Environmental Science

Fawu Wang
Masakatsu Miyajima
Tonglu Li
Wei Shan
Teuku Faisal Fathani *Editors*

Progress of Geo-Disaster Mitigation Technology in Asia

Springer

Environmental Science and Engineering

Environmental Science

Series Editors

Rod Allan
Ulrich Förstner
Wim Salomons

For further volumes:
http://www.springer.com/series/3234

Fawu Wang · Masakatsu Miyajima
Tonglu Li · Wei Shan · Teuku Faisal Fathani
Editors

Progress of Geo-Disaster Mitigation Technology in Asia

Springer

Editors
Fawu Wang
Department of Geoscience
Shimane University
Matsue
Japan

Masakatsu Miyajima
Kanazawa University
Kanazawa
Japan

Tonglu Li
Department of Geological Engineering
Chang'an University
Xi'an
People's Republic of China

Wei Shan
Institute of Engineering Geology Explora
Northeast Forestry University
Harbin
People's Republic of China

Teuku Faisal Fathani
Department of Civil and Environmental Engineering
Universitas Gadjah Mada
Yogyakarta
Indonesia

ISSN 1431-6250
ISBN 978-3-642-29106-7 ISBN 978-3-642-29107-4 (eBook)
DOI 10.1007/978-3-642-29107-4
Springer Heidelberg New York Dordrecht London

Library of Congress Control Number: 2012944387

Printed on acid-free paper

Springer is part of Springer Science+Business Media (www.springer.com)

Preface

Japan Sea Region Research Institute was established 9 years ago in 2003 with the sole objective of bringing geoscience and geotechnically based researchers together. The founding members shared the idea of having an international research meeting which would accommodate other research areas that are related to the field of geotechnical engineering. Target participants and contributors were Japanese and foreign researchers around Japan Sea. The first international symposium was held in December 2003, in Kanazawa University Japan, under the title: "First International Symposium on Mitigation of Geo-hazards in Areas around the Japan Sea". Though the opening ceremony was missed by some foreign researchers due to heavy snowfall in and around the venue city, the symposium recorded huge success as everyone, through lively discussions, shared views and opinions on current scientific problems, and the participants unanimously decided to make the symposium an annual event.

With success established, there was need to expand the research area to accommodate studies in geohazard mitigation and prevention like seismology and earthquake, building and pipeline engineering, and the target area was expanded beyond the countries around Japan Sea to larger areas including Indonesia, Iran, and so on.

Scientific research has no end. The more we probe and solve environmental problems, the more we discover more unsolved problems. This is why we must not relent in providing answers and solutions to pertinent geoenvironmental challenges. In commemoration of the tenth annual symposium, we are very happy to present to you the results of our latest research works. On behalf of the first chairpersons of the Steering and Organizing Committee in 2003, I would like to thank everybody so far present at the symposium and those who have in one way or the other contributed to the success of this event.

序 文

今から９年ほど前、筆者らの何名かが所属していた金沢大学に日本海域研究所があった。地盤の研究をしている仲間で、研究所の名前に相応しい国際的な研究集会を始めようと図り、知っている外国の研究者に声をかけ、１２月に金沢で、第一回日本海域地盤破壊軽減国際シンポジウムを開催した。あいにく豪雪が金沢を来襲し、外国の研究者の中には開会式に間に合わなかった人もいた。活発な討議を通じて、多くの課題のあることをみんなが認識し、来年以降も開催することを決めた。その後、研究のテーマは地盤のみでなく、地域も日本海域にとどまることはなかった。今回、第１０回を記念して、われわれの最近の到達点を紹介できることを非常にうれしく思う。しかし研究に終わりはない。研究を進めると、また新しい課題が出てくる。われわれはこれからも研究を続ける。

これまでにこのシンポジウムで発表し、サポートしてくださったみなさまに心からの感謝を捧げる。

第一回目の実行委員会と組織委員会を代表して
金沢大学名誉教授　北浦　勝

Japan, May 22, 2012

Masaru Kitaura
Chairperson of the First Steering and
Organizing Committees
Professor emeritus of Kanazawa University

Foreword

This book presents up-to-date research results of geo-disaster mitigation technologies in Asia. Most of the contributions in this paper are from the core members and participants of the International Symposium on Mitigation of Geo-disasters in Asia (MGDA) in the 10 years, with some keynote papers from notable researchers who are very active in this region.

As rightly introduced by Prof. Emeritus M. Kitaura, the first International Symposium on Mitigation of Geo-disasters in Areas around Japan Sea was held in 2003 at Kanazawa University, Japan. This pioneer event drew the attention of researchers and engineers from China, Korea, and Japan who were then interested or working on disaster mitigation around the Japan Sea region. The second, third, and fourth symposiums were held in the Kanazawa University while the fifth and sixth symposiums were held in 2007 and 2008 in Xi'an and Kunming cities both in China. In 2009, the name of the symposium was changed to "The International Symposium on Mitigation of Geo-disasters in Asia" to include more countries. The seventh event was held in Harbin city of China. Then, the eighth and ninth symposiums were held in Vladivostok city of Russia in 2010, and Yogyakarta city of Indonesia in 2011, respectively.

The Department of Geoscience in Shimane University, Japan got the chance to organize the tenth event of the symposium in 2012. To celebrate the tenth anniversary of the symposium, we made a proposal to publish a book with Springer to show the progress we have made in the past 10 years in the geo-disaster mitigation technologies in Asia. The idea was approved by the current steering committee which is made up of Prof. M. Miyajima (Kanazawa University, Japan), Prof. T. L. Li (Chang'an University, China), Prof. W. Shan (Northeast Forestry University, China) and Associate Professor T. F. Fathani (Gadjah Mada University, Indonesia), and an editorial committee for the book was formed.

For the past 10 years, the continent of Asia has experienced a lot of geohazards like earthquakes, typhoons, and volcanic eruptions which have caused serious disasters. The reader is therefore enjoined to see some contributions made by the core members as we try to improve our efforts in providing timely results and suggestions on hazard assessment and disaster prevention.

It is very important to acknowledge that all scientific approaches and methods employed in the study of hazard analysis and risk management are relevant in disaster mitigation. In Asia, many research institutes and investigation centers have presented diverse research methods and results based on their specific areas of interest. Our core members also made important contributions to geo-disaster mitigation. For example, the Kanazawa University research group concentrated on earthquakes and seismology and made major progress in lifeline earthquake engineering; the Chang'an University research group has made enormous contributions on disasters associated with loess deposits; the Northeast Forestry University research group are working on landslide disasters in cold regions; the Gadjah Mada University research group concentrated on tsunami caused by earthquakes, lahar by volcano eruption and landslide warning; the Jilin University research group conducted many research works on geotechnical and civil engineering problems, while the Shimane University group are working on submarine to localized landslides through experimental approach to numerical analysis, and the complex earthquake/rainfall-triggered landslides. It is our belief that the results and conclusions presented in these research areas will be of great benefit to the readers of the book.

We also admitted the limitation of our existing network formed in the annual events, and are trying to enlarge the network so that we can include the key researchers of geo-disaster in the Asian region. So, in addition to the core members in our network, we invited Dr. A. Strom from Russia, Dr. Z. Q. Yue from University of Hong Kong, Dr. K. F. Liu from National Taiwan University, Dr. R. K. Dahal from Tribhvuan University, and so on to contribute some very comprehensive research results for the book.

We appreciate the financial support from Kanazawa University, Chang'an University, and Northeast Forestry University which made it possible for us to publish this book. The Tenth International Symposium on Mitigation of Geo-disasters in Asia is also supported by a joint research fund courtesy of Disaster Prevention Research Institute, Kyoto University, and a germinating research project for disaster prevention of Shimane University. The San'in Disaster Prevention Forum based on Shimane University fully supported this important event. Mr. Austin Chukwueloka Okeke, Mr. Fikri Faris, and Mr. Hufeng Yang of Graduate School of Shimane University assisted the editing committee in editing this book.

To celebrate the tenth anniversary of this annual event, we are organizing a field trip from Sendai city to investigate the 2011 disaster triggered by tsunami in the coastal area of eastern Japan, and also, analyze the achievements of Japan in earthquake-proof building designs. We enjoin everybody to join us to Mt. Bandai to see a deep-seated landslide triggered by volcanic eruption, and then move to Hotaka town to see debris flow countermeasures and monitoring systems. The field excursion will end with a trip to Shimane Prefecture to see the peaceful countryside and a world heritage center: the Iwami Silver Mountain, where participants will directly feel the local people's keenness to harmoniously live with natural hazards.

Finally, we would like to dedicate this book to the founding members of the symposium: Prof. M. Kitaura and Prof. M. Miyajima for their academic foresight, leadership ability, and courage in mitigating disasters in Asia. We also appreciate the continued participation of our core members who have contributed so much to the success of this professional body. We believe that in the nearest future, our network will be much stronger, so that our scientific findings will not only benefit Asia, but will also be usefully applied in global disaster mitigation.

May 28, 2012

Fawu Wang
On behalf of the Chairpersons of the Tenth Steering
and Organizing Committees

Contents

Part I
Comprehensive Study

Damage by the 2011 Great East Japan Earthquake and Tsunami

Masakatsu Miyajima and Akira Murata

Abstract This paper deals with an outline of damage induced by the 2011 great east Japan earthquake and tsunami. An earthquake with a magnitude of 9.0 occurred in the north-western Pacific Ocean at a relatively shallow depth of 32 km on March 11, 2011 at 14:46 on local time. The earthquake generated a tsunami of unprecedented height and special extent along the coast of the main island of Japan. The earthquake and tsunami caused about 20,000 deaths and missing and injured about 6,000 people. This paper reports an outline of the earthquake, tsunami and damage, then, focuses on the damage to water supply pipelines.

Keywords The 2011 great east Japan earthquake · Earthquake damage · Tsunami · Water supply pipeline

1 Introduction

An earthquake with a magnitude of 9.0 occurred off the coast of northeast Japan on March 11, 2011 at 14:46 on local time. Its epicenter was located at 38.1N, 142.9E. A Japan Meteorological Agency (JMA) seismic intensity of 7, that is a maximum level, was recorded at K-NET Tsukidate observation station in Kurihara City, Miyagi Prefecture. The earthquake generated a tsunami of unprecedented height and special extent along the coast of the main island of Japan. The earthquake and tsunami caused 15,821 deaths and 3,931 missing, and wounded 5,940 people

M. Miyajima (✉) · A. Murata
School of Environmental Design, Kanazawa University,
Kakuma-machi, Kanazawa 920-1192, Japan
e-mail: miyajima@se.kanazawa-u.ac.jp

F. Wang et al. (eds.), *Progress of Geo-Disaster Mitigation Technology in Asia*,
Environmental Science and Engineering, DOI: 10.1007/978-3-642-29107-4_1,

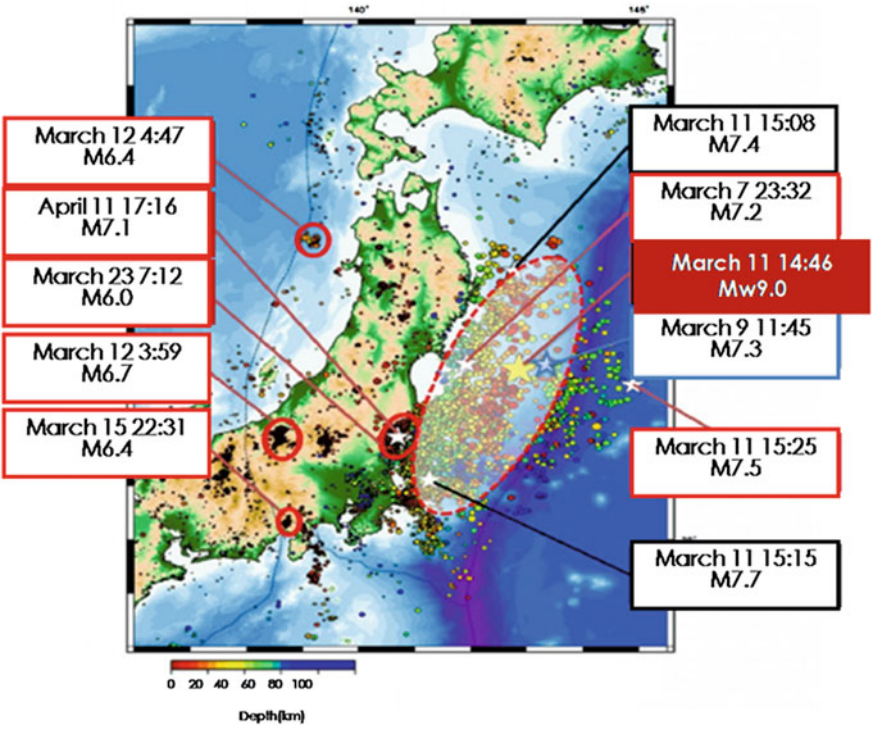

Fig. 1 Major earthquakes before and after March 11 (http://outreach.eri.u-tokyo.ac.jp/eqvolc/201103_tohoku/eng/aftershocksofpast/)

(As of October 4, 2011, Japanese Government). The major cause of death was the tsunami. The completely collapsed houses numbered 118,480 (As of October 4, 2011, Japanese Government). This paper gives an outline of the earthquake, tsunami and damage, then, focuses on the damage to water supply pipelines.

2 Outline of Earthquake and Ground Motion

The earthquake occurred on March 11, 2011 at 14:46 JST in the north-western Pacific Ocean at a relatively shallow depth of 32 km, with its epicenter approximately 72 km east of the Oshika Peninsula of Tohoku, Japan. The earthquake was initially reported as 7.9 M_W by the United States Geological Survey (USGS) before it was quickly upgraded to 8.9 M_W, then finally to 9.0 M_W. Sendai was the nearest major city to the earthquake, 130 km from the epicenter. This earthquake is the fourth largest in the world since 1900 and largest in Japan since recording started 130 years ago. Major earthquakes before and after March 11 plot in Fig. 1 (USGS 2011). This figure shows that the main earthquake was preceded by a

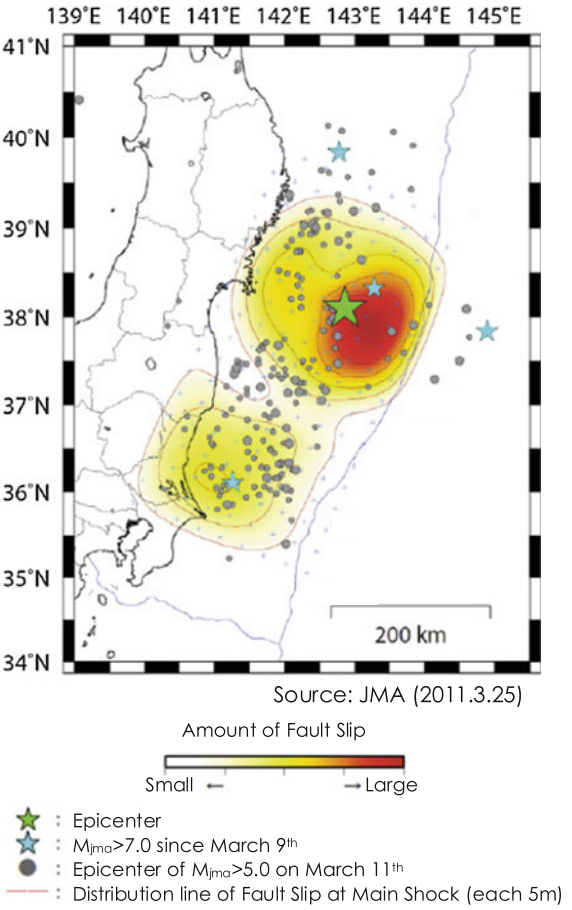

Fig. 2 Distribution contour of fault slip at main shock (Japan Meteorological Agency: http://www.seisvol.kishou.go.jp/eq/2011_03_11_tohoku/index.html#0311data)

number of large foreshocks, with hundreds of aftershocks reported. The first major foreshock was a 7.2 M_W event on March 9, approximately 40 km from the epicenter of the main earthquake, with another three on the same day in excess of 6.0 M_W. Following the main earthquake on March 11, a 7.0 M_W aftershock was reported at 15:06 JST, succeeded by a 7.4 M_W at 15:15 JST and a 7.2 M_W at 15:26 JST. Figure 2 shows distribution contour of fault slip at the main earthquake (JMA 2011). This figure suggests that the size of fault is approximately 450 km length and 200 km width. The fault slip is about 30 m as maximum. And two large slip parts, that is, two asperities exist on this fault, so strong motion records can be categorized several types as the observation site. Figure 3 shows distribution maps of peak ground acceleration (PGA) and peak ground velocity (PGV) by the main eartqhuake (NIED 2011). These figures indicate PGA was over 2,000 cm/s^2 at Miyagi, Iwate and Ibaraki Prefectures and PGV was over 166 cm/s at Miyagi Prefecture. Figure 4 shows distribution of JMA seismic intensity (JMA 2011). This figure shows large seismic intensity over 6- exists at many sites not only at

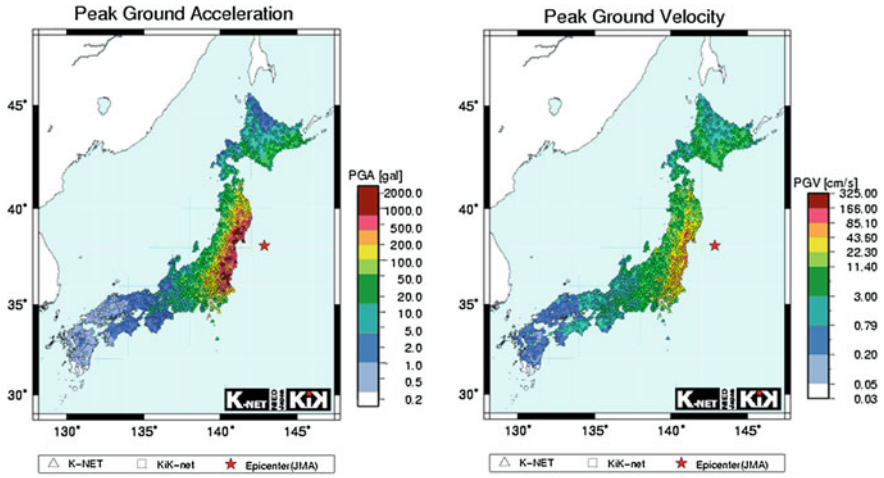

Fig. 3 Distribution of peak ground acceleration and peak ground velocity (National Research Institute for Earth Science and Disaster Prevention: http://www.kyoshin.bosai.go.jp/kyoshin/topics/html20110311144626/main_20110311144626.html)

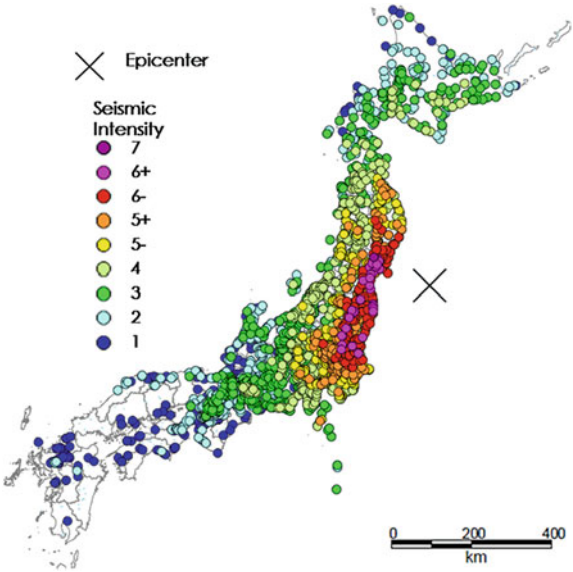

Fig. 4 Distribution of seismic intensity (Japan Meteorological Agency: http://www.seisvol.kishou.go.jp/eq/2011_03_11_tohoku/index.html#0311data)

Tohoku region but also at Kanto region. Figure 5 shows strong motion records of the main earthquake at K-NET Tsukidate (MYG004), K-NET Shiogama (MYG012), K-NET Hitachi (IBR003) and K-NET Sendai (MYG013), respectively (NIED 2011). These figures show the duration time of strong motion were over

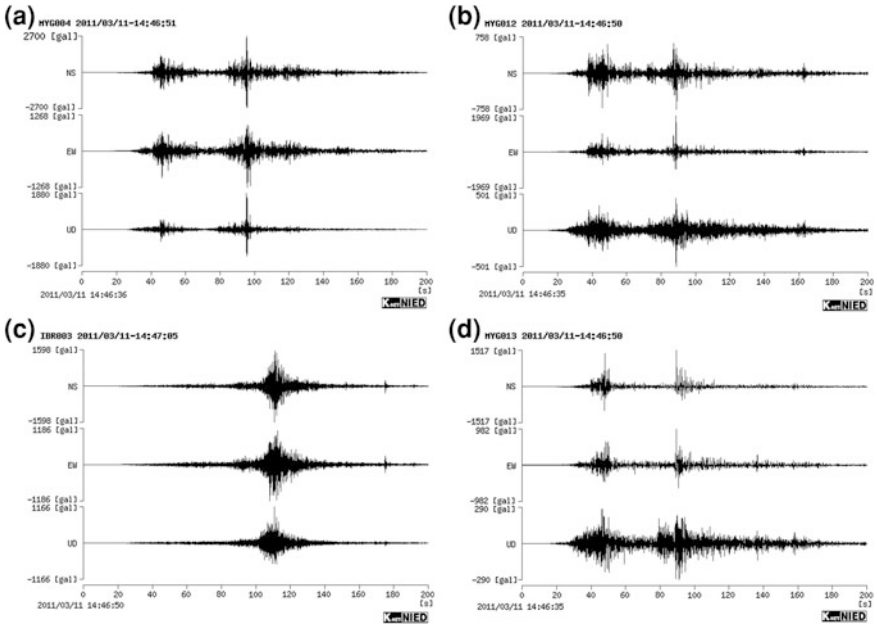

Fig. 5 Strong motion records of main shock (National Research Institute for Earth Science and Disaster Prevention: http://www.kyoshin.bosai.go.jp/kyoshin/topics/html20110311144626/main_20110311144626.html)

three minutes. Three sites at Miyagi (MYG) show two peaks of strong motion and Hitachi site shows one peak of strong motion. This phenomena seems to be related to a location of asperites of the seisemic fault.

3 Outline of Tsunami

The earthquake occurred at 14:46 JST around 67 km from the nearest point on Japan's coastline, and initial estimates indicated the tsunami would have taken 10–30 min to reach the areas first affected, and then areas farther north and south based on the geography of the coastline.

Fig. 6 shows inundation and run-up heights in Hokkaido, Tohoku and Kanto regions surveyed by Tohoku Earthquake Tsunami Joint Survey Group (JSCE Tohoku Earthquake Tsunami Joint Survey Group 2011). According to their survey, the maximum run-up height was 39.7 m at Miyako City. The maximum inundation height at the Sendai Plain was 19.5 m and the mean inundation height near the shoreline was about 10 m.

It has been estimated from areal and satellite photography that almost 535 km^2 of land were inundated in according to the Ministry of Land, Infrastructure,

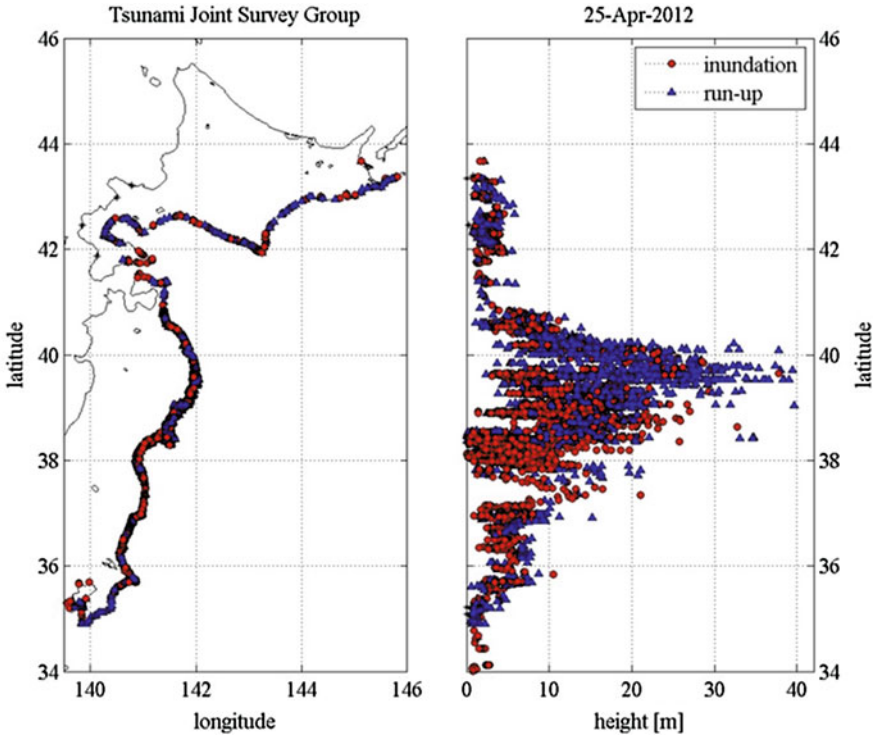

Fig. 6 Distribution map of inundation and run-up heights (The 2011 Tohoku Earthquake Tsunami Joint Survey Group: http://www.coastal.jp/tsunami2011/)

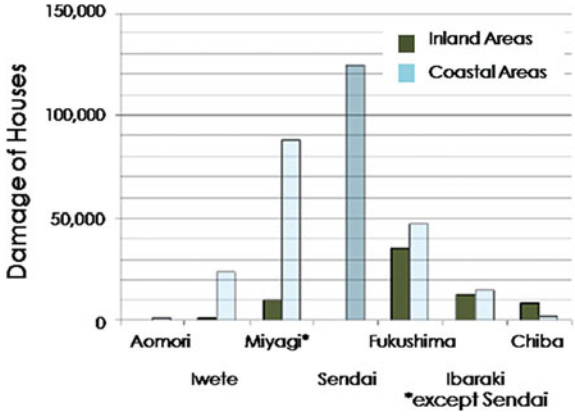

Fig. 7 Damage of houses comparing between inland areas and coastal areas (Building Research Institute: http://www.kenken.go.jp/japanese/contents/topics/20110311/0311report.html)

Transport and Tourism. The tremendous tsunami caused a catastrophic destruction in Tohoku region. At least 101 designated tsunami evacuation sites were hit by the wave.

Photo 1 Damage to house by soil liquefaction

4 Outline of Damage by the Earthquake and Tsunami

The completely collapsed houses numbered 118,480 (As of October 4, 2011, Japanese Government). Figure 7 shows number of damage to houses in each prefecture of the affected areas in comparison of damage in inland and coastal areas (BRI 2011) This figure indicates that most of the damage were caused by tsunami. The soil liquefaction occurred from Tohoku to Kanto regions, and severe damages such as an inclination of houses (Photo 1) and suspension of water supply occurred. Especially, reclaimed land in Urayasu city of Chiba prefecture was severely liquefied and many houses were damaged.

The number of damage to road such as national road and prefectural road was 3918 as of April 25, 2011. The collapse of road caused isolated persons, at least 16,000 in Iwate, Miyagi and Fukushima prefectures. Many bridges was washed away by the tsunami (Photo 2). A lot of damage to highway (NEXCO East) was also occurred and the highway was closed in wide areas.

A railway of East Japan Railway area suffered damage at 28 stations including Sendai station, and about 1,100 electric poles were also damaged. The railroad track flowed out about 60 km in 7 railroad sections such as Kesennuma line by tsunami.

A suspension of water supply was occurred at about 2,300,000 houses in the wide area from Tohoku to Kanto regions just after the earthquake. The restoration

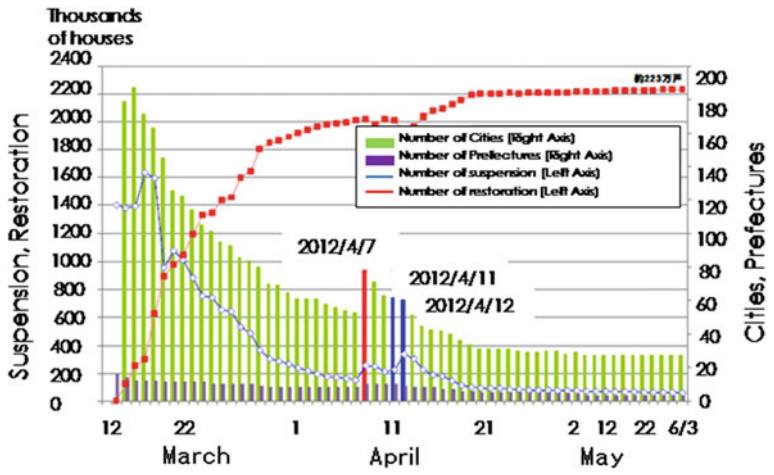

Fig. 8 The restoration situation of water supply (Japan Water Works Association: http://www.jwwa.or.jp/houkokusyo/pdf/higashinihon_daishinsai/higashinihon_2.pdf)

of water supply is shown in Fig. 8 (JWWA 2011). About 90 % of water outrage was recovered after one month from the event except flooded areas by the tsunami. Newly damage, however, occurred by the strong aftershocks happed in the middle of April 16, 2011. Sewarage plants in the area along the shore in Iwate, Miyagi, and Fukushima prefectures suffered damage and shut down by the tsunami. The sewarage pipelines of 550 km were damaged in 64,730 km of 129 cities. The numbers of gas stoppage of deliveries were totally 401,976 houses in 16 entrepreneurs. The restoration was done by May 3, 2011.

5 Damage to Water Supply Facilities

5.1 Causes of Damage to Facilities

The damage caused by the earthquake and tsunami seems to be classified into five categories. Firstly the causes of damage are divided by earthquake and tsunami. Causes of damage by earthquake are classified into ground shaking itself and ground failure such as liquefaction, slope failure and etc. Photo 5 shows damage to expansion joint of steel pipe with 2400 mm diameter. This damage seems to be caused by ground shaking and/or ground deformation. Photo 6 shows an uplift of underground water tank induced by liquefaction.

Causes of damage by tsunami are classified into three categories; inundation, washing away and scouring of surface ground. Some intake facilities were inundated by tsunami and became malfunction for long time because of high density of calcium chloride in water. Photo 3 shows damage to a water pipe bridge by

Photo 2 Damage to bridge by tsunami

Photo 3 Damage to steel pipe with 2400 mm diameter (http://www.pref.miyagi.jp/kigyo/)

tsunami. The water pipe bridge was completely washed away. Photo 4 shows damage to a buried pipeline. The pipeline appeared above ground after tsunami because of scouring caused by tsunami. The mechanism of damage to pipeline, that is, how much force acts on a pipeline is not sure. The mechanism of this kind of damage must be clarified in the future (Photos 5, 6).

6 Damage to Pipeline in Sendai City

Since the damage to pipeline of Sendai City was obtained except the flooded area, damage rate of pipelines in Sendai City is discussed here. The water supply system of Sendai City has approximately 472,775 m of transmission and distribution main pipelines. About 74 % of the total piping length is made up of ductile cast iron pipe (DIP), 24 % steel pipe (SP).

The number of damage to transmission and distribution main pipelines was 10 and that of damage to air valve and hydrant was 43. The damage rate of pipelines, defined as the locations of damage divided by piping length, was 0.02 (locations/km).

The total number of damage to transmission main, distribution main and branch pipelines was 264 except the flooded areas, and the piping length is 3,761 km. The damage rate of transmission main, distribution main and branch pipelines was, therefore, 0.07 (locations/km) The damage rate in relation to pipe type and pipe diameter is shown in Figs. 9 and 10, respectively. Figure 9 indicates that the damage rate of polyvinyl chloride pipe (VP) is high. Figure 10 reveals that the smaller the pipe diameter is, the higher the damage rate.

Figure 11 illustrates a comparison of damage rate of Sendai City with those of other cities suffered damage to pipeline in the past earthquakes in Japan. Kobe, Ashiya and Nishinomiya Cities suffered damage to water supply pipeline in the 1995 Hyogo-ken Nambu Earthquake, Nagaoka City in the 2004 Niigata-ken Chuetsu Earthquake, Monzen Town in the 2007 Noto-hanto Earthquake and Kashiwazaki City in the 2007 Niigata-ken Chuetsu-oki Earthquake, respectively. This figure revels that the damage rate of Sendai City was very low in comparison with another cities. Magnitude of earthquake and seismic intensity in each city were different. PGA of K-NET Sendai observation station was, however, not small; 1,808 (cm/s/s). This value is higher than most of cities listed in Fig. 11. One of reasons of low damage rate in Sendai City seems to be high earthquake-proofing rate. The earthquake-proofing rate is defined as the piping length of ductile cast iron pipe with earthquake resistant joint and welded steel pipe divided by the total piping length. The earthquake-proofing rate of Sendai City is 51.2 %.

Figure 12 illustrates the relation between the earthquake-proofing rate and damage rate of each waterworks bureau suffered damage in the 2011 great east Japan earthquake. The damage rate shown in this figure is calculated by using the damage to transmission and distribution main pipeline, that is, distribution branch pipeline is not included. This figure shows JMA seismic intensity scale in each

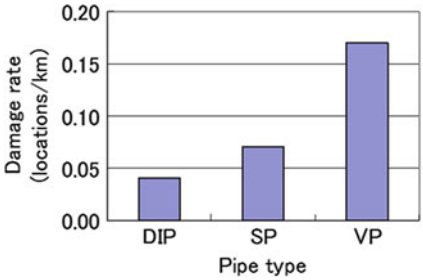

Fig. 9 Damage rate related to pipe type in Sendai City

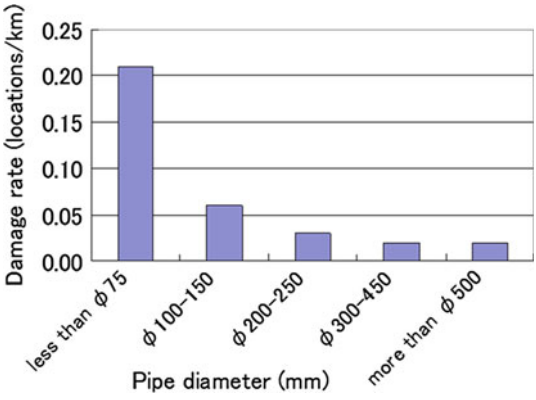

Fig. 10 Damage rate related to pipe diameter in Sendai City

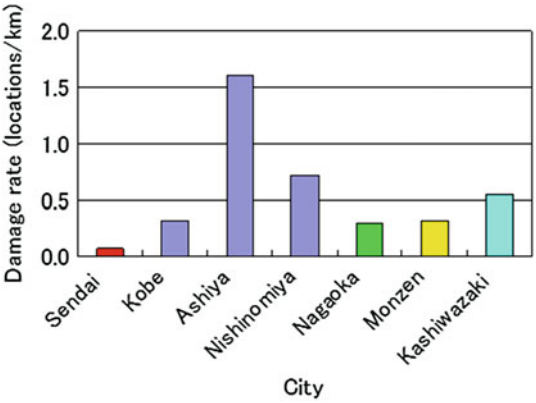

Fig. 11 Comparison of damage rate in the recent damaging earthquake in Japan

area. This figure indicates that the higher the earthquake-proofing rate, the lower the damage rate is. There was no damage to the ductile cast iron pipe with earthquake resistant joint. Effect of earthquake-proofing pipe was, therefore, verified by the earthquake.

Photo 4 Uplift of underground water tank

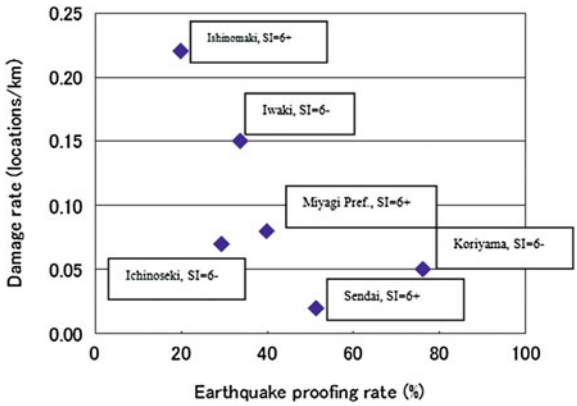

Fig. 12 Relation between earthquake proofing rate and damage rate

7 Conclusions

An outline of the damage to water supply facilities from the 2011 great eat Japan earthquake and tsunami was presented and the damage rate of pipeline was discussed. The following conclusions may be drawn based on the present study.

Photo 5 Damage to water pipe bridge

Photo 6 Damage to pipe by scouring of tsunami

(1) The entire damage to water supply pipelines is not revealed, especially flooded areas by tsunami. We must collect all damage data and analyze it to learn the lessons from this disaster.
(2) Effect of earthquake-proofing for pipeline was verified. We must accelerate the earthquake proofing, especially for aged facilities.
(3) Force of tsunami acted on a buried pipe is not clear. The effect of tsunami must be studied soon.

Acknowledgments The present paper is based on the collected from an investigation by reconnaissance team of the Ministry of Health, Labour and Welfare, Japan. Many individual and organizations generously helped with this investigation. This study was supported in part by the Grant-in-Aid for Scientific Research from the Ministry of Education, Culture, Sports, Science and Technology, Japan (No. 20310108).

References

Building research institute (BRI) http://www.kenken.go.jp/japanese/contents/topics/20110311/0311report.html (Written in Japanese)

Japan meteorological agency (JMA) About the 2011 off the pacific coast of Tohoku earthquake (28th Report), 25 March 2011 (Written in Japanese)

Japan water works association (JWWA) http://www.jwwa.or.jp/houkokusyo/pdf/higashinihon_daishinsai/higashinihon_2.pdf (Written in Japanese)

National research institute for earth science and disaster prevention (NIED) Strong motion observed by 2011 Tohoku district-off the pacific ocean earthquake, emergency meeting of headquarters for earthquake research promotion, 13 March 2011. (Written in Japanese)

The 2011 Tohoku earthquake tsunami joint survey group, JSCE field survey tsunami results http://www.coastal.jp/tsunami2011/, 11 March 2012 access (Written in Japanese)

2011 Tohoku earthquake, Earthquake Research Institute, The University of Tokyo (http://outreach.eri.u-tokyo.ac.jp/eqvolc/201103_tohoku/eng/aftershocksofpast/)

Geological Prerequisites for Landslide Dams' Disaster Assessment and Mitigation in Central Asia

Alexander Strom

Abstract Landslide dams' hazard assessment aimed to disaster mitigation requires knowledge of the origin of hazardous phenomena, its triggering factors, magnitude, spatial distribution, recurrence, as well as characteristics of their possible secondary and tertiary effects. These hazards identification and quantification can be derived from detail geological and geomorphic study of the present and past river-damming landslides and related phenomena such as evidence of outburst floods. Several historical catastrophes that occurred in the Central Asian region due to formation and/or breach of landslide dams are described briefly and case studies demonstrating various manifestations of landslide damming in the Central Asia region are discussed with special emphasis on those topics, which still remain unsolved or controversial. These are: (1) the landslide versus moraine interpretation of the Pamirs' natural blockages origin, (2) the relationship between formation of large-scale bedrock landslides and seismicity, which is critically important for both landslide and seismic hazard assessment, (3) morphological and structural peculiarities of large-scale bedrock landslides—the main type of river-blocking slope failures that predetermine magnitude of river damming, its longevity and character and rate of dams' breach. The importance of the detailed study of the past breached dams, as the analogues of the existing and future hazardous blockages is discussed in the conclusive remarks.

Keywords Landslide dam · Inundation · Dam breach · Outburst flood · Landslide hazard assessment

A. Strom (✉)
Geodynamic Research Center—Branch of JSC, Hydroproject Institute,
Volokolamsk Highway, 2, Moscow, Russia 125993
e-mail: a.strom@g23.relcom.rua_strom2002@yahoo.co.uk

F. Wang et al. (eds.), *Progress of Geo-Disaster Mitigation Technology in Asia*,
Environmental Science and Engineering, DOI: 10.1007/978-3-642-29107-4_2,

1 Introduction

A "disaster" is defined as "a sudden calamitous event bringing great damage, loss, or destruction" (Merriam-Webster's 11 Collegiate Dictionary). Those, classified as "Geo-disaster", are of natural origin, mainly, and their mitigation must be considered as an important task of the mankind and, at the first place, of the geo-hazard scientific community. The disaster mitigation requires correct identification of type, location, magnitude, timing (recurrence), primary and secondary effects of the natural phenomena that can be considered as being potentially disastrous. Based on these data, measures aimed to prevent or predict such phenomena can be elaborated. The prevention is preferable, however, if it is impossible from technical or economical reasons, timely prediction via site monitoring and early warning must be arranged.

Large-scale landslides and, especially, those that cause river damming are among the most disastrous natural phenomena in mountainous regions all over the world (Schuster and Costa 1986; Costa and Schuster 1988, 1991; Evans et al. 2011). The Central Asia region that includes the Pamirs and the Tien Shan Mountains (Fig. 1) is not the exclusion (Delaney and Evans 2011; Strom 2010b).

Various aspects of identification and quantification of hazards related to landslide dams' formation and evolution are described and discussed hereafter with special emphasis on those topics, which still remain unsolved or controversial. After brief description of some historical catastrophes that occurred in the Central Asian region due to formation and/or breach of landslide dams I will dwell on the controversial interpretation of the Pamirs' natural blockages origin (landslide vs. moraine), which determines at a great extent possibility of future disasters. Another problem is the relationship between formation of large-scale bedrock landslides, those that cause rivers' damming in particular, and seismicity, which is critically important for both landslide and seismic hazard assessment.

High emphasis is placed on the morphological and structural peculiarities of large-scale bedrock landslides (rockslides and rock avalanches)—the main type of river-blocking slope failures (Hermanns et al. 2011; Fan et al. 2012). These characteristics predetermine magnitude of river damming, its longevity and character and rate of dams' breach. Besides, analysis of rockslides morphology and internal structure allows assumptions on their motion mechanism(s) (Strom 2006, 2010a). The importance of the detailed study of the past breached dams, as the analogues of the existing and future hazardous blockages will be discussed in the conclusive remarks.

2 Brief Overview of the Historical Disasters Associated with Landslide Dams in the Central Asia Region

Several catastrophes associated with large-scale slope failures and breach of landslide-dammed lakes occurred in the Pamirs and the Tien Shan in the twentieth Century exemplifying basic primary and secondary effects of these hazardous natural phenomena.

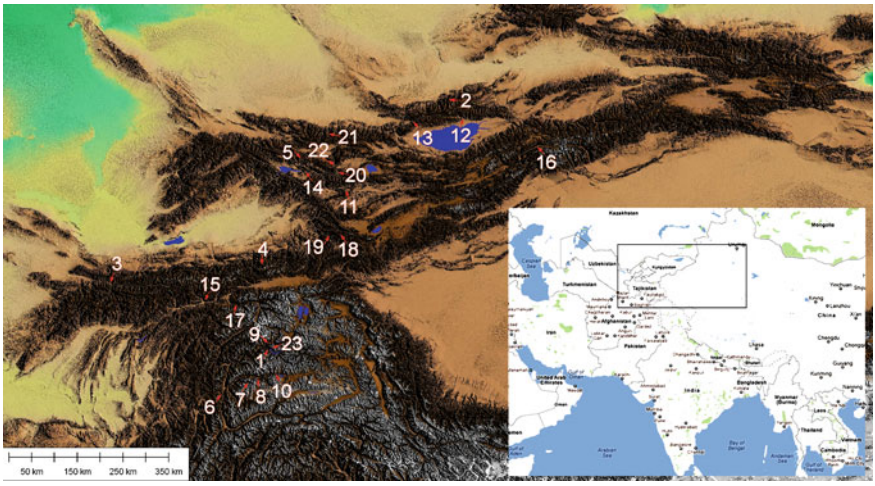

Fig. 1 General map of Central Asia with location of all features mentioned in this chapter (*Red arrows*). The study region is marked on the inset. *1* the 1911 Usoi landslide and Sarez Lake; *2* the 1963 Issyk outburst flood; *3* the 1964 Aini landslide and its prehistoric predecessor; *4* the 1966 Yashinkul outburst flood; *5* the 1992 Belaldy landslide and 1993 debris flow; *6* the Shiva dam and Lake; *7* the Rivakkul dam and Lake; *8* the Imom rockslide; *9* the Kudara-Pasor landslide; *10* the Yashilkul dam and Lake; *11* the Beshkiol landslide; *12* the 1911 Ananievo landslide; *13* the 1911 Kaindy landslide; *14* the Djuzumdybulak rock avalanches; *15* the 1949 Khait rock avalanche; *16* the Upper-Inylchek landslide cluster; *17* the Muksu landslide cluster; *18* the Kulun landslide-dammed lake; *19* the Kulun mouth silted landslide-dammed lake; *20* the Lower Aral landslide; *21* the Aksu landslide; *22* the Kokomeren landslide; *23* the Murgab assumed landslide

2.1 Usoi Dam and Sarez Lake

The most known case study is the formation of the Usoi landslide and the Sarez Lake in Central Pamirs. The world largest historical non-volcanic landslide originated on February 18, 1911, when large earthquake with $M_w = 7.7 \pm 0.2$, according to the recent analysis of the macroseismic and instrumental data performed by Ambraseys and Bilham (2012), caused catastrophic wedge-like failure of about 2.2 km^3 ($\sim$6 billion tons) of rocks (Fig. 2) and formation of the 567-m high Usoi natural dam named after the small Usoi village that was buried with 54 inhabitants. Only three men who spent that night in the Sarez village survived (Luknitskiy 1955). This should be considered as a primary disastrous effect of the landslide.

The 5-km long (across the valley) and 3.75-km wide dam (Fig. 3) have blocked the Murgab River valley at 38°16.5′ N, 72°36′ E (1 on Fig. 1). Despite the remoteness and inaccessibility of the site, Russian researchers performed first studies of this unique feature soon after the event (Bukinich 1913; Shpilko 1915; Preobrajensky 1920). Its regular studies started in sixtieth of the twentieth Century (Scheko and Lekhatinov 1970; Gaziev 1984; Agakhanjanz 1989).

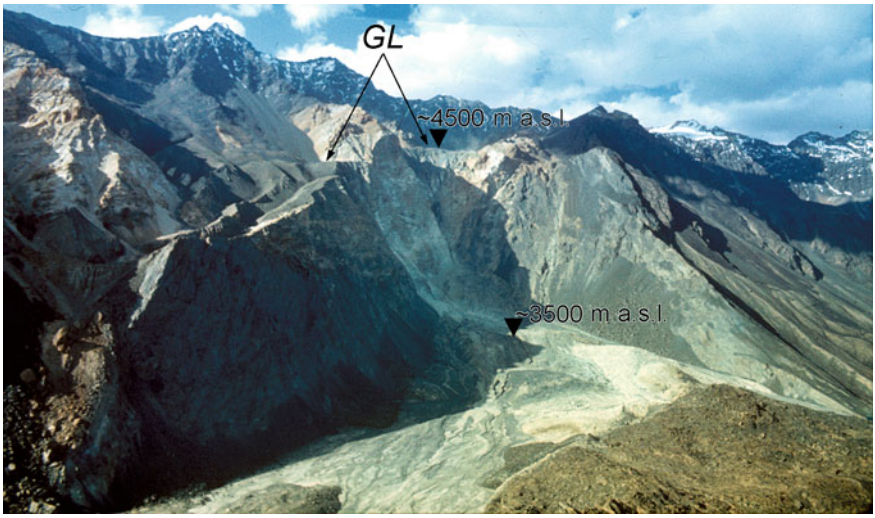

Fig. 2 The Usoi rockslide headscarp. *GL*—glacial valleys remaining above the headscarp

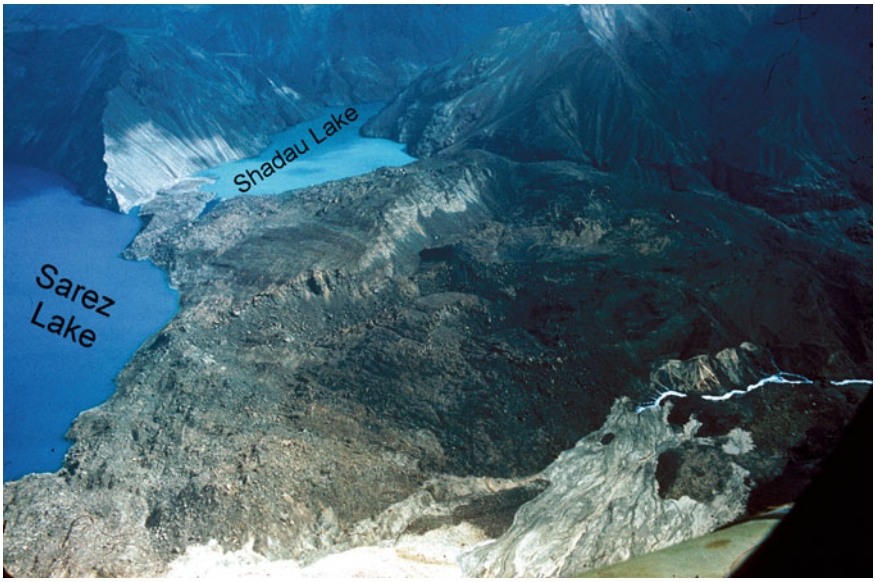

Fig. 3 The Usoi natural dam. Helicopter view from north. Giant block retaining original structure is visible on top of the dam in front of the Shadau Lake. Seeping water forms springs at the left bank of the erosion canyon. Whitish flat area above the canyon—deposits of debris flows that came in this direction before their diversion towards the Lake in 1947. Steep scarp that crosses the dam body indicate its transverse spreading likely due to impact over the steep opposite slope of the Murgab River valley

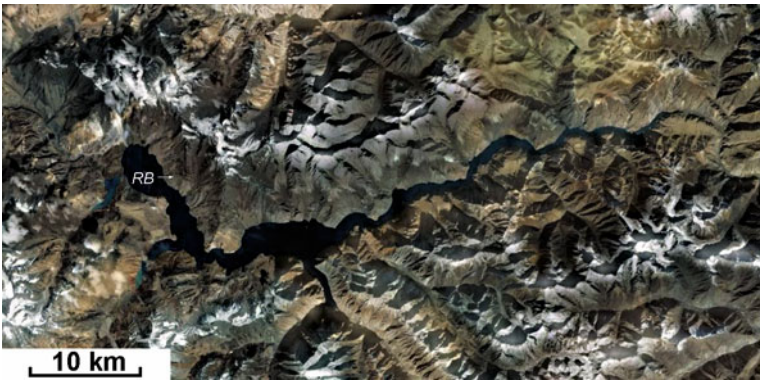

Fig. 4 The Sarez Lake. Google Earth space image. *RB*—location of the assumed Right-Bank landslide

The 500-m deep and 60-km long lake containing almost 17 km^3 of water (Fig. 4) was named after the Sarez village that was submerged along with several other minor settlements. Such inundation represents secondary disastrous effect of landslide river damming, which, though being not sudden and, thus, *sensu stricto*, not "catastrophic", produced complete damage not only of the local people property, but of the entire inhabited environment, forcing people to resettle to other kishlaks (villages) in the Bartang River valley and in the Gunt River valley, passing south from the Rushan Range. In high mountains economic and social losses due to such secondary effects could be much higher than that of the landslide itself. All these however, are negligible in comparison with what could happen if the Usoi dam will be breached and water stored in the lake released.

Fortunately, the enormous size of the blockage, especially of its upper permeable part (seepage takes place through the uppermost ~140 m of the dam only with most permeable zones within the uppermost 50–70 m, while the dams body bellow is practically impermeable) provides nearly balanced values of the mean inflow and outflow. However, according to regular observations, lake level increases gradually (up to 20 cm/year) and is now 3261 m a.s.l., only 38 m below the lowermost part of the blockage (at maximal water level) (Ischuk 2011). Significant filtration through the dam started around 1925. Present day estimates of mean discharge passing through the dam range from 45.8 to 47 m^3/s (State Water Inventory 1964–1981; Hanisch and Söder 2000). During the flood period water rises for about 5 m above the mean annual level, but, simultaneously, filtration increases up to 84 m^3/s (Hanisch and Söder 2000). Present state of the dam is considered as safe. There are, however, several factors that do not ensure the stability of the Usoi dam "forever". Besides the above-mentioned gradual rise of water level, the seeping water forms powerful springs ~140 m below the lake level in the canyon cutting the downstream slope of the blockage (see Fig. 3). Its head erodes both the dam body and sediments left by debris flows fed by the streams from glacier valleys remaining above the headscarp. After 1947, when a

rockfall from the headscarp wall blocked the channel and diverted these debris flows towards the lake (Paramonov 1969), intensive growth of the canyon stopped but, anyhow, filtering water erodes it. Recently several new powerful springs were identified in the canyon (Anatoly Ischuk, personal communication).

Downstream slope of the blockage is crossed by steep bow-shape scarps (see Fig. 3) indicating some transverse (down-valley) spreading of the landslide body (Paramonov 1969). Largest of them could originate when rapidly moving rockslide collided with the opposite bank of the Murgab River valley (Strom 2010a). It can be assumed that such secondary deformations decrease the overall stability of the dam, producing potential sliding surfaces. Along with the gradual development of the canyon it is difficult to predict how the stability of the downstream slope of the blockage will evolve in decades and centuries.

In 1960s it was hypothesized that large-scale slope failure might occur on the lakes' right bank, 4–5 km from the blockage (RB on Fig. 4), which would cause the huge displacement wave that can gash over the dam at its lowermost section resulting in the dam's partial or complete breach (Sheko 1968; Sheko and Lekhatinov 1970; Fedorenko 1988), as it occurred, for example, in the Las Conchas valley (Argentina) in the prehistoric times (Hermanns et al. 2004). Different researchers estimated volume of this "Right-bank landslide" from 0.3 to 2.0 km^3. However, possibility of such a large-scale failure, its volume and rate estimates are still controversial and require more studies (Alford and Schuster 2000; Ischuk 2011; Strom 2012c). Additional uncertainty of the Lake banks stability assessment is associated with high seismic activity of Central Pamirs. It should be mentioned that none of several gigantic past rockslides that had blocked the Murgab River valley close to the Usoi dam (Fedorenko 1988) remain intact, proving the assumption that long-term stability of the dam and lake can not be guaranteed without special security arrangements.

Recently the early warning system have been installed within the frames of the World Bank Project, aimed to record various indicators of the dams' instability (seismic strong motion, rapid increase of water level in the Lake, etc.) and to allow people living downstream to escape to special shelters arranged above the endangered level. It should mitigate the disastrous consequences if dams breach would occur (Zaninetti 2000).

Since the potential risk of the blockage breach and of the devastating outburst flood exists, special measures should be undertaken to ensure long-tem safety of the Lake Sarez regardless of any dynamic effects such as strong earthquake or impact of the displacement wave caused by large-scale failure in the lake. Possible solutions, which are under discussion, envisage not only risk reduction measures, but also use the Lake Sarez water for irrigation and power production. Construction of a spillway tunnel through the left bank bedrock massif from the small Shadau Lake formed in the tributary valley (visible at the background on Fig. 3) seems to be the most reliable variant (the Sarez Lake could be linked with the Shadau by a channel) that allows not only lowering of the Sarez Lake up to the safe level (i.e. outburst flood disaster prevention) but also the integration of a powerhouse (Strom 2012c).

2.2 Outburst Floods Caused by Landslide Dams' Breach

The most disastrous effect of landslide river damming is an outburst flood caused by dams' breach. Numerous case studies from the Alps, Karakorum, Himalayas, Central American and Argentinean Ands, Tibet and Longmanshan mountains are described, for example, in various chapters of the book "Natural and Artificial Rockslide dams" (Evans et al. 2011a, b).

Three outburst floods caused by rockslide dams breach had occurred in Central Asia in 1960s (Pushkarenko and Nikitin 1988; Strom 2010b) and two of them were really devastating. One more disastrous breach occurred in 1993.

On July 7, 1963 the catastrophic breach of the Issyk Lake (43°15.3′ N, 77°28.9′ E) occurred east from the former capital of Kazarhstan, the Almaty City (2 on Fig. 1). Evidence of a devastating debris flow that passed through the Issyk valley could be visible till now, almost 50 years after the disaster.

The prehistoric landslide dam about 0.6 km^2 in size and up to 200 m high (about 50 Mm^3 in volume), composed of diorite blocks (on top) and same rock crushed at a high extent in the dams' interior (Eugen Gaspirovich, personal communication), was breached by overtopping caused by debris flow that originated in the upper reaches of the catchment due to the Jarsai glacial lake breach. Up to 6–7 million m^3 of debris was brought into the Issyk Lake within 3–4 h resulting in rapid increase of the lake level and creation of waves that destroyed the upper part of the blockage. Water stored in the lake rushed downstream eroding the dam body as well as river banks and valley bottom (Gerasimov 1965). Peak discharge recorded about 10 km downstream, close to the Issyk town, was 745 m^3/s, while mean discharge of the river at this site is 4, 96 m^3/s (from (State Water Inventory 1964–1981). Only small remnant lake has remained after the disaster. Later on an artificial dike was built in the eroded canyon to protect downstream valley and the Issyk town from new debris flows and to renew this beautiful touristic site (Fig. 5).

Next year, on April 24, 1964, 20 Mm^3 of rock debris blocked the Zeravshan River valley in Tajikistan close to the junction of the Zeravshan and Fandaria Rivers just upstream from the Aini town (39°23′ N, 68°32.5′ E) (3 on Fig. 1). The dam was up to 150 m high (maximal height, the effective one was much lower, about 50–60 m) and 1.3 km along the stream. Dammed lake fed by both rivers with cumulative discharge of about 90 m^3/s (in April–May, 1964; mean annual discharge at this gauge is 147 m^3/s, according to (State Water Inventory 1964–1981) could store up to 126×10^6 m^3 of water, which release would devastate lower part of the Zeravshan River valley with the historical Samarkand City. To take the situation under control the 865-m long and up to 23 m deep trench across the dams' crest was excavated by directed blasts. On May 6 water started passing through this artificial channel and 2 days later the discharge exceeded the inflow. The peak discharge of 1,200 m^3/s was recorded on May 31. Lake was almost emptied at June 20, when its level dropped for 325 m. 3 millions cubic meters of debris was eroded from the dam resulting in significant aggradation of the

Fig. 5 The Issuk dam and Lake after restoration of the dam. The rockslide headscarp is on the left. Large alluvial fan was formed by debris flow that caused the dam's breach in 1963. 3D Google Earth view

Zeravshan River channel downstream (Neshikhovskiy 1988; Strom 2010b). This case study is one of the first examples of the successful prevention of the rockslide dam breach disaster.

I want to point out that there are evidence of both past and future slope failures at this site. First, it is clearly seen that the 1964 rockslide occurred within the headscarp of a much larger prehistoric rockslide (Fedorenko 1988). Second, an arcuate scarp above the headscarp of ancient rockslide (marked by small red arrow on Fig. 6) and upslope-facing scarps at the upper part of the opposite—south-facing slope of the watershed indicate possibility of the formation of new large rockslides at this site.

One more catastrophic outburst flood caused by the rockslide dam breach occurred on June 18, 1966 in the Isfairamsay River basin in Kyrgyzstan (4 on Fig. 1). The rockslide dam 20–30 Mm^3 in volume (the entire rockslide volume was about two times larger, but almost half of it rests within the headscarp—see Fig. 7) originated about 300 years ago, likely being triggered by an earthquake, and formed a dam about 100 m high that had blocked the Tegermach River valley (right tributary of the Isfairamsay River) at 39°55.6′ N, 72°18′ E (Rezvoi and Rezvoi 1969; Rezvoi et al. 1971; Reizvikh et al. 1971; Strom 2010b). The dam of the Yashinkul Lake was overtopped due to continuous raining. Outburst flood lasted for about 7 h with peak discharge of 5000 m^3/s and caused significant damage not only in Kyrgyzstan but also in Uzbekistan farther downstream. The breach canyon is up to 90 m deep, 50–60 m wide at its bottom and 280–340 m wide at the dams' crest level (Neshikhovskiy 1988) (measurements on the Google

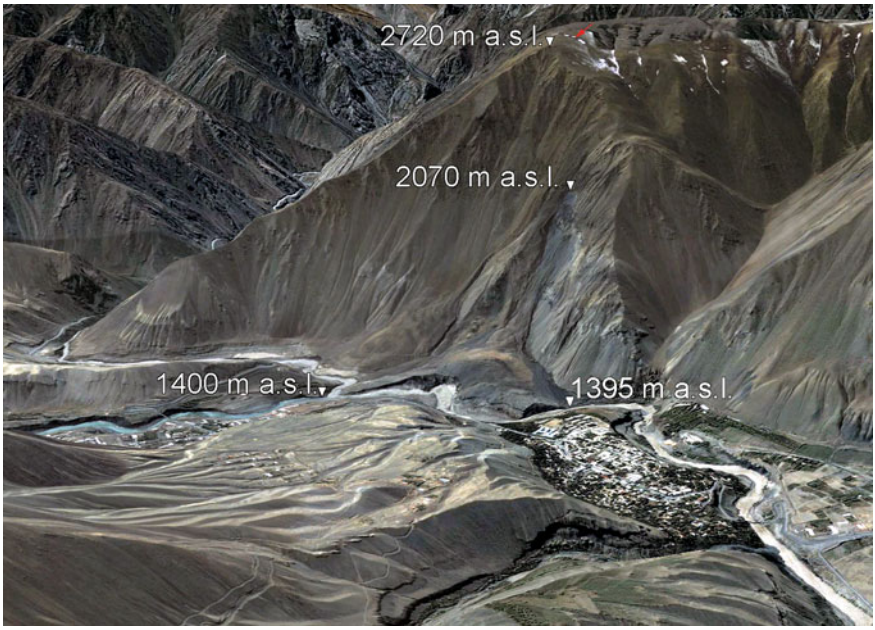

Fig. 6 Remnant of the 1964 rockslide dam at the Aini town (Tajikistan) immediately downstream from the junction of the Zeravshan river (coming from the left with clear blue water) and the Fandarya River (with muddy water, coming from the gorge at the background). *Red arrow marks* an arcuate scarp indicating possibility of slope failure at this site in future. 3D Google Earth view

Earth image returns width value up to 370 m). Thus, about 10×10^6 m^3 of debris (much more than in the Aini and Issyk cases) was removed from the dams' body causing significant aggradation downstream.

The most recent disaster associated with landslide river damming in Central Asia region occurred in the Belaldy River valley—small right-bank tributary of the Naryn River than now falls in the Toktogul reservoir (5 on Fig. 1). The M7.3 Suusamyr earthquake triggered rockslide about 40 Mm^3 in volume on August 19, 1992. Its debris formed $\sim$500 m wide and 1000 m long body that filled steep but wide glacial valley bottom forming blockage about 100 m high (Fig. 8). Rockslide killed few people who tended a herd in the upper reaches of the valley. Unlike other case studies described above where large water bodies had been impounded, this rockslide dam formed two minor lakes up to 200–300 m^2 in size only. Nevertheless, 10 months later, in June 1993, likely after intensive snowmelt at elevations exceeding 3000 m a.s.l., these lakes burst out producing powerful debris flow that partially devastated the Belaldy village 17 km downstream and the Torkent village 30 km downstream from the dam site (Korjenkov et al. 2004).

This case study demonstrates that rockslide-damming phenomena causing small-size impoundment could have, nevertheless, quite severe tertiary consequences (considering upstream valley inundation as secondary effect).

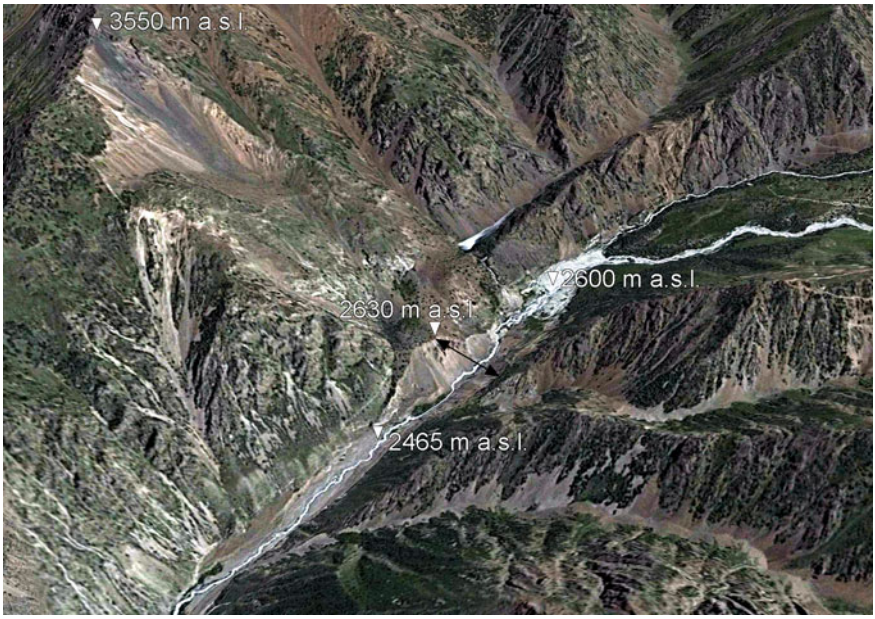

Fig. 7 The Yashinkul dam breached in 1966. Note large difference of the benchmarks elevations upstream and downstream from the dam resulting from the significant sedimentation of the 300-years old lake (compare with the Aini landslide dam on Fig. 6). Just downstream from the dam evidence of valley aggradation are still visible. 3D Google Earth view

3 Origin of Natural Blockages

Correct determination of the river-damming feature origin plays a critically important role in the entire process of the related hazards and risks assessment. Several basic problems must be solved. First, is the blockage(s) in question a landslide dam(s) or drainage disturbance was caused by any other process (glaciation, tectonics)? The correct solution would foreordain most of further analysis and practical actions aimed to study the feature and to elaborate disaster mitigation measures if necessary. If features in question are glacial landforms, they would not have any relation to seismic events. If landslide origin of the dam(s) is substantiated, next question arises—what is the cause/trigger of such event(s). Here possibility of their seismic origin must be taken into consideration and either proved or disproved in each particular case (see, e.g. Strom and Stepanchikova 2008; Strom 2012b).

If rockslides are caused/triggered by earthquakes, then, due to unpredictability of large earthquakes, prediction of future slope failures place and time could be performed, most likely, at a regional scale based on probabilistic approach rather than at a local scale using site-specific deterministic analysis. If, in contrast, slope failures result from gradually developing processes, site-specific landslide prediction and, possibly, prevention, seems to be more realistic. The following sections address to these problems.

Fig. 8 1992 rockslide at the upper reaches of the Belaldy River—source of the powerful debris flow of June 1993. 3D Google Earth view

3.1 Landslides Versus Moraines

Genesis of natural blockages in mountain valleys has been a debatable topic for a long time. Two main processes are considered as being responsible for their formation—glaciation (either retreat of large along-valley glaciers leaving end moraines as barriers, or such a glaciation-related phenomena as rock glaciers—see e.g. Owen and England 1998; Burger et al. 1999), and large-scale slope failures. It was discussed in details for the Karakoram region where rockslide nature of such barriers was proved by Hewitt (1998, 2002, 2006). However, recently the problem was raised again, this time for the Pamirs, in publications of Nikolai Ischuk (2008, 2011a, b) who considers almost all of them, including well-known features such as the existing dams of the Yashinkul and Shiva Lakes and the breached Kudara-Pasor blockage as being formed by end moraines. His main argument in favor of such assumption is the presence of large amounts of moraine material in these dams.

Correct solution of the contradictory interpretation of dams' landslide versus moraine origin provides the basis for hazard assessment of such phenomena. If most of the Pamirs natural blockages, both intact and breached were formed by end moraines—no hazard of large rivers' blocking is anticipated in the near future, since present day glaciation degradation makes the formation of new similar features in the main river valleys impossible and only small lakes in the glaciated tributary valleys may originate with ongoing glaciers' retreat or being dammed by gradually moving rock glaciers. If the opposite—rockslide—origin of these features is true, then, in contrast, no general restrictions of river damming at any time in future exist and related risks should be much higher.

Fig. 9 Rockslide dam of the Shiva Lake in the Afghan Badahshan at 37°23′ N, 71°24′ E (6 on Fig. 1). It is clearly visible that the headscarp is a unique feature which relief is much younger than that of other parts of the valley slope. 3D Google Earth view

Several reasons do not allow me to agree with interpreting valley barriers either as end moraines or as a combination of end moraines as main river-damming features accompanied by subordinate rock slope failures as proposed by Ischuk (2011a, b). First, all (!) natural dams are associated with the concave lowering on the valley slopes just above these bodies, which are distinctly younger than the adjacent slopes and are nothing else than the rockslide headscarps (Figs. 9, 10). I cannot accept so high probability of association of end moraine and subsequent rockslides—there is no reason to interconnect these totally different phenomena. Moreover, in most of cases nothing similar to such a spoon-shape lowering could be found on the adjacent slopes. Ischuk (2011a, b) interpreted these features as being formed by small cirque (niche) glaciers or "pre-glacial" nivation hollows. But glaciation that forms such geomorphic features is a climate-driven process that depends (at a valley scale) on elevation and slope aspect. Thus, if niche glacier or nivation hollow exits on a slope at one site, similar and same age topographic features *must* exist on the adjacent similarly-facing slopes at the same elevation. However, as mentioned above, nothing similar can be found and headscarps from where rockslides originated are unique for the particular segments of river valleys (see Figs. 9, 10). It excludes interpreting these geomorphic features as being left by niche glaciers or nivation phenomena.

Presence of large amount of moraine material in the dams' bodies can be explained as follows. Since most of the Pamirs valleys had been intensively glaciated in the past, lower parts of their slopes are covered by the material from the lateral and/or bottom moraines of these past glaciers. When large-scale slope failure occurs, moving bedrock material bulldozes moraine material and often overrun and overlay it (Strom 1994, 2006). Additional possibility of the appearance of rounded and semi-rounded boulders in the damming barriers can be exemplified by the Usoi rockslide that involved some material from the modern glacier valleys above the headscarp crest (see Fig. 2).

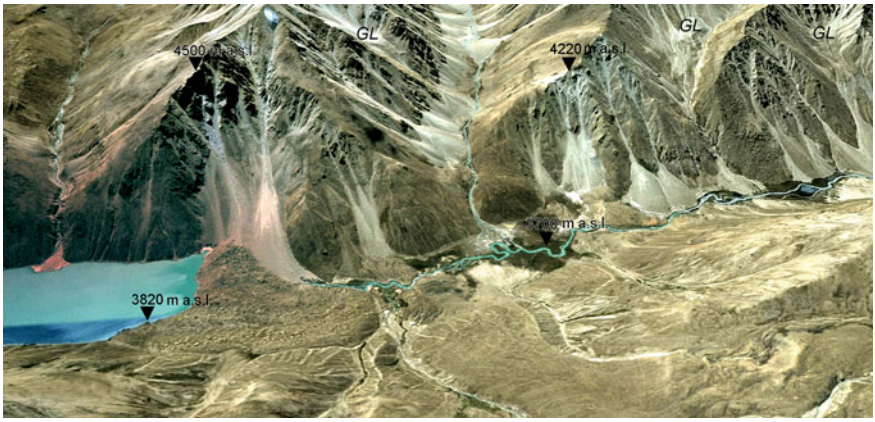

Fig. 10 The Rivakkul Lake dam in the Gunt River basin at 37°37′ N, 72°03.5′ E (7 on Fig. 1). One more smaller blockage can be seen immediately downstream from the dam and one more—downstream from the small green plane at 3700 m a.s.l., which is the bottom of the small emptied lake. *GL*—modern glacier deposits contemporary with the damming features develop much higher than rockslides that blocked the valley. 3D Google Earth view

This mechanism—pushing-out of old moraine material resting at the feet of valley slopes in front of moving rockslide debris can be seen very clearly at the Imom rock avalanche in the Gunt River valley (31°41.5′ N, 72°19.6′ E, 8 on Fig. 1, Fig. 11). This 2.5 km long and 20–30 Mm^3 in volume rockslide caved from the 700 m high slope composed of Precambrian crystalline rocks. The inner part of its body is composed of angular blocks and rubble of crystalline rocks while the frontal 300 m and 50–100 m wide 'stripes' bounding the main body from both sides are composed of typical moraine material—rounded and semi-rounded boulders with sandy-rubbly matrix. This material originated from the remnants of lateral moraine that rest on the slope and, partially, of the alluvial fan that is now overlaid by rockslide body, but originally was formed at the slopes' foot.

In several cases distinct zoning of the deposits in question clearly indicates that their motion was directed across the valley, not along it, as at the Kudara-Pasor dam at 38°24′ N, 72°34.3′ E (9 on Fig. 1, Fig. 12), which also contradicts glacier hypothesis but is in line with the rockslide one.

One more case study, mentioned by Ischuk (2011b) that allows alternative interpretation is the Yashinkul dam and Lake—the source of the Gunt River (37°47′ N, 72°44′ E, 10 on Fig. 1). Here about 50 Mm^3 of gneiss caved from the 1 km high slope, hit the spoor at the opposite bank of the river and spread up- and downstream for about 4 km in total (Fig. 13). Moving gneiss debris scraped up large amount of moraine material from the slope foot, but, unlike the Imom case, did not just pushed it in front as a bulldozer, but overrun and overlaid it (Strom 1994, 2006). So, it looks as if the river channel is filled by moraine material just blanked by rock avalanche debris. But in fact the entire blockage was formed by rock avalanche that involved large amount of moraine material. Moreover, some

Fig. 11 The Imom rockslide at the left bank of the Gunt River valley. Frontal and flank parts of its body are composed of moraine material resting at the slope base that had been bulldozed by moving rockslide debris. 3D Google Earth view

part of the latter spread outside the limits of the blocky gneiss zone forming microrelief that differs significantly from the intact terrain outside (Figs. 13, 14). Besides, here we can also see that the headscarp is a unique feature at this slope within its elevations range, which indicate non-climatic cause of its origin.

Case studies described above demonstrate that presence of moraine material in the river-damming barriers does not exclude their rockslide origin. Combination of blockages and headscarps just above them proves that most of large natural barriers in the Pamirs river valleys, both existing and breached have been formed by rockslides, not by end moraines.

I should note that in much less elevated Tien Shan, which have not experience so strong glaciation either at present or in the past (except its central highest segment with Victory and Khan Tengri peaks), some rockslide and rock avalanche deposits were also mapped as "moraines", on State geological maps compiled in 1960s–1970s in particular. Argumentation refuting such interpretation is the same as discussed above.

One more controversial issue is the possibility of long-term and large-scale river damming due to active tectonics. Diversion or temporary damming of streams by local anticlines and surface ruptures has been described after several earthquakes (Florensov and Solonenko 1963, 1965; King and Vita-Finzi 1981; King and Stein 1983; Meghraoui and Doumaz 1996). However, since largest terrestrial single-event

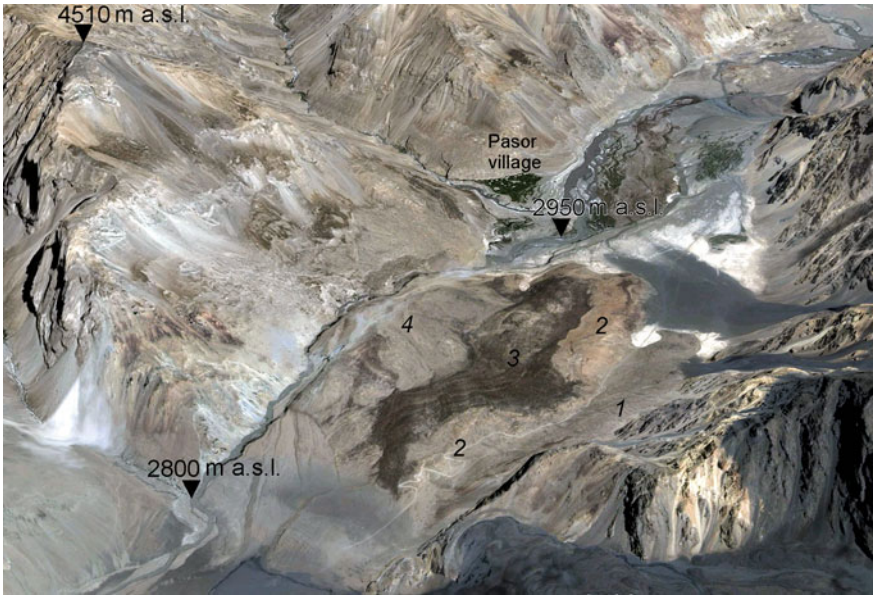

Fig. 12 Breached dam in the Kudara River valley downstream from the Pasor village (9 on Fig. 1). Numbers *1–4* mark various lithologies in the dam's body, which position clearly indicates that material moved across the valley from the headscarp with top mark 4510 m a.s.l. 3D Google Earth view

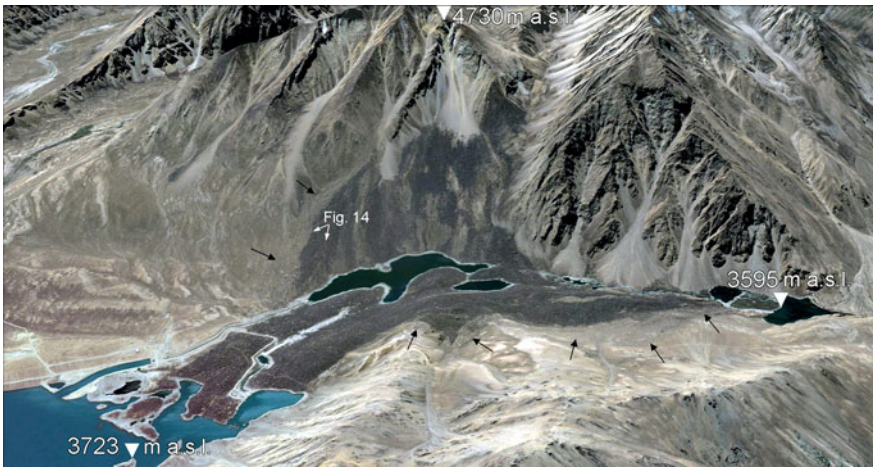

Fig. 13 Yashilkul rockslide dam. Dammed lake is the source of the Gunt River. Gneiss rock avalanche debris is *dark brown*; *black arrows* mark the outer limit of light-brown moraine material spread in front and sidewise from gneiss debris and being part of rock avalanche; *white arrows mark* the site from where photograph shown on Fig. 14 was made. 3D Google Earth view

Fig. 14 Wide thin stripe of moraine material bounding central part of the Yashilkul rock avalanche debris composed of gneiss blocks. Its microrelief differs significantly from old moraine material (outer limit of rock avalanche is marked by *arrows*). Photograph was made in 1980s before the construction of the spillway visible on Fig. 13

vertical offsets associated with earthquakes do not exceed ca. 10 m (Wells and Coppersmith 1994; Strom and Nikonov 1997) such phenomena do not provide same hazard as landslide river damming. In particular, the assumption that large-scale disturbance of the Naryn River at the Alabuga River mouth resulting in accumulation of thick lacustrine succession could be caused by continuous, long-term, and relatively rapid faulting (Makarov 1977) appeared to be erroneous, since long-term blocking that lasted for about 3000 years was caused, in fact, by a gigantic Beshkiol landslide about 10 km^3 in volume that had blocked the valley at 41°26.5′ N, 74°30′ E (11 on Fig. 1), about 15 km downstream from the site where active fault crosses the Naryn River (Korup et al. 2006; Strom and Korup 2006).

3.2 Possible Triggering Factors: Seismic Versus Aseismic

Large-scale bedrock slope failures in rugged terrain could be a culmination of a continuous deformation process driven by gravity force and sometimes accelerated by an abnormal rainstorm, snowmelt, permafrost degradation or human activity (McColl 2012). On the other hand they could be triggered or even caused by an "external" force—earthquake strong motion. It should be mentioned that slowly moving landslides generally do not cause river damming being eroded gradually

by a stream, thus just catastrophic events produce features that are the topic of this paper. One more important point is that most of large-scale seismically triggered catastrophic slope failures were associated with large earthquakes, not with small or medium ones.

Large earthquakes triggered most (but not all) of the large historical rockslides in the Pamirs and the Tien Shan Mountains. Besides the Usoi and Belaldy rockslides described above they accompanied the 1887 Verniy earthquake (Mushketov 1890), the 1911 Kemin earthquake (Bogdanovich et al. 1914; Delvaux et al. 2001), the 1946 Chatkal earthquake (Leonov 1970), the 1949 Khait earthquake (Leonov 1960; Evans et al. 2009b). Same occurred in many other regions—in the USA where the 1959 M7.1 Hebgen Lake earthquake in Montana triggered the Madison Canyon landslide (Hadley 1964), in Alaska in 1964 and 2002 when earthquakes with M9.4 and M7.9 triggered spectacular rock avalanches (McSaveney 1978; Jibson et al. 2006), in Peru where the 1970 M8.0 Ankash earthquake produced the Huaskaran ice-rock avalanche (Plafker and Eriksen 1978), in China during the 2008 M8.0 Wenchuan earthquake that triggered the giant Daguangbao rockslide 0.75–1.1 km^3 in volume and numerous smaller landslides and rockslides (Wu et al. 2010; Yin et al. 2011). The list can be expanded. Such a distinct association led to the situation when presence of large and/or long runout prehistoric rockslide is often equalized with an evidence of strong past earthquake without providing any additional reasons in favor of such assumption—just due to enormous size and expressiveness of these features.

However, numerous large bedrock landslides had occurred without seismic triggering—the 1903 Frank rockslide 30 Mm^3 in volume in Canada (Krahn and Morgenstern 1976), the above mentioned 1964 Aini landslide $\sim$20 Mm^3 in volume in Tajikistan (Fedorenko 1988) (Prof. Zolotariov—one of the leading landslide experts in the Soviet Union, who studied the Aini rockslide, said in late 1970s that if he would not know that this slope failure was not triggered by a strong earthquake, he would, likely, considered it as seismically induced feature), the 1962 Huaskaran ice-rock avalanche—the aseismic predecessor of the larger 1970 event (Evans et al. 2009a), the 1974 Mayumarka rockslide 1.6 billion cubic meters in volume in Peru (Hutchinson and Kojan 1975), the 1987 Val Pola rock avalanche $\sim$40 Mm^3 in volume in Italy (Crosta et al. 2011), the 2000 Yigong landslide 300 Mm^3 in volume and about 10 km long in Tibet, China (Shang et al. 2003), etc. Thus, neither size nor runout of landslide can prove its seismic origin itself. It is confirmed by data, presented by McColl (2012) that numerous large bedrock landslides all over the world have occurred not only without earthquakes, but without any observable triggering.

I must point out that if the assumption of a particular landslide or group of landslides seismic origin is erroneous, it would cause not only an overestimation of seismic hazard, but, also, underestimation of an overall landslide hazard. Direct linking of large-scale rock slope failures' formation with large earthquakes only, which are relatively rare events with typical recurrence intervals at a particular causative fault varying from several hundred to several thousands of years, means that large bedrock landslides should occur with more or less the same recurrence.

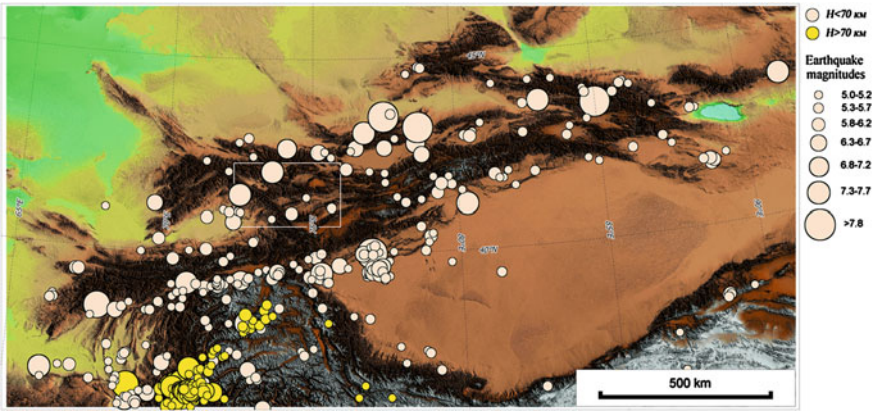

Fig. 15 Seismicity of the Tien Shan Region. Notice lack of earthquakes in the Central Tien Shan (75°–79° E, 40.5°–42° N), in the Zeravshan River basin (67°–70° E, 38.5°–40° N) and in some other parts of this mountain system with high concentration of large-scale landslides (outlined area is shown on Fig. 16)

However, other natural phenomena that can trigger such slope failure (e.g. rainstorms, hurricanes, abnormal snowmelt, etc.—see McCall 2012 for the detailed review) are much more frequent. For example, 3 typhoons hit Taiwan annually on average (Jan and Chen 2005) while large earthquake occur at this island several times per century only (Hung 2000; Cheng et al. 2007). In the area where the 1999 M7.6 Chi–Chi earthquake had triggered large Tsao-Ling landslide, 5 large-scale slope failures occurred since 1862, but only three of them—in 1862, 1941, and 1999—were triggered by earthquakes. Two others—in 1942 and in 1979 were rain-induced phenomena (Hung 2000).

No doubts that seismicity, strong earthquakes in the first place, is one of the main factors leading to slopes' instability. But such origin of large-scale bedrock landslides should be not just postulated, but substantiated somehow. It is especially important in the Central Asia region where historical data on various natural phenomena are available for a short time, generally, less than for 200 years, much shorter than the recurrence period of large earthquakes at a particular causative fault.

Distinguishing of seismic and aseismic rockslides and rockslide dams is a critical problem in the internal parts of the Tien Shan mountains, occupied by the Naryn, Zeravshan and Sarydzhaz River basins. Unlike northern and southern limits of this mountainous system and the Ferghana depression rim where numerous large earthquakes have been recorded in the historical times (Ignatiev 1886; Mushketov 1890; Bogdanovich et al. 1914) and, later on, instrumentally (Fig. 15), no similar large earthquakes are known in the inner parts of the Tien Shan. Thus, its seismic hazard assessment is based, at a large extent, on the paleoseismological data (Korjenkov 2006; Abdrakhmatov et al. 2007). Those include analysis of both surface ruptures and bedrock landslides, which are as widespread in the inner parts of the region as in its boundary zones with high modern seismic activity. Some

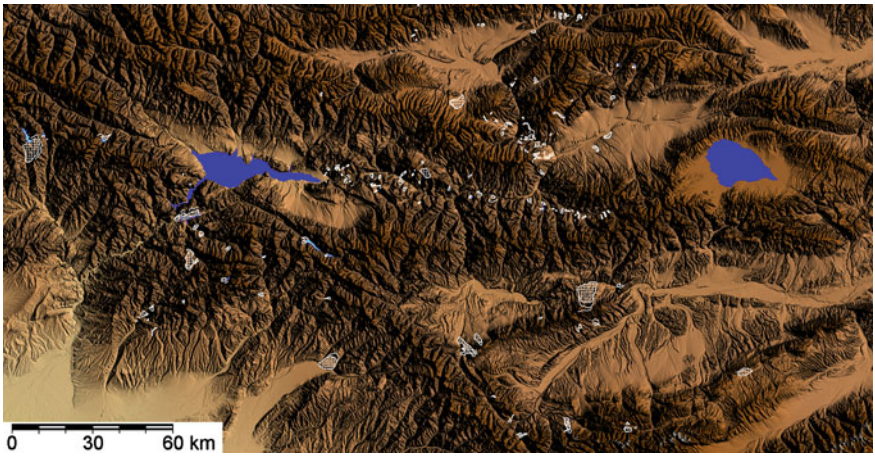

Fig. 16 Spatial distribution of large-scale bedrock landslides (*white-colored* features) in the central part of the Naryn Ricer basin. This region is characterized by low seismic activity during last ca. 200 years. *Dark blue*—the Toktogul reservoir and the Sonkul Lake impounding central part of the neotectonic depression. *Light blue*—largest landslide-dammed lakes visible at this scale

zones of the inner Tien Shan, such as those stretching along the Zeravshan River valley (Fedorenko 1988) or along the Naryn—Lower Kokomeren—Minkush River valleys (Strom 2012a) feature abnormally high concentration of large-scale rockslides and rock avalanches (Fig. 16).

The most unequivocal evidence in favor of seismic origin of a particular rockslide dam is a direct spatial and temporal coincidence of slope failure on the one hand and of the surface rupture on the other hand. Such historical coincidence could be exemplified by the 1911 Kemin earthquake when the Ananievo (12 on Fig. 1) and Kaindy (13 on Fig. 1) rockslides occurred on slopes directly undercut by surface ruptures (Bogdanovich et al. 1914; Delvaux et al. 2001). Spatial closeness and, likely, simultaneity of the prehistoric surface ruptures and of rockslide dams was found at the Talas-Feghana fault zone and in the western part of the Naryn-Sonkul fault zone (Fig. 17a) (Belousov et al. 1994; Korjenkov 2006; Abdrakhmatov and Strom 2006).

However, quite often large rockslides originate far from the surface rupture, like, for example, the above mentioned Belaldy rockslide triggered by the 1992 Suusamyr earthquake. No direct data on the location and even on the formation of surface ruptures are available for the well known 1911 Sarez (Ambraseys and Billham 2012) and the 1949 Khait (Leonov 1960; Evans et al. 2009b) earthquakes in Central Asian accompanied by large landslides—the Usoi rockslide dam and the Khait 7.3 km long rock avalanche (15 on Fig. 1).

Therefore in most cases sound conclusions on a particular landslide(s) seismic origin could be derived from the set of indirect evidence mainly (Fedorenko 1988; Strom and Stepanchikova 2008; Strom 2012b). One of such evidence is the close ages of several large rockslides distributed over more or less large area, especially

Fig. 17 **a** The Djuzumdy rock avalanche site (14 on Fig. 1, 41°47′ N, 73°24′ E) in the Naryn River valley, east from the Ketmen-Tiube depression. 3D Google Earth view. Large-scale slope failures from the headscarp on the *right* (bellow point at 1620 m a.s.l.) had occurred twice. Approximate frontal edges of these rock avalanche deposits are marked by dashed lines. According to lichenometric studies the younger body was formed more than 1000 years ago, which does not contradict to the age of the latest rupturing event along the adjacent active fault (marked by *red arrows*), that had happened roughly from 105 BC to 238 AD (2σ range). Trenching was performed at the site marked as (**A**). Evidence of recurrent surface faulting were found at the site marked as (**B**). **b** Sketch of landslides and active fault developed at this area. Three rockslides about 3 km north from the Naryn River, at the opposite side of the ridge, affected by the Djuzumdy rock avalanches and surface rupture, rest on the deposits of the older landslide dam. The charcoal sample collected from these deposits returned age of 3629-3337 BC (2σ range). Thus, they should be younger than ~5000 years. Calibration of radiocarbon ages was performed by Calib 5.0 (Stuiver and Reimer 1993). "C" marks the Djuzumdy caldera-like cavity (Strom and Groshev 2009) ▶

if they are located close to a large active fault (Crozier 1992; Belousov et al. 1994; Bull 1996). Strictly speaking the above Naryn-Sonkul fault zone case exemplified by the Djusumdybulak landslides (see Fig. 17a) also represents indirect evidence of various features simultaneity—landslide ages determinations just bound the age of faulting with better precision (Fig. 17b).

We must consider also that, according to Malamud et al. (2004), strong earthquakes and other energetic triggering phenomena like typhoons usually produce one or few large and extra-large landslides along with numerous medium and minor features. Indeed, many earthquakes were accompanied by only one extremely large slope failure without anything else comparable (Ischuk 2011; Owen et al. 2008), or by few large landslides located at a significant distance from each other (Bogdanovich et al. 1914; Wu et al. 2010; Yin et al. 2009, 2011; Huang and Li 2009). It is evident that hundreds and thousand years after the event it would be difficult to proof large-scale slope failures simultaneity, even if we would be able to date them directly, considering accuracy of sampling and precision of dating methods that can be used for such studies (Walker 2005).

Additional (though, of course not the alternative) approach is based on thorough analysis of the basal units of lacustrine sediments in the drained landslide-dammed lakes where one can find features closely timed to master events (Strom 2012b). Simultaneity of large-scale slope failure and of other slope failures or liquefaction phenomena that occur at a rather large distance provides sound reasons to considering all these phenomena, each of which could be caused by ground shaking, to be triggered by strong earthquake that had affected large area.

At present relations of most of the prehistoric river-damming bedrock landslides in the Pamirs and the Tien Shan with large earthquakes are still unknown. Solution of this problem requires extensive and regular studies of such features including their dating, detailed analysis of their relationships with nearby active faults and reconstruction of the pre-slide slope morphology and internal structure that could be used for retrospective numerical modeling of slope stability. The latter is a powerful tool for revealing real nature of the phenomena in question, but its reliability strongly depends on the input parameters accuracy and reliability.

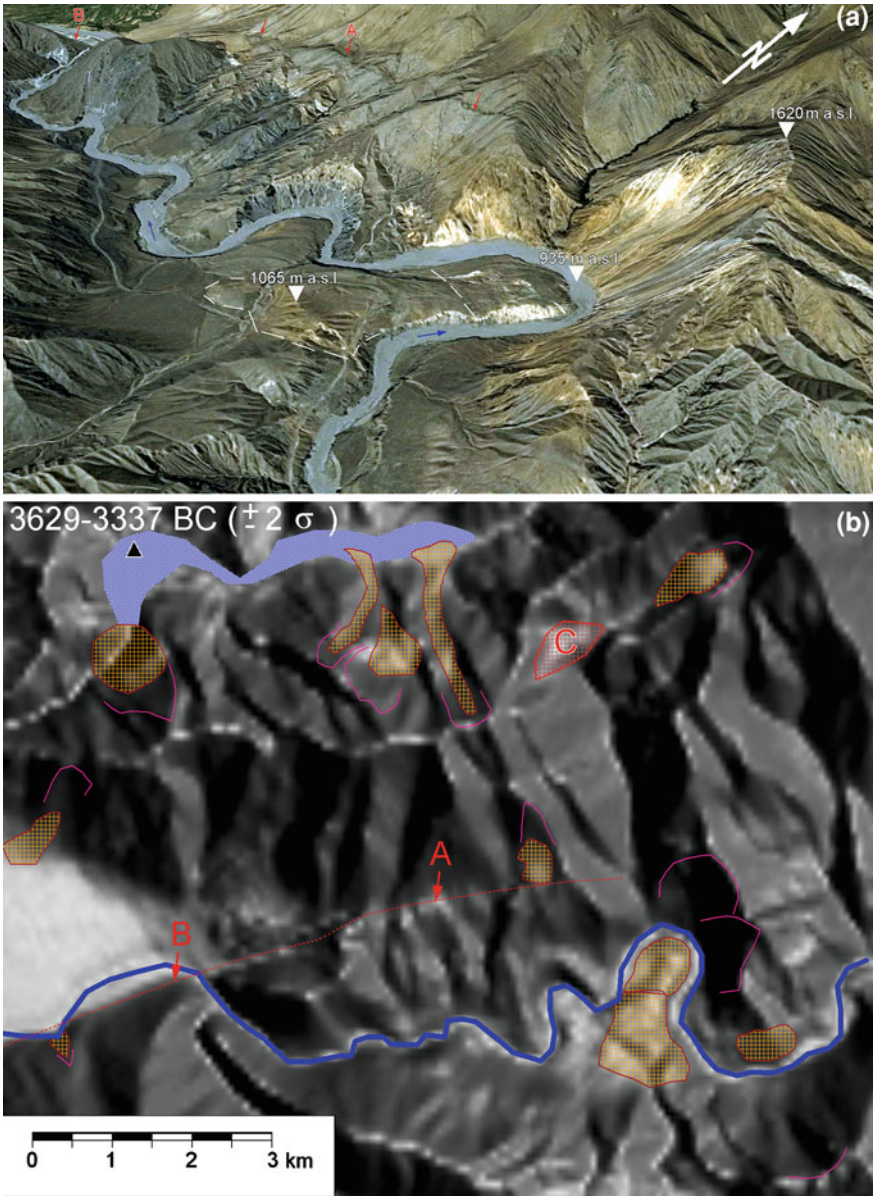

4 Spatial Distribution of River-Damming Landslides

The first step of the landslide hazard assessment in general and of hazard assessment related to landslide river damming, in particular, is regular mapping of landslides and compilation of their representative inventories. The preliminary

studies carried out in the Central Asian region revealed significant unevenness of landslide distribution throughout these mountainous systems—zones of their extreme concentration alternate with areas with similarly rugged terrain but lacking such features (see Fig. 16).

Most of zones featuring high concentration of bedrock slope failures coincide with large fault zones, with some exceptions, however. For example, east–west trending belt with numerous landslides stretching along the Naryn, Lower Kokomeren and Minkush River valleys visible on Fig. 16 follows the Naryn-Sonkul fault zone. However, numerous landslides in the upper part of the Kokomeren River valley (Strom and Abdrakhmatov 2009) do not follow any regional fault zone though some of them are close to local active faults.

Areas where deep river valleys follow large fault zones seems to be the most susceptible for the formation of large landslide dams due to combination of several factors: (A) presence of high steep slopes formed due to the powerful streams' incision; (B) wide distribution of rocks weakened by faulting and fracturing typical of large fault zones; (C) complex groundwater conditions supported by differently oriented aquifers and aquicludes. All these factors favor formation of very large landslide dams and landslide-dammed lakes. Seismicity, which is, often, associated with same fault zones, is an important, but not obligatory factor. Thus, as discussed above, while active fault zone with known high seismic activity should be definitely considered as a landslide-prone area, opposite conclusion, i.e. consideration of a fault zone with high concentration of landslides as being seismically active requires additional argumentation.

Sometimes, landslide distribution within fault zones is uneven too and distinct clustering could be observed along their strike (Strom and Abdrakhmatov 2004; Abdrakhmatov and Strom 2006). While numerous multiple-aged landslides could be found within such clusters, nothing similar exists between them, despite similarly rugged topography, presence of active faults with surface ruptures, and complex geological structure. It can be exemplified by the Inylchek River valley blocked by large successive rock avalanches that collapsed from both slopes of the valley at 42°09.5′ N, 79°27.5′ E, about 17 km downstream from the present day terminus of the Southern Inylchek glacier (16 on Fig. 1, Fig. 18). Both geology and topography of the valley just at this section and outside, where no similar slope failures have occurred, look similar (Fig. 19). Absence of any recognizable geological and geomorphic anomalies at those sections of the river valleys following along large fault zones were recurrent large-scale rockslides occur allows assumption that an abnormally high slopes' instability is caused by an "external" factor, notably by increased strong motion effect governed by some peculiarity of source rupturing process. It follows thence that these sites should be considered as most hazardous during future large earthquakes.

Even if these speculations about role of seismicity in landslide clustering is wrong, and real causes of any particular slope failure and of their concentration at this site are not fully understood, areas featuring recurrent large-scale slope failures are characterized by an abnormally high landslide hazard level and should be, thus, the first priority sites for hazard assessment and monitoring. It can be exemplified by the Aini

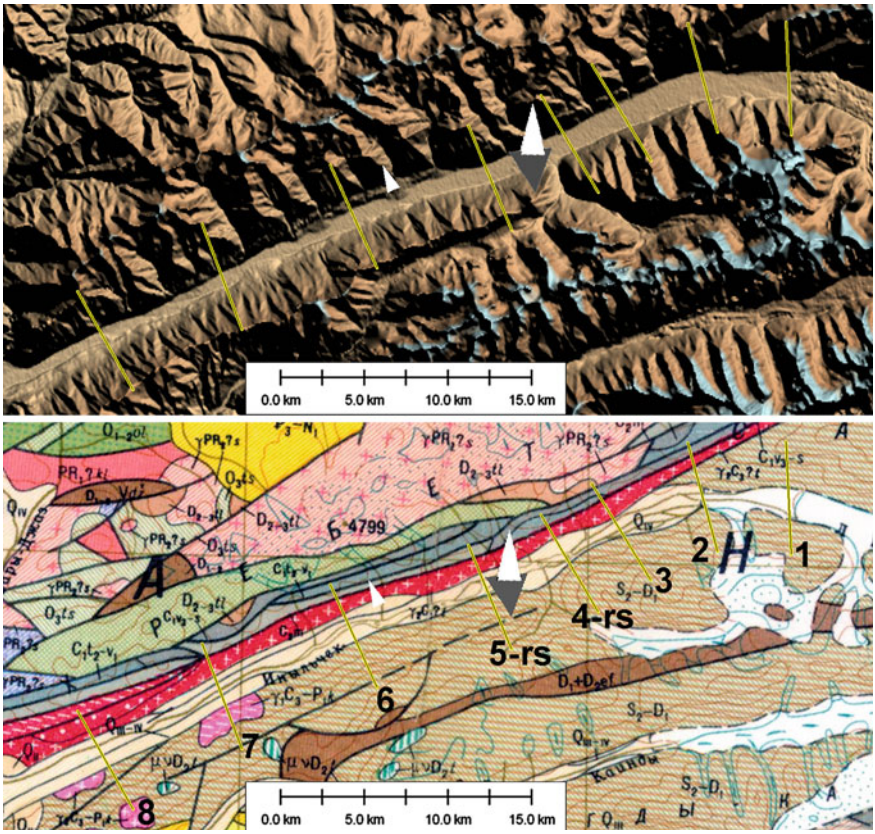

Fig. 18 SRTM DEM (*above*) and fragment of 1:500,000 geological map of the Inylchek River valley. Triangles show the position of large rockslides identified in the valley. Rockslide from the right bank (*larger white triangle*) is younger than that from the *left* bank (*grey triangle*). *Numbered yellow lines* profiles shown on Fig. 19

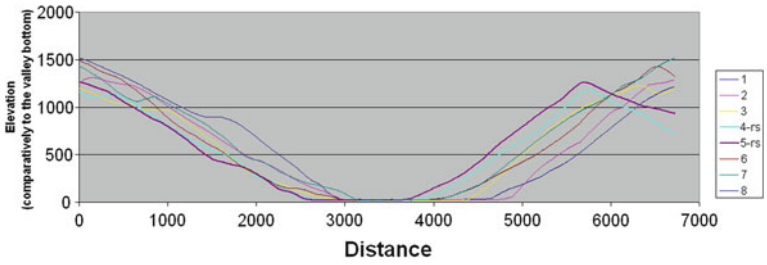

Fig. 19 Superposed cross-sections of the Inylchek River valley (see their location on Fig. 18). Profiles 5-rs and 6-rs cross the valley close to the landslide dam formed by *right-bank* rockslide that overlaid the *left-bank* one. Note that slopes' steepness is almost the same all over the valley

town area in the Zeravshan River valley in Tajikistan, described above (see Fig. 6). The 1964 river-damming landslide was preceded by much larger prehistoric one and indications of future instabilities are evident on the left-bank watershed.

Similar clusters could be identified not only in the Tien Shan, but in the Pamirs as well. One of the largest of them includes the Usoi dam—the most recent river-damming feature, the preceding giant Murgab landslide (23 on Fig. 1), the Kudara breached dam in the adjacent river valley (9 on Fig. 1) and several smaller breached dams nearby. Such an abnormal concentration increases probability of the new large landslides within this area, including the Sarez Lake banks, though it is unlikely that we can quantify this hazard with reasonable substantiation. Landslide dams' distribution in other parts of the Western Pamirs is more even, in general, while the plateau-like Eastern Pamirs almost lacks such features.

Ambraseys and Bilham (2012) noted that almost all large-scale slope failures in the vicinity of the Usoi dam have occurred on south-facing slopes and linked this effect with stronger weathering depending on slope aspect. This assumption is opposed, however, by inverse orientation of slopes most affected by large rockslides in the upper part of the parallel Gunt River valley and its tributaries. Here many large-scale slope failures including river-damming features took place on the north-facing slopes. Among them are the Yashinkul (see Fig. 13), the Rivakkul (see Fig. 10), the Imom (see Fig. 11) rockslides and several others that could not be described herein due to paper length limitations. In contrast, westward, in the downstream part of the Gunt valley and in the lower reaches of its largest tributary—the Shakhdara River valley, most of bedrock slope failures affected south-facing slopes—similar to the Murgab-Kudara (Usoi) cluster.

Such differentiation allows assumption, though just speculative at present, that slope failures orientation could be governed by directivity of seismic shaking, rather than by the influence of any exogenous processes (weathering, nivation phenomena, etc.). In case of the Murgab-Kudara (Usoi) cluster this hypothesis is in line with the assumption that the source zone of the 1911 Sares earthquake was located somewhere west from the Usoi landslide site (Ambraseys and Bilham 2012, their Fig. 4), likely within the fault zone that stretches in the NE direction towards the Karakul Lake tectonic depression. If so, just right (south-facing) slopes of the river valleys would be "lighted" by seismic waves spreading from their foci.

Voluminous outburst floods could provide especially high risk for the hydraulic schemes located downstream. Thus, identification of sites with increased possibility of future river damming within the catchment should be performed within the frames of corresponding engineering surveys. In the Central Asia region such analysis was carried out for the Rogun Dam in Tajikistan (Besstrashnov et al. 2011; Zhirkevich et al. 2011). Cluster of several past rockslide dams and evidence of the potential future failures was identified in the central part of the Muksu River valley in the northern Pamirs at 39°08′ N, 71°45′ E (17 on Fig. 1,) and rough estimates of the volume of possible landslide-dammed lake and of the outburst flood parameters were obtained. It was shown that, due to significant distance from this site to the Rogun reservoir and the dam site, even worst scenario would not

pose a real threat for the dam. Nevertheless, considering centuries-long life-time of most of hydraulics structures, such analysis must be obligatory for hydraulics engineering and should be included in the national and international guidelines and regulations (Besstrashnov et al. 2011; Zhirkevich et al. 2011).

5 Effects of Bedrock Landslide Dams' Morphology and Internal Structure on Their Hazard Assessment

Geological conditions discussed above determine formation of large-scale bedrock landslides which is the main type of slope failures in mountainous regions of Central Asia responsible for river damming. However, as mentioned above, effects of valley inundation and of subsequent outburst floods are, in most cases, much more disastrous than direct effects of slope failure itself. As soon as landslide occurs and blocks the valley, further evolution of the blockage depends on hydrological characteristics of the stream on the one side and on dimensions, shape and internal structure of the blockage on the other side (Hermanns et al. 2011; Dunning and Armitage 2011). Though most of such dams have been breached rather soon (Schuster and Costa 1986; Costa and Schuster 1988; Schuster and Evans 2011; Evans et al. 2011a, b), many of them exist for decades, centuries and millennia. At the same time, even centuries-long survival of a landslide-dammed lake does not ensure its further stability that was exemplified tragically in the region in question by the above mentioned Issyk and Yashinkul disasters.

5.1 Critical Morphological Peculiarities

In the overview of the Central Asian landslide dams (Strom 2010b) it was shown that most of them behave as predicted according to the DBI value (Ermini and Casagli 2003). However, several landslide dams demonstrate inverse behavior. Some of features that have large DBI values indicating their instability have existed for a very long time, and, likely, will be stable in future, while some other with low DBI (i.e. within the stability domain) have been breached soon after formation. Analysis of such abnormal behavior reveals several additional factors and parameters (besides landslide dam volume and height, and stream discharge described in terms of catchment area), which must be considered as prerequisites for landslide dams' disaster assessment and mitigation.

An important factor influencing a landslide-dammed lake lifetime and risk of an outburst flood is the presence of another dam upstream. Such cascade location can either decrease risk or increase it significantly. The first scenario can be exemplified by the Kulun River that had been dammed twice—in its upper reaches at 40°32′ N, 74°17.2′ E, where the 90-m deep Kulun Lake still exist (18 on Fig. 1) and at 40° 27.6′

N, 74° 04.2′ E, just upstream from its mouth where 70-m high rockslide dam formed by rockslide from the upper part of its right bank composed of Paleozoic limestone (19 on Fig. 1), created 6.5-km long lake. The dam was overtopped but not breached and the lake have been silted completely (Strom 2010b). Here the stable upstream dam forms the lake large enough to cut off seasonal floods that reduces possibility of a downstream lake outburst significantly.

In contrast, breach of even rather small upstream lake of any origin (landslide, moraine, etc.), especially if it causes a debris flow, could have a dramatic effect on the downstream water body and its damming feature, resulting sometimes in the outburst flood much more powerful than the initial one. Just such chain catastrophe occurred in 1963 in the Issyk River basin (see Sect. 1.2).

One of landslide dams' characteristics quite important for assessing their longevity and style of breach is the cross-valley profile of the dam (Hermanns et al. 2011; Korchevskiy et al. 2011), which, in turn, depends at a large extent on rockslide motion mechanism (Strom 2006). Perhaps the main mechanism of dams breach is their erosion due to overtopping, which starts at a lowermost part of the dams crest. Under otherwise equal conditions landslide dams formed in relatively narrow valleys by rock avalanches of the primary type (Strom 2006) with distinct proximal lowering are more subjected to catastrophic breach than those with distal lowering (formed by rock avalanches of the secondary and jumping types, ibid). While in the first case erosion would cut through landslide body composed of crushed debris and this process can be quite rapid and catastrophic, in the second case it is much more likely that stream incision will start at the frontal edge of the landslide body and will affect the bedrock of the opposite slope. Thus, the outlet channel will develop gradually, like it happened in case of the Beshkiol (Korup et al. 2006) and Kokomeren (Hartvich et al. 2008) landslides. In the latter case the gigantic ($\sim$1.5 km^3 in volume) Late Pleistocene Kokomeren rockslide (41°55.5′ N, 74°13.5′ E, 22 on Fig. 1) likely experienced dual style of breaching—upper part of the dam composed of rockslide debris could fail catastrophically while its lower part several tens meters high was eroded gradually being protected by the bedrock spur at the upstream edge of the blockage (Fig. 20).

Slower breach of the dams with distal lowering is not obligatory, however, it strongly depends on the shape of the buried valley. For example, the Holocene Lower Aral landslide that had blocked the Kokomeren River valley at 41°47.9′ N, 74°17.3′ E (20 on Fig. 1) by the 70-m high dam with distal lowering was, nevertheless, breached catastrophically, producing powerful debris flow with peak discharge about 28,000–30,000 m^3/s (calculations were performed by A. Zhirkevich) that left large boulders on top of a 10-m high cliff $\sim$2 km downstream from the dam (Fig. 21). In this case the landslide had filled just the lowermost box-shape part of the river gorge with very steep slopes. In any case this factor—the across-valley dam profile—should be taken into consideration when predicting blockage evolution and elaboration of possible disaster mitigation measures.

One more important morphological characteristic of landslide dams is the along-valley debris distribution (Hermanns et al. 2011; Strom 2010a). Dams' stability and its possibility to sustain erosion dew to overtopping and/or internal

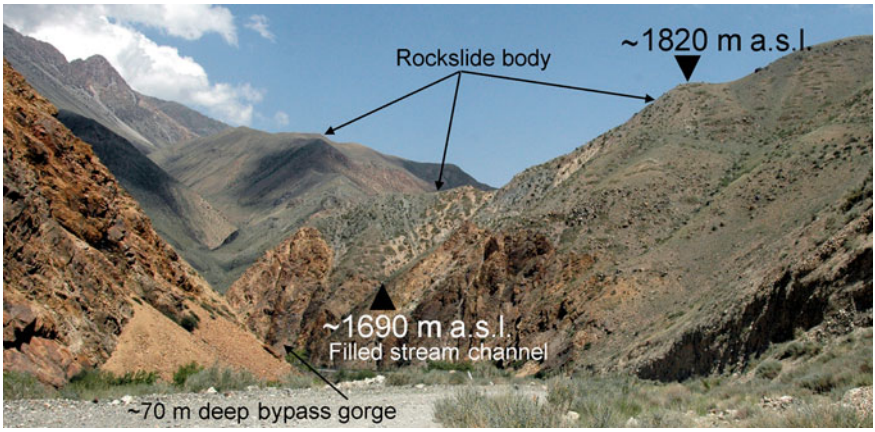

Fig. 20 Bypass gorge eroded through the bedrock at the upstream limit of the Late Pleistocene Kokomeren rockslide dam

piping strongly depend on its compactness. It can be well exemplified by two extreme case studies—the Yashinkul dammed Lake in Pamirs described above (10 on Fig. 1) and the Aksu breached dam in the Tien Shan (42°32.5′ N, 74° E, 21 on Fig. 1). Both of them demonstrate behavior, opposite to that expected according to the DBI of features in question (Strom 2010a). The fist one (see Fig. 13), with DBI = 3.71, much more than 3.08—the lower bound of the instability domain (Ermini and Casagli 2003) is, nevertheless, quite safe and stable feature. Its debris collided with rocky spur at the opposite bank of the river and spread for 3.7 km up and downstream the valley, which decreased dams' height significantly—up to ~50 m maximum. Difference between the lake level and the downstream tip of rock avalanche is about 130 m that returns water table gradient of 0.035, which corresponds to its inclination angle of about 2° only. Such a weak flow is unable to erode blocky carapace that covers the dam body (see Fig. 14), thus there is no possibility for this dam to be breached in any reasonable time.

The giant Aksu dam more than 400 m high (it is a minimal—effective dams' height) and about 1.5 km^3 in volume (Fig. 22) that had blocked rather small river demonstrates opposite behavior. With DBI = 1.94 this feature should be in the stability domain, which upper limit is 2.75 (Ermini and Casagli 2003). Nevertheless the dam was breached and, judging from the absence of lake sediments in the valley upstream, soon after its formation. Most likely that after overtopping rapid turbulent flow at the downstream slope of this very compact dam with along-stream length of 2.5 km only (compare with ~4 km long Usoi and ~3.5 km long Shiva dams of the same order of size) had eroded its proximal lower part very fast.

Analysis of dams' morphology allows optimization of the disaster mitigation measures. For example, if the crest level of the newly formed dam at its distal and proximal parts would be more or less equal, it would be more reasonable to excavate an artificial outlet channel at the distal edge of the blockage, rather than at

Fig. 21 Debris left by outburst flood after breach of the Lower Aral Holocene landslide dam on the isolated ~10 m high cliff about 2 km downstream from the breached dam. *Dark blue arrow* shows river flow direction. *Left* inset—large angular blocks of granite up to 1 m in size carried by the fist, most powerful surge of the debris flow formed by outburst and deposited immediately downstream from the cliff in its 'shadow'. This material was, likely, eroded from the dams' outer part. *Right* inset—cliff is covered by stony angular granite debris left by the following part of the debris flow enriched by smaller fragments, likely from the internal part of the dams' body. Orientation of flattened fragments clearly indicates direction of debris flow motion (*brown arrows*). Note that debris flow was thick enough to leave about 2-m thick debris 10 m above the river level

its central or proximal parts. In this case we can expect slower incision prevented by the bedrock of the valley opposite slope, and, thus, lower peak discharge of the outburst flood (of course, not in the case of the U-shape or box-shape valley).

5.2 *Basic Characteristics of the Landslide Dams' Internal Structure*

The majority of bedrock landslide deposits that form large natural dams both in the Central Asia region and all over the World are characterized by dual internal structure—their lower/internal parts are composed by intensively comminuted and compactly embedded debris that forms giant low permeable blockage core overlaid by

Fig. 22 Breached Aksu dam in the Aksu River valley at the northern slope of the Kyrgyz Range. Remaining part of the dam's body is the smooth hill with top mark at 2150 m a.s.l. 3D Google Earth view

coarse blocky carapace or, sometimes, by huge intact bedrock massifs (McSaveney and Davies 2006; Poschinger et al. 2006; Poschinger 2011; Dunning and Armitage 2011; Hewitt 2006, 2011; Abdrakhmatov and Strom 2006; Strom 1994, 2006, 2010b; Crosta et al. 2011; Davies and McSaveney 2011; Weidinger 2011).

Such internal structure predetermines water filtration pattern and, in favorite cases, possibility of the dam to sustain the superficial and internal erosion. Coarse blocky carapace with large void space supports filtration, while intensively crushed and densely compacted angular fragments of the internal core could form almost impermeable body. Permeable blocky carapace, along with significant up- and downstream debris spreading ensure long-term stability of the above mentioned Yashinkul dam in Pamirs. In general, higher the dam is, wider its upper filtering zone would be and, at favorite conditions, its dimensions could be large enough, so that filtration can compensate the inflow as in the Usoi case (Ischuk 2011). It can explain longevity of some giant dams in Nepal Himalaya (Weidinger 2011), Karakoram (Hewitt 1998, 2006, 2010, 2011) and Argentina (Hermanns et al. 2011) that had blocked rivers with rather large discharge. In such case the higher dam could be much safer than the lower one.

If, however, outer coarse blanket is removed naturally or by excavation and powerful turbulent flow affects the internal comminuted debris directly, dam fails catastrophically, unless the outflow channel incises the bedrock (as on Fig. 20). Such catastrophic breach occurred, in particular, in 1963 at the Issyk Lake (see

Fig. 5) where waves generated by debris flow entering in the lake removed blocky carapace armoring the blockage surface. Subsequent dams breach was quite rapid (Gerasimov 1965). Presence of large amount of intensively fragmented bedrock debris, which is entrained in the water flow leads to its immediate transformation in the rapidly moving debris flow, which was observed during the 1985 Bairaman dam breach in Papua New Guinea (King et al. 1989) and was described above in the Lower Aral landslide case (see Fig. 21). Such debris flows, besides extremely hazardous direct effects on the population and infrastructure, result in significant flood plane aggradation.

On the other hand, intensive debris comminution typical of dams' interiors could support the internal erosion and piping, especially considering sharp contact between comminuted and coarse facies that was observed at some deeply eroded landslide bodies (Strom 2006). Free turbulent water flow through the voids in the blocky carapace could remove fines from the underlying crushed material causing deformations and settlement of the dams' crest.

Sometimes landslide dams' stability is difficult to predict. For example, the 1964 Aini dam described above, the 2002 Yigong dam (Shang et al. 2003), the Tangjiashan dam, formed during the 2008 Wenchuan earthquake (Yin et al. 2011) fail shortly after streams started passing through the spillway trenches excavated across their crests to reduce possible amount of water release. In contrast, the 2010 Attabad dam that blocked the Hunza River still exist while significant discharge passes through the spillway channel built for the same purpose (Delaney and Evans 2011).

In the region in question the most critical problem is the structure and grain-size composition of the interiors of the Usoi dam. Some researchers believe that dams' lower part is composed of a gigantic intact bedrock block(s) (Papirin 1990; Negmatullaev and Ischuk 2011). From my point of view, based on observations of numerous deeply dissected rockslides (Strom 1994, 2006; Abdrakhmatov and Strom 2006), the internal part of this natural dam is composed, most likely, of the intensively crushed and densely compacted rock debris, preventing seepage through more than 3/4 of its body. Objective solution of this issue is urgently necessary both for dam long-term stability assessment and for disaster mitigation measures elaboration.

6 Conclusions

Case studies described herein exemplify geological and geomorphic factors that predetermine formation of river-damming landslides, magnitude of the impoundment (lakes' depth and volume), its longevity and style of dams' breach. All these form the basis of the identification and quantification of hazard related to landslide dams' formation and evolution and plays an important role in selection of technical and social measures aimed to predict and/or to prevent related disasters.

If we consider not only present-day hazard provided by the existing landslide-dammed lakes that might breach, at least hypothetically, but also the long-term hazard stipulated by large-scale slope failures that could occur in future (which is

quite important, in particular, for hydraulic structures with, sometimes, centuries-long life cycle), we must, first, identify areas with higher possibility/probability of such phenomena occurrence. It requires, first, regular regional mapping of landslides, those that caused river-damming in particular and creation of their complete inventory for the entire Central Asian mountainous region. Emphasis must be placed on those zones and more localized areas where recurrent large-scale landslides have occurred in the past and, especially, if there are evidence indicating future instabilities. Regardless of real nature of such clustering, they must be considered as first priority sites for detailed studies of slope stability and monitoring. Extensive dating of past landslides should be considered as an important topic of these investigations providing information, necessary for time-dependant hazard and risk assessment.

Besides, such regional mountain-system-scale studies provide relevant data for statistical analysis of various parameters of landslide dams and dammed lakes relationships in the mountainous region characterized by arid climate, which could differ somehow from those typical of the Mediterranean region or of the Longmenshan mountains with much more humid climate for which such analyses were performed at a regional scale like in the Apennines (Casagli and Ermini 1999) or for one extraordinary triggering event—the 2008 Wenchuan earthquake (Fan et al. 2012).

Site-specific landslide dams' hazard assessment and elaboration of disaster prevention/mitigation measures require data that can be revealed from the detailed analysis of the geology and geomorphology of both existing and past (breached) landslide dams. I want to point out that deeply eroded breached dams are most informative for this purpose, especially in case of extremely large features (Abdrakhmatov and Strom 2006). Same size intact landslide dams like the Usoi blockage, could be hardly studied with same details, due to extreme difficulty of either deep drilling or deep geophysical exploration of such complex and irregular bodies. Better knowledge of how past landslide dams were breached could help in elaboration of optimal disaster mitigation measures in case of similar phenomena in future.

Emptied landslide-dammed lakes also provide unique opportunity to search features at the basal units of lake sediments that can be almost simultaneous with blockage formation, thus providing additional data that can shed light on the nature of triggering event (Strom 2012b). Such studies link landslide damming hazard assessment with seismic hazard assessment which is another critically important prerequisite of disaster mitigation in Central Asia region.

Acknowledgments My work on landslide dams in the Central Asia regions was supported by the International Program on Landslides (IPL) Projects M111, M126 and C106-2, by NATO Science for Peace LADATSHA Project "Prevention of Landslide Dam Disasters in the Tien Shan, Kyrgyz Republic", and by the GEF/UNEP/UNU PALM Project "Sustainable Land Management in the High Pamir and Pamir-Alai Mountains". Field work in the Tien Shan would be impossible without continuous support of Dr. Kanatbek Abdrakhmatov and his colleagues from Kyrgyz Institute of Seismology. I also want to thank my colleagues from Hydroproject Dr. Anatoly Zhirkevich, Dr. Ivan Lobodenko, Mr. Danil Remeniak and Ms. Natalia Pribylova for useful discussions and Prof. Fawu Wang for his suggestion to write this article and thorough review of the manuscript.

References

Abdrakhmatov K, Strom A (2006) Dissected rockslide and rock avalanche deposits; Tien Shan Kyrgyzstan. In: Evans SG, Scarascia Mugnozza G, Strom A, Hermanns RL (eds) Landslides from massive rock slope failure. NATO science series: IV: earth and environmental sciences, vol 49. Springer, Heidelberg, pp 551–572

Abdrakhmatov KE, Tompson C, Weldon P (2007) Active tectonics of the Tien Shan. Bishkek, Ilim, 72 pp (in Russian)

Agakhanjanz OE (1989) Sarez. Hydrometeoizdat Press, Leningrad 110 pp (in Russian)

Alford D, Schuster RL (2000) Introduction and summary. In: Alford D, Schuster RL (eds) Usoi Landslide Dam and Lake Sarez. An assessment of hazard and risk in the Pamir mountains, Tajikistan. ISDR Prevention Series, No 1. UN, New York and Geneva, pp 1–18

Ambraseys N, Bilham R (2012) The Sarez-Pamir earthquake and landslide of 18 February 1911. Seismol Res Lett 83(2):294–314

Belousov TP, Skobelev SF, Strom AL (1994) On estimation of the recurrence period of strong earthquakes of the central Tien Shan (according to the data of absolute geochronology). J Earthq Predict Res 3:226–236

Besstrashnov V, Zhirkevisch A, Strom A (2011) The potential landslide and glacial blockages breach assessment: its influence on the Rogun HPP safety. The Second World Landslide Forum Abstract Book, p 384

Bogdanovich KI, Kark IM, Korolkov BYa, Muchketov DI (1914) Earthquake of the 4th January 1911 in the northern districts of the Tien Shan. Tr Geol Com Ser 89, 270 pp (in Russian)

Bukinich DD (1913) Usoi earthquake and its consequences. Russian Gazette, No 187 (in Russian)

Bull WB (1996) Prehistorical earthquakes on the Alpine fault, New Zealand. J Geophys Res 101(B3):6037–6050

Burger KC, Degenhardt JJ, Giardino JR (1999) Engineering geomorphology of rock glaciers. Geomorphology 31:93–132

Casagli N, Ermini L (1999) Geomorphic analysis of landslide dams in the Northern Apennine. Trans Jpn Geomorphol Union 20(3):219–249

Cheng C-T, Chiou S-J, Lee C-T, Tsai Y-B (2007) Study on probabilistic seismic hazard maps of Taiwan after Chi–Chi earthquake. J GeoEng 2(1):19–28

Costa JE, Schuster RL (1988) The formation and failure of natural dams. GSA Bull 100:1054–1068

Costa JE, Schuster RL (1991) Documented historical landslide dams from around the world. United States Geological Survey Open-File Report 91–239:486

Crosta GB, Frattini P, Fusi N, Sosio R (2011) Formation, Characterisation and Modeling of the Val Pola Rock-Avalanche Dam (Italy). In: Evans SG, Hermanns R, Strom AL, Scarascia-Mugnozza G (eds) Natural and artificial rockslide dams. Lecture Notes in Earth Sciences, vol 133. Springer, Heidelberg, pp 347–368

Crozier MJ (1992) Determination of paleoseismicity from landslides. In: Landslides (Glissements de terrain), Bell DH (ed). Proceedings of the 6th international symposium, vol 2, Christchurch, New Zealand, pp 1173–1180

Davies TR, McSaveney MJ (2011) Rock-avalanche size and runout—implications for landslide dams. In: Evans SG, Hermanns R, Strom AL, Scarascia-Mugnozza G (eds) Natural and artificial rockslide dams. Lecture Notes in Earth Sciences vol 133. Springer, Heidelberg, pp 441–462

Delaney KB, Evans SG (2011) Rockslide dams in the northwest Himalayas (Pakistan, India) and the adjacent Pamir mountains (Afghanistan, Tajikistan), Central Asia. In: Evans SG, Hermanns R, Strom AL, Scarascia-Mugnozza G (eds) Natural and artificial rockslide dams. Lecture Notes in Earth Sciences, vol 133. Springer, Heidelberg, pp 205–242

Delvaux D, Abdrakhmatov KE, Lemzin IN, Strom AL (2001) Landslides and surface breaks of the 1911, Ms 8.2 Kemin earthquake, Kyrgyzstan. Russ Geol Geophys 42(10):1167–1177

Dunning SA, Armitage PJ (2011) The grain-size distribution of rock-avalanche deposits: implications for natural dam stability. In: Evans SG, Hermanns R, Strom AL, Scarascia-Mugnozza G (eds)

Natural and artificial rockslide dams. Lecture Notes in Earth Sciences, vol 133. Springer, Heidelberg, pp 479–598

Ermini L, Casagli N (2003) Prediction of the behavior of landslide dams using a geomorphological dimensionless index. Earth Surf Proc Land 28:31–47

Evans SG, Bishop NF, Smoll LF, Murillo PV, Delaney KB, Oliver-Smith A (2009a) A re-examination of the mechanism and human impact of catastrophic mass flows originating on Nevado Huascarán, Cordillera Blanca, Peru in 1962 and 1970. Eng Geol 108:96–118

Evans SG, Roberts NJ, Ischuck A, Delaney KB, Morozova GS, Tutubalina O (2009b) Landslides triggered by the 1949 Khait earthquake, Tajikistan, and associated loss of life. Eng Geol 109(3–4):195–212

Evans SG, Delaney KB, Hermanns RL, Strom A, Scarascia-Mugnozza G (2011) The formation and behavior of natural and artificial rockslide dams; implications for engineering performance and hazard management. In: Evans SG, Hermanns R, Strom AL, Scarascia-Mugnozza G (eds) Natural and artificial rockslide dams. Lecture Notes in Earth Sciences, vol 133. Springer, Heidelberg, pp 1–75

Evans SG, Hermanns R, Strom AL, Scarascia-Mugnozza G (eds) (2011) Natural and artificial rockslide dams. Lecture Notes in Earth Sciences, vol 133. Springer, Berlin, pp 1–642

Fan X, van Westen CJ, Xu Q, GorumT, Dai F (2012) Analysis of landslide dams induced by the 2008 Wenchuan earthquake. J Asian Earth Sci (Submitted)

Fedorenko VS (1988) Rockslides and rockfalls and their prediction. Moscow State University Publishing House, Moscow (in Russian)

Florensov NA, Solonenko VP (1963) The Gobi-Altai earthquake, Akademiya Nauk USSR, Moscow, 391 pp (in Russian)

Florensov NA, Solonenko VP (1965) The Gobi-Altai earthquake, Israel program for scientific translations (in English). U.S Department of Commerce, Washington, p 424

Gaziev E (1984) Study of the Usoi Landslide in Pamir. In: Proceedings of the 4th international symposium on landslides, vol 1, Toronto, pp 511–515

Gerasimov V (1965) The Issyk catastrophe in 1963 and its effects on geomorphology of the Issyk River Valley. Trans All-Union Geogr Soc 97(6):541–547 (in Russian)

Hadley JB (1964) Landslides and related phenomena accompanying the Hebgen Lake earthquake of August 17, 1959. USGS Professional Paper 345-K, pp 107–138

Hanisch J, Söder C-O (2000) Geotechnical assessment of the Usoi landslide dam and the right bank of Lake Sarez. In: Alford D, Schuster RL (eds) Usoi Landslide dam and lake Sarez. An assessment of hazard and risk in the Pamir mountains, Tajikistan. ISDR Prevention Series, No 1. UN, New York and Geneva, pp 23–42

Hartvich F, Mugnai F, Proietti C, Smolková V, Strom A (2008) A reconstruction of a former rockslide-dammed lake: the case of the Kokomeren River valley (Tien Shan, Kyrgyzstan), Geophysical Research Abstracts 10 EGU General Assembly 2008

Hermanns RL, Niedermann S, Ivy-Ochs S, Kubik PW (2004) Rock avalanching into a landslide-dammed lake causing multiple dam failure in Las Conchas valley (NW Argentina)—evidence from surface exposure dating and stratigraphic analyses. Landslides 1:113–122

Hermanns RL, Hewitt K, Strom A, Evans SG, Dunning SA, Scarascia-Mugnozza G (2011) The Classification of rockslide dams. In: Evans SG, Hermanns R, Strom AL, Scarascia-Mugnozza G (eds) Natural and artificial rockslide dams. Lecture Notes in Earth Sciences, vol 133. Springer, Heidelberg, pp 581–593

Hewitt K (1998) Catastrophic landslides and their effects on the Upper Indus streams, Karakoram Himalaya, Northern Pakistan. Geomorphology 26:47–80

Hewitt K (2002) Postglacial landform and sediment associaton in a landslide-fragmented river system: the Transhimalayan Indus streams, Central Asia. In: Hewitt K et al. (eds) Landscapes of transition. Kluwer, Dordrecht, pp 63–91

Hewitt K (2006) Rock avalanches with complex run out and emplacement, Karakoram Himalaya, Inner Asia. In: Evans SG, Scarascia Mugnozza G, Strom A, Hermanns RL (eds.) Landslides from massive rock slope failure. NATO science series: IV: earth and environmental sciences, vol 49. Springer, Heidelberg, pp 521–550

Hewitt K (2010) Gifts and perils of landslides. Am Sci 98:410–419
Hewitt K (2011) Rock avalanche dams on the Trans Himalayan Upper Indus streams: a survey of Late Quaternary events and hazard-related characteristics. In: Evans SG, Hermanns R, Strom AL, Scarascia-Mugnozza G (eds.), Natural and artificial rockslide dams. Lecture Notes in Earth Sciences, vol 133. Springer, Heidelberg, pp 177–204
Huang RQ, Li WL (2009) Analysis of the geo-hazards triggered by the 12 May 2008 Wenchuan earthquake, China. Bull Eng Geol Environ 68:363–371
Hung JJ (2000) Chi–Chi earthquake-induced landslides in Taiwan. Earthq Eng Eng Seismol 2(2):25–33
Hutchinson JN, Kojan E (1975) The Mayunmarca landslide of 25th April 1974, Peru, Report Ser. No. 3124/RMO. RD/SCE, UNESCO, Paris
Ignatiev IV (1886) The earthquake in the Tokmak district in the 1885. In: Proceedings of the Russian imperial geographic society, vol 22, issue 2 (in Russian)
Ischuk NR (2008) Blockages of river valleys in Tajikistan and their role in assessment of the regional seismicity. In: Proceedings of the 4th international symposium "geodynamics of the intracontinental orogens and geoecological problems", Bishkek, June 15–20, 2008, pp 244–245
Ischuk AR (2011) Usoi rockslide dam and lake Sarez, Pamir mountains, Tajikistan. In: Evans SG, Hermanns R, Strom AL, Scarascia-Mugnozza G (eds) Natural and artificial rockslide dams. Lecture Notes in Earth Sciences vol 133. Springer, Heidelberg, pp 423–440
Ischuk NR (2011b) The origin of the mountain river closures in Tajikistan. Abstract book of the Second World Landslide Forum, Rome 393 p
Ischuk NR (2011b) The Role of glacial deposits in forming modern mountain lake dams in the Pamirs. Georisk No 1, pp 16–29 (in Russian)
Jan CD, Chen CL (2005) Debris flows cased by Typhoon Herb in Taiwan. In: Jacob M, Hungr O (eds) Debris-flow hazards and related phenomena. Praxis, Springer, Berlin, pp 539–556
Jibson RW, Harp EL, Schulz W, Keefer DK (2006) Large rock avalanches triggered by the M 7.9 Denali Fault, Alaska, earthquake of 3 November 2002. Eng Geol 83:144–160
King GCP, Stein RS (1983) Surface folding, river terrace deformation rate and earthquake repeat time in a reverse faulting environment. Spec Publ Calif Div Mines Geol 66:165–176
King GCP, Vita-Finzi C (1981) Active folding in the Algerian earthquake of 10 October 1980. Nature 292:22–26
King J, Loveday I, Schuster RL (1989) The 1985 Bairaman landslide dam and resulting debris flow Papua New Guinea. Q J Eng Geol 22:257–270
Korchevskiy VF, Kolichko AV, Strom A, Pernik LM, Abdrakhmatov KE (2011) Utilisation of data derived from large-scale experiments and study of natural blockages for blast-fill dam design. In: Evans SG, Hermanns R, Strom AL, Scarascia-Mugnozza G (eds) Natural and artificial rockslide dams. Lecture Notes in Earth Sciences, vol 133. Springer, Heidelberg, pp 617–637
Korjenkov AM (2006) Seismogeology of the Tien Shan (within the limits of the Kyrgyztan and ajacent regions). Bishkek, Ilim 289 pp
Korjenkov AM, Mamyrov E, Omuraliev M, Kovalenko VA, Usmanov SF (2004) Rock avalanches and landslides formed in result of strong Suusamyr (1992, M = 7,4) earthquake in the Northern Tien Shan-test structures for mapping of paleoseismic deformations by satellite images. In: Buchroithner MF (ed) High Mountain Remote Sensing Cartography VII (HMRSC VII). Kartographische Bausteine, Band 23, Dresden, pp 117–136
Korup O, Strom AL, Weidinger JT (2006) Fluvial response to large rock-slope failures—examples from the Himalayas, the Tien Shan and the New Zealand Southern Alps. Geomorphology 78:3–21
Krahn J, Morgenstern NR (1976) Mechanics of the Frank slide. In: Rock Engineering for Foundations and Slopes, American Society of Civil Engineers vol 1, pp 309–331
Leonov NN (1960) The 1949 Khait earthquake and geological conditions of its occurrence. In: Proceedings of Russian academy of sciences, geophysical series, No 3, pp 409–424 (in Russian)
Leonov NN (1970) The 1946 Chatkal earthquake. Problems of the engineering seismology 13:64–77 (in Russian)
Luknitskiy PN (1955) Travel over the Pamirs. Molodaya Gvardia Publishers, Moscow (in Russian)

Makarov VI (1977) Newest tectonic structure of the Central Tien Shan. Science Publishers, Moscow. 172 pp (in Russian)
Malamud BD, Turcotte DL, Guzzetti F, Reichenbach P (2004) Landslides, earthquakes and erosion. Earth Planet Sci Lett 229:45–59
McColl ST (2012) Paraglacial rock-slope stability. Geomorphology 153–154:1–16
McSaveney MJ (1978) Sherman glacier rock avalanche. In: Voight B (ed) Rockslides and avalanches, natural phenomena, vol 1. Elsevier, Amsterdam, pp 197–258
McSaveney MJ, Davies TRH (2006) Rapid rock-mass flow with dynamic fragmentation: inferences from the morphology and internal structure of rockslides and rock avalanches. In: Evans SG, Scarascia Mugnozza G, Strom A, Hermanns RL (eds) Landslides from massive rock slope failure. NATO science series: IV: earth and environmental sciences, vol 49. Springer, Heidelberg, pp 285–304
Meghraoui M, Doumaz F (1996) Earthquake-induced flooding and paleoseismicity of the El Asnam, Algeria, fault-related fold. J Geophys Res 101(B8):17617–17644
Mushketov IV (1890) The Vernyi earthquake of 28/05 (9/06) 1887. In: Proceedings of Geological Committee, 10(1), St. Petersburg, 154 pp (in Russian)
Negmatullaev SH, Ischuk NR (2011) The Sarez Lake: sizing up the investigations. Georisk 1:8–14 (in Russian)
Neshikhovskiy RA (1988) Floods on rivers and lakes. Hydrometeoizdat, Leningrad, 184 pp (in Russian)
Owen LA, England J (1998) Observations on rock glaciers in the Himalaya and Karakoram mountains of Northern Pakistan and India. Geomorphology 26:199–213
Owen LA, Kamp U, Khattak GA, Harp EL, Keefer DK, Bauer MA (2008) Landslides triggered by the 8 October 2005 Kashmir earthquake. Geomorphology 94:1–9
Papirin LP (1990) Main regularities of water seepage through the Usoi blockage. TajikNIINTI, Dushanbe, pp 6–11 (in Russian)
Paramonov BA (1969) Formation of the Usoi blockage relief. Bull Moscow State University 5:110–112 (in Russian)
Plafker G, Eriksen GE (1978) Nevados Huascaran avalanches, Peru. In: Voight B (ed) Rockslides and avalanches, vol 1. Elsevier, Amsterdam, pp 277–314
Poschinger Av (2011) The flims rockslide dam. In: Evans SG, Hermanns R, Strom AL, Scarascia-Mugnozza G (eds) Natural and artificial rockslide dams. Lecture Notes in Earth Sciences, vol 133. Springer, Heidelberg, pp 407–421
Poschinger A von , Wassmer P, Maisch M (2006) The flims rockslide: history of interpretation and new insights. In: Evans SG, Scarascia Mugnozza G, Strom A, Hermanns RL (eds) Landslides from massive rock slope failure. NATO science series: IV: earth and environmental sciences, vol 49. Springer, Heidelberg, pp 329–356
Preobrajensky J (1920) The Usoi Landslide. Geol. Comm., Papers on Applied Geol., vol 14, 21 pp (in Russian)
Pushkarenko VP, Nikitin AM (1988) Experience in the regional investigation of the state of mountain lake dams in Central Asia and the character of breach mudflow formation. Landslides and mudflows (in two volumes), UNESCO/ UNEP, Moscow (in Russian)
Reizvikh VN, Krukovskiy GL, Nikitin AM (1971) Causes and conditions of the Yashinkul Lake outburst. Collection of papers of the Tashkent Hydro-Meteorological Observatory (4):49–95 (in Russian)
Rezvoi DP, Rezvoi PD (1969) Lake that disappeared. Priroda(Nature) 7:81–83 (in Russian)
Rezvoi DP, AlexeenkoAV, Bolgar BD, ErmolenkoYuA, Marushkin IA, Rezvoi PD, Soloshenko II (1971) Rockfall-dammed lakes of the Alai Range—important factor of the high mountain relief formation. Reports and News of the L'vov branch of the Ukraine Geographical Society (1968–1969). Lvov University Publishing House, pp 71–73 (in Russian)
Schuster RL, Costa JE (1986) A perspective on landslide dams. In Schuster RL (ed) Landslide dams: processes, risk and mitigation. American Society of Civil Engineers, New York, NY, Geotechnical Special Publication No. 3, pp 1–20

Schuster RL, Evans SG (2011) Engineering measures for the hazard reduction of landslide dams. In: Evans SG, Hermanns R, Strom AL, Scarascia-Mugnozza G (eds) Natural and artificial rockslide dams. Lecture Notes in Earth Sciences, vol 133. Springer, Heidelberg, pp 77–100

Shang Y, Yang Z, Li L, Liu D, Liao Q, Wang Y (2003) A super-large landslide in Tibet in 2000: background, occurrence, disaster, and origin. Geomorphology 54:225–243

Sheko AI (1968) The Usoi blockage stability and the Lake Sarez breach assessment. Bull Moscow Nat Invest Soc Geol Sect 4:151–152 (in Russian)

Sheko AI, Lekhatinov AM (1970) Current state of the Usoi blockage and tasks of future studies. In: Materials of Scientific-technical meeting on the problems of study and forecast of the mudflows, rockfalls and landslides, Dushanbe, pp 219–223 (in Russian)

Shpilko GA (1915) New data on the Usoi blockage and the Sarez Lake. In: Proceedings of the Turkestan Department of Russian Geographical Society, vol 11, pp 11–17 (in Russian)

State Water Inventory (1964–1981) Annual data on the mainland superficial water regime and resources 5 (basins of the Central Asian Rivers)

Strom AL (1994) Mechanism of stratification and abnormal crushing of rockslide deposits. In: Proceedings of 7th international IAEG congress, vol 3, Balkema, Rotterdam, pp 1287–1295

Strom AL (2006) Morphology and internal structure of rockslides and rock avalanches: grounds and constraints for their modeling. In: Evans SG, Scarascia Mugnozza G, Strom A, Hermanns RL (eds) Landslides from massive rock slope failure. NATO science series: IV: earth and environmental sciences, vol 49. Springer, Heidelberg, pp 305–328

Strom AL (2010a) Evidence of momentum transfer during large-scale rockslides' motion. In: Williams AL, Pinches GM, Chin CY, McMorran TG, Massei CI (eds) Geologically active. In: Proceedings of the 11th IAEG Congress, Auckland, New Zealand, 5–10 September 2010, Tailor & Francis Group, London, pp 73–86

Strom A (2010b) Landslide dams in Central Asia region. Landslides. J Jpn Landslide Soc 47(6):309–324

Strom AL (2012a) Effects of rockslides and rock avalanches on hydropower schemes in the Naryn River valley. Proc 11 ISL (in press)

Strom AL (2012b) Use of indirect evidence for the prehistoric earthquake-induced landslides identification. In: Proceedings of the international symposium on earthquake-induced landslides, Kiryu, Japan, November 7–9, 2012

Strom A (2012c) Usoi landslide and Lake Sarez. In: Bobrowsky P (ed) Encyclopedia of natural hazards. Springer, Heidelberg (in press)

Strom AL, Abdrakhmatov KE (2004) Clustering of large rockslides: the phenomenon and its possible causes. In: Lacerda WA, Ehrlich M, Fontoura AB, Sayao A (eds) Landslides: evaluation and stabilization. Taylor & Francis Group, London, pp 317–320

Strom AL, Abdrakhmatov KE (2009) International summer school on rockslides and related phenomena in the Kokomeren River valley, Tien Shan, Kyrgyzstan. In: Sassa K, Canuti P (eds) Landslide disaster risk reduction. Springer, Berlin, pp 223–227

Strom AL, Groshev ME (2009) Mysteries of rock massifs destruction. In: Abbie M, Bedford JS (eds) Rock mechanics: new research. Nova Science Publishers, Hauppauge, pp 211–231

Strom AL, Korup O (2006) Extremely large rockslides and rock avalanches in the Tien Shan, Kyrgyzstan. Landslides 3:125–136

Strom AL, Nikonov AA (1997) Relations between the seismogenic fault parameters and earthquake magnitude. Izvestia Phys Solid Earth 33:1011–1022

Strom AL, Stepanchikova P (2008) Seismic triggering of large prehistoric rockslides: pro and con case studies. In: Proceedings of the international conference on management of landslide hazard in the asia-pacific region (satellite symposium of the first world landslide forum), pp 202–211

Stuiver M, Reimer PJ (1993) Extended ^{14}C data base and revised CALIB 3.0 14C age calibration program. Radiocarbon 35:215–230

Walker M (2005) Quaternary dating methods. Willey, New York, 286 pp

Weidinger JT (2011) Stability and life span of landslide dams in the Himalayas (India, Nepal) and the Qin Ling Mountains (China) In: Evans SG, Hermanns R, Strom AL, Scarascia-Mugnozza G (eds)

Natural and artificial rockslide dams. Lecture Notes in Earth Sciences, vol 133. Springer, Heidelberg, pp 243–277

Wells DL, Coppersmith KJ (1994) Empirical relationships among magnitude, rupture length, rupture area, and surface displacement. Bull Seis Soc Am 84:974–1002

Wu S, Wang T, Shi L, Sun P, Shi J, Li B, Xin P, Wang H (2010) Study on catastrophic landslides triggered by 2008 great Wenchuan earthquake, Sichuan, China. J Eng Geol 18(2):145–159

Yin Y, Wanf F, Sun P (2009) Landslide hazards triggered by the 2008 Wenchuan earthquake, Sichuan, China. Landslides 6:139–151

Yin Y, Zheng W, Li X, Sun P, Li B (2011) Catastrophic landslides associated with the M8.0 Wenchuan earthquake. Bull Eng Geol Environ 70(1):15–32

Zaninetti A (2000) Monitoring and early warning system. In: Alford D, Schuster RL (eds) Usoi landslide dam and Lake Sarez. An assessment of hazard and risk in the Pamir mountains, Tajikistan. ISDR Prevention Series, No 1. UN, New York and Geneva, pp 63–72

Zhirkevich AN, Besstrashnov VM, Shilina EN, Strom AL (2011) Discharge assessment of outburst floods caused by the existing and potential natural blockages breach in the Vakhsh River basin upstream from the planned Rodun Dam. Hydrotech Constr 12:38–46 (in Russian)

Social Benefits of Landslide Prevention and Mitigation in Hong Kong, China

Zhong Qi Yue

Abstract The urban development and infrastructure of Hong Kong are basically built on hillside slopes of 20–50°. Landslide is the severest geohazard in Hong Kong. Since 1977, engineers and researchers in Hong Kong have done tremendous work and investigations in landslide prevention and mitigation. They have made many significant contributions to Hong Kong. At present, Hong Kong slope safety standard has become one of the highest standards in the world. This paper gives a brief summary of landslide disaster prevention and mitigation history in Hong Kong. It discusses in detail eight social benefits. They are the lowest landslide fatality in mountainous urban developments, enhancing social stability and governance, job and training opportunities, sustainable development and prosperity, rehousing squatters for resolving social issues, self-restricted land use for urban development, technology innovation and advancement, and local and international recognitions. It points out five difficulties encountered during landslide disaster prevention and mitigation. They are incorrect landslide causes and mechanisms, change in slope safety standard, dramatic change in rainfall, doubts about long term investment nature, and no right on land use. Finally, it is remarked that Hong Kong has established, trained and maintained a team of hundred or thousand competent geotechnical engineers who can address any technical challenges in future urban developments in the sea and/or on the mountains for Hong Kong.

Keywords Landslides · Disaster prevention and mitigation · Land use · Social benefits · Slope safety · Urban model

Z. Q. Yue (✉)
Department of Civil Engineering, The University of Hong Kong,
Hong Kong, People's Republic of China
e-mail: yueqzq@hku.hk

F. Wang et al. (eds.), *Progress of Geo-Disaster Mitigation Technology in Asia*,
Environmental Science and Engineering, DOI: 10.1007/978-3-642-29107-4_3,

1 Introduction

Hong Kong is located on east side of Pearl River Delta Mouth in China (Fig. 1). Its land area is 1,104 km^2, about 6 and 9 % of the total land areas of New York and Beijing, respectively. It consists of Hong Kong Island, Kowloon Peninsula, New Territories, Lantau Island and other 230 small islands. Their mountains respectively have the highest peaks of 552, 602, 957, and 934 m above the surrounding sea level. At present, Hong Kong has populations of seven millions and is recognized as an international centre for finance, trade, business, dense urban development and tourism. On the other hand, Hong Kong has also well known for its effort in landslide prevention and mitigation in geotechnical community (GEO 2007; Yue 2003, 2004a, 2006).

In the past, Hong Kong experienced several severest landslide disasters. Landslide is the most common and severest geological hazards. The urban developments in Hong Kong are mainly on hilly natural terrains of slope angles from 20–50°. The massive excavation and build-up of platform lands for urban developments over past 150 years have resulted in many man-made slopes and retaining walls. People are living on potentially dangerous slopes. Hilly terrains, strong storms, dense land use, roads on hill slopes, thick and abnormally weathered soils, groundwater and surface runoff are the factors leading common occurrences of landslide hazards. In particular, the rainfall is about 2,000–3,000 mm annually and falls mainly during the wet season from May to September. High rainfall intensity of more than 50 mm/h or 200 mm/day is common. Each landslide can cause disasters in Hong Kong due to its dense urban development and can cause a loss of confidence in Hong Kong dense urban development on mountains. Therefore, the term “Landslide prevention and mitigation” is used in Hong Kong and includes the conventional concept or term “landslide disaster prevention and mitigation”.

2 Brief History of Landslide Prevention and Mitigation in Hong Kong

History of landslide prevention in Hong Kong can be divided into two periods (GEO 2007). Before 1977, the government did not have a specific organization or office specialized in slope safety and landslide prevention. Then slope design and construction in general were not needed to be controlled, checked and approved by the Government for quality and safety standards. After 1977, the government established a specific organization to control slope safety and prevent landslide disaster.

Fig. 1 Topographic map of Hong Kong and surrounding areas (based on Google Map)

3 First Period Without Specialized Governmental Control Office

This first period can be sub-divided into five stages: the first stage before 1989 when Hong Kong changed from a fishing village to a town; the second stage from 1889 to 1937 before the World War II; the third stage from 1937 to 1946 during the World War II; the fourth stage from 1946 to 1971 post the World War II; and the fifth stage from 1972 to 1976 for the establishment of the governmental control on landslide hazards.

Before 1889, the population was about 200,000. Reports and records on landslide hazards were not available at present. The earliest known record on landslide hazards was in 1889. The earliest complete record of landslide disaster is the event happened on July 17, 1925 at middle levels of Hong Kong Island. The disaster destroyed five buildings and reduced 75 fatalities. Before the landslide, there were continued heavy rains for 3 days in Hong Kong. Two hours before the landslide occurrence, Hong Kong Observatory recoded a rainfall of 126 mm.

During the World War II, there were few records about landslides in Hong Kong. After the World War II, more and more people migrated to Hong Kong. From 1945 to 1971, the populations increased from 0.5 to 4 millions. Many squatters and buildings were constructed on hillside slopes. The recorded fatalities by landslide were more than 230. The severest disaster event was caused by a landslide occurred on June 12, 1966. The heavy rainfall triggered more than 700 landslides that caused a total of 64 fatalities, 2,500 people homeless and 8,000 people relocated to other places. However, the government did not put landslide disaster prevention onto the agenda.

Consequently, from 1972 to 1976, landslides further killed about 200 people. On June 18, 1992, two devastating landslides occurred. One was at the weathered volcanic hillside slope with dense high-rise buildings at the upper west middle level of Hong Kong Island. The soil and rock debris flows killed 67 people and destroyed a high-rise building. The other was at a fill slope forming a part of a hillside road embankment at Sau Mau Ping in Kowloon. The mud avalanche killed 71 people and injured 60 people. Moreover, on August 25, 1976, a devastating landslide occurred at an adjacent fill slope forming a part of another hillside road embankment at Sau Mau Ping. The mud avalanche killed 18 people and injured 24 people. Some details of old landslides in Hong Kong can be found in Lumb (1975).

4 Second Period with Specialized Governmental Control Office

4.1 Establishment of GEO in 1977

According to Morgenstern (2000), the 1976 road fill slope disaster had wider implications because the 1972 road fill slope disaster was located nearby and also in man-made fills. The final report of the commission of inquiry concluded about the cause of the 1972 road fill slope failure that no fault was found in the design and construction of the road embankment. Therefore, the 1976 road fill slope failure made this conclusion suspect. Furthermore, Hong Kong had developed well and become richer. The populations were up to five millions. Landslide risk was much higher. The public had much higher expectations on slope safety and landslide disaster reduction. For example, Hong Kong Independent Commission Against Corruption (ICAC) was established on February 15, 1974.

Consequently, the government appointed an Independent Review Panel on Fill Slopes to advise on the cause of the 1976 road fill slope failure. Finally, the Panel recommended that "a control organization be established within the government to provide continuity throughout the whole process of investigations, design, construction, monitoring and maintenance of slopes in Hong Kong". In July 1977, the government established the Geotechnical Control Office (GCO) to control man-made slope safety. In 1991, GCO was renamed as Geotechnical Engineering Office (GEO). The establishment of GCO (GEO) has been proved to be the first major turning point in the evolution of landslide prevention in Hong Kong. GEO has grown to be an internationally recognized centre of excellence (Morgenstern 2000).

4.2 Five Stages of Landslide Prevention and Mitigation

Since 1977, Hong Kong has done tremendous works on landslide prevention and urban slope greening. The development of landslide prevention can be further divided into six stages. Details of the six stages are discussed below.

After the GEO establishment in 1977, Hong Kong introduced legislations and regulations to check and approve each new slope design and construction projects and site inspections and supervisions. Building ordinance was revised in 1980 and further revised in 1995. So, checking and inspection of slope construction for private projects can be carried out by the Government Departments without early notice. Slope projects for the Government can be checked and approved internally. The technical aspects are consulted with GEO. In addition, registration of man-made slopes was carried out. At present, more than 39,000 government and 1,800 private man-made slopes have been registered in the Hong Kong Slope Safety Website at http://hkss.cedd.gov.hk. The slope safety and related geotechnical information are open to public free of charge. Third, a long-term landslide prevention project was lunched to assess and upgrade existing (old) man-made slopes to current safety standards. From 1977 to 1981, 104 old slopes were upgraded with a total cost of HK$321 millions.

In 1982, the annual rainfall was 3,200 mm. In May and August 1982, heavy rainfall caused more than 700 landslides which resulted in 27 fatalities. Among them, 23 fatalities were people living in squatters on hillside slopes. Consequently, the government lunched rehousing squatters and upgraded and greened squatter slopes. From 1982 to 1991, 327 old slopes were upgraded with a total cost of HK$605 millions.

From 1992 to 1995, several fatal landslide disasters occurred and killed 11 fatalities. Four landslides were well noted. They are the Banguio Villa mudflow in 1992, the Kwun Long Lau old masonry retaining wall collapse in 1994, the Fei Tsui Road landslide-debris flow in 1995, and the Shum Wan Road landslide-debris flow in 1995. Since 1992, the government has launched public educations on slope safety. From 1992 to 1995, 238 old slopes were upgraded with a total cost of HK$ 435 millions. The independent view reports on the fatal landslides recommended the government to undertake a systematic approach on the landslide risk in Hong Kong. This is a second major turning point in the evolution of landslide prevention in Hong Kong.

Subsequently, the government launched a 5 years accelerated landslip prevention programme. From 1996 to 2000, 1,003 old slopes were upgraded with a total cost of HK$3656 millions. In addition, the government launched a long-term project on systematic landslide investigations in 1997. Private consultants are contracted to investigate each fatal or economically important landslide. The purposes are to understand landslide mechanism, to learn lessons from nature for better slope design, to clarify responsibilities for different parties involving a failure case, and to obtain factual data. The findings are published by the government for public use. The report can be used in court or arbitration.

In 2000, the government further lunched a 10-year extended landslip prevention project. From 2001 to 2009, 2,273 old slopes were upgraded with a total cost of HK$ 8445 millions. Quantitative risk assessment method was also developed and used in the planning and selection of substandard slopes to be upgraded. The objective is to reduce the quantitative landslip risk to 25 % of that in 1977. On November 30, 2007, the government further announced to spend HK$600 millions for landslip prevention on both man-made and natural slopes from 2010 to 2020. The landslip prevention project was renamed to the landslip prevention and mitigation project. The focus only on man-made slopes has been changed to both man-made and natural terrain slopes, which is the third major turning point.

4.3 Slope Safety Management System

As summarized by Malone (1998), a slope safety management system has been developed and used in Hong Kong. They can be used by others for better and effective preventing and mitigating of landslide hazards and developing green cities. The components of the system include the following items.

Upgrade existing sub-standard slopes and retaining walls, geotechnical control on new slope works, public educations, landslide investigation, and natural terrain studies are the five items discussed above. Each landslide event is a natural experiment of slope instability and failure. It gives researchers and engineers the opportunity to learn the landslide mechanisms and to better understand the landslide characteristics of a site or region. Landslide investigation likes a doctor to see patients and to accumulate experience about the slope stability. The findings have been used to update the standards and regulations.

The sixth is the standards and regulations for slope safety. Hong Kong learnt the best methods and experience in the world and attracted various talents. Based on the specific local geological and urban conditions, HK developed many standards and regulations and techniques for better slope safety system and management. The seventh is the Slope Safety Technical Review Board launched in 1998. Three persons of high international reputations in slope engineering and landslide prevention are appointed to be the members of 3 year term. They review GEO work and make comments and suggestions for improvements and refinements. The eighth is slope safety audit and maintenance. The government employed consultants to check private slopes for their safety and upgrading if they were found not up to the current standards. A Dangerous Hillside Order (DHO) with liability will be issued to the private owners to force them for further investigations and upgrading. GEO checks and audits slope maintenance works of other government works department. The ninth and tenth are respectively the public landslide warning system and the emergency service on landslide disasters, which are discussed below.

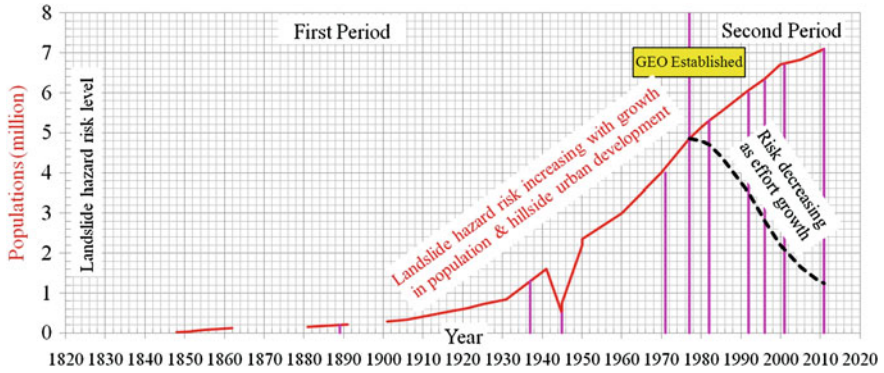

Fig. 2 Variation of landslide hazard risk with growth in population and hillside urban development and effort in landslide prevention and mitigation in Hong Kong

5 Social Benefits of Landslide Prevention and Mitigation in Hong Kong

Landslide prevention and mitigation are a long term non-profit driven work of social importance and urban relevance. They cover the fields of natural science, engineering, construction, social science, urban planning and development, economy, tourism, law, landscaping. Better and effective slope safety can offer invaluable assets to the sustainable development and properties of mountainous cities and people oriented harmonic society. The landslide prevention in Hong Kong over the past 35 years has brought many social benefits and added values to the stability and property. Some of them are discussed below.

5.1 No. 1 Lowest Landslide Fatality

The primary objective of landslide prevention is to save lives. The second objective is to reduce landslide hazards and economic loss. From 1949 to present, the total number of landslide fatalities recorded in Hong Kong is 473. About 90 % happened before 1977. From 1984 to present, the number of landslide fatalities is 21. As shown in Fig. 2, the populations increased from about 2 millions to 5 millions from 1949 to 1976. The populations further increased from 5 millions to 7 millions from 1977 to 2012. The population density is about 7000 person per kilometre square, which is one of the highest population densities in the world. These data can show that the landslide risk and fatality had increased quickly as the populations increased, when there was no specialized governmental control on landslide hazards before 1977. The landslide risk and fatality have decreased quickly when a specialized government control has been imposed on landslide

hazards since 1977, although the populations are still increasing. At present, Hong Kong is a large mountainous city of the highest population density and the lowest landslide fatality.

5.2 No. 2 Enhancing Social Stability and Governance

In this media-dominated and free society of Hong Kong, public awareness on landslide risk and hazard has been raised. As a majority of people are living and working on high hillside slopes, they demand a stable, safe and environmental-friendly slope ground. Such demand and need can be further magnified by the extremely high property values for their houses and/or flats in high-rise building. Over the last 35 years, in particular since 1995, geotechnical engineers have upgraded the man-made slope grounds with the highest safety standards in the world. Furthermore, they have also landscaped these slope grounds with many techniques for natural appearance and integrating their visual impacts with the surrounding environments. The numerous man-made slopes in urban areas have been greener and greener. For many years, Hong Kong has not experienced any public demonstration because of landslide disasters, although public demonstrations can take place almost everyday. Such fundamental changes and achievements have contributed to the social stability and prosperities and won the confidences of general public that geotechnical engineers can make their home slopes safe and green with limited financial resources.

5.3 No. 3 Job and Training Opportunities

Slopes are everywhere in Hong Kong. Each slope must occupy a piece land. Hence, the public investments in slope safety and landslide prevention and mitigation have to be carried out by many local technical staff and engineers. Techniques and methods from overseas have to be tested and examined for local use. Such long term and stable investments have offered jobs and training opportunities to many university graduates, young engineers and workers. The practical experiences on slope design, construction and management have been invaluable assets for young people to grow up and become professional engineers or managers. They are of the noticeable importance when economic activities turned downward in Hong Kong during the several world financial crises in the past 15 years. Furthermore, engineers have been the leaders responsible for the landslide hazard prevention and remediation projects. As a result, a strong team of many hundreds or several thousands engineers equipped with slope safety expertise and landslide prevention experience have been developed and accumulated in Hong Kong. They are readily available for various urban developments of the society in difficult grounds of mountains or sea beds.

5.4 No. 4 Sustainable Development and Prosperity

For a developed and rich society, it is important to undertake sustainable development and to make further prosperity. However, how to make sustainable development and prosperity for such society with huge economic size is not an easy task. Different people can have different opinions or ways on this issue/task. Promoting social awareness on landslide hazard risks can be one natural way to frequently alert and educate people that their developed society is vulnerable to disasters.

About 106 auto-rainfall gauges are installed and maintained by the government across Hong Kong. Their data are used for landslide warning publicly via media. The criteria for issuing a landslide warning are (1) the 24 h rainfall is greater than 175 mm in large area or (2) the 60 min rainfall is greater than 70 mm. For example, a landslide warning was issued on June 24, 2005. The maximum hourly rainfall reached 150 mm. The maximum daily rainfall was about 700 mm. There were 240 flooding events and 28 landslides. 90 airplanes were delayed and 50 ships were cancelled. All schools were closed in the afternoon. The landslides did not cause any injury. The day became an unexpected public holiday.

In addition, the government keeps a 24-hour and year-round emergent service to provide slope stability advice on actions to be taken in case of danger arising from landslides. The actions have closure of roads, evacuation of buildings, and/or urgent slope repair works. Consequently, the general public can be protected from landslide hazards and public services disrupted by landslides can be restored. For example, emergence services were provided on June 7, 2008 when Hong Kong encountered a rainfall of 1100 years return period. From 8:00 am to 9:00 am, the rainfall was 145.5 mm. The daily rainfall was 307.1 mm. The new expressway for Hong Kong International Airport on north Lantau Island was blocked by landslide debris from the above natural terrains. The term-contractor for the landslide prevention works was deployed to undertake the road debris clearance and re-open the expressway quickly. This emergence service by the contractor had a 20 % increase over the normal fee, which was written in the term-contract document in advance.

5.5 No. 5 Rehousing Squatters

As discussed above, severe landslide disasters occurred in squatters in 1982. Subsequently, the government launched rehousing squatter project. About 74,000 people were relocated into public house buildings, which restored a large amount of hillside land areas for beautifying the natural environment. An example is shown in Fig. 3 where the squatters on the hillside in 1970s were demolished and the slope has been restored into the natural green environment.

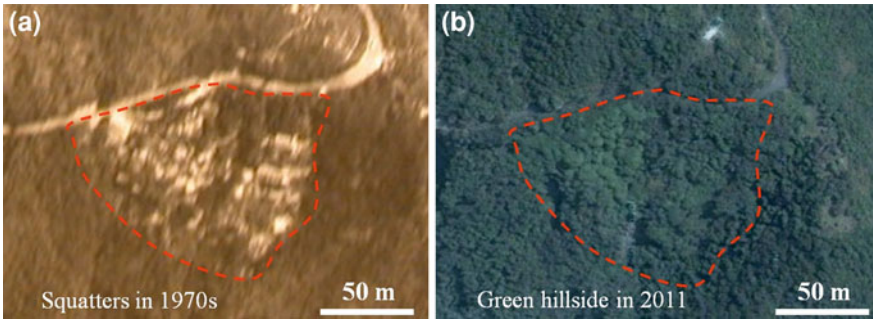

Fig. 3 Comparison of a hillside slope with squatters in 1970s and greening in 2011

As shown in Fig. 2, after the World War II, populations in Hong Kong have continuously increased from about 0.5 to 7 millions. Demanding for lands and houses has been extremely high. Land is extremely valuable in Hong Kong. In the old days, hundred thousands people migrated to Hong Kong and constructed their squatter homes on hillside slopes. The property values in Hong Kong have been unavoidable for many people. Therefore, clearance and demolishing the squatters are also important but difficult to undertake. They have been social issues that the government has not been able to resolve it for many years. The landslide disasters in 1982 was used as an opportunity for initiating, executing and demolishing some squatters on unsafe hillside slopes and re-settling the residents into high-rise public buildings, which resolved the issues partially and peacefully. At present, there are still hundred and thousands people living in various squatters across Hong Kong.

5.6 No. 6 Self-Restricted Land Use for Urban Development

Among the total land area of 1,104 km^2, Hong Kong has used only about 263 km^2 for urban development, about 14 % of the urban area of London. In other words, about 23.8 % of the total land area is urban or built-up land (HKSARG 2010). It can be further broken down as about 6.9 % for residential use, 5.1 % for roads, railways and airport, and 5.0 % for commercial, industrial and institutional use. The rest 7.8 % is for open space, cemeteries, vacant and other uses. The 79 % un-developed lands are woodland, shrubland and grassland, agricultural land, fish ponds, wetland, barren land and reservoir water area. A majority of these un-developed lands (about 66.7 %) are woodland, shrubland and grassland (country parks) have been protected by laws and regulations for many years. The agricultural land is about 4.6 %. In addition, Hong Kong has a total sea area of 1,650 km^2. The reclamation land is 68 km^2, 4.1 % of the total sea area.

Therefore, the land use in Hong Kong is self-confined and restricted, which protects and benefits the natural ecological environments. Such land use can reduce landslide hazard areas so that limited landslide prevention and mitigation resources can be concentrated onto the most needed urban areas. For example,

Fig. 4 Large banyan trees growing out of old masonry retaining walls on Bonham Road, Hong Kong Island

large trees have been growing up in old masonry retaining walls, which has been an important and beautiful landscape and heritage element witnessing the dense urban history (Fig. 4). Consequently, a dense urban development model on hilly terrains has been developed and established (Fig. 5). The large amounts of people, activities and resources have been concentrated on small land areas on both sides of Victoria Harbour, which has made Hong Kong internationally well known and become a tourism centre and a convenient business and goods centre.

5.7 No. 7 Technology Innovation and Advancement

The demands for best landslide prevention and mitigation and highest slope safety standards have enabled geotechnical engineers and researchers to use and develop the best slope stabilization measures, techniques and standards. They are applicable to local geological and dense urban conditions. They are changeable to accommodate the public needs. For example, pre-stressed ground anchors were commonly used in 1970 and 1980s. Due to their high maintenance cost, they have been almost abandoned. On the other hand, the urban environments and trees on slopes have become mature and the land spaces are limited. Consequently, soil nailing has become a slope

Fig. 5 Dense urban development with high-rise buildings on Victoria Harbour and below the Peak of 552 m above the sea level on Hong Kong Island

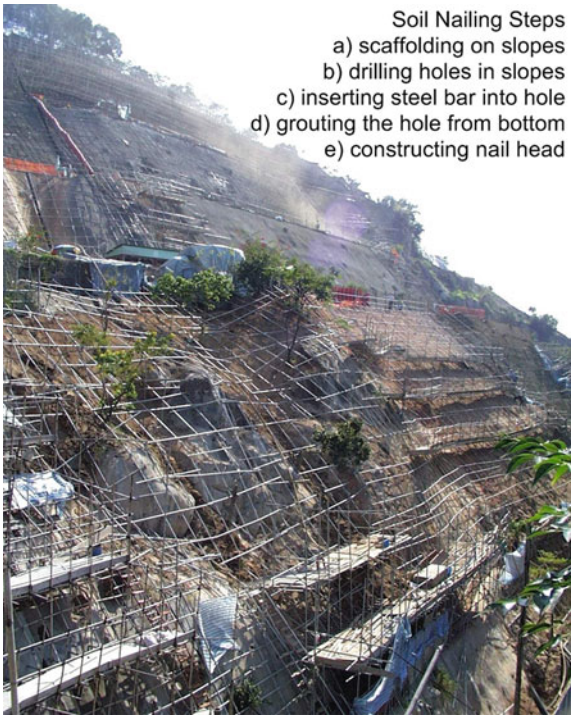

Fig. 6 Ongoing construction of soil nails for stabilizing existing cut slope in Hong Kong

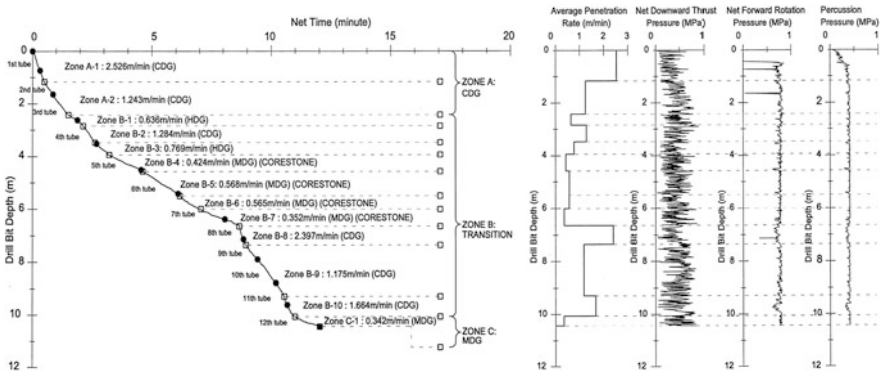

Fig. 7 Results of automatic process monitoring for drilling a soil nail hole in weathered granite slope by air-driven rotary-percussive drill with down-the-hole hammer in Hong Kong

upgrading measure of choice because its flexibility and robustness since 1995 (Fig. 6). Landscaping treatment and bioengineering on slopes with hard covers (such as shotcrete) have been widely adopted since 2000. In recent years, many large check dams have been constructed at stream toes for mitigating debris flow hazards on natural terrains. Two examples are briefly discussed below.

Geotechnical engineering requires an accurate knowledge of the mechanical behaviour of soils and rocks and of their spatial distributions in the ground. Delineating the spatial distribution of different geomaterials in depth has always been an important yet difficult task. Unforeseen ground conditions have been cited as the most significant factor in causing construction delays and large slope failures in Hong Kong. The formation of soil nail holes requires mechanically detaching and removing geomaterial from the cut face of drill bit in the hole, which is a mechanical failure process of the in situ geomaterials with depth. Therefore, automatic drilling process monitoring (DPM) technique has been developed and used to delineate the strength distribution of geomaterials along each soil nail hole (Yue et al. 2002). Figure 7 shows an example of the DPM results, where the Zone B-8 at the depth 7 m is clearly a weak zone. The DPM is shown to be an in situ technique for continuous measurement of mechanical strength and spatial distribution of ground geomaterials covering caverns, soft or weak soils to hard rocks. More details can be found in Yue (2004b, 2005, 2006, 2010, 2011) and Yue et al. 2003, 2004a–c, 2006, 2007, 2008).

The second example is about the design calculation of soil nailing for slopes. Since 1979, it has been recommended and stipulated that "(2) Low and high risk slopes. Non-circular analytical methods, such as those by Janbu (1972) or Morgenstern and Price (1965), are recommended for most soil slopes in Hong Kong. However, a sliding block or Bishop (1955) circular analysis may occasionally be more appropriate." (GEO 2000). It was well accepted that the different slice methods would result in slight differences in the critical and minimum factor of safety values for slopes. The difference was normally less than 10 %.

Consequently, both simplified Janbu and Morgenstern and Price methods were used in soil nailing design in Hong Kong. However, Wan and Yue (2004, 2005) showed that the two different slice methods would result in substantial differences in the soil nail design results and the associated construction costs for upgrading the cut slopes to the same current safety standards. The simplified Janbu method based soil nail design would be 10–90 % more expensive than that based on the Morgenstern–Price method. They suggested the geotechnical industry to use Morgenstern–Price method in soil nail design since it satisfies both moment and force equilibriums of slices. Savings could be achieved, which would not sacrifice the design standards. Shiu et al. (2006) carried out further parametric studies on this issue. Consequently, GEO (2008) recommended and stipulated that "The calculated factors of safety given by methods that consider force equilibrium or moment equilibrium only may not give correct results. Therefore, only methods that satisfy both force and moment equilibrium should be used for the analysis (Shiu et al. 2006)."

5.8 No. 8 Local and International Recognitions

Investments in landslide prevention and mitigation cannot obtain direct returns. Such efforts are non-profit oriented. They are for public and community at large and need long term effort and investment by the society and government. It is roughly estimated that the government has directly invested a total of HK$16–30 billions in landslide prevention and mitigation since 1977. A majority of the cost are for salaries of local personnel working on landslide prevention and mitigation. As result, everyone in the society has benefited the safe and green environments of urban slopes and retaining walls. Large trees growing out of old masonry retaining walls look like bonsais among high-rise buildings (Figs. 4 and 5).

The society and government have further won recognitions regionally and internationally. For examples, the Mayor of North Vancouver came to Hong Kong for experience of landslide prevention and mitigation on April 15, 2006. The Mayor of Taibeia came to Hong Kong twice for experience of landslide prevention and mitigation in 2001 and 2005. On February 13, 2001, he commended the slope safety management of Hong Kong in his speech to the public.

6 Difficulties Encountered in Landslide and Mitigation Prevention in Hong Kong

The efforts of preventing and mitigating landslides in Hong Kong have also experienced some difficulties and problems. The society and government have to be persistent and firm on the long-term effort and investment.

Fig. 8 Collapse of Kwun Long Lau old masonry retaining wall in 1994 (modified after GEO)

6.1 First Difficulty

The first difficulty is that the past experience based causes and mechanisms of landslides can be incorrect. Some slope stability assessments can be incorrect and some landslide preventive measures can be ineffective. For example, the Kwun Long Lau old masonry retaining wall, the Fei Tsui Road cut slope, and the Lung Cheung Road cut slope were assessed by qualified geotechnical engineers. However, they failed and caused disasters in 1994, 1995 and 1997, respectively (Figs. 8–10). These man-made slopes were assessed to be safe by qualified geotechnical engineers. But, they failed and caused disasters afterwards.

6.2 Second Difficulty

The second difficulty is about the change in slope safety standard. It is clear that safety standard is normally determined on the basis of affordability of a society. So, slope safety standard is changeable with time. Prior to 2000, the minimum value of factor of safety for upgrading existing slopes was 1.2. After 2000, it has been increased to 1.4. Since the establishment of GEO in 1977, more than 15,000 new slopes were constructed under its geotechnical control. GEO engineers checked and approved their design and monitored their construction. They could be up to the slope safety standards when they were made. However, occurrences of landslides in these new slopes are not uncommon, which also shows the difficulties in slope safety management.

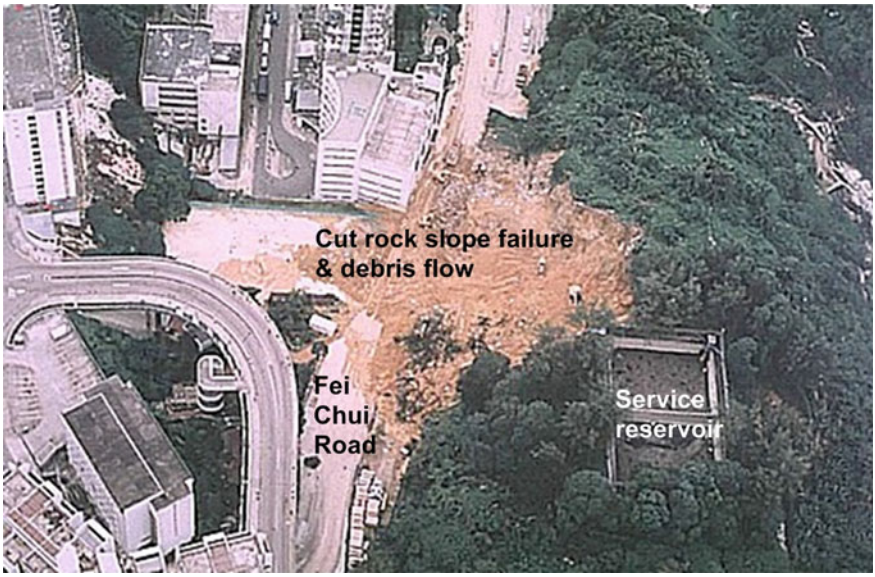

Fig. 9 Landside and debris flow in a cut rock slope above Fei Chui Road in 1995 (modified after GEO)

Fig. 10 Landslide in a cut slope above Lung Cheung Road in 1997 (modified after GEO)

Fig. 11 Blockage of newly constructed North Lantau Express by channelized debris flow on streams from above mountain on June 7, 2008 (modified after web video)

6.3 Third Difficulty

Due to climate change, the recorded maximum rainfalls in Hong Kong have been frequently updated. For example, on June 7, 2008, Hong Kong encountered a storm rainfall of 1100 years return period. Landslides caused 2 fatalities and 16 injures. The North Lantau Highway was blocked by debris flow from the above mountain slope (Fig. 11). This demonstrates the long-term and difficulty nature of landslide prevention and mitigation.

6.4 Fourth Difficulty

The fourth difficulty is about the long term nature of landslide prevention and mitigation. Landslides are mainly triggered or caused by rainfall in Hong Kong. During dry weather conditions, some people in charge may consider landslide prevention and mitigation less important and put less resource on this task. If the dry weather conditions continue for many years, such demand and requirement for reducing the resource can become higher and higher. Public attentions on landslide hazards can also become weak and weak.

For example, from 1983 to 1990, Hong Kong encountered dry weather conditions. The rainfalls were not high. So, the resource and investment to landslide prevention and mitigation became less and less. However, since 1991, Hong Kong

encountered wet weather conditions. The rainfall became higher and higher. Landslide disasters frequently occurred. So, much more resources and investments including the 5-years accelerated programme were channelled to landslide prevention and mitigation. However, from 2000 to 2007, Hong Kong re-encountered dry weather conditions. The rainfall was less. Landslide disasters also became less and less. During this period, there were informal arguments or discussions to reduce the resources on landslide prevention and mitigation. Once again, on June 7, 2008, Hong Kong experienced the heavy rainfall and landslide disasters. More resources were put on to landslide prevention and mitigation again.

6.5 Fifth Difficulty

However, it must be pointed out that the new urban development model concentrated on limited and restricted small land area has a severe limitation. A majority of people living and working in very small space are always under extremely high pressure. They are sufferings much on many aspects including (a) almost no personal privacy, (b) extremely inconvenient for family or personal activities in homes, (c) difficulties for gathering of friends and relatives at homes, and d) high psychological pressure for spacing. The prices are high. Some times, tragedies can happen.

For examples, on Nov. 29, 2007, a girl of 11 years old jumped out of her public housing flat of 300–360 feet square on ninth floor of a public housing building because of too small space. Her six persons' family of three generations lived in the small flat. She wrote "I will leave! Nice things or romantic love on this world would not happen to me!" On April 13, 2012, a young man (30 years old) jumped out of his public housing flat on ninth floor after he killed his wife (26 years old). Their public housing flat was about 400 feet square and lived by seven people of three generations with two couples. His wife was unhappy about small flat and wanted to devoice. Before jumping, he put his 6 year old son to his mother and said "I have done a wrong thing that is an irreversible mistake!"

Therefore, the fifth difficulty is that although they can make mountainous slope safe, form platforms and insert solid foundations for high-rise residential buildings, geotechnical engineers cannot make decisions on how to use the lands. As discussed before, more than 66.7 % land areas in Hong Kong are country parks (natural terrains). Only about 6.9% land areas are used for residential building for more than seven million people. It is ridiculous, isn't it?

7 Concluding Remarks

The landslide disasters in 1970s not only forced the government to allocate resources on landslide prevention and mitigation but also triggered many young university graduates in Hong Kong to address the challenges. For more than

35 years, many geotechnical engineers have made non-stopped efforts and activities for landslide prevention and slope safety in Hong Kong. They have treated that the slope safety is their primary career objective. They have worked hard for achieving this objective. Their contributions to the development and prosperity of Hong Kong are significant. However, their personal returns are limited. Their highest official post so far is a deputy director of Civil Engineering and Development Department (i.e., Head of GEO).

Many facts discussed above have demonstrated that the establishment of GEO for controlling slope safety in 1977 was a wise decision of the society. Landslide prevention and mitigation are a long-term social work for urban development and prosperity in the mountainous city of Hong Kong. Comparing to their social benefits, the government investments on landslide prevention and mitigation so far are very limited. Especially, they cannot be counted if they are compared to the incomes from urban developments, property markets and tourism. The government has obtained huge returns for its very limited investments on landslide prevention and mitigation. Everyone has benefited from the safe and green slope urban environment at present. Finally, it is also remarked that Hong Kong has established, trained and maintained a team of hundred or thousand geotechnical engineers who can address any technical challenges in future urban developments in the sea and/or on the mountains for Hong Kong. Since Hong Kong has many unused and undeveloped land areas and sea areas, geotechnical and civil engineers will still be much needed and play an important role in the sustainable development and prosperity of Hong Kong as its population grow to more than 10 millions.

Acknowledgments The author would like to thank Mr. Y. C. Chan, Mr. G. Daughton, Dr. D.X. Pan, and Mr. J. D. Legge for their advices and cares when he came to Hong Kong from Canada and practiced landslide prevention projects from 1996 to 1999. The work is financially supported by The University of Hong Kong and the National Basic Research Program of China (973 Program, Grant No. 2011CB710600).

References

Bishop AW (1955) The use of the Slip Circle in the Stability Analysis of Slopes.Geotechnique 5:7–17

GEO (2000) Geotechnical manual for slopes. Fourth reprint, Geotechnical Engineering Office (GEO), The Government of HK SAR. 300 pp

GEO (2007) Thirty Years of slope safety practice in Hong Kong. Geotechnical Engineering Office (GEO), The Government of Hong Kong SAR 625 pp

GEO (2008) Guide to soil nail design and construction, Geoguide 7, Geotechnical Engineering Office (GEO), Government of HKSAR. Hong Kong, China, 97 pp

Janbu N (1972) Slope stability computations. Embankment dam engineering:casagrande volume. Wiley, New York, pp 47–86

HKSARG (2010) Hong Kong year book, by Government of HKSAR, Hong Kong, China. 494 pp. (http://www.yearbook.gov.hk/)

Lumb P (1975) Slope failures in Hong Kong. Q J Eng Geol 8(1):31–65

Malone AW (1998) Risk management and slope safety in Hong Kong. In: Li KS (ed) Slope Engineering in Hong Kong. Balkema, JN Kay and KKS Ho, pp 3–17

Morgenstern NR (2000) Common ground, Keynote address. In: Proceedings of international conference on GeoEng, Melbourne, vol 1, pp 1–30

Morgenstern NR, Price VE (1965) The analysis of the stability of general slip surfaces.Geotechnique 15:79–93

Shiu YK, Chang GWK, Cheung WM (2006) Review of limit equilibrium methods for soil nail design, Special Project Report SPR 3/2006, Geotechnical Engineering Office (GEO), Government of HKSAR, Hong Kong, China, 105 pp

Wan SP, Yue ZQ (2004) Significant cost implications in using Janbu's simplified or Morgenstern–Price slice methods for soil nail design of cut slopes. Trans Hong Kong Inst Eng 11(1):54–63

Wan SP, Yue ZQ (2005) Significant cost implications in using Janbu's simplified or Morgenstern-Price slice methods for soil nail design of cut slopes, replies to discussions. Trans Hong Kong Inst Eng 12(1):49–51

Yue ZQ (2003) HKU Jockey Club Research and Information Centre for landslip prevention and land development. Mainland–Hong Kong Academic Exchange, Edited and published by Beijing–Hong Kong Academic Exchange Centre, Hong Kong, March 2003, vol 57, pp 32–35 (in Chinese)

Yue ZQ (2004a) Landslide hazard management and prevention in Hong Kong.Operating mechanism for disaster management, Qunyan pressing, pp 139–162 (inChinese)

Yue ZQ (2004b) Automatic monitoring of drilling process for optimizing ground anchorage. In: Proceedings of the 8th conference of Chinese Association of Rock Mechanics and Engineering, Chengdu, Science Press, pp 879–886 Oct 2004 (in Chinese)

Yue ZQ (2005) Automatic drilling process monitoring for soil and rock strengths and their spatial distribution in ground. In: Proceedings of the 2nd world forum of Chinese scholars in Geotechnical Engineering, Nanjing, China, pp 85–90, 22–22 Aug 2005 (in Chinese)

Yue ZQ (2006) Hong Kong landslip prevention and its social benefits. JEng Geol 14(Supplements):12–17 (in Chinese)

Yue ZQ (2010) Automatic monitoring of drilling process for mechanical profiles of grounds composing both soils and rocks. In: Proceedings of the 4th Japan–China geotechnical symposium, Okinawa, Japan, pp 230–235, 12–14 April 2010

Yue ZQ (2011) Optimization of pre-stressed ground anchors or grout-in-type soil nails with drilling process monitoring. In: Proceedings of the third international conference on Geotechnical Engineering for Disaster Mitigation and Rehabilitation (3ICGEDMAR 2011) together with the fifth international conference on Geotechnical and Highway Engineering—practical applications, challenges and opportunities (5ICGHE), Semarang, Indonesia, 18–20 May 2011, pp 573–578

Yue ZQ, Lee CF, Law KT, Tham LG, Sugawara J (2002) Use of HKU drilling process monitor in soil nailing in slope stabilization. Chin J Rock Mech Eng 21(11):1685–1690

Yue ZQ, Guo JY, Tham LG, Lee CF (2003) Application of HKU DPM in automation of geotechnical design and construction. In: Proceedings of the first national congress on GeoEng China, vol 1, pp 147–155. China Communications Press, ISBN 7-114-04724-X. Beijing, China, 22–25 Oct 2003

Yue ZQ, Lee CF, Tham LG (2004a) Automatic drilling process monitoring for rationalizing soil nail design and construction. In: Proceedings of the 2004 annual seminar of HKIE geotechnical division, Hong Kong, China, 14 May 2004, pp 217–234

Yue ZQ, Guo JY, Tham LG, Lee CF (2004b) Drilling process monitoring for ground characterizations during soil nailing in weathered soil slopes, Geotechnical and geophysical site characterization. In: Viana Da Fonseca A, Mayne PW, Proceedings of the 2nd international conference on site characterization (ISC-2), Porto, Portugal, vol 2, 1219–1224, 19–22 Sept 2004

Yue ZQ, Lee CF, Law KT, Tham LG (2004c) Automatic monitoring of rotary-percussive drilling for ground characterization—illustrated by a case example in Hong Kong. Int J Rock Mech Min Sci 41:573–612

Yue ZQ, Gao W, Chen J, Lee CF (2006) Drilling process monitoring for a wealth of extra factual data from drillhole site investigation. In: Proceedings of the 10th international congress of the International Association of Engineering Geology (IAEG2006 Engineering Geology for Tomorrow's Cities), Nottingham, UK, 6–10 Sept 2006. Theme 5—Urban site investigation, paper number: 5–746, pp 1–10 (CD RAM softcopy); Abstracts: p 87 (hardcopy)

Yue ZQ, Chen J, Gao W (2007) Automatic drilling process monitoring (DPM) for in situ characterization of weak rock mass strength with depth. In: Proceedings of the 1st Canada-US rock mechanics symposium (Rock Mechanics: meeting society's challenges and demands), Eberhardt E, Stead D, Morrison T (eds) Vancouver, Canada, 27–31 May 2007, Taylor & Franics, London, vol 1, pp 199–206

Yue ZQ, Chen J, Gao W (2008) An innovative approach combining geological mapping and drilling process monitoring for quantitative assessment of natural terrain hazards, In: Proceedings of the 10th international symposium on landslides and engineered slopes, June 30–July 4, 2008, Xi'an, China, pp 535–541

Advances of Geo-Disaster Mitigation Technologies in Taiwan

Ko-Fei Liu, Chyan-Deng Jan, Ping Sien Lin and Hsin-Chi Li

Abstract Taiwan is located in the typhoon district of the Pacific Ocean and is hit by typhoons averaged 3.6 times annually. Many large scale hillside development projects were undertaken in the past decades. These areas have become very vulnerable to natural hazard and usually are subject to heavy damage under slope-land disasters. The loss of people's lives and properties are severe. The average death toll was 8.26 casualties per event from 1981 to 1999. Starting from 1992, huge resources had been spent in the research of debris flows and landslides. After the assessment and warning system started on 2000, the number of casualties decreased to an averaged 2.23 per event between 2000 and 2008 and the average decreased as time progress. There were 22 large landslides or debris flows in 2008, but the average casualty was only 0.55 per event. This paper describes the technology advances from 2000 to 2010 in Taiwan. The most important advances are in the assessment technology, warning technology and mitigation concepts. The assessment method started with pure empirical formula, then improved to delimiting hazard zone numerically. The most recent change is to include social vulnerability in assessment. The warning system started with very local monitoring

K.-F. Liu (✉)
Department of Civil Engineering, National Taiwan University,
No.1, Sec. 4 Roosevelt Rd, 106, Taipei, Taiwan
e-mail: kfliu@ntu.edu.tw

C.-D. Jan
Department of Hydraulic and Ocean Engineering, National Cheng Kung University,
No.1, University Road, 701, Tainan City, Taiwan

P. S. Lin
Department of Civil Engineering, National Chung Hsing University,
No.250, Kuo Kuang Road, 40227 Taichung, Taiwan

H.-C. Li
National Science and Technology Center for Disaster Reduction, 9F., No.200, Sec. 3,
Beisin Rd., Sindian District, 231 New, Taipei City, Taiwan

F. Wang et al. (eds.), *Progress of Geo-Disaster Mitigation Technology in Asia*,
Environmental Science and Engineering, DOI: 10.1007/978-3-642-29107-4_4,

to nationwide warning with fine resolution quantitative precipitation estimation with multiple sensor radar system. The warning time has improved to more than 24 h before the disaster. The concept for mitigation changes from traditional structure countermeasures to ecological means. However the most fundamental change is the shifting emphasis from structure mitigation to non-structure mitigation with planning, education and drills.

Keywords Debris flow · Warning criterion · Hazard assessment · Social vulnerability · Counter measurements

1 Introduction

Taiwan is located at the interface between the Philippine Sea Plate and the Eurasia Plate. It is in the Pacific Rim seismic zone and experiences almost 1,000 sensible shocks annually. Taiwan is noted for its young topography and fragile geology. Climate change and earthquakes increase the amount of bare land and number of landslides in mountainous area. Mountainous areas account for 72 % of the total area of Taiwan. The slopes are steep in mountain. Mean annual rainfall is 2,515 mm. The temporal distribution of rainfall is extremely uneven. It is usual to have a total of 1500 mm rainfall in 5 days just by a typhoon event. Therefore, debris flows are a frequent phenomenon because of steep streams, abundant sediment, and high intensive rainfalls. Furthermore, most of the mountainous areas near cities are developed into agricultural and recreational areas; the threat of this natural phenomenon becomes a major social and economical problem (Fig. 1).

To face the challenge of these natural phenomena, the fifth National Technology Conference in 1998 in Taiwan concluded that Taiwan should put more effort on natural disaster mitigation and application research. Therefore, all related bureaus and agencies should have special fundings devoted in this area. The application of academic research should also be closely examined. Thus, the National Science Council (NSC from hereon) in Taiwan had devoted a lot of budget into the study of slope-land hazard since then. From year 2000 to 2010, NSC funded close to one million US dollars annually on slope-land hazard related projects. On the average, 28 projects annually were supported. The peak research activity was at 2005 at which there were 47 projects with total budget about 1.2 million US dollars (National Science Council 2011) . Most of the budget in this period was spent on debris flow assessment, simulation, warning and monitoring. Later, monitoring becomes part of the warning system and simulation becomes part of the assessment system.

The Soil and Water Conservation Bureau (SWCB from here on) is responsible for all landslide and debris-flow related engineering projects and the planning of a comprehensive nationwide mitigation strategy. So SWCB sponsored projects for fundamental as well as application research on structure and non-structure

Fig. 1 Debris flow disaster at Song-Her village in central Taiwan. The village is partially buried by debris flows and an original small stream outbursts into debris flow river of more than 30 m wide. This scenario is typical in Taiwan

countermeasures. Structure countermeasures include the installation of debris barriers, debris breakers, debris basins, deflection berms, slit dams, check dams, and/or Sabo dams in debris-flow gullies and alluvial fans (Jan and Chen 2005). Non-structure measure contains delimiting debris-flow hazard zone, village and road warning, land utilization limitation, evacuation plans, evacuation drills and education. The idea of non-structure countermeasures is to increase the self protecting ability of local residents against debris flow. The structure countermeasures are to decrease debris flow occurrence or change its characteristics or the flow path by engineering approaches to reduce the degree of disaster associated with it. The methodology and concept of structure countermeasures changed in time. The most popular traditional method is to build Sabo dames. Later, ecological measurements become popular after the Chi–Chi earthquake in 1999. However, it was found that ecological engineering is not so effective on the areas of steep slope, so it was restricted to be one option for regions with a slope less than 45° recently. But the concept of near natural river construction had already become the most important concept in hazard mitigation. It was enforced in every reconstruction and protection measurements.

In what follows, we shall describe the advances of geo-hazard mitigation-technologies in the views of assessment, non-structure countermeasures and structure countermeasures respectively in the following sections.

2 Assessment of Debris Flow Hazard

Assessment of landslide hazard begins in Taiwan with nationwide investigation on potential debris flow streams by the Soil and Water Conservation Bureau (SWCB) and landslide area investigation by the Central Geological Survey in Taiwan. The investigation of debris flows revealed 370 potential debris flow streams in 2000 and the number increased to 1660 in 2011. The field investigation of landslides in 2011 showed that the total landslide area in Taiwan was about 39,429 ha.

2.1 Assessment: Delimiting

The affected length for landslide is considered to be 1.5 times the height of the landslide. Anything longer than that is treated as flowing effect in Taiwan. Therefore, most research focus their effort on the affected area of debris flows. To find the potential debris flow stream, Hsieh et al. (1992) based on their field investigation, they suggested the very first criterion for identifying potential debris flow streams in Taiwan. The two necessary criterion they suggested are a watershed with average slope between 10° and 15°, and the total areas with slope greater than 10° larger than 5 ha. If these criteria are satisfied in a watershed, it is identified as a potential stream that will induce debris flows. If there are public construction or residents to be protected within the area, it is treated as a potentially dangerous area. With this method, 370 potential debris flow streams were identified. Hsieh (1992) used equal slope method and deposition pattern to delimit the dangerous area and determine the possible deposition depth for a potential stream. Shih et al. (1997) suggested that area with deposition depth greater than 3 m is extremely dangerous and tagged the area as a red zone. If the deposition depth is smaller than 3 m, it is not fatal but still dangerous and is named yellow zone. Yu and Lein (1999) studied the nature of deposition fan and used it to improve Hsieh's method. Hsieh (1999) improved his own method with combined analysis of field investigation and the concentric circular method. The method is compared with a real case. These methods are considered semi-empirical methods and used for fast analysis and preliminary designs.

Tsai (2002) used numerical simulation to analyze the Fong-Chu debris flow and obtained good comparison result but the parameters needed to be calibrated with real cases. Liu and Huang (1996) developed a numerical simulation program DEBRIS-2D for debris flows with the nonlinear constitutive relationship from Julien and Lan (1999). The numerical simulation results were compared with analytical solutions, lab experiments and real field cases, and very good agreement were obtained for all cases (Fig. 2). One convenient characteristic for DEBRIS-2D is that no calibration of parameters is required. Therefore, all physical parameters can be measured before debris flow event. After the user interface for DEBRIS-2D was developed, this program was used by many consulting companies and numerous agencies in the

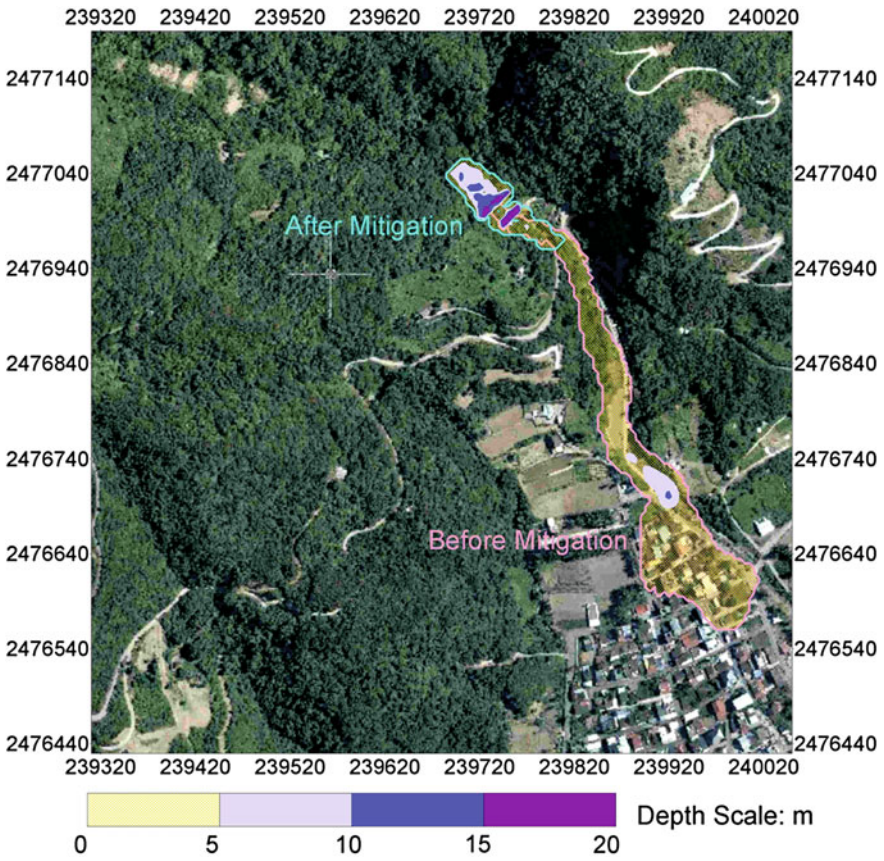

Fig. 2 A typical numerical simulation output for detailed hazard assessment (from DEBRIS-2D). This figure shows the affected area after debris flows completely stopped. *Lower right* is the village to be protected. *Pink* area indicates the area affected by debris flow originally. *Blue* area is the area affected by debris flow after construction of designed mitigation measures. *Different colors* indicate the depth of the final deposition. The area and depth contour are the necessary features hazard assessment

fields of geo-disaster mitigations. It even successfully predicted the hazard zone and deposition depth accurately in Taitung, Taiwan 3 years before the actual disaster occurred (Liu et al. 2009). DEBRIS-2D can also be used to estimate the effect from simple counter measurements. Now, this program has been used by researchers of several universities within the Asian area.

Numerical methods are used for detailed design especially for important countermeasures. The confirmation of design effect and precise delimiting of dangerous area are extremely important for areas with a lot of residents and buildings such as a hillside village. A good simulation result also enables a possible monetized loss assessment. Sometimes all approaches mentioned above are used and different decision making procedures are applied to reach the final delimiting results.

Table 1 The seven different types for land utilization

Land law	The type of land use		Content
Type 1	Construction		Such as house, industry, commerce, etc.
Type 2	Agricultural		Such as paddy field, dry land, fruit land, betel field, etc.
Type 3	Forest	Developed	Bamboo field, the cutting area, etc.
		Original	Such as broadleaf wood, coniferous wood, bush woods, collapse place, wasteland, etc.
Type 4	Tourism		Such as holiday villages, forest attraction area, etc.
Type 5	Other production		Such as ore land, herd ground, salt industry, etc.
Type 6	Transportation and hydraulic		Such as road, bridge, irrigation canals, dyke weir, watercourse, etc.
Type 7	Other		Not included in the above-mentioned areas, for instance desert or snow-covered mountain, etc.

2.2 Assessment: Financial Loss Assessment

If there is a real disaster, one can itemize the loss according to the real situation. However to estimate the monetized loss before a disaster is a complicated procedure. The first monetized assessment in Taiwan was proposed by Liu and Li (2006). They combined hazard zone delimiting method with the flow depth vs loss curve (Tsai 2002) to establish the assessment procedure.

There are many different kinds of losses in a real disaster. Liu and Li (2006) first classify the loss into two categories, human loss and property loss. Then the property loss was further divided into land loss and ground surface property loss. By consulting land law (The Land Act, Article 2, Taiwan), land loss is again divided into seven different types based on land utilization: construction use, agricultural use, forest use, tourism use, other production use, transportation and hydraulic use and other uses (Table 1). Different values can be found for different types of land use according to government bulletins. The ground surface property is separated into construction and non-construction property. For non-construction properties such as plants, they will be destroyed completely by a debris flow. But constructions are a recoverable loss for small scale debris flows or mud flows. Therefore, a simple standard suggested by Shih et al. (1997) was used. The construction is regarded as completely destroyed if debris flow depth is greater than 3 m, half destroyed if depth is between 1 m and 3 m and slightly damaged if the depth is less than 1 m (Table 2). This standard is subject to change according to the characteristic of particular regions.

After this classification, the loss of land and ground surface properties can be quantified. The procedure is first to simulate the debris flow affected area and deposition depth for a given rainfall event or a given rainfall return period. Then within the affected area, different zones are identified (Fig. 3) and loss in different zones under different categories are calculated. The sum of all losses gives the financial loss for a given event or a financial loss for a specified rainfall. But at the

Table 2 The suggested standard for evaluating the ground surface property loss

Final buried depth (m)	Objects on the ground	
	Construction	Non-construction (such as agriculture)
More than 3	Destroyed completely	Destroyed completely
1–3	Half destroyed (loss reduce by half)	Destroyed completely
Under 1	Slightly damaged (loss is down to legal fee)	Destroyed completely

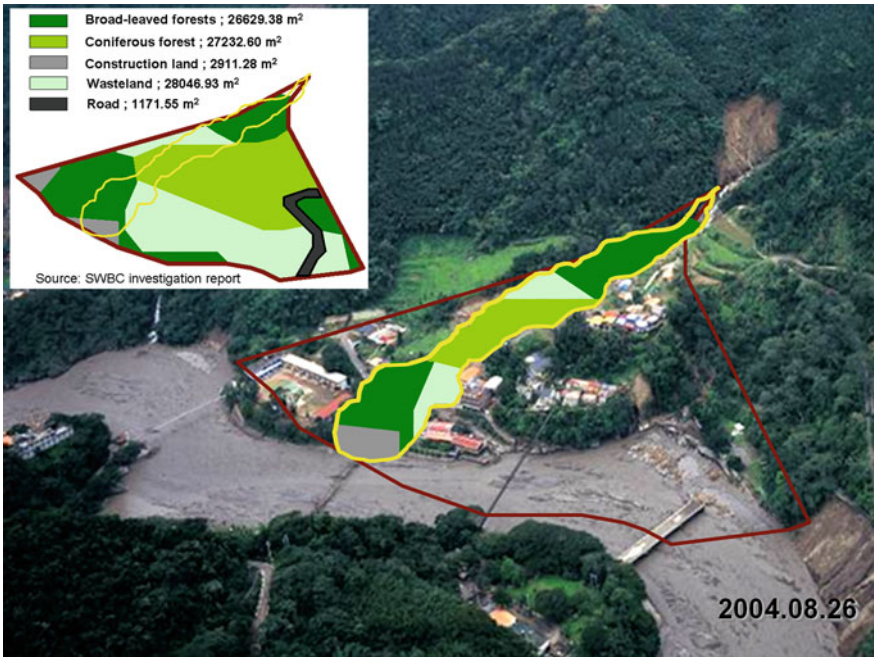

Fig. 3 The different zones of land utilization within debris flow hazard zone

same location, the loss can be different from debris flows under different rainfall amount. Therefore, to predict the most possible loss is equal to calculate the statistically expected loss. So we need to calculate the statistically averaged value of loss. In the case of natural hazard, we use the following formula,

$$\text{The expected loss of disaster} = \sum_{t=1}^{\infty} p(x_t)[\beta_t C_t] \qquad t = 1, 2, 3, \ldots \infty \quad (11)$$

$p(x_t)$: The probability distribution function of rainfall;

β_t: The probability for debris flow to occur under the given return period;

C_t: The total loss under a specified return period, obtained by adding losses from all catagories;

t: The recurrence interval of rainfall.

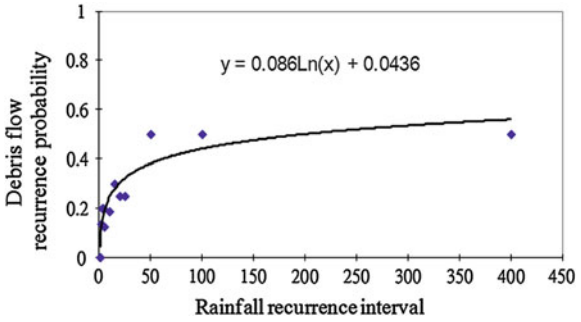

Fig. 4 The probability coefficient of debris flow occurrence under different rainfall return frequencies y is β_t and x is time

The probability coefficient β_t for debris flow must be computed from the actually debris flow records. After collecting data in Taiwan for the past 20 years, the values of β_t is found to be $\beta_t = 0.086\ln(x) + 0.0436$ (Li and Liu 2010) as shown in Fig. 4. As we define the statistical expected value as the hazard loss, repeated simulation with different return periods is necessary. Therefore, it is required that the delimiting method used must reflect the difference from different rainfalls.

This method had been tested against several real disasters; the expected loss value is within 10 % of all the money spent by government in the target area within 3 years after disaster. This means that this method is reasonable to use as an estimation for direct disaster loss. To estimate the indirect loss, there is more work to be done. Li (2011) further combined GIS system with the above method to create a fast and object based evaluation system TLAS Taiwan. TLAS TAIWAN is now a standard tool used by National science and technology center for disaster reduction in Taiwan. A simpler version of TLAS is also available on website for the public. It can provide all interested people with itemized calculation of total loss. This method becomes the backbone of the social vulnerability assessment system in Taiwan.

2.3 Assessment: Social Vulnerability

As the assessment technology improves, the human based factors become more and more important. It was discovered that the same scale of hazard can induce completely different disasters in neighboring locations. Therefore, it is believed that a true assessment of disaster must contain human factors in order to reflect the real situations or to estimate the possible loss. The focus becomes the social vulnerability.

During early periods, the concept of vulnerability was based on biophysical vulnerability, which included three dimensions: hazard, exposure and sensitivity (Adger et al. 2004). However, in recent years, discussions have gradually turned towards the state of the subject (the human social system) before a disaster and how such a state affects its vulnerability, which is social vulnerability (SV). In other words, SV is independent from the forces of a natural disaster, and originates from the characteristics inherent in a social system. Cutter (1996) summarized research

Table 3 Summary of social vulnerability influencing factors in disaster-isolated areas

Influence dimension		Influencing factors
Social vulnerability	Vulnerable population	Including elderly living alone, mentally and physically disabled, household of medium and low income, children and teenagers; the elderly and the invalid; economic power, poorer individuals etc.
	Engineering construction and geographic environment	Slope-land infrastructure construction, irrigation system and retaining walls; limitations on development in areas prone to disaster, and the development of early warning systems; effective slope-land management system; outgoing roads in slope-land area etc.
	Disaster management and community disaster prevention	Regional economy, land use planning, risk assessment, the implementation of government disaster assistance policies and insurance, promotion and advocacy, planning of evacuation route, community disaster prevention topics and promotion etc.
	Individual risk perceptions and adaptability	Risk perceptions, hazard perceptions, evacuation decision making capabilities, previous experience, living cost and environment, etc.
	Social support	Social network, official social support (medical system and social service institutions), non-official social support (family members, relatives, neighbors, colleagues) catering assistance, financial support, transportation assistance, etc.

between 1980 and 1995, but it still shows very diversified opinions. If it comes to application on slope-land hazard, there is hardly any research. According to previous literature, major slope-land vulnerability factors can be divided into vulnerable population (Li et al. 2012), engineering project and geographical environment, disaster management and community disaster prevention, individual risk perception and adaptability and social support five dimensions as listed in Table 3.

2.4 Social Vulnerability Index in Taiwan

Based on previous researches, Li et al. (2012) define social vulnerability as the degree of damage and resistance of a community against slope-land hazard event. Li invited experts from many different disciplines such as experts from social system, transportation, urban design and environment to have a formal discussion. The final result for Social Vulnerability Influencing Factors in disaster-isolated areas is summarized in Fig. 5. The four most important factors are exposure to potential maximum loss, resistance ability, recovery ability and engineering protection. These four factors contain all vulnerable factors of slope-land disaster.

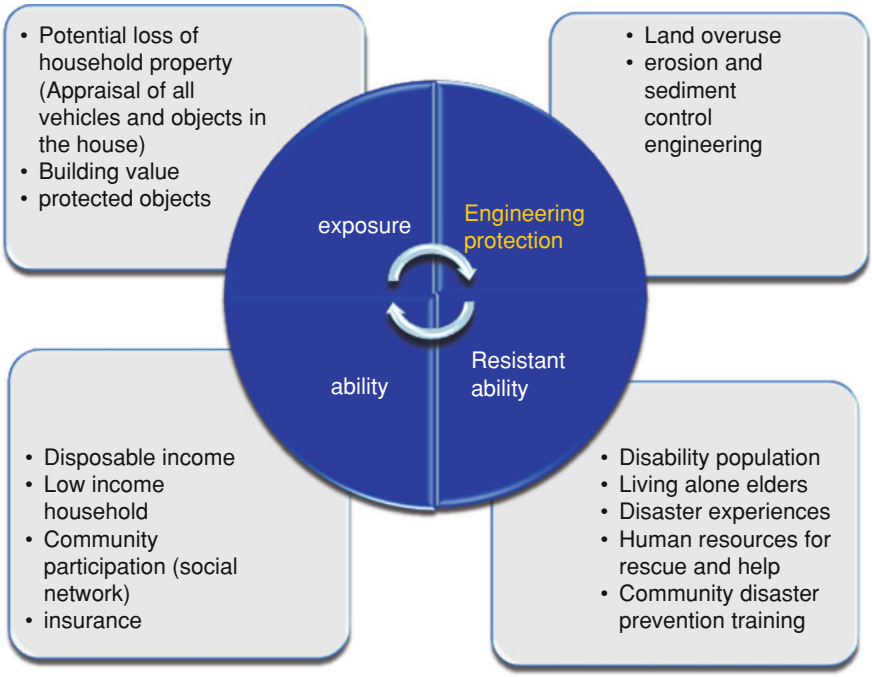

Fig. 5 Social vulnerability index of slope-land disaster

1. Maximum possible loss: This factor measures the maximum damage that can occur and can be divided into human causalities and property loss in the debris flow danger zone.
2. Engineering construction and geographic environment: Any countermeasures can protect people to a certain degree, so it is still one of the important factors. The engineering construction and geographic environment includes slope-land infrastructure, effective slope-land management system, early warning system, stability of outgoing road system in slope-land area etc.
3. Self-preservation ability: This factor measures the people's ability of resisting disasters. Self-preservation ability is an individual ability to protect his/her own life and property, the less they are able to protect themselves the less they are able to resist the impact of a disaster. Indexes of self-preservation ability include females, elders, the disabled, homeless, risk awareness and disaster preparations, disaster drills, community disaster education etc.
4. Recovery and adaptive capacity: This measures resilience in the concept of social vulnerability. After sustaining damages from a disaster, households that are able to withstand the damage and recover rapidly are less vulnerable than those cannot recover. Here, recovery means to return to their normal lives rapidly. Adaptation means to learn from the disaster experience, turn it into effective disaster prevention knowledge, and use the knowledge to prevent damage when the disaster occurs again. Recovery and adaptive capacity can be

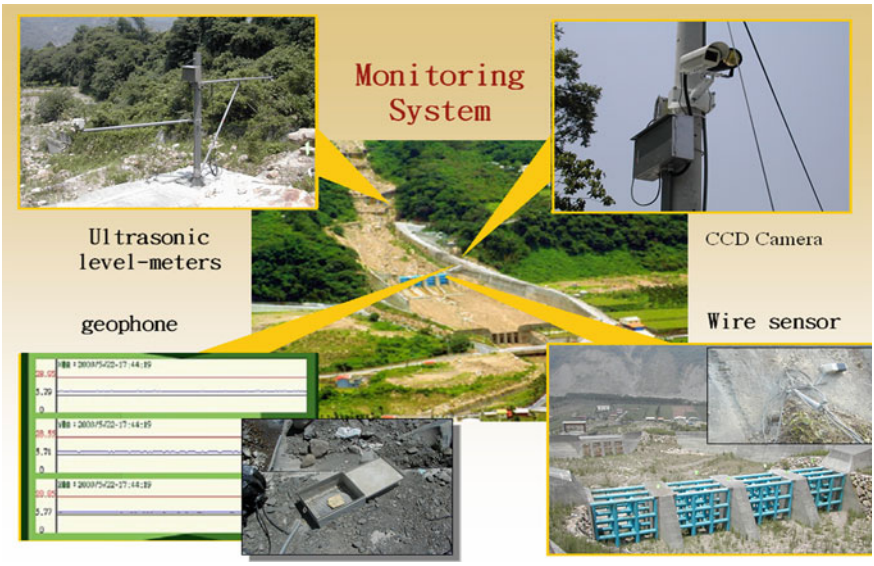

Fig. 6 Standard SWCB monitoring system. Equipments include CCD camera, geophone, wire sensor and ultrasonic level-meter, installed at Fengqiu debris-flow potential stream in the Chenyoulan stream watershed,Taiwan

evaluated by measuring several variables, including disposable income, low income household, community participation (social network) and insurance.

To calculate the value of SV indexes, most common aggregation average method (Clark et al. 1998) is adopted. First step is to normalize the obtained SV statistical data by (Eq. 1), and then uses the aggregation average method to calculate the comprehensive indicator (Eq. 2). Finally the social vulnerability index of every Taiwan's county is calculated.

$$Z_{ij} = \frac{(X_{ij} - M_j)}{SD_j} \tag{1}$$

Z_{ij}: The normalized value of different social vulnerable factors (j) in certain assessed area (i);

X_{ij}: The value of different social vulnerable factor (j) in certain assessed area(i);

M_j: The average value of certain social vulnerable factor (j);

SD_j: The standard deviation of certain social vulnerable factor (j);

i: The different area of assessment;

j: The different social vulnerable factors.

$$SVI_i = \frac{\sum_{j=1}^{N} Z_{ij}}{N} \tag{2}$$

SVI_i: The Social Vulnerability Index of the assessed area;

Z_{ij}: The normalized value of different social vulnerable factors (j) in certain assessed area (i);

N: The number of social vulnerable factors;

j: The different social vulnerable factors.

So far, this method is used in NCDR, a social vulnerability map for Taiwan by an adopted statistical method which is constructed. It has already been useful for many non-structure mitigation applications, such as implementation of evacuation and refuge-related job, strengthen the disaster prevention education, reinforce the disaster resources of the disadvantaged minority and revision of regional disaster prevention and emergency response plan etc. But it is still not good enough for detailed assessment of the social impact from slope-land disasters. In the future, quantifying the loss for social impact would be the major important direction.

3 Non-Structure Countermeasures

With a good assessment on the location and the possible magnitude of the disaster, a decision on countermeasures can be made. Non-structure measurements are the most cost effective method against disaster. It also increases the resistance of the whole community against disaster. Therefore, more and more emphasis has been put on non-structure countermeasures in Taiwan.

3.1 Monitoring Stations

The first rainfall-based warning/monitoring system was installed in Hualien County, eastern Taiwan in 1992. The first monitoring/warning system with multiple sensors and systematic operation was developed in 1992 (Liu 1998). The system consists of geophones, rain gauges, video cameras, water level meters, ground water level sensors and ultra light sensors. That system was installed in Shen-Mu village, central Taiwan and was sponsored by NSC as a pioneer system. Soon it was adopted by SWCB and became a nationwide system. The standard monitoring station of SWCB consists of a rain gauge, a geophone, and a video camera. Although the monitoring stations have functioned reasonably well for some subsequent debris-flow events, but it did not have a warning ability and was only a monitoring system. So the system was improved (as shown in Fig. 6) and a rain gauge, ultrasonic airborne level-meters, geophones, wire sensors, infrared Charge-Coupled-Device (CCD) cameras, and a satellite communication were added into the system. All data were transmitted to the Debris Flow Emergency Operation Center of the SWCB. These data can be analyzed and the results can be used in making decisions on how to mitigate possible debris-flow hazards during emergency time (Fig. 7).

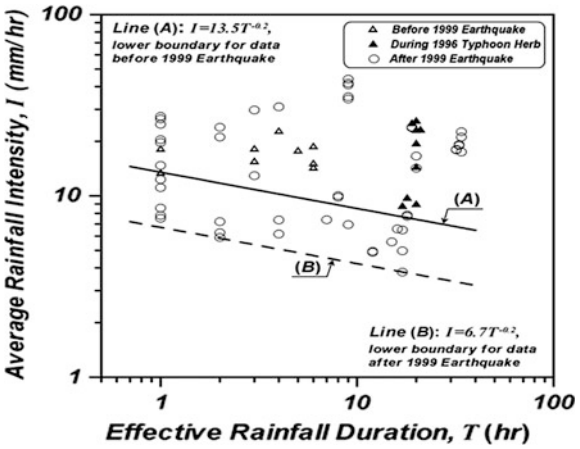

Fig. 7 Empirical relation between duration and intensity of debris-flow causing rainstorms for the entire Chenyoulan stream watershed (Jan and Chen 2005)

3.2 Early Evacuation

However, because streams are short in Taiwan such a warning system can only provide local residents with at most a 15 min evacuation time. It is too short to be useful. Therefore, a criterion based on rainfall record was developed as the major tool for early warning in 2000. To cope with the early warning policy, planning of an evacuation route followed by evacuation drills in potential hazard areas became important. The planning of evacuation routes for Taiwan is completed for every potential hazard area around 2005 by a 6-year project. After that, an evacuation map can be modified by local authorities. Education programs have become essential because that is the only effective way for people to understand the whole policy and details of evacuation. The budget for evacuation drills and education is small but effective, so it has become the required regular activities annually for local townships.

3.3 Variation of Rainfall Based Warning System

Before 2000, researchers in Taiwan used the early USGS method. The hydro-meteorological threshold of debris-flow initiation can be defined by rainfall intensity versus rainfall duration relation (Caine 1980; Wieczorek 1987; Keefer et al. 1987). An example is shown in Fig. 7 for Chenyoulan Stream watershed in central Taiwan. This particular watershed was affected seriously by the Chi–Chi earthquake. A line (A) relating the rainfall intensity against the rainfall duration on a log–log scale describes an envelope of debris-flow-causing storms before the 1999 earthquake. The critical line (A) can be expressed using an empirical rainfall intensity-duration formula with linear regression analysis as

$$I = 13.5T^{-0.2} \tag{3}$$

in which I is the average rainfall intensity in mm/hr and T the rainfall duration in hours. After the 1999 Chi–Chi earthquake, new data has lowered the threshold of rainfall amount needed to trigger debris flows significantly. This reflects the fact that abundant supply of loose material due to earthquake can be mobilized more easily under lighter rains. Therefore, a new critical line (B) shown in Fig. 3 is found as

$$I = 6.7T^{-0.2} \tag{4}$$

Comparing Eqs. (3) with (4), we found the debris flow triggering rainfall intensity is decreased by 50 %. This is equivalent to the increase in the number of debris-flow events in subsequent years after the 1999 Chi–Chi earthquake. This threshold line (B) has gradually moved upward, approaching asymptotically to the original threshold line (A) as time goes. But the recovery was interrupted by another strong earthquake or typhoon (Jan and Chen 2005).

3.4 Rainfall Triggering Index, RTI

The rainfall parameters commonly used to set up the rainfall-based debris-flow warning models are the rainfall intensity I, the rainfall duration T, the accumulated rainfall R in a rainfall event as well as the antecedent rainfall P of the considered rainfall event. To calculated the accumulated and antecedent rainfall, one needs to define the starting and ending points of a rainfall event. To issue warning, we need to know when debris flow will occur. The definition of a rainfall event and occurrence time are indicated in Fig. 8 (Jan and Lee 2004; Jan and Chen 2005).

It had been observed several times that debris flows initiated just at the time of the peak of hourly rainfall in Taiwan. In many other occasions, the time for peak hourly rainfall is within the possible occurrence time domain described by residents. Since for most cases, it is impossible to record the exact time of debris flows initiation, so the time of the peak hourly rainfall is assumed to be the time of debris-flow occurrence in Taiwan.

The starting-time of a rainfall event is defined as the hourly rainfall just becomes larger than 4 mm. The ending-time for the rainfall event is at the time where the hourly rainfall just becomes less 4 mm, but this must be maintained for at least 6 h.

An effective accumulated rainfall contributing debris-flow occurrence should include the considered rainfall event and its antecedent rainfall. The effective accumulated rainfall $R_t(t)$ at time t in a rainfall event is defined as the sum of the accumulated rainfall $R(t)$ at time t of the considered rainfall event and its seven-day effective antecedent rainfall (Jan and Lee 2004). It can be expressed as

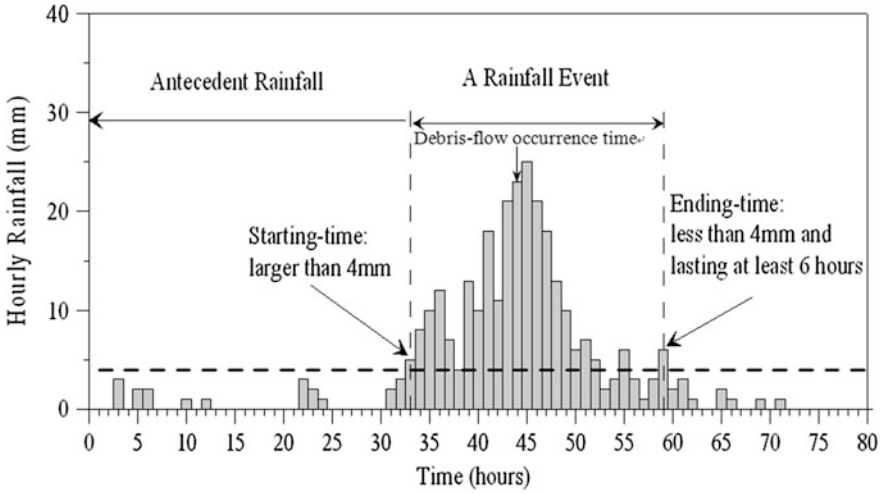

Fig. 8 Definition of a rainfall event used to analyze rainfall-induced debris flows

$$R_t(t) = R(t) + \sum_{i=1}^{7} \alpha^i R_i \tag{5}$$

in which $R(t)$ is the amount of the accumulated rainfall at time t in the considered rainfall event; R_i is the amount of the antecedent i day's rainfall; α is a weighting factor and is set to be 0.8. An instant rainfall triggering index (*RTI*) at time t for judging debris-flow occurrence potential is defined as the product of hourly rainfall intensity $I(t)$ and the effective accumulated rainfall $R_t(t)$ at time t, i.e.,

$$RTI(t) = I(t)\ (\text{mm/hr}) \times R_t(t)(mm) \tag{6}$$

The value of *RTI* for debris flow occurrence depends on historical data. Since the occurrence time for debris flow is considered to be at the peak hourly rainfall, so the critical value of RTI for a rainfall event is defined as the product of the hourly rainfall intensity I (mm/h) and the effective accumulated rainfall R_t (mm) at the time of debris-flow occurrence or at the peak of rainfall intensity. A scatter-plot of the rainfall triggering index *RTI* (mm^2/h) for historical rainfall events versus rainfall-event consecutive number N is shown in Fig. 9. The lower critical line of *RTI* (RTI_{10}) is defined as the lowest *RTI*-values of rainfall events that had triggered debris flows. An upper critical warning line of *RTI* (RTI_{90}) is defined as 90 % of *RTI*-values for the historical rainfall events (regardless of occurrence of debris flow). If RTI value is in between RTI_{10} and RTI_{90}, the associated probability of debris flow occurrence is calculated as

$$P(RTI) = 0.1 + 0.8\left(\frac{RTI - RTI_{10}}{RTI_{90} - RTI_{10}}\right) \tag{7}$$

With this probability, one can plot the RTI values as a function of time as in Fig. 10. This warning model had been adopted by SWCB in Taiwan in 2004. The result for Typhoon Mindulle is listed in Table 4. As can be seen, more than 20 h is available to evacuate residents and all events occurred after RTI_{90} was reached. This method is still used by many agencies now. In 2008, this method was used for road warning by Directorate General of Highways. They apply the method on Su-Hwa high way. When yellow warning is issued, officers from Directorate General of Highways must standby. When red warning is issued, the dangerous sections of road will be blocked. No one can pass the section until red warning is released.

However, starting from 2005, in real application related to general public, SWCB announced the warning based on accumulative rainfall only due to the difficulty in public awareness of hourly intensity. This means taking $I = 1$ in Eq. (6). Then RTI values changes to Rainfall threshold value (RTV). But the probability concept remains the same. The official warning value is RTV_{70}. Warning is separated into two stages. Whenever the Central Weather Bureau predicted an accumulative rainfall exceeds RTV_{70}, a yellow warning is issued. If the current accumulative rainfall exceeds RTV_{70}, then a red warning is announced. In yellow warning area, residents are advised to leave. In red warning area, residents are forced to leave. This system has been used since then. If there is extraordinary events such as huge earthquake or Typhoon, RTV value will be recalibrated and modified.

3.5 QPESUMS and Emergency Response System

The system of Quantitative Precipitation Estimation and Segregation Using Multiple Sensors (QPESUMS) was initiated in 2006 for calculating and analyzing the predicted rainfall within 1–3 h and provide quantitative prediction of rainfall for the next 72 h. Gourley et al. (2002) explain the structure of the system. This system is the combined research result of SCWB, Water Resource Agency in Taiwan and National Severe Storm Laboratory, NSSL, USA. The radar system is composed of five Doppler radars build around Taiwan island. With this system, the path of typhoon and precision of rainfall forecast become much better. As a result, all subsequent warning using rainfall data become much better. Especially, the precipitation data has a 1 km by 1 km resolution and is corrected by ground level rain gauge records. So it can represent the real ground level precipitation. The resolution is also suitable for landslides and debris flows. With this good precipitation forecasting and the debris flow warning system, this whole system worked very well in recent years.

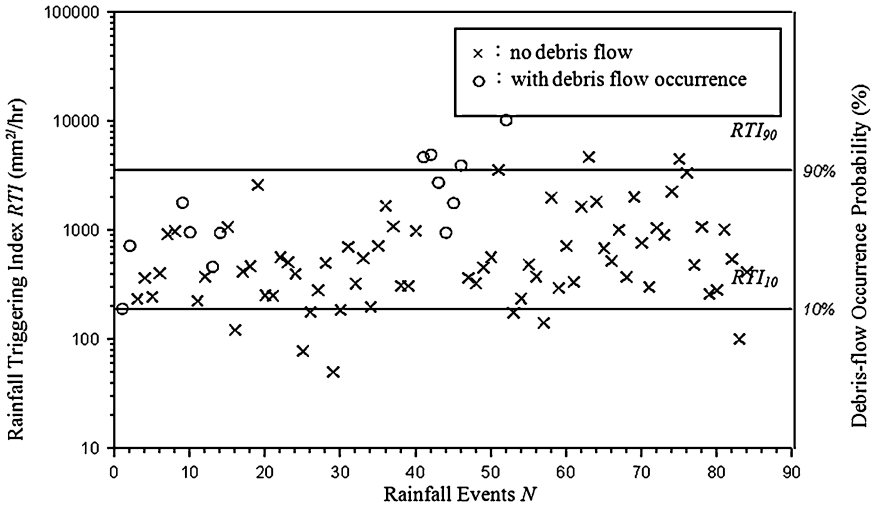

Fig. 9 Distribution of rainfall triggering index for historical rainfall events in a watershed, and the determination of critical lower and upper RTI values

4 The Structure Countermeasures of Debris Flow

Non-structure countermeasures can help local residents to increase their own defense against hazard. But the structure countermeasures are still necessary when we face large amount of lose material and unstable geology.

4.1 The Past (Before 1991): Closed-Type Sabo Dams

Reports from the SWCB (1992, 1996) showed 97.51 % of the debris-flow mitigation dams used during 1964–1991 in Taiwan are closed-type sabo dam (gravity concrete dam, steel dam, etc.). The closed-type sabo dam, which are often non-porous, can be divided into regular and submerged sabo dams.

Regular sabo dam is a dam with height more than 5 m. Its purpose is to store and regulate the sand in the river to stabilize the riverbed as well as to prevent scouring and further to eliminate debris flow. Submerged dams are a series of dams with each height less than 5 m. The purpose is to stabilize rivers by preventing erosion to protect the foundation of revetments or other structures (Liu 1998).

Despite the abilities of stabilizing slopes, increasing scouring base and changing sedimentation pattern, closed-type gravity dam is more susceptible to filling-up. During hazard, these dams are usually filled completely and overflow can induce damages at the downstream. A few disasters were caused by partial dam failure. The investigation (Forestry Bureau 1992) showed that 85.01 % of the sabo dams in

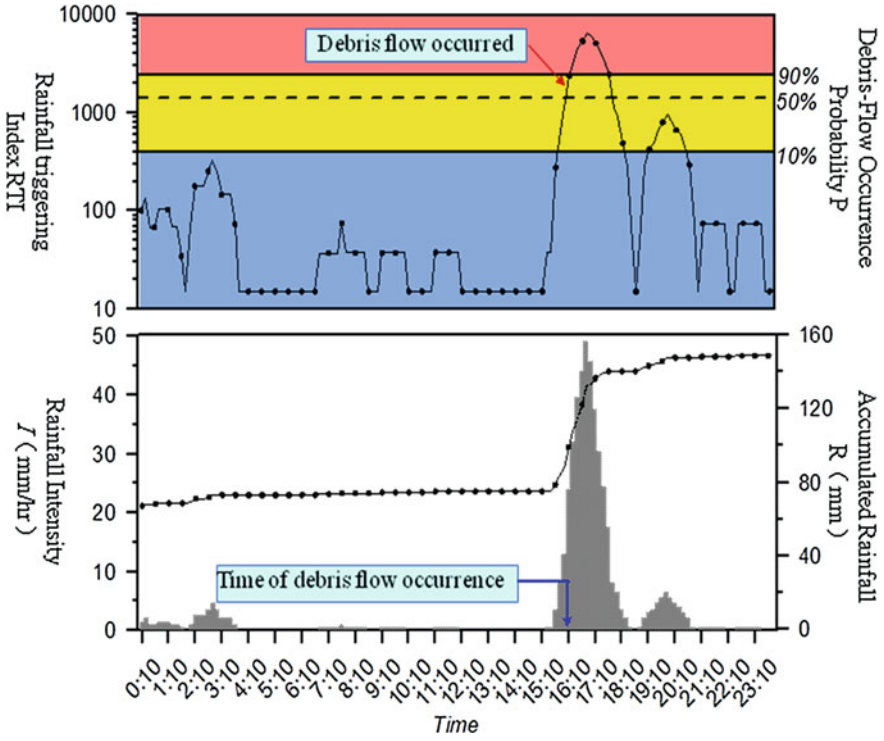

Fig. 10 Temporal variations of the rainfall intensity, the effective accumulated rainfall, the rainfall triggering index and its corresponding debris-flow occurrence probability. This record is for Typhoon Mindulle, 2004. The real occurrence time of debris flow is marked. It occurred at RTI_{90}. The time difference between debris-flow occurrence and the peak rainfall intensity was about 1 h

Taiwan built between 1964 and 1991 had reached their full capacities. Therefore, other countries such as Austria and Japan, often choose the open-type dam to replace the traditional closed-type gravity dam to avoid the aforementioned problems. Submerged dams have similar weakness, but with somewhat less retaining effect.

4.2 Present (1992 Till Now): Open-Type Sabo Dam

Since closed-type sabo dams are often washed off or filled up, they are gradually replaced by open-type sabo dams. Open-type sabo dam, often porous dam, is also known as grille dam (Chou et al. 1991). Grille dam is named as having grille (vertical and horizontal) or grid (flat or three-dimensional) as a whole. A typical open-type dam is shown in Fig. 11. As a usual practice, scrap tires will be installed in front of the dam to decrease the impact of debris flow on the dam (Fig. 12).

Table 4 Comparison of the time of debris-flow warning and the time of debris-flow occurrence for four debris-flow-prone areas in the Typhoon Mindulle event

Location	Time of debris flow occurrence	Rainfall intensity and effective accumulated rainfall at the time of debris-flow occurrence		Debris-flow warning time by the SWCB, based on the RTI model	Length of warning time ahead the time of debris-flow occurrence
		I (mm/h)	R_t (mm)		
Heping	07/03 08:30	81.5	472	07/02 10:40	26 h 50 min
Dongshi	07/03 08:00	34.0	421	07/02 16:10	15 h 50 min
Ren-ai	07/03 09:10	55.5	380	07/02 09:50	28 h 20 min
Guosing	07/03 08:00	125.0	419	07/02 10:50	21 h 10 min

Some investigations showed that the impact on slit dam is reduced by 20 % with scrap tires (Lin et al. 2007).

The most common open-type sabo dam is the concrete slit dam. The span between the slits is designed to be 2–2.5 times the maximum size of the boulders. The greater the dam angle, the greater the impact of debris flow exerted on the dam. On the other hand, when the dam angle is smaller, the impact of debris flow on the dam is decreased, and the maximum impact is at the 3/8–1/2 height of the the dam (Chen 2000). Even used open-type sabo dam to protect rock shed. As a result, the life time for the rock shed with the protection of open-type sabo dam can be significantly increased (Figs. 13 and 14).

Today, there are many different types of open-type sabo dams in Taiwan, and each has its own specific functions. Through researches and field observations, the main performance of the open-type sabo dam can be summarized.

1. It can store a large quantity of gravels to reduce total output of debris flows.
2. For an open-type dam, sediments of smaller size can be transported to downstream so that the storage space on upstream of the dam can be used to store sediment with larger size.
3. The local scouring phenomena at the downstream of the open-type sabo dams is minor as compared with the closed-type dams.
4. Since fine sediment and water can pass through the sabo dam freely, this helps the ecological balance of stream, as well as sediment transportation.
5. Open-type dam has smaller area directly facing the flow and a smaller impact force compared with the closed-type dam.

In view of the ability to withstand the impact force while maintaining ecological balance, it is indeed a versatile method of conserving the environment. Because of these benefits, open-type dam has become the most often seen in Taiwan nowadays. However the design of open-type dam is always composed of a series of different types of dames (Fig. 15). So the design can be safe and satisfy different requirements of residents.

Fig. 11 Typical dimension of open-type sabo dams: steel slit dam

Fig. 12 Slit dam with scrap tires installed to reduce debris flow impact. Huashan River at Kukeng Township of Yunlin County, Taiwan

Fig. 13 The installation of accelerometers in the slit dam

4.3 Future: Flexible Barrier System

Flexible barrier system originated from a flexible system consisting of rock falling prevention. The flexible barrier system, which replaced traditional rigid retaining structure, has been developed for 50 years. In recent years, Europe and the United States have started applying flexible barrier system to the mitigation of debris flow. The characteristic is to absorb the impact of the falling rocks by circle-type steel net and elastic plastic deformation of steel ropes. These energy dissipating units can further absorb remaining energy by friction. However, the only drawback for flexible barrier system is its cost. Damping performance depends on the structure of these steel nets, and this net structure is usually patented or requires special material. As a result, to use imported flexible barrier system in Taiwan is very expensive compared with sabo dams.

Recognizing its future application in Taiwan, researchers have started studying the flexible retaining structures. The impact of flexible retaining structures with energy-absorbing network is compared with the impact of rigid retaining structures using concrete slit dam. The result showed that the impact on flexible structures is only about 20 % of that on concrete slit dam. (Lin 2006). It is believed that, the flexible barrier system will be popularly used to against geo-harzards in Taiwan in the near future.

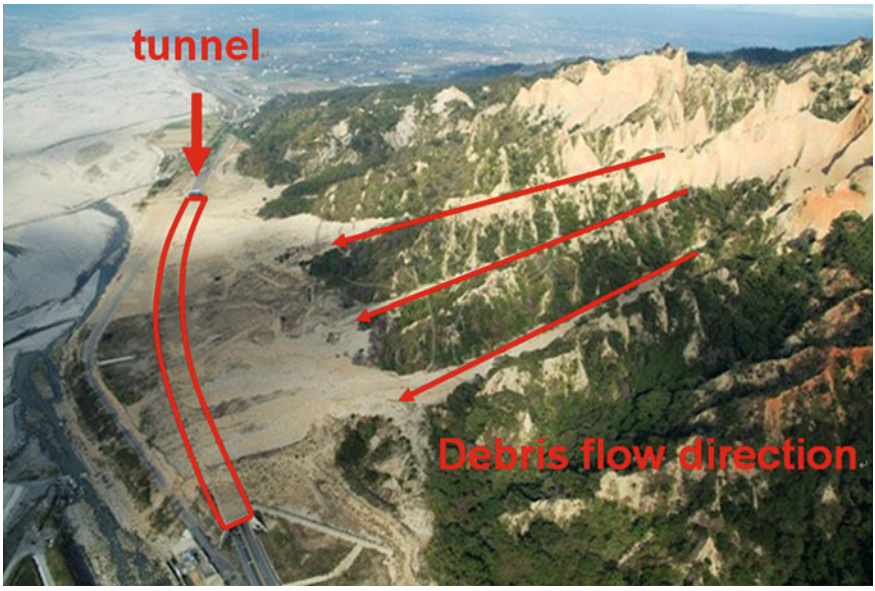

Fig. 14 Rock shelter (*open tunnel*) at Huo Yan Mountain—operational life can be extended with the impact of debris flow reduced

4.4 Systematic Ecological Mitigation Method

The Chi–Chi earthquake in 1999 created many bare collapses in the central mountainous area. The 921 Earthquake Recovery Committee determined to apply ecological engineering techniques based on the concept proposed by Guo (2001). The recovery plan starts from the highest catchment as the first priority and goes downwards for landslide rectification. The principles of mitigation are as follows (Lin and Chiou 2003):

1. Source of landslides and collapsed area: (Hung and Chen 2002) Filling up the cracks and cutting off water flow at the source of landslide are the most important. Re-direct water through location with good vegetation. Unstable plants are trimmed or removed and replaced by shrubs and gramineous grass.
2. Collapsed slope: Collapsed slope should be flattened locally through cutting it to a less steep slope. Then methods such as driving piles, making wattles and intercepting surface water with gutters can be used. Surface water is redirected to the vegetation area. Final step is to re-plant vegetation to stabilize the slope.
3. Debris accumulating fan formation downhill: The same methods applied on slope are used again. Driving piles and making wattles on the apex of the fan are applied to block newly collapsed debris and to ensure a stable environment for the follow-up vegetation on the fan to grow. Surface water intercepting and

Fig. 15 Debris-flow control structures, such as Sabo dams, debris barriers, and debris basins, at Fengqiu in the Chenyoulan Stream watershed (Jan and Chen 2005)

stabilization of the fan foot should be enforced. Upon completion of the above steps, vegetation may start.

These principles achieved very good results. Bare land recovered quickly in a year. This results in a 5 year boom of ecological engineering researches. However in 2001, typhoon brought heavy rainfall, many of the previous mitigated area failed again. This indicated that ecological engineering has its limitation. In recent years, only slope less than 45° will apply ecological engineering as mitigation measures.

By combining the past experience, Wu (2003) proposed the systematic mitigation concept for slope. Wu proposed that hazard mitigation should start from the landslide source area in the watershed. The mitigation method used on source area should be one of the ecological engineering methods. These methods include filling up the cracks, cutting off water flow at the source of landslide, driving piles and making wattles with vegetation, facilitating groundsill stabilization at the river toe, rectifying landslide deposition area by dredging method and growing plants on sides of the river to increase the stability of the slope. This becomes the center of the concepts in any of the SWCB mitigation project now. The influence is deep. Mitigation in debris flow streams is required to use local material such as boulders and woods. A typical groundsill work is shown in Fig. 16 where boulders along the river are used. Other mitigation methods such as revetment and retaining earthwork have to

follow the same principles. For example, the type and the material used for revetment should be determined based on hydraulic properties and the natural resources used to protect the river bank. Besides, one must use basket, cage and riprap to create the diversity of the pore structure in order to create an environment suitable for vegetation and survival of insects, birds and fishes. When the slope of the river bank is greater than 30 degrees, retaining structures should be built. For ecological considerations, porous gravity retaining structure is adopted. to avoid an excessive use of reinforced concrete while making use of local debris material. This gravity structure can also be made into a porous panel with opening, in which rooted plants or branches can be placed to serve as a habitat for living things.

4.5 Viaduct Across Potential Debris Flow Area

Many roads in the mountain areas pass through potential debris flow streams. These cross sections of road and debris flow streams must be rebuilt every debris flow occurs. The Directorate General of Highways learned from the lesson. Now, roads through debris flow region should be built as a viaduct or an arc bridge. No bridge pier is allowed inside potential debris flow streams. One of the famous example is the viaduct on route 21 along Chenyoulan River between Eighteen Chong Bridges and Ai-Yu Bridge. The road was completely destroyed during Typhoon Toraji (2001). To ensure the road safety, the Highway Bureau rebuilt a full-scale viaduct across the whole potential debris flow area. This steel bridge is as high as 40 m and was constructed in areas where several landslides took place. There is no bridge pier along the 110 m span. This is the largest road reconstruction project of debris flow mitigation and was completed in October, 2006 (Fig. 17).

5 Conclusion

After 15 years' research, Taiwan has built its own system of geo-hazard mitigation system. The newly established QPESUMS system can provide 1Km × 1Km rainfall predictions and a forecast up to 72 h. This could significantly improve the rainfall prediction so as to improve geo—disaster prediction and mititgation. A rainfall-based debris-warning model and system is established for preventing or migrating debris-flow hazards. The Soil and Water Conservation Bureau and the Doctorate General of Highways both have used it with good results. Evacuation plans are completed in Taiwan and the evacuation drills as well as education programs will ensure that people know what to do during the disaster. The assessment system has provided accurate monetized estimation for engineering decision making. The mitigation design can be evaluated before its completion which saves a lot of government budget as well as decreases the chance of faulty

Fig. 16 Continuous stone-beam groundsill work (Hsieh 2008)

design. The completion of social vulnerablity index will make our assessment system closer to people and thus to real situation. The most used structure mitigation method is the open-type dams. The concept of geo-hazard mitigation is a systematic mitigation towards the whole watershed. Mitigation should start from the landslide source area with natural ecological engineering methods. The flexible retaining structures, such as energy-absorbing network will be the future trend. Viaduct or arc bridge will be used to pass potential debris flow area for any highways. No piers for bridge is allowed in the debris flow potential stream.

However, there are still weak points in Taiwan's system. For example, QUESUMS still has its weak point in mountainous area where there is no rain gauge for calibration. Thus, it is not easy to have a precise rainfall forecast there. As a result, warning criterion tends to be more conservative which decreases the accuracy for warning. Then, people's trust in warning will decrease and eventually, the effectiveness for the warning system would be reduced. Assessment requires a lot of information and some of the information is still not easy to obtain. So assessment for certain area will be rough. These subtle points are everywhere for geo-hazard mitigation. But we believe that as long as we treat the disaster prevention as a human business, we shall improve ourselves towards ultimate safety even we live on a special Island full of hazards.

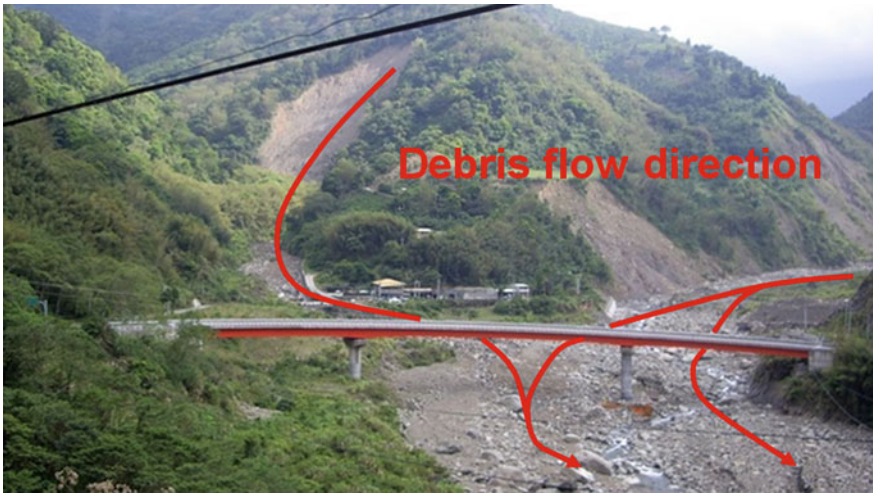

Fig. 17 The viaduct on route 21 along Chenyulan River between Eighteen Chong Bridge

Acknowledgments This paper requires a lot of information, special thanks should be given to Dr. Wei Liang-Rung from the National Science Council in Taiwan and Dr. Yin Shao-Yun from the Bureau of water and soil conservation.

References

Adger WN, Brooks N, Graham B, Agnew M, Eriksen S (2004) New indicators of vulnerability and adaptive capacity. Final project report, Norwich UK: Tyndall Centre for Climate Change Research

Caine, N (1980) The rainfall intensity-duration control of shallow landslides and debris flows. Geografiska Annaler 62A(1/2):23–27

Clark G, Moser S, Ratick S, Dow K, Meyer W, Emani S, Jin W, Kasperson J, Kasperson R, Schwarz H (1998) Assessing the vulnerability of coastal communities to extreme storms: the case of revere, MA., USA. Mitig Adapt Strat Glob Change 3(1):59–82

Chen ZY (2000) The impact force of debris flow on the slit dam, Department of Civil Engineering, National Chung-Hsing University, Taichung, Taiwan

Chou BV, Li DJ, Lo DF, Lu JJ, Yang CH (1991) Guide of prevention for debris flow. Science Press, Beijing, pp 96–108

Cutter SL (1996) Vulnerability to environmental hazards. Prog Hum Geogr 20(4):529–539

Gourley JJ, Maddox RA, Burgess DW, Howard KW (2002) An exploratory multisensory technique for quantitative estimation of stratiform rainfall. J Hydrometeor 3:166–180

Guo (2001) Introduction to ecological engineering methods, The 921 Earthquake Post-Disaster Recover Commission, Executive Yuan, Taiwan (in Chinese)

Hsieh CL (1999) Potential Debris flow evaluation and classification. I, Project report National Science Council

Hsieh PY (2008) The effect stability of channel-bed equipted with incline type ground sills. Feng Chia university water resources engineering and conservation. Taichung, Taiwan (in Chinese)

Hsieh CL, Wang CH, Chen LL (1992) Investigation and analysis of debris flows in Huai-Lien and Taitung. J Chin Soil Water Conserv 23(2):109–122

Hung YS, Chen JH (2002) Investigate into safety and engineering method of ecological engineering methods. Ecological engineering method conference. Taipei, Taiwan, pp 41

Jan CD, Chen CL (2005) Debris flow caused by Typhoon Herb in Taiwan. In: Jakob M, Hungr O (eds) Chapter 21 in the book of Debris-flow hazards and related phenomena. Springer, published by Praxis Publishing Ltd., London, pp. 539–563

Jan CD, Lee MH (2004) A debris-flow rainfall-based warning model. J Chin Soil Water Conserv 35(3):273–283

Julien PY Lan Y (1991) Rheology of hyperconcentrations, J Hydraul Eng ASCE 117:346–353

Keefer DK, Wilson RC, Mark RK, Brabb EE, Brown WM, Ellen SD, Harp EL, Wieczorek GF, Alger CS, Zatkin RS (1987) Real-time landslide warning during heavy rainfall. Science 238:921–925

Li HC, Chen Z.E, Lin SW, Lee CH, Chen HL, Yu LF, (2012) A study of the Social Vulnerability in Disaster-isolated Areas — the Case of Sanjhan Tribein Hualien", 13th Cross-Strait symposium on Environmental Resources and Ecological Conservation, Haulien, Taiwan P 33

Li HC, Liu KF (2010) Evaluation of the indirect loss from debris flow hazard—with Song-He village as an example. J Chin Inst Civ Hydraul Eng 22(2):159–166

Li HC, Young HH (2011) Establishment and application of household loss model for slope-land hazard. J Chin Inst Civ Hydraul Eng 23(4):437–444

Lin PS, Lin JY, Chan KF, Chou WH (2007) An experimental study of the impact force of debris flows on slit dams, The Fourth International Conference on Debris-Flow Hazards Mitigation, China

Lin JY (2006) Flexible retaining structure for evaluation of debris-flow hazards mitigation. National Science Council, Council of Agriculture, Taiwan

Lin CY, Chiou YW (2003) Introduction of ecological engineering methods. Mingwen Press, Taipei, Taiwan

Liu KF, Huang MC (2006) Numerical simulation of debris flow with application on hazard area mapping. Computat Geosci 10:221–240

Liu KF (1998) The countermeasures of debris flow. Technique of civil, first issue, 178–183

Liu KF, Li HC (2006) Assessment of direct loss from debris flow hazard. Chin J Soil Water Conserv 37(2):143–155

Liu KF, Li HC, Hsu YC (2009) Debris flow hazard assessment with numerical simulation. Nat Hazards 49:137–161

National Science Council "Project result summary from 2000–2010" (2011)

Shih BJ, Jern KY, Shieh CL, Chen LJ (1997) A study on the hazardous debris flow zoning. In: Proceedings of the 1st National debris flow conference Taiwan, pp 141–155

Soil and Water Conservation Bureau (1992) The specifications of conservatively technique of soil and water. Council of Agriculture, Executive Yuan, Taiwan

Soil and Water Conservation Bureau (1996) The guide of soil and water conservation. Council of Agriculture, Executive Yuan, Taiwan

Tsai YF (2002) Delimiting debris flow hazard zone. Chin J Mech 18(2):91–102

Wieczorek GF (1987) Effect of rainfall intensity and duration on debris flows in Central Santa Cruz mountains, California. In: Costa, JE, Wieczorek GF (eds) Debris flows/avalanches: process, recognition, and mitigation. Rev Eng Geol 7:103–114. Geological Society of America, Boulder, Colorado

Forestry Bureau (1992) Survey report of current status of dam in Taiwan. Council of Agriculture, Executive Yuan, Taiwan

Wu HL (2003) Using the ideal of natural ecological engineering methods to straighten on the landslides of debris flow and case study. Soil and Water Conservation Bureau, Council of Agriculture, Executive Yuan, Taiwan

Yu FC, Lein HB (1999) Discussion of delimiting dangerous debris flow deposition fan. Geotech Res 74:7–66

The Mechanisms for Initiation and Motion of Chinese Loess Landslides

Tonglu Li, Peng Wang and Yu Xi

Abstract Loess is a wind-blown sediment with characteristic loose structure and low water content. Moisture content and confining stress are the key factors controlling the mode of its deformation and failure. CU tri-axial tests suggest that in low moisture content and low confining stress, loess fails by cracking with the development of vertical fissures while if fails by shearing in moderate moisture content and moderate confining stress, with a decline shear plane. Also, loess fails by slow creep in high moisture content and high confining stress. Therefore, the failure mode of the loess in a critical slope varies with the moisture content and confining stress which defines the initiation of a loess landslide. Loess landslides can be recognized as four types: rapid long run-out slide, rapid flow slide, slow creep slide and quick slump slide. The mechanism of the landslide movement is also controlled by the moisture state on the sliding path. The rapid long run-out slide is that the sliding mass slides on a saturated loose ground, where the pore water pressure caused by undrained loading and undrained shear inside the ground is much higher than that inside the sliding mass. Therefore, the shearing may take place in the ground because of liquefaction of the loose material, such as sand and gravel, which may cause a rapid and long run-out movement. The quick flow slide is that the saturated sliding mass slides on an unsaturated or dry ground, which produces a lower or even negative pore pressure, a film of fluidized soil is stuck on the ground, and the slide occurs in the sliding mass. It also causes a quick movement because liquefaction occurs at the base of the sliding mass. The slow creep slide is that the sliding mass slides on an impermeable sliding bed, such as red clay or bedrock, where the pore pressure at the slip path neither generate nor dissipate, so the driving force are almost equal to the resisting force along the slip path, and the movement could be very slow or off and on. The slump slide is that

T. Li (✉) · P. Wang · Y. Xi
Department of Geological Engineering, Chang'an University, 710054 Xi'an, China
e-mail: dcdgx08@chd.edu.cn

F. Wang et al. (eds.), *Progress of Geo-Disaster Mitigation Technology in Asia*, Environmental Science and Engineering, DOI: 10.1007/978-3-642-29107-4_5,

the unsaturated or dry sliding mass slides on an unsaturated or dry ground. Because there is a sharp reduction from peak strength to residual strength for the unsaturated sliding surface, the sliding mass has a quick fall and then stops at the toe of the slope where none or even a negative pore water pressure generated on the sliding surface because of water dissipation.

Keywords Loess · Landslide · Pore water pressure · Mechanism · The Chinese loess plateau

1 Introduction

Loess is deposited in arid and semi-arid areas and is a typical unsaturated soil. The physical and mechanical properties of loess are determined by its material composition and moisture content. Consequently, the initiation and the motion mechanism of loess landslide are largely determined by moisture distribution within the slopes. In dry states, the loess could have a high strength and the slopes can be stable at a steep angle, so we can often see the vertical loess cliffs in loess area. However, the strength could decrease as the moisture content increases. The moisture content in a loess slope varies spatially implying that the deformation mode and strength varies with the change in moisture content down a slope. Therefore, the deformation, failure characteristics and strength of the loess in different level of moisture content were investigated using CU tri-axial tests. The motion mechanism of loess landslide is also clarified based on the moisture state along the failure plane.

2 Deformation and Failure Modes of Loess Specimens

For a loess slope, the moisture on the potential sliding surface within it changes with depth. The upper part is dry and has a low stress level, the middle is humid and has a moderate stress level, and the lower is wet and has a high stress level. As shown in Fig. 1.

To determine the effect of the moisture on the deformation and the failure mode, a group of intact samples were taken from the fifth loess bed (L_5) at a loess slope for laboratory study. The particle size of the sample was analyzed with the Laser Grain Size Analysis Equipment. The curves of particle size versus content accumulation and distribution in percentages are shown in Fig. 2. It suggests that the loess consists of 2 % fine sand (>50 μm), 60 % silt (5–50 μm), and 38 % clay (<5 μm), of which silt takes up the main portion. The general physical character of the sampled loess is shown in Table 1.

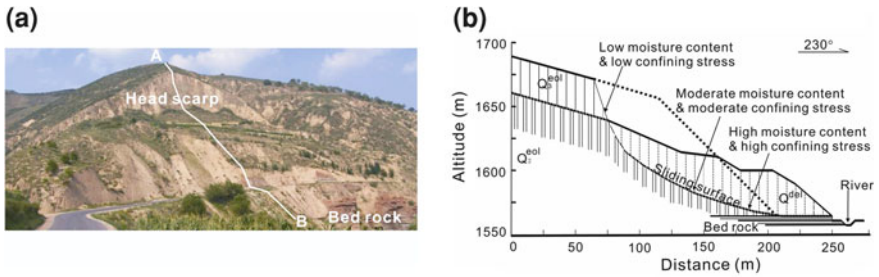

Fig. 1 The moisture content and stress level on the sliding surface of a failure slope

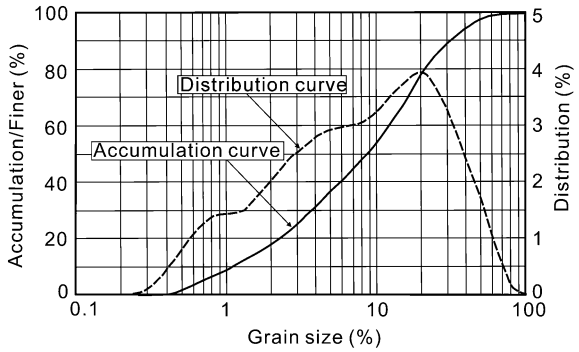

Fig. 2 Accumulative and distribution of the specimen's grain size for CU test

Table 1 The general physical properties of the sampled loess

Clay content (l%)	Density (γ/g. cm^{-3})	Moisture content (wl%)	Liquid limit (w_L%)	Plastic limit (w_P/%)	Plastic index (I_P/%)	Liquid Index (I_L)	Dry density (ρ_d/g.cm)$^{-3}$	Void ratio (e)
27.4	1.53	13.9	37.0	22.8	14.2	−0.62	1.37	0.972

The samples were carefully cut to cylindrical shape with a height of 8 cm and a diameter of 3.9 cm for CU tri-axial tests. The saturated moisture content of the specimen was calculated to be about 32 %. The specimens were divided into eight groups. Each group has 13 specimens with moisture contents of 3, 6, 11, 16, 21, 26, 30, 32 %, respectively and tests in different confining stress. The moisture content of the specimens were controlled to the expected value by the follow processes: First, dry all the specimens in oven for 12 h, then put one of them on electronic balance as it cool down, and calculate the bulk weight with the expected moisture content and the dry weight of the specimen. In the beginning, the dry weight was showing on the balance, then, drop water on the specimen with an injector till the balance shows the specimen get to the bulk weight. At last, enclose

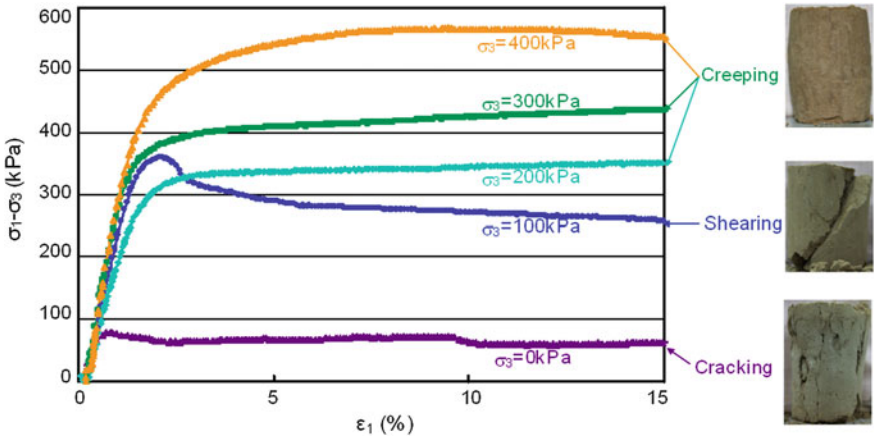

Fig. 3 Failure modes of the loess specimens under CU tri-axial tests

the specimen with a rubber film for keeping the water from escaping and making the water in the specimen uniform. As the water added in the specimen is exceeded, just put it for a while for the water releasing till satisfied quantity. The specimens of 1–7 groups are unsaturated, all of which were conducted with the above processes. Those of the 8th group are completely saturated which were saturated by injecting CO_2 for 30 min and then slowly filling de-aired water in 20 cm pressure head. Saturation was ensured by obtaining a B value of exceeding 0.95 (Skempton 1954).

The specimens of each group were consolidated under a given confining stress (σ_3) of 0, 50, 100, 150, 200, 250, 300, 350, 400, 450, 500 and 550 kPa., and then sheared by constant axial strain rate of 0.04 mm/min in undrained condition. Termination condition of the test at each confining stress is as the axial strain reaches 15–20 %. The tests were conducted on the LSB-1 Stress–strain controlled seepage tri-axial equipment (made in China).

The results of CU tri-axial tests suggest that there are three types of failure mode for the loess specimens. These are cracking, shearing and creeping. For the cracking mode, the specimen is cracked vertically, and the stress–strain curve has a typical strain-softening character with a clear peak value and a reduction to residual after the peak point, and the yield point is very close to the peak point, as shown in Fig. 3a. For the shearing mode, the specimen is sheared along a decline plane, and the stress–strain curve also has a typical strain-softening character similar to the former case, as shown in Fig. 3b. For the creeping mode, the specimen is laterally expanded without clear failure traces, and the stress–strain curve has a strain-softening, perfect plasticity or strain-hardening characters, as shown in Fig. 3c, in this case, there is no clear peak point on the curve, even for the strain-softening, the strain transit gentle without sharp reduction.

Figure 4 shows the failure modes of all the specimens of confining stress versus moisture content. It shows that the failure mode of loess is dependent on the

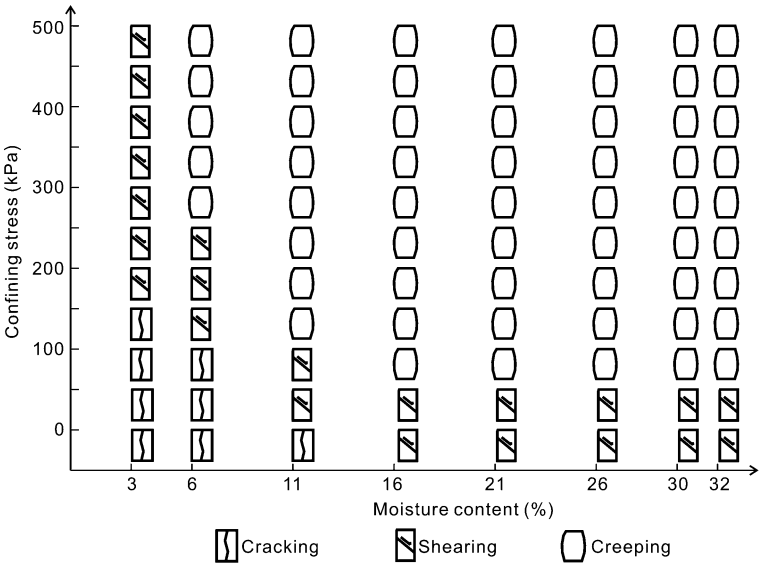

Fig. 4 The failure mode of the specimen in certain moisture content and confining stress

moisture content and confining stress. Loess with low moisture content and low confining stress equivalent to the upper part of a slope fails by cracking; loess with moderate water content and moderate confining stress equivalent to the main portion of the slope in the middle fails by shearing; loess with high moisture content and high confining stress equivalent to that at the slope base fails by creeping. As loess slopes get to critical state, stress at the upper part of the slope are released first, then followed by the deformation and failure mechanism control by the shearing portion in the middle and the creeping portion at the base.

It is also found that the moisture content in the specimen controls the shearing strength by pore water pressure. Figure 5 shows that the results of the specimens with moisture content of 3 % are almost dry. All the stress–strain curve are strain-softening, and the *p*–*q* curves show there are no pore water pressure produced during the shearing process. Figure 6 shows that those of the specimens with moisture content of 26 % are humid. The stress–strain curve are from perfect plastic to strain-hardening, and the *p*–*q* curves shows that the pore water pressure produced as the shearing stress get to certain level. Figure 7 shows that those of the specimens with moisture content of 32 % are completely saturated. The stress–strain curves are all strain-softening, and the *p*–*q* curves show that pore water pressure is produced at the beginning of the shear. Extra pore pressure is also produced in the process.

The red line on p–q curves are the residual strength line for the group of the specimens from the parameters of which, the c' and φ' can be calculated. The results are shown in Table 2 and Fig. 8. It can be seen that the effective friction angle φ' is independent of moisture content, while the effective cohesion c' has a

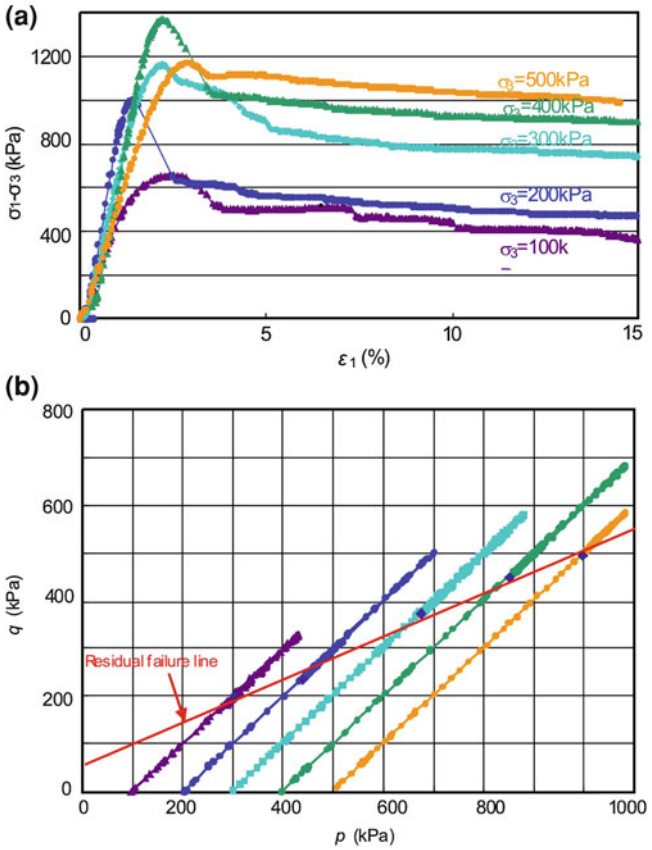

Fig. 5 The CU tri-axial tests results of the specimens with the moister content of 3 %. **a** The principal stress difference (σ_1–σ_3) versus axial strain (ε_1). **b** Maximum shearing stress (q) versus Mean principal stress (p)

reverse correlation with the moisture content. As the moisture content exceeds plastic limit, c′ is kept constant.

The motion characteristics are also defined by the pore water properties on the failure path. Kinetically, Li et al. (2007) proposed that loess landslides can be divided into four type which include: rapid long run-out slide, rapid flow slide, slow creep slide and quick slump slide.

3 Rapid Long Run-Out Slide

Rapid long run-out slide often occurs on the sides of the loess platforms where the loess slope is high and steep. High river terraces are eroded to leave the wide and flat terrace lying between the toe of the slope and the river. The grounder water

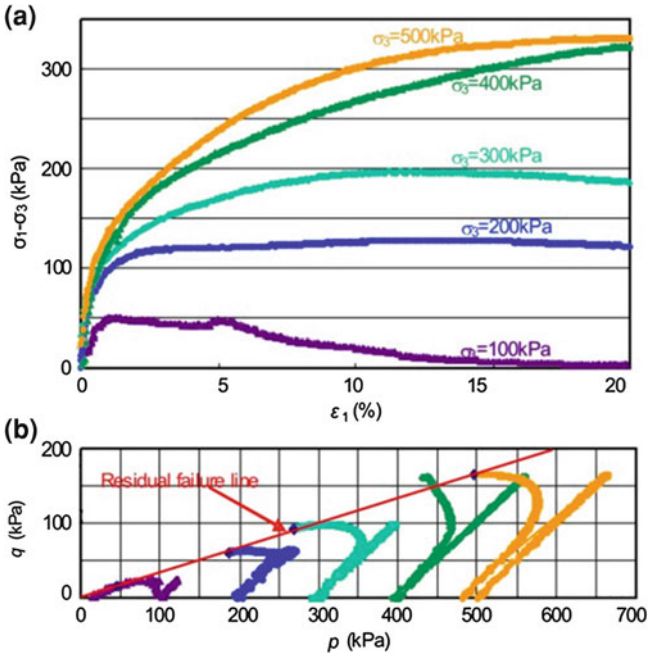

Fig. 6 The CU tri-axial tests results of the specimens with the moister content of 26 %. **a** The principal stress difference (σ_1–σ_3) versus axial strain (ε_1). **b** Maximum shearing stress (q) versus Mean principal stress (p)

level in the first terrace is generally very shallow. The main triggering factors are either groundwater level rise or surface water. The sliding process can be divided into two phases. The first phase is that the sliding mass separates from the sliding-bed of the slope and slumps down rapidly; the second phase that is as it hits on the first terrace in front of the slope toe, liquefaction of the saturated gravels and silt-clay may reduce the shear resistance which causes the sliding mass to move with high velocity. So this type of landslide has a very high speed and long moving distance (Sassa 1988; Sassa et al. 1997).

In this case, pore water pressure generated by undrained loading and undrained shear inside the ground is much higher than that inside the sliding mass, therefore the shearing takes place in the ground. The high pore pressure causes liquefaction of the ground material, and then produces a big difference between the driving force and resisting force. Therefore, the sliding mass could achieve a high acceleration to move as a floating body with a high speed and long run-out. The mechanism is shown in Fig. 9.

Saleshan landslide in Gansu province, China is a well known case which has been mentioned by many authors. It failed in March 17, 1983, destroyed four villages, took 277 lives and 300 domestic animals, filled up two small reservoirs and covered more than 20 million square meters of farmland in a few minutes

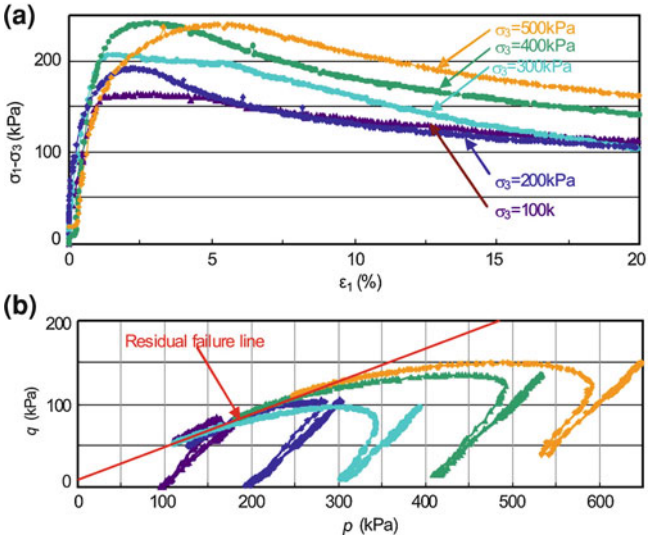

Fig. 7 The CU tri-axial tests results of the specimens with the moister content of 32 %. **a** The principal stress difference (σ_1–σ_3) versus axial strain (ε_1); **b** Maximum shearing stress (q) versus Mean principal stress (p)

Table 2 The Effective cohesion c' and friction angle φ' measured at different moisture content

Group no.	1	2	3	4	5	6	7	8
Moisture content (wl%)	3.0	6.0	11.0	16.0	21.0	26.0	30.0	32.0
Effective cohesion (c′/kPa)	167.9	120.5	67.4	35.2	16.6	16.6	16.4	16.2
Effective friction angle (φ'/°)	22.6	21.5	20.1	20.0	20.1	20.1	21.3	22.6

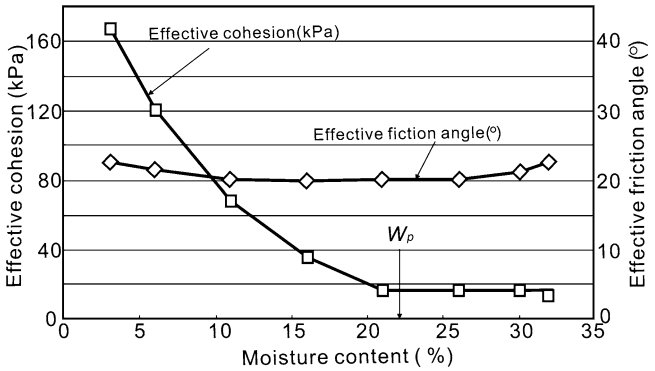

Fig. 8 The Effective cohesion c' and friction angle φ' measured at different moisture contend

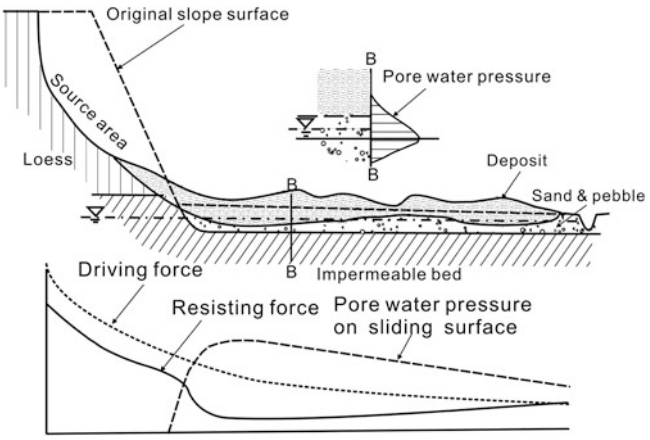

Fig. 9 The motion model for a rapid long run-out slide

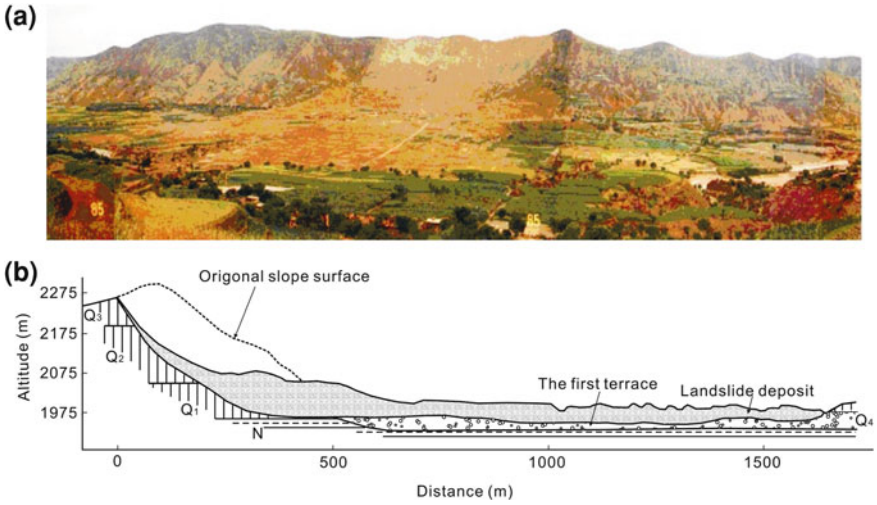

Fig. 10 A rapid long run-out slide, Saleshan landslide occurred in 1983. **a** Overview. **b** The main section

(Liu et al. 2000). The landslide slipped from 300 m high slope with a speed of 30 meters per second and moved 1600 m down-slope getting to the opposite bank of Baxie river. It is a typical rapid long run-out slide. The stratum of the failed slope is that the loess on the above and the Tertiary red clay lying under the loess. The red clay is a relative impermeable bed, on which the groundwater accumulated and softened the loess and the clay. So the groundwater action caused the quick sliding. The front of the slope toe is the first river terrace of the Baxie river which consists

Fig. 11 A typical topography preferring for the rapid long run-out landslide, the side slope of a loess platform to the south bank of the Jinghe river

of loose sand with shallow groundwater, Liquefaction of the loose sand on the sliding path is the cause of its long run-out as shown in Fig. 10.

This type of landslide also popularly distributes at the side of a loess platform to the south bank of the Jinghe river. Those happening in recent decade are Shutangwang (in 2001), Xiuchidu (in 2002), Dongfeng (in 2003) and Taiping (in 2005) landslides. Figure 11 shows a part of the bank that the whole slope is composed of loess, from Holocene to early Pleistocene, with the slope height of 70–90 m and slope angle of 50–70°. The first terrace is composed of 1 m Q_4 alluvial silt-clay upper and 2–3 m or more gravel bed down underlying with old clay, and the grounder water level is of 0.5–1.0 m in depth. The flow water of irrigation is the triggering factors of the slides. Before failing, the top of the slop have developed many fissures by unloading process and water erosion, which allowed a mount of irrigation water flowing in the slope. Rising of the groundwater level and reducing of the loess strength resulted in the failure of the slope at first. As the sliding mass separated from the slope and slumped down quickly, it hit on the first terrace and caused liquefaction of the saturated gravels and silt-clay, which produced a very high speed and a long distance.

4 Rapid Flow Slide

Rapid flow slide is not popular but occasionally occur in areas with suitable topographic conditions. It is characterized by the change of its motion functions in the source area and the path. This type of slide initially starts as a landslide but quickly changes to a flow slide moving down along a gully to the outlet or a slope

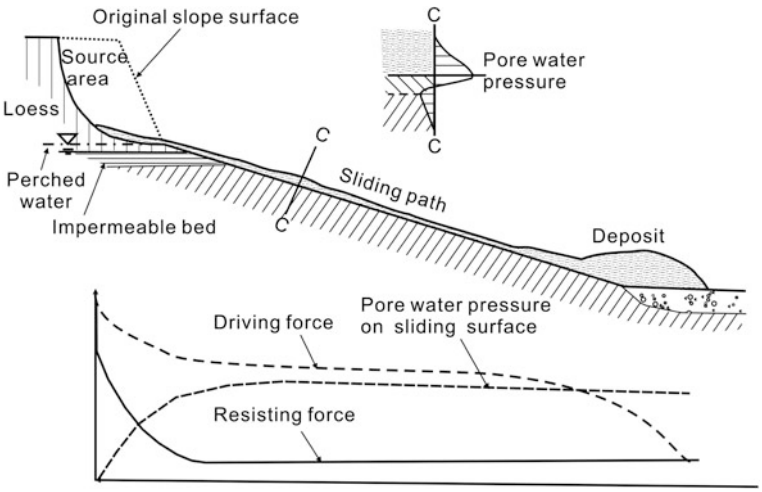

Fig. 12 The motion model for rapid flow slides

to the toe. Rapid flow slide often breaks suddenly and results in damages to properties and houses down the slopes.

For this type of landslide, the lower portion of the sliding mass is saturated. Especially for the loess in the Upper Pleistocene (Q_3) and the top of the Middle Pleistocene (Q_2) which has a loose structure with the saturated water content higher than the liquid limit. As the sliding mass starts to move, the structure of the loess near the sliding surface is damaged and the state is changed from solid to liquid. This process is called static liquefaction because it occurs with a very little strain. Static liquefaction may results in a remarkable reduction of shear strength with the sliding mass moving out of the sliding bed with a very high speed. As it moves down, the slope surface in the path may be dry or unsaturated. The pore pressure between the slope surface and sliding mass dissipates easily which causes a lower or even negative pore pressure. But the pore water pressure in the lower sliding mass could maintain higher value and the sliding mass keeps in liquid state during the moving process, so the friction between sliding mass and the ground could be little higher than that in the liquefied sliding mass. A film of liquid soil is stick on the ground and the sliding occurs in the sliding mass, which conducts a high speed and a long run-out, the sliding mass finally gets to the toe of the slope and deposit there. The mechanism is illustrated as Fig. 12.

The rapid flow slide dominates the sides of the HeiFangtai loess platform which is located in Yongjin county, Gansu province of China. It is the fourth terrace of the yellow river where the Huangshui river joins the Yellow River. The top of the platform is 120 m high relative to yellow river bank (top of the first terrace) and was used as farmland in 1970's. The irrigation system was also built to pump up the yellow river to irrigate the farmland, so the water penetrates into the slope to induce a large number of landslides. Of which, the rapid flow slides are at most in

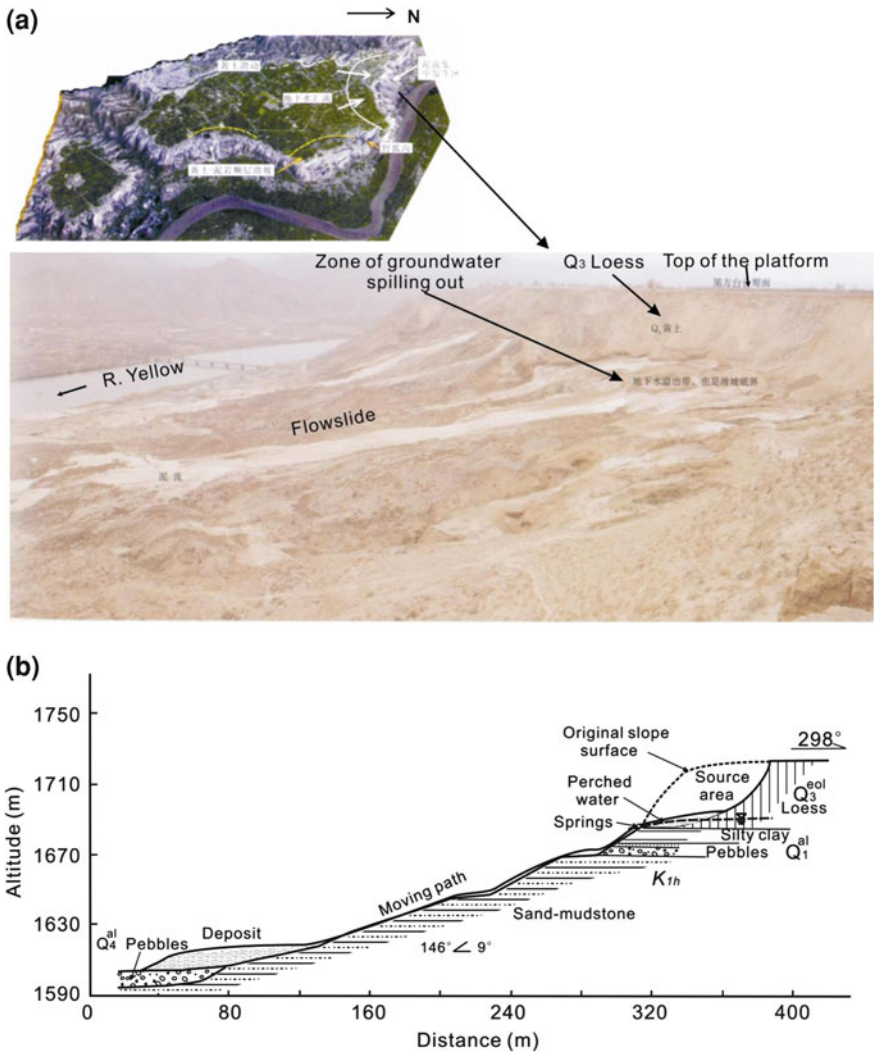

Fig. 13 The landscape of Heifangtai loess platform and the flow slides on the side **a**, The Jiaojia flow slide is the nearest one in the graph, **b** shows the main geological profile of the Jiaojia flow side

number, our investigation observed that there are 15 such slides distributed on the north and east sides of the platform.

We measured the geological profile of the side slope as shown in Fig. 14. It shows that the slope materials are composed of Q_3 loess with thickness of 20 m, a bed of Q_2 red clay with thickness of 4 m, a bed of Q_1 gravel with thickness of 8 m and the Cretaceous inter-beds of sandstone and mudstone underneath. Because the red clay is relative impermeable, as water penetrates down the loess, then accumulates on top of

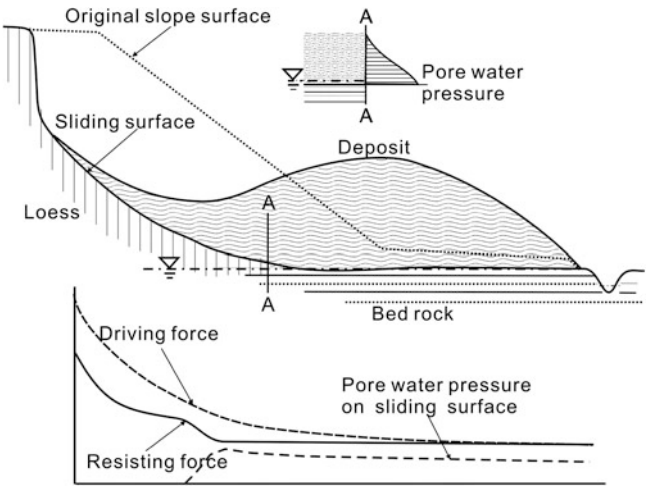

Fig. 14 The motion model for slow creep slide

the clay and spills out on the side slope (Fig. 13a). Therefore, the loess above the red clay is easily saturated and softened. As the sliding mass slumps down, it quickly changed to a mudflow rushing down along the slope. The lower slope being the flow path is sandstone and mudstone, which is relatively stiff, and even though gentle, the mud remains along the path.

Figure 13b shows Jiaojia landslide. The 1:10,000 aerial images were taken in April 1977, July 1997 and July 2001 by Gansu provincial survey bureau and 1:10,00 3D laser scanning topographic imagine was taken in April 2010 by the Xi'an geological survey for this landslide. The images were transferred to DEM models to calculate the failure process by comparing the models in different periods (Zhang et al. 2011). The results suggest that the volume of sliding mass from the source area is 2516665.6 m^3 between 1977 and 1997, 267733.1 m^3 between 1997 and 2001 and 493895.0 m^3 between 2001 and 2010; and the average retrogressive distance of the back scarp is 88.4 m with the rate of 4.42 m/a between 1977 and 1997, 23.2 m with the rate of 5.81 m/a between 1997 and 2001, 14.8 m with the rate of 1.64 m/a between 2001 and 2010. The total retrogressive distance is 126.4 m during the past 33 years, even so the rate in recent decade is much lower than that in before, but the failures still occur in every irrigating season. Similar loess flow slides also occur in the other loess area.

5 Slow Creep Slide

The slow creep slides are characterized by its slow moving rate. In general, the horizontal displacement is usually longer than the vertical and often occurs in areas where slopes are composed of Quaternary loess underlain by impermeable clay or bedrock. The sliding surfaces are usually on top of the impermeable bed, so

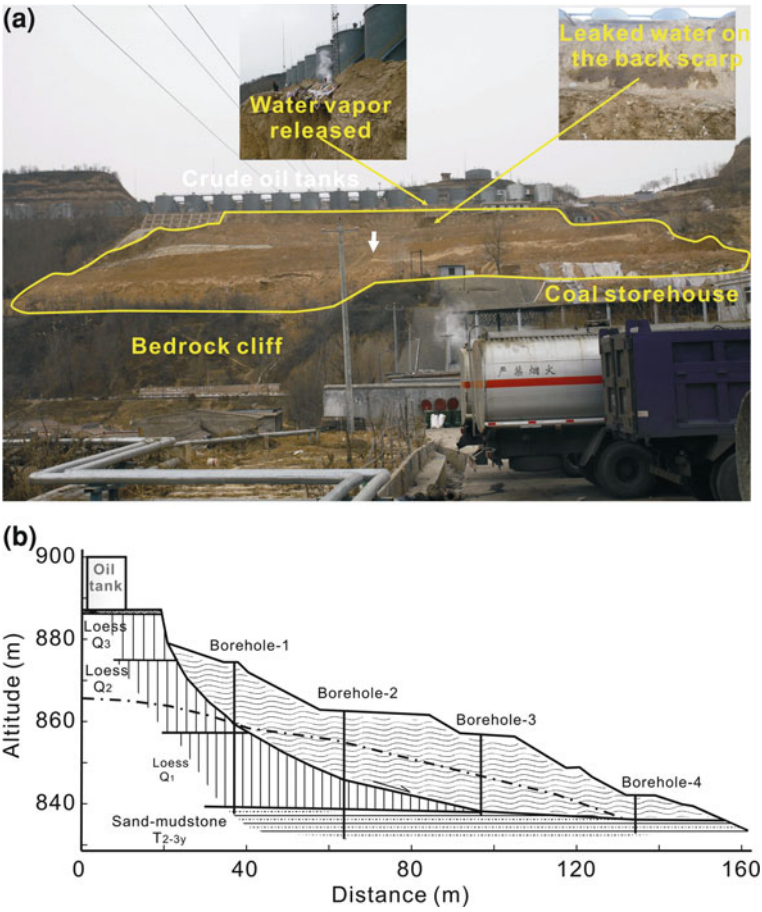

Fig. 15 A slow creep slide of the Yanlian landslide: **a** Overview. **b** The main geological profile of the Yanlian landslide

the ground neither generates nor dissipates pore pressure, and the pore water pressure maintains a constant. The shear strength on the sliding surface is almost equal to the shearing stress, so the landslides have a low speed and move in a long or a short length as illustrated by Fig. 14.

This type of landslide is prominent in the Chinese loess area, especially around the northern loess plateau. They generally dominate the sides of riverbanks where the loess coves on the high river terraces, which are composed of gravels, Tertiary red clays and Miocene bedrocks. The lateral erosion or human excavations at the foot of slopes often trigger the landslides.

A typical case is the Yanlian landslide which occurred on October 21st 2010. The landslide is located in Hungling county, Shaanxi province of China, on the right side of the Luohe river. It is 150 m in length, 240 m in average width,

28,885 m^2 in plane area, 13.8 m in average thickness, and 400 thousand cubic meters in volume. It moved off and on for 2 days and 20 m forward at the toe and 8–12 m down at the back scarp. The movement was very slow that there is enough time for persons within there to escape, nobody died in this accident (Fig. 15).

The district in which the landslide occurred belongs to the Yan'an oil refinery. There are 33 huge crude oil tanks built on top of the slope with 14 oil-transfer pipes crossing over the slope toe; a large coal storehouse and a heat-supply workshop is situated next to the toe of the slope. The landslide destroyed the 14 oil-transfer pipes causing the Yan'an oil refinery to stop production for a week. The landslide also buried part of the wall of the coal storehouse, affected some parts of the oil tanks near the head scarp, and cut off a county road.

Site investigation and boreholes revealed that the material of the failed slope is composed of 30 m thickness of loess, a 1 m of gravel and bedrock underneath. The gravel bed is the deposit of the third Luohe River terrace and the surface of the bedrock is gentle. The landslide has an armchair-landform that the back scarp is 8–10 m high, steep and concave in shape. It sheared out on the top of the bedrock, so the sliding surface is steep at the back and gentle at the base as Fig. 10 shown.

The landslide was induced by water infiltration. We have drilled some boreholes within and without the landslide just after failure, which suggests that the groundwater is rich in the sliding area but shortage out of the area. Loess has a very low permeability (mainly 10^{-4}–10^{-5} cm/s) and the inclination of the slope is relative steep (30°–40° before failure), so most of the precipitation runs off other than penetrates into ground. If the source of the groundwater in the sliding area is not the rainwater, where does it come from? As we looked up the platform on the top of the slope on which the crude oil tanks set, there is a water heating system working in winter for keeping the crude oil in the transfer pipes from solidifying. The system has pressure-release valves releasing water vapor and part of the vapor condenses to water as it meets the cold air. The condensed water penetrated into ground drop by drop for 2–3 decades. The water accumulated on the surface of bedrock and caused rising of the groundwater level, which consequently reduced the shear strength of the loess. Therefore, the groundwater is the essential cause of the slide.

Before the slope failed in 2010, it had deformed for 2 years with some fissures appearing on the slope surface. Anchor-frameworks and micro-piles have been used to stabilize the slope. However the reinforced work did not extend to the sliding surface which made the countermeasures ineffective. As shown in Fig. 11, the sliding surface of the slope is steep at the back and gentle at the base. The back rupture is in the unsaturated loess that has a relative high strength and shows softening feature at the stress–strain curve, which has a remarkable reduction from peak strength to residual strength. The base rupture is on the base of the loess slope and at the top of the bedrock where the completely saturated loess has a relative low strength and shows ideal elasto-plastic features at the stress–strain curve which shows a steady strength as strain increased. Because the base rupture takes up the main part of the whole sliding surface, the initial failure developed slowly. After the failure, the movement of the slide was mainly controlled by the residual

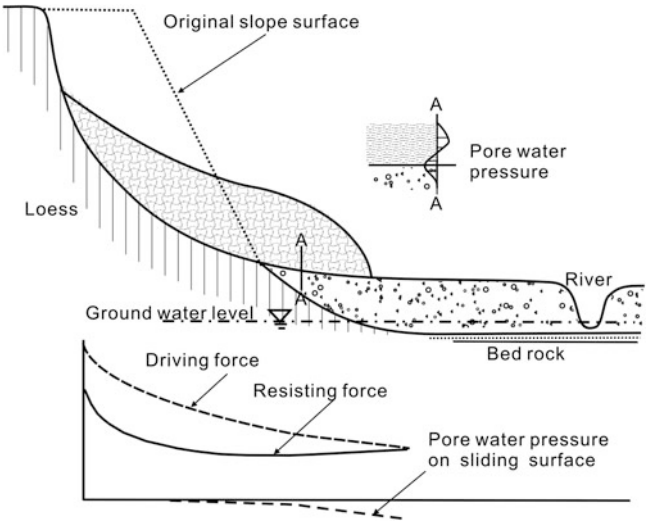

Fig. 16 The motion model for quick slump slides

strength that was constant during the process, so the landslide appears as slow creep movement as illustrated in Fig. 15b.

6 Quick Slump Slide

The feature of this type of landslide is that it has a short run-out distance, and the vertical displacement is larger than that horizontal. The recent landslides induced by both natural agents and human activities on the Chinese loess plateau failed as slump slides. The quick slump slides generally occur on steep loess slopes, with steep sliding surfaces. In this case, the ground water level is far below the toe of the slope, so both the sliding surface and the sliding path were unsaturated, which indicates that no pore water pressure was created during the failure and movement. As the sliding mass slumps down, the pore water pressure even become negative because of water dissipation, so it will get to a new equilibrium soon after. Therefore, it has a short run-out distance (Fig. 16).

A typical case is the Sanmutai landslide in Fuxian county, Shaanxi province, which occurred at 22 h on May 6th 2006 (Fig. 12). The landslide is located at the side of a loess ridge or the side of a stream valley. From measured geological profile of the landslide (Fig. 17b), it can be seen that the material of the sliding slope is composed of a 28 m thick loess bed on the upper layer and 5 m thick pebbles at the lower layer. The loess bed can be further distinguished as 10 m Q_3 loess and 18 m Q_2 loess from top to lower, in which there have plenty of vertical joints. The pebbles are the deposit of the second terrace of the stream. The slope

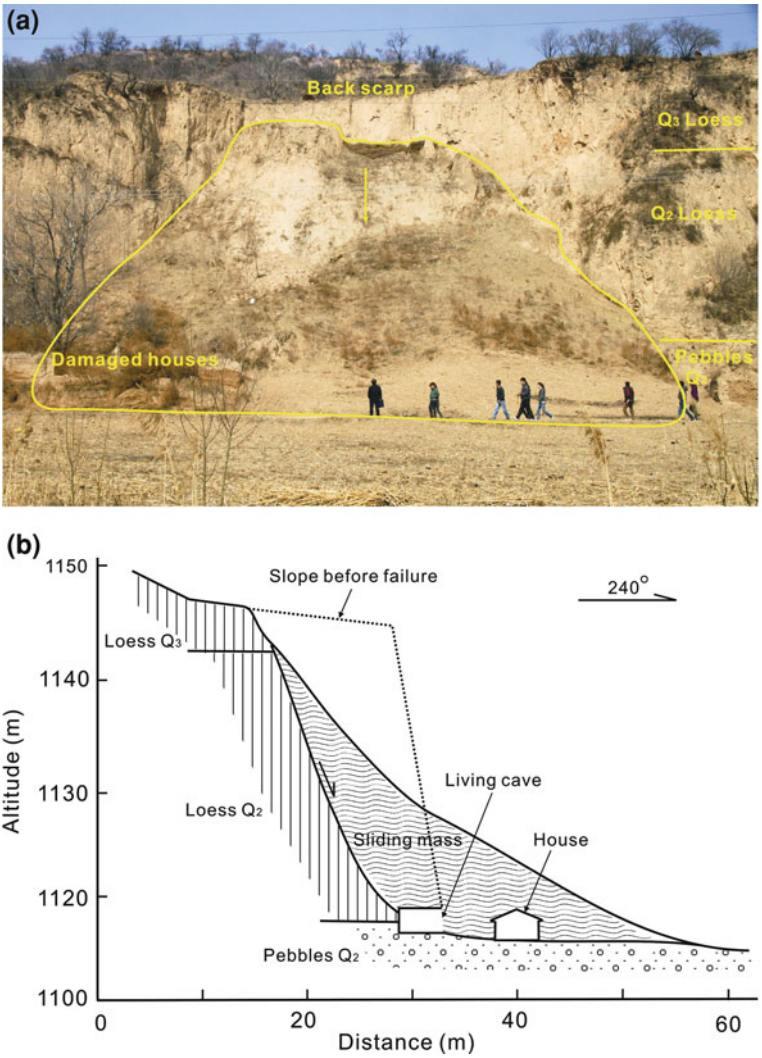

Fig. 17 The Sanmutai landslide in Fuxian county, Shaanxi province occurred on May 6th 2006. **a** Overview. **b** The main profile

has a vertical height of 33 m and slope angle of 50°. Before the slope failed, there were four living caves excavated on the toe of the slope and a row of five houses built infront of the slope in which four families lived. The slope material slid and stopped at the foot of the slope; the failed mass shows a cone-shaped structure (Fig. 17a), with a vertical height of 26 m, bottom width of 37 m and thickness of 15 m. It destroyed all the living caves and the surrounding houses and also killed two persons. There was no rainfall, irrigation channels or springs around the slope. The main causes of the landslide are slope undercutting and excavations carried

out at the slope toe. The sliding occurred in the dry loess which has a relative high strength, but shows a big difference between peak and residual strength. Cutting and Caving may have caused the slope to be in a critical state condition.

In the Chinese loess area, heavy casualties made by this type of landslides are recorded every year, a large part of them were due to engineering activities, such as road-cut, site leveling and underground mining/surface excavations. In addition, quick slump slides also occur near the sides of the loess gullies which have been affected by erosion in recent geological time. The slopes of the gully sides are very steep because of the effect of erosion, so failures often occur there. The gullies are generally far from the towns and resident areas, so there are no casualties and serious loss caused by the landslides, but they are the main sources of soil erosion.

7 Conclusion

Loess landslides are the most developed geological disaster in the Chinese loess area. They are divided into four types: slow creep slide, rapid long run-out slide, quick slump slide, and rapid flow slide. These four types occur in different geological and hydro-geological conditions. Pore water pressure controls the motion types of the sliding masses. The slow creep slide is that the sliding mass slides on an impermeable sliding bed. The rapid long run-out slide is that the sliding mass slides on a saturated loose ground. The quick slump slide is that the less saturated sliding mass slides on a less saturated or dry ground. The rapid flow slide is that the saturated sliding mass slides on an unsaturated or dry ground.

Acknowledgments This research work was supported by National natural science foundation of China (NSFC-40972182). The support from this agency is gratefully acknowledged.

References

Li TL et al (2007) The types of loess landslides and their spatial prediction method. Chin J Eng Geol (in Chinese), 15(4):500–505

Liu ZY et al (2000) Kinematical block model of long run-out prediction for high-speed landslides. Chin J Rock Mech Eng (in Chinese) 19(6):742–746

Sassa K et al (1997) Landslide hazard assessment in cultural heritage,Lishan, Xian. In: Sassa K (ed.) Proceedings of international symposium on landslide hazard assessment, Xi'an 13–16 July, pp 1–24.

Sassa K (1988) Geotechnical model for the motion of slides. In: Proceedings of the 5th international symposium on landslides 1:37–56

Skempton AW (1954) The pore–pressure coefficient A and B. Geotech 4(4):143–147

Zhang MS, Dong Y, Sun PP, Liu J (2011) Risk analysis and control of the Zhaojia'an landslide through controlling water levels. Hydrogeol Eng Geol 38(1):123–138

Geo-Disaster and Its Mitigation in Nepal

Ranjan Kumar Dahal and Netra Prakash Bhandary

Abstract Geologically young and tectonically active Himalayan Range is characterized by highly elevated mountains and deep river valleys. The mountainous terrains of Nepal Himalaya are characterized by dynamic physical processes, and therefore, mitigation of geo-disaster is a big challenge. A better understanding of the geological nature of the terrain and the interaction of various triggering factors of geo-disaster will greatly help in the development of safer infrastructures, mitigation of geo-disaster, and control of land degradation in the Himalaya. Over the years, Nepal has gained a significant amount of experiences in geo-disaster studies, especially in design and survey of geo-disaster mitigation programs, in the fields of hazard and risk assessment, in low cost rural road engineering; in community based river training work and in slope maintenance incorporating indigenous techniques. This chapter provides an overview of geo-disasters in Nepal and their mitigation efforts. In this chapter, all geological zones of Nepal are evaluated from the perspective of geo-disaster occurrences. Geo-disaster mitigation efforts of both governmental and non-governmental sectors are also evaluated. People's perception for geo-disaster mitigations efforts are also discussed in this chapter.

R. K. Dahal (✉)
Department of Geology, Tribhvuan University, Tri-Chandra Campus, Ghantaghar, Kathmandu, Nepal
e-mail: ranjan@ranjan.net.np

R. K. Dahal · N. P. Bhandary
Ehime University, 3 Bunkyo-cho, Matsuyama, Ehime, Japan 790-8577

F. Wang et al. (eds.), *Progress of Geo-Disaster Mitigation Technology in Asia*, Environmental Science and Engineering, DOI: 10.1007/978-3-642-29107-4_6,

1 Introduction

Nepal is a highly mountainous country between China in the north and India in the south, east and west with an area of 147,181 sq. km. It occupies about 800 km long central part of the Himalayan arc, which has been formed by the collision of Indian and Eurasian plates. Nepal is mainly characterized by rugged topography, very high relief, variable climatic conditions, complex geological structures affected by active tectonic process and seismic activities. Topographic elevation changes from 60 m in the southern plain to 8,848 m at the Mt Everest within a north–south horizontal distance of less than 200 km. This kind of topography is highly prone to geo-disaster. The seasonal monsoon rains, intense but improper land use practices make the Nepalese Himalayas the most unstable landscapes in the world.

Steep slopes are the key features of the Himalayan geomorphology. Rapid uplift from Miocene, which continues even today, has created local relief measurable in kilometres from river valleys to peaks. As a result, large-scale valley slope creeping (large-scale landslides) due to gravity has been prolonging from the early uplift of mountains, and it is a common feature. Thus, landslides may be regarded as one end of the spectrum of slope modification processes in the Nepal Himalaya (Waltham 1996). The combination of the weak rock and thick soil cover and monsoon climate makes each physiographic zone of Nepal prone to geo-disaster (Dahal 2006, Dahal et al. 2009). In these contexts, for development of safer infrastructures, mitigation of geo-disaster and environmental degradation in the Himalaya, a better understanding of geological nature of terrain and interplay of prime triggering factor with soil and rock is indispensable.

Nepal suffers from tremendous natural disasters every year, especially landslides and floods. In Nepal, landslide, floods, earthquakes and snow avalanche are considered as major geo-disasters. Floods are included in geo-disasters in Nepal, particularly, because both geological and hydro-metrological causes involve in flooding. A great number of people are affected by large- and small-scale geo-disaster throughout the country, particularly during monsoon periods. The measured values of mean annual precipitation in Nepal range from a low of approximately 250 mm in north of the Himalaya to exceeding 6,000 mm in western Nepal. The annual rainfall in capital city Kathmandu (central Nepal) generally exceeds 1,350 mm. The mean annual rainfall varying between 1,500 mm and 2,500 mm predominate over most of the country. The daily distribution of precipitation in the country during rainy season is also uneven. Sometimes, 10 % of the total annual precipitation can occur in a single day. Similarly, 50 % of the total annual rainfall can also occur within 10 days of summer. Such an uneven rainfall pattern is thought to play an important role for geo-disasters in Nepal (Dahal 2009). In 1988, a huge landslide at Darbang of Myagdi District, about 250 km west of Kathmandu, killed 109 people and temporarily blocked the Myagdi River (Yagi et al. 1990). Likewise, one such event of debris flow along Arniko Highway (at Larcha, Bhotekoshi) of central Nepal, killed 54 people in 1996 (Adhikari and Koshimizu 2003).

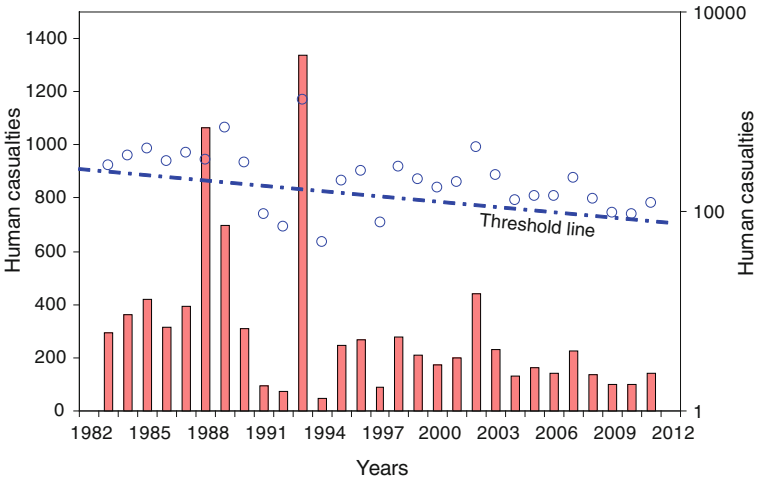

Fig. 1 Annual human life loss from geo-disaster in Nepal form 1983 to 2011. The data in right y-axis is human casualties due to landslide and floods only

Nepal lies in the seventh position for deaths resulting as consequences of floods, landslides and debris avalanches and in the eighth position for flood-related deaths alone (Upreti 2010). The record of loss of lives due to various types of disasters in Nepal between 1983 and 2011 is presented in Fig. 1. In the last 30 years, every year about 860 people lost their lives due to geo-disasters. Unlike landslides and floods, earthquake, glacial lake outbrust floods (GLOFs) and snow avalanche do not occur every year. Landslides and floods are most prominent geo-disasters in Nepal and on an average, they kill 270 people per year. The records reveal that in South Asia, Nepal stands third in having highest number of average annual human deaths per million living population, behind Sri Lanka and Bangladesh (Upreti 2010).

During the past 100 years, three great earthquakes (Table 1a) occurred along the Himalayan front. From east to west, the sequence includes 1905 Kangra earthquake (Mw *7.8), 1934 Bihar-Nepal Earthquake (Mw = 8.1), and the 1950 Assam Earthquake (Mw *8.6). After 1934 Bihar-Nepal Earthquake, seven major earthquake hit Nepal and the lastest is Sikkim/Nepal Border Earthquake of September 18, 2011. In this earthquake, 14, 544 houses were damaged (6, 435 completely destroyed), 6 people were killed and 30 people were injured in Nepal only (Table 1b).

Similarly, various studies show that global warming effect in the Nepal Himalaya has increased the temperature by 0.15–0.6 °C per decade in last three decades (Shrestha et al. 1999), which is two to eight times higher than the rise in the global average temperature presented by International Panel of Climate Change (IPCC 2001). As melting of glaciers are one of the indicators of global warming, the impact is clearly seen in the Himalayan glaciers. About 6 % of glacier area has been decreased in the glacial basins and sub-basins of eastern Nepal from 1970s to 2000. Shrinking, retreating and decreasing of glacier surface

Table 1 Earthquakes in Nepal

A. Magnitude-Frequency data on Earthquakes in Nepal and the surrounding region in the period of 1911–1991 (BCDP, 1994)

Earthquakes of Magnitudes in Richter Scale	*5–6*	*6–7*	*7–7.5*	*7.5 to 8*	*>8*
No. of Events	41	17	10	2	1
Approximate Recurrence Interval, year	2	5	8	40	81

B. Past earthquakes of 80 years and damage records

Year	*Epicenter*	*Magnitude*	*Deaths*	*Houses Destroyed*
1934	East Nepal	8.1 (M_W)	8,519 people died out of which 4,296 died in Kathmandu Valley alone	Over 200,000 buildings and temples etc. damaged, about 55,000 buildings affected in Kathmandu Valley (12,397 completely destroyed).
1936	Annapurna	7.0 (M_L)	Record not available	Record not available
1954	Kaski	6.4 (M_L)	Record not available	Record not available
1965	Taplejung	6.1 (M_L)	Record not available	Record not available
1966	Bajhang	6.0 (M_L)	24	6,544 houses damaged (1,300 collapsed)
1980	Chainpur	6.5 (M_L)	103	25,086 buildings damaged (12,817 completely destroyed)
1988	Udayapur	6.5(M_L)	721	66,382 buildings damaged
2011	Sikkim/ Nepal border	6.9(M_L)	6 died and 30 injury (2 died in Kathmandu valley alone)	14, 544 house damaged (6, 435 completely destroyed)

M_L: Richter Magnitude, M_W: Moment Magnitude

are seen after 1970s and the process is faster in 2001 onwards. As a result, Nepal has already faced 12 glacial lake outburst floods (GLOFs) events and it is damaged by another 10 GLOFs of Tibet which drain to Nepalese rivers in the north (Bajracharya et al. 2006, 2009).

These data clearly suggest that there is a very harsh situation of geo-disasters in Nepal. Particularly, situation of landslide and flood disasters are creating serious threat in lives and properties. In this context, this chapter provides comprehensive information about geo-disaster in Nepal and their mitigation efforts.

2 Physiography and Geology of Nepal

The Himalaya forms a sharp geographic boundary between high Tibetan plateau of east-central Asia in the north and subdued Asian subcontinent in the south. This narrow, rugged and young mountain range of Asia was formed by latest mountain building activity in the geological history. The Himalaya was formed by the collision of the northward moving Indian plate with the giant Asian landmass. This convergence builds up the force to push the Himalaya upward as well as

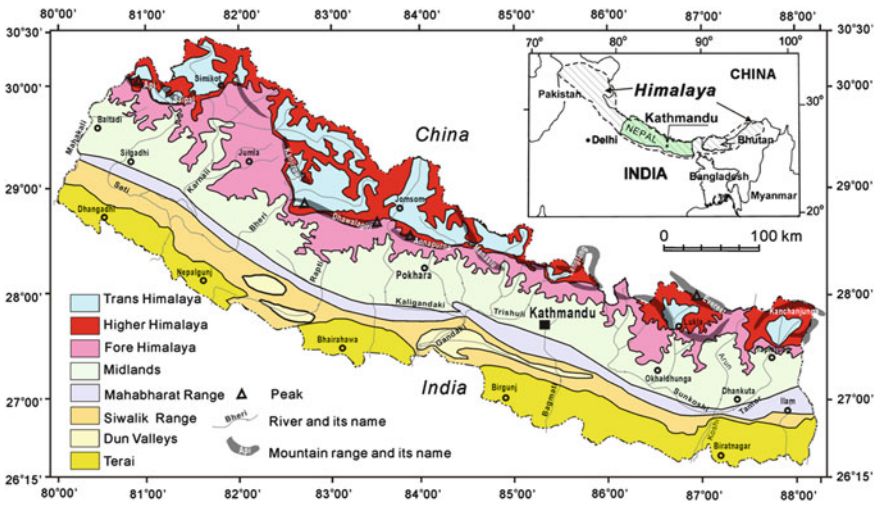

Fig. 2 DEM based physiographic map of Nepal (after Dahal and Hasegawa, 2008)

horizontally, thereby making it the most restless mountain range in the world. The orogenic process is continuous from the collision of Indian plate with the giant Asian landmass and the mountains are still in building process. This is noticeable by present day northward movement of India at the rate of 15 mm to 50 mm per year and the occurrences of frequent seismic shakes all along the Himalaya and its surroundings (Bilham et al. 1998). Most part of the drift is accommodated within the Himalaya by various thrusts as well as rising peaks.

Nepal is located in the central part of the Himalayan arc and occupies nearly one-third of the mountain range. Physiographically, 83 % of Nepal falls within the mountainous terrain and the remaining 17 % lies in the northern edge of the alluvial plains of the great Gangetic Basin. Nepal is well defined into eight physiographic provinces from south to north; namely, (1) Terai (the northern edge of the Indo-Gangetic plain), (2) Siwalik (Churia) Range, (3) Dun Valleys, (4) Mahabharat Range, (5) Midlands, (6) Fore Himalaya, (7) Higher Himalaya, and (8) Trans Himalaya. Each of these units has unique altitudinal variation, slope, relief characteristics, and climatic pattern. The physiographic maps of Nepal with major mountain peaks are given in Fig. 2. Geologically, Nepal can be divided into five tectonic zones from north to south: the Tibetan-Tethys Himalayan Zone, Higher Himalayan Zone, Lesser Himalayan Zone, Siwalik Zone, and Terai Zone (Fig. 3). The main structural framework of the Himalaya is formed by three northerly inclined major breaks in the upper crust of the Indian Plate namely, the Main Central Thrust (MCT), the Main Boundary Thrust (MBT) and the Main Frontal Thrust (MFT). Each of the geological zones is characterized by their own lithology, tectonics, structures and geological history. All these tectonic zones are separated from each other by the thrust faults. The southernmost fault, the MFT separates the Sub-Himalayan (Siwalik) Zone from Gangetic Plains; the MBT

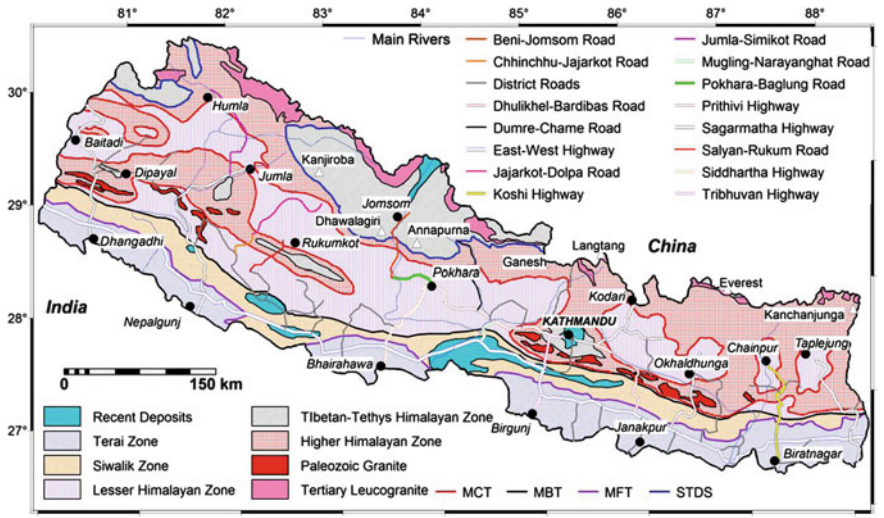

Fig. 3 Geological map of Nepal (modified after Dahal and Hasegawa 2008)

separates the Lesser Himalayan Zone from Siwalik; the MCT separates the Higher Himalayan Zone from the Lesser Himalayan Zone; the South Tibetan Detachment System (STDS) marks the boundary between the Higher Himalayan Zone and the overlying sedimentary sequence of the Tibetan-Tethys Himalayan Zone (Fig. 3).

The Terai Zone is also known as Gangetic Plain and it is the Nepalese portion of the Gangetic Plain that extends from the Indian Shield in the South to the Sub-Himalayan (Siwalik) Zone to the North. The plain is in less than 200 meters above sea level and usually has thick (nearly 1500 m) alluvial sediments. The alluvial sediments contain mainly boulder, gravel, silt and clay.

The Sub-Himalaya Zone is also known as Siwalik Zone and it consists basically of fluvial deposits of the Neogene age (14 millions years–1 millions years old). This Zone extends all along the Himalaya forming the southernmost hill range of 8–50 km. The Lesser Himalayan rocks thrust southward over the rocks of Siwalik along the MBT. Main rock types of Siwalik are mudstone, sandstone and conglomerate.

The rocks of Lesser Himalayan Zone have been transported southwards in several thrust slices. Generally, two tectonic sequences namely autochthonous and allochthonous can be distinguished in this zone throughout the Himalaya. Both the sequences of the Lesser Himalayan Zone mainly consist of sedimentary and metasedimentary rocks such as slate, phyllite, schist, quartzite, limestone, dolomite, etc., ranging in age from Precambrian to Eocene. There are some granitic intrusions also (Cambrian-Ordovician age) in this zone.

The Higher Himalayan Zone mainly consists of huge pile of strongly metamorphosed rocks. This zone is separated with Tibetan-Tethys Zone by normal fault system called as South Tibetan Detachment System (STDS). It extends continuously along the entire length of the country as in whole Himalaya, and its

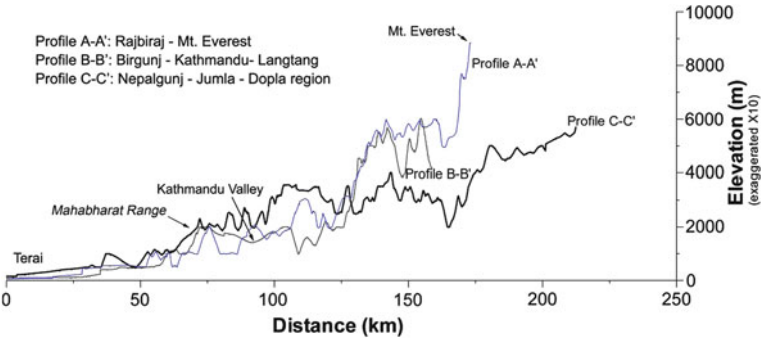

Fig. 4 Topographic profile of eastern, central and western Nepal. The location of profile lines are given in, Fig. 5**a**. Usually, eastern and central Nepal has highly elevated monsoon barrier within 100 km distance from Indo-Nepal boarder to north whereas western Nepal has elevated mountain range at 200 km distance from boarder

width varies from place to place (Fig. 3). The gneisses, schists, and marbles of the zone form the basement of the Tibetan-Tethys Zones. Miocene leucogranite intrusions are also found in this zone.

The Tibetan-Tethys Zone lies in northern part of the country and extends to the north in Tibet (Fig. 3). This zone is composed of sedimentary rocks, such as shale, limestone, and sandstone, ranging in age from Cambrian to Eocene. In eastern part, there is very few exposure of the Tibetan Tethys Zone. Most of the other great Himalayan peaks of Nepal such as Everest, Annapurna, and Dhaulagiri have rocks of Tibetan-Tethys Zone.

3 Geo-Disaster in Each Physiographic Provinces

Rainfall is the major trigger of geo-disasters in Nepal. Orographic effect of mountains is the main cause of extreme rainfall in Nepal during monsoon. The prevailing winds (moisture-laden vapour) from the Arabian Sea and the Bay of Bengal get intercepted to mountains. As the air hits higher land, it is forced to rise. When the air rises above the dew point, it can no longer hold all its water, and then it starts to condense. This process results in high rainfall across the southern flanks of the Himalayan range (windward face) and low rainfall behind the Himalaya (leeward face). The orographic effect of the Mahabharat Range is also significant in whole Nepal and the windward face of the range usually gets high rainfall in monsoon. The orographic effect of the Fore Himalaya is responsible for extreme monsoon rainfall in the Midlands. The topographic profile of eastern, central and western Nepal clearly suggests these phenomena (Fig. 4).

Moreover, in southern part of central Nepal, the topography is relatively lower than other parts of the country (Fig. 5) but abruptly rises in north as Dhaulagiri, Annapurna and Manaslu ranges. As a result, Pokhara area generally gets more

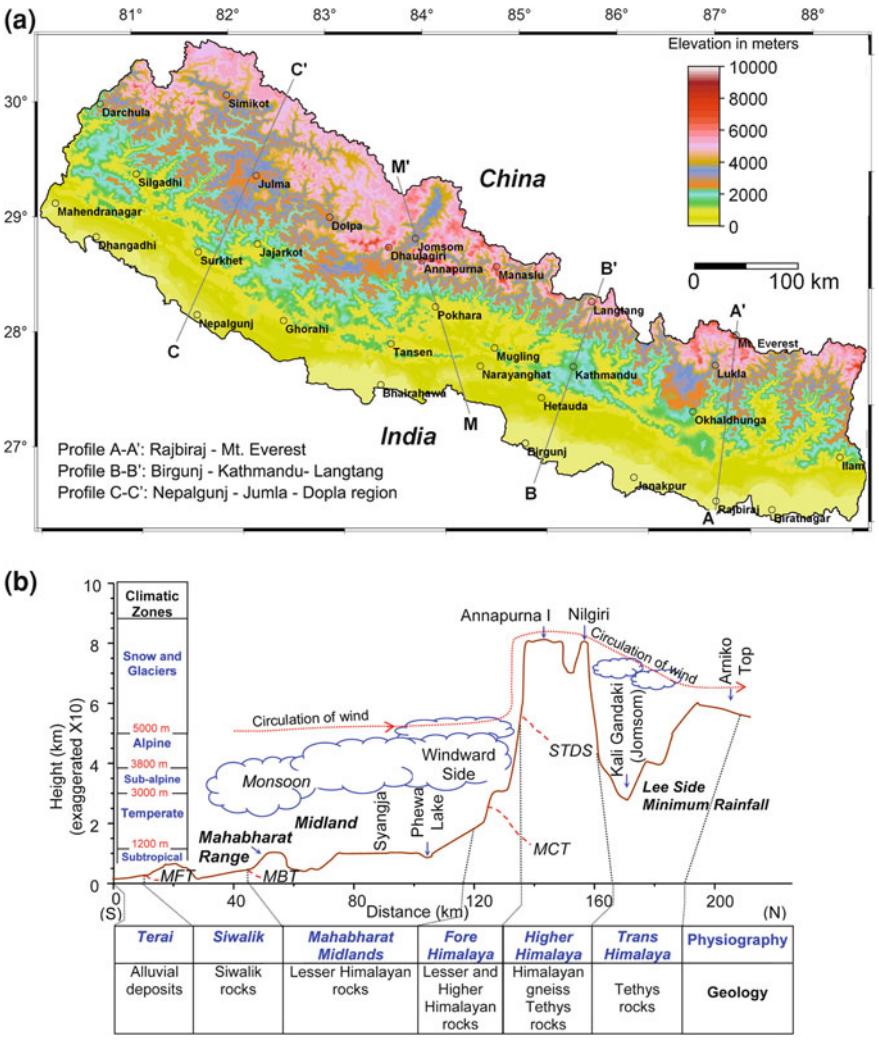

Fig. 5 **a** Relief map of Nepal, a lower altitude area is situated in the area between west of Kathmandu and Pokhara. The topographical profile of line AA', BB' and CC' already given in Fig. 4**b** Topographical profile (through line MM' in Fig 5**a**) of Nepal Himalaya with illustration of climatic zones, main geology and physiography

rainfall than other parts of Nepal due to strong orographic effect of Annapurna and Dhaulagiri ranges (Fig. 5b). As a result, central Nepal always has high values of both mean annual rainfall and extreme 24 h rainfall (Figs. 6).

Geologically young mountains of Nepal have wide range of issues related to geo-disaster. However, the problems are different in each physiographic province. Brief scenarios of geo-disaster problems in various physiographic provinces are given below.

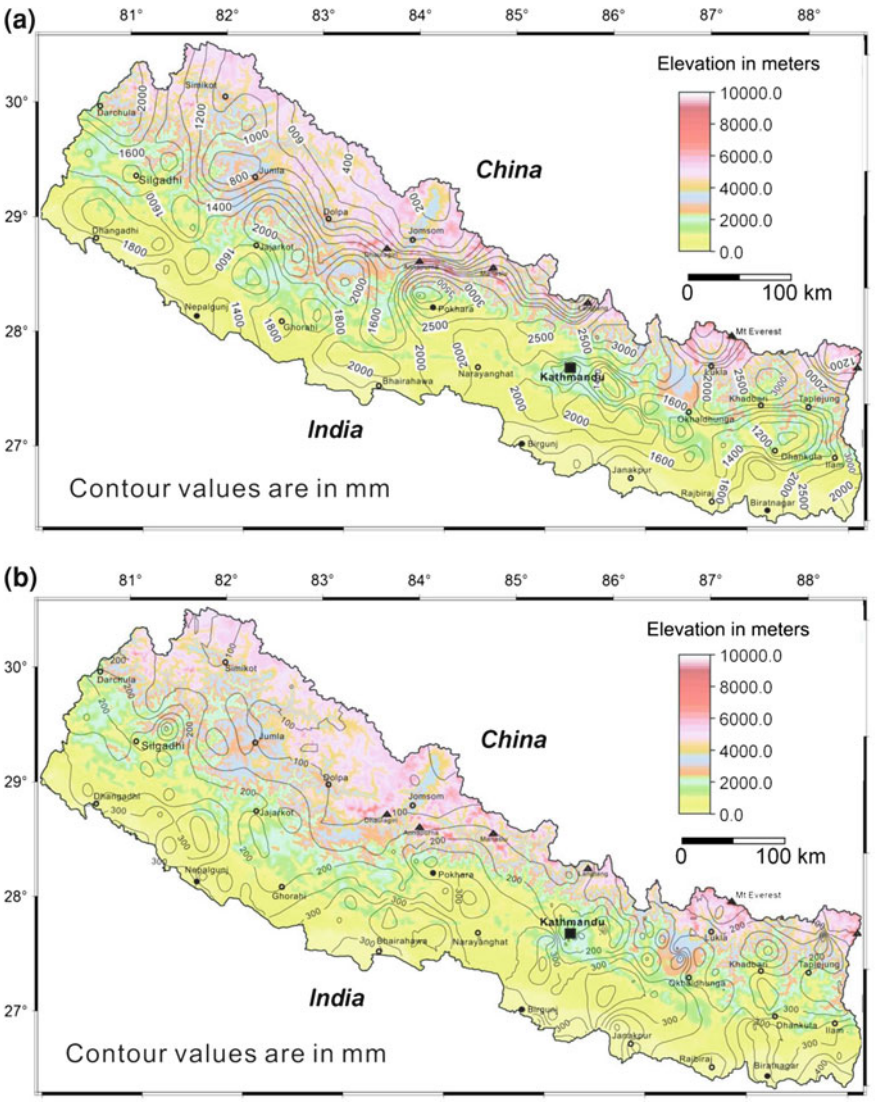

Fig. 6 **a** Mean annual precipitation and **b** Maximum rainfall of 24 h, in the both figures, peak value is around central Nepal

3.1 Terai

The Terai is made up of recent river deposits and consists of coarse sediment in the north, near the base of Siwalik Range and fine sediment in the south, near the Indian border. The elevation of Terai varies from 60 m in eastern Nepal to 200 m in western Nepal with broad plain area. All rivers of Nepal drain into the Ganga River of India

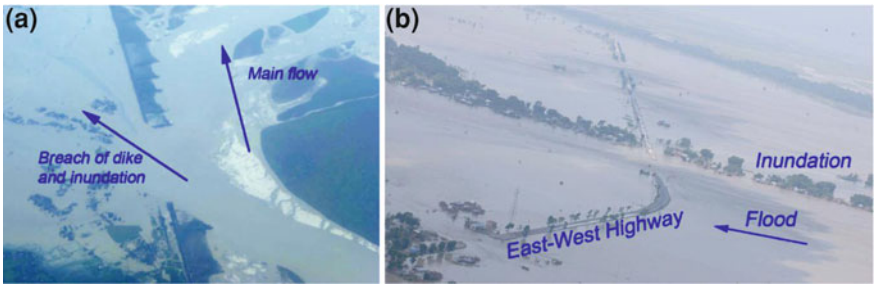

Fig. 7 Bird's-eye view of Koshi Barrage dike breaching in 2008, **a** Dike of breaching (photo Courtesy: World Health organisation) and **b** Flooding in downstream (Photo Courtesy: Buddhi Narayan Shrestha)

through Terai. As a result, every year, Terai faces extreme problems of floods and river bank erosion (Fig. 7). Areas near Siwalik Range also confront to problems of debris flows. Moreover, both small and large rivers in the Terai have nature of shifting channel. Riverbeds in the Terai may rise at annual rates of 15–30 cm. Satellite imagery clearly shows that in 250 years, the Koshi River in eastern Nepal has shifted about 125 km west of its original course (Joshi 1985). There was a worst incident of flood management in Koshi River on August 18, 2008. On that day, the river breached from its Koshi Barrage embankment and carved a channel of destruction. More than 70 thousand people were affected in Nepal by this worst flooding in five decades. Over 9,000 hectares of paddy, sugar cane, corn and jute (used from making burlap) field were destroyed. The channel picked up by the Kosi river was an old channel that it had abandoned over 100 years ago. Nearly 95 % of total flow of the Koshi was reported to have flowed through the new course. 15 km of the East–West highway was impassable and 3 km section was completely destroyed. Traveling to Kathmandu from the east was not possible. All business in the flooded area was stagnant during the disaster. Such devastating floods occasionally hit the Terai area and therefore, river channel management is the main disaster mitigation issue in the Terai.

3.2 Siwalik

The Siwalik (Churia) Range is made up of geologically very young sedimentary rocks such as mudstones, shale, sandstones, siltstones and conglomerates. These rocks are soft, unconsolidated and easily disintegrable. The Upper Siwalik contains thick beds of conglomerates and they are loose and fragile. Similarly, Lower Siwalik and Middle Siwalik have problem due to alternating beds of mudstones and sandstone (Fig. 8a). In such alternating bands, mudstone can flow when saturated with water which results overhanging sandstone beds. Such overhang jointed sandstone beds easily disintegrate into blocks (Fig. 8b). Similarly, throughout Nepal, the rainfall within Churia Range is normally in the range of 2000–2500 mm per year.

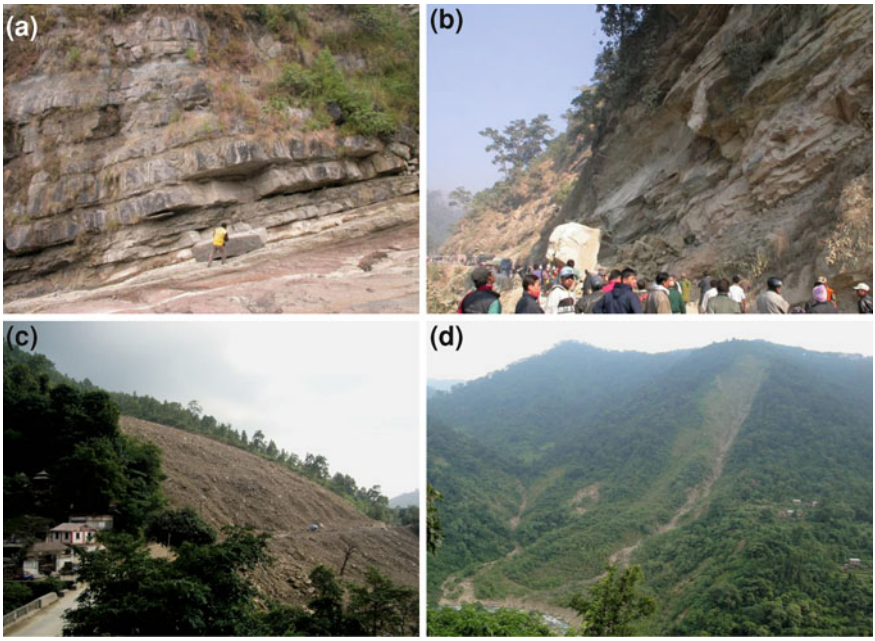

Fig. 8 **a** Alternating bands of hard (sandstone) and soft rock (mudstone) in Siwalik, **b** rock block fall in roadside slope and blockage of the Butwal-Tansen Road in western Nepal, **c** Huge debris flow in Siwalik along Butwal-Tansen Road near Siddababa Temple, Butwal in 2009., and **d** A typical debris flow in Siwalik

As a result, geological conditions and the climate render the Churia Range highly susceptible to geo-disaster processes. Basically, rock failures, shallow slides and debris flows are common in Siwalik Range (Fig. 8b, c and d).

3.3 Mahabharat Range and Midlands

The Mahabharat Range is a narrow but elongated physiographic province (see Figs. 2 and 4) belongs to the Lesser Himalayan Zone. It is the most important barrier of the monsoon clouds and it greatly influences the rainfall distribution pattern in Nepal (see Fig 4). Almost in whole Nepal, southern face of Mahabharata Range gets extensive rainfall in comparison to Midland. The annual rainfall in Mahabharat Range area is comparatively higher and the frequency of high intensity rainfall is also higher. Thus, these areas are getting extensive problem of floods, debris flows and shallow landslides. These events are periodically causing big disasters. Disaster of south and south-east Kathmandu in 1993 and disaster of the Mugling-Narayanghat Road of central Nepal in 2003 are examples of such problems. Not only rainfall but geological condition and steep slopes (slope

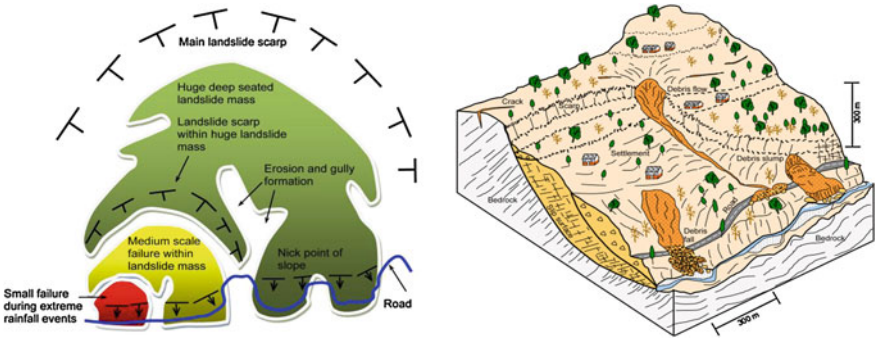

Fig. 9 Typical models of landslide terrain of Mahabharat Range and Midlands of Nepal

angle >25°) also play major role in soil slips and debris flows in the Mahabharat Range. From field observation, it is understood that in areas of rocks such as limestone, dolomite marble and granites, the slopes are stable in the Mahabharat Range, whereas areas consisting of rocks such as phyllites, slates, intercalation of phyllites and quartzites render the terrain most prone to landslides.

The Midlands also belong to the Lesser Himalayan Zone and situated at north of the Mahabharat Range. It has a gentle topography compared to Churia and Mahabharat ranges. The slopes are also comparatively less steep than in other zones of the Himalaya. Thick soil formations are found in slopes of the Midlands because of deeply weathered rocks. As a result, the slopes are very prone to landslides after intense rainfall. Usually, the Midlands are considered as rain shadow zone of the Mahabharat Range; it only receives rainfall between 1,000 and 2,000 mm, but some area has high rainfall record too. Most of the population of Nepal live in the Midlands, and this zone is intensively cultivated also. Irrigation system can be found in every terrace on slope as well as on old landslide debris and mismanagement of irrigation canals can be found everywhere. These improper agricultural practices generally cause landslides or reactivate old landslide masses, and usually damage the whole settlement.

Both the Mahabharat Range and the Midlands have many numbers of deep-seated landslides. Many of them are still active and possess slow moving creep nature (Fig. 9). Likewise, most of the shallow landslides in the Mahabharat Range and the Midlands basically occur on deep-seated landslides mass. This phenomenon has been well understood during the study of landslides in major highways of central Nepal (Fig. 10). Almost all landslides of 2003 in Mugling-Narayanghat Road were found on deep - seated landslides debris. These deep-seated landslides are basically found as huge valley collapsing structures. The slip surface of such landslides has remarkable amount of clay mineral accumulation (Hasegawa et al. 2009; Yatabe et al. 2005). The economical landslide mitigation measures employed in such failure sites were found to have been less effective due to large-scale landslides. The Midlands usually face extreme rainfall events and many shallow-seated landslides can occur in the specific area. An example of such events was seen in Phewa Lake catchment of Pokhara city in 2007 (Fig. 11).

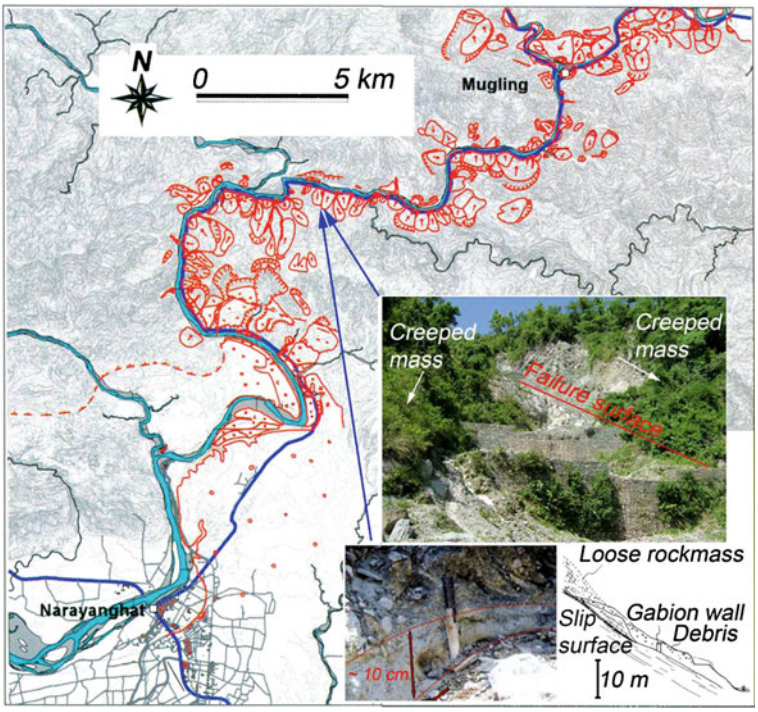

Fig. 10 Example of landslide inventory map some section of Prithivi Highway and Mugling–Narayanghat road (see Figs. 3 and 5 for locations). From field observations, aerial photographs and topographical maps, it was noticed that almost all section of Mugling–Narayanghat Road section passes through the numbers of deep–seated landslides (modified after Yatabe et al. 2005)

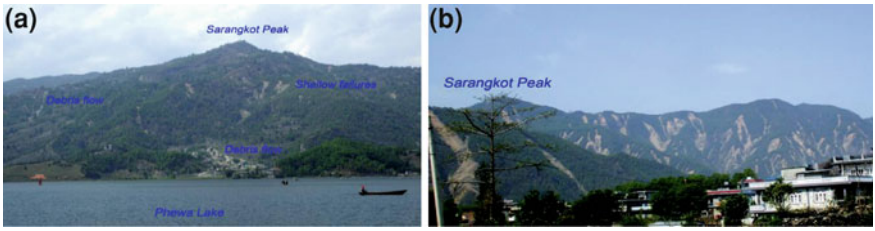

Fig. 11 **a** Many shallow failures at Phewa Lake (Pokhara) catchment after extreme rainfall in 2007, **b** Same events triggers many shallow failures in the northern part of Phewa Lake

3.4 Fore Himalaya

The Fore Himalaya is northern part of Midlands and it is the frontal portion of the Higher Himalaya. Geologically, it belongs to the Lesser Himalayan Zone in many places and in some places it belongs to the Higher Himalayan Zone. Thus, main rock types of this province are phyllites, schists, marble, quartzites, and gneisses. Tectonically, this zone

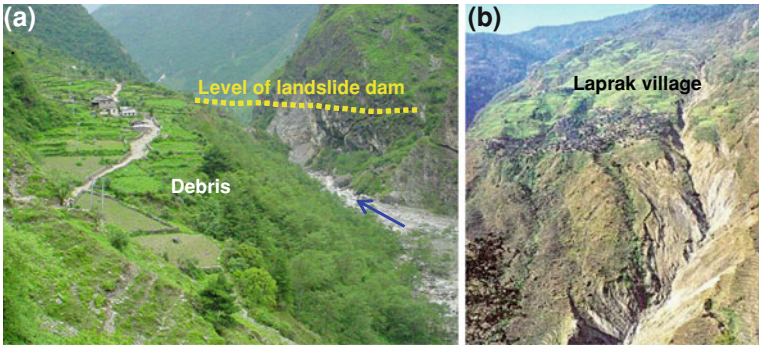

Fig. 12 **a** Old landslide dam of Kaligandaki River in the Fore Himalaya and **b** Laprak landslides in 2000 (Laprak photo courtesy: Narayan Gurung)

is very active and uplifting at a high rate and the topography is steep and rugged. Similarly, like the south faced slope of the Mahabharat Range, the Fore Himalaya also gets high rainfall in the range between 2,000 and 3,500 mm. This province is another vulnerable area for geo-disaster occurrence, but because of less soil deposit on steep slopes, only rock-related failure problems are very frequent.

Deep-seated landslides (see Fig. 9) are also frequent in this zone. Some landslide dams can be also noticed in narrow river valleys. Fig. 12**a** shows a typical landslide dam in the Kaligandaki River. Reactivated deep-seated landslides are also a serious problem in this zone. A typical example of reactivated deep-seated landslide is shown in Fig. 12**b**. It is Laprak landslide of Gorkha district of central Nepal. Laprak is a remote village in the northern part of Gorkha district it takes about 3 days by walking to reach there from the district headquarter. There are some 520 households and the population is 3,900. Following a continuous rainfall for more than 24 h, Laprak landslide reactivated on 3rd July 1999. The landslide is situated on a steep slope facing north at an elevation of 2,100 m from the Mean Sea Level. The Raizo River is draining out from the toe of the slope and it is responsible for toe undercutting problems of whole slope of Laprak village. In fact, it is a large-scale valley collapse which probably initiated hundreds of years ago. The soil deposit varies from place to place within the landslide area presumably from 5 to 15 m. The rock type consists of mica schist, phyllitic quartzite and gneiss. The bedrock is estimated to be at a depth of 5–15 m from the top soil and foliation is semi parallel to the slope. Although the Laprak Landslide first took place in July 1999, it is still active and continuously expands, especially during the monsoon period.

3.5 Higher Himalaya

The Higher Himalaya province is the highest area of the Nepal Himalaya. It includes all elevated peaks and their slopes exceeding 5000 m in altitude. Geologically, this province belongs to the Higher Himalayan Zone and the

Tibetan-Tethys Himalayan Zone into some extent and main rock types of this zone are gneiss, schist, marble and quartzite. Vertical or steeps rocky slopes are very common in this province. Usually, the southern face of province generally receives high precipitation. This zone has many glaciers, which are in retreating state along with the glacier lakes. As a result, this zone is prone to glacial lake outburst floods (GLOFs). Occurrence of snow avalanche is also very frequent in this zone; however, only few settlements can be found in this zone and they are rarely hit by snow avalanche. Similarly, in this province, there is no or little soil cover on slopes, so only very large rock-related failure phenomena are common in this Himalaya. For example, mega landslide of Lete village in the Kaligandaki River, which is believed to have been responsible for damming up of the Kaligandaki River for a long time, is also a huge wedge failure. Because of this landslide dam, the Kaligandaki River channel is broad and braded in Larjung, Jomsom and Kagabeni area of Mustang (Fig. 13). There is a similar type of landslide dam in Manag district also (Waltham, 1996). Because of very low population and few infrastructure development programs, the degradations in the Higher Himalaya are not attentive for planners and researchers.

3.6 Trans Himalaya

The province behind (north) the Higher Himalaya is called Trans Himalaya. Geologically, this province belongs to the Tibetan-Tethys Himalayan Zone. This area is situated in the rain shadow zone of the Higher Himalayan Range. This zone has average annual rainfall very low in comparison to the Midlands and the Fore Himalaya. Thus soil related landslides are less frequent but debris flow in a snow fed stream is quite common. The river bank made of alluvial and glacial moraine possesses bank failure problem.

4 Rainfall and Landslide Relationships in Nepal

As already described, orographic effects are the main cause of monsoonal rainfall in Nepal, which usually begins in June and ends in September. This effect is largely dependant on the topography. For example, the southern part of central Nepal is gentler than the other parts but rises abruptly in the north to form steep Himalayan peaks like the ranges of Dhaulagiri, Annapurna and Manaslu (see Fig. 3). As a result of the orography of these ranges, the Pokhara area on the south generally gets higher rainfall than the other parts of Nepal. For this reason, central Nepal has high values of mean annual rainfall and extreme 24-hour rainfall.

Until 2007, for the Himalaya, no generalized studies exist for landslide and debris-flow initiating precipitation thresholds although these mountains have tremendous landslide problems compared to other parts of the world. Considering

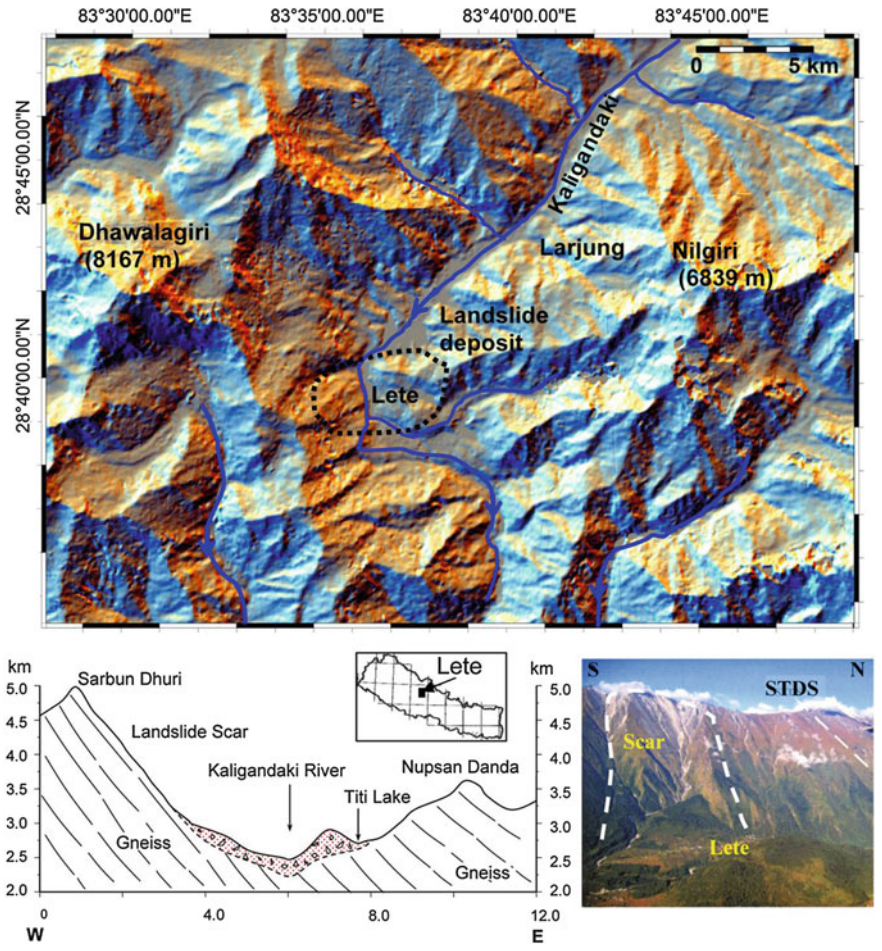

Fig. 13 Huge landslides in the Lete village. The broad and braided channel of the Kaligandaki River can be noticed on upstream from Lete whereas downstream has steep and narrow valley. The photograph on lower right of figure (Photo Courtesy: Bishal Nath Upretti) also shows rock slide scar. Location map of Lete area in Nepal is also shown in inset

rainfall as a main factor triggering landslides in Nepal, Dahal and Hasegawa (2008) have established relationship between landslide occurrence and rainfall characteristics in the form of empirical equations. The empirical thresholds refer to relational values based on statistical analysis of the relationship between rainfall and landslide occurrences (Campbell 1975; Caine 1980; Larsen and Simon 1993; Guzzetti et al. 2004), whereas physical thresholds are usually described with the help of hydrologic and stability models that take into account the parameters such as relationships between rainfall and pore-water pressure, suction, infiltration, slope morphology, and bedrock structures. Dahal and Hasegawa (2008) considered 193 landslide events through 55 years (1951–2006) for establishing rainfall

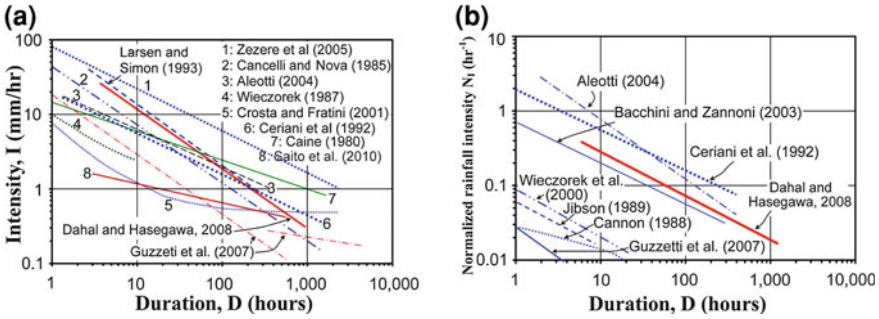

Fig. 14 Comparison of the landslide triggering thresholds; **a** rainfall intensity–duration thresholds from various studies for the Nepal Himalaya and **b** Comparison of the normalized rainfall intensity–duration thresholds from various studies (modified after Dahal and Hasegawa, 2008)

threshold relationships. The method employed by Dahal and Hasegawa (2008) in establishing the rainfall thresholds is similar to that by other researchers (e.g., Caine 1980; Cancelli and Nova 1985; Larsen and Simon 1993; Aleotti 2004; Guzzetti et al. 2007) for such estimations in different parts of the world (Fig. 14a).

Dahal and Hasegawa (2008) have described rainfall threshold for Nepal in two different approaches: intensity-duration threshold and normalized rainfall intensity threshold. They have defined intensity-duration threshold for the Nepal Himalaya as Eq. 1:

$$I = 73.90D^{-0.79}. \quad (1)$$

Where, I is hourly rainfall intensity in millimeters (mm hr^{-1}) and D is duration in hours.

According to this threshold relation, for rainfall events of shorter duration, such as below 10 h, a rainfall intensity of 12.0 mm/hr is necessary to trigger landslides, while an average precipitation of less than 2 mm/hr appears sufficient to cause landsliding if continued for more than 100 h. Moreover, for continuous rainfall of more than one month, landslides may be triggered even by an average rainfall of less than 1 mm/hr and this is quite possible during monsoon periods.

Dahal and Hasegawa (2008) have also analyzed the landslides and the corresponding rainfalls respect to the mean annual precipitation (MAP), which is another approach to rainfall-threshold analysis. The ratio between the critical rainfall of the event and the mean annual precipitation of the site is defined as normalized critical rainfall (NCR), and it is expressed in percentage of annual rainfall. By normalizing rainfall intensity with NCR, Dahal and Hasegawa (2008) have expressed following threshold (Fig. 14b) for landslides in Nepal (Eq. 2):

$$NI = 1.10D^{-0.59}. \quad (2)$$

Where, NI is normalized rainfall intensity (hr^{-1}) and D is duration in hours.

It is useful in estimating rainfall intensity for a landslide event in the form of a percentage of MAP. The threshold relation indicates that for rainfall events of short duration, such as less than 10 h, a normalized rainfall intensity of 0.28 h-1 (i.e. 28 % of MAP) is required to trigger landslides, while a normalized rainfall intensity of less than 0.07 h-1 (7 % of MAP) appears sufficient to cause landslides if continued for more than 100 h.

When monsoon rainfall and landslide relationship was taken into consideration, it was noticed that a considerable number of landslides were triggered in the Himalaya by continuous rainfall of 3–90 days. It has been noticed that continuous rainfall of few days (5 days or 7 days or 10 days) are usually responsible for landsliding in the Nepal Himalaya. Monsoon rains usually fall with interruptions of 2–3 days and are generally characterized by low intensity and long duration. Thus, there is a strong role of antecedent rainfall in triggering landslides. Dahal and Hasegawa (2008) suggest that a moderate correlation exists between the antecedent rainfalls of 3–10 days and the daily rainfall at failure in the Nepal Himalaya.

5 Infrastructures and Geo-Disaster

Disasters always result in economical burden to the country. Usually, a geo-disaster is directly responsible to the losses of lives, buildings, industry, and agriculture in Nepal. As a result, losses in production, income-earning activities, employment, including the cost of relief and recovery indirectly affects the socio-economic condition of the country. Consequently, each large geo-disaster can potentially set Nepal back several years in terms of development efforts. Therefore, mainstreaming of geo-disaster management, incorporating elements of risk reduction into infrastructure planning and poverty eradication programs are already emphasized in Nepal.

A high proportion of Gross Domestic Product (GDP) of the country is lost every year due to geo-disaster. The reason for this loss in Nepal is attributed to inadequate public awareness, lack or inadequacy in preparedness, inadequate financial resources, lack of scientific and technical knowledge and lack of skills in mitigation of geo-disasters. The infrastructure damages due to landslide and flood related disasters in Nepal are mostly, (i) damage in road sectors, (ii) sedimentation during flood, (iii) canals and dam breaching, (iv) damage to powerhouse of hydropower station, (v) transmission tower collapse and (vi) damages to public and private buildings. The systematic data of loss and damage due to geo-disaster is not available in Nepal. The Ministry of Home Affairs (MoHA) compiles data only on the number of houses destroyed and loss of agriculture land by various types of disasters. Even these data do not specify the type of houses or whether they are public, private or school buildings and these data also do not separate landslide and flood damages and losses. Similarly, the Department of Roads of Nepal takes care of all kinds of road maintenance, but it does not have any systematic data record system for landslide and flood damages in roads. Most of the time, researchers collect data from various sources and evaluate geo-disaster consequences in Nepal.

Table 2 Historical records of flood events in Nepal (modified after Shrestha, 2010)

Type of Flood	No. of events	Events
Extreme weather event	4	Lele in 1981; Kulekhani in 1993; Larcha in 1996 and Syangja and Butwal in 1998.
Outburst of landslide dam	11	Budhigandaki in 1967 and 1968; Tinau in 1970; Phalangku in 1971; Baglung in 1976; Balephi in 1982; Trisuli in 1985; Tadi in 1986; Sunkosi in 1987; Myagdi in 1988; and Tarukhola (Bajhang) in 1989.
Outburst of glacial lake	22	Taraco (Sunkosi) in 1935; Gelhaipoci (Arun) in 1964; Longda (Trisuli) in 1964; Zhangzangbo (Sunkosi) in 1964; Ayico (Arun) in 1968; Nare Drangka (Dudhkosi) in 1977; Phucan (Tamor) in 1980; Zhangzangbo (Sunkosi) in 1981; Jinco (Arun) in 1985; Dig Tsho in 1985; Kaligandaki in 1987; Chubung (Tamakosi) in 1991 and Tamapokhari (Inkhu Khola) in 1998 and so on.
Infrastructures and its failure	8	Kosi barrage almost every year (latest major one in 2008); River embankment and dam construction near boarder area in Dhanusa, Rautahat, Nepalgunj, Bardiya and Kailali almost every year; Irrigation dam (Bagmati) in 1993; Check dams and bridges in Dhading, Rapti, Chitwan in 1990 and 1993; Check dams in Butwal in 1970 and 1981 and so on.
Flash flood	1	Flooding in the Seti River on 5th of May, 2012, killed morethan 70 person in Pokhara area, western Nepal. SnowAvalanche in the Annapurna Greater Depression (AGD) of theAnnapurna Himalayan Range induced this flash flood in theSeti River.

Based on the disaster records of 1980–2008, the annual frequency of disastrous flood in Nepal is found to be 0.97 (Shrestha, 2010). Table 2 lists some of the major flood events in Nepal.

There are various causes of floods in Nepal. These causes can be broadly classified into natural and anthropogenic. The natural causes of floods in Nepal include intense monsoonal rainfall, fragile geological setting, landslide dam outburst, wide catchment, steep slope, snow avalanche and GLOFs. The anthropogenic causes of floods in Nepal include deforestation, improper land use and agricultural practices, line settlements along the river bank, unfavorable design of bridges, and chocked drains. On 5th May 2012, debris-mixed snow avalanche in the Annapurna Greater Depression (AGD) of the Annapurna Himalaya Range induced flash flood in the Seti River and killed more than 70 persons in Pokhara area. this flash flood aso damaged bridges and settlements.

Dahal and Hasegawa (2008) have collected data of various landslides in last 55 years, which were responsible for infrastructure damages and human casualties. They have evaluated more than 677 landslide events and have found that disastrous landslide events are concentrated mainly in central Nepal (area between Pokhara and Kathmandu) where mean annual rainfall is high (Fig. 15). Although this database does not include all landslide events since 1951 in Nepal, most landslides caused slight to severe damage. Some debris flow events were so devastating that they killed more than 50 people, while some events resulted in

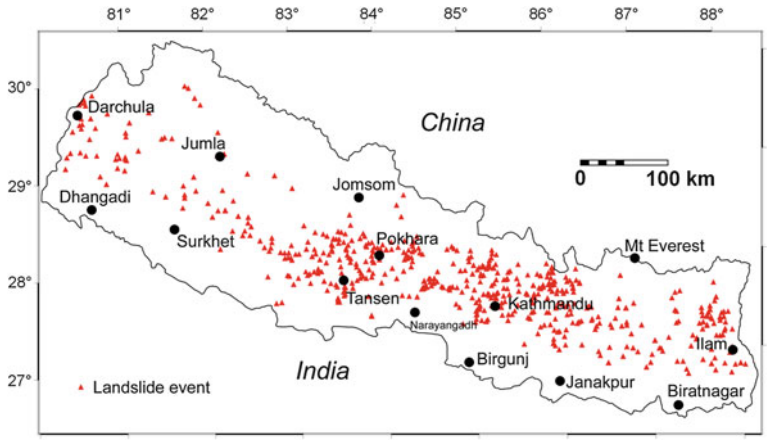

Fig. 15 Landslide distribution in Nepal. This map was prepared using 677 landslide events. Major concentration of landslides events is noticed in central Nepal. The map does not represent total landslides events in Nepal

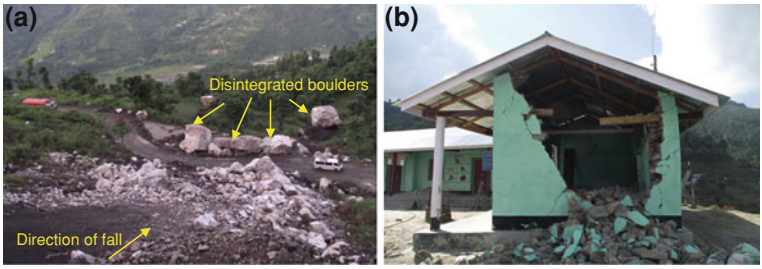

Fig. 16 Road and school building damages due to the Sikkim/Nepal Earthquake of September 18, 2011, **a** Rock fall in the Koshi highway and **b** Damag building of Sumnima pre-secondary School in eastern Nepal

blockade of highways for only a few hours. As per the available data, a total of 143,554 houses in Nepal have been destroyed by floods and landslides during a period from 1983 to 2003. This amounts to an average of 7,329 house destruction per year and the average annual infrastructure damage in Nepal due to landslides and floods in terms of financial loss is approximately US$ 20 million.

As already mentioned in earlier section, last earthquake in Nepal was Sikkim/Nepal Border Earthquake of September 18, 2011. The shake map produced by the United States Geological Survey (USGS) immediately after the earthquake suggests that the earthquake shaking was moderate to strong in east Nepal, Sikkim (India) and a few parts of south Tibet (China). Many roadside slopes along the highways were damaged along with private and public buildings, especially schools and police post (Fig. 16). Many longitudinal as well as transverse cracks were also observed in the ridge part of the roadside slopes of the Mechi Highways during the field visit of the authors.

Study of infrastructure damages by geo-disasters reveal that the major damages are mainly concentrated in roads and in the present context, roads arer the major infrastructures in Nepal. Therefore, brief information of road construction and related geo-disasters are discussed separateiy in the subsequent section.

6 Roads in Nepal

Road development history is not long in Nepal. Up mentioning until 1951, the total length of roads was only 376 km. Even the capital city, Kathmandu, was isolated from rest of the country and outside world. Only by 1956, Kathmandu was made accessible by road from the Terai in the south. The road network gradually increased from this meager length to more than 21,455 km in 2011, which is exclusive of village roads constructed by the local bodies. Out of this 6,874 km is black topped, 5,036 km is graveled, and 9,545 km is fair weathered roads. While developing road network, only economic parameters were considered for selection of road construction projects without giving much consideration to the social aspects and travel time. Anticipated economic development with the construction of roads was almost neglected. Many roads were of seasonal type earthen standards, and these roads lacked reliability. In the global human and economic development scenario, the region which has paved road accessibility in terms of serving the people is high; the socio-economic condition of the people is also large better off. But in context of Nepal, the roads are there but only usable for six months. Thus, still people could not exploit the roads for socioeconomic development of their area. With, half of the total road length as earthen roads, the Nepal Road Standards.

In Nepal, half of total road length is earthen roads. Nepal Road Standards classifies roads as follows:

- National Highway across length and width of the country
- Feeder Road providing access to important trade centers and district headquarters from the national highways
- District Road providing access to trade centers within the district as well as district headquarter
- Urban Road within the city area
- Rural Road to provide access to rural settlements and agricultural centers

The national highways and feeder roads are included in Strategic Road Network (SRN) under the jurisdiction of the Department of Roads (DoR). Nearly one-third of the total road length is incorporated in SRN. Other remaining two-third of the total roads are considered as district roads, rural roads, urban roads, and agricultural roads which are under the jurisdiction of the Department of Local Infrastructure Development and Agricultural Roads (DoLIDAR) and local bodies (District Development Committee, Village Development Committee and Municipalities).

Recently, road construction has extensively increased in Nepal from central level to district and then to village level. Highway construction has also increased. Nepal Government is also giving due importance to highway maintenance. Major highways

of Nepal (see Fig. 3) such as Prithivi Highway, Tribhuvan Highway, Siddhartha Highway, and East–West Highway are in maintenance phase. New highways like Dhulikhel-Sindhuli Road, Chhinchu-Jajarkot Road, Dumre-Chame Road, Jajarkot-Dolpa Road, Beni-Jomsom Road, Jumla-Simikot Road, Salyan-Rukum Road, Sagarmatha Highway and Beni-Jomsom (see Fig. 3) are also in construction phase. Similarly, it is not surprising to note that more than 70 % Village Development Committees (VDCs) of Nepal have Users Committees for rural road construction.

International donor agencies are also giving immense priority for rural road construction in community level. These road construction and maintenance programs are widely affected by both shallow- and deep-seated landslides. The failures also vary in severity and losses. Roadside slope failures have not frequently resulted in greater loss of life because most catastrophic failures have occurred in less populated areas. Economical and financial losses are however substantial. Generally, a shallow failure that occurs along a road, both in uphill and downhill slopes is a main problem in single to double lane roads of Nepal. These problems are excessive both in major highways and in rural roads. During road construction, a rocky terrain is usually cut vertically, so the steep vertical cliffs with potential rock fall hazard are very common in present roads of Nepal (see Fig. 8b).

The road construction in Nepal is not responsive to the rapid technological changes and project perceptions. There is a lack of innovation and dynamism in the road agencies. Road agencies are reluctant to face the new technological and social challenges within the country. Fund constraints are always there for construction and maintenance. Rural and agricultural roads pose challenges for operation and maintenance of roadside slopes. Likewise, up until now, there is no single road tunnel in Nepal, so road tunnel-related issues are absolutely new for Nepalese engineers and technicians.

6.1 Site Investigation Practice in Road

In Nepal, standard methods of site investigation for a road construction project are not well adopted. In many cases, site specific geological problems are investigated without the help of a geologist or geological expert, which often leads to missing of many parameters. As a result, applied preventive measures fail to serve. An integrated approach is necessary to understand the mechanism and to conceive affordable solutions for the mitigation of the geo-disaster. In every case, problems on roadside slopes are only due to poor management of surface and subsurface water. Detailed topographic survey is necessary at problematic areas. An engineering geological survey is also necessary along the road. But such surveys are not in practice in district and rural roads. Even in highways, such surveys are not considered during primary investigation period. In general, geotechnical investigations like test pitting, subsoil sampling, field and laboratory testing to obtain index properties and strength parameters of the soil material should be performed for each landslide before implementation of preventive measures. But such

investigations are almost not in practice for district roads and rural roads. Clear understanding of groundwater flow pattern in cut slope is also necessary, but very few works have been done in this aspect during road constructions in Nepal.

7 Mitigation of Geo-Disasters

Many steps have been initiated towards geo-disaster mitigation in Nepal. Priority has been given to low cost and indigenous technology rather than sophisticated engineering design. Several line agencies have been assigned specific tasks towards geo-disaster mitigation, including mitigation of flood disasters. Many non-governmental organizations are involved in various tasks towards reducing the vulnerability and increasing disaster resilience of communities living in the flood prone zone. Different academic and research institutions are involved in activities related to geo-disaster risk reduction, including scientific publications and public awareness enhancement. In general, three approaches are in practice to mitigate geo-disaster in Nepal and each approach is briefly introduced in the following suheadings.

7.1 Institutional Setup and Awareness Approach

The MoHA, Government of Nepal is the nodal agency of various activities related to all kinds of disaster mitigation in Nepal. Therefore, it is responsible for preparation and implementation of central level policies and programs of geo-disaster mitigation. It coordinates rescue, relief, and rehabilitation works immediately after any geo-disaster event through district and local level institutions all over the nation. It also coordinates its activities with the Nepal Army, Nepal Armed Police Force, Nepal Police, Trauma Centers of different hospitals, Nepal Red Cross Society (NRCS), and other institutions for rescue and distribution of relief materials. The Department of Hydrology and Meteorology (DHM) collects, analyzes and publishes different hydrological and meteorological data from all over Nepal, which are essential for estimating flood values of different return periods, flood forecasting, and early warning of floods. Nowadays, it gives giving real time data of river discharge. Likewise, the Department of Water Induced Disaster Prevention (DWIDP) has been established as a central agency for formulation of policies and plans and implementation of programs related to reduction of geo-disaster excluding earthquake. The DWIDP is preparing flood and landslide hazard maps in heuristic approach, conducting river training works including Sabo check dam structures, conducting training activities and publishing various literatures including training materials, journals, and pamphlets. It is also involved in providing local-scale early warning in close coordination with the Department of Roads. Early warning system installed in Mugling-Narayanghat Road with a real time monitoring of rainfall intensity, landslide and debris flow is an excellent example. The Department of Soil Conservation

and Watershed Management (DSCWM) is also implementing community-based integrated watershed management, river training work and soil conservation in the small catchment level which results in lower flood values and lower sedimentation in the downstream area.

Considering very high risk of earthquake, the Government of Nepal has started Kathmandu Valley Earthquake Risk Management program. It was created with active participation of about 82 concerned institutions of Kathmandu, including the main emergency response institutions and agencies of the government. This program was initiated to start the process of systematically reducing seismic risk over time in the capital city of Kathmandu. Likewise, the Government of Nepal has also stared a few school earthquake safety programs in close coordination with non-governmental organizations, such as National Society for Earthquake Technology (NSET).

Many non-governmental organizations (NGOs) and international non-governmental organizations (INGOs) in Nepal are also involved in various activities related to earthquake and flood disaster mitigations. These organizations are spending millions of dollar for information disseminations, public awareness campaign, disaster toolkit distribution and training. They usually get funds from international donor agencies, and their budget is generally more than national budget for geo-disaster mitigation. However, they are facing extreme criticism in their programs because they use nearly 80 % of the total funds for their office maintenance and hiring international consultants and remaining 20 % of the fund is used for awareness and training programs.

7.2 Research and Implementation Approach

The academic institutions in Nepal are also involved in geo-disaster related research and they are suggesting various suitable approaches for geo-disaster mitigation. Institute of Engineering (Tribhuvan University), Department of Geology and Department of Geography (Tribhvuan University) and Nepal Engineering College (Pokhara University) are in regular research activities for geo-disaster mitigation. Recently, Kathmandu University has also initiated research works on glaciers and glacial lakes of Nepal. An International non-governmental organizations, ICIMOD (International Centre for Integrated Mountain Development) is also preparing database of glacial lakes in the Himalayan Regions. The academic institutions are mostly involved in applied research and public awareness enhancement activities. Some research on seismic hazard mapping through microtremor survey has been also started in Kathmandu valley as a joint research project of Tribhuvan University and Ehime University, Japan (Poudyal et al. 2012a, Poudyal et al. 2012b).

Department of Geology of Tribhvuan University is preparing an integrated early warning model for rainfall-induced landslides (Dahal, 2009) for the Nepal Himalaya. Similarly, various models (both deterministic and statistical) for landslide hazard zoning are already developed (Dahal et al. 2008a, 2008b, 2009, 2010, 2012; Paudyal et al. 2012) and it is found that these models and zonation maps are suitable to use in

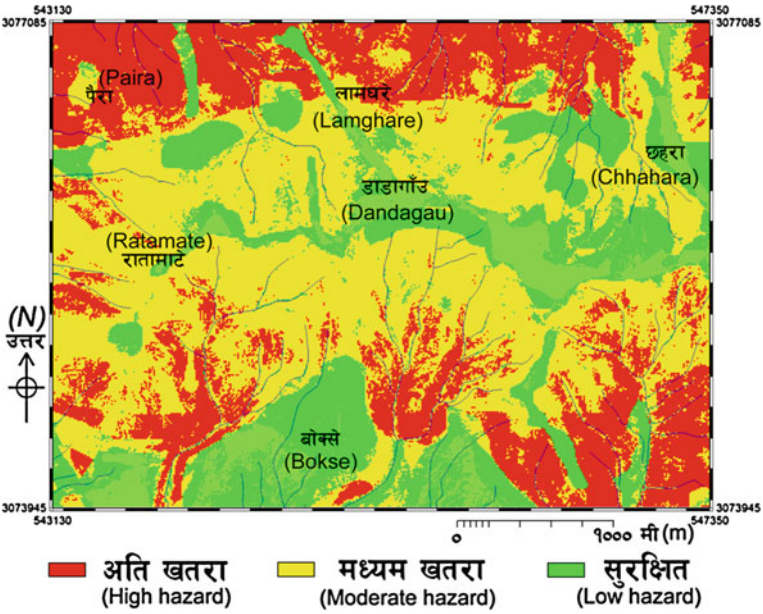

Fig. 17 Proto-type landside hazard zonation map of a fictitious village of Nepal developed by Department of Geology, Tribhuvan University. The map is in Nepali language and red color is for high hazard zone, yellow color is for medium hazard zone and green color is for low hazard zone

planning level and community level geo-disaster mitigation. Hazard zonation map is useful to prepare land use planning. Moreover, the planning engineers can take care of required remedial measures for existing infrastructures of high hazard zones and can also suggest precautions for medium hazard area. Once cost involvement in the structure is known, the hazard zonation maps can be transferred to the landslide risk maps and depending on existing code of risk level, planner can take necessary decision for construction of infrastructure on slopes.

In Nepalese context, this kind of risk evaluation is still not in practice. Planning without evaluation of landslides hazard level already brought extensive loss in economy. For the community level use, the landslide hazard or susceptibility zonation maps can be refined to only three hazard class by using red (for high hazard), yellow (for medium hazard) and green (for low hazard) colours. As a result, the non-technician also can read the map easily. Example of the proto-type community level landslide hazard maps of a fictitious village is shown in Fig. 17. This kind of refined hazard map can be also used in planning of villages on slopes. At least, Village Development Committee (VDC) can legislate some rules and regulations to utilize slopes for settlement and other infrastructures. For instance, a VDC can ask people not to build houses in red zone and ask people to utilize red and yellow zones for agricultural and forest development and green zone for housing.

Implementation of mitigation approaches needs many rules and regulations. Therefore, several laws related to disaster risk mitigation have been enacted in Nepal.

Natural Disaster Relief Act, Soil and Water Conservation Act, Water Resources Act, Forest Act, Environment Protection Act, and Local Self Governance Act are some of the main acts related to geo-disaster. On the basis of these acts, governmental and non-governmental organizations are working for geo-disaster mitigation.

7.3 Engineering Approach

Engineering approach of geo-disaster mitigation in Nepal is still in primitive stage. Basically, river training and management of landslides in roadside slopes are two major works in engineering approach of geo-disaster mitigation. However, modern structural preventive designs are very few in these works. In many cases, traditional technology and locally available materials are used to mitigate floods and landslides and structures are not indestructible in extreme weather conditions. Following subheadings explain the details of engineering approach for geo-disaster mitigation in Nepal.

7.3.1 Drainage Management

There are some accepted practices of drainage measures in landslides and cut slopes of Nepal. Mainly, major highways have better management of surface runoff at cut slopes and landslides than the district and rural roads. In these roads, surface runoff of up to 1 m^3/s is drained through lined catch drains and riprap channels designed for minimum 25 years return period (Fig. 18). Drainage of subsurface/surface water has been managed using french drains (depth 1.5 m to 2.5 m). General effective depth of a network of french drains is down to lower saturation level from ground surface. Excellent performance of french drains were observed at both landslides and cut slope of Arniko Highway (Fig. 18), whereas some unlined catch drain around the cut slope along the rural roads were possessing adverse effect on slope. Nowadays, adopting similar technology, DWIPD is also practicing water management on problematic landslide sites of villages and successfully managing landslides.

7.3.2 Structural Support

In roadside slopes of Nepal, structural support measures are also applied in combination with drainage and bioengineering measures. Various types of walls such as gabion, stone masonry, composite masonry, etc. have been used to mitigate failure. Few support structures such as reinforced concrete crib wall, shortcreting, rock bolts, earth anchors, anchored walls, retaining wall, prop wall etc. are also found to be used in some highways (Fig. 19). Not only for landslides, but structural measures are also used in flood mitigation. There are few successful cases also. For example, more than a quarter of the Arniko Highway section between 62 km and 87 km section was totally washed away in some portion and partially

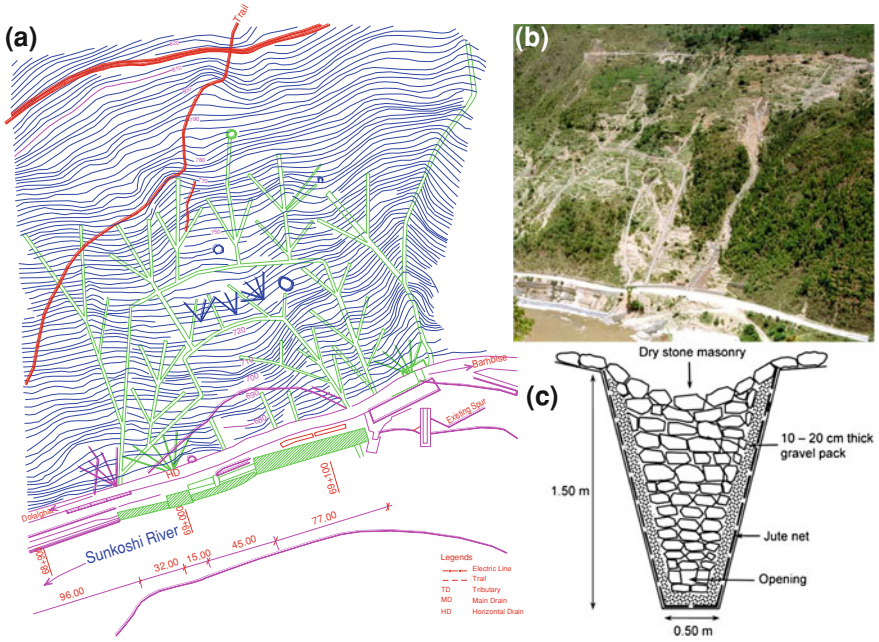

Fig. 18 Drainage management for landslide stabilization at km 69 + 000 stretch of the Arniko Highway, connecting capital Kathmandu with Chinese boarder in North, **a** Engineering drawing of the site prepared by Department of Roads, **b** Photographic view of the site, **c** Section view of catch drain (Figure courtesy: Tuk Lal Adhikari)

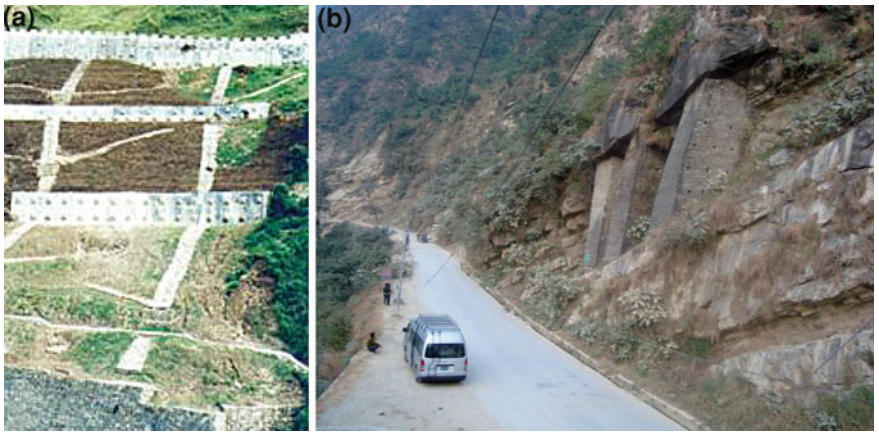

Fig. 19 **a** Various anchored structures and toe walls in a roadside slope (Photo: Department of Roads, Nepal), **b** Prop wall to support hanging sandstone beds in Siwalik

damaged in other portions following a catastrophic cloudburst in the area between June 30 and July 1, 1987. A maintenance program was initiated in 1991 and completed in 1993. Before the rehabilitation work, the landslides were surveyed

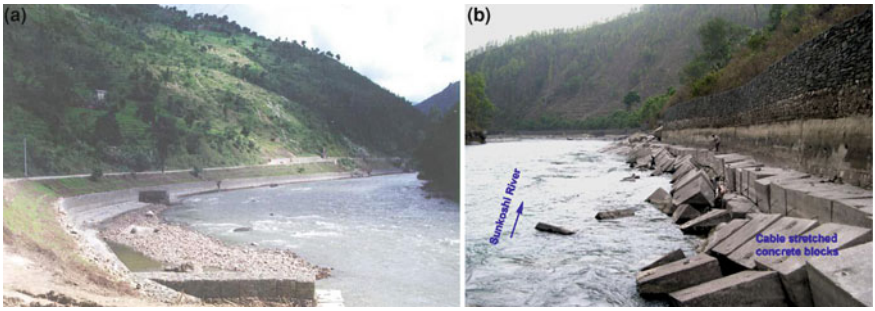

Fig. 20 Bank Protection work at km 69 + 000 of the Arniko Highway, **a** Upstream view of the site in 1992 after construction and **b** Downstream view of the same site after 12 years (Photo courtesy: Tuk Lal Adhikari)

and monitored, and engineering geological mapping, geophysical surveys, exploratory drillings, geotechnical testing and piezometric monitoring were carried out. Based on these studies and monitoring, the final design work for rehabilitation was carried out. This was one of the pioneer major roadside slope stabilization works in Nepal. The site is successfully restored and the site was found stable when it was evaluated after 15 years (Fig. 20). Similar kind of engineering design is now being implemented in various landslide and flood management programs of Nepal.

7.3.3 Bioengineering Works

Bioengineering is the use of living plants for engineering purposes. It may be used in controlling soil erosion and landslide stabilization. Bioengineering does not replace standard civil engineering structures, but it helps in slope stability in combination with small-scale engineering structures. In Nepal, comprehensive bioengineering work has been carried out for the last 35 years and a great extent of large experience has been collected in slope stabilization using vegetation (Howell 1999; Dahal 2001; Florineth et al. 2002). It was found to be a very useful technique for a country like Nepal in the initial stage of road construction and slope management. It is a cheap and simple technology and locally available materials are used to prepare bioengineering structures. It also helps to limit the lateral extent of instability and acts to improve the environment of roadside slope. However, it is not effective to control deep-seated landslides.

There are different methods of using vegetation to protect and stabilize slopes. The main categories are (Howell, 1999):

- Simple planting (e.g. grass seeding, planting trees, shrubs and bamboos)
- Structure using vegetating (e.g. lines of grasses or shrub cuttings, in the form of brush layering)
- Composite system (e.g. planted jute netting or vegetated stone pitching).

Fig. 21 Bioengineering works to mitigate landslide disaster and applied to various roadside slopes of highways and roads, **a** French drain and grass plantation in a landslide site of the Arniko Highway, **b** Drainage measure and tree grass plantation in Krishnabhir landslide (Photo courtesy: Anjan Kumar Dahal), **c** Coir netting and grass plantation in roadside slope of a rural road

Many of the low cost roads (rural roads) in Nepal extensively apply bioengineering and form it a part of the design. One of the early major applications of bioengineering was along the Koshi Highway in 1991–1992 for the rehabilitation work and along the western section of the East–West Highway in the Siwalik. A great deal of experience was acquired during this work. Encouraged with this success, the

Table 3 Bioengineering measures practiced for landslide and flood mitigation in Nepal

Type of plants	Bioengineering system
Hard wood plant	Palisades, tree planting, bamboo planting, fascines, live check dam
Shrub	Shrub planting, vegetated riprap, brush layering, live staking
Grass	Grass seeding or broadcasting, diagonal lines of grass planting, horizontal lines of grass planting, downward lines of grass planting, chevron lines of grass planting, herring bone lines of grass planting, random pattern of grass planting

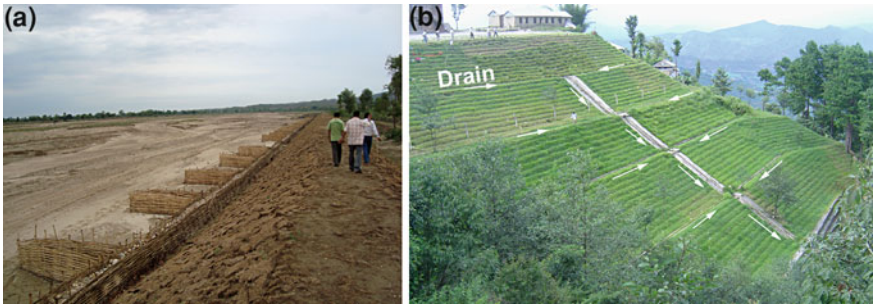

Fig. 22 **a** Community based river training work with bioengineering systems for flood protection in Terai and **b** Bioengineering work for the protection of problematic slope in a settlement area, east of Kathmandu

work was extended further to other major highways such as Prithivi Highway and Pokhara-Baglung roads (see Fig. 3 for location). The projects succeeded in controlling slope failures and erosion. A problematic landslides of Prithivi Highway (Krishnabhir landslide, Fig. 21) was also managed by bioengineering works in conjunction with civil engineering structures. Many on-going road projects are also extensively using bioengineering in combination with engineering structures to control cut slope failures and soil erosion. Bioengineering works, which are generally found to be applied in roadside slopes of Nepal as low cost mitigation measures, are presented in Table 3. Some examples of bioengineering in roadside slopes can be seen on Fig. 21. Figure 22**a** illustrates a successful case of community based river training work with bioengineering systems for flood protection in Terai. The community used local materials to prepare this embankment for river training work. Not only roadside slopes, but problematic slope in a settlement area is also successfully protected by bioengineering work and Fig. 22**b** illustrates a case of a village (Patlekhet) situated in eastern part of Kathmandu.

8 Concluding Remarks

Highly dynamic physical processes dominate the mountainous terrain of Nepal, and therefore, mitigating geo-disaster is a challenge. Construction, maintenance and rehabilitation of infrastructure under the unique Himalayan condition require

innovative and more pragmatic approach compared to less critical terrains in other parts of the world.

Many earlier projects of geo-disaster mitigation have faced various problems during conception and implementation process, and in this process, invaluable experience has been gained during the last three decades. New research findings, concepts, approaches and techniques appropriate to this unique Himalayan terrain are gradually emerging. These techniques and experience are important and far-reaching, and may be applicable in similar regions of the developing world. Over the years, Nepal has gained a significant amount of experience in geo-disaster studies, in design and survey of geo-disaster mitigation programs, in the fields of hazard and risk assessment, in low cost rural road engineering, in community-based river training work, and in slope maintenance incorporating indigenous techniques.

In the changing political and economic scenarios since 2006, Nepal has been appertaining the new aspect of development from villages and cities. Basically, road construction has become a major component of infrastructure development in Nepal. In fact, this construction practice of roads is not that primitive; it is partly copied from developed countries also. In the new concept of development with international standard of construction activities, more geo-disaster related issues will be confronted, which are not well understood in present day practices.

The governmental agencies involved in geo-disaster management must change their status from implementer to facilitator. Government should enhance institutional capacity building at local level to enable local bodies to undertake the immense responsibility of geo-disaster mitigation. Strengthening geo-disaster management capacity in both governmental and non-governmental level at par with ambitious road development plan is very necessary.

In Nepal, due to lack of fund for structural measures, the bioengineering approach is always considered as prime measure of landslide mitigation. However, bioengineering is only suitable to stabilize shallow-seated landslides and to protect erosion on earth embankments during flood. In Nepal, the Department of Roads is considering bioengineering as an indefectible approach for roadside slope management. Due to lack of resources and funds, the Department of Roads attempted to stabilize large-scale landslides, such as Krishnabhir landslide with bioengineering measure and in total 7 years were spent to acheive stabilization. During this stabilizing process, the road, which is the only road connecting the capital city with other parts of country, was blocked for many days. If the indirect loss due to traffic (more than 8,000 vehicles per day) disruption and continued maintenance of bioengineering system was compared with total cost of probable structural measure on the site during project design, the structural measure would be cheaper than the bioengineering system. Thus, modern concept of geo-disaster mitigation in roadside slope of Nepal should take into account of structural measures as primary mitigation system, and bioengineering system should be only considered as an accessory component of geo-disaster mitigation system.

Non-governmental organization involved in geo-disaster management, especially, earthquake and floods need to emphasize research and engineering

approaches for geo-disaster mitigation along with awareness and training programs. A sensational incident about the awareness program happened in one of the flood disaster risk reduction program in Banke district of western Nepal. People were not happy with the training and capacity building programs for disaster awareness and disaster resilience and they were demanding engineering approaches for geo-disaster mitigation such as river training and embankment construction in their villages. They started to boycott all non-governmental organizations involved in geo-disaster awareness programs. This kind of people's perception is increasing in many villages of Nepal and they are putting pressure on the government for prioritizing engineering approach to geo-disaster mitigation.

References

Adhikari DP, Koshimizu S (2005) Debris flow disaster at Larcha, upper Bhotekoshi Valley, central Nepal. Island Arc 14:410–423

Aleotti P (2004) A warning system of rainfall-induced shallow failure. Eng Geol 73:247–265

Bajracharya SR, Mool PK, Shrestha BR (2006) The impact of global warming on the glaciers of the Himalaya. In Proceedings of the International Symposium on Geodisasters, Infrastructure Management and Protection of World Heritage Sites, 25–26 Nov 2006, Kathmandu: Nepal Engineering College, National Society for Earthquake Technology Nepal, and Ehime University Japan, 231–242

Bajracharya SR, Mool PK (2009) Glaciers, glacial lakes and glacial lake outburst floods in the Mount Everest region. Nepal. Annals of Glaciology, London, UK 50(53):81–86

BCDP (1994) Building Code Development Project: Seismic Hazard Mapping and Risk Assessment for Nepal; UNDP/UNCHS (Habitat) Subproject: NEP/88/054/21.03. Min. Housing Phy. Planning, Kathmandu

Bilham R, Blume F, Bendick R, Gaur VK (1998) Geodetic constrains on the translation and deformation of India: Implications for future great Himalayan Earthquakes. Curr Sci 74(3):213–229

Caine N (1980) The rainfall intensity–duration control of shallow landslides and debris flows. Geogr Ann 62A:23–27

Campbell RH (1975) Soil slips, debris flows, and rainstorms in the Santa Monica Mountains and vicinity, Southern California. US Geol. Surv. Prof. Paper, vol. 851:1–20

Cancelli A, Nova R (1985) Landslides in soil debris cover triggered by rainstorms in Valtellina (Central Alps -Italy). In: Proceedings of IV International Conference and Field Workshop on Landslides, Tokyo, August 1985, pp 267–272

Cannon SH (1988) Regional rainfall-threshold conditions for abundant debris-flow activity. In: Ellen SD, Wieczorek GF (Eds.), Landslides, floods, and marine effects of the storm of January 3–5, 1982, in the San Francisco Bay Region. Geol Surv Prof Paper, vol 1434, pp. 27–34

Ceriani M, Lauzi S, Padovan N (1992) Rainfall and landslides in the Alpine area of Lombardia Region, central Alps, Italy. In: Interpraevent International Symposium Bern 2:9–20

Crosta G, Frattini P (2001) Rainfall thresholds for triggering soil slips and debris flow. In: Proceedings of EGS 2nd Plinius Conference 2000, Mediterranean Storms, Siena, pp 463–488

Dahal RK (2001) Use of Bioengineering in Watershed Management. Bulletin of Nepal Geological Society 19:68–72

Dahal RK (2006) Geology for Technical Students. Bhrikuti Academic Publication, Kathmandu, p 756

Dahal RK, Hasegawa S (2008) Representative rainfall thresholds for landslides in the Nepal Himalaya. Geomorphology 100(3–4):429–443

Dahal RK, Hasegawa S, Nonomura A, Yamanaka M, Dhakal S, Paudyal P (2008a) Predictive modeling of rainfall-induced landslide hazard in the Lesser Himalaya of Nepal based on weights-of-evidence. Geomorphology 102(3–4):496–510

Dahal RK, Hasegawa S, Nonomura A, Yamanaka M, Dhakal S (2008b) DEM-based deterministic landslide hazard analysis in the Lesser Himalaya of Nepal. Georisk: Asses Manage Risk Eng Syst Geohazards 2(3):161–17810.1080/17499510802285379

Dahal RK (2009), Evaluation of rainfall-induced landslides from the perspectives of stability analysis, rainfall threshold and hazard in the Nepal Himalaya and Shikoku, Japan, Ph.D. thesis, unpublished, p 246

Dahal RK, Hasegawa S, Yamanaka M, Dhakal S, Bhandary NP, Yatabe R (2009) Comparative analysis of contributing parameters for rainfall-triggered landslides in the Lesser Himalaya of Nepal, Environ Geol 58(3):567–586

Dahal RK, Hasegawa S, Bhandary NP, Yatabe R (2010) Low-cost road for the development of Nepal and its enginrin geological consequences, IAEG 2010 conference, Geologically Active Williams et al. (eds), Taylor and Francis Group, London, 4085–4095

Dahal RK, Hasegawa S, Bhandary NP, Poudel PP, Nonomura A, Yatabe R (2012) A replication of landslide hazard mapping at catchment scale. Geomatics, Natural Hazards Risk 3(2):161–192 10.1080/19475705.2011.629007

Florineth F, Rauch HP, Staffler HP (2002) Stabilization of landslides with bio-engineering measures in South Tyrol/Italy and Thankot/Nepal. In: Interpraevent 2002 in the Pacific Rim (Ed.): Interpraevent 2002 in the Pacific Rim, 2002, Matsumoto/Japan; Congress publication, Matsumoto/Japan, Vol 2, pp 827–837

Guzzetti F, Peruccacci S, Rossi M, Stark CP (2007) Rainfall thresholds for the initiation of landslides in central and southern Europe. Meteorol Atmos Phys 98(3–4):239–267

Hasegawa S, Dahal RK, Yamanaka M, Bhandary NP, Yatabe R, Inagaki H (2009) Causes of large-scale landslides in the Lesser Himalaya of central Nepal. Environ Geol 57(6):1423–1434

Howell J (1999) Roadside Bio-engineering, HMG Nepal, Department of Roads, Babar Mahal, Kathmandu, Nepal, Reference Manual p 216 and Site Handbook p 160

IPCC (2001) Climate Change, The Scientific Basis, Cambridge University Press, Cambridge, pp 881

Jibson RW (1989) Debris flow in southern porto rico. In: Schultz AP, Jibson RW (Eds.), Landslide processes of the Eastern United States and Puerto Rico. Geol Soc Am, Special Paper 236:29–55

Joshi MD (1985) Environment of Nepal, edited by Majupuria. Kathmandu, TU Natures Paradise

Larsen MC, Simon A (1993) A rainfall intensity-duration threshold for landslides in a humid-tropical environment. Puerto Rico. Geografiska Annaler 75(1–2):13–23

Paudyal YR, Yatabe R, Bhandary NP, Dahal RK (2012) A study of local amplification effect of soil layers on ground motion in the Kathmandu Valley using microtremor analysis, earthquake engineering and engineering vibration (Accepted for publication in 27 Mar, 2012a)

Paudyal YR, Bhandary NP, Yatabe R (2012b) Seismic Microzonation of densely populated area of Kathamandu Valley of Nepal using microtremor observations. Journal of earthquake Engineering, available online 21 May 2012 10.1080/13632469.2012.693242

Poudyal CP, Chang C, Oh H-J, Lee S (2010) Landslide susceptibility maps comparing frequency ratio and artificial neural networks: a case study from the Nepal Himalaya. Environ Earth Sci 61:1049–1064

Saito H, Nakayama D, Matsuyama H (2010) Relationship between the initiation of a shallow landslide and rainfall intensity-duration threshold in Japan. Geomorphology 118:167–175

Shrestha HK (2010) Floods in Nepal and their impact on National Economy. In Bhandary NP. Disasters and Development, Investing in Sustainable Development in Nepal, Ehime University, Japan and Bajra Publication Kathmandu, Nepal, Subedi JK (ed) pp 109–133

Shrestha AB, Wake CP, Mayewski PA, Dibb JE (1999) Maximum temperature trends in the Himalaya and its vicinity: an analysis based on temperature records from Nepal for the period 1971–94. J Clim 12:2775–2787

Upreti BN (2010) Impact of natural disaster on development of Nepal, in Bhandary NP. Disasters and development, investing in sustainable development in Nepal, Ehime University, Japan and Bajra Publication Kathmandu, Nepal, Subedi JK (ed), pp 11–33

Waltham T (1996) Very large landslides in the Himalayas, Geol Today (Sep–Oct):181–185

Wieczorek GF (1987) Effect of rainfall intensity and duration on debris flows in central Santa Cruz Mountains, California. In: Crosta, G., Wieczorek G.F. (eds.), Debris flows/avalanches: processes, recognition and mitigation. Reviews in Engineering Geology, Geol Soc Ame 7:23–104

Wieczorek GF, Morgan BA, Campbell RH (2000) Debris flow hazards in the Blue Ridge of Central Virginia. Environ Eng Geosci 6(1):3–23

Yagi H, Maruo Y, Saijo K, Nakamura S (1990) The September 1988 large landslide in the vicinity of MCT, Darbang, Nepal. J Japan Geol Soc 26:45–49

Yatabe R., Bhandary NP, Bhattarai D (2005) Landslide Hazard mapping along major highways of Nepal—A reference to road building and maintenance, Ehime University and Nepal Engineering College, 164p

Zezere JL, Trigo RM, Trigo IF (2005) Shallow and deep landslides induced by rainfall in the Lisbon region (Portugal): assessment of relationships with the North Atlantic Oscillation. Nat. Hazards Earth Sys. Sci. 5:331–344

Yatabe R., Bhandary NP, Bhattarai D (2005) Landslide Hazard mapping along major highways of Nepal—A reference to road building and maintenance, Ehime University and Nepal Engineering College, 164p

Hybrid Socio-Technical Approach for Landslide Risk Reduction in Indonesia

Dwikorita Karnawati, Teuku Faisal Fathani, Wahyu Wilopo and Budi Andayani

Abstract This paper highlights the importance of integrating social and technical approaches (which is so called a "**hybrid socio-technical approach**") as one innovative and strategic program with respect to landslide disaster risk reduction. Such program mainly based on multi-disciplinary action-research to support the community empowerment program through public education. The technical approach was mainly conducted for geological and geotechnical investigation to analyse and predict susceptibility levels of the disaster prone area, as well as to develop an appropriate technology for hazard mapping and disaster early warning. Meanwhile, the social approach was necessary to be undertaken for analysing and mapping the psychosocial conditions of the disaster prone area, and accordingly an appropriate strategy and program to implement the produced technology can be formulated. Moreover, it is also important to establish a "community task force" as the driving power for landslide disaster risk reduction, which can sustain the program at the village level.

Keywords Hybrid socio-technical system · Indigenous technology · Life and environmental protection · Community empowerment

D. Karnawati (✉) · W. Wilopo
Geological Engineering Department, Universitas Gadjah Mada,
Jl. Grafika No. 2, Yogyakarta 55281, Indonesia
e-mail: dwiko@ugm.ac.id; dwiko2007@yahoo.co.id

T. F. Fathani
Civil and Environmental Engineering Department, Universitas Gadjah Mada,
Jl. Grafika No. 2, Yogyakarta 55281, Indonesia

B. Andayani
Faculty of Psychology, Universitas Gadjah Mada, Bulaksumur,
Yogyakarta 55281, Indonesia

F. Wang et al. (eds.), *Progress of Geo-Disaster Mitigation Technology in Asia*,
Environmental Science and Engineering, DOI: 10.1007/978-3-642-29107-4_7,

1 Introduction

Situated in such a dynamic geological region, which is occupied by high density of population, Indonesia is frequently struck by various types of geological disasters, which leads to substantial death tolls, casualties and socio-economical loss. According to the Indonesian National Agency for Disaster Management, Indonesia has been struck by 6,632 events of natural disasters (mainly geological disasters), within the period of 1997–2009, with the total death tolls of 151,277 people. Therefore, it is very urgent to develop appropriate geo-disaster mitigation for life protection and environmental sustainability, through the improvement of society resilient in such disaster prone area.

2 Socio-Technical Challenges for Landslide Disaster Risk Reduction

Landslide is one of the most frequent disasters in Indonesia. Because of the geological conditions and the high rain precipitation, more than 50 % of Indonesian region is prone for this particular disaster. It is commonly found that the soil condition in this area is fertile with significant amount of water resources and the beautiful panorama to stay. That is why, most of the landslide prone areas have been developed as the villages or cities with high population density, such as in Java and Sumatera. As the results, the risk of landslide disasters seriously increases in response to the continuous growing of population and uncontrolled land use changing. Indeed, it has been thousands of people died, several thousands of houses damages and thousand hectares of land buried due to landslide disasters. Accordingly, the improvement of community resilience in landslide prone area has become critical challenges that should be tackled through the implementation of appropriate approach, technology and capacity development program as suggested by Karnawati et al. (2009), Anderson et al. (2010, 2011) and also Halcombe et al. (2012), in order to ensure the human survivability and environmental sustainability.

The development of hazard map and the application of an appropriate technology for early warning system are considered as the crucial efforts to reduce the risk of landslide disasters. Unfortunately, the effectiveness in implementing hazard maps and an early warning system cannot be guaranteed due to less consideration on the social-cultural and socio-economical conditions at the disaster prone area. Accordingly, the needs to integrate social considerations into technical system should be addressed in order to assure the effectiveness in the implementation of such hazard map and early warning system for disaster risk reduction.

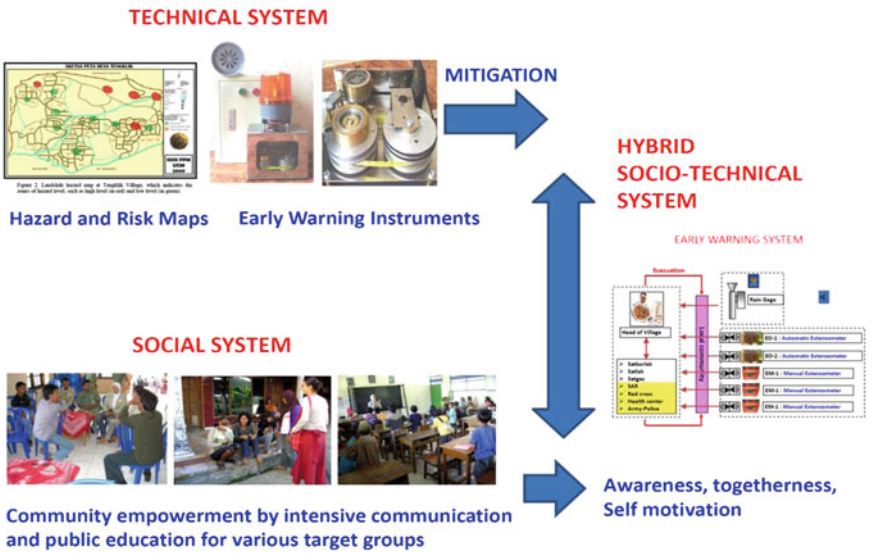

Fig. 1 The concept and key component of a hybrid socio-technical system for landslide mitigation and early warning system Karnawati et al. (2009, 2011)

3 Hybrid Socio-Technical Concept for Landslide Disaster Risk Reduction

To ensure the effectiveness in the implementation of any technology for disaster risk reduction, a combined (hybrid) system, which considers both social and technical conditions has been developed by Karnawati et al. (2009, 2011). Such approach mainly consists of the development of technical system for providing community landslide hazard/risk map and early warning system, and also the social system for developing appropriate community empowerment program. The technical system is recommended to address the development of the existing indigenous or local knowledge and technology, by considering the simplicity of such system and technology. More over, the utilization of the local material is promoted, by encouraging the local knowledge (local experts and local operators) to drive the local participation program. Indeed, it is important that the hybrid system should be performed with a low cost and simple technology, approach and method, so that it can be easily understood, reproduced, operated and maintained by the local community, such as suggested by Karnawati et al. (2009, 2011) This empowerment program relies on the public education, encouraging community participation in developing and implementing action plan for disaster mitigation and risk reduction. Schematic concept of this approach is illustrated in Fig. 1.

All of this concept can be done only if the local community has been empowered. Therefore, process of technology development can be carried out during or as a part of the process of community empowerment.

4 Implementation of the Hybrid Socio-Technical System

A hybrid socio-technical system has been implemented in one pilot area in Central Java, especially in Karanganyar Regency. This Regency is situated at the western slope of Lawu Volcano, in which 30 % of the region is highly risk for landslide due to the high susceptibility condition (indicated by red colour in the map of Fig. 2). The landslide risk in this area is controlled by the geology and climate conditions, and also consequence of high vulnerability of socio-economical conditions in the landslide prone area Karnawati et al. (2009, 2011). Managing the social-conditions for reducing the socio-economical vulnerability in the landslide prone area is considered to be more feasible, instead of changing the natural conditions, such as the geology and climate. Thus, the landslide disaster risk reduction in the pilot study area was conducted by targeting the social conditions through the adaptive management as suggested by Andayani et al. (2008), Karnawati et al. (2009, 2011), and also Halcombe et al. (2012), which emphasized on the improvement of community resilience by implementing the ***hybrid socio-technical approach.***

5 Development of Technical System

The technical system for landslide disaster risk reduction was developed by Karnawati et al. (2009, 2011, 2012), consisting of several technical components such as the instruments for landslide early warning system recommended by Fathani et al. (2008) and also Fathani and Karnawati (2009), supported by the smart-grid for landslide hazard communication, monitoring and early warning developed by Karnawati et al. (2012) as well as the community-based landslide hazard map suggested by Karnawati et al. (2010).

5.1 Early Warning Instruments

The early warning instruments was designed by relying on the manual extensometers (5 sets) connected with the alarm generated by dry battery as illustrated in Fig. 3. Each of these instruments is facilitated with the automatically pull able wire installed across the progressive crack (Fig. 4), so that the progress of crack development due to the slope movement can be monitored. The instalment of extensometers was also supported by the rain-gauge (1 set) as illustrated in Fig. 3b

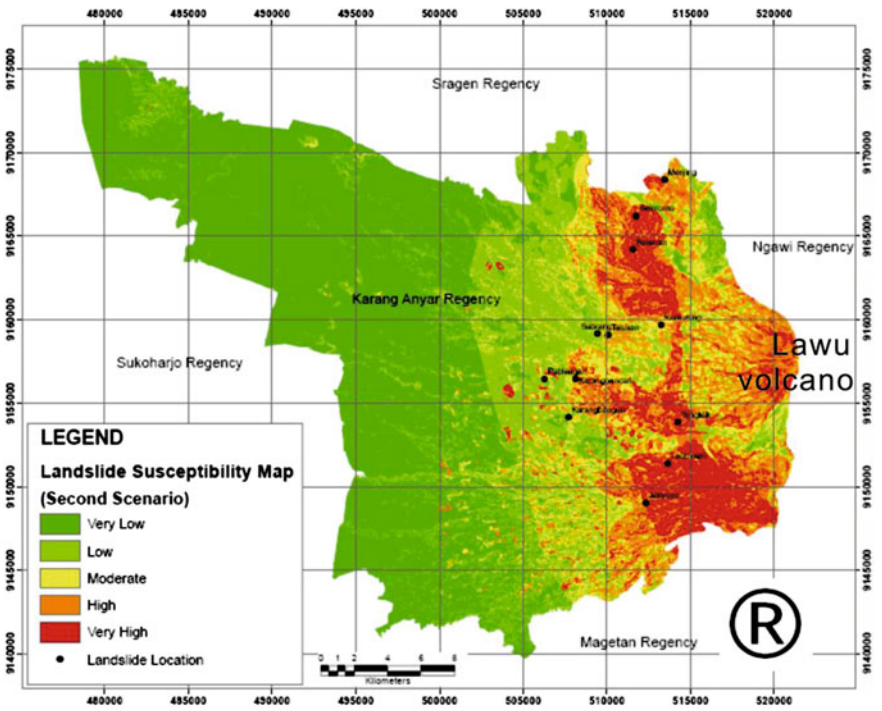

Fig. 2 Landslide susceptibility map of Karanganyar regency, central java, Indonesia, developed in regional scale of 1:100,000 Karnawati et al. (2009, 2011)

and solar panel (1 set); so two different stage of warning levels can be defined. The first threshold of warning was set-up by setting the ON alarm in response to the rain precipitation of 70 mm/h or the accumulative rain precipitation of 100 mm, whilst the second threshold was defined when the extension of pull able wire reached the distance of 5 cm. The function of first alarm was used for raising the community alert, and the second alarm was set-up for starting the evacuation process in the landslide prone zone.

Admittedly, the numbers of early warning instruments are limited which were not sufficient to cover the large area of prone zone. Therefore, a smart grid for landslide early warning has been developed by Karnawati et al. (2012).

5.2 Smart Grid for Landslide Hazard Monitoring and Early Warning

Smart Grid is a participatory cyber-based communication and information system, developed as a system of handling networks of information nodes consisting of local experts, local surveyors, or selected members of local task force and the

Fig. 3 **a** Above, the manual extensometer (generation 1 on the *left* and generation 2 on the *right*), connected with alarm system in the *middle*, and **b** *below*, the rain gauge with the alarm system (Fathani et al. 2008; Fathani and Karnawati 2009)

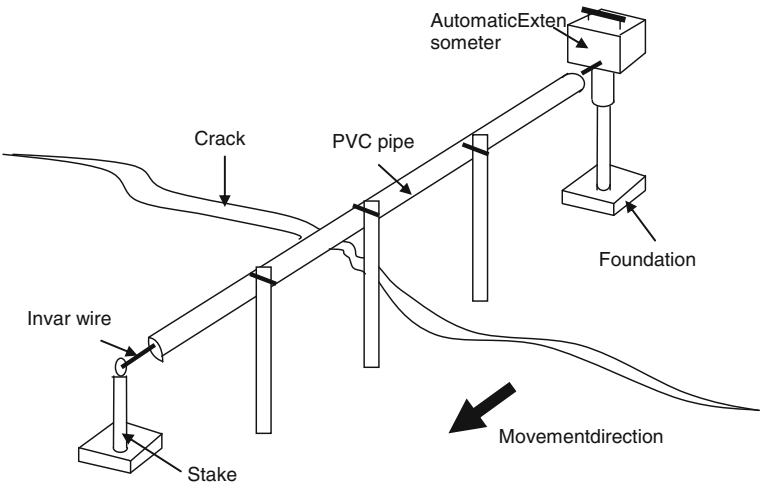

Fig. 4 The automatically pull able wire, protected inside the PVC pipe and installed across the progressive crack (Fathani et al. 2008)

contact person in the local communities. The information is sent to the 'online' web or cyber system, with the specific functions to facilitate the participatory data reporting via the online web, mobile phone (text message), or other various social media, and also to store and analyse those participatory input-reports (related to the geological/geotechnical conditions and process, which considered as the symptoms or early indications of landslides), for defining the landslide hazard and risk level in any particular site or zone. Results of the analyses are required to provide the emergency-decision supports, which relate to the information of the zone and level of landslide hazard/risk, evacuation route and shelter, as well as the recommendation of method or approach for mitigation, preparedness and emergency actions. All of the information about hazard/risk and the guidance for response will be blasted/transmitted back to the respective-reporting node as well as to the other relevant registered nodes. This participatory system can also be connected to various types of social media (mobile phone call/text, Twitter, Facebook, Google+, Yahoo, etc.).

It is also important that the multi-two way direction facilitates the communication flow in this participatory smart grid system. Such system can also be linked to the existing community-based landslide early warning instruments developed in parallel with this smart grid system.

Concept of the smart grid design is illustrated in Fig. 5, whilst the example to the web performance of smart grid is displayed in Fig. 6.

5.3 Community-Based Hazard Map

The understanding and simplicity of the approach and method of mapping is the most critical part to guarantee the effectiveness of disaster risk reduction program.

Unfortunately, it is apparent that most of the technical landslide hazard map was not easy to be understood by the local community. That is why a simple participatory hazard mapping method was developed by Karnawati et al. (2010), to facilitate the community landslide hazard mapping, which also addressing the Landslide Risk Assessment and Mitigation Strategy suggested by Lacasse and Nadim (2008). Therefore, the standard technical method for landslide hazard mapping was simplified to prepare a simple landslide hazard map which can be conducted by the local community on the existing village base-map (i.e. the village "situation" map), through the participatory mechanism. Such map was presented without any contour, but mainly showing the lay out of roads, rivers, houses and land farming areas which were very easy to be identified by the local community. Identification of the high susceptible zone (red zone) and low susceptible or safe zone (green zone) for landslides was carried out by the community task force through public participation, which is advised by the local expert. Figure 7 shows the landslide hazard map which was developed by the local community in Tengklik Village, Tawangmangu District, Karanganyar Regency, Central Java.

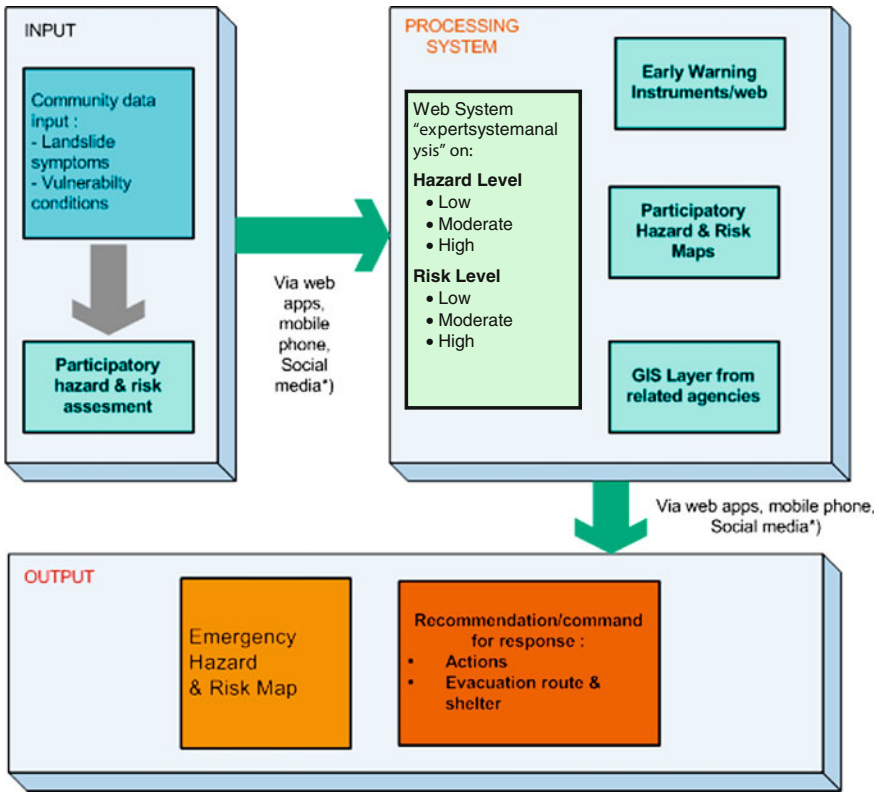

Fig. 5 Concept of expert system in the smart grid design developed by Karnawati et al. (2012)

This map is also very important to decide where the early warning instruments should be installed and how the evacuation route should be decided.

6 Development of Social System

Development of the social component in the hybrid system was initiated by social survey, to identify the existing knowledge about the landslide hazard, which will affect the community's perception about landslide risk and their expectation on the proposed developed-technology for landslide disaster risk reduction. Identification on all of those aspects significantly control their motivation or willingness for actively participating in any disaster risk reduction program. Results of this social survey will be crucial to formulate the appropriate and effective strategy for public education related to the effort for raising the community awareness and also for conducting community empowerment program.

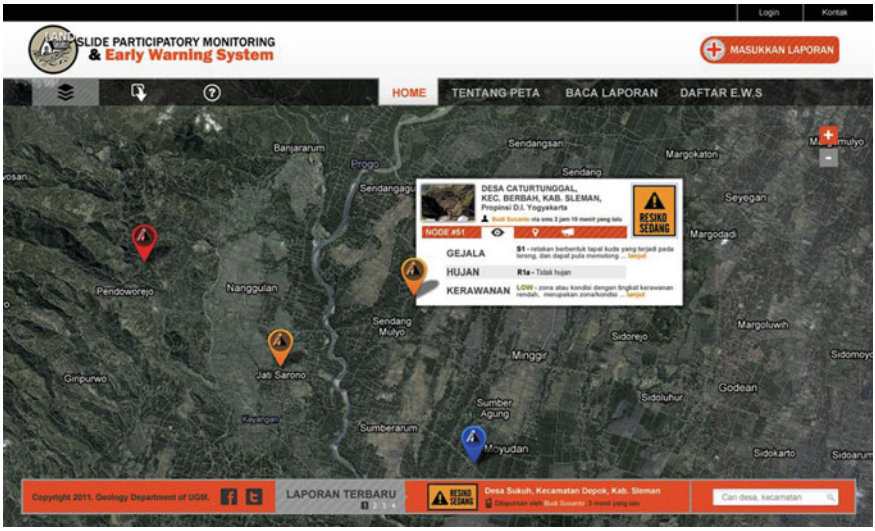

Fig. 6 Web performance showing the geographical position of the reporting nodes

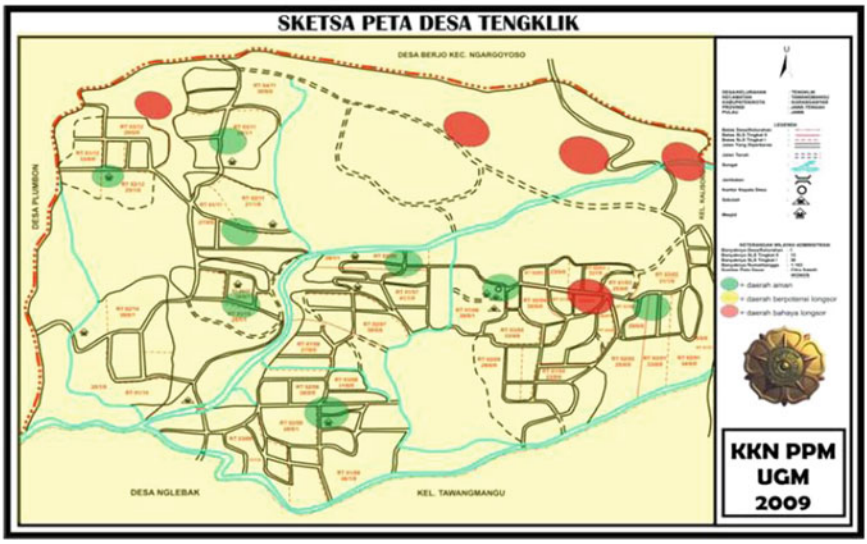

Fig. 7 Community-based landslide hazard map of Tengklik Village, Karanganyar regency, central java, indicating zones of hazard level (red is high level and green is low level), recommended by Karnawati et al. (2010)

Various target groups were defined, and those comprise the group of women (as the key person in the family), teachers, children as well as the young and senior

leaders. The local government of Karanganyar Regency also continuously and actively supported this social development program.

Results of the social survey indicated that most of the community members had been quite aware with the potential occurrence of landslides at the rainy season, because the landslide disasters have quite frequently struck their living area, especially under the heavy or long continuous rainfall. Nevertheless, most of the community members preferred to remain living in their vulnerable region, instead of being relocated to the other safer areas. Obviously, the fertility of soil, the abundance of water resources, the beauty of mountainous panorama and the strong psychological engagement with their homeland or home-heritage, strongly prevented their willingness to leave their dangerous homeland. Unfortunately, they did not have enough knowledge, skill and capacity to decide about "what should" and "what should not do" for preventing the landslide as well as for protecting their life and environment from the landslide occurrences. Although, they had not yet been capable to identify the sites (slopes), which were susceptible for landslide, and to recognize the initial symptoms of landslide. Therefore, the hybrid socio-technical approach for community-based landslide early warning was applied to develop their capacity for implementing the appropriate landslide disaster risk reduction program, which will support the improvement of the community resiliency in this landslide prone area.

A community task-force for disaster risk reduction at the village level was also established under the coordination with the Agency for Disaster Management at the Regency level (Fig. 8). This network is also linked to the local hospital (health centre), the local army and police, and also the Search and Rescue Team (SAR team) at the local Regency. Indeed, this task force played an important role as the driving power for the disaster risk reduction program, and also to effectively implement and sustain the technical system for landslide risk reduction.

7 Evaluation

It was apparent that the existence of a community task force for landslide disaster risk reduction at each village level was the most important factor to ensure the affectivity and sustainability of landslide mitigation and risk reduction program. This task force had an important role as the driving agent in the empowerment and mitigation program. In fact, since this proposed hybrid socio-technical approach implemented in several pilot areas in Karanganyar Regency, such as in Ledoksari Village in 2008, Tengklik Village in 2009, Matesih Village in 2010 and also Gempolan and Plosorejo Village in 2011, the community resilience for landslide disasters has gradually increased, the socio-economical losses due to landslides can be minimised and the numbers of landslide victims have been dropped to zero. It seems that this approach could effectively empowered to local community to mitigate the landslides. Furthermore, the key person who is also the member of the community task force and was in charged for the mitigation program was also

Fig. 8 Activities to develop and empower the community task force at Tengklik Village which were facilitated by the student community service program conducted by Universitas Gadjah Mada

invited to share their experiences in facilitating the community empowerment actions to tackle the landslide problems in another landslide disaster area in Tanjungsani Village at Agam Regency, West Sumatera.

Therefore, the Hybrid Socio-Technical approach is also very applicable to be developed in several other disasters area in developing countries, although several adjustments may be required to address the social and environmental characteristics at the specific site. Moreover, the importance of commitment and leadership of the local Agency for Disaster Management at the Regency and District levels to support the effectiveness of the disaster management program at the village must be highlighted.

It was also obvious that the socio-cultural and socio-economical constrains during the mitigation program can be minimized by implementing the hybrid socio-technical approach. Indeed, the introduction and implementation of a new technology for early warning and disaster management system can be conducted more effectively through the public participation actions. That is why more enthusiastic response of the local community and local authority to actively participate in the landslide disaster risk reduction program can be performed as illustrated in Fig. 8.

8 Conclusion

One of the most critical considerations on disaster risk reduction in Indonesia is the assurance for the effectiveness and sustainability of the disaster management program. It is apparent that the proposed model, which is so called as the combined (hybrid) socio-technical approach has been quite effective and strategic to improve the community resilience at the landslide vulnerable village. It is also crucial that the system should be developed through community participation and the provision of simple and low cost technology for landslide hazard mapping and early warning. Indeed, the establishment of community task force at the village level is very important to ensure the effectiveness, continuity and sustainability of this proposed system. This approach may also be applicable to tackle similar problems for landslide risk reduction in other developing countries in Asia.

Acknowledgments Special thanks are directed to the Indonesian Agency of National Disaster Management, the British Council Delphe Program as well as the Directorate General of Higher Education—the Indonesian Ministry of National Education and the Fulbright Senior Research Program funded by US Department of State's Bureau of Education and Cultural Affairs for providing financial supports to carry out the pilot studies. The acknowledgments are also extended to Universitas Gadjah Mada for the provision of academic facilities, as well as to the research assistant at the Laboratory of Environmental Geology and the Computing Laboratory of Civil and Environmental Engineering at Faculty of Engineering, Universitas Gadjah Mada. This research can be successfully conducted was due to the continuous and intensive assistance of Mr. Sani Tanaka Ismawanto—the student of Magister Instrumentation at the Faculty of Engineering, Universitas Gadjah Mada.

References

Andayani B, Karnawati D, Pramumijoyo S (2008) Institutional framework for community empowerment towards landslide mitigation and risk reduction in Indonesia. In: Proceedings of the 1st world landslide forum, Tokyo, global promotion committee of the international program on landslide (IPL)—ISDR, pp 57–59

Anderson MG, Halcombe E, Esquivel M, Toro J, Ghesquire F (2010) The efficacy of a program of landslide risk reduction in area of unplanned housing in the eastern of Caribbean. Environ Manag 45:807–821

Anderson MG, Halcombe E, Blake JR, Ghesquire F, Holm-Nielsen N, Fisseha T (2011) Reducing landslide risk in communities; evidence for the eastern Caribbean. Appl Geogr 31:590–599

Fathani TF, Karnawati D (2009) Early warning of landslide for disaster risk reduction in central java Indonesia. In: Proceedings of international workshop on early warning for landslide disaster risk reduction in the eastern Asian region, Kunming, China

Fathani TF, Karnawati D, Sassa K, Fukuoka H, Honda K (2008) Landslidemonitoring, prediction and earlywarning in Banjarnegara, Indonesia. In: Proceedings of 1st world landslide forum, Tokyo, pp 195–198

Halcombe E, Smith S, Wright E, Anderson MG (2012) Integrated approach for evaluating the effectiveness of landslide risk reduction in unplanned communities in the Caribbean. Nat Hazards 61:351–385

Karnawati D, Fathani, TF, Andayani B, Burton PW, Sudarno I (2009) Strategic program for landslide disaster risk reduction; a lesson learned from central java, Indonesia. In: Duncan K, Brebbia CA (ed) Disaster management and human health risk; reducing risk, improving outcomes, WIT Transactions on the Built Environment Transaction, WIT Press, Southompton, pp 115–126

Karnawati D, Setianto A, Wilopo W, Andayani B, Suharto (2010) Development of community landslide hazard map for landslide risk reduction. In: Proceeding of 11th international association of engineering geologist congress, Auckland, 5–10 Sept 2010, Auckland, New Zealand, pp 1203–1208

Karnawati D, Fathani TF, Andayani B, Legono D, Burton PW (2011) Landslide hazard and community-based risk reduction effort in Karanganyar and the surrounding area central java, Indonesia. J Mt Sci 8(2):149–153

Karnawati D, Frost EG, Fathanni TF, Subroto (2012) Smart grid for landslidemonitoring and earlywarning system in Indonesia. In: Proceedings of the 10th Anniversary of ICL—January 2012, Kyoto

Lacasse S, Nadim F (2008) Landslide risk assessment and mitigation strategy. In: Sassa K, Canuti P (eds) Landslide disaster risk reduction. Springer, Berlin, pp 31–61

Damage and Recovery from the 1999 Chichi Earthquake in Taiwan

Jiin-Song Tsai, Lap-Loi Chung and Karl Gee-Yu Liu

Abstract This article briefs some experiences and the lessons learned from the disaster of the Chichi earthquake that hard struck central Taiwan on September 21, 1999. Most of the contents are on the basis of many existing literatures. Presented first herein are issues of damages resulted in by the earthquake, including damages to buildings, bridges and ground problems, etc. The aftermath reconstruction and recovery works are described in the following. Finally, the important achievement and preparedness for mitigating future earthquakes are also delineated.

Keywords Chichi earthquake · Damage · Recovery

1 Introduction

The Chichi earthquake, also known as Jiji earthquake (集集大地震) or 921 earthquakes (九二一大地震) in some literatures, was the strongest earthquake with epicentre on the Taiwan Island in the 20th century. The earthquake, with the focal depth about 7 km (4.5 miles) and a magnitude of $M_S = 7.3$ (Richter scale by USGS) or $M_W = 7.6$ (Central Weather Bureau of Taiwan), occurred at 01:47 a.m. on September 21, 1999 near the town Jiji (集集), Nantou County, Taiwan. The earthquake occurred along the Chelongpu Fault (車籠埔斷層) that stretches along

J.-S. Tsai (✉)
Department of Civil Engineering, National Cheng Kung University, 70101 Tainan, Taiwan
e-mail: jstsai@mail.ncku.edu.tw

L.-L. Chung · K. G.-Y. Liu
National Center for Research on Earthquake Engineering (NCREE), 200, SECT 3, Xinhai RD, 106 Taipei, Taiwan

F. Wang et al. (eds.), *Progress of Geo-Disaster Mitigation Technology in Asia*, Environmental Science and Engineering, DOI: 10.1007/978-3-642-29107-4_8,

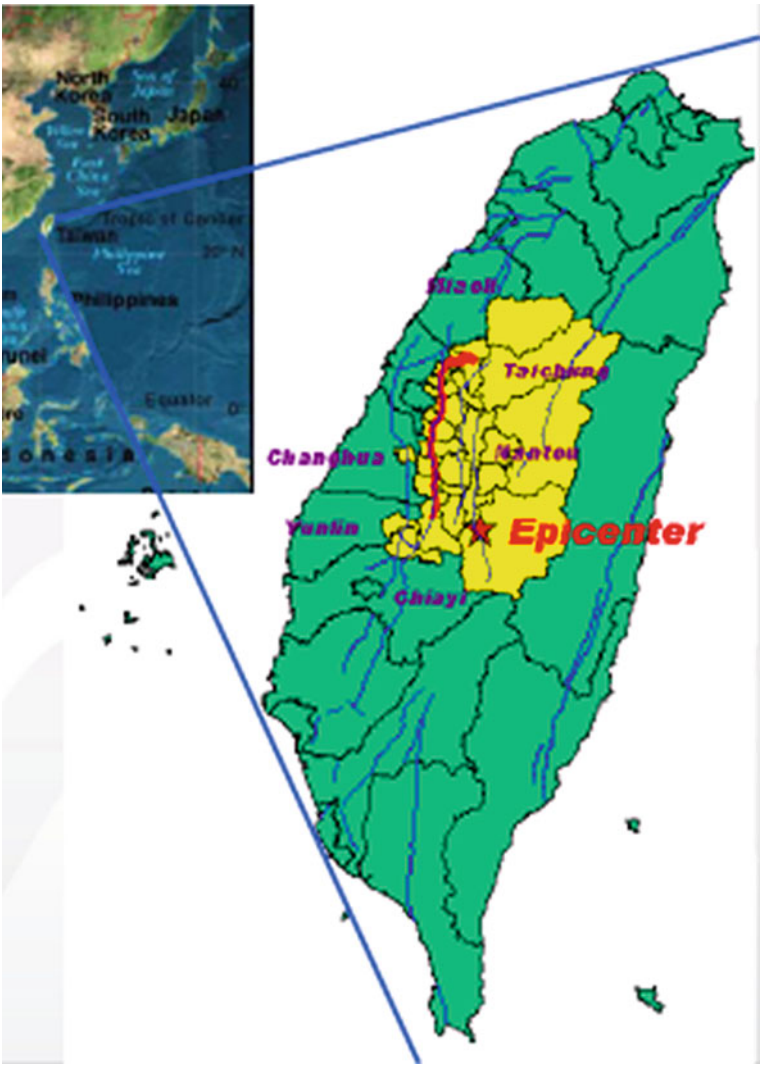

Fig. 1 Chelongpu fault and epicenter of Chichi earthquake (Chen and Liu 2009)

the west foothill of the Central Mountain Range in the longitudinal direction of the island (Fig. 1). It is unique for its rupture length over 100 km and the ground near the fault were tremendously raised, up to 9.8 m heave. A new waterfall of 7 m (23 ft) high was formed then near the northern end of the fault at Dongshih (東勢). Figure 2 shows the geological section (east–west) at the epicenter. This devastating earthquake caused more than twenty four hundreds death toll and over ten thousands injured people. Around fifty thousand buildings were destroyed and another fifty thousands were seriously damaged. The total economic lost was to an

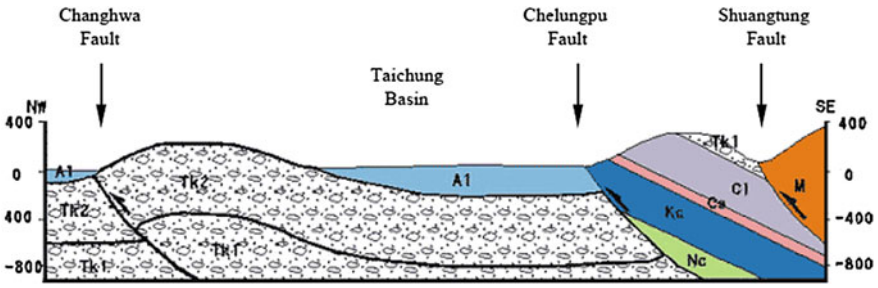

Fig. 2 Geological section at epicenter (Moh et al. 2002)

order of US$10 billion (NT$300 billion) estimated by many governmental agencies (e.g. the Directorate General of Budget Accounting and Statistics of Executive Yuen). This quake brought in unprecedented disaster that seriously impacted people's social and economic life. Until today, it is recognized as the "Quake of the Century" to us without doubt.

In this event, the ground shaking has been well recorded by the installed sensors and monitoring stations of the Taiwan Central Weather Bureau's Seismic Network (CWBSN) and many purposefully installed strong motion networks including SMA-I, SMA-II, TSMIP, LSST, and the downhole arrays in Taipei. The collected high quality data were soon adopted in various studies of the characteristics of ground motion, wave propagation, and site effects. In particular, the data of pulse-like near-field ground motions contributed solid evidences to many studies of source effects in the near fault zone (e.g. Loh et al. 2000; Wen 2003) to solve a long-time puzzle in seismology.

According to the recorded data, the strongest shaking lasted for more than 40s with a peak horizontal acceleration of 989 gals (east–west direction of Station TCU084) and a peak vertical acceleration of 716 gals (Station CHY080). In particular, recorded peak ground accelerations generally exceeded 100 gals in Taipei, which is more than 100 km away from the epicentre, due to amplification of the basin effect (NCREE 2000). As a result of the tremor, one 12-story building, which was later found to be poorly constructed, collapsed and caused 87 people died in the rubbles.

The earthquake and the wide spreading damages, including building, infrastructure, lifeline, etc., have been extensively investigated and studied by researchers and professionals from domestic to international societies. A large body of data have been collected, making it a well organized documentation for studies in many aspects. A series of reconnaissance reports were published by the National Center for Research on Earthquake Engineering (NCREE) of Taiwan and Multidisciplinary Center for Earthquake Engineering Research (MCEER) of the United States. A commemorate Symposium was held in the next year (2000) with over 100 papers presented in four volumes, one each on science, geotechnical, structural and human aspects of the earthquake. In the following, a brief summary of the damage is mainly based on the above information and many other reports and articles published later. We attempt to give a brief review on the event and its consequences and influences.

2 Damage

The central areas of Taiwan suffered the most severe impact, particularly those near Nantou and Taichung. Towns such as Puli (埔里) was under huge consequences, and the majority of the casualties associated with collapsed buildings were found in this area. In the following, the first described is the heavy damage to buildings, and next are others including many public service facilities, such as transportations and bridges, utility systems, and others.

3 Damage to Buildings

In this event, most of damaged structures along the fault were non-engineered old structures constructed prior to the implementation of modern design codes. But modern structures near the rupture were unable to resist the large ground movements and the intensity of shaking exceeding what was specified in the design code.

This resulting high damage rate of structures is from a large percentage of buildings that collapsed were one-to-three story reinforced concrete frame structures constructed with brick infill partitions and exterior walls. Many of them had pedestrian corridors and open front at the ground floor. More than two dozen modern high-rise apartment buildings overturned or collapsed because of inadequate design. Some of the buildings collapsed because of the so-called "short-column effect" as the spaces between columns were partly filled by windowsills (Fig. 3). These windowsills trap the columns preventing the development of their normal flexural behavior over their height and allowing them to only deform over their free-height, i.e., the length of the column not surrounded by windowsills. As a result, although the shorter length of the trapped column would make it possible to resist higher lateral forces before the flexural strength of the column is reached, the ultimate shear strength of a short column is thus first reached and typical non-ductile shear failures ensue.

Among various kinds of building damages, one important category was identified: school building. Roughly nine hundreds school buildings in total were damaged, and over one hundred of them were severely damaged and resulted in closing many down for months or even permanently in a few cases. Like those elaborated above, they mostly suffered the damage from the "short-column" effect too. This phenomenon is because of an ill-design in which the lower part of the space between columns were infilled by windowsills leaving the upper part open for windows. This type of damage in school building was rather common in the direction parallel to the exterior corridor outside the classrooms (Fig. 4). The severity of damage to school buildings exceeded that of other types of structures due to the similarity of the design and construction of school buildings. The eccentricity of most school buildings associated with cantilevered corridors at upper floors made the situation worse.

Fig. 3 Short-column effect

4 Damage to Highways and Bridges

To the aspect of inland transportation, the Central Cross-Island Highway, at the time the only major complete route across the mountains in central Taiwan, was badly damaged. Subsequent storm damage and the high cost of restoration mean that the highway remains closed so far to public use and is not expected to be reopened in the near future. Instead, a national freeway has been continuously built since then to fulfil the demand of cross-island transportation. In the mountain area, there were a total of 132 landslides during the main quake and the aftershocks, some causing loss of life as rock-falls crushed houses.

Along the highway routes, there were about one thousand bridges suffered strong shaking, and over one hundred of them were badly damaged. Among them, twenty bridges were seriously damaged and required extensive repairs or had to be demolished and rebuilt. Most of them are located on Route 3 which is a major north–south highway running the length of Taiwan from Taipei in the north to Pingtung in the south. There are approximately 65 bridges on this route as it passes through Taichung and Nantou counties. Five of these bridges suffered collapsed spans or cracked piers. Another five bridges on county and city highways experienced similar distress, including one cable-stayed bridge under construction. All these ten bridges are within 10 km of the fault zone and most are within 5 km. Seven are located directly on the causative fault or on one of its branches. All are considered to be in the near field and thus subjected to intense ground motions

Fig. 4 Heavily damaged Guangfu elementary school in Wufeng (wikipedia: 921 earthquake)

or/and movements in both horizontal and vertical directions. The average fault dislocations were up to an order of 1.5 and 3 m in the horizontal and vertical directions, respectively.

5 Damage to Power and Water Systems

Other damages included many public service systems (utility lifelines) and crucial facilities. Among them, power and water systems had much impact to the people's daily life and the country's economics. In the following, we brief the consequences of the two aspects.

Power was cut to a large proportion of the island, due to damage to power stations, transmission stations, and the automatic shutdown of Taiwan's three nuclear power plants, which were restarted 2 days later. Damage to power facilities in the epicentral region in central Taiwan caused extensive power outages in the region. Power was also disrupted in northern Taiwan despite suffering much less earthquake effects. Damage to transmission lines that traverse mountainous areas with unstable ground caused extensive failure to the foundation of transmission towers. The inability to transport adequate power to the large population centers in the north required rotating blackouts for several weeks. Disruption of

power to semiconductor fabricating facilities in Hsinchu Science Park impacted world trade in computers and other products that were dependent on the products produced by these facilities. The loss of power also caused widespread communication disruptions.

Immediately after the earthquake all power in the northern and central part of the island was disrupted. The national electricity provider Taipower quickly restored their service. On September 20 Taipower was supplying 22,000 MW to users. Shortly after the earthquake Taipower could only supply 5,000 MW because of loss of capacity due to power stations tripping offline, damage to switchyards at substations and power generating stations, and the loss of lines to carry power. On September 22 through September 26, 13,000 MW was supplied, and it took two more weeks till early October to achieve 19,000 MW (Schiff and Tang 2000) .

Regarding water supply system, lack of water service in Taichung area was due to water pipe ruptures, damage to the Shih Kang Dam and the impounding reservoir, damage to Fengyuan Water Treatment Plant. The Fengyuan Water Treatment Plant was the only water treatment facility suffering significant damage from the earthquake. Damage to the Shih-Kang Dam, described later, reduced the raw water supply for the Taichung area by about 40 %. More deatails of the damage to the water supply system due to fault rupture are described in the following.

In Taichung City, water supply was resumed on a rationed basis on the second day after the earthquake, and full supply resumed in 9 days, except in a few isolated high elevation areas where water was supplied by truck. But water loss due to leakage in the water distribution system was up to 25 % after the earthquake and the poor situation lasted for nearly two months. Restoration of water service to rural area was slower than in urban areas due to damage to access roads and bridges. Therefore, in the rural area (Taichung County) about 80 % of the customers (about 700,000 families) suffered much longer duration without water service. In Nantou County, water supply from the distribution systems was still unavailable 2.5 weeks after the quake.

6 Hazards of Ground Movement

Hazards of the result of ground movement, including fault rupture, liquefaction and landslide causing many structure/foundation failures were rather widespread.

7 Fault Rupture

The Chelungpu Fault, a mapped active fault, roughly follows the topographic break along the western edge of the Central Mountain Range. The fault ruptured from Shih-Kang in the north to Tungtou in the south. The hanging wall of the

Fig. 5 Damage to Shih-Kang dam

thrust fault moved westward and upward by 1–2 m along the entire length of the rupture. Tectonic warping, or folding, associated with the faulting caused additional upward ground deformations of 6–7 m, particularly in the northern reaches of the rupture. The tremendous ground deformation associated with this earthquake's faulting caused major destruction to buildings and lifelines across a wide zone, as much as 120 m wide, along the entire rupture length.

No human-made structures were able to sustain such rupture, and Shih-Kang Dam (Fig. 5), located close to the north end of the rupture, was the one suffered the most. It is a gravity dam, about 25 m high, and has about 18 gated bays that serve as a spillway. The dam was directly intersected by fault rupture, with a differential movement of about 9 m vertically and 2 m horizontally under bays 16–18. The fault had not been mapped at the site prior to the earthquake. Bays not affected by the fault rupture survived essentially undamaged. A peak ground acceleration (PGA) of 0.56 g was recorded in a town nearby.

It is noted that the fault rupture also passed by about 20 m from the easternmost end of the Fengyuan Water Treatment Plant described above. At this location the faults run nominally in the north–south direction. The vertical offset at the fault trace was about 4 m (east portion moving up with respect to the west portion) and the horizontal offset was between 1–2 m (left lateral offset). These offsets were large enough to sever four steel pipelines with diameters of 400, 1100, 1500, and 2000 mm which traversed the fault and ran nominally in a NW–SE direction. Figure 6 show the distored 2000 mm steel pipe, and a remnant of it is now exhibited in Taipei.

Fig. 6 The distorted 2000 mm steel pipe in Fengyuan (*left*) is now exhibited at the museum of drinking water, Taipei (*right*)

Other substantial damage to water pipe was also found along the fault rupture trace, especially when water lines crossed the fault. For example, a 700-mm steel water main supported on its own piers crossing Yi Jiang River was broken into several sections. A new 1000-mm DIP pipe, supported by new piers, was reconstructed at the location in about 2.5 weeks. In a damage statistics, a total of 50 repairs were required for a heavily damaged pipe over a 3 km length section. It is expected that this exceeding high damage rate was the result of fault rupture or other similar near fault ground deformation effects.

8 Liquefaction

One of the causes for the heavy damage to buildings, lifeline systems, and harbor facilities is the widespread liquefaction caused by the earthquake. Figure 7 shows a survey on foundation damages by the NCREE (2000). Among the 467 foundation damage cases reported, 67 cases (14 %) were caused by earthquake-induced liquefaction.

Evidences of widespread liquefaction such as sand boiling, settlement and lateral spreading were observed after the earthquake. As shown in Fig. 8, the areas suffering the most severe liquefaction were Yuanlin, Wufeng, and Nantou.

In Yuan Lin, liquefaction was the most dramatic with an area of near 60 km^2 seriously affected. More than two hundreds of dwellings were either destroyed or were damaged beyond repair. Most of the dwellings destroyed were poor single-story houses made of bricks or adobes. Modern buildings performed rather well and suffered only tilting with little structural damage. At a nearby ground motion monitoring station (Station TCU110), a peak acceleration of 187 gals was registered.

In Nantou, a section of levee along the Maolo River was seriously damaged as a result of liquefaction. The monitoring station (TCU076) at a distance of 15 km away recorded a peak acceleration of 420 gals and strong motion lasted for 41s. Liquefaction was found to be limited within depths of 4–8 m. There was no

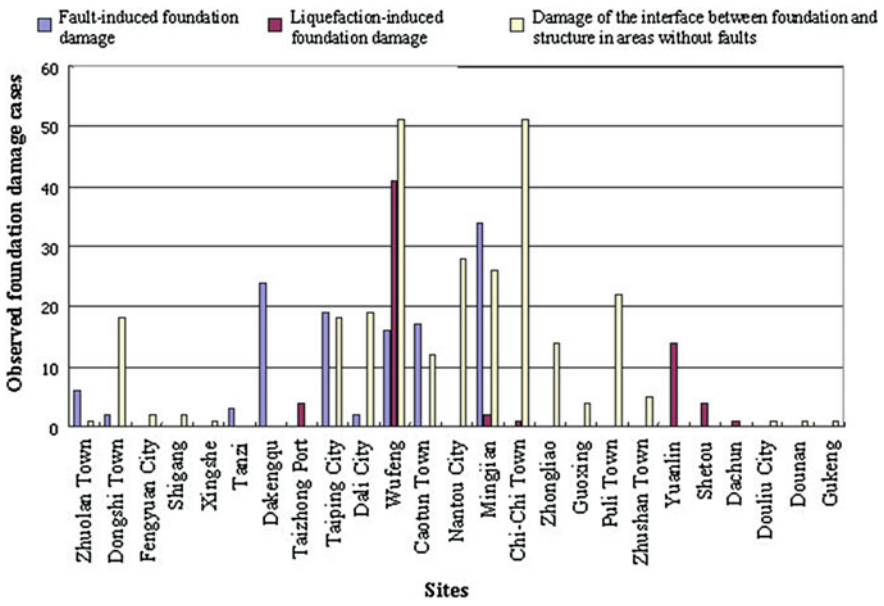

Fig. 7 Foundation damage survey after the Chichi earthquake (NCREE 2000)

indication of liquefaction in the underlying gravel layer. Post-liquefaction settlement ranged from 5–26 cm.

In Wufeng which is within 1 km from the Chelungpu fault, liquefaction resulted in lateral spreading at four locations along the Koniaokeng Creek and damaged a few low-rise structures. A nearby monitoring station (TCU065) measured peak acceleration of 774 gals in the east–west direction, 563 gal in the north–south direction and 257 gals in the vertical direction.

The most severe liquefaction-induced damage occurred at the port of Taichung (台中港), one of Taiwan's major commercial harbours located about 55 km northwest of the epicenter. During the earthquake, liquefaction badly damaged four of its 45 docking wharves. The port was built on a reclaimed land in four stages. The hydraulic fill behind the four wharves are retained by caissons which sit on a thin layer of cobbles and boulders. The loosely dumped sands behind the caissons were liquefied and sand boils occurred all over the places. Sands erupted from the ground can be found as far as 150 m from the waterfront. Due to liquefaction, the caissons moved seaward by 1 m on average and the backfill behind these caissons settled by about 70 cm. Due to the outward movements of the caissons, gaps were created at the interlocks between caissons and permitted the materials behind the caissons to be washed away by tides resulting in cavities of, up to, 30 m in diameter and 4 m in depth (Fig. 9).

The nearest seismology station located at a distance of 4.7 km southeast of the Port registered a peak acceleration of 165 gals in the east–west direction and 152 gals in the north–south direction. The vertical component of the ground motion was small.

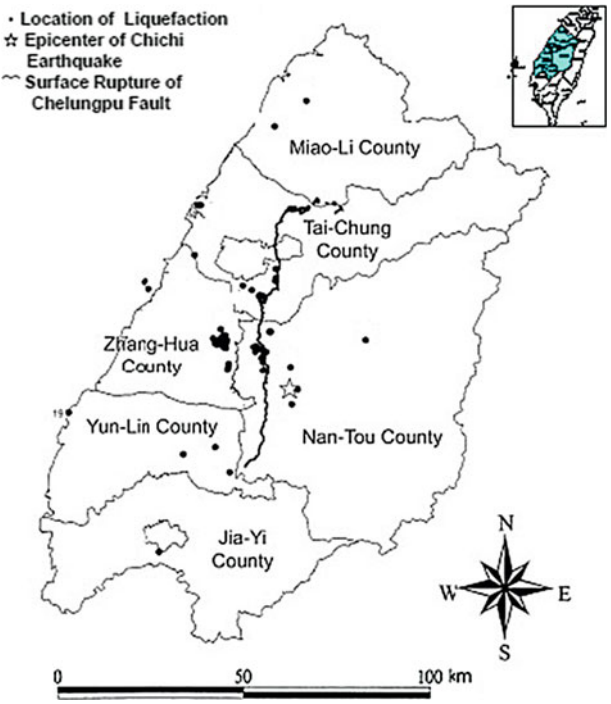

Fig. 8 Distribution of liquefaction sites in the Chichi earthquake (NCREE 2000)

9 Landslide

Strong ground motions on the land mass east of the Chelungpu Fault generated more than 1,800 landslides throughout the region of the Central Mountain Range within and adjacent to the epicentral area. A total of 436 scores of slope failure were investigated and documented in the reconnaissance report coordinated by NCREE. The Bureau of Water and Soil Conservation reported more than 2,300 items of variation based on the satellite photos taken before and after the earthquake (Ueng et al. 2001). Nearly all of the slope failures are located to the right of Chelungpu fault, i.e., on the hanging wall, and most slides were relatively shallow slips in residual soils, typically involving depths of 1–5 m.

It should be specially mentioned herein that two phenomenal landslides occurred near the epicenter. They are parts of a massive landslide involving 120 million cubic meters of debris occurred at Tsao-Ling. In one, a large section of mountain slide 2–3 km and swept away everything in its path, including entire villages. About eighty percent of the sliding mass (about 100 million cubic meters), and 39 people who lived behind the crest of the dip slope, flew over the Ching-Shui River, and landed on the other side of the river. Thirty two people were killed and seven survived after the sliding-flying-landing process. Air-blast or

Fig. 9 Damage of Taichung port by liquefaction

release of compressed air cushion under the sliding mass is believed to be responsible for this abnormal phenomenon (Hung 2000).

The other involved twenty percents (about 25 million cubic meters) of the sliding mass dropped into the valley of the Ching-Shui River and blocked the flow causing flooding of the upstream valleys (Hung 2000). It slid down more than 100 m, damming up a river and forming an artificial lake.

10 Recovery from the Disaster

To recover the damaged homeland, a new governmental agency: the 921 Earthquake Post-Disaster Recovery Commission, Executive Yuan was formed soon after the quake to take the lead. It became a full-fledged central government agency later in the next year (2000). In the meantime, the Provisional Act on the 921 Earthquake Post-disaster Reconstruction was promulgated on February 3, 2000 to promote the work of reconstruction effectively, rebuild the society and communities quickly, and revitalize the economy. Figure 10 shows the process of the recovery actions after the Chichi earthquake along the time line of the laws and the organizations of the governmental agency to advance the mission goal.

The Taiwan government allocated a total budget of around NT$212.36 billion (around US$6.63 billion) for the post-disaster reconstruction work. Private sector donations amounted to around NT$33.9 billion (around US$1.06 billion). The recovery program was classified into the following five categories: public

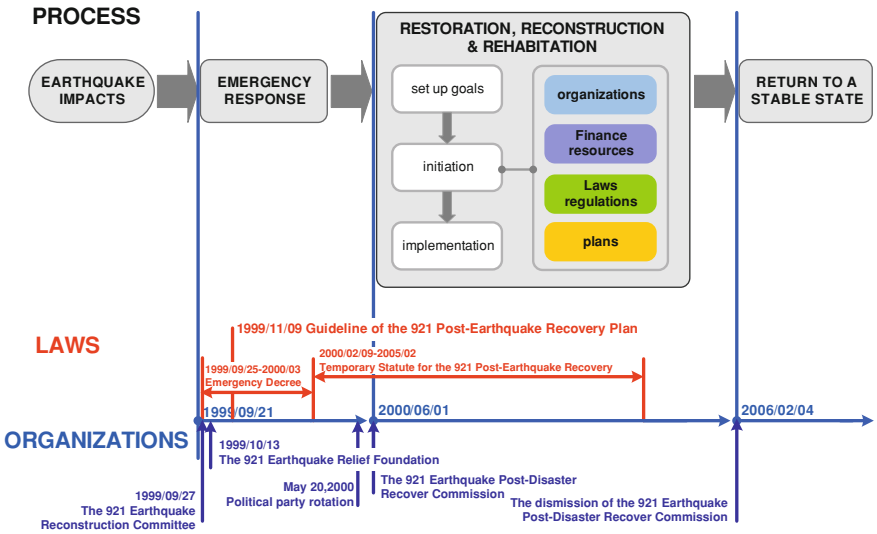

Fig. 10 Timeline of the recovery works (Chen and Liu 2009)

construction, geotechnical engineer, economic revitalization, life reconstruction, and house and community reconstruction (Fig. 11). Regarding detail items, Fig. 12 shows an overall progress of the post-earthquake recovery works from immediately after quake to 2005, by then most works had been nearly accomplished.

Among those many recovery works, housing homeless people was on top the line. In order to settle the survivors after the quake, temporary houses (prefabricated units) were built in 112 different settling areas (5,824 housing units). Among these, 38 were built by government agency, 56 by charity organizations, and 18 by private enterprises. The settling areas were mostly on public estates. Yet there were landowners willingly to provide their own lands amounting to 46 settling areas to accommodate the prefabricated housing units. It is worthy noted that Japan donated 1,003 prefabricated housing units formerly used in the Hanshin-Awaji Earthquake to our 14 settling areas.

Beyond temporary housing works, the urban renewal and reconstruction works in the following were mainly sponsored by the government's no-interest construction financing loans and credit guarantees through a special program offered by the 921 Relief Foundation (a semi-official organization) in November 2002. Merging with private sector donations, the governmental fund was to finance the urban renewal construction of congregate housing buildings and to buy existing buildings to settle people. Till February 2006, 99 applications for urban renewal reconstruction had been filed. A total of 63 communities (5,142 units) were sponsored by the special program.

Besides housing the survivors, recovery of damaged schools were another important issue (Fig. 12). A total 293 schools had been reconstructed. The government reconstructed 185 schools consuming a total budget of NT$33.506 billion.

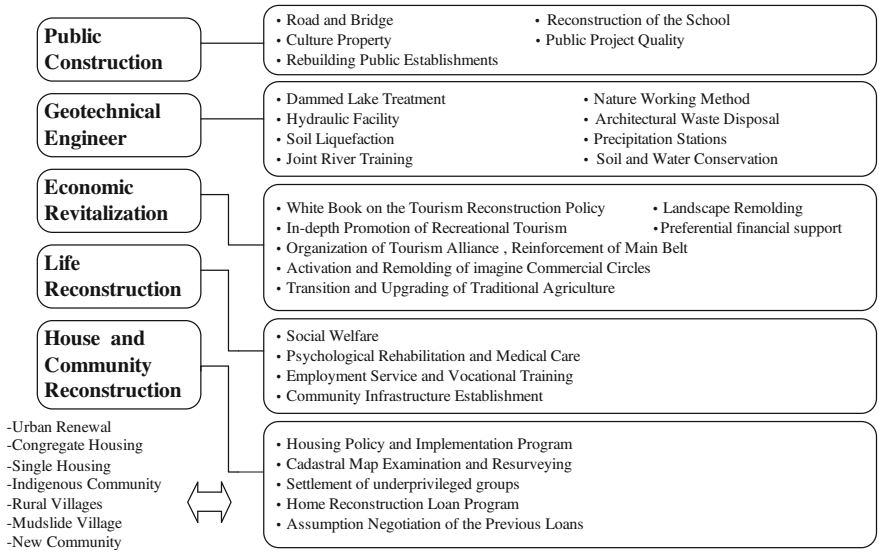

Fig. 11 Post-Chichi-earthquake disaster recovery program (Ding 2007)

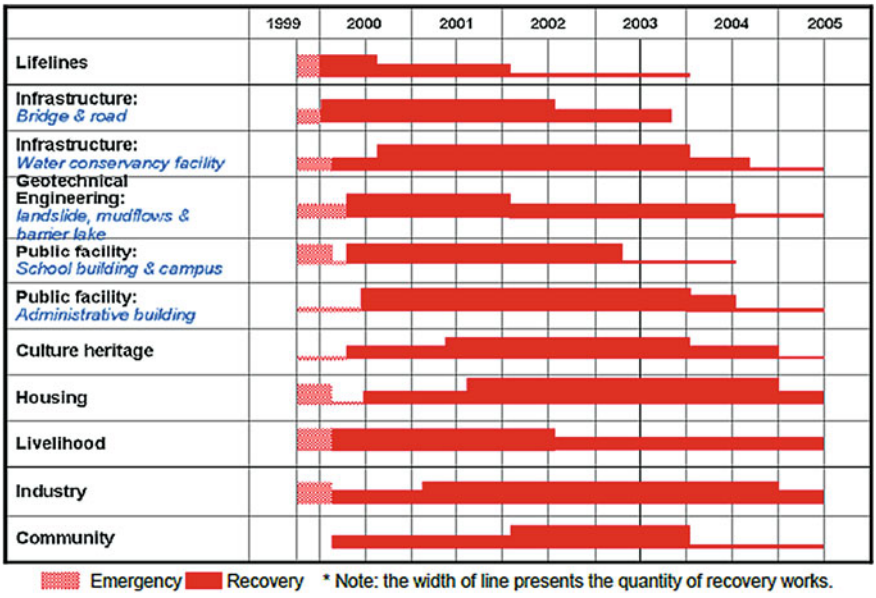

Fig. 12 Overall progress of post-Chichi-earthquake recovery works (Chen and Liu 2009)

The rest 108 schools were handled by charity organizations. In comparison, the private sectors performed better than the public sectors by injecting new idea of sustainability to the new schools.

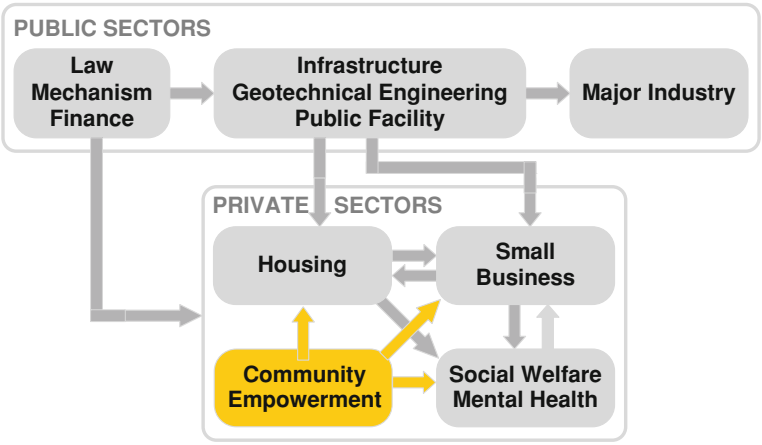

Fig. 13 Long-term recovery concept learnt from Chichi earthquake (Chen and Liu 2009)

According to a recent report (Chen and Liu 2009), the path of the recovery was indeed tough and tedious. The 10-year long recovery tells that intensive collaboration between individuals and organizations is the essential to integrate efforts from both public and private sectors. On one hand, the major portion of infrastructure recovery can be carried out by public sectors who can mobilize high capacity equipment and abundant resources through a simple and linear process under a good plan. On the other hand, special structural and most non-structural recovery is better carried out by private sectors since this portion needs a much complicate process and takes a long while to implement. In fact, the non-structural recovery has great impact on both the reconstruction and rehabilitation of communities. Therefore, how to empower the people in the communities has become a crucial factor to the success of the entire recovery (Fig. 13).

11 Conclusions

The Chichi earthquake certainly increases the awareness of people of potential threat of earthquake and provides an opportunity for improving the preparedness for earthquakes in future. The path of recovery further points out the importance of collaboration between public and private sectors and provides another opportunity for learning the empowerment of communities for strengthening the resilience against disasters. Through the painful experience of disaster and the rough path of recovery from the earthquake, people in Taiwan have learned how to live with the nature, in good and bad, and sincerely prepare to deal with what may happen in the future.

References

Chen LC and Liu YC (2009) Conceptualizing long-term earthquake recovery: what we learned from the 1999 Chi–Chi earthquake in Taiwan. In: Proceeding of the 9th IIASA-DPRI conference on integrated disaster risk management, October 2009, Kyoto University and International Institute for Applied Systems Analysis, Japan

Ding YC (2007) The Chi–Chi (Taiwan) earthquake experiences on post-disaster reconstruction for the 921 earthquake. In: The 2nd international conference on urban disaster reduction, Taipei, Taiwan, 27–29 November 2007

Hung JJ (2000) Chi Chi Earthquake induced landslides in Taiwan. In: Proceedings of international workshop on annual commemoration of Chi–Chi earthquake,Taipei, Taiwan, ROC

Loh CH, Lee ZK, Wu TC, Peng SY (2000) Ground motion characteristics of Chi–Chi earthquake of 21 September 1999. Earthq Eng Struct Dynam 29:867–897

Moh ZC, Hwang RN, Ueng TS, Lin ML (2002) 1999 Chi Chi earthquake of Taiwan.In: The 17th Australasian conference on the mechanics of structures and materials, Gold Coast, Australia, pp 12–14

NCREE (2000) Reconnaissance report of the geotechnical hazards caused by Chi–Chi earthquake, national center for research in earthquake engineering (NCREE), Taipei, Taiwan (in Chinese)

Schiff AJ, Tang AK (2000) Chi Chi Taiwan earthquake of September 21, 1999: lifeline performance (Monograph (American Society of Civil Engineers. Technical Council on Lifeline Earthquake Engineering), No 18). American Society of Civil Engineers, USA

Ueng TS, Lin ML and Chen MH (2001) Some geotechnical aspects of 1999 Chi–Chi, Taiwan earthquake. In: Proceedings 4th international conference on recent advances in geotechnical earthquake engineering and soil dynamics and symposium in honor of Professor W D Liam Finn, San Diego, California, USA

Wen KL (2003) Strong motion observations in Taiwan & ground motion characteristics of the 1999 Chi–Chi earthquake, NCREE03-027. International training program for seismic design of structures, Oct 13–17, Taipei, Taiwan, ROC

Key Factors Influencing the Mechanism of Rapid and Long Runout Landslides Triggered by the 2008 Wenchuan Earthquake, China

Fawu Wang, Ping Sun, Lynn Highland, Hongshuai Liu, Laizhen Pei and Qiangong Cheng

Abstract The 2008 Wenchuan earthquake triggered many rapid and long runout landslides, which directly caused great loss of properties and human lives and were responsible for a large percentage of total damages caused by the earthquake. It is very important for future landslide mitigation programme to understand the earthquake-induced mechanism of initiation and motion of rapid and long runout landslides, which can potentially be the deadliest of ground failures. In this paper, field investigations of some typical landslides caused by the Wenchuan earthquake are introduced first, and followed by data from ring shear tests used to simulate the initiation and motion of one landslide in particular, the Donghekou landslide. It was found that valley water and groundwater played key roles in the rapid motion and long runout process of this landslide during the great earthquake. It was also observed that hazardous effects from the slowing of movement and/or a short runout, due to various geologic and hydrologic

F. Wang (✉)
Department of Geosciences, Faculty of Science and Engineering,
Shimane University, Matsue, Japan
e-mail: wangfw@riko.shimane-u.ac.jp

P. Sun
Institute of Geomechanics, Chinese Academy of Geological Sciences,
100081 Beijing, China

L. Highland
National Landslide Information Center, U. S. Geological Survey, Denver, USA

H. Liu
Institute of Engineering Mechanics, China Earthquake Administration, Harbin, China

L. Pei
Institute of Mountain Hazards and Environment, Chinese Academy of Sciences, Chengdu, China

Q. Cheng
School of Civil Engineering, Southwest Jiaotong University, Chengdu, China

F. Wang et al. (eds.), *Progress of Geo-Disaster Mitigation Technology in Asia*,
Environmental Science and Engineering, DOI: 10.1007/978-3-642-29107-4_9,

conditions of other landslides caused by the Wenchuan earthquake, contrasts with those which caused more deaths and damages due to rapid, long runout movement. Implications from this analysis suggest that decision-makers for future hazard mitigation and land use planning should be advised to be aware of the geotechnical and hydrological properties of their local areas where possible.

Keywords Wenchuan earthquake · Rapid and long runout landslides · Initiation · Motion · Hydrogeological condition

1 Introduction

The 2008 Wenchuan earthquake caused heavy damages in Sichuan Province and the nearby areas in China. According to the official statistics (as of 6 July 2008), the earthquake caused 69,197 deaths, and 18,340 were declared missing. About one-third of this total was caused by earthquake-induced landslides, directly and indirectly. Typical examples are the rapid and long runout Wangjiayan landslides which caused devastating damages in Beichuan county the Donghekou landslide in Qingchuan County and the Jiufeng-cun landslide in Pengzhou City (Wang et al. 2009; Yin et al. 2009; Cui et al. 2009). These landslides killed all the people and destroyed all the villages in their travel paths. Very few people in these areas survived these landslides due to their catastrophic, fast-moving and widespread characteristics. Understanding the mechanism of initiation and motion of rapid and long runout landslides, especially the key factor controlling the travel distance, is extremely important for purposes of disaster mitigation and land-use planning for these areas of probable future seismic activity. In this paper, the landslide field investigation results are introduced first, followed by presentation of experimental results using ring-shear apparatus to simulate landslide initiation and motion. Finally, some suggestions are made to the local communities for land-use guidance during the reconstruction process of the damaged areas.

2 Field Investigation Results on Some Typical Landslides

After the Wenchuan earthquake, the authors investigated the earthquake affected areas at five different points in time. The first time was June 2008, 1 month after the earthquake occurrence. At this time, most of the large scale landslides remained in their original shape after initial occurrence, making the observation and investigation more closely attuned to conditions which occurred immediately after the earthquake initiated the landslides. During the field investigations, there was strong indication that the hydrogeological conditions associated with the landslides controlled the initiation and motion of the landslides. In order to verify this hypothesis, characteristics of some of these typical landslides are presented here to show the importance of hydrogeological conditions to the landslide process.

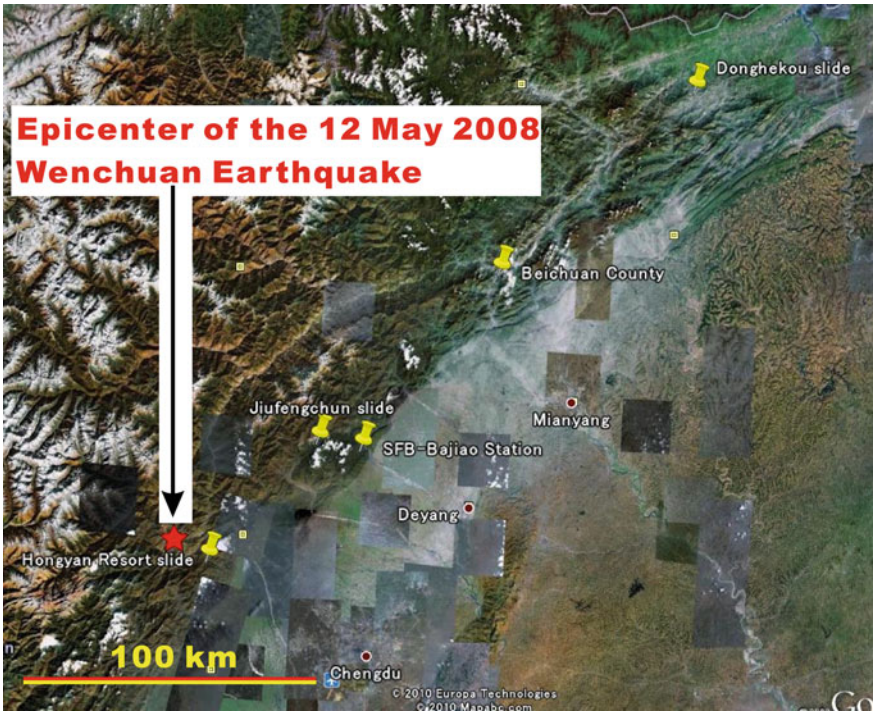

Fig. 1 Map of the area affected by the 2008 Wenchuan earthquake, showing locations of the epicenter, the SFB-Bajiao strong-motion station, and the landslides and rockfalls studied

Figure 1 shows the location map of the earthquake-affected area. The epicenter of the main shock of the Wenchuan earthquake is shown, as well as the location of landslides and rockfalls in Hongyan Resort Village, Dujiangyan City, in Jiufengcun Village, Pengzhou City, in Donghekou Village, Qingchuan County. The Wangjiayan earth flow/slide and the Jingjiashan rockslide in Beichuan County town are also shown in this figure. In addition, the location of the SFB-Bajiao station for strong earthquake monitoring is also included in this figure. During the Wenchuan earthquake, the SFB-Bajiao station recorded the three components (E–W, S–N, and Up–Down) of the seismic wave, and the monitored wave is used in the geo-simulation test of the Donghekou rockslide—debris flow for the landslide initiation study discussed in this paper.

2.1 Rockfall Occurrence in Hongyan Resort Village

Hongyan Resort Village in Qingcheng-Houshan is located on an old landslide dam. Using information from Google Earth, typical landslide topography can be recognized. Because the slope was relatively gentler than the nearby area, large

Fig. 2 This rockfall occurred in Hongyan Resort Village, located on an old landslide dam. The *dashed white line* shows where the road existed before the landslide

scale development was conducted and a large resort village was constructed here. During the Wenchuan earthquake, rockfalls occurred at the roadside, killed about 40 persons, and totally blocked the road, effectively cutting off the transportation route to the area (Fig. 2). From field observations, it was found that the road was built along the erosional path of a torrent which passed through the old landslide dam area (it is a local road constructed of concrete).

Moreover, the buildings in this village were heavily damaged and none are useable for the foreseeable future. From site evaluation it is very clear that old landslide areas (especially those landslides that moved for long distance as this one in Hongyan Resort Village) are very prone to large-scale slope failure caused by earthquake shaking, and old landslides can easily be reactivated.

From the viewpoint of hydrogeology, the landslide occurred in a dry slope. Because the slope here is steep (about 60°), groundwater should be very deep if it exists. From Fig. 2, it can be seen that the displaced rock mass deposited at the foot of the slope is on an angle of repose. It can be classified as a rapid failure because of the steep slope angle, but the travel distance is limited because the displaced rock mass is dry and the travel path is also dry, and does not have the extended flow effect that a wet mass would cause.

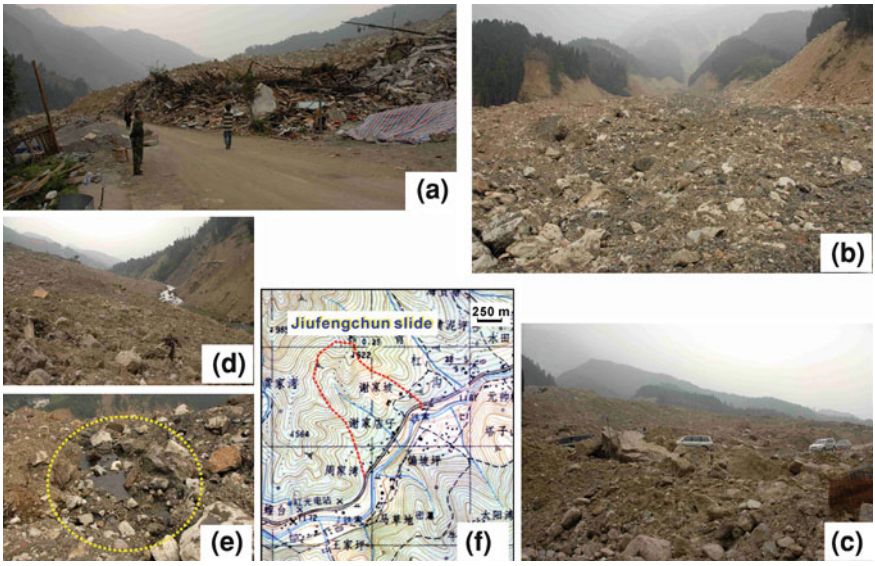

Fig. 3 Photos of rock deposits from the rock flow in Jiufeng-cun Village. **a** Toe of the rock flow, **b** Travel path of the rock flow, **c** Oblique view, **d** Dammed Jin-he river, **e** Water in the sliding mass, **f** Old map showing a valley located along the travel path

2.2 Rockslide: Rock Flow in Jiufeng-cun Village

In Jiufeng-cun Village Pengzhou City, rockslides occurred at the source area at first, and became rock flow during the sliding process, at least partly due to the source area having a topographical characteristic for the accumulation and impounding of water. The total traveling distance is about 1.6 km, and more than 100 deaths resulted from the rapid motion, as people did not have time to evaculate. In Fig. 3a, the smashed houses and displaced sliding mass looked very dry, and a witness did not see any water seep out from the displaced sliding mass. However, as shown in Fig. 3e, in a photo taken 1 month after the earthquake, we found water pockets existing on the sliding mass. Also as seen in Fig. 3f, which is an old map created before the earthquake, a gully has existed in this area. As shown in Fig. 3b–e, the displaced sliding mass consists of large gravels and boulders, and thus, the permeability of the sliding mass should be very high. The high permeability will not allow groundwater to be distributed throughout the sliding mass, but will exist near the sliding surface. As indicated by the geo-simulation test presented in this paper, a thin saturated sliding zone will be enough for rapid and long travel motion.

In Fig. 3f of the old map, it can be noted that a similar slope failure had occurred previously. The evidence includes the straight local road and densely populated village, because in mountainous areas, roads are always naturally curved if there is no debris flow deposits and the existence of a densely-populated village

Fig. 4 The rockslide—debris flow in Donghekou Village (the photo was taken in July 2008, 2 months after the earthquake). The flow-path was considered to be fully saturated

hints that a gentle slope and rich groundwater can be found. It can be estimated that the Wenchuan earthquake effects are just a repeat of the previous event, and most likely, it will occur again in the same valley in the future. It is very important to recognize this phenomenon of susceptible pre-conditions affected by prevalent seismicity for future landslide disaster mitigation.

2.3 Rockslide: Debris Flow in Donghekou Village

A large-scale rockslide occurred on the mountain in back of Donghekou Village. Movement was triggered by the earthquake, and the initial rockslide became a debris flow as it moved down the mountain. Seven villages were destroyed and more than 400 people were killed. The photo in Fig. 4 shows the Donghekou rockslide/debris flow. The source area of the landslide looks dry, while the travel path is full of water. When the sliding mass entered the valley bottom, the deposit was estimated to be in a fully saturated state, based on the post-earthquake investigation and information in a photo showing the village before the earthquake.

Soil samples were taken from the site, and simulation tests on the initiation and motion mechanism of this landslide were conducted. The test results are presented in the following section.

Fig. 5 The Wangjiayan earth fall/slide (*left*) and the Jingjiashan rockfall (*right*) in Beichuan county town. The Wangjiayan landslide killed 1,600 people and the Jingjiashan landslide killed 400 people. The *dashed lines* show the travel path and the extent of each landslide

From the viewpoint of village location, this site is similar to Jiufeng-cun Village. The flat valley probably was formed by ancient debris flow(s), and the access to a water source attracted more people and the seven villages were formed.

2.4 The Wangjiayan Earth Fall/Slide and the Jingjiashan Rockslide in Beichuan County Town

The damages caused by landslides triggered by the Wenchuan earthquake in Beichuan County are the most severe of the entire disaster (Fig. 5). At Wangjiayan, an earth flow occurred in the weathered shale and sandstone, and it became a long runout and rapid landslide at the bottom of the slope. This landslide destroyed the old town and caused 1,600 deaths. The shallow groundwater table and low permeability of the sliding mass are factors that are considered to have played key roles in the landslide motion. While the Jingjiashan rockslide occurred in dolomite/limestone, and also because the displaced rock mass was almost dry, it slowed and stopped at about 25°. The Maoba Senior High School was destroyed and about 400 students and teachers were killed, because the school was located very close to the bottom of the slope. Additionally, the school was in very close proximity to the earthquake fault, and most likely experienced a damaging level of shaking from the earthquake.

Fig. 6 Air photo of the Donghekou landslide. Refer to Figs. 7 and 8 for scale

3 Simulation Tests for the Initiation and Motion Mechanism of the Donghekou Rockslide: Debris Flow as a Case Study

Using the undrained ring shear apparatus developed in Kyoto University, Japan (Sassa 1997; Sassa et al. 2004), two types of simulation tests were conducted. They are: (a) Simulation test to clarify the initiation mechanism of the Donghekou rockslide triggered by the Wenchuan earthquake; (b) Test to simulate the moment when the failed sliding mass loaded onto the valley deposits, and to clarify the motion mechanism for long runout and high speed.

3.1 The Simulation Test for Landslide Triggered by the Real Seismic Wave

In this test, the initial stress condition was set according to the longitudinal section of the Donghekou rockslide considering the capacity of the experimental apparatus. The real seismic wave components of the Wenchuan earthquake monitored at Bajiao Town in Shifang City by Seismic Monitoring Network, China Earthquake Administration were used (Wang 2008). By transforming the three components of the seismic wave to two components occurring along the sliding surface (increment of shear stress) and perpendicular to the sliding surface (increment of normal stress), the input signals were formed (Wang et al. 2000), and applied to the sample (sample A from the source area of the Donghekou rockslide).

Figures 6 and 7 are an air photo and topographic map of the Donghekou rockslide—debris flow, respectively. The debris flow dammed the Xiasihe River

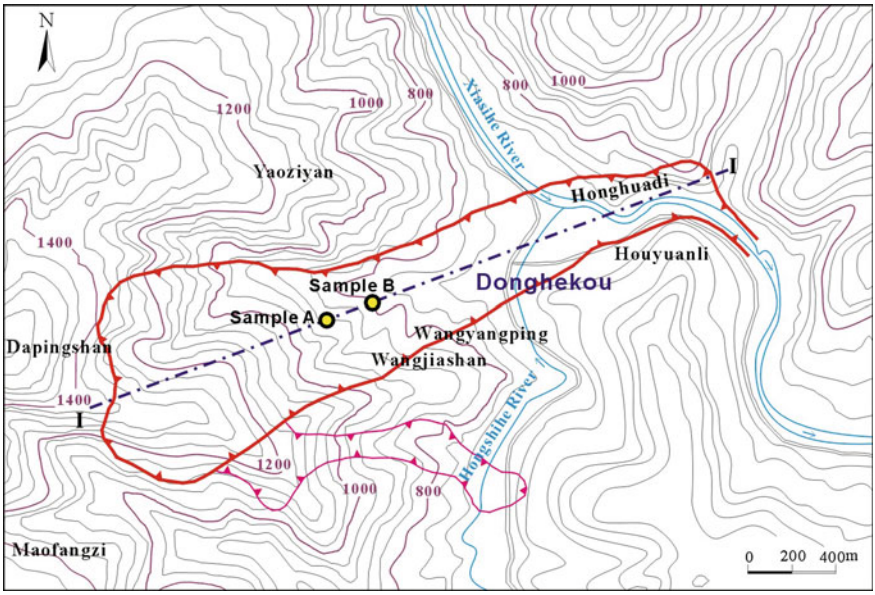

Fig. 7 Topographic map of the Donghekou rockslide—debris flow showing towns, rivers, and areas where samples A and B were taken (landslide boundaries are outlined in *lines* with *triangle marks*)

and its tributary, and formed two landslide lakes, and part of the displaced slide mass entered the Xiasihe River, and flowed down the stream. Fortunately, the landslide dam in the main stream of the Xiasihe River is not very thick. Because of the long travel distance, the debris flow deposits became wide and thin. The Donghekou Town is located at the junction of the tributary and the Xiasihe River, and it is reasonable to consider that the surrounding deposits were fully saturated before the earthquake, a situation that can occur, even in dry season. From Fig. 7, it can be seen that the scale of the rockslide can be estimated. In the source area, the average length is about 1 km, and the width is about 1 km, and the total length of the rockslide and debris flow reached about 3 km.

Figure 8 shows the geological components of the Donghekou rockslide—debris flow and the surrounding area. The source area of the rockslide is located in dolomite limestone and sericite limestone of the Yuanji Formation of the Sinian Period (Pre-Cambrian). The displaced sliding mass moved in weathered tuff sandstone and phyllite and carbon-siliceous slate, which has a high potential for grain crushing, and relatively low permeability.

Figure 9 shows the central longitudinal section of the Donghekou rockslide—debris flow. The average thickness of the sliding mass in the source area is about 50 m, and the total volume of the Donghekou rockslide is about 50 million m^3. Also as shown in Fig. 9, by means of connecting the upper part of the rockslide and the toe of the debris flow, the apparent friction angle of the rockslide—debris flow of 11° was obtained. This value indicates a high mobility for the

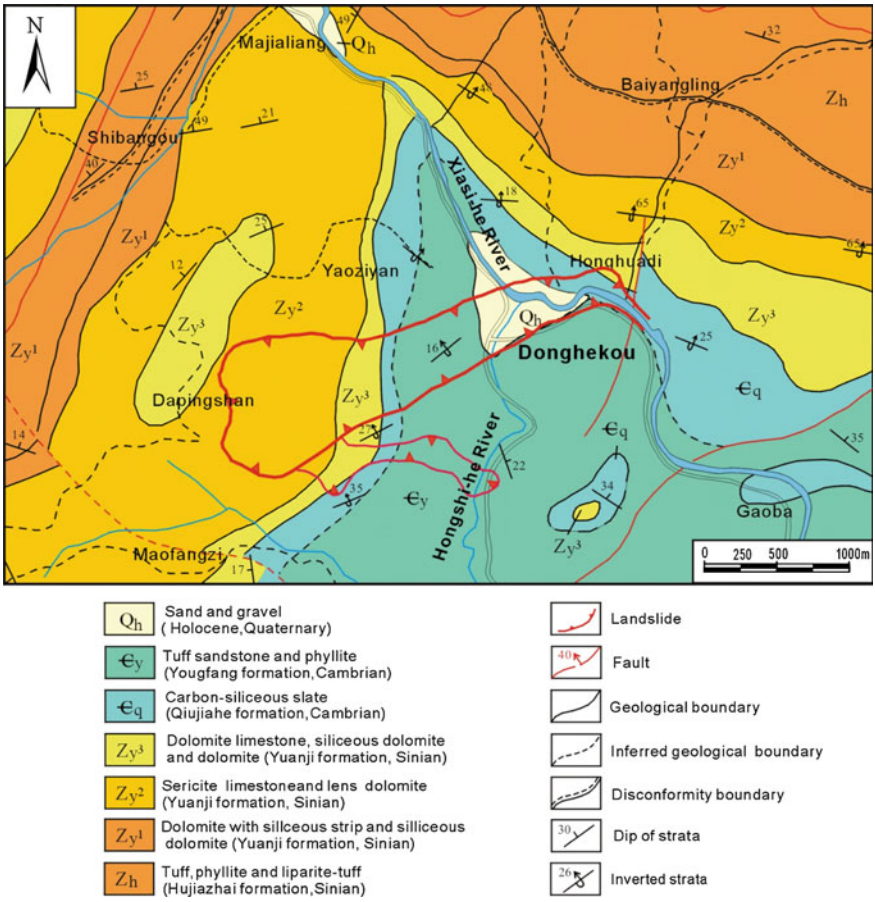

Fig. 8 Geological map of the Donghekou rockslide—debris flow and surrounding area

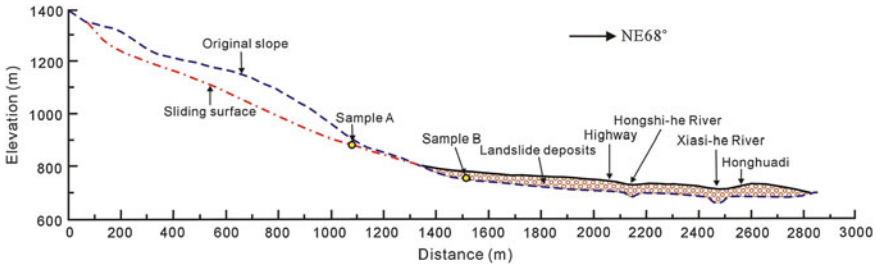

Fig. 9 Longitudinal section of the Donghekou landslide showing landslide topographical characteristics, and locations from which samples A and B were taken

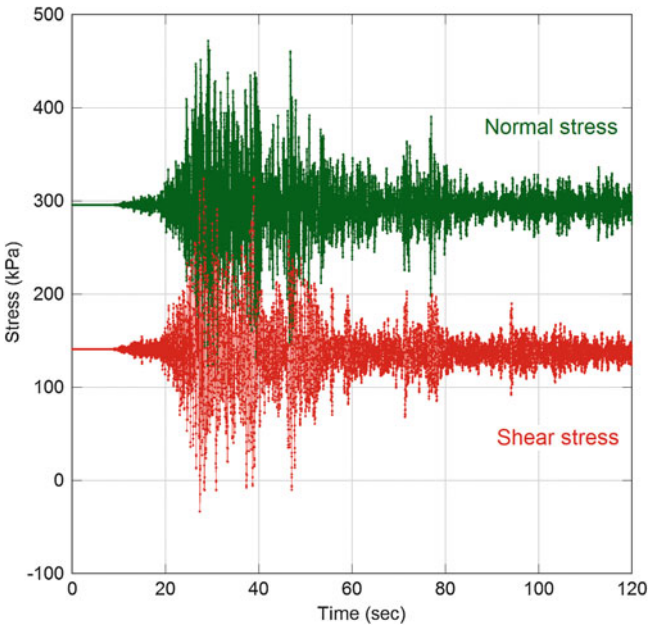

Fig. 10 Components of the real seismic wave, which was recorded by China Administration of Earthquake, were used as the input signal for the simulation test

rockslide—debris flow. From the source area, sample A was taken for geo-simulation test for landslides initiated by earthquake, while sample B was taken for the test to simulate the travel process when it is loaded by a displaced moving mass from the upper slope. As confirmed from an investigation conducted in March 2009, it was found that although there was a generally dry season in this area, and groundwater existed around sample A and B.

For the initial condition of the Donghekou rockslide, slope angle of 25° was used at the source area. With the consideration of the capacity of the apparatus, a thickness of 20 m was used to replace the actual average thickness of 50 m. The unit weight of the sliding mass was assumed to be 18 kN/m^3. For the seismic accelerations, generally, it was attenuated by distance, and amplified by standing elevation. Considering the distance of the Donghekou from SFB-Bajiao monitoring station, and the topographic condition, the seismic wave monitored at SFB-Bajiao monitoring station was used to form the input signal for the simulation test without amplification and attenuation. Figure 10 shows the normal stress component and shear stress components acting on the sliding surface of the Donghekou rockslide at the source area. The initial normal stress is 295.7 kPa, and the initial shear stress is 137.9 kPa.

The test was conducted with sample A from the source area. After consolidation, the initial shear stress was loaded gradually while keeping the sample in a drained condition to avoid excess pore-water pressure generation. Then, the

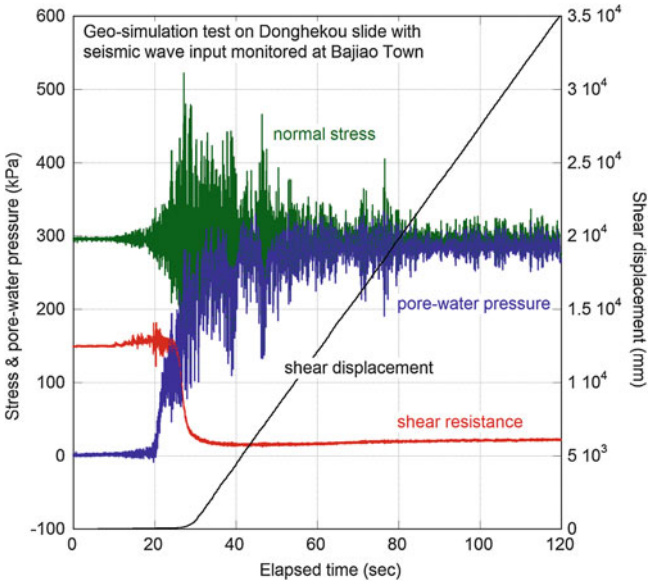

Fig. 11 Geo-simulation test results for the Donghekou landslide using the real seismic wave components as the triggering process

sample was changed to an undrained condition, and the input signals were loaded to simulate the condition of the original slope when the earthquake motion was applied as the initiation factor.

Figure 11 is the entire data series for the geo-simulation test on the Donghekou rockslide. A large decrease of the shear resistance and a rapid generation of excess pore-water pressure to the value of normal stress can be observed. Figure 12 shows a close-up, magnified view of the first period of the data from 18 to 30 s. From the two figures, it can be seen that the sample failed at about 10 s from the beginning of the earthquake (10 s in Fig. 11, and 20 s shown in Figs. 10, 11), and the shear displacement accelerated at about 25 s. At the same time (from 20 s), pore-water pressure shows a rapid increase, and reached the same value with normal stress at about 45 s, reaching the point of full liquefaction. Corresponding to rapid increase in pore-water pressure, shear resistance decreased rapidly, and reached a very low value of about 15 kPa. At the end of the seismic loading, the shear displacement reached a value of 35 m with a high speed (the maximum speed of the apparatus at the selected gear).

After undrained shearing for 35 m was completed, the sample in the shear box was removed, and grain size distributions were analyzed (Fig. 13). Compared with the original sample, it is evident that grain crushing occurred throughout the whole material of the samples, those at the shear zone being finer. It is evident that grain crushing can occur under undrained conditions, and it may contribute to liquefaction of the soil during shearing.

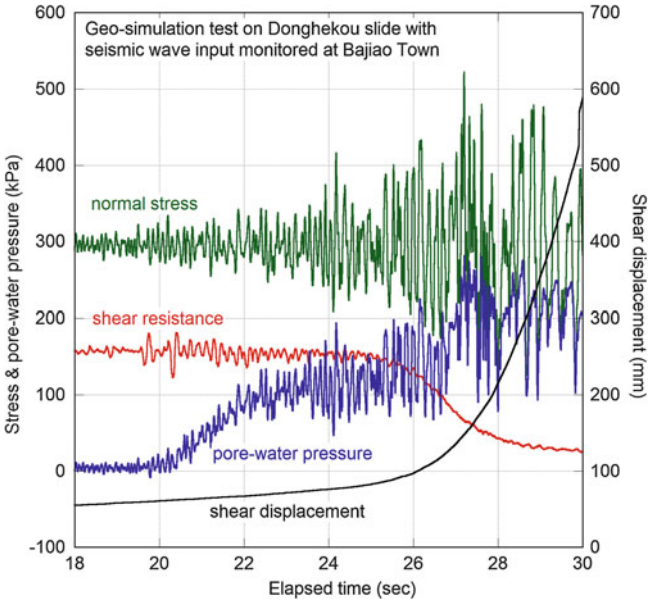

Fig. 12 Close-up magnification of part of the Geo-simulation test results for the Donghekou landslide

3.2 Results of the Simulation Test Showing the Process and the Point at Which the Failed Sliding Mass Loaded into the Valley Deposit

To simulate the process of debris flow triggered by rockslide, the model proposed by Sassa et al. (1997) was applied. The sliding mass moved down the slope (I), and applied load onto the torrent deposits at the foot of the slope (II). Because a surface-water stream or subsurface flow existed and some of the deposits were saturated, the torrent deposit was sheared by undrained loading and transported downstream together with the sliding mass (III) (Sassa et al. 2004). In this study, we changed the saturated condition of torrent deposits to three patterns: dry, partially saturated, and fully saturated, to observe the significance of the Hydro-geological conditions. A column of unit width, which is part of the torrent deposit, was considered. In position (I) of the sliding mass, the weight of the column (W0) was in effect. When the sliding mass rode on to the torrent deposit (II) with a certain velocity, it provided dynamic loading of the column. Here, it is assumed that the applied stress on the torrent deposits was the sum of the static stress, W, (load due to the weight of the sliding mass) and the dynamic (impact) stress, F_d, working in the direction of motion of the sliding mass (Fig. 14).

Graphs 2–4 shown in Fig. 15 illustrate the results for the three conditions (dry, partially saturated, fully saturated). When the failed sliding mass traveled down to

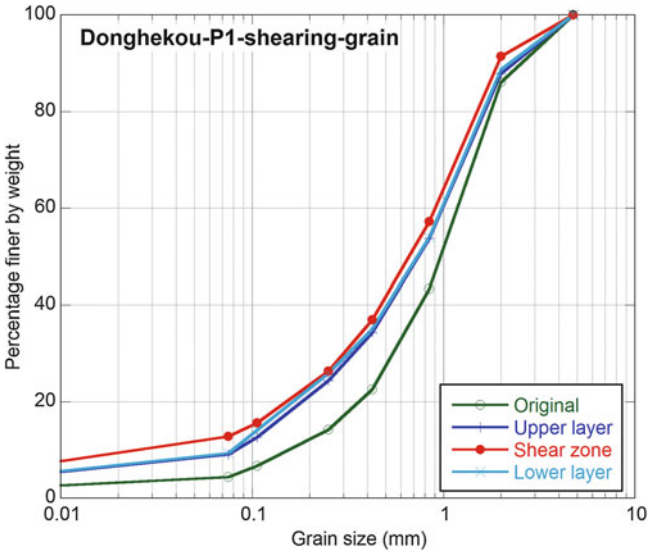

Fig. 13 Grain size distribution of the source area sample from the Donghekou landslide. The original sample, consisting of soils from the *upper layer* of the shear box, the *lower layer* of the shear box, and the shear zone are shown

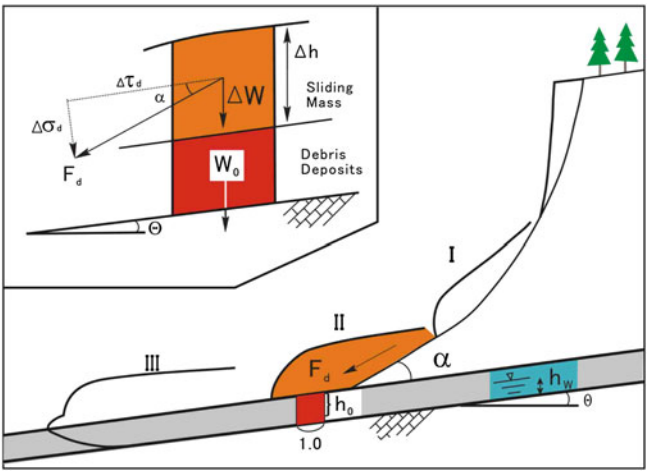

Fig. 14 Model of the landslide triggered by debris flow (Sassa et al. 1997)

the valley deposits, in a dry condition, only very limited shear displacement occurred, and when the valley deposit were fully saturated, a large travel distance together with high speed motion occurred. The high pore-water pressure was measured, and the shear resistance was very small (about 45 kPa). This should be a

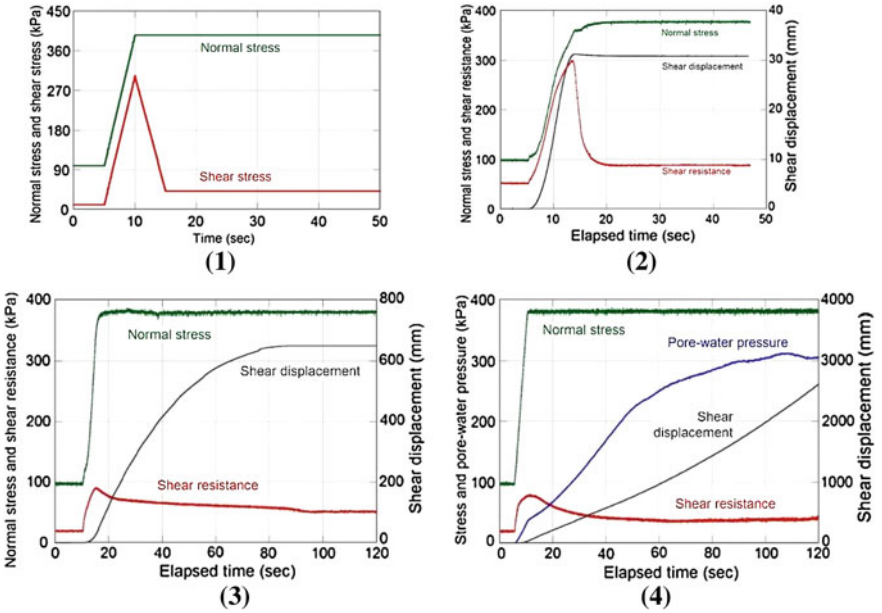

Fig. 15 Loaded stress signals (shown in graph 1) and results of the Donghekou landslide motion simulation test using sample B. Graph (2) shows results of dry condition, graph (3) shows results of unsaturated condition, graph (4) shows results of fully-saturated condition

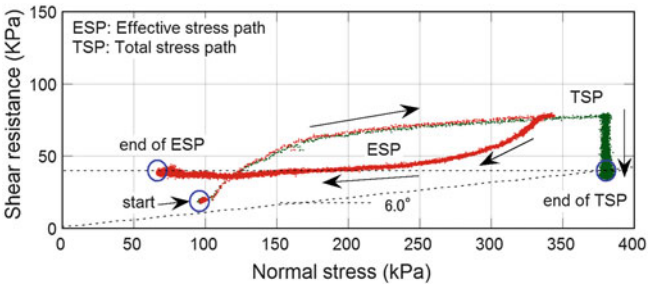

Fig. 16 Total stress path and effective stress path of the simulation test for fully-saturated sample B

possible reason for the long runout motion for more than 2 km-length of the Donghekou rockslide debris flow. Figure 16 shows the total stress path and effective stress path of the test with the fully-saturated soil sample. The apparent friction angle (the inclination of the line connecting the end of TSP and the original point) is only 5.4°, which means the landslide would keep moving until a position where the angle to the source area is smaller than this value.

As mentioned previously, the angle from the toe of the Donghekou landslide and the source area is about 11°. Considering the dissipated energy caused by the

impact of collision with each other, some parts may not be in a fully saturated condition, and this result is acceptable for explaining the actual situation. This test shows that the existence of the water is a very important factor for the rapid movement and long travel distance.

4 Conclusions and Suggestion for Land Use in the Reconstruction Process to Mitigate Landslide Disaster

Through field investigation of the long runout landslides triggered by the Wenchuan earthquake and experimental study on the Donghekou rockslide—debris flow in particular, it was observed that the valley water and groundwater played key roles in the long runout and rapid landslide motion process during the great earthquake. Impacts and losses depended upon whether the landslide occurred but abruptly stopped, and whether the landslides moved for long distance with high speed, a situation which seemed to kill large numbers of people. It would be useful if more earthquake-induced landslide case studies using methods outlined in this paper were to be analyzed. We could then be closer to concluding whether there are similar and/or additional variables that affect rate of movement, extent of movement and their relationships to the rates of deaths and damage.

For the purpose of landslide disaster mitigation during earthquake, we strongly suggest that:

(a) Avoid locating villages or other structures in the landslide motion path, because the same event or very similar, will most likely occur in the future;
(b) Avoid locating villages and people on landslides even if they look stable, because they will most likely deform or fail easily with the triggering action of seismic activity;
(c) Caution should be exercised because of the possibility of landslide and debris flows occurring during the reconstruction activities, as well as for long-term, future disaster mitigation. We found that some new villages were located in debris flow-prone areas such as the case with the Qian-tribe minority village in Beichuan County, and this could possibly be of future concern. Average people as well as community and emergency planners would benefit greatly from education about the landslide vulnerability of their areas.

Acknowledgments The field investigation and sampling was partially supported by Chinese State Key fundamental Research Program project (2008 CB425802, representative: P. Cui). The authors deeply appreciated the discussions with Prof. XY Wu of Southwest Jiaotong University, China, Prof. K. Konagai of University of Tokyo, Prof. S. Tsuchiya of Shizuoka University, Japan in the field investigation. The ring shear tests were conducted when the first author worked in Disaster Prevention Research Institute of Kyoto University, Japan.

References

Cui P, Zhu YY, Han YS, Chen XQ, Zhuang JQ (2009) The 12 May Wenchuan earthquake-induced landslide lakes: distribution and preliminary risk evaluation. Landslides 6(3):209–223

Sassa K (1997) A new intelligent-type dynamic-loading ring-shear apparatus. Landslide News 10:33

Sassa K, Fukuoka H, Wang FW (1997) Mechanism and risk assessment of landslide-triggered-debris flows: lesson from the 1996.12.6 Otari debris flow disaster, Nagano, Japan. In: Cruden DM, Fell R (eds) Landslide risk assessment. Proceedings of the international workshop on landslide risk assessment. Honolulu, 19–21 Febr, pp 347–356

Wang ZF (2008) A preliminary report on the Great Wenchuan Earthquake. Earthq Eng Eng Vib 7(2):225–234

Sassa K, Fukuoka H, Wang G, Ishikawa H (2004) Undrained dynamic-loading ring-shear apparatus and its application to landslide dynamics. Landslides 1(1):9−17

Wang FW, Sassa K, Fukuoka H (2000) Geotechnical simulation test for the Nikawa landslide induced by 1995.1.17 Hyogoken-Nambu earthquake. Soils Found 40(1):35–46

Wang FW, Cheng QG, Highland L, Miyajima M, Wang HB, Yan CG (2009) Preliminary investigations of some large-scale landslides triggered by the 2008 Sichuan earthquake. Landslides 6(1):47–54

Yin YP, Wang FW, Sun P (2009) Landslide hazards triggered by the 2008 Wenchuan earthquake, Sichuan, China. Landslides 6(2):139–152

Part II
Specified Studies

Strong Ground Motion Prediction for Scenario Earthquakes

Masato Tsurugi

Abstract Strong ground motion is the most basic information to estimate seismic damage and examine the earthquake-resisting capacity of buildings. It's very important to predict strong ground motions, estimate seismic damage and conduct earthquake countermeasures for a future large earthquake. Firstly, three basic components of seismic motions, i.e., source, path and site characteristics are mentioned to understand essence of method for strong ground motion prediction. Secondary, methods of strong ground motion prediction based on fault rupture propagation model such as empirical Green's function method and stochastic Green's function method are explained. In empirical Green's function method, seismic motion from large earthquake is synthesized using that from small earthquake according to scaling laws of spatial and temporal growth of fault rupture. These are scaling laws of fault parameters for small and large earthquakes and the omega-squared source spectra. When there is no suitable observed record as Green's function, stochastic Green's function method can be adopted to predict strong ground motions. Instead of observed seismic motions from small earthquake, the method uses simulated motions as Green's function and synthesizes seismic motions from a large earthquake using the same concepts of empirical Green's function method. Thirdly, recipe for predicting strong ground motion from future large earthquakes is introduced. The recipe is summarized standard methodology for prediction of strong ground motions. The broadband strong ground motions can be predicted accurately by applying the recipe. Moreover, theoretical and empirical methods to evaluate path and site characteristics are explained. Finally, the stochastic Green's function method is demonstrated on example of strong ground motion prediction for existing active fault in Iran.

M. Tsurugi (✉)
Geo-Research Institute, 4-3-2 Itachibori, Nishi-ku, Osaka 550-0012, Japan
e-mail: turugi@geor.or.jp

F. Wang et al. (eds.), *Progress of Geo-Disaster Mitigation Technology in Asia*, Environmental Science and Engineering, DOI: 10.1007/978-3-642-29107-4_10,

Keywords Strong ground motion prediction · Source–path–site characteristics · Empirical Green's function method · Stochastic Green's function method · Recipe for predicting strong ground motions

1 Introduction

Strong ground motion is the most basic information to estimate seismic damages and examine earthquake-resisting capacity of buildings. It's very important to predict strong ground motions, estimate seismic damage and conduct earthquake countermeasures for a future large earthquake. There are three methods to predict strong ground motions. The first method is empirical method, such as attenuation equation of peak ground acceleration, peak ground velocity, and response spectrum. The second method is semi-empirical method such as empirical Green's function method and stochastic Green's function method. The third method is theoretical method such as finite different method and finite element method. The empirical method is simple and useful to know average aspect of strong motions. But specific source, path, and specific site characteristics cannot be considered. The theoretical method is based on theoretical fault mechanism and wave propagation theory. However, this method can be applied for only long period seismic motion (about >1 s), because short period seismic motions are affected by randomness of propagation path route and site condition. On the other hand, in the semi-empirical method, specific source, path and site characteristics can be considered and strong ground motion in important frequency range for engineering use can be predicted accurately. Then, the semi-empirical methods of strong ground motion prediction and example of its application for existent active fault are presented in this chapter.

Firstly, three basic components of seismic motions, i.e., source, path and site characteristics are mentioned to understand essence of method for strong ground motion prediction. Secondary, methods of strong ground motion prediction based on fault rupture propagation model such as empirical Green's function method and stochastic Green's function method are explained. Thirdly, recipe for predicting strong ground motion from future large earthquakes is introduced. Moreover, theoretical and empirical methods to evaluate path and site characteristics are explained. Finally, the stochastic Green's function method is demonstrated on example of strong ground motion prediction for existing active fault in Iran.

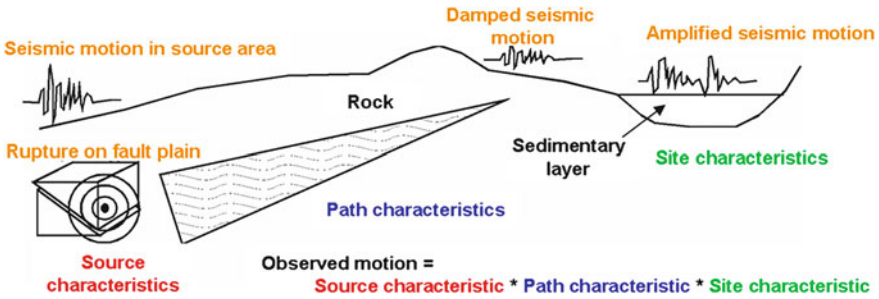

Fig. 1 Source-path-site characteristics (the *asterisk* indicates convolution)

2 Three Basic Components of Seismic Motions (Source, Path, and Site Characteristics)

Seismic motions are composed by three characteristics i.e., source, path, and site characteristics (Fig. 1). Source characteristics is joint effect of various parameters, such as source fault length, seismic moment, non-uniformity of slip distribution and location of rupture starting point etc. Path characteristics are attenuation characteristics on propagation path route, i.e., geometrical spreading and internal damping. Site characteristics are general term of various effects of sedimentary layers to seismic motions such as amplification of seismic motion and extension of duration, or generation of surface waves etc.

3 Methods of Strong Ground Motion Prediction

Attenuation equation of peak ground acceleration, peak ground velocity, duration, and response spectra have been used for strong ground motion prediction widely. The method is simple and useful to know average aspect of strong motions. However, specific source, path, and site characteristics cannot be considered. Other methods, which can consider specific source, path, and site characteristics, such as empirical Green's function method (Hartzell 1978; Irikura 1986; Irikura et al. 1997) and stochastic Green's function method (Boore 1983; Kamae et al. 1991) are introduced in this chapter.

3.1 Empirical Green's Function Method

If two conditions below are satisfied, empirical Green's function method can be used for predicting of strong motions.

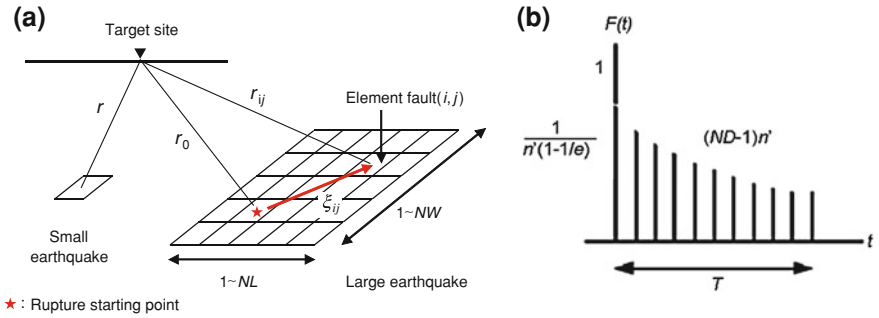

Fig. 2 Schematic illustration of the empirical Green's function method. **a** Faults of large earthquake and small earthquake; **b** filtering function with an exponentially decay function

1. A small earthquake occurred in same source area and by same source mechanism with a target large earthquake.
2. Seismic motion from the small earthquake observed at target site.

In this case it is assumed that observed seismic motions from small earthquake include path characteristics and site amplification which are the same with those from target large earthquake. Therefore, strong ground motion from a large earthquake can be simulated by considering only differences of source characteristics between small and large earthquake. Main differences of source characteristics between small and large earthquake are rupture area and slip displacement, which are small and large respectively. In empirical Green's function method seismic motion of a large earthquake, $U(t)$ is calculated from that of a small earthquake, $u(t)$ by Eqs. (1)–(3). The concept of the method and the variables of the equations are shown in Fig. 2. Seismic motion from large earthquake is synthesized using that from small earthquake according to scaling laws of spatial and temporal growth of fault rupture. These are scaling laws of fault parameters for small and large earthquakes (Kanamori and Anderson 1975) and the omega-squared source spectra (Aki 1967).

$$U(t) = \sum_{i=1}^{NL} \sum_{j=1}^{NW} \frac{r}{r_{ij}} F(t) * \{C.u(t)\} \tag{1}$$

$$F(t) = \delta(t - t_{ij}) + \frac{1}{n'\left(1 - \frac{1}{e}\right)} \sum_{k=1}^{(ND-1)n'} \cdot \left[\frac{1}{e^{\frac{k-1}{(ND-1)n'}}} \delta\left\{ t - t_{ij} - \frac{(k-1)T}{(ND-1)n'} \right\} \right] \tag{2}$$

$$t_{ij} = \frac{(r_{ij} - r_0)}{V_s} + \frac{\xi_{ij}}{V_R} \tag{3}$$

where, NL, NW, and ND are numbers of subdivisions of fault length, fault width, and slip on fault plain, obtained by Eqs. (4) and (5). NL and NW are determined by dividing a target earthquake's fault to almost square shape subfaults. C is ratio of

stress drops between large and small earthquakes, and the asterisk indicates convolution. $F(t)$ is filtering function (correction function) to adjust difference in slip velocity time functions between large and small earthquakes. The shape of $F(t)$ is shown in Fig. 2b. V_s and V_r are S-wave velocity near source area and rupture velocity on fault plain, respectively. T is rise time for large earthquake, and defined as duration of filtering function $F(t)$ (Fig. 2b). It corresponds to the duration of slip velocity time function on subfault. Parameter n' is an appropriate integer to weaken artificial periodicity of N, and to adjust interval of the tick to the sampling rate. ξ_{ij} is distance from rupture starting point to center of subfault (i, j). r, r_0, and r_{ij} are distance from hypocenter of small earthquake, rupture starting point, and center of subfault (i, j) to target site, respectively.

$$\frac{M_o^L}{M_o^S} = CN^3 = C(NL \times NW \times ND) \tag{4}$$

$$ND = \sqrt{NL \times NW} \tag{5}$$

where, M_o^L and M_o^S are seismic moment of target large earthquake and small earthquake. Kamae and Irikura (1998) applied this method to simulate seismic motions during the 1995 Kobe earthquake, Japan. The effectiveness of the method is confirmed by comparing simulated motions to observed ones (Fig. 3).

3.2 Stochastic Green's Function Method

It's very rare case to satisfy the two basic conditions of the empirical Green's function method above. When there is no suitable observed record as Green's function, the stochastic Green's function method (Kamae et al. 1991) can be adopted to predict strong ground motions. Instead of observed seismic motions from small earthquake, the method uses simulated motions (Boore 1983) as Green's function and synthesizes seismic motions from a large earthquake using the same concepts of empirical Green's function method. Sato et al. (2001) applied this method to simulate seismic motions during the 2000 Tottori-Ken Seibu earthquake, Japan. The effectiveness of the method is confirmed by comparing simulated motions to observed ones (Fig. 4).

4 Recipe for Predicting Strong Ground Motions

Recipe is summarized standard methodology for prediction of strong ground motions from future large earthquakes (Irikura et al. 2004; Irikura and Kurahashi 2008; Headquarters for Earthquake Research Promotion directed by Ministry of Education, Culture, Sports, Science, and Technology 2008) and composed from four main items shown below.

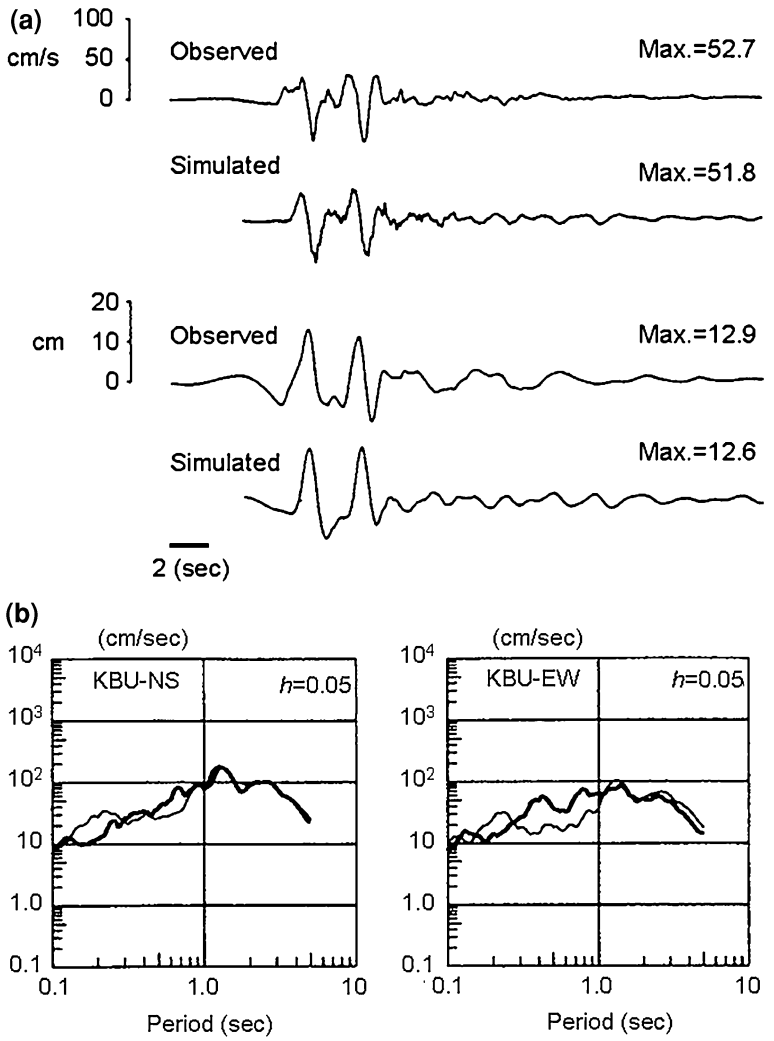

Fig. 3 Comparison of simulated motions calculated by empirical Green's function method and observed one at KBU during the 1995 Kobe earthquake, Japan (Kamae and Irikura 1998). **a** Velocity (*upper*) and displacement (*lower*) waveform; **b** velocity response spectra ($h = 5$ %) (*thick line*−observed, *thin line*−simulated)

1. Characterization of source
2. Modelling of ground structure
3. Strong ground motion simulation method
4. Verification of predicted ground motion

The broadband (0.1–10 s) strong ground motions can be predicted accurately by applying the recipe. For predicting strong ground motions, two sets of source

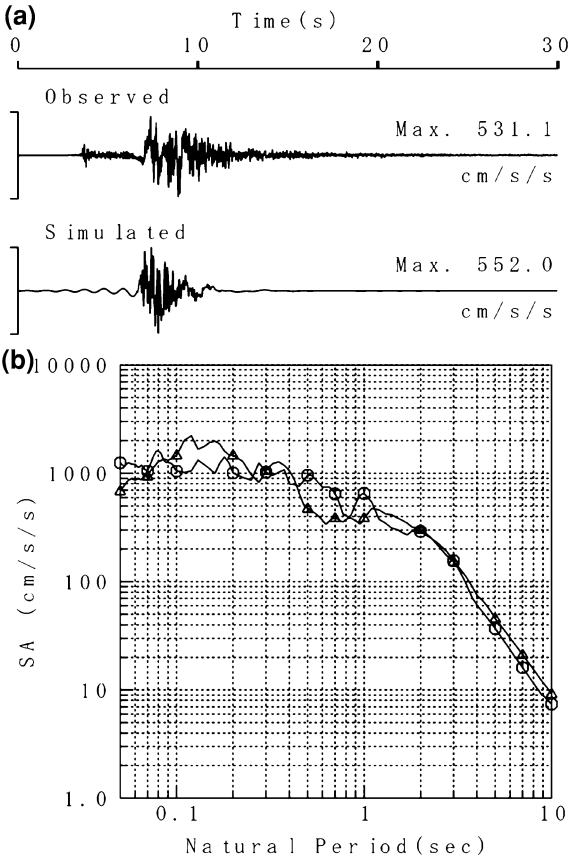

Fig. 4 Comparison of simulated motions calculated by the stochastic Green's function method and observed one at Kasyo dam during the 2000 Tottori-Ken Seibu earthquake, Japan (Sato et al. 2001). **a** Acceleration waveform (*upper*−observed, *lower*−simulated); **b** acceleration response spectra ($h = 5$ %) (*open circle*−observed, *open triangle*−simulated)

parameters, outer and inner fault parameters, are needed. Settings of outer and inner fault parameters for inland crustal earthquakes are described in this chapter.

4.1 The Outer Fault Parameters

The outer fault parameters are parameters characterizing the entire source area such as total rupture area and seismic moment.

Source location, strike angle, source segment, and dip angle

These parameters are given from geo-morphological and geological survey of active faults.

Fault length, L (km)

Fault length is given by fault location.

Fault width, W (km) and fault area, S (km^2)

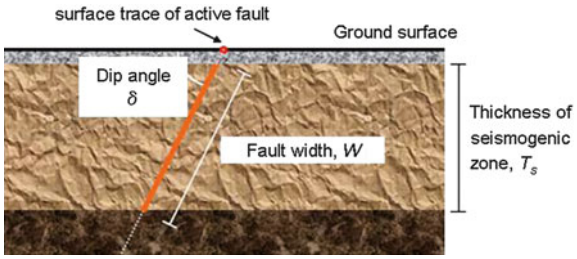

Fig. 5 Relationship between thickness of seismogenic zone and fault width

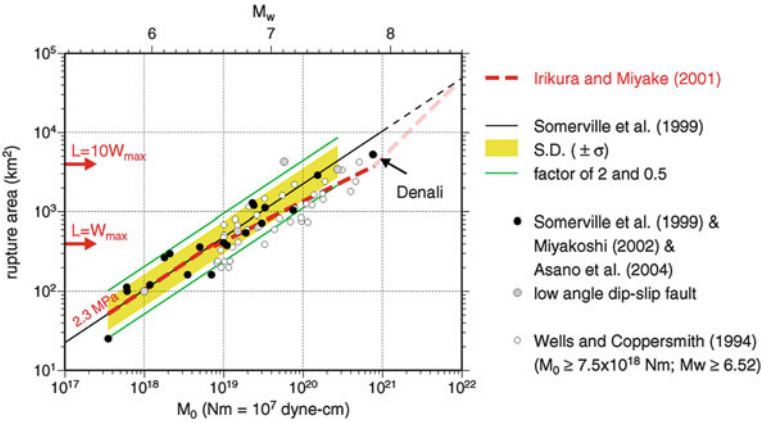

Fig. 6 Empirical relationship between fault rupture area, S and seismic moment, M_o

Fault width is estimated from thickness of seismogenic zone and dip angle such as shown in Fig. 5 and below and then fault area ($S = LW$) is calculated.

$$W = L \quad (\text{For} \quad L < W_{\max}) \tag{6}$$

$$W = W_{\max} \quad (\text{For} \quad L > W_{\max}) \tag{7}$$

$$W_{\max} = T_s / \sin\delta \tag{8}$$

$$T_s = H_d - H_s \tag{9}$$

where, T_s is thickness of seismogenic zone (km) and δ is dip angle (degree). H_d and H_s are depths of lower and upper boundaries of seismogenic zone (km).

Total seismic moment, M_o $(\mathrm{N} \cdot \mathrm{m})$

Total seismic moment is given from the empirical scaling relation, M_o $(\mathrm{N} \cdot \mathrm{m})$ versus total fault area, S (km^2) such as shown in Fig. 6 and below (Somerville et al. 1999; Irikura and Miyake 2001).

$$M_o = (S/2.23 \times 10^{15})^{3/2} \times 10^{-7} \quad (\text{For } < 7.5 \times 10^{18}(\text{N} \cdot \text{m})) \tag{10}$$

$$M_o = (S/4.24 \times 10^{11})^{2} \times 10^{-7} \quad (\text{For } \geq 7.5 \times 10^{18}(\text{N} \cdot \text{m})) \tag{11}$$

Average stress drop, $\Delta\sigma$ (MPa)
Average stress drop is estimated by the Eq. (12).

$$M_o = \frac{16}{7 \times \pi^{3/2}} \times \Delta\sigma \times S^{3/2} \tag{12}$$

Average slip on fault plain, D (m)
Average slip is estimated by the Eq. (13).

$$M_o = \mu D S \tag{13}$$

where, μ is rigidity (N/m^2) ($\mu = \rho\beta^2$), ρ is density (kg/m^3), β is S-wave velocity (km/s).

4.2 The Inner Fault Parameters

Inner fault parameters define slip heterogeneity inside the fault, and have much more influence on strong ground motions than the outer fault parameters.
Combined asperity area, S_a (km^2)
Fault slip displacement on asperity area is greater than that in other area; more seismic energy is generated from asperity area. Combined asperity area is estimated from acceleration source spectra level based on empirical relation (14):

$$A = 2.46 \times 10^{17} \times (M_o \times 10^7)^{1/3} \tag{14}$$

$$r = \frac{7\pi}{4} \times \frac{M_o}{A \times R} \times \beta^2 \tag{15}$$

$$S = \pi R^2 \tag{16}$$

$$S_a = \pi r^2 \tag{17}$$

where, A is acceleration source spectra level ($\text{N} \cdot \text{m/s}^2$). R and r are equivalent radius of total fault area and asperity area (km).
Stress drop on asperity, $\Delta\sigma_a$ (MPa)
Stress drop on asperity area is given by the Eq. (18).

$$\Delta\sigma_a = (S/S_a)\Delta\sigma \tag{18}$$

Slip on asperity area and off-asperity area, D_a, D_b (m)
Slip on asperity area, D_a, and slip on off-asperity area (background), D_b, are estimated by the equations below.

$$D_a = 2D \tag{19}$$

$$M_{oa} = \mu D_a S_a \tag{20}$$

$$M_{ob} = M_o - M_{oa} \tag{21}$$

$$D_b = M_{ob}/(\mu S_b) \tag{22}$$

where, M_{oa} and M_{ob} are seismic moment on asperity and off-asperity area (N · m). S_a and S_b are area of asperity and off-asperity (km^2).

5 Path and Site Characteristics

Path characteristics are attenuation characteristics on propagation path route, i.e., geometrical spreading and internal damping. Internal damping (Q factor) is estimated by empirical methods using observed seismic records such as spectral inversion method (Iwata and Irikura 1988) and double spectral ratio method (Matsuzawa et al. 1984; Chun et al. 1987). Q factor is usually modelled as a function of frequency such as Eq. (23).

$$Q(f) = Q_0 \times f^{\alpha} \tag{23}$$

Site characteristics are general term of various effects of sedimentary layers on seismic motions such as amplification of seismic motion and extension of duration, and generation of surface wave etc. Site amplification factor can be calculated theoretically and empirically. The multiple reflection theory of one dimensional ground structure (Schnabel et al. 1972; Sugito 1993) is one of the theoretical approaches. Spectral inversion method (Iwata and Irikura 1988) and the method of removing source and path characteristics from observed records (Tsurugi et al. 2000) are some methods of the empirical approaches.

6 Example of Strong Ground Motion Prediction

Application of the strong ground motion prediction method for future large earthquake is demonstrated on example from Iran. The target site is historical masonry building, Bazaar (BZR), in Tabriz, Northwest of Iran, and target fault is North Tabriz fault (Fig. 7). Because there is no observed record from small earthquake occurred in target fault, North Tabriz fault, the stochastic Green's function method is adopted for the prediction.

6.1 Source Characteristics

The target fault is North Tabriz fault, its whole length is over 200 km. The location of North Tabriz fault is decided by an active fault map (Hessami et al. 2003). The fault closest distance to BZR is about 2 km. The fault is divided into six segments

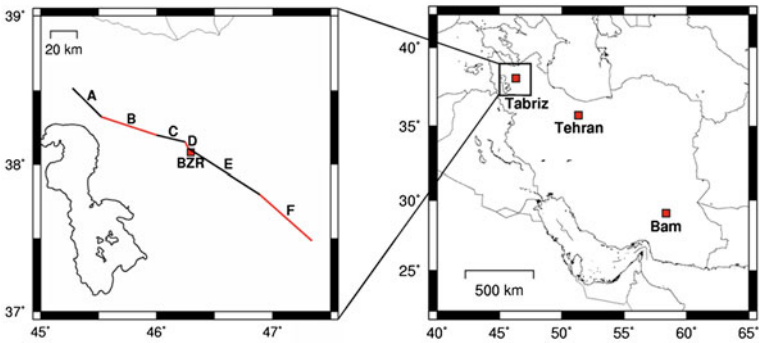

Fig. 7 Location of target fault and target site (BZR) for Tabriz, Iran

Table 1 General source parameters of each scenario

Scenario No.	No. 1	No. 2	No. 3	No. 4	No. 5	No. 6
Rupture area	Segment C	Segment E	Segment C Segment D	Segment D Segment E	Segment C Segment D Segment E	All segment
Length (km)	22	64	28	70	92	218
Width (km)	15	15	15	15	15	15
Area (km^2)	330	960	420	1,050	1,380	3,270
Seismic moment ($N \cdot m$)	5.69×10^{18}	5.13×10^{19}	9.81×10^{18}	6.13×10^{19}	6.70×10^{19}	1.36×10^{20}
Moment magnitude	6.4	7.1	6.6	7.1	7.2	7.4

(from segment A to segment F) based on the changes of strike angle. The author made six rupture scenarios. Two scenarios are for two nearest segments ruptured individually, and four scenarios are for case when a few segments ruptured simultaneously. The rupture area and the other parameters of each scenario are shown in Table 1 and Fig. 8. Moment magnitudes of each scenario are in the range from 6.4 to 7.8. The outer and inner fault parameters are given according to the recipe for predicting strong ground motions above. For example, the fault parameters of scenario No. 2 are shown in Table 2. Fig. 9 shows the location of asperities and rupture starting points of the scenario No. 2. The asperity area is deployed on fault plane in the nearest location to the target site, because this location is considered as most critical case for the target site. Several points are selected as the rupture starting points and then parametric study is done. For example, eight points are selected as rupture starting points in scenario No. 2 (from R1 to R8).

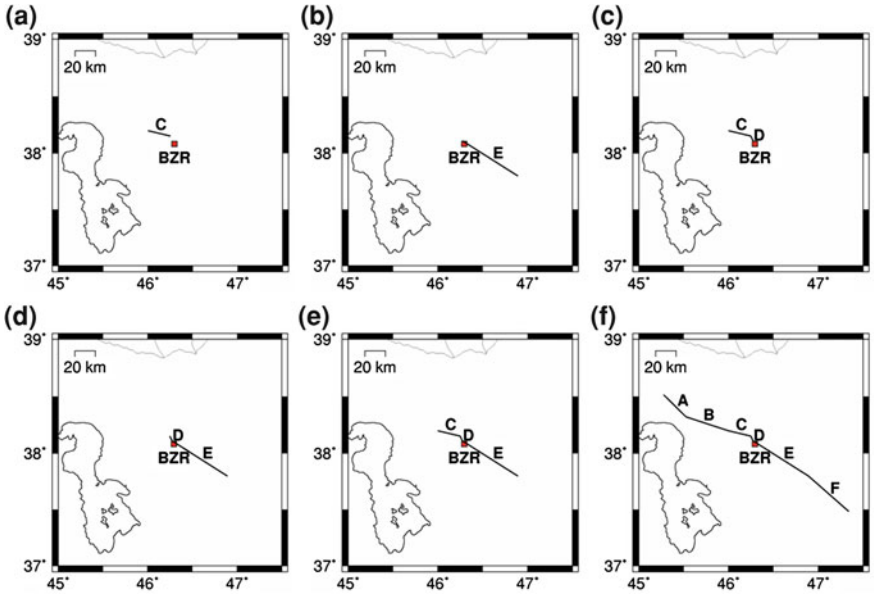

Fig. 8 Fault ruptures scenarios. **a** Scenario No. 1, **b** scenario No. 2, **c** scenario No. 3, **d** scenario No. 4, **e** scenario No. 5, **f** scenario No. 6

6.2 Path, Site, and Other Characteristics

Path characteristic is evaluated by spectral inversion method (Iwata and Irikura 1988) using observed records of four small earthquakes (Table 3) at three sites around Tabriz. Q-factor is obtained as a function of frequency,

$$Q(f) = 17.4 \times f^{1.00} \tag{24}$$

where, f is frequency.

Site amplification factor is evaluated by one dimensional seismic response analysis (Schnabel et al. 1972; Sugito 1993). Ground structure model is constructed by receiver function method (Petukhin et al. 2011) and the result of PS logging test and cyclic tri-axial tests (Table 4).

High cut filter, $P(f)$, due to cut-off frequency, $f_{\max}$, (Tsurugi et al. 2008) is adopted in the prediction.

$$P(f) = \frac{1}{\sqrt{1 + \left(\frac{f}{6.5}\right)^{2\times 0.90}}} \tag{25}$$

Table 2 Outer and inner fault parameters of the scenario No. 2

Outer fault parameters		
Upper depth (km)		2
Lower depth (km)		17
Fault length (km)		64
Fault width (km)		15
Fault area (km^2)		960
Strike angle (°)		122.4
Dip angle (°)		90
Rake angle (°)		172
Seismic moment ($N \cdot m$)		5.13×10^{19}
Moment magnitude		7.1
Average slip (cm)		161.5
Average stress drop (MPa)		4.2
Inner fault parameters		
Asperity area		
Number	2	
Total area (km^2)	318	
Asperity area ratio (%)	33.1	
	Asperity 1	Asperity 2
Area (km^2)	210	108
Moment ($N \cdot m$)	2.49×10^{19}	9.20×10^{18}
Slip (cm)	359.0	257.5
Stress drop (MPa)	12.7	12.7
Rise time (s)	2.08	1.79
Off-asperity area		
Area (km^2)	642	
Moment ($N \cdot m$)	1.71×10^{19}	
Slip (cm)	80.7	
Stress drop (MPa)	2.5	
Rise time (s)	2.98	

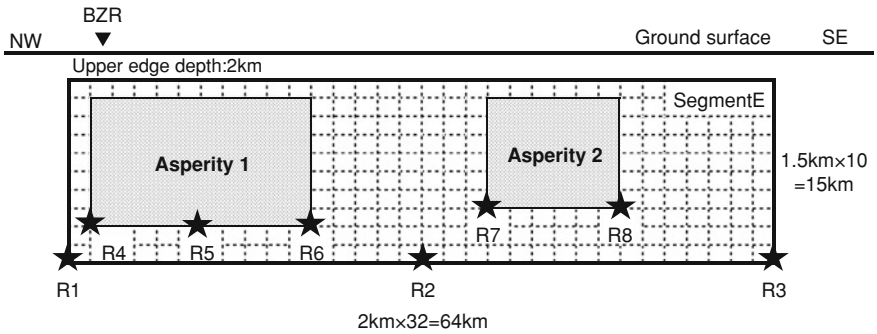

Fig. 9 Location of asperities and rupture starting points (*star*) of the scenario No. 2

Table 3 Observed records used in spectral inversion analysis

No.	Origin time	Epicenter		Depth (km)	Magnitude
		Latitude	Longitude		
1	2007.09.16 05:20:01	38.100	46.360	24	4.1
2	2007.12.01 18:22:17	38.150	46.410	22	4.2
3	2007.12.01 18:45:11	38.130	46.430	22	4.8
4	2007.12.02 10:00:02	38.090	46.430	16	4.1

Lat.: Latitude (degree), Lon.: Longitude (degree)

Table 4 Ground structure model

	Layer No.	Upper depth (m)	Thickness (m)	V_S (m/s)	ρ (g/cm^3)	
Shallow structure	1	0	2	222	1.5	From PS logging test
	2	2	1	238	1.5	
	3	3	2	238	1.7	
	4	5	2	278	1.7	
	5	7	2	400	1.7	
	6	9	2	229	1.7	
	7	11	1	173	1.7	
	8	12	1	278	1.7	
	9	13	2	278	1.7	
	10	15	2	333	1.8	
	11	17	2	327	1.8	
	12	19	4	305	1.8	
	13	23	3	594	1.9	
	14	26	3	594	1.9	
	15	29	2	784	1.9	
	16	31	2	784	1.9	
	17	33	72	784	1.9	
Deep structure	18	105	155	1,040	2.1	From receiver function method
	19	260	390	1,420	2.2	
	20	650	–	3,500	2.7	

6.3 Results

Predicted acceleration waveform and acceleration response spectra (damping 5 %) for the fault rupture scenario No. 2 are shown in Fig. 10. The predicted peak ground accelerations of EW component for scenario No. 2 are in the range from 400 to 850 cm/s/s. The peak ground velocities are in the range from 37 to 81 cm/s. The acceleration response spectra in short period range ($T < 1$ s) are about 2,000 cm/s/s for one case, and in the range from 600 to 1,200 cm/s/s for other cases.

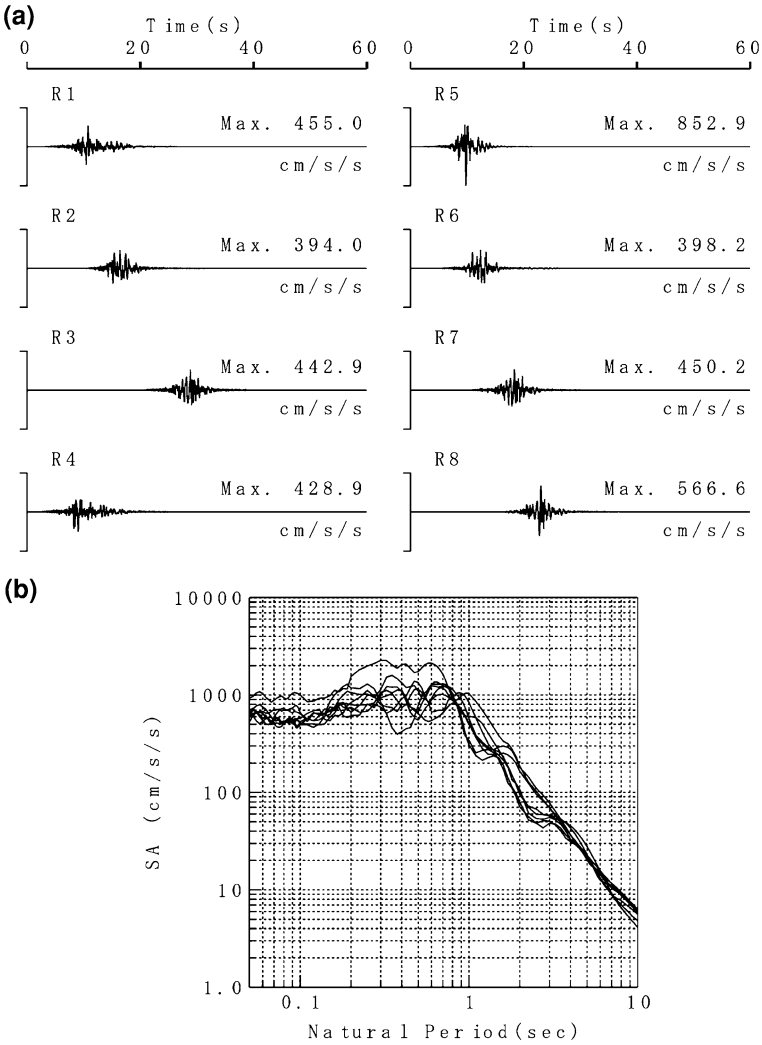

Fig. 10 Predicted motions for scenario No. 2 (EW component). **a** acceleration waveform; **b** acceleration response spectra ($h = 5\ \%$)

7 Conclusions

Strong ground motion is the most basic information to estimate seismic damages and examine earthquake-resisting capacity of buildings. It's very important to predict strong ground motions, estimate seismic damage and conduct earthquake countermeasures for a future large earthquake. Methods of strong ground motion prediction and example of its application for existing active fault are presented in this chapter.

Firstly, three basic components of seismic motions, i.e., source, path and site characteristics are mentioned to understand essence of method for strong ground motion prediction. Secondary, methods of strong ground motion prediction based on fault rupture propagation model such as empirical Green's function method and stochastic Green's function method are explained. Thirdly, recipe for predicting strong ground motion from future large earthquakes is introduced. Moreover, theoretical and empirical methods to evaluate path and site characteristics are explained. Finally, the stochastic Green's function method is demonstrated on example of strong ground motion prediction for existing active fault in Iran.

I hope this chapter will contribute for protecting life and property and improving earthquake-resisting capacity of buildings in Asia.

Acknowledgments This chapter is presented with reference to some chapters written by emeritus Prof. Irikura in Kyoto University. I express gratitude to Prof. Irikura. The clarity and completeness of this chapter was improved by comment from Prof. Kagawa in Tottori University and Dr. Petukhin in Geo-Research Institute. The project for predicting strong ground motions from future large earthquake at Tabriz Bazaar was supported in part by the grant-in aid for Science Research from the Ministry of Education, Culture, Sports, Science and Technology, Japan (No. 21254001). Prof. Miyajima in Kanazawa University and Dr. Fallahi in Azerbaijan University of Shahid Madani lead the project energetically. I'm grateful to Prof. Miyajima and Dr. Fallahi. Ground structure model at Tabriz bazaar constructed by Dr. Yoshida in Fukui National College of Technology, and Dr. Solitani Jigheh in Azerbaijan University of Tarbiat Moallem. Generic mapping tool by Wessel and Smith (1998) was used for making several figures.

References

Aki K (1967) Scaling law of seismic spectrum. J Geophys Res 72:1217–1231

Boore DM (1983) Stochastic simulation of high-frequency ground motion based on seismological models of the radiated spectra. Bull Seismol Soc Am 73:1865–1894

Chun KY, West GF, Kokoski RJ, Samson C (1987) A novel technique for measuring L_g attenuation: results from Eastern Canada between 1 to 10 Hz. Bull Seismol Soc Am 77:398–419

Hessami K, Jamali F, Tabassi H (2003) Major active faults of Iran. International institute of earthquake engineering and seismology

Hartzell SH (1978) Earthquake aftershocks as Green's functions. Geophys Res Lett 5:1–4

Headquarters for Earthquake Research Promotion (Director: Ministry of Education, Culture, Sports, Science, and Technology) (2008) Strong ground motion prediction method ("Recipe") for earthquakes with specified source faults. http://www.jishin.go.jp/main/index-e.html (in Japanese)

Irikura K (1986) Prediction of strong acceleration motion using empirical Green's function. Proceedings of the 7th Japan earthquake engineering symposium, pp 151–156

Irikura K, Kagawa T, Sekiguchi H (1997) Revision of the empirical Green's function method by Irikura (1986). Programme and abstracts, seismological society of Japan, 2, B25 (In Japanese)

Irikura K, Miyake H (2001) Prediction of strong ground motions for scenario earthquakes. J Geogr 110:849–875 (In Japanese with English abstract)

Irikura K, Miyake H, Iwata T, Kamae K, Kawabe H, Dalguer LA (2004) Recipe for predicting strong ground motions from future large earthquakes. Proceedings of the 13th world conference on earthquake engineering, Paper No. 1371, Vancouver, Canada

Irikura K, Kurahashi S (2008) Validity of strong motion prediction recipe for inland-crust earthquakes. Proceedings of the 14th world conference on earthquake engineering, Beijing, China

Iwata T, Irikura K (1988) Source parameters of the 1983 Japan sea earthquake sequence. J Phys Earth 36:155–184

Kamae K, Irikura K, Fukuchi Y (1991) Prediction of strong ground motion based on scaling law of earthquake−by stochastic synthesis method. J Str Constr Eng (Trans AIJ) 430:1–9 (In Japanese with English abstract)

Kamae K, Irikura K (1998) Source model of the 1995 Hyogo-Ken Nambu earthquake and simulation of near source ground motion. Bull Seismol Soc Am 88:400–412

Kanamori H, Anderson DL (1975) Theoretical basis of some empirical relations in seismology. Bull Seismol Soc Am 65:1073–1095

Matsuzawa T, Hasegawa A, Takagi A (1984) Estimation of Q-factor by double spectral ratio method. Proceedings of the annual meeting of seismological society of Japan, 2:C75, 247 (In Japanese)

Petukhin A, Tsurugi M, Abdolhossein F, Miyajima M (2011) Receiver function method for estimation of the shallow structure: example for Tabriz, Iran, Japan Geoscience Union Meeting 2012, HDS004-P09

Somerville PG, Irikura K, Graves R, Sawada S, Wald D, Abrahamson N, Iwasaki Y, Kagawa T, Smith N, Kowada A (1999) Characterizing crustal earthquake slip models for the prediction of strong ground motion. Seismol Res Lett 70:59–80

Sato N, Yonezaki F, Harita K, Tsurugi M, Kagawa T, Toki K (2001) Strong motion simulation at dam site during the 2000 Tottori-Ken Seibu earthquake. Proceedings of the 26th JSCE earthquake engineering symposium, Sapporo, pp 341–344 (in Japanese)

Schnabel PB, Lysmer J, Seed HG (1972) SHAKE a computer program for earthquake response analysis of horizontally layered sites. EERC 72–12

Sugito M (1993) Frequency-dependent equivalent strain for earthquake response analysis of soft ground. Proceedings of the 3rd Republic of China and Japan joint seminar on natural hazards mitigation, Tainan, pp 409–422

Tsurugi M, Tai M, Kowada A, Tatsumi Y, Irikura K (2000) Estimation of empirical site amplification effects using observed records. Proceedings of the 12th world conference on earthquake engineering, 1243

Tsurugi M, Kagawa T, Irikura K (2008) Study on high-cut frequency characteristics of ground motions for inland crustal earthquakes in Japan. Proceedings of the 14th world conference on earthquake engineering, Beijing, 02-0036

Wessel P, Smith WHF (1998) New, improved version of generic mapping tools released. Am Geophys Un, EOS

Stability Analysis of Loess Slopes Based on Reliability Concepts

Ping Li, Yanan Zheng and Tonglu Li

Abstract In engineering designs for cut slopes excavated in loess areas during highway construction, knowledge of the strength of the loess, including cohesion and friction angle, are essential, but these parameters are often very uncertain. Thus, the slope design needs to be based on field data rather than calculation. Field survey data on natural loess slopes could be used as a basis for cut slope design. This paper defines the natural limit state slope, and investigates the natural slopes in the field in Shaanxi province of China. Based on critical slopes, the reliability of loess slopes is calculated by the Monte Carlo method for various combination of loess strength parameters. The criterion of probability of failure is suggested for the loess slope design. Probability theory can be used to deal with the variation of soil properties in the loess slope design.

Keywords Loess · Slope · Reliability · Probability

1 Introduction

1.1 Loess Properties and Their Influence on Highway Construction

Loess is a kind of loose aeolian deposit largely found in arid and semi-arid areas. In China, loess and loess-like soil are distributed over an area of about 64×10^4 km^2. Because of its aeolian origin, loess has characteristic properties such as a loose structure, high water sensitivity, collapsibility and well developed vertical joints.

P. Li (✉) · Y. Zheng · T. Li
Department of Geological Engineering, Chang'an University, 710054 Xi'an, China
e-mail: dcdgx08@chd.edu.cn

F. Wang et al. (eds.), *Progress of Geo-Disaster Mitigation Technology in Asia*, Environmental Science and Engineering, DOI: 10.1007/978-3-642-29107-4_11,

The skeletal structure of the loess is composed of coarse silt particles, which are cemented at grain contact points by clay and chemical materials, and the sediments generally have high porosity. As surficial water infiltrates, the clay and chemical cementation disintegrate quickly and the structure can collapse into the pores to cause collapsibility. The loose skeletal structure makes loess very susceptible to water and consequently, it is easily eroded. The Yellow River in China carries 1.6 billion tones of mud and sand away annually when it flows through the loess area. The gently inclined slope surfaces are more easily eroded than the steeply inclined slope surface because water can easily infiltrate in the former. There are many vertical joints in loess, especially on tops of the slopes. Water that seeps into the slopes along the fissures softens the loess, and decreases the shear strength to a large extent. Therefore, water, either through rainfall or irrigation, is the main factor leading to failure of loess slopes. Loess has large variability in the shear strength parameters which is related to water content and the original structure including the cement matrix. Groundwater level is so deep that most of the loess is unsaturated. The coefficients of variation (COV) for the strength parameters of unsaturated loess with variation in water content and original structure are high. The loess properties result in a fragmented topography cut by deep crisscrossed gullies and valleys. Three typical types of loess topography are recognized: loess plateaus; loess ridges; and loess domes.

New highways have been rapidly constructed in recent years in China. A 1,497 km long Expressway has been constructed in a loess area in Shaanxi province. Many cut slopes were excavated where the highway goes through loess gullies. For example, the Huanglin-Yan'an Expressway (Fig. 1), has cut slopes in 26 places along the 24 km highway between Gongjiayuan village and Xiaquangou village. Five of the cut slopes are 20–30 m high and 16 of them are higher than 30 m; the highest is up to 90 m. Except for bridges and tunnels, cut slopes occur along 75 % of the total length of the road. At present, specifications and manuals provide guidance just for the design of slopes lower than 30 m but not for higher slopes. Most cut slopes unload at the foot of the natural slopes, often inducing new landslides and reactivating old landslides. There have been numerous failures in loess cut slopes. Along the Tongchuan–Huanglin Expressway (Fig. 1), 22 old landslides were reactivated and eight new landslides were induced. An additional 130 million ¥RMB had to be invested to stabilize the landslides. Taking the experience of building the Tongchuan–Huanglin Expressway into account in the construction of the Huanglin-Yan'an Expressway, engineers paid more attention to surveys in the planning period, and tried to get rid of the old landslides. However, 18 landslides still occurred, most of them first-time slides. The design of loess cut slopes is consequently a major problem for highway construction in loess areas.

1.2 Loess Slope Design Conditions

Engineers have to consider three aspects in designing cut slopes in loess. The first is to take up the least area of land possible, which demands a steep cut slope.

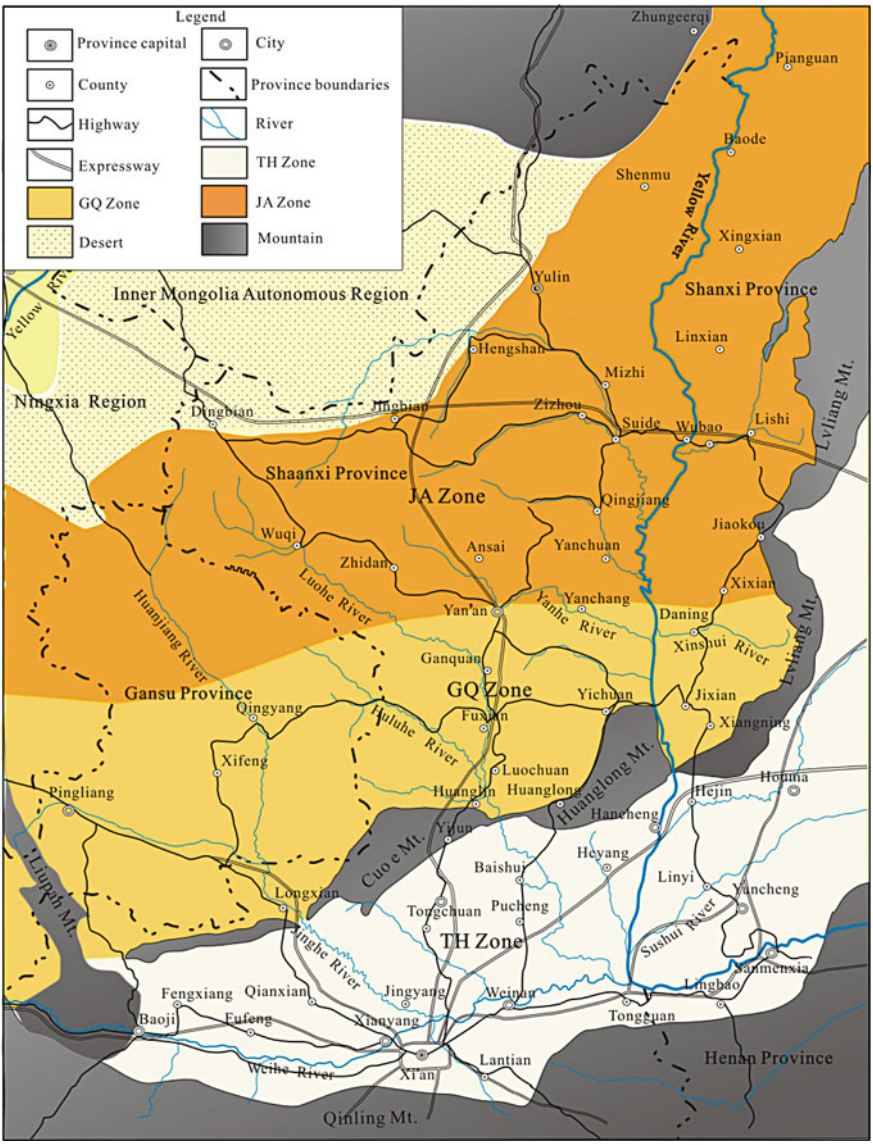

Fig. 1 Shaanxi loess zones and highways

The second however, is to keep the whole slope permanently stable which requires a gentle slope. The third is to avoid erosion to protect the slope surface and keep it stable.

Loess has sensitive structures and well developed vertical joints. Commonly a slope ratio of about 1:0.5 is used on slopes about 10 m high. The stable slope ratio varies with soil properties. Steep slopes are less prone to erosion by rainwater and

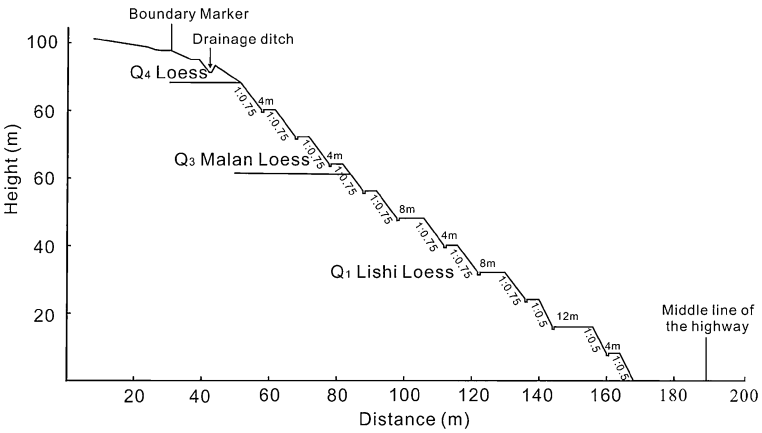

Fig. 2 High cut section in Huanglin-Yan'an Expressway

so protect the slope surface well, but high slopes must have a low slope ratio to ensure that the whole slope is stable. To solve the problem of both surface erosion and slope stability, engineers create wide steps with steep slopes between the steps. The cut slope in K170 + 900–989 on the Huanglin-Yan'an Expressway is an example that illustrates the case. This cut slope is 90 m high and 89 m long. The designed slope ratio [height (H)/horizontal distance (L)] is 1:1.69. The cut slope is stepped, with ten levels of steps and eleven slopes between the steps, as shown in Fig. 2. Each slope is 8 m high and three of them have a slope ratio of 1:0.5, while eight having a ratio of 1:0.75. The widest step is 12 m wide, with drainage ditches constructed on the inner sides of each step. This stepped design can deal with the contradiction of slope surface erosion and whole-of-slope stability well.

When observing natural loess slopes, it is obvious that the slopes on the eroded banks of the rivers are steeper than those on the depositional banks and most highways are constructed on the depositional banks. Engineers suggest a whole-slope ratio for their design slopes generally by referring to the slope on eroded river banks. Commonly the designed slope ratio is the same or a little gentler than the surveyed natural slope ratio. It is called the method of natural analogy (Li et al. 2009a, b). To give the recommended factor of safety of 1.2–1.3 (JTG D30 2004), the slope ratio calculated by Bishop's simplified method is lower by 10° than that of a similar natural slope. The difficulty in the calculation is to choose an appropriate set of values for cohesion (c) and internal friction angle (φ) because of their large natural variability. Usually, natural analogy is adopted in engineering designs rather than calculation. But the engineer who lacks experience with natural analogy may be confused when faced with loess cuts with complex topography. If the method is combined with reliability theory, it can consider the variations of c and φ values in the slope design.

Based on reliability theory, the probability of failure (P_f) can be employed in evaluating the stability of slopes. The natural-analogy method can be combined

with the reliability approach by incorporating the criterion of P_f. By using reliability concepts, engineers can gain an increased awareness of the uncertainties when they work on the slope design.

2 Critical Slope

First, it is necessary to define the natural critical slope, by using the method of natural analogy. From field investigations of natural loess slopes and detail surveying of the slope ratio in the loess areas in Shaanxi province, the concept of "critical slopes" can be identified and defined as slopes that are in critical state—they would fail if they were a little steeper and be stable if gentler, even when experiencing rain and other dynamic agents. The critical slopes can be found on erosive river banks. Four criteria of field identification of the critical slopes are proposed, which include: (a) those slopes having a series of open cracks at the top; (b) those slopes having local damage and failures on the surface; (c) those slopes having the same geological conditions as slopes with landslides near them; (d) those slopes being reconstructed topographically by landslides. Using these criteria, we have surveyed the central sections of 79 critical slopes and reconstructed those of 16 loess landslides in the areas investigated.

The investigation area can be divided into three zones from south to north, based on topography and soil properties (see Fig. 1). These are the Tonghuang (TH) zone (south of Huanglin county), Ganquan (GQ) zone (from Huanglin county to Yan'an city) and Jin'an (JA) zone (north of Yan'an city). The TH zone has loess–plateau topography, with thick loess strata, well developed vertical joints, and steep slopes. The loess in this zone has high cohesion and a clay content of about 12 %. The GQ zone has a loess–ridge topography, with Lishi loess strata overlying the bedrock, and gently inclined slopes. The loess in this zone has a clay content of about 18 % and the cohesion deceases sharply when the loess is saturated with water. The JA zone has a loess–dome topography. The loess has low cohesion and a high internal friction angle, a clay content of about 9 % with low water sensitivity. A logarithmic regression between height and slope ratio was obtained (Li et al. 2009a, b). Table 1 lists mean values of slope ratios and their 25, 15, and 5 % confidence limits for slope ratios in critical slopes of different heights in the three zones.

3 Calculation of Probability of Failure

3.1 Model and Parameters

Here a Monte Carlo simulation method is used to analyze the probability of loess–slope failure. The critical equation is defined by Bishop's simplified method, and the approach proposed by Li et al. (2003) is used to search for the critical slip surface.

Table 1. Slope ratios (H/L) used in reliability calculation

H /m	Slope ratios											
	Mean critical slope			5 % confidence limit			15 % confidence limit			25 % confidence limit		
	TH	GQ	JA	TH	GQ	JA	TH	GQ	JA	TH	GQ	JA
20	1:0.54	1:0.84	1:0.92	1:0.80	1:1.25	1:1.25	1:0.72	1:1.12	1:1.14	1:0.68	1:1.05	1:1.09
30	1:0.69	1:0.99	1:1.01	1:0.99	1:1.49	1:1.38	1:0.90	1:1.33	1:1.26	1:0.85	1:1.25	1:1.20
40	1:0.81	1:1.12	1:1.08	1:1.15	1:1.70	1:1.49	1:1.04	1:1.51	1:1.35	1:0.99	1:1.41	1:1.29
50	1:0.91	1:1.23	1:1.14	1:1.30	1:1.90	1:1.57	1:1.17	1:1.67	1:1.43	1:1.11	1:1.56	1:1.37
60	1:1.00	1:1.33	1:1.20	1:1.44	1:2.09	1:1.65	1:1.30	1:1.82	1:1.50	1:1.23	1:1.70	1:1.43
70	1:1.09	1:1.43	1:1.24	1:1.57	1:2.27	1:1.72	1:1.41	1:1.97	1:1.56	1:1.33	1:1.83	1:1.49
80	1:1.16	1:1.51	1:1.28	1:1.70	1:2.46	1:1.79	1:1.52	1:2.11	1:1.62	1:1.44	1:1.96	1:1.54
90	1:1.24	1:1.60	1:1.32	1:1.82	1:2.64	1:1.85	1:1.63	1:2.26	1:1.67	1:1.54	1:2.09	1:1.59
100	1:1.31	1:1.68	1:1.36	1:1.95	1:2.83	1:1.91	1:1.74	1:2.40	1:1.72	1:1.64	1:2.21	1:1.63

The strength parameters; cohesion and internal friction angle (c and φ) are considered as random variables. There are 1,635 groups of loess mechanical data gathered from exploration reports for the Tongchuan–Huanglin, Huanglin-Yan'an and Jinbian-An'sai Expressways. Table 2 is a statistical summary of results for cohesion and internal friction angle determined by direct-shear tests. It is assumed that the c and φ obtained by back analysis represents the real strength parameters and those obtained by direct-shear tests need to be altered. Comparing test results of samples from boreholes shafts with the results from back analysis, the c and φ values measured by direct-shear tests of the borehole samples in the TH zone are mostly close to the back-analysis results which can be adopted directly. Because of the special soil properties, those in the GQ zone are systematically higher than the back-analysis results which should be reduced and those in the JA zone are systematically lower than the back-analysis results which should be raised in some extent.

3.2 Results and Design Charts

Statistics from c and φ indicate that their probabilistic distributions could be either normal or log normal (Ni et al. 2001; Li et al. 2009a, b). A normal distribution is adopted here. Based on the variability of loess strength parameters; c and φ, a series of combinations of c and φ COVs were applied in the Monte Carlo simulations. For each set of c and φ COV, 5,000 sets of random c and φ were extracted for the calculation of the corresponding factors of safety (Chen 2003). The calculated factors of safety are fit in a normal distribution, from which the P_f can be computed. Table 3 shows the P_f ($Fs \leq 1$) for the slope ratios listed in Table 1 with the combination of $\mathrm{COV}_c = 0.1$ and $\mathrm{COV}_\varphi = 0.1$. For this combination of variation, the P_f is about 50 % for mean critical slope, lower than 12.5 % for the slope ratio of 25 % confidence, lower than 6.98 % for the slope ratio of 15 % confidence and lower than 1.72 % for slope ratio of 5 % confidence.

Table 2 The statistics for direct shear strength

Zones and shearing method	Age	Num.	*c*/ kPa					*φ*/ (°)				
			Max.	Min.	Mean	Dev.	COV_c	Max.	Min.	Mean	Dev.	COV_φ
TH-Q[a]	Q_4	134	65.9	0.8	21.6	12.9	0.59	30.9	3.0	19.7	6.3	0.32
	Q_3	230	98.0	6.0	32.6	17.8	0.55	43.0	11.0	25.7	5.5	0.22
	Q_2	241	100.4	6.9	40.6	18.3	0.45	47.0	13.0	26.8	6.5	0.24
	Q_1	71	147.0	6.0	59.5	29.9	0.50	46.9	11.9	26.3	8.42	0.32
	N	48	132.6	6.9	76.3	30.5	0.40	27.9	14.2	22.9	3.0	0.13
TH-CQ[b]	Q_3	162	83.0	11.0	39.7	14.6	0.37	35.5	2.3	21.4	4.7	0.22
	Q_2	393	102.0	16.0	44.1	13.9	0.31	45.3	11.9	21.4	4.0	0.19
	Q_1	18	103.0	24.0	60.1	21.2	0.35	30.9	18.4	24.0	3.5	0.15
GQ-Q	Q_4	19	75.0	3.0	28.0	18.0	0.64	31.4	10.5	23.9	5.8	0.24
	Q_3	22	54.0	3.0	27.0	15.1	0.56	40.7	16.7	30.6	6.2	0.20
	Q_2	121	87.0	3.0	38.4	18.3	0.48	43.6	8.1	26.9	7.3	0.27
	N	19	100.0	11.0	54.0	25.7	0.48	37.4	12.3	26.5	8.5	0.32
JA-Q	Q_3	28	37.0	4.0	17.1	8.0	0.47	30.0	20.9	26.0	2.4	0.09
	Q_2	73	49.0	10.1	21.9	9.4	0.43	37.5	17.6	27.9	4.8	0.17
JA-CQ	Q_3	45	42.0	12.0	24.9	9.1	0.37	40.0	15.0	29.1	5.5	0.19
	Q_2	11	27.0	12.0	15.5	4.4	0.28	29.0	21.0	25.6	2.9	0.11

[a] *Q* quick direct shearing
[b] *CQ* consolidated quick direct shearing

Table 3 Probability of failure as $COV_c = 0.1$ and $COV_\varphi = 0.1$

H/m	P_f ($Fs \leq 1$) / %											
	Mean limit state slope			5 % confident limit			15 % confident limit			25 % confident limit		
	TH	GQ	JA	TH	GQ	JA	TH	GQ	JA	TH	GQ	JA
20	1.42	31.96	1.44	0.02	0.26	0	0.10	1.32	0.06	0.12	3.08	0.10
30	17.42	56.86	15.52	0.36	0.66	0.20	0.98	3.76	0.92	2.20	8.16	1.82
40	37.14	61.42	33.98	0.82	0.54	0.72	3.24	3.72	3.02	6.38	8.34	5.18
50	48.52	59.72	46.96	1.14	0.34	1.22	4.86	2.82	4.68	9.28	6.50	8.78
60	53.18	53.56	53.66	1.10	0.18	1.56	4.76	1.46	6.00	10.10	4.30	11.20
70	53.12	46.48	57.80	0.82	0	1.72	4.02	0.72	6.64	8.84	2.62	12.48
80	49.62	38.32	59.78	0.56	0	1.68	2.92	0.42	6.98	6.82	1.64	12.26
90	44.66	30.36	60.62	0.32	0	1.64	2.32	0.22	6.52	4.72	0.66	12.50
100	39.58	22.32	60.38	0.18	0	1.36	1.44	0.06	6.28	3.46	0.42	11.78

The P_f of slopes ratio of 5 % confident were performed using four kinds of COV combinations. The results for the three zones are shown in Figs. 3, 4, 5 respectively. The mean values of c and φ are the same in these calculations. Figures 3, 4, 5 show that the influence of COV_c and COV_φ on the P_f in a large difference when slope heights are changed. COV_c influences on the P_f of lower slopes in a larger intensity as well as COV_φ on the P_f of higher slopes. It implies that P_f is more influenced by the value of c in the lower slopes and more influenced

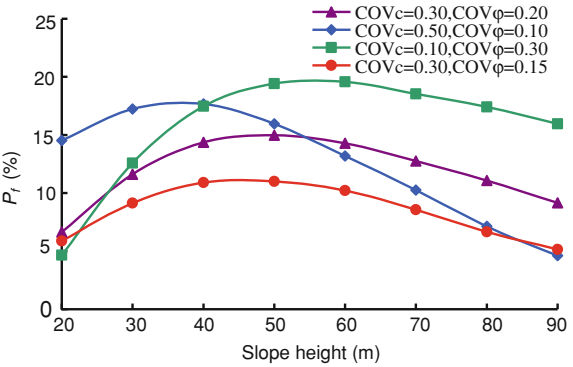

Fig. 3 Probability of slope failure P_f for the TH zone under the four COV_c and COV_φ combinations

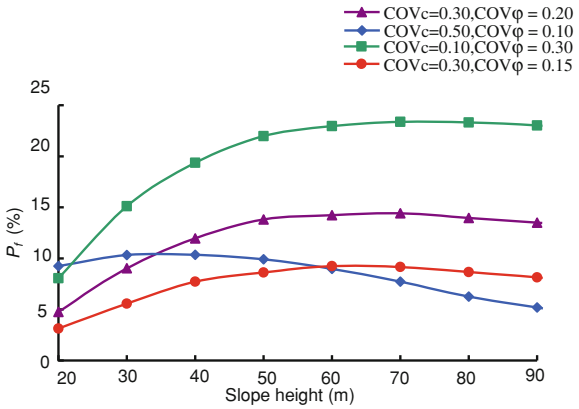

Fig. 4 Probability of slope failure P_f for the GQ zone under the four COV_c and COV_φ combinations

by the value of φ in higher slopes. In the middle range of slope heights, the values of c and φ influence the P_f of slopes about equally. The P_f is highest in the mid-range of slope heights, but the height with the largest P_f changes when the COVs are changed.

Generally the 5 % confidence level is applied in engineering design. At this degree of confidence and in different combinations of COV, P_f is 1.1–25.5 % in the TH zone, 0.7–22.5 % in the GQ zone and 1.7–25.4 % in the JA zone. The larger the coefficients of variation, the higher the probability of failure P_f.

Table 2 shows that loess COV_c and COV_φ are high, but they cover a large area. Nineteen typical sites in the Shaanxi province show that the mean value of COV_c is 0.27, of which 63 % sites have a COV_c lower than 0.30 and 80 % lower than 0.40. As the mean value of the COV_φ equals 0.098, 58 % sites have a COV_φ lower than 0.10 and 84 % lower than 0.15. The P_f with the combination of $COV_c = 0.30$ and $COV_\varphi = 0.10$ is lower than 7.6 % at 5 % probability of failure in the three zones. That of $COV_c = 0.30$ and $COV_\varphi = 0.15$ is lower than 10.0 %. That of $COV_c = 0.40$ and $COV_\varphi = 0.15$ is lower than 14.8 %. So, a reliability criterion is proposed for loess slope design based on three variant combinations of $COV_c = 0.3$

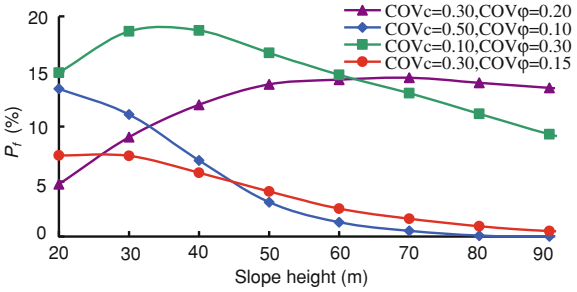

Fig. 5 Probability of slope failure P_f for the JA zone under the four COV_c and COV_φ combinations

and $COV_\varphi = 0.10$; $COV_c = 0.30$ and $COV_\varphi = 0.15$, and $COV_c = 0.40$ and $COV_\varphi = 0.15$. The P_f is less than 7–10 % for the Expressway and first-grade highways while the P_f is less than 14–16 % for second-grade highways and the sub-grades. In the condition of $COV_c = 0.30$ and $COV_\varphi = 0.15$, the $P_f = 7$ % corresponds to a 1.30–1.35 factor of safety, a $P_f = 10$ % corresponds to 1.25–1.30 and a $P_f = 14$–16 % to about 1.2.

Also, because of the unpredictability of the geotechnical soil properties (Sivakumar et al. 2004, 2005; Gorden et al. 2003; Raymond et al. 2005; Christian et al. 1994), the fixed criteria do not apply to all the projects, so Figs. 3, 4 and 5 can be referred to provide reasonable estimates of P_f for different loess slope designs.

4 Conclusion

The authors defined the concept of "critical slope" based on field investigations and surveys of natural loess slopes in the Shaanxi province of China. From the cross sections of the critical slopes, the values of the probability of failure P_f were obtained by Monte Carlo simulation for a series of combinations of coefficients of variation for cohesion and internal friction angle (COV_c and COV_φ).This paper proposes certain reliability criteria analyzing the variability of strength parameters for loess–slope design using critical slopes for 5 % confidence limit of the slope ratio as a design reference. The criteria are that the P_f is less than 7–10 % for Expressways and first-grade roadways, while the P_f value is less than or about 14–16 % for second-grade and sub-grade roadways. Determination of the reliability index provides a systematic method for evaluating the influence of uncertainties in the various parameters and can be used to assist engineers in assessing the acceptable level of risk in loess areas.

Acknowledgments This research work was aided by National natural science foundation of China (No.NSFC-40772181 and NSFC-40972182). The support of this agency is gratefully acknowledged.

References

Chen ZY (2003) Soil slope stability analysis. Press of water conservancy and electric power. Beijing, pp 150–160 (in Chinese)

Christian JT, Charles CL, Gregory BB (1994) Reliability applied to slope stability analysis. J Geotech Eng 120(12):2180–2207

Gorden AF, Griffiths DV, Anthony U (2003) A slope stability model for spatially random soils, applications of statistics and probability in civil engineering. Mill press, Rotterdam

Li P, Wang BG, Li TL (2009a) Study on analogism used in highway cutting loess slope design. J Highw Transp Res Dev 26(2):2–5

Li P, Wang BG, Li TL (2009b) Study on the reliability for the highway cutting loess slopes in Shaanxi province. Chin J Highw Transp 22(6):18–25

Li et al (2003) A new method for quick searching potential sliding surface of the simple earth slope. J Chang'an Univ (Earth Sci Edn), 25(3): 56–59 (in Chinese)

Ni WK, Han QL (2001) Statistical analysis of physical and mechanical indexes of the typical loess. J Eng Geol Chin 9(1):62–67

Raymond WMC, Wilson HT (2005) Reliability of deteriorating slopes. Geotech Geoenviron Eng 131(5):589–597

Sivakumar BGL, Mukesh MD (2004) Effect of soil variability on reliability of soil slopes. Geotechnique 54(5):335–337

Sivakumar BGL, Murthy DSN (2005) Reliability analysis of unsaturated soil slopes. Geotech Geoenviron Eng 131(11):1423–1428

Loess Deposit and Loess Landslides on the Chinese Loess Plateau

Tonglu Li, Changye Wang and Ping Li

Abstract Chinese Loess is a wind origin deposit which records the continuous Quaternary history. In the past 30 years, the loess stratigraphy has achieved a great advantage that the absolute age and the litho-strata were well defined by dating and correlating with deep sea core isotopic curves. That set up a formed basis for further study in the loess properties and geological hazards in view of origin and mechanism. Loess has special characters of typical topographies, vertical joints, loose texture and water sensitivity, which makes it easy to slide. Landslides on the Chinese Loess Plateau are the most severe geological hazards, which deprive people of life, damage gas and oil routes, destroy roads and railways and decrease farmlands. Control of landslides is a long-term strategy. Besides the general used structural methods being applied in the slides related to some engineering, improvement of ecological environment, innovation of irrigation way and availability of drainage systems are more significant. Building of early warning system based on monitoring is a practical and economic way to check landslides as much as possible in considering of the present natural environment and national condition.

Keywords Loess · Stratigraphy · Loess Plateau · Landslide · Deposit

1 Introduction

Loess is an aeolian sediment formed by the accumulation of wind-blown fine sand and clay components. Loess is distributed in arid and semi-arid regions where favourable weather conditions help in its generation and deposition. Globally, loess

T. Li (✉) · C. Wang · P. Li
Department of Geological Engineering, Chang'an University, Xi'an 710054, China
e-mail: dcdgx08@chd.edu.cn

F. Wang et al. (eds.), *Progress of Geo-Disaster Mitigation Technology in Asia*, Environmental Science and Engineering, DOI: 10.1007/978-3-642-29107-4_12,

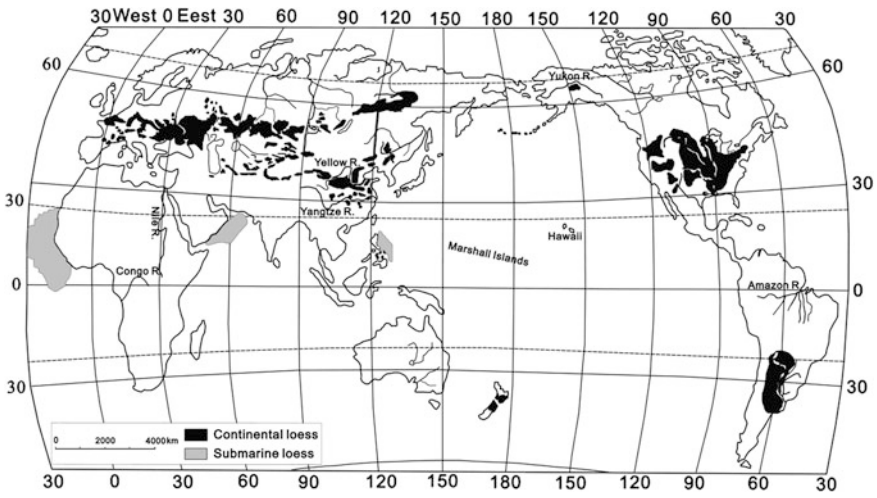

Fig. 1 Global deposits of Loess (After Sun 2005)

covers 10 percent of the earth surface and is distributed mostly in regions spanning 30–55° North and 30–40° South latitudes, which are monsoon dominated zone. As shown in Fig. 1, loess deposits are mainly distributed in the northern hemisphere, from Europe to Siberia in Russia, northern China and north America, with relative lesser deposits in the southern hemisphere, such as the center of New Zealand and the South America. In addition, loess deposits have been discovered in the ocean floor, such as the Atlantic ocean around west Africa, the north Arabian sea, the Japan sea and the sea around eastern Philippine. Loess deposits, unlike water-deposited sediments, are not only distributed in river basins; they are also distributed in the seas and oceans, which strongly prove its wind-blown origin.

Loess in China covers a total area of approximately 631,000 km^2, occupies 4.4% of the national land (Liu 1996), of which, the Loess Plateau has the best developed deposit in the world (Fig. 2). The thickness of loess deposits in this area vary from few meters to more than 300 m.

The Loess Plateau of northern China, which has an area of approximately 430,000 km^2, is located in the center of the Yellow River and is bordered by the Tengeri Desert, Wuqiao Ridge and Riyue Mountain to the west; Taihang Mountain to the east, Qinlin Mountain to the south and Yinshan Mountain to the north (Fig. 3). As monsoon winds generate fine sediments from the northern and north-western deserts, it is barred by the eastern and southern mountains; this causes the fine material to be deposited on the plateau. Field investigations and laboratory analysis have shown that particle sizes of the loess deposit changes from coarse-grained to fine-grained for sampling done from the northwestern part to southeastern end. Recently, the Loess Plateau has become an important economic zone in the western part of China, where there are plenty of natural resources such as oil and gas, coal, hydro-energy and also serves as an important site for agricultural development.

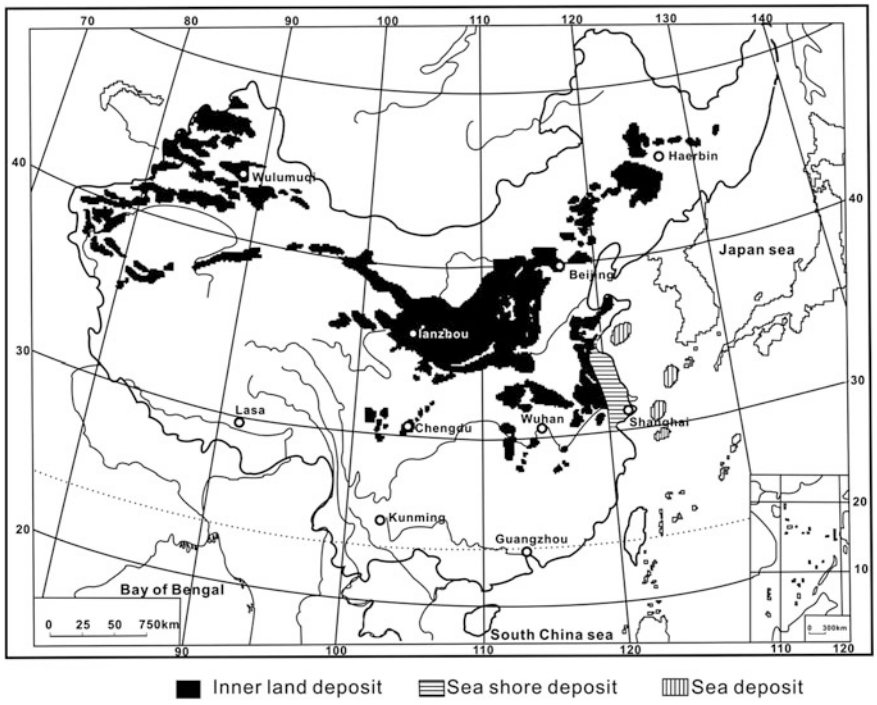

Fig. 2 Loess deposits in China (After Liu 1985)

The Loess Plateau and its environs have been affected by oil and gas explorations, mining of solid mineral deposits, civil construction and urbanization. These activities have greatly influenced the geomorphology of the Plateau, making the area prone to geological hazards. These geohazards, such as landslides, mud-flows, ground-collapses and tension cracks have continued to cause untold havoc to the economic and other developmental activities within the area. In China, landslide disaster, apart from earthquake, has recorded the highest number of fatalities in recent years.

2 Loess Stratigraphy on the Chinese Loess Plateau

In the Miocene epoch, area around the present Loess Plateau was a deep inner basin, called Ordos Basin, which received the Cretaceous-Tertiary deposits made up of sandstones, shales, mudstones and coal interbeds. At the end of the Cretaceous, the Yanshan tectonic movement led to the uplifting of the Ordos Basin to close the deposition and to suffer a long period of weathering and erosion which lasted till the end of the Pliocene and formed peneplain. Therefore, the area generally lacks the early and middle Tertiary deposits. At the end of the Pliocene, the area was still a paleo-plain of denudation, in which there were a lots of

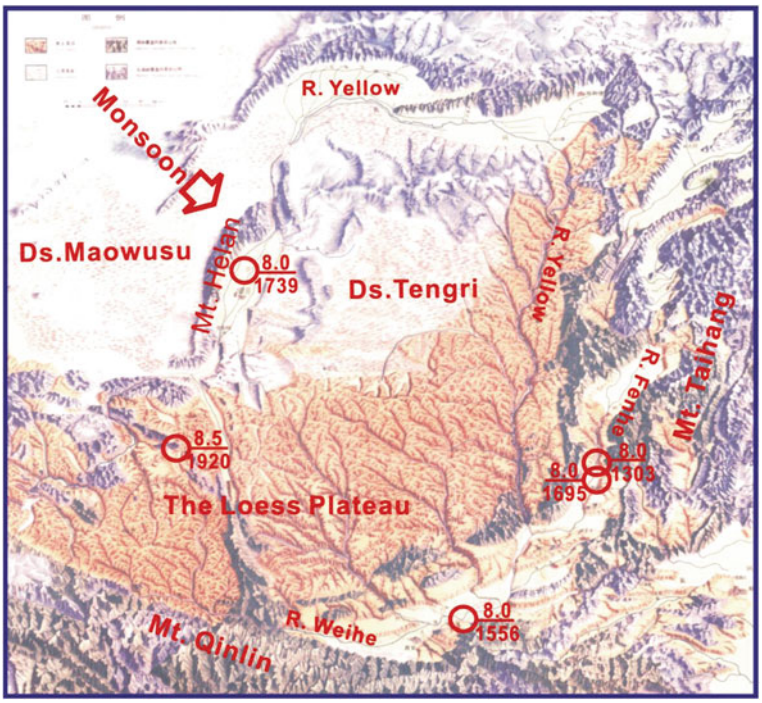

Fig. 3 The landscape of the Chinese Loess Plateau

denudation basins and rift basins. There were a inner river system which flowed from around to the center. Hipparion-red-clay, a wind-transported sediment, was deposited around the surrounding lake and river basins with thicknesses varying from tens of meters to hundreds of meters.

During the Quaternary, the climate became dry and cold and loess began to deposit. In the early Quaternary, the basins and the river beds were filled with lacustrine and alluvial deposits, while the surrounding high lands received the loess sediment, which made up the present loess platform. Luochuan loess platform is one of the largest loess deposits in northern Shaanxi, with successive loess sediment in the Quaternary. A loess profile in Potou village, Luochuan County, located at the western side of Heimugou gully, has been considered as a standard loess section on which the Quaternary paleo-climatic and stratigraphic studies have been carried out in detail (Kukla and An 1989). Liu and Zhang (1962) divided the loess strata into three lithostratigraphic units based on observed field characteristics. They are: the Wucheng loess (Q_1), Lishi loess (Q_2), and Malan loess (Q_3). Beside these three typical units, a layer of 2 m of Holocene deposit (Q_4) covers the upper part of the deposit. The upper part of this layer consists of brownish-yellow thin bed while the lower part consist of dark brown bed, of which the former is called Holocene loess(L_0) and the later is called black loam (S_0).

Due to incessant changes in climate during the Quaternary, the sediments are not uniform in color, composition and structure on the section. They occur as alternating beds of brownish-yellow loess and brownish-red paleosol. Loess represents the product of dry-cold climate, while paleosol, as well as the loam, represents that of warm-wet climate. Loess strata on Potou profile is made up of more than thirty loess-paleosol sequences indicating that the climate must have changed for more than thirty periods during the Quaternary. The Malan loess is the first layer of typical loess which is a set of uniform loose material corresponding to the last glaciation. Lishi loess includes the first paleosol to the fifteenth loess sequences. Of all the above loess sections, the ninth (L_9) and fifteenth (L_{15}) loess beds have a relative higher thickness and coarse particles indicating deposition under harsh weather conditions, while the fifth paleosol (S_5) is a thick layer consisting of three sub-paleosols with two thin loess beds among them. L_9, L_{15} and S_5 are considered to be the marked beds for easy identification of the loess stratigraphy in the field. Wuchen loess consists of thin interbeds of paleosol and loess with high content of calcium and stiff of properties, so it is called as lithoid loess. Below the Wuchen loess underlies Neocene red clay.

Since 1980, a detailed age dating of the loess strata has been recorded through the combined application of radioactive (C^{14}) and paleo-magnetic dating methods, and the correlation of isotope curves along the oceanic bore holes and loess sections. From the result, loess in the Quaternary are divided into Holocene (Q_4), Upper Pleistocene (Q_3), Middle Pleistocene (Q_2) and Lower Pleistocene (Q_1) series. The boundary of the Holocene and Upper Pleistocene is located at the basal section of the black loam, dating more than 11,000 years ago. The Upper and Middle Pleistocene are located at the lower part of the first paleosol (S_1), with ages dating more than 128,000 years ago. Also, the Middle and Lower Pleistocene are located in the eighth loess (L_8), with ages dating more than 730,000 years ago which corresponds to the B/M boundary of paleo-magnetism. The Lower Pleistocene boundary and the Upper Pliocene is located at the lower part of the loess, a little higher than the M/G boundary of paleo-magnetism. The age of the M/G boundary is about 2.47 million years, therefore, the boundary of the Quaternary and Tertiary is considered as 2.50 million years or so. It can be observed that there is a wide difference between the early lithologic units and the present chrono-stratigraphic units. The stratigraphic profile of the Luochuan loess is shown in Table 1. The profile also shows that the loess-paleosol sequences from different parts of the Loess Plateau are spatially correlative, as shown in Fig. 4 (Liu 1996).

As mentioned above, in the early Quaternary, the area of the present Loess Plateau has many inner basins which vanished in about 1.70 MaBP due to extensive uplift in the area corresponding to the second episode of the Himalaya movement. Meanwhile, the present pattern of the Yellow River system began to form with water flow out of the basins as loess is being deposited. Because the Plateau uplifts intermittently and the river terraces have been developed. There are generally five to six terraces along the main river and their tributaries in the Loess Plateau. The loess covers these terraces like mantles bordered by the Liupanshan Mountains. The rivers in the western region have six terraces while those in the eastern region have five terraces which shows that the whole plateau are not uniform.

Table 1 Stratigraphy of the Luochuan standard loess section

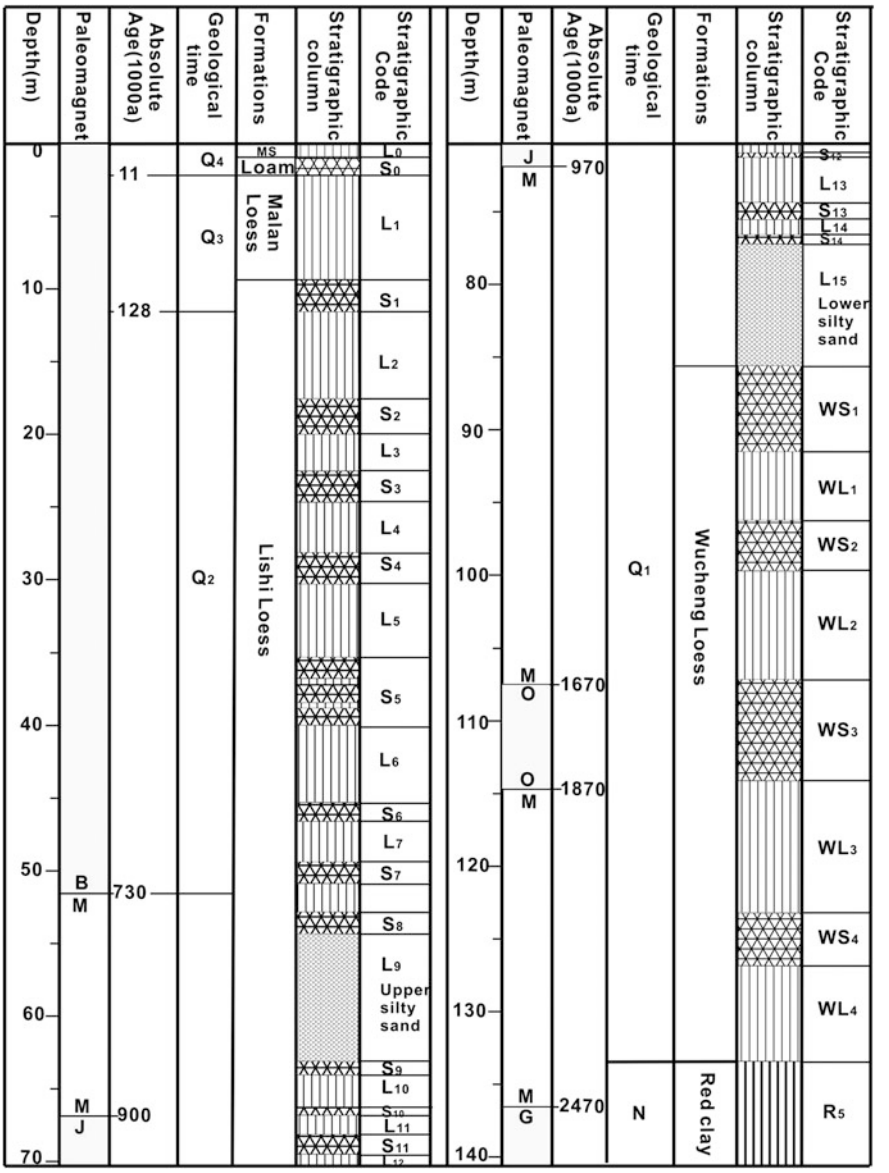

In the western region, 6 terraces can be distinguished along the river sides. The height is terrace VI, on which loess is about 310–505 m thick with 21–23 layers of paleosol, presently, the thickest loess deposits in the world. Loess on terrace VI began to sediment at 1.43 MaBP. Loess on terrace V consists of L_0 to S_{14} or S_{16}, 200–400 m in thickness, and dated at 1.23 MaBP. Loess on terrace IV consists of

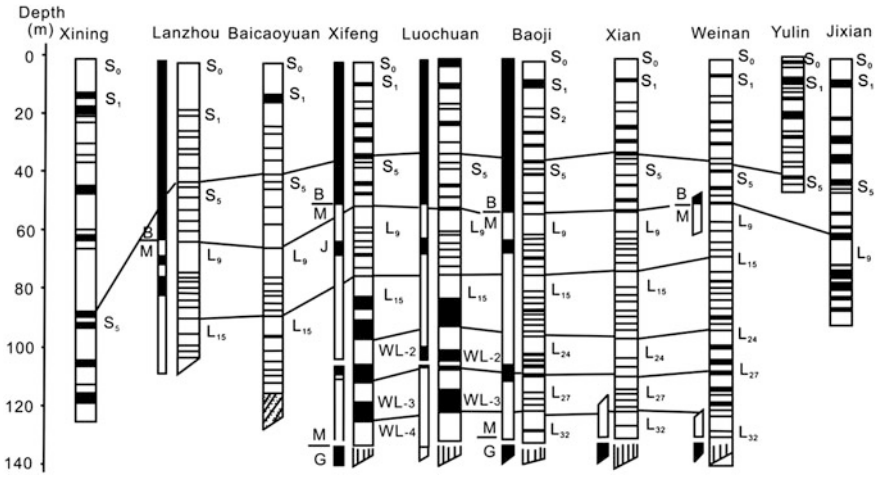

Fig. 4 Correlation of the loess stratigaphy on the Loess Plateau (After Liu 1996)

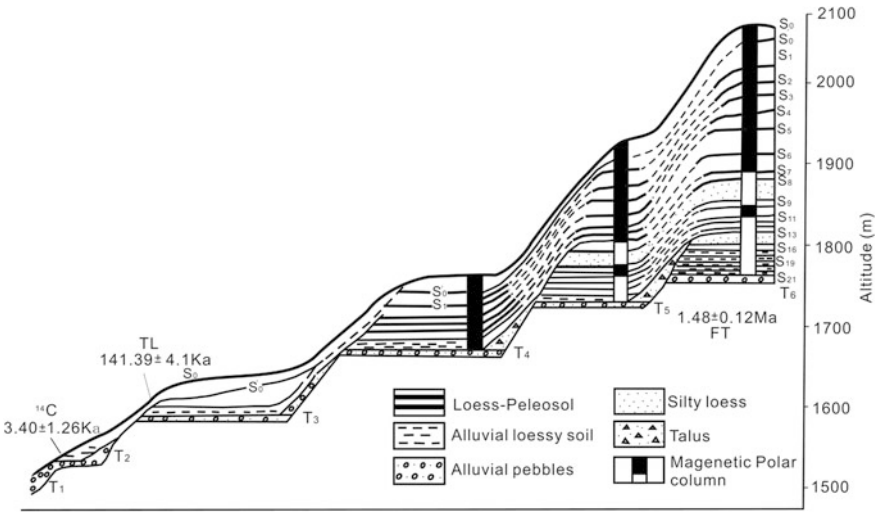

Fig. 5 Loess section on the terraces of the Yellow river (After Zhang 1989)

L_0 to S_5 or S_6, 100–200 m in thickness, and dated at about 0.62 MaBP. Loess on terrace III consists of L_0 to S_1, about 40–60 m in thickness, and dated at about 0.12 MaBP. Loess on terrace II is a layer of loessial soil with thickness of 20–35 m and dating at about 0.03 MaBP. Loess on terrace I consist of present loess L_0 and black loam S_0, about 2.0 m in thickness, and dated at about 0.01 MaBP. Figure 5 is a typical section of the Yellow River terrace near Lanzhou city, which represent the loess on terrace six in the west region.

In the west region, there are generally 5 terraces covered by loess, but loess thickness is thinner than that in the west. Loess on terrace V consists of L_0 to S_{11}–S_{16} (Varied in places), about 70–90 m in thickness, and dated at 1.23 MaBP. Loess on terrace IV consists of L_0 to S_8 or S_9, about 40–70 m in thickness, and dated at about 0.80 MaBP. Loess on terrace III consists of L_0 to S_6, about 25–45 m in thickness, and dated at about 0.62 MaBP. Loess on terrace II consists of L_0 to S_1, 10–17 m, dated at about 0.12 MaBP. Loess on terrace I consists of present loess L_0 and black loam S_0, about 2.0 m in thickness, and dated at about 0.01 MaBP.

The processes of a terrace consist of two episodes: lateral erosion and down-cut. In the tectonic static period, a river has lateral erosion and the riverbed is widened, while during the uplift period, it cut down vertically to form a new narrow riverbed and the original riverbed and floodplain becomes a terrace. The new riverbed would be the next terrace in the forth coming static-uplift cycle. Therefore, on the record of river terraces, the Loess Plateau have experienced at least six cycles of uplift which implies the 6 periods of down erosion at the same time. The erosion cases can also be demonstrated by the interaction among some new loess bed with the old ones.

3 The Effects for Landslide Initiation on the Loess Plateau

Loess has typical landforms like vertical joints and loose textures, as well as special physical and mechanical properties, such as low water content, strong structural strength, loose textures and weaker water resistance, high compressive strength which reduced the shear strength of the material.

3.1 Typical Topographies

Loess mainly forms three characteristic types of geomorphic structures. These are loess platform, loess ridge and loess dome, as showing in Figs. 6, 7, 8. Another form of geomorphic structure, loess Karst is not common.

It could be seen that on the sides of the platforms, ridges and domes are the steep slopes which could easily slide in favorable conditions, such as infiltration of rain water, irrigation water and earthquake effects. Generally, loess landslides occur on the slopes steeper than 35° and higher than 40 m. Our investigation in the northern Shaanxi Province shows that 80 % of loess landslides occurred in slopes with dip angles exceeding 35°. As the slope angle becomes greater than 50°, failure style is normally collapse-sliding or purely collapse; the slopes are stable for slope angles lower or close to 35°. The sliding is more preferable to occur in concaves slopes. The landslides are often continuously distributed on the sides of the loess valleys as the side being the rims of loess platforms, ridges and domes, hence forms the so-called “slide-skirts” or “slide-zone”. The loess slides on the southern part of the valley with strike direction trending East–West are more than those on the north because of its less sunshine effect and higher moisture content.

Fig. 6 Loess platform

Fig. 7 Loess ridges

3.2 Vertical Joint Structure

One unique structural feature of the Loess Plateau is the existence of vertical joints (Fig. 9), which is both primary in origin due to loess formation by wind-blown processes and tectonic in origin due to neo-tectonic movement (Wang 1985). Vertical joints in the loess deposits constitute weak planes along which rainfall easily infiltrate into the loess. The joints are the main erosion path in the loess slopes especially on the margins of the platforms and ridges; the joints generally connect the upper and the lower part of the slopes. Rainfall infiltrates into the slope through the joints and moves down along the joint planes as meet a relative impermeable bed as paleosol, the water would move horizontally out on the impermeable bed. As a result, a lot of sinkholes (Fig. 10) form on the slope surface with outlets appears on the slope toe (Fig. 11). The process enlarges the joints into wide fissures which allow more water to flow in and form temporary waterfall during rainy periods. Erosion along the joints not only affects the slopes, but also allows more water to flow into the slope which essentially affects the stability of the slope.

Fig. 8 Loess domes

Fig. 9 Loess joints

3.3 Loose Texture

Loess materials have a characteristic porous texture. The upper Q_2 and Q_3 loesses, L_1 to L_2 generally have void ratios of 0.8–1.1, that means the ratio of pores to solid particles is about 1:1, so it is a very loose material. As viewing on Scan Electric Micrograph photos, the micro-holes can be identified clearly (Figs. 12, 13). The particles are mainly aggregation of silts around the holes contacting at points with weak connection by clay minerals. The connection is water-sensible. As soaked in water, the particles will lose their connection and also disintegrate. At last, they become more fine granules and fall in the holes (Figs. 14, 15). This typical texture make loess has a special quality of collapsibility, which means as the loess has consolidated under given load, if soaked by water, it will creates an additional depression.

Fig. 10 Sinkholes on the ground

Fig. 11 Erosion along loess joints

The skeleton-porous texture of loess formed in arid climate, which has a relative high structural strength in general condition. But the strength decreases obviously as it is saturated. Therefore, continuous raining or irrigation always causes large numbers of loess slides.

Fig. 12 Micro-texture of undisturbed loess, rounded particles of aggregation of silts support each other, pores are among them

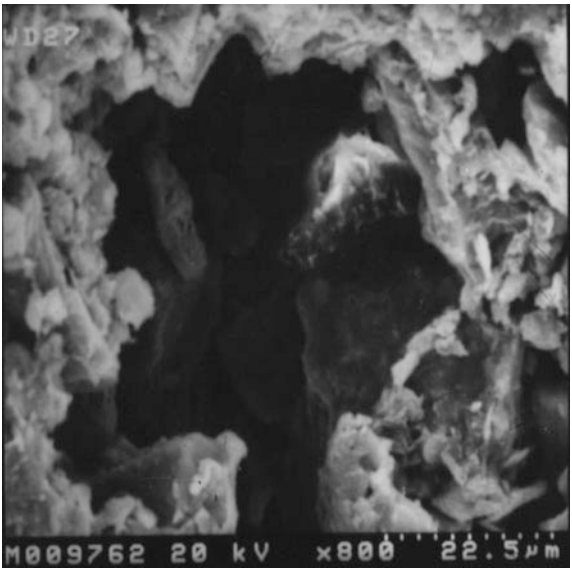

Fig. 13 Micro-texture of undisturbed loess, a single pore

Fig. 14 Micro-texture after water soaked loess, the rounded aggregations disintegrate, parts of them fall in the pores

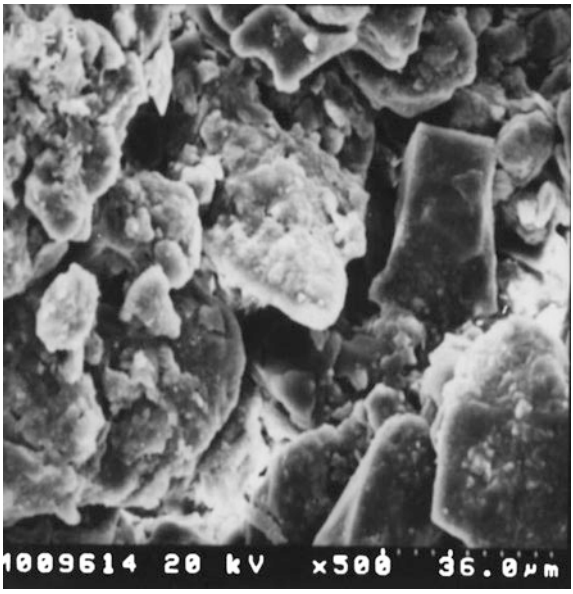

Fig. 15 Micro-texture after water soaked loess, pores were filled up

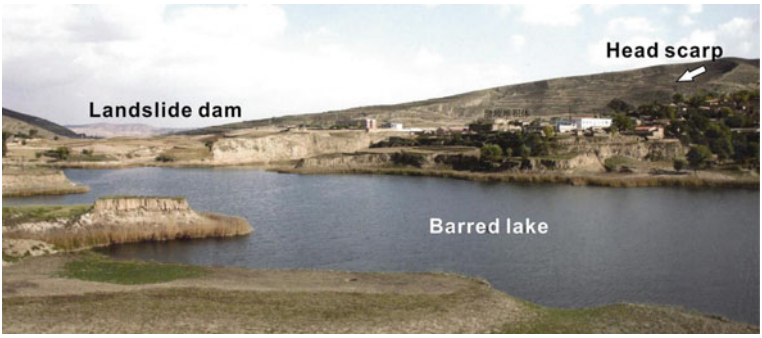

Fig. 16 Landslide dam and barrier lake formed in 1920 Haiyuan 8.5 Ms earthquake. (Subao Village, Xiji County, Ningxia autonomous Region, Photo by Yin YP)

4 Triggering Factors of the Loess Landslides

The loess landslides are initiated by four triggering factors. They are earthquakes, rainfalls, irrigation and civil engineering activities (Li and Li 1997).

4.1 Earthquakes

The eastern part of the Loess Plateau is surrounded by a major active zone. The eastern and southern part lies next to the Fenhe and Weihe Rifts respectively, the north is the Hetao rift, the west is the Yingchuan rift and the southwest is the Liupanshan thrust structure. Five earthquakes with magnitude of equal or larger than 8.0 Ms degree occurred in these active zones. They are: the 1303 Hongtong 8.0 Ms in the Fenhe rift, the 1556 Huaxian 8.0 Ms in Weihe rift, the 1695 Linfen 8.0 Ms in Fenhe rift, the 1739 Pingluo 8.0 Ms in Yinchuan rift, the 1920 Haiyuan 8.5 Ms in the liupanshan thrust zone (Fig. 3).

The latest and most catastrophic is the 8.5 Ms Haiyuan earthquake, which triggered 675 loess landslides and killed more than 100,000 lives. The landslides formed 40 huge barrier lakes, with 27 of them still very active (Fig. 16) Extensive earthquake vibrations and liquefaction have been considered to be the main triggering factors which initiated the landslides. After the 2008 Wenchuan earthquake, the area around the Loess Plateau has been considered to be a potential region of strong earthquakes.

4.2 Rainfalls

Rainfall is a common triggering factor of landslides. The Loess Plateau has an annual precipitation between 450 and 720 mm, which is not really high. High rainfalls are recorded between June and September and often occur as storms. Most of the loess landslides are related to rainfall effect, but loess has a very low

Fig. 17 Ground saturated zone after decades of intermittent rainfall, the observed site is located in Ganquan County, Shaanxi Province

permeability. The coefficient of permeability of loess is generally lower than 10^{-4} cm/s. In situ observation and test indicates that the depth of the saturated zone at the loess ground generally no more than 1 m even after a long term of raining, as Fig. 17 shows. However, the vertical joints on the tops of loess slopes are the main for the rainfall down moving. Erosion along the joints forms sink holes and opened fissures to permit much rain water flowing in (Fig. 18). As the water encountering a relative impermeable bed, such as paleosol, Tertiary red clay or bed rock, it would accumulate on the bed to soften the soil and induce landslide.

4.3 Irrigations

With developing of the irrigation systems in the loess region in recent 40 years, agricultural irrigation has become a prominent agent to induce landslides. Hei-Fang platform in Gansu province is a typical area for this case. The platform is composed of two high flat lands with the total irrigation area of 13.4 km^2. Since the irrigation system began to run in 1968, the loess landslides around the platform occurred frequently. Investigation revealed that in the 15 years between 1968 and 1983, 15 landslides occurred with average 1 one a year which are relative small in dimension and short in run distance with run-out length between 20–50 m, in the 6 years between 1984 and 1989, 15 cases occurred with average 1.5 ones a year which are larger in dimension and longer in run distance with run-out length between 50–100 m, in the 9 years between 1990 to 1998, 31 cases occurred with average ones a year which are large in dimension and far in run distance with run-out length between 250–400 m. According recently investigation, the 10 km long margin of the Hei-Fang platform has 72 landslides (Fig. 19).

Fig. 18 The flow of rain water along vertical joint in the loess, root also grows along the joint

The landslides caused reduction of farmland and loss of lives and properties. In about 40 years, more than 1 km^2 area of the top land of the platform slid away, caused 20 more person death and injured.

In the Guanzhong irrigation area of central Shaanxi province, there is the same problems. Guanzhong irrigation area is accords with the Weihe rift area. There are many pieces of highlands among the branches and the trunk of the Weihe River in the rift area, those highlands are the dissected loess platforms. The surfaces of the most loess platforms are irrigating farmlands. The area has a long history of irrigation and now has a very dense canal system. Leakage of the canals and free-flow irrigations induced a large number of landslides at the side slopes of the loess platforms, such as the north sides of the loess platforms at the south of the Jinghe river (Fig. 20), Bahe river, and Weihe river.

4.4 Engineering Activities

Engineering cut mainly carried out in highway and railway infractions, as well as dwelling sites.

There are 4 main national highways and many other provincial roads as well as 3 railways rendering on the Loess Plateau connecting this region to the around of

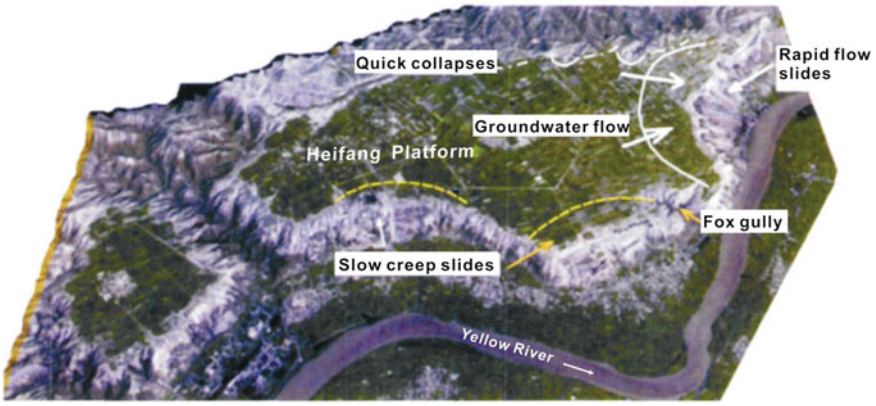

Fig. 19 The landscape of Hei-Fang platform

Fig. 20 The topography of the south bank of Jinghe River and the north side of a loess platform with the slope height of 70–90 m and slope angle of 50–70°. The top is an irrigation farmland, which often induces landslides at the side

the country. Construction of the roads induced a large number of landslides and caused a huge loss. Tongchuan-Huanglin highway is the first high grade road constructed on the Loess Plateau. In the period of design, the landslide problem was far low estimated; only 3 landslides were designed to stabilize. While the highway being constructing, there were 27 landslides occurred actually. More than 200 million yuan RMB was added to control the landslides. Almost all kinds of measures, such as piles, pile-anchors, block-anchors, frame-anchors, beam-anchors and retaining walls, were practiced in the landslides (Fig. 21).

Fig. 21 The piles applied to stabilizing a landslide on the Tongchuan-Huanglin highway

Fig. 22 The living caves (Abandoned) in the top and the foot of the loess slope

In addition, the people in the loess area have a tradition from ancient time to live in digging caves (Fig. 22), which also induced slides to cause a large number of causalities as not properly worked out. The living caves mostly dig either on the top or on the foot of a slope around platforms or ridges. As there are a good drainage ways around living caves to get rid of water penetration, and the thermos released by living activity to keep the soil of the inner wall always dry, the living caves are solid enough to living.

Fig. 23 A new excavated building site located in Longshou village, Huanglin County, Shaanxi. The west side has a shearing plane at the top by unloading (**a**); the toe of the north side was spited to slices by the concentrated stress (**b**)

But people often neglect some potential or unseen intakes of water, so landslides often damage living caves and kill peoples in loess area. In recent years, the living caves destroyed and people killed by loess slides every year, especially in autumn.

Our investigation revealed that about 380 were killed and 70 injured in the collapse of 400 living caves during 1985 to 2010. Figure 23 shows a new excavated site for digging living caves. It can be seen that the toe of the north side has been split to slices by the concentrated stress, the west side has a shearing plane at the top by unloading, and the east side has dug caves at the toe. All the traces imply that the slope close to equilibrium state, digging of the caves would cause damage without reinforcement.

5 The Hazards of Loess Landslide on the Loess Plateau

Loess landslide is a prominent geological disaster in the Loess Plateau, which caused deaths of lives, damage to lifelines, transportation routes and destruction of farmlands.

5.1 Causing Direct Death of Lives

The reports of the loess landslides caused causalities are released almost every year. Of which, the Saleshan landslide in Gansu Province broken in 1983 is the well known one, which is a high rapid long run-out slide with the run distance of 1600 m in a few minutes. The landslide destroyed four villages, took about 200 and 77 lives and 300 domestic animals, and filled up two small reservoirs. In 2005, another loess landslide occurred in Shuidonggou village, Jingxian County, Shanxi Province on May 9th killing 24 people. In 2006, the loess flow-slide occurred in Gaolou village, Huaxian County, Shaanxi Province on October 6 killing 12 people. In 2009, a loess landslide occurred in Lanzhou city, Gansu Province on May 16th killing seven people. In 2010,

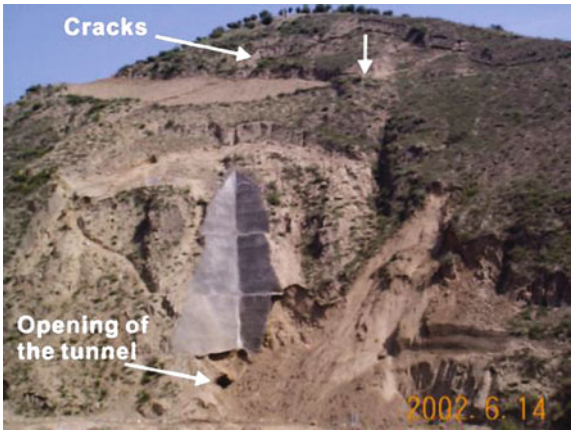

Fig. 24 Collapse and slide occurred in the opening as the tunnel being driven after a heavy rain

another geodisaster occurred in Shigou village, Zizhou County, Shaanxi Province on January 10 killed 27 people. In 2010, the accident occurred in Baqiao district, Xi'an city on September 17 killed 32 workers of two factories located at the foot of a slope.

The population in loess area is relatively dense. Before 1980's, almost all peasants, even rich ones, lived in living caves, but now most of them move out to live in houses, even buildings, which did not reduced the casualties by landslide. Because of house land limitation, most of the new houses were built on the foot of slopes. Cutting of slopes for enlarging sites and keeping the wasted living caves still open often make the houses in front the slope in danger.

5.2 Damage of Lifeline

There are plenty of gas and oil transfer routes entombed underground on the Loess Plateau, such as the West-East Gas Transfer Route, Jingbian–Beijing and Jingbian–Xi'an Gas Transfer Routes, Jingbian–Xianyang oil Transfer Route and many other oil Transfer Routes between gathering wells and oil refining plants. Landslides are the most headache problems in the route lines.

Figure 24 shows a tunnel crossing a loess ridge in the West-east Gas Transfer Route. As the tunnel was driving in June 2002, after 30 h continuously raining of 60 mm rain fall from June 8 to 9, a collapse fell down to cover half of the opening of the tunnel, further more, a 60 m high, 100 m width slide was appeared on the slope. The cracks bordering the slide opened 10–30 cm, and the top part of the sliding mass fell down 60–80 cm. The steel supports and the inner line were seriously twisted (Fig. 25). At last, the tunnel was abandoned; instead of entombing along the river valley beside, more than 10 millions Yuan RMB was added for the revision.

Another big accident being gotten rid of is that a landslide on the Jingbian–Xianyang oil Transfer Route which crosses the whole Loess Plateau with 460 km long. To the north of Xianyang City, the route was designed crossing beneath the

Fig. 25 Steel supports were twisted by deformation of the inner wall of the tunnel

Jinghe River and then climbing up a 90 m high slope which is the north side of Jingyang Plantform. A series of linear distributed sinkholes and cracks developing on the top of the slope told us a potential huge landslide was there. Then we persuaded the designer move the route a kilometer away on a stable old landslide, even though the route should be elongates 3 km and costs 6 millions Yuan additional money. The oil route was completed and put into work in the beginning of year 2002 (Fig. 26), while the slope slipped in March 2002, with irrigating on the top of the platform. The slide not only fell 50 m down, but also squeezed the Jinghe River bed to thrust up (Fig. 27). It would be a disaster as the oil route was entombed on the original site.

5.3 Obstruction of Transportation

The Loess Plateau is located in the central of China. The 4 main national highways and the 3 railways of Long-Hai, Bao-Zhong and Xi-Tai connecting this region to others around the country. Because of the complicated landforms and rapid highway and railway development, construction of the road induced a large number of landslides and caused huge loss. On Tongchuan-Huanglin highway, there were 27 landslides occurred during construction in 1990 s. Almost all kinds of possible measures, such as piles, pile-anchors, block-anchors, frame-anchors, beam-anchors and walls for anti-sliding, were practiced in the slides. Unfortunately, part of the control structures was invalid at last. Since the road was completed to utilize on May 2001, it has troubles in every rain season, some of the piles were broken down, and some of the anchors were pulled out, and the slides were still moving foreword. The reason of the failures is that drainage system is not sufficiently available, both ground and underground. In any cases, drainage of water is the most necessary, but simple and less cost measure in loess sliding control because of its sensibility to water. After of all, all the roads passing the Loess Plateau face the problems of landslides which either large or small (Figs. 28, 29).

Fig. 26 The landslide on the north side of Jingyang loess platform occurred in March 2002

Fig. 27 The Jinghe river bed was squeezed up by the landslide

Fig. 28 The damaged beam-anchors for stabilizing the landslide

Fig. 29 A loess slide in No.309 National Road (K2075 + 100)

Railway has the same problem. The 150 km length of Baoji-Tianshui railway has 22 landslides, of which 13 ones are loess slides. Wolongsi landslide, slipped on August 8,1955 near Baoji City, is the largest one on the railway line. It is primary an old landslide, re-slipping after several days rainstorm. The slipping process continued half an hour. The railway on the foot of the slide was pushed forward 110 m, and all the living caves, houses and farmland on the slide were destroyed. The slide has size of 20 million cubic meters and area of 3.3 million square meters. In addition, landslides often cause railway accidents on the Loess Plateau.

5.4 Deduction of Farmland

Land-slipping is a kind of gravity erosive process, which not only moves away the good land on the top of the slope, but also covers that on out of the slope foot. With the landslide progressively developing, the cultivable land is decreasing, which is so-called "worm-eating" of the farmland. The process is more severe on the side slope of loess platforms. Generally the top of the loess platform is gentle and suitable for irrigation, while the foot of the side slope is first terrace of river, which has very loose deposits and shallow ground water. The slides in such a condition have a high rate and a long run distance. Landslides along the platform are almost continuously distributed, forming slide zones along the sides of platforms. There several such slide zones around Xi'an city, such as North bank of Weihe River slides zone; South bank of Jinghe River slides zone, South bank of Bahe River slides zone, North bank of Chanhe River slides zone

Take the South bank of Jinghe River slides zone as example. This slides zone extends 45 km long east to west. Because of side erosion of Jinghe River, the slope has dip angle of 45–70° and 70–90 m high. The top is the gentle Jingyang Platform, a good irrigating farmland. Since the irrigation system was built up in 1976, large amount of water penetration caused hundred of slides along this zone, of which the large slides with size of greater than 30 thousands cubic meters are 30 more. Until present, the total size of the sliding mass is 45 million cubic meters, 30 persons dead, 240 living caves damaged and nearly 1000 mu farmland on the top slipped, 2500 mu farmland on the foot of the slope covered.

Fig. 30 A loess slide in South bank of Jinghe River sliding on May, 2003. Slipped away 80 mu, and covered 200 mu farmland

Fig. 31 A loess slide in South bank of Jinghe River sliding on April, 2006. Covered 5 mu farmland

Now there are still 20 potential landslides creeping in dangerous state. Because local government pays much attention to the slide zone and set ones on duty to observe the change of the slope. They gave alarm to the villagers on time, so relative few people dead in the slipping along this zone. In recent years, Large slides almost happens every year in the fall, the follow photos (Figs. 30, 31) shows the ones in 2002 and 2006.

6 Countermeasures for the Loess Landslides

6.1 Hazard Risk Management

Now we pay too much attention to the engineering countermeasures and skills to control landslides when the hazards of landslide coming. However, as investigating origins of the hazards, it is not surprised that most of them were related to

human activities. So, "A Great Debate" on the topic of "Disaster Mitigation Is A Waste of Money" was conducted at the end of the 2010 11th IAEG conference. I agree with the point of view because "People are the main problem" just as some delegates argued (Sergio 2010; Kalsnes et al. 2010). We make the disaster today with a little money; we cure them tomorrow with great money. Is it a waste of money? Therefore, hazard risk management should be more essential than hazard mitigation, which means we should control the action of ourselves to keep from producing new hazards in the long run. So reasonable planning of land use, immigration of the people out of hazard threatening, improvement of ecological environment, innovation of irrigation skill may be more significant. The government has stepped going on but far more from the necessity of economic development.

Since 1990 s, the government has been prohibited to herd on the loess slope of steeper than 25° on the Loess Plateau instead of planting trees. Now the north of Loess Plateau is greener than before. Covering of vegetations would obstruct erosion of loess to improve stability of slope.

Since 2008 Wenchuan 8.1 Ms earthquake and thereafter 2010 Zhouqu huge debris flow, the government has appropriated special funds for immigrating the people suffering inclement geological conditions to the new planned site. But some planned sites were still unsuitable for residence, hazards triggered by construction at the new site made the problems severe. Because the land resources are owned by government, but held by privates, which limits the choice of reasonable sites in a broad range. So the problems may be solved under further reformation of the land policy.

The present overflow irrigation way applying in most farmland on the Loess Plateau not only wastes water resource, but also induces landslides. Replacement by dropping or spraying irrigation could create more social and economic benefits.

That Large amount of cutting for road construction can be replaced by under ground tunnels, cutting for leveling house foundation by littlie cutting and more filling may reduce the risk of landslide in a large extent.

6.2 Monitoring and Pre-alarm

For landslides which have potential risk to the residents but not confident for their stability, monitoring and pre-alarm is a practical way to reducing their risk as much as possible. There are many successful experiences on this way. In the remote areas, the heads of the local government were trained to respond to any observation on the slope movement. People could be alarmed before slipping which saved many lives. As to slides related to some important project such as highways, railways and reservoirs, besides periodical observation, monitoring by equipments such as total station is often applied. Some equipment were fixed in the sites, such as extension meter, incline meter and rainfall meter. The monitoring

Fig. 32 An extensometer installed at a landslide in Heifangtai, Gansu province

Fig. 33 A borehole inclinometer installed at a landslide in Heifangtai, Gansu province

data were obtained on real time with remote controlled unit from the field. Figures 32 and 33 shows the monitoring system of surface extensometer and borehole inclinometer installed at the landslides in Heifangtai, Gansu province.

7 Conclusions

1. Loess is a wind blown deposit which is best developed in the Chinese Loess Plateau. The loess highlands of the Plateau have a continuous stratigraphy in the whole Quaternary which reflects the climatic change in the geological record of the deposits, while loess on the river terraces reflect the intermittent uplift of the Plateau and consequent lateral and downward erosion.
2. Loess landslide occurred extensively on the Loess Plateau due to the topographic effect, vertical joint structures, loose texture and water sensibility.
3. Loess landslides are triggered by earthquakes, rainfalls, irrigations and engineering activities. Most of the landslide hazards are caused by human activities.

4. The countermeasures for landslide hazards should be hazard risk management for controlling man-made hazards, such as reasonable planning of land use, immigration of the people out of hazard threatening, improvement of ecological environment, innovation of irrigation skills and best design for constructions.

Acknowledgments This research was funded by the National Science Foundation (Project No. 40972182). Postgraduate students Xing Xianli, Wang Changye, Wang Peng, Zhang Yaguo, Wang Adan, Chen Chunli attended the field investigation. Wang Hong, Zhou Yichao, Wang Ning, Zhang Ziran drew some of the figures. Our appreciation also goes to all those that contributed to the success of this project.

References

Kalsnes B, Nadim F, Lacasse S (2010) Managing geological risk. In: Willams AL, Pinches GM, Chin CY, McMorran TJ, Massey CI (eds) Geological active–proceedings of the 11th IAEG congress, Auckland, 5–10 Sept 2010, pp 111–126

Kukla G, An ZS (1989) Loess stratigraphy in Central China. Palaeogeogr Palaeoclimatol Palaeoecol 72:203–225

Liu DS, Zhang ZH (1962) Chinese loess. J Geol 42(1):1–14 (in Chinese)

Liu DS (1985) Loess and environment. Science Press, Beijing, pp 17 (in Chinese)

Liu DS (1996) Geological environments in China and global change. Keynote speech on the 30th IGC, Beijing, pp 1–9

Li XS, Li TL (1997) The characteristics and analysis of loess landslide in China. In: Sassa K (eds) Proceedings of the International Symposium on Landslide Hazard Assessment, Xi'an, China, 13–16 July 1997, pp361–366

Sergio M (2010) Disaster should not be the protagonists of Disaster Risk. In: Willams AL, Pinches GM, Chin CY, McMorran TJ, Massey CI (eds) Geological active–proceedings of the 11th IAEG Congress, Auckland, 5–10 Sept 2010, pp 89–110

Sun JZ (2005) Loessology. Hong Kong Archaeological Society Press, Hong Kong, pp 1–10 (in Chinese)

Wang JM (1985) On loess joints. J Xi'an Coll Geol 7(2):15–19 (in Chinese)

The Application of Monitoring and Early Warning System of Rainfall-Triggered Debris Flow at Merapi Volcano, Central Java, Indonesia

Teuku Faisal Fathani and Djoko Legono

Abstract The 2010 Mt. Merapi eruption has produced approximately 140 million m^3 of pyroclastic deposit, in which more than 10 million m^3 deposits are potential to move downstream through Boyong/Code River towards Yogyakarta City. The flow behavior of Code River may be affected by the presence of accumulated sediment at the upstream of the river (namely Boyong River). By rainfall trigger, this potential source can cause debris flow disaster that may contribute damage to the settlement areas in Yogyakarta City. This paper presents the application of monitoring and early warning system to mitigate the impact of debris flow disaster along Boyong/Code River as revealed by most adaptive, low cost, and collaborative-based technology. The real-time monitoring equipment consists of automatic rainfall recorder, automatic water level recorder, debris sensor, and interval camera. The system was developed by considering the community aspiration in determining the types and placement of monitoring equipment, and maintaining its sustainability. The information flow of the proposed early warning system has been introduced accordingly. The central station receives the results of the real-time monitoring and the information through radio communication from the focal points located along Boyong/Code River. Afterward, the warning alert is sent to focal points and the debris flow monitoring radio. This newly built system is expected to be integrated with the monitoring system of other volcanic rivers at Merapi Volcano.

Keywords Volcanic debris flow · Real-time monitoring · Early warning system · Community preparedness

T. F. Fathani (✉) · D. Legono
Department of Civil and Environmental Engineering, Universitas Gadjah Mada, Jalan Grafika No. 2, Yogyakarta 55281, Indonesia
e-mail: tfathani@gmail.com

F. Wang et al. (eds.), *Progress of Geo-Disaster Mitigation Technology in Asia*, Environmental Science and Engineering, DOI: 10.1007/978-3-642-29107-4_13,

1 Introduction

Mt. Merapi is one of the most active volcanoes in Indonesia. It has a long history of frequent eruptions with avalanche type pyroclastic flows caused by collapsing lava mass. Mt. Merapi eruption induced pyroclastic, tephra, laharic flow, and debris flooding have often occurred with a cycle of approximately 9–16 years for larger scale flows and 1–3 years for smaller scale ones. During the eruption period, Mt. Merapi produces a large number of sediment volumes which can move downstream in various mechanisms, such as through natural flow by bed load transports and debris flows, and flow through human-related activities by sand mining (Wardoyo et al. 2010).

It was reported that the 2006 Mt. Merapi eruption (from April through October 2006) had produced approximately 8 million m^3 of sediment, which has high potential to move downstream towards the southern part of the mountain (Legono et al. 2008). Meanwhile, the 2010 Mt. Merapi eruption (from 25 October through 2 December 2010) produced approximately 140 million m^3 of pyroclastic deposit toward the southern and western part of the mountain (Legono et al. 2011a). Since then, the volcanic debris flow has caused severe damage to the inhabitants and residents living on the foot slopes. Figure 1 shows the Merapi volcano before and after 2010 eruption.

Due to 2010 Mt. Merapi eruption, a large number of sediment is deposited at the upstream of several volcanic rivers, hence the secondary disaster in term of rainfall-induced debris flow may occur in a long period. The presence of river bends also increases the possibility of inundation in some river flood plains in the city area or may create a new stream, causing significant damage to various infrastructures and settlements. Figure 2 shows the collapsed bridge at the west side of Mt. Merapi, while the damage on houses is shown in Fig. 3. These damages were due to the destructive power of rainfall-induced debris flow. Considering the large deposit accumulation in the upstream part of volcanic rivers, there is a necessity to monitor the hydraulic and hydrology parameters, which may be used to predict the occurrence of debris flow. The monitoring results can be used for both anticipating the debris flow disaster and developing the criteria of rainfall characteristics induced debris flow for early warning system. Therefore, both types of monitoring, i.e. historical and real-time, are very much needed.

2 Debris Flow at Boyong/Code River

The distribution of pyroclastic flow towards the southern part of Mt. Merapi appears dominantly in Boyong/Code River in which the 1994 Mt. Merapi eruption hit the upstream part of the river severely. Since then, several numbers of sediment control structures were built to ensure that Yogyakarta City would be sufficiently safe from debris flow disaster. There are 41 sabo dams provided with river training structures such as groundsills and retaining walls along Boyong River.

Fig. 1 Merapi volcano before the 2010 eruption

Fig. 2 Collapsed bridge due to the destructive power of rainfall-induced debris flow

The 2010 Mt. Merapi eruption is predicted to contribute more than 10 million m^3 pyroclastic deposits on the upstream (Legono et al. 2011a). By rainfall trigger, this potential source can cause debris flow occurrence that may contribute damage to the settlement areas at the surrounding Boyong/Code River in Yogyakarta City (Fig. 4). Although local communities in this area have been experiencing various flood disasters, such preparedness of flood disaster by means of debris flow is far beyond sufficient because such debris flow phenomenon is a very rare case. Such insufficient preparedness was found on 29 November 2010 afternoon, where the first flood after the 2010 Mt. Merapi eruption occurred. The flood carried various materials from fine sediment to coarse sand, but no boulder was found. The sediment was assumed to be originated from dust particles fallen in the catchment area of Boyong/Code River and accumulation of sediment in the upstream of Boyong/Code River (Fig. 5). In fact, local communities have initiatives to anticipate the debris flow disaster by identifying the debris occurrence at the upstream part of the river.

Fig. 3 Damage on houses near the volcanic river

Apparently, during the days after 29 November 2010, increase in rainfall intensity occurred, triggering a more intensive debris flow that caused significant damages in several infrastructures at some rivers (Pabelan River and Putih River). Fortunately, no casualty was reported. However, the damage of important infrastructures such as roads, bridges, paddy fields, and settlements was very significant. A hyper-concentrated flow in Boyong/Code River occurred several times that made the local people evacuate themselves (Fig. 6).

3 The Characteristic of Rainfall-Induced Debris Flow

Rainfall plays an important role in contributing the possibility of massive soil mass movement both in the form of debris flow and landslide. In many occurrences of debris flow or landslide, rain contribution can be in the form of heavy rain (commonly expressed in rain intensity, in mm/h), or relatively long rain (which is expressed in time unit of hour). Depending on the characteristic of soil mass movement, usually defined as soil mass stability (function of mass density, shear strength characteristic, soil water content, soil embankment shape, etc.), the rain intensity and duration will trigger the process of debris flow occurrence.

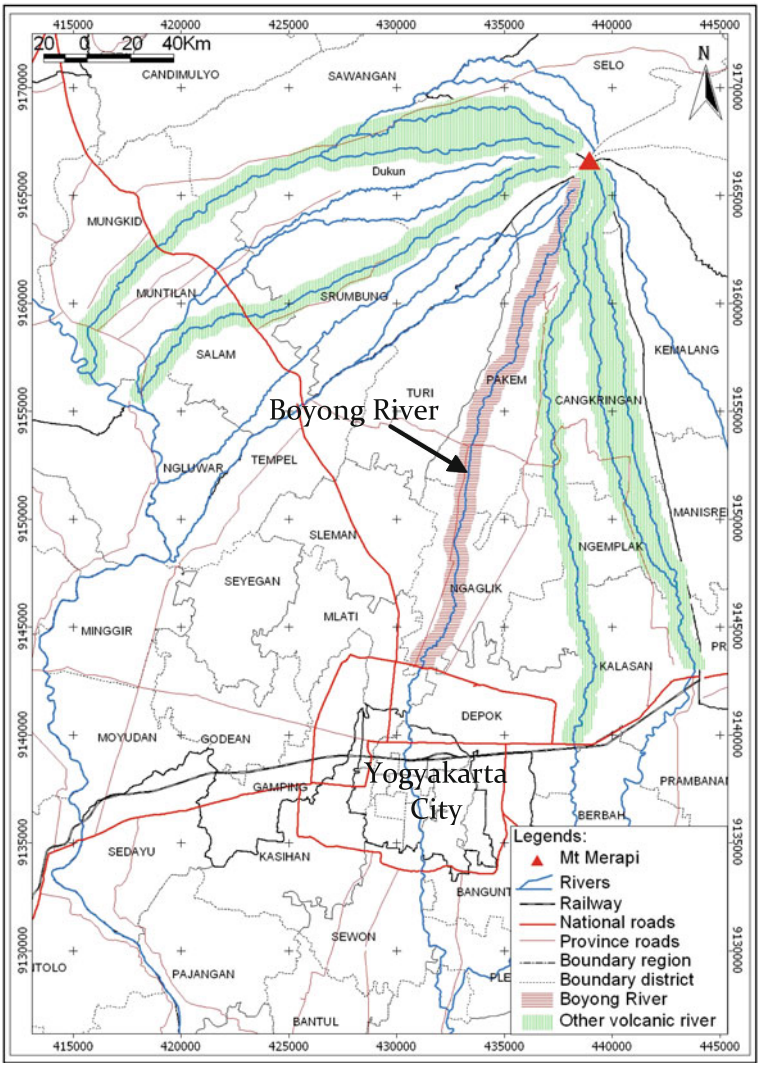

Fig. 4 Volcanic rivers toward southern and western part of Mt. Merapi which have potential impact of debris flow. Boyong River is directed toward Yogyakarta City and change the name to Code River

Three different approaches might be used to develop criteria of debris flow occurrence as described by MLIT (2004), i.e. based on the information of relationship between the rainfall intensity and rainfall accumulation, rainfall intensity and antecedent rainfall, and rainfall intensity and the soil moisture. As an illustration, before 2010 Mt. Merapi eruption, the criterion used as a sign of possibility of debris flow occurrence in the upstream of volcanic rivers at Mt. Merapi area was rainfall with intensity of 25 mm/h (Takahashi 1991) or 50 mm/h with the duration

Fig. 5 Upstream condition of Boyong River: Sabo dam BOD4 on 14 January 2011

of more than 2 h (Legono et al. 2008). However, at the present, after the 2010 Mt. Merapi eruption, the criterion changes due to the position of the sediment, in which instability increases significantly due to a large number of very loose granular materials forming a very steep slope formation upstream. Such condition may cause debris flow occurrence even in rainfall intensity of less than 50 mm/h and duration of less than 2 h. Based on two events on lahar flow occurrence at Kali Putih on 9 January and 23 January 2011, the rainfall intensities at upstream were 9 mm/h for 2 h duration and 40.9 mm/h for 2 h duration.

In order to obtain historical and real-time information, the rainfall monitoring should show rainfall intensity value in mm/h. Similarly for debris flow, as the wave propagation of debris flow is very fast (e.g. 3–5 m/s order), the monitoring of water elevation in stream should have very high accuracy, e.g. at 1.00 cm, with a reliably short frequency, e.g. every 10 s, particularly if such equipment is dedicated for the development of early warning system.

As the flow monitoring system will be transferred into discharge information (in volume units per unit time), the rating curve establishment, which represents the correlation between the water depth and the discharge, should be conducted and updated periodically. The necessary calibration is a part of "rule of thumb" of each system development; therefore, it is an obligatory requirement.

Fig. 6 Downstream condition of Code River: Jogoyudan area in the Yogyakarta City on 30 November 2010

4 Early Warning System Against Debris Flow

At the moment, the development process which considers reliable sustainability is the involvement of community participation in a form of highly local self-assessment, planning and action (Wisner 2006). In this development of debris flow early warning system, a collaborative-based process is introduced (Legono et al. 2011b). Although it is similar to community involvement process, the term "collaborative" is used to emphasize that community together with local government should be involved in solving a problem, i.e. debris flow early warning.

The collaborative-based debris flow early warning system of Boyong/Code River was developed with the following process.

(a) Public consultation meeting on Boyong/Code River debris flow (the people living along the Code River requested information on debris flow occurrence).
(b) Determination of key persons (hereinafter referred as focal point: FP) whose task is to receive the earliest news on debris flow phenomenon by SMS blasting.
(c) Construction and installation of integrated monitoring equipment (water elevation sensor, pendulum, camera interval) and its socialization to focal points.

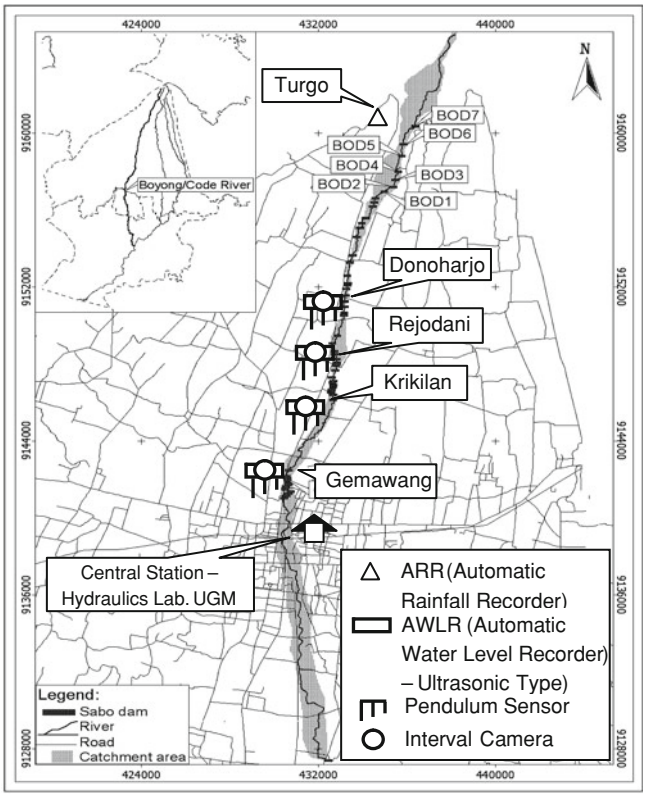

Fig. 7 The proposed location of the instrument for debris flow monitoring and warning system at Boyong/Code River

Figure 7 shows the proposed location of the instrument for debris flow monitoring and early warning, i.e. one real-time Automatic Rainfall Recorder (ARR) at Turgo, four sets cross-sectional monitoring system (comprising one real-time Automatic Water Level Recorder-AWLR, one real-time debris sensor, one interval camera) at Donoharjo, Rejodani, Krikilan, and Gemawang. A central station was set up in the Hydraulics Laboratory, Department of Civil and Environmental Engineering of Universitas Gadjah Mada which further addresses in maintaining the sustainability of the system.

Figure 8 shows the information flow of the proposed early warning system. Rainfall station in Turgo and cross-sectional monitoring system in four locations along Boyong River will transmit the result of real-time monitoring to the central station. In addition, the central station also receives information through radio communication from the focal points who monitor debris flow visually. After analyzing the received data, the central station then sends a warning alert to focal points located along Boyong/Code River and to the debris flow monitoring radio of 149.940 MHz. This warning can be sent automatically by the system or trigged

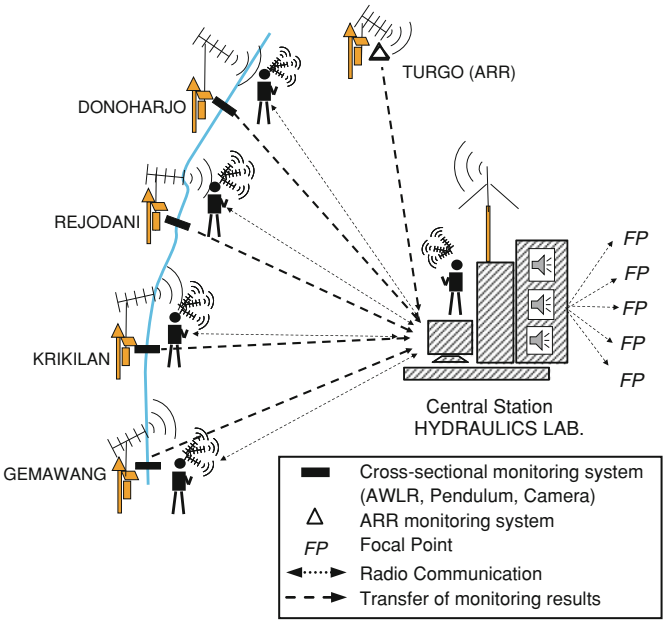

Fig. 8 Proposed information flow for monitoring and early warning of debris flow at Boyong/Code River

manually by the operator. The system built in Boyong/Code River is expected to be integrated with the monitoring system of other volcanic rivers at Mt. Merapi area.

Figure 9 shows the current warning system pursued by the community at surrounding Code River. The community living near the river has tried to carry out debris flow monitoring with the simplest way. Based on the previous experience, "caution" and "evacuation" elevation are marked on the river slope protection; hence, they can decide the right time to evacuate. The presence of integrated debris flow early warning system indeed helps the community to increase their awareness and preparedness in facing the disaster.

As shown in Figs. 7 and 8, the ideal version of early warning system against debris flow in Boyong/Code Rivers may comprise water level monitoring system at four locations, i.e. Donoharjo, Rejodani, Krikilan, and Gemawang, and provide with the pendulum type sensor to confirm the high degree of flow, i.e. the flow depth equal to 1.50, 2.25, and 3.00 m. In addition, one additional interval camera was also installed to confirm the flow occurrence visually. The sequence of alert should be arranged in such that the debris flow propagation time is sufficiently long to issue the warning that gives significant benefit to community, so that they have sufficient time to take necessary actions for evacuation.

Furthermore, the establishment of collaborative-based debris flow early warning system consists of the following process:

Fig. 9 Existing community warning alert in anticipating debris flow

(a) Installation of interval camera on the river side, accompanied by the local people (the installation was witnessed by the local people who are also members of an NGO, Jalin Merapi. At the same time, local people awareness and aspirations were studied).
(b) After the installation, the data on the river flow was collected for several days, and a collaborative review of the data was then conducted (the local people saw the benefits and asked for a higher specification, not the historical/logger type, but the real-time one).
(c) The development and installation of equipment were carried out taking into account community aspiration, at least types and locations (the local people showed the best location for the installation. Also, due to the necessity on the early debris flow monitoring, the local people avail facilities such as electricity accessibility and key-persons for the socialization of the equipment function and their maintenance).

Due to the insufficient budget, only the Automatic Rainfall Recorder (ARR) in Turgo and the Automatic Water Level Recorder (AWLR) in Rejodani were then established in the beginning of 2011. Figures 10 and 11 show some readings obtained from the installed ARR in Turgo and AWLR in Rejodani, respectively.

Automatic Rainfall Recorder (ARR) in Turgo recorded rainfall intensity every 6 min in the logger and then sent the data to the central station by radio telemetry. Rainfall intensity over 50 mm/h occurring between 14:00 and 16:00 PM on 13 May 2011 can be monitored from the website (Fig. 10). With this information, focal points should increase their awareness on the possibility of debris flow occurrence in the downstream.

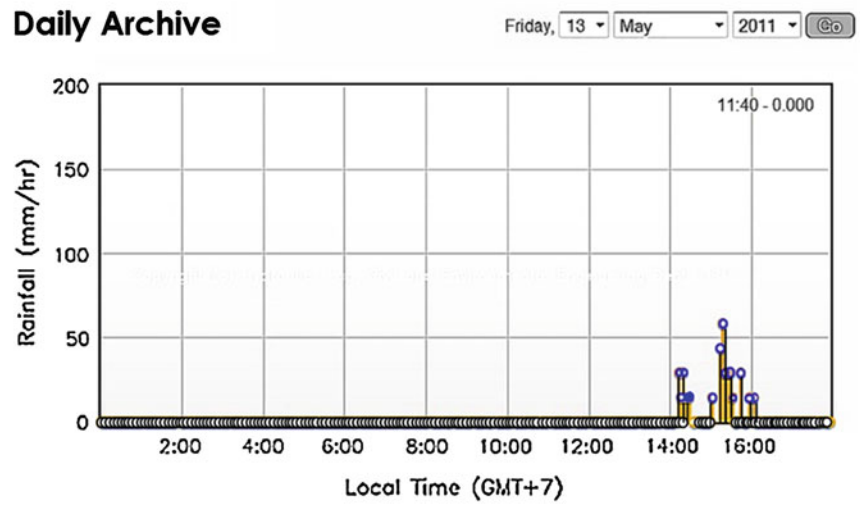

Fig. 10 Example of online reading obtained from Turgo ARR monitoring system

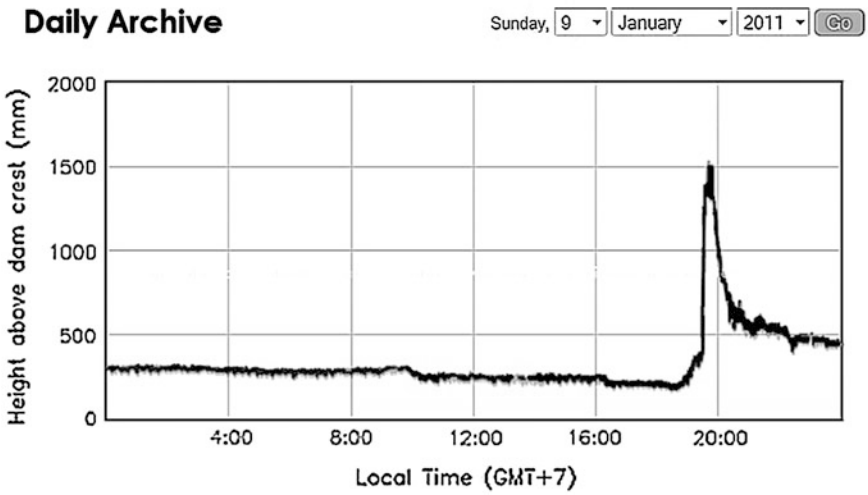

Fig. 11 Example of online reading obtained from Rejodani AWLR monitoring system

In Fig. 11, the rising of the flow monitored by the ultrasonic equipment every 15 s is shown real-time on the website. On 9 January 2011, the water elevation to dam crest rose from 39 to 130 cm in only 20 s. Further study should be carried out to determine the time needed for the debris to reach Yogyakarta City and the elevation of the flow in the downstream.

Figure 12 shows the cross-sectional monitoring system at Rejodani. Ultrasonic monitoring equipment, interval camera, and three different levels of pendulum are

Fig. 12 Cross-sectional monitoring system at Rejodani

placed in one river cross-section. This system transfers the monitoring results regularly to the central station. The whole system was built by prioritizing most adaptive and least cost technology. Through this system, a debris flow monitoring system of Boyong/Code River for community at Yogyakarta City is implemented. This monitoring system is easy to replicate for rivers threatened by debris flow disaster at the surrounding of Mt. Merapi area.

5 Conclusions

The monitoring on hydrology and hydraulic parameters (including debris flow and rainfall characteristic) should be carried out with consideration to the physical phenomenon laws of the parameters. Information from the monitoring results should be quantitative and complimentary to the existing system. Both the

historical logger type and the real-time monitoring system are necessary for further study in determining rainfall and debris flow characteristic for warning criteria. Collaborative-based debris flow early warning system is considered more sustainable as community understands the value of the information they receive. However, support from the local government is still required. More integrated and effective application in the future is still vastly needed, including completion of monitoring system along Boyong/Code River and also the integration of this system to the others debris flow monitoring at Mt. Merapi area. Further establishment of Standard Operating Procedure utilizing the established early warning system in collaboration with the local community is considered important. By this mechanism, such effort in maintaining its sustainability will be gained.

References

Legono D, Rahardjo AP, Fathani TF, Prabowo IE (2008) Development of community-based early warning system against debris flow at Mt. Merapi Indonesia. In: Proceeding of the first world landslide forum, 18–21 Nov 2008, Tokyo, Japan, pp 404–406

Legono D, Prabowo IE, Karnawati D, Fathani TF, Rahardjo AP (2011a) Lahar flow disaster monitoring and mitigation based on community collaboration. In: Proceeding of symposium Merapi, 21 Feb 2011, Yogyakarta, Indonesia pp 11–16

Legono D, Prabowo IE, Fathani TF, Karnawati D, Rahardjo AP (2011b) Development of collaborative-based lahar flow early warning system for Code River at Yogyakarta City. In: Proceeding of international seminar on water related risk management, 15–17 July 2011, Jakarta, Indonesia

Ministry of Land, Infrastructure and Transport—MLIT (2004) Development of warning andevacuation system against sediment disasters in developing countries, Guidelines for constructiontechnology transfer, Infrastructure Development Institute, Japan

Takahashi T (1991) Lahar flow—monograph. IAHR, AA Balkema, Rotterdam, The Netherlands

Wardoyo W, Legono D, Fathani TF, Jayadi R (2010) Pyroclastic deposit characteristics of volcanic rivers and its affect to the transport mechanism. In: Proceeding of IAHR-APD international seminar, 21–24 Feb 2010, Auckland, New Zealand

Wisner B (2006) Self-assessment of coping capacity: Participatory, proactive and qualitative engagement of communities in their own risk management. Measuring vulnerability to natural hazard. United Nations University Press, Tokyo, pp 316–328

Assessment of the 2004/2011 Earthquakes and Tsunamis in Indonesia and Japan: Lesson Learnt and Way Forward

Iman Satyarno

Abstract Two great of around magnitude nine earthquakes those followed by big tsunamis have happened in Indonesia on December 24, 2004 known by Aceh earthquake and in Japan on March 11, 2011 known by Tohoku earthquake. Unlike Japan, Indonesia has hardly any preparedness in terms of people capacity and tsunami countermeasure structures technology at that time, therefore the number of infrastructure damages and casualties in Aceh tsunami is very high. However, the number of infrastructure damages and casualties due to Tohoku tsunami is still considered very high too. It was noted because the current preparedness and developed tsunami countermeasure structures including the natural ones like mangrove forest or coastal vegetations did not work well during the tsunami. The lesson learnt from these two tsunamis bring to a conclusion that further studies are still required to find better and more appropriate analysis, design and applications of countermeasures structures. Currently, there are still many areas around the world which are potential to be hit by tsunami like West Sumatra province in Indonesia.

Keywords: Casualties · Evacuation · Inundation · Preparedness · Seawall · Tsunami

I. Satyarno (✉)
Department of Civil and Environmental Engineering, Gadjah Mada University, Jl. Grafika No. 2, Yogyakarta, Indonesia
e-mail: iman@tsipil.ugm.ac.id; iman_arno@eudoramail.com

F. Wang et al. (eds.), *Progress of Geo-Disaster Mitigation Technology in Asia*, Environmental Science and Engineering, DOI: 10.1007/978-3-642-29107-4_14,

1 Introduction

A 9.1 magnitude earthquake that happened in the West Coast of Northern Sumatra of Indonesia which is also known as Aceh Earthquake on Sunday, December 26, 2004 at 07:58:53 AM had shocked people all over the world reminding that a great earthquake which was followed by a big tsunami can definitely happen again. The epicentre of the earthquake was 3.316°N, 95.854°E at 30 km depth as noted by United State Geology Survey (www.usgs.gov). In Indonesia this earthquake is well known as Aceh Earthquake or Tsunami as the earthquake epicentre was close to the nearest city called Banda Aceh. According to USGS it is the third largest earthquake in the world since 1900 and is the largest since the 1964 Prince William Sound, Alaska earthquake. The impact of the earthquake and tsunami left more than 227,898 people dead with Indonesia recording the highest death toll of more than 170,000. On a global scale, the combined effect of the earthquake and tsunami were felt in more than 14 countries around south Asia and far away Africa (Kenya, Madagascar, South Africa, Somalia and Tanzania), with about 1.7 million people displaced. It is informed in January 2005 that the death toll was 286,000. Then in April 2005, Indonesia reduced its estimate for the number of missing by over 50,000. The earthquake was felt (IX) at Banda Aceh, (VIII) at Meulaboh, (IV) at Medan, Sumatra and (III–V) in parts of Bangladesh, India, Malaysia, Maldives, Myanmar, Singapore, Sri Lanka and Thailand.

Further USGS mentions that the tsunami caused more casualties than any other in recorded history and was recorded nearly world-wide on tide gauges in the Indian, Pacific and Atlantic Oceans. Saatcioglu et al. (2005) mention that the quake itself was the second strongest ever recorded since 1900, with a Richter magnitude of 9.3 noted by North-western University, though USGS suggested a magnitude of 9.1 as mentioned above. As the earthquake is caused by the rupturing of the subduction zone between the India plate and the overriding Burma micro plate with a vertical uplift of 7.0–10 m at the India plate that made a massive tsunami with wave height reaching up to 24 m. Borrero (2005) even stated that the maximum runup on the open west coast near the town of Lhoknga exceeded 30 m.

Not long after the December 26, 2004 Aceh Earthquake and Tsunami, another great 9.0 magnitude earthquake happened in eastern coast of Japan on Friday, March, 11 2011 at 02:46:24 PM, which is also known as Tohoku Earthquake. The epicentre of the earthquake was noted by USGS at 38.297°N, 142.372°E at a depth of 30 km (18.6 miles) set by location program earthquake and tsunami. Like the one in 2004, this earthquake was also followed by big tsunami so that at least 15,703 people killed, 4,647 missing, 5,314 injured, 130,927 displaced and at least 332,395 buildings, 2,126 roads, 56 bridges and 26 railways destroyed or damaged by the earthquake and tsunami along the entire east coast of Honshu from Chiba to Aomori. The majority of casualties and damages occurred in Iwate, Miyagi and Fukushima. It is noted that a maximum tsunami runup height was 37.88 m at Miyako. ERRI (2011a, b) even noted that the maximum runup might reached +40 m.

Further USGS noted that the total economic loss in Japan was estimated at 309 billion US dollars. Electricity, gas and water supplies, telecommunications and railway service disrupted and several reactors severely damaged at a nuclear power plant near Okuma. Several fires occurred in Chiba and Miyagi. At least 1,800 houses destroyed when a dam failed in Fukushima. Maximum acceleration of 2.93 g recorded at Tsukidate. Horizontal displacement and subsidence was observed. Landslides occurred in Miyagi and Liquefaction was observed at Chiba, Odaiba, Tokyo and Urayasu. The tsunami destroyed or severely damaged many coastal towns in the Kuji-Minamisanriku-Nami area. It was felt (VIII) at Fukushima, (VII) at Agui, Hiratsuka, Kiryu, Komae, Oyama, Sendai and Tsukuba and (VI) in much of eastern Honshu, including the Tokyo-Yokohama area, Japan.

The two earthquakes that followed by big tsunamis in Indonesia and Japan mentioned above have passed away, but what can we do to anticipate the near future ones. This paper discuss the lesson learnt from the two earthquakes where the two countries have different preparedness and tsunami countermeasure structures technology background. While Indonesia has inadequate preparedness and tsunami countermeasure structures at that time, Japan shall have been more advance. Moreover, it is believed that many expertises from Japan were to have had learnt much on what happen in 2004. However, in fact Japan still experienced big losses from the 2011 tsunami. Why this could have happened, are the current preparedness and tsunami countermeasure structures technology applied in Japan are still not enough? This is important to know because there are still many places around the world like West Sumatra Province in Indonesia which are susceptible to be hit by tsunami. While it is still debatable about the potential big tsunami to happen in West Sumatra, in fact the vulnerability of its infrastructure is considered very high as what has been shown in Miyagi Prefecture during March 11, 2011 tsunami. More proper and better preparedness and tsunami countermeasure structures technology shall be implemented in West Sumatra to minimize the number of infrastructure damages and casualties in case of a big tsunami does really happen.

2 Lesson Learnt from December 26, 2004 Aceh Tsunami

The tsunami that happened on December 26, 2004 has indeed caused a tremendous impact to Aceh people in terms of the number of casualties and the number of infrastructure damages. It is estimated that between 130,000 and 150,000 people of Aceh lost their lives, 370,000 missing, estimated 500,000–700,000 people were displaced, and the total damage and losses was US$ 4.45 billion or around Rp 41.4 trillion (Masyrafah and McKeon 2008; BRR and Partners 2006; Saatcioglu et al. 2005; Scheper 2006; UNICEF 2006).

According to BRR and Partners (2006), the earthquake and tsunami had caused 3,000 km of road impassable, 14 of 19 sea ports badly damaged, 8 of 10 airports and airstrips damaged, 120 arterial bridges and 1,500 minor bridges destroyed.

Saatcioglu et al. (2005) found that most of severely damaged buildings caused by hydrodynamic pressures generated by tsunami and impact forces induced by floating debris were non-engineered reinforced concrete structures, low rise timber frames and unreinforced masonry buildings. The damaged bridges and roads have paralysed the relief effort after the tsunami particularly the 150 km coastal Meulaboh that was washed away and the bridges on the way lost their super structures due to the tsunami wave pressure. It was also found that water supply in Banda Aceh was disrupted due to failure of water mains as most of the main pipelines were broken as they were attached to bridges to cross the rivers that pass through the city.

The high number of damaged infrastructures and casualties due to 2004 Aceh earthquake and tsunami mostly came due to the tsunami and some smaller number because of the earthquake itself (Bate 2005). The huge impacts could have happened because at that time there was inadequate preparedness and lack of tsunami countermeasure structures were introduced and implemented in this tsunami potential area due to the following factors.

1. The people had inadequate capacity and education to face such big tsunami as some resident were attracted by a large amount of fish trapped on the seabed when the sea withdrew from the land up to 1.5 km and they were unable flee the ensuing tsunami (Bate 2005).
2. There was hardly any tsunami early warning system along the coast areas so that very few people in Banda Aceh realised that a large tsunami had occurred until after the inundation (Bate 2005).
3. There was hardly any tsunami countermeasures structure such as tsunami seawalls and vertical evacuation structures were built in the coast areas, see Fig. 1.
4. People density was higher in the areas closer to the coast.
5. Hardly any infrastructure was designed to consider loads caused by such big tsunami hydrodynamic pressure.

Currently the daily life of people in Aceh has been back to normal and almost no sign of damages and ruins can be seen. Some monuments of damaged infrastructures have been preserved as shown in Fig. 2 as memorial signs to keep reminding the people about the big earthquake and tsunami that might come again one day in the same place or in other places in other time. A tsunami research centre like TDMRC (Tsunami and Disaster Mitigation Research Centre) has been established by the local Syiah Kuala University in Aceh. Its building has vertical evacuation facilities, as shown in Fig. 3. However, it is felt that much more works must be carried out in Aceh to minimise the impact of future earthquake and tsunami, especially when it is learnt from 2011 Japan earthquake and tsunami discussed below.

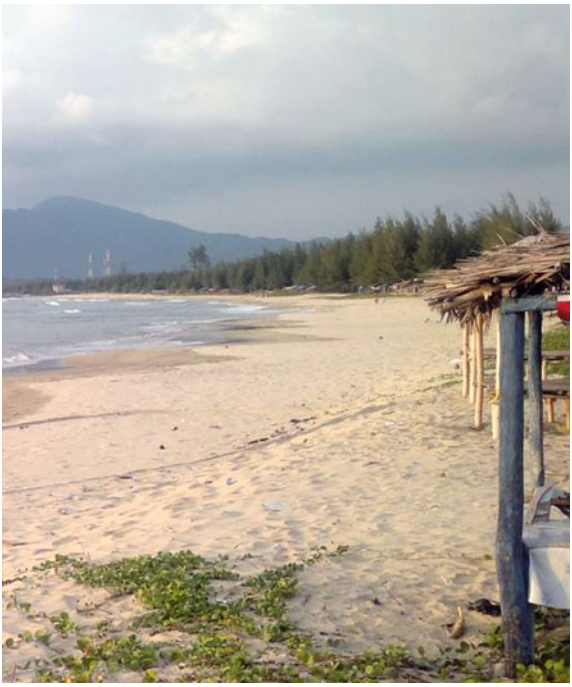

Fig. 1 Hardly any tsunami countermeasure structures like tsunami seawall can be found in Aceh coast

Fig. 2 Current situation of a ship on top of a building as a monumental sign

Fig. 3 Tsunami and Disaster Mitigation Research Centre (TDMRC) established after 2004 earthquake and tsunami where the building is made as a vertical evacuation structure

Fig. 4 Washed out community houses in Yuriage

3 Lesson Learnt from March 11, 2011 Tohoku Earthquake and Tsunami

ERRI report (2011a, b) mentions that current loss estimates in March 11, 2011 Tohoku earthquake and tsunami indicate 22,626 persons were killed or missing nationwide of which 15,534 are confirmed deaths, 107,000 buildings collapsed and another 11,000 partially collapsed that also includes government buildings, emergency centres, hospitals, and other emergency facilities such as the nuclear power plants. Some of the washed houses and damaged buildings caused by this tsunami can be seen in Figs. 4 and 5. More over there are many infrastructures such as road, bridge, airport, and sea port damaged due to the tsunami.

The highest casualties happened in Ishinomaki which was 5,867 or 3.7 % of its 160,700 population perished due to the earthquake and tsunami (EERI 2011). In fact, the community had actually high levels of tsunami awareness, pre-disaster mitigation including structural works and preparedness. However, they had

Fig. 5 Overturned building caused by tsunami hydrostatic and hydrodynamic forces in Onagawa

Fig. 6 Fixed tsunami seawall that have been overtopped during March 11, 2011 tsunami

assumed and planned for a smaller tsunami or in other words the size of the actual event overwhelmed communities pre-disaster risk reduction.

In terms of tsunami countermeasure structures technology, Japan is much more advanced than Indonesia to reduce the tsunami impact on the infrastructures and on the people themselves. Some of the following tsunami countermeasure structures (ATEP 2006–2010) may have been built or prepared in Japan.

Fig. 7 Watergate that manually or automatically closed during tsunami warning

Fig. 8 School buildings are commonly taken as vertical evacuation structures but some of them have been overtopped during tsunami inundation on March 11, 2011

Tsunami defensive structures:

1. Tsunami seawalls, as wall or curved barriers that block waves from inundating coastal areas and redirect wave energy back towards the sea, see Fig. 6.
2. Watergates, see Fig. 7 as constructions to protect against tsunami waves that can be closed manually or can begin to automatically close within second after earthquake shaking triggers its seismic sensors.

Fig. 9 The broken handrail remains in the footsteps of the overtopped high ground level designed for vertical evacuation facilities due to the March 11, 2011 tsunami

3. Tsunami breakwaters, as offshore structures that restrict the inflow of tsunami and storm waves into a harbour by narrowing the entrance.
4. Tetrapods, as one type of concrete armours unit with four legs.
5. Natural protectors like coastal vegetations of mangrove forest.

Vertical evacuation structures:

1. Elevated shelters, such as buildings which are built with some height of elevated floor to hold people during the occasion of tsunami, see Fig. 8.
2. Towers, almost the same as elevated shelters but have different shape.
3. Elevated platforms, as tsunami evacuation site where in tsunami-free times they also serve as scenic view points.
4. High ground level as shown in Fig. 9 or beam as artificial high ground to accommodate people during tsunami occasions.

Although countermeasure structures have been established in Japan, the number of infrastructure damages and casualties are still high due to March 11, 2011 tsunami. Of course, this matter need to be evaluated for developing more proper tsunami countermeasure structures in Japan itself or in other country as will discussed in the next section.

4 Discussion

4.1 Effectiveness of Current Tsunami Preparedness and Tsunami Countermeasure Structures

As mentioned above the number of infrastructure damages and casualties are still high in March 11, 2011 Japan tsunami although some tsunami countermeasure structures have been established prior to tsunami occasion. This could happen probably because the tsunami countermeasure structures have been inadequately designed quantitatively and or qualitatively.

For communities along the coast areas with potential tsunami of 20 ft or more that would be impossible to evacuate them within 20 min, FEMA P646 (2008) suggests to construct special structures called vertical evacuation structures to reduce significant loss of life. These structures shall have sufficient height to elevate evacuees and be designed and constructed with the strength and resiliency needed to resist the effects of tsunami waves and the earthquake itself.

The FEMA considers this approach after the experience of the 2004 Aceh tsunami. Some factors to be considered in constructing vertical evacuation structures are as follows:

1. the likelihood of a region being affected by a tsunami event,
2. the potential consequences of a tsunami event (e.g. damage, injury, and loss of life),
3. the elements of a local emergency response plan, including available evacuation alternatives,
4. the planned and potential uses for refuge facility, and
5. the cost of constructing a tsunami-resistance structure.

Besides the above factors, it is also required to consider the required travelling time of tsunami from its source to the community area. Based on the required travelling time of tsunami from its source to reach the community areas, FEMA P646 (2008) divides it into three categories:

1. more than 2 h for far-source-generated tsunami,
2. between 30 min and 2 h for mid-source-generated tsunami, and
3. less than 30 min for near-source-generated tsunami.

In case of near-source-generated tsunami, the vertical evacuation structures might not be effective as the community might have no time to reach the vertical evacuation structures. This is because the effectiveness of vertical evacuation structures very depends on critical available time between tsunami warning and tsunami inundation, and the level of inundation itself. These two factors can cause a big catastrophe if the vertical evacuation structures do not satisfy them. Therefore it is required to choose the appropriate locations or spacing between vertical evacuation structures so that the people can safely reach them before the tsunami inundation.

FEMA P646 (2008) suggests the maximum distance shall consider the required time of the people to reach the level in the structure to be higher than the tsunami inundation level including the time for ingress and vertical circulation in a crowded and possibly chaos situation. To achieve safe site level, it is recommended that the level of vertical structures shall be the maximum predicted tsunami runup at the site, plus 30 %, plus one storey height or 10 ft (3 m).

The vertical evacuation structures are not necessary to be new structures as they can be soil berms or naturally high existing ground, parking garages, community facilities, commercial facilities, school facilities, or existing buildings as shown in Figs. 8 and 9. Among these types of structures, the parking garages are probably the most ideal ones (FEMA P646 2008). This is because normally parking garages were built as open structures that will allow water to flow through with minimal resistance. More over they also commonly have interior ramps that will allow more than enough opportunity for entrance with easy vertical circulation to higher levels within the structures and large open area on the top level or top deck.

However, it is important to note that all tsunami countermeasure structures shall strong enough to resist the loads caused by the earthquake and tsunami, and shall have adequate height above the tsunami inundation. Therefore, it is necessary to consider the following factors in designing the tsunami countermeasures structures (EERI 2011; FEMA P646 2008).

1. Direct hydrostatic and hydrodynamic forces from water inundation.
2. Impact forces from water-borne debris.
3. Fire spread by floating debris and combustible liquids.
4. Scour and slope or foundation failure (Okamoto et al. 2008).
5. Wind forces induced by wave motion.

Among the above factors that made several tsunami countermeasure structures in general did not work well during the March 11, 2011 Japan tsunami are mostly the inadequate level (EERI 2011). However the structural damages caused by direct hydrostatic and hydrodynamic forces from water inundation and or impact forces from water-borne debris was possible as shown in Fig. 5. The ones caused by fire probably spread by floating debris and combustible liquids are also noted as can be seen in Fig. 10, while significant scour phenomena is found as can be seen in Fig. 11.

All of these tsunami countermeasure structures damages shall be further studied and evaluated for more appropriate design and application in other places or countries. This is very important because once a structure is declared as a tsunami countermeasure structure, the local community will confidentially make it as an evacuation point to safe their life during a tsunami occasion. Of course, the failure of this structure will bring to a big catastrophe, as noted that several cases of four storey buildings being overtopped in northern Sanriku coastal area (EERI 2011). Even some tsunami evacuation buildings, a hospital, and local emergency management centres were overtopped, resulting in loss of life amongst those with expectations of safety in those buildings.

Fig. 10 Three storey school building that was set on fire spread by probably floating debris and combustible liquids

4.2 Effectiveness of Coastal Vegetations such as Mangrove Forest

It is a common perception in Indonesia and may also be the same in other countries that coastal vegetations like mangrove forest can effectively protect or reduce an area from tsunami impact. However, Bate (2005) noted that mangrove forest was completely destroyed and did not reduce the impact during the December 26, 2004 Aceh tsunami. The same finding can also be noted during the March 11, 2011 Tohoku tsunami. Figure 12 shows the remains of the coastal vegetations that could not really protect the area from tsunami impact. EERI (2011) noted that tsunami mitigation forest planted along the coastline of Natori and Minamisanriku appeared to be ineffectual given the depth and velocity of the tsunami inundation. Moreover, even it was found that the tree trunks were snapped off or uprooted and became large wooden debris missiles brought inland by the tsunami that make higher hydrodynamic forces on structures.

Fig. 11 Scour phenomena around a structure's foundation in a coastal are due to tsunami

Fig. 12 Remains of coastal vegetations that did not effectively protect the area from tsunami hit

Fig. 13 An example of a vulnerable building during September 30, 2009 Padang earthquake that shall not be assigned as tsunami vertical evacuation structures

4.3 Vulnerability of West Sumatra Infrastructures

Based on the lesson learnt from December 26, 2004 and March 11, 2011 tsunamis discussed above, it now is appeared that much more studies need to be carried out to reduce the impact of tsunami. This is because some current natural tsunami protection like mangrove forest or manmade ones like tsunami seawall structures and vertical evacuation structures have not yet effectively protect an area from tsunami hit. Meanwhile, there are a number of vulnerable infrastructures in tsunami potential areas like West Sumatra province in Indonesia for instance. The location of West Sumatra with the city of Padang in the west coast of Sumatra is quite similar to the position of Aceh and Miyagi prefecture that have been badly hit by tsunami. Some of the vulnerable infrastructures to tsunami hit in West Sumatra province are as follows.

1. Buildings in Padang city, note that a quite number of them collapsed during September 30, 2009 earthquake as shown in Fig. 13. Without any thorough investigation of their actual earthquake resistance, it is not a good idea to make them as vertical evacuation structures.
2. Minangkabau Airport in the north of Padang City which is very close to the coast. Note that Sendai Airport in Miyagi Prefecture, which is the location is similar to the Minangkabau Airport, was badly smashed by the tsunami and could not operate for several time after that.
3. Port of Teluk Bayur in the south of Padang city, which is susceptible to be damaged by tsunami like the Port of Sendai in Miyagi Prefecture.

4. Roads and bridges, which are close to the coast as the main lines to enter the Padang city and to connect with the Minangkabau Airport in the north and Teluk Bayur Port in the south. The damage of these roads and bridges may paralyse the transportation into and out of Padang city.

If no appropriate preparedness and tsunami countermeasure structures are developed in West Sumatra, what have happened in Aceh in 2004 and in Tohoku in 2011 may also happen in this area in case of a big tsunami.

5 Conclusions

1. Two big tsunamis those happened in Indonesia on December 26, 2004 and in Japan on March 11, 2011 have caused a lot of infrastructure damages and casualties.
2. Lack of preparedness and tsunami countermeasure structures in Indonesia might have caused the high number of infrastructures damages and casualties due to the December 26, 2004 tsunami.
3. Although better preparedness and tsunami countermeasure structures have been developed in Japan, the number of structural damages and casualties are still considered high in March 11, 2011 tsunami.
4. Further studies need to be carried out to evaluate the current preparedness and design of tsunami countermeasure structures including the natural mangrove forest or coastal vegetation so that they can be more effective to protect an area from tsunami hit.
5. Like Miyagi prefecture with Sendai city in Japan, the West Sumatra Province with Padang City in Indonesia has vulnerable infrastructures which are susceptible to tsunami hit.

Acknowledgments I would like to thank to TDMRC (Tsunami and Disaster Mitigation Research Centre) and Syiah Kuala University Aceh for their invitation to Aceh to have a seminar and visiting some areas affected by December 26, 2004 earthquake and tsunami on December 22–24, 2011. Special thanks also to JICA (Japan International Cooperation Agency) and ICUS (International Center for Urban Safety Engineering) Institute of Industrial Science, The University of Tokyo for their invitation to visit some areas affected by March 11, 2011 earthquake and tsunami from November 24 to December 3, 2011, especially for Mr Watanabe and Mr Numada who always guided the travelling. Also thanks to New Zealand Aid Program who funded the Local Government Training for Capacity Building in Disaster Risk Management in Padang, West Sumatra on February 24–28, 2012.

References

ATEP (2006–2010) Structural countermeasures, UAF Geophysical Institute
Bate RF (2005) Assessment of Banda Aceh, Sumatra, Indonesia following the earthquake and tsunami of 26 Dec 2004, Tsunami Safe Hills 103 Etherington Road HULL, East Yorkshire HU6 7JO, United Kingdom
Borrero JC (2005) Field survey Northern Sumatra and Banda Aceh, Indonesia and after the tsunami and earthquake of 26 Dec 2004, Preliminary report prepare for earthquake Engineering Research Institute, 9 Feb 2005
BRR, Partners (2006) Aceh and Nias two years after the tsunami, 2006 progress report, United Nations, Office of the Secretary-General's Special Envoy for Tsunami recovery
EERI (2011) Learning from earthquake, the 11 March 2011, Great East Japan (Tohoku) earthquake and tsunami: societal dimensions, EERI Special Earthquake Report, Aug 2011
ERRI (2011a) Learning from earthquake, the Tohoku, Japan, tsunami of 11 March 2011: effect on structures, EERI Special Earthquake Report, Sept 2011
ERRI (2011b) Learning from earthquake, the Japan Tohoku tsunami of 11 March 2011, EERI Special Earthquake Report, Nov 2011
FEMA P646 (2008) Guidelines for design of structures for vertical evacuation from Ttsunamis, applied technology council 201 Redwood Shores Pkwy, Suite 240 Redwood City, California 94065
Masyrafah H, McKeon JM (2008) Post-tsunami aid effectiveness in Aceh- proliferation and coordination in reconstruction, Wolfensohn Center for Development at Brookings, Working Paper 6
Okamoto O, Oda K, Kumagai K (2008) Study on scour by tsunami-example of port and harbor structures. In: Fourth international conference on scour and erosion
Saatcioglu M, Ghobarah A, Nistor I (2005) Reconnaissance report on the 26 Dec 2004 Sumatra earthquake and tsunami, CAEE, The Canadian Association for Earthquake Engineering
Scheper E (2006) Impact of the tsunami response on local and national capacities, Indonesia Country Report (Aceh and Nias), Tsunami Evaluation Condition
UNICEF (2006) The 2004 Indian Ocean tsunami disaster, evaluation report May 2006. Evaluation of UNICEF's Response (Emergency and Initial Recovery Phase), Indonesia

Liquefaction Countermeasure Technique by Using Logs

Masaho Yoshida, Masakatsu Miyajima and Atsunori Numata

Abstract During 2011, Great East Japan Earthquake in Japan, extreme liquefaction caused extensive damage to residential houses in the Kanto Plain region and resulted settlements and tilts larger than that was observed during past earthquakes. This paper deals with a proposal of ground improvement technique by installing logs into loose sand layer as a soil liquefaction countermeasure for residential houses. Small-scale shaking table tests in a 1-g gravity field were carried out using some model grounds. It was clarified that the wooden pile could increase the resistance of ground against liquefaction due to the increase of ground density by piling and the dissipation of excess pore water pressure along the surface of piles. As a result, the magnitude of settlements of the house which was set on the improved ground by piling logs became quite small.

Keywords Liquefaction · Countermeasure · Shaking table test · Log · Residential house · Global warming

M. Yoshida (✉)
Department of Civil Engineering, Fukui National College of Technology, Geshi, Sabae, Fukui 916-8507, Japan
e-mail: masaho@fukui-nct.ac.jp

M. Miyajima
School of Environmental Design, College of Science and Engineering, Kanazawa University, Kakuma, Kanazawa, Ishikawa 920-1192, Japan

A. Numata
Research Institute of Technology, Tobishima Corporation, 5472 Kimagase, Noda, Chiba 270-0222, Japan

F. Wang et al. (eds.), *Progress of Geo-Disaster Mitigation Technology in Asia*, Environmental Science and Engineering, DOI: 10.1007/978-3-642-29107-4_15,

1 Introduction

Liquefaction is a phenomenon in which the strength and stiffness of a soil is reduced by earthquake shaking and causes a lot of ground failures and structural damage during past earthquakes. Therefore, various liquefaction countermeasure techniques based on soil improvement are proposed to mitigate liquefaction risk by improving the strength, density, and drainage characteristics of the soil. From this point of view, if some piles are installed into loose saturated sand layer, it is expected that the characteristics of ground may be changed as the composite ground of sand and piles.

Global warming is one of the most serious problems in this century. Because a tree can store carbon within itself, the utilization of wood in the engineering field for the carbon stock may contribute to the mitigation of global warming. As a way of extending and increasing the usage of wood, the authors consider that wood should be used in the construction project, because a huge amount of materials are used and soft ground scattered in many different locations. However, modern civil engineering constructions seem to be using lesser amount of wood compared to those in the previous times. Therefore, the authors consider that one of the most effective ways to utilize wood is installing the wood into the soft ground as a material for ground reinforcement. Generally, one of the major reasons that affect the reliability of wood is decay and insect damage. However, it is reported that decay and insect damage of wood do not occur below the ground water level (Numata et al. 2008). Because the water level in the soft ground is very high, logs can act as a pile or material for ground improvement without having to concern for decay or insect damage of wood.

The Great East Japan Earthquake in March 11, 2011 caused severe damages and loss of life. Damages observed in the Kanto Plain region, which includes the Tokyo Bay and Tone River areas, were dominated by the effects of liquefaction-induced ground failures. Liquefaction-induced damages were observed around the northern shorelines of Tokyo Bay and at communities along the Tone River. Liquefaction caused extensive damage to light residential structures in many of these areas and resulted settlements and tilts larger than that was observed during past earthquakes. The authors proposed a ground reinforcement technique by piling logs into loose saturated sand layer as a countermeasure against liquefaction. This technique has advantage to be applied for the residential house which has narrow space around structure because this technique does not need large construction equipment.

In this paper, a series of small-scale shaking table tests were conducted in a 1-g gravity field in order to evaluate the performance of this technique in liquefiable sand layers during an earthquake. From the test results, it was confirmed that the ground improvement by piling logs could be treated as one of the countermeasures to restrain the magnitude of settlements and tilts for the residential houses.

Photo 1 Settlement and tilt of residential house in Chiba city

2 Structural Damage Due to Soil Liquefaction

Liquefaction during earthquakes induces such damage of existing structures as uplift or settlement, depending on the weight of structure. It is very important to mitigate damage occurring by liquefaction to take some countermeasures against vertical displacement. Liquefaction caused extensive damage to light residential and light commercial structures with the magnitudes of the settlements and tilts during the 2011 Great East Japan Earthquake as shown in Photo 1 taken in Chiba city. Many of these structures use mat-type foundations with limited damage of superstructures; however, the large settlement of 50 cm over and tilt of 5 % over. Photo 2 shows the uplift of manhole in Urayasu city. The manhole was lifted up to 1 m and settlement of surrounding pavement was at most 30 cm. Liquefaction-induced damage to utilities caused widespread disruptions for homeowners.

While those of damage were observed in many places, a structure supported by wood piles which was not damaged by soil liquefaction was existed in devastated area during the 2011 Great East Japan Earthquake. Photo 3 shows a sedimentation basin of Hebita Purification Plant in Ishinomaki city. Though liquefaction occurred around the structure, the settlement and tilt of the basin were not observed. As a result of site investigation, it is clarified that this basin was constructed in 1969 supported by wood piles. About 900 pine logs measured 15 mm diameter and 3000 mm long were piled at the interval of 900 mm for the foundation of this basin. It seems that this is the evidence that wood pile is applicable to the liquefaction countermeasure technique.

3 Retrieving Wood Piles from Ground

Photo 4 shows Kida Bridge across the Asuwa River that flows in Fukui city, Japan. The bridge was completed in December, 2008. It can be seen that there are a lot of head of piles made of wood in the riverbed near piers. These wood piles were used

Photo 2 Uplift of manhole and settlement of pavement in Urayasu city

Photo 3 Sedimentation basin of the Hebita purification plant in Ishinomaki city

Photo 4 Former wood pile foundations near Kida Bridge

as foundations of the former Kida Bridge which was completed in 1949. It is assumed that they were placed underneath the riverbed through 59 years (Yoshida et al. 2009).

Photo 5 shows the wood pile which was retrieved from Kida Bridge. The length and diameter of the pile was about 3.5 m and 30 cm, respectively. By using optical

Photo 5 Wood pile retrieved from Kida Bridge

microscope, it was clarified that the species of wood pile is Japanese cedar (*cryptomeria*). According to the visual observation, it is assumed that the top of the pile was stuck up out about 1 m from the riverbed, because the area between about 1 m from the top had a mark that water scraped the surface of the wood pile. The wood pile was in the gravelly sand and clay layer, and the bottom of the pile was assumed to reach sandy silt layer or sand layer by referring to a borehole data near this site.

4 Investigation for Soundness of Wood Piles

4.1 Visual Observation Test

Figure 1 shows a result of visual determination method of decay level according to JIS K 1571:2004 (Yoshida et al. 2007). Three evaluators of A, B, and C were observed and were considered the decay level referring to the standard shown in the figure. The positions of riverbed and water level presumed by site investigation are also shown in the figure. Because the decay level was one or less under the riverbed, it is confirmed that wood pile can keep soundness in the soil under the water level.

4.2 Pylodin Penetration Test

Figure 2 shows a result of the penetration test by using a Pylodin which can examine the level of decay (Yoshida et al. 2007). The Pylodin was a device to compare the depths of penetration by a pin stricken with a certain force. If the level of decay is high, the surface of wood become soft and the depth of penetration

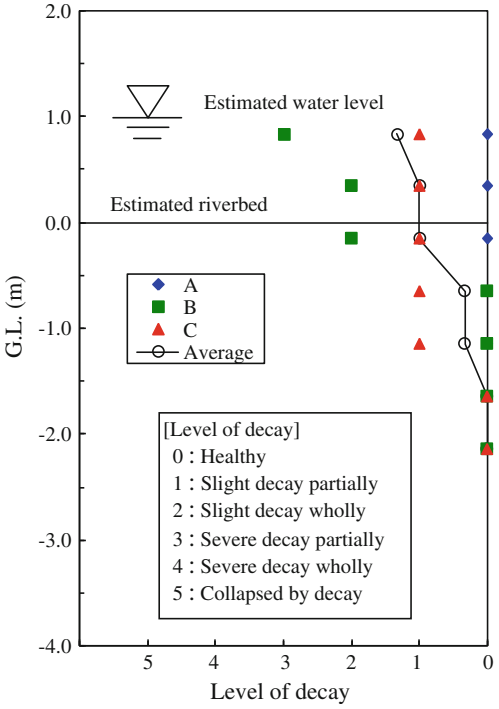

Fig. 1 Results of visual observation test

become large. The standards of decay are considered that the depth of penetration is 30 mm or more. The shape of the test piece was a discoid by cutting out the wood pile and the thickness of the piece was 10 cm. The penetration tests were conducted on two sides of wood piles. One was the side of cut end and the other was the orthogonal side of cut end. Although the values vary widely at the same ground level as shown in Fig. 2, it is clarified that the wood piles keep health because most of the average values were less than 30 mm.

4.3 Compression Test

Figure 3 shows a result of compression test according to JIS Z 2101:1994 (Yoshida et al. 2008). The size of the test piece was 30 mm^2 and 60 mm in height, and they were made by cutting out the discoid which was used for the Pylodin penetration test. The standard compression strength of Japanese cedar and allowable stress used for the design of wood pile foundation are also shown in the figure. It is considered that the test pieces are three to five times the strength of the allowable strength.

Therefore, it is clear that the wood piles made of Japanese cedar that had been buried in soil under the water through 59 years did not decay and still had enough

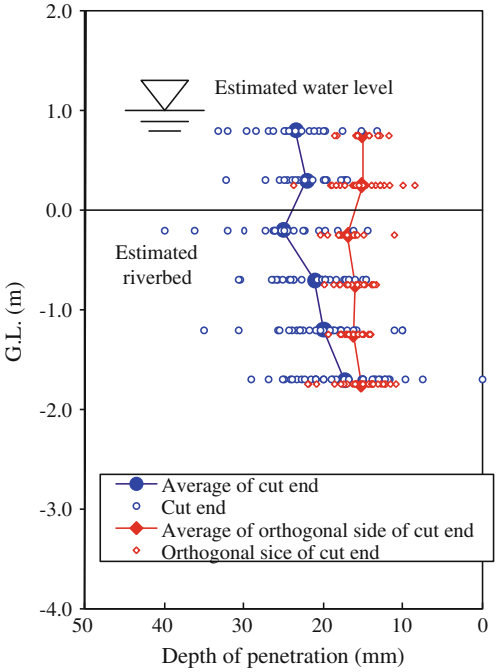

Fig. 2 Results of pylodin penetration test

strength as a pile foundation. In the past, pines have been often used as wood pile in Japan. Because civil engineers usually use pine for pile now, it is very valuable evidence that Japanese cedar used to be used as pile foundation and existed in the ground with no decay. On the other hand, some physical damage and minor decay were found on the top part of the piles where the pile was stuck up out from ground. It means that the wood including Japanese cedar can be used as a construction material in the ground under the water level for at least more than 50 years. Therefore, civil engineers should consider using wood as a construction material instead of steel, concrete or other artificial chemical materials for the future, under the condition that the wood is in the soil under the water level.

5 Shaking Table Test to Clarify Effectiveness of Installing Logs into Liquefiable Ground

Figure 4 illustrates the cross-sections of top and side view of a model ground with locations of transducers (Yoshida et al. 2008). The model ground was set up in a rigid acrylic container that measured 800 mm long, 400 mm wide, and 540 mm high. The tests were conducted by using a composite ground which consists of two parts. One was improved area that model of logs made of Japanese cedar got by thinning in Fukui prefecture were installed in loose sand layer which was shown in

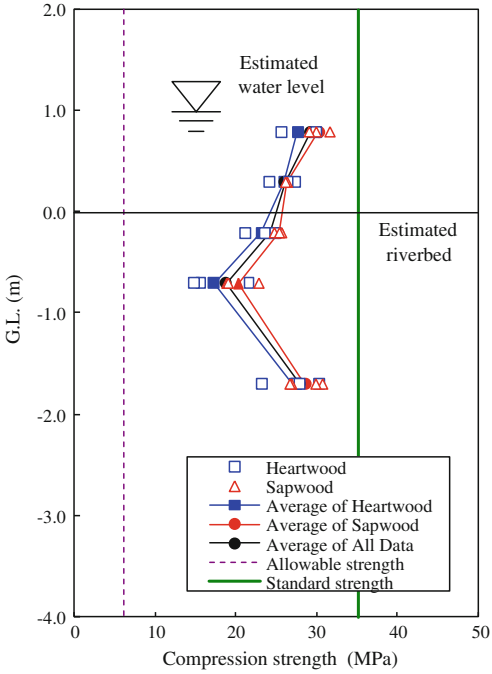

Fig. 3 Results of compression test

left side of Fig. 4 and the other was an unimproved area. The loose liquefiable sand layer was made of silica sand No.7 and the relative density was about 35 %. The physical properties of sand are listed in Table 1. The model of log made by scaling down 1/25 of the wood pile of Kida Bridge and measured 12 mm diameter and 220 mm length.

The shaking table tests were conducted as follows: (1) Pore water pressure transducers were installed at the locations as shown in Fig. 4. (2) The container was first filled with water up to 300 mm high from the bottom. Then a sieve with a 2 mm mesh was moved back and forth below water surface, pouring wet sand through water to form a uniform sand layer with 300 mm thick. (3) Excess water above the sand layer was soaked up so that the water surface was leveled with the surface of the sand layer. (4) Accelerometers were installed at the locations as shown in Fig. 4. (5) Thirty-six logs of 20 mm long were installed into the loose sand layer slowly with an interval 30 mm, except the top of log. (6) No. 5 gravels were laid over the loose sand layer with 20 mm thick. (7) The model ground was shaken in the horizontal direction with the sinusoidal wave of 100 gal in peak amplitude, 5 Hz in frequency, and 5 s in duration time as shown in Fig. 5. The pore water pressures and the response accelerations were recorded simultaneously on the data recorder. (8) After the excess pore water pressure had completely dissipated, the vertical displacements of logs and ground surface were measured by a point gauge. (9) The processes of (7) to (8) repeated five times with different amplitude which was 100–180 gal at the intervals of 20 gal.

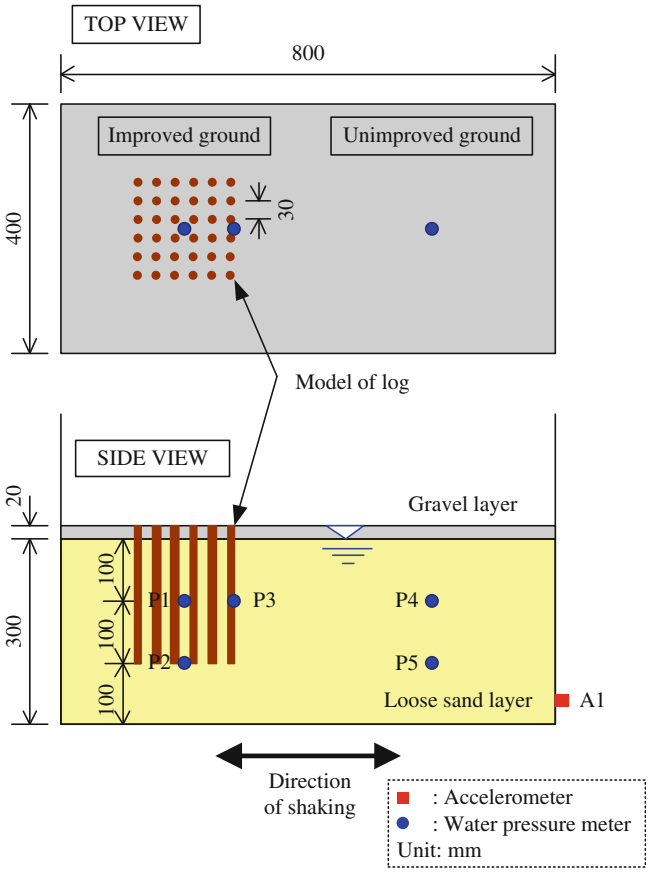

Fig. 4 General view of model ground and transducers

Table 1 Physical properties of sand

Density (g/cm^3)	Average diameter (mm)	Coefficient of permeability (cm)
2.63	0.17	4.79×10^{-3}

Figure 6 shows time histories of excess pore water pressure ratios located at 100 mm deep from the ground surface after undergoing shaking of 120 gal. In case of unimproved ground, the excess pore water pressure ratio reached 1.0 and the ground completely liquefied. However, in case of improved aground, the maximum value of excess pore water pressure ratio decreased, and the velocity of dissipation was extremely fast.

Figure 7 shows the accumulation of settlement in soil layer. The settlement ratio is defined as a vertical displacement of soil layer divided by initial thickness

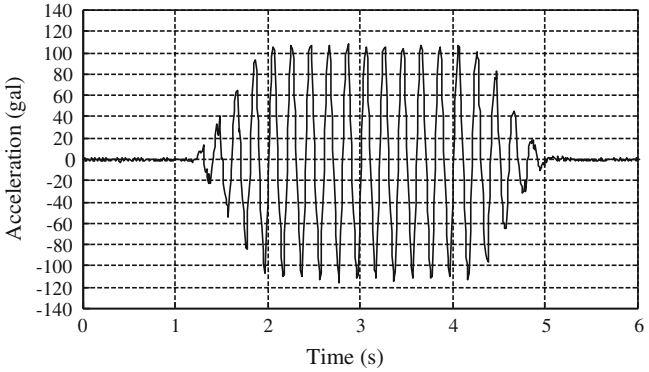

Fig. 5 Time history of input acceleration

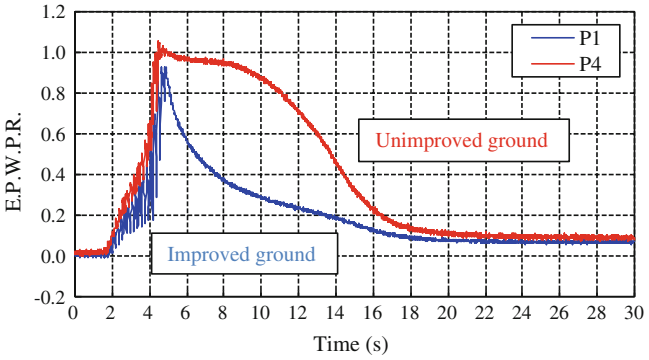

Fig. 6 Time histories of excess pore water pressure ratio

of the ground, and the residual vertical displacement was accumulated after fifth shaking. The negative value in the figure means upheaval of ground. Though the settlement became about 60 cm after fifth shaking in unimproved ground, the upheaval occurred due to the floatation of logs.

Accumulated vertical displacement of logs at the left, center, and right part of the improved area after fifth shaking is shown in Fig. 8. All of the displacement means flotation of logs. It is clear that the flotation occurred because the input acceleration exceeded 140 gal. The flotation of logs in the center part enclosed with a lot of logs was less than that in the outer part of improved ground. It seems that the flotation of logs caused the upheaval of ground in the improved area.

It is clarified that the resistance against soil liquefaction increased by installing the logs into the loose sand layer. It is considered that the resistance was caused by the following four effects: (1) replacing the loose sand with logs, (2) densifying the

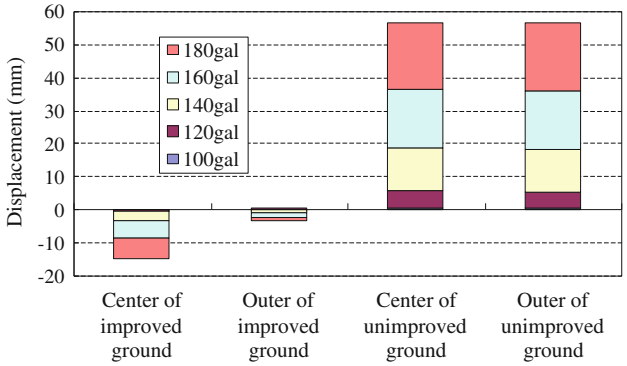

Fig. 7 Vertical displacement of ground surface

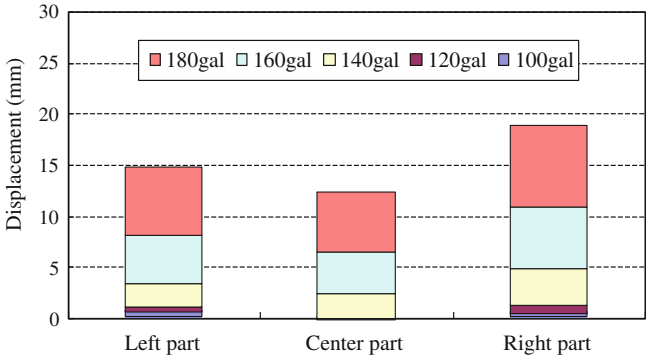

Fig. 8 Vertical displacement of logs

loose sand by installing the log, (3) restraining the shear deformation by fixing the top of logs into gravel layer, and (4) dissipating the water pressure along the periphery of logs.

6 Shaking Table Test to Clarify Effectiveness as Bearing Pile of Structure

Figure 9 illustrates cross-sections of top and side view of a model ground with locations of transducers (Yoshida et al. 2009). The container and sand were same as Fig. 4. The tests were conducted by using a composite ground which consists of

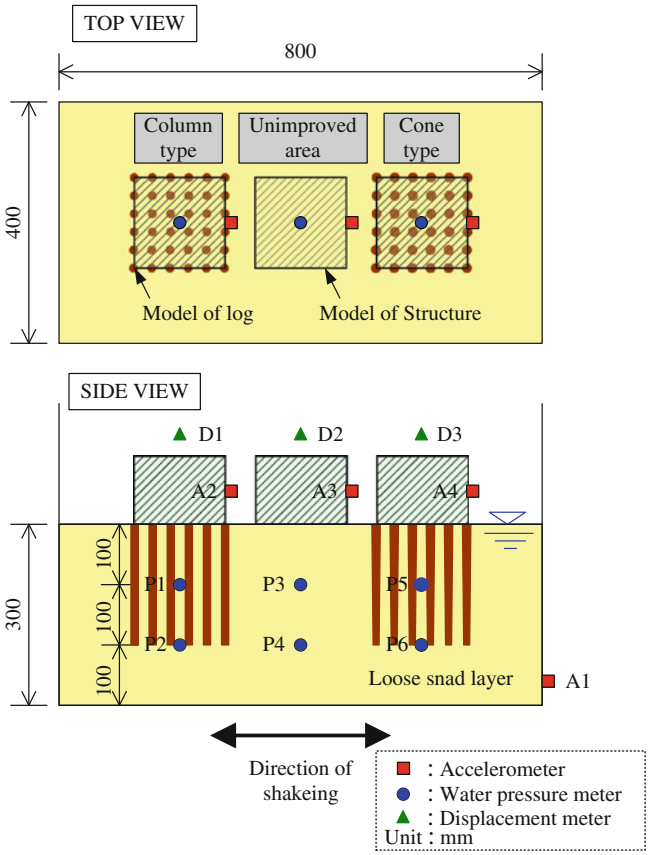

Fig. 9 General view of model ground and transducers

three parts. The left part was improved area installed by column type logs, the right part was also improved area installed by cone type logs, and the center part was unimproved ground. The shape of cone-type log was copied from real wood pile. The model of log in case of the column type measured 12 mm diameter and 200 mm long. The diameter of top was 14 mm and the bottom was 10 mm in case of cone type. The volume of both the models were the same. The underside of structure model was 150 mm^2 and the weight was 6000 g.

The shaking table tests were conducted as follows: (1) Pore water pressure transducers were installed at the locations as shown in Fig. 9. (2) The container was first filled with water up to 300 mm high from the bottom. Then a sieve with a 2 mm mesh was moved back and forth below water surface, pouring wet sand through water to form a uniform sand layer with a thickness of 300 mm. (3) Excess water above the sand layer was soaked up so that the water surface was

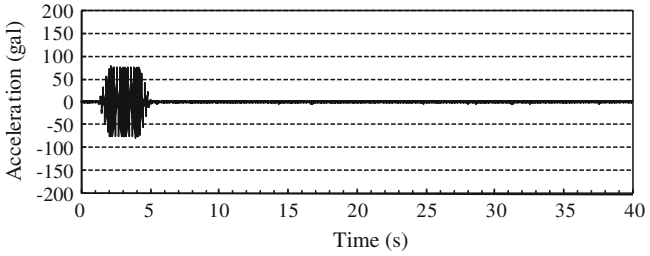

Fig. 10 Time history of input acceleration

leveled with the surface of the sand layer. (4) Thirty-six logs were gradually installed into the loose sand layer with an interval 30 mm. (5) The models of structure were placed over each area. (6) Accelerometers and displacement meters were installed at the locations as shown in Fig. 9. (7) The model ground was shaken in the horizontal direction with the sinusoidal wave of 80 gal in peak amplitude, 5 Hz in frequency, and 5 s in duration time as shown in Fig. 10. The pore water pressures and the response accelerations were recorded simultaneously on the data recorder. A vertical displacement of structures was also measured by a laser displacement meter. (8) After the excess pore water pressure had completely dissipated, the vertical displacements of logs and ground surface were measured by a point gauge. (9) The processes of (7) to (8) repeated three times with different amplitude which was 60–100 gal at the intervals of 20 gal.

Figure 11 shows the time history of excess pore water pressure located at 100 mm deep from ground surface after undergoing shaking of 80 gal, and the result of comparing the column-type log, unimproved ground, and the cone-type log. Figure 12 also shows the time history of settlement of model structures in the same case. The excess pore water pressure reached maximum value after 2 s when the shaking began. It seems that the ground did not liquefied because the pressure did not reach the effective overburden pressure of 3.4 kPa. However, the pressures decreased rapidly after indicating the maximum value and increased again. The start time of this phenomenon correspond to the settlement of structure model as mentioned below. The settlement of structure model started when the excess pore water pressure reached maximum value and it stopped with the end of shaking in the case of improved ground. However, the settlement of the unimproved ground increased continuously until the pressure completely dissipated. It is confirmed that the settlement of structure was mitigated due to the friction of logs eve if the ground softened by generating the excess pore water pressure. Moreover, it seems that the effect of cone-type log was relatively low as compared to the column-type log. It is considered that the cone-type log has the advantage of the area of facing the ground. However, because the excess pore water pressure generated in the ground dissipated from the lower layer of the ground toward the upper layer, the dissipation time of column-type log which had small drainage area became longer than the column type.

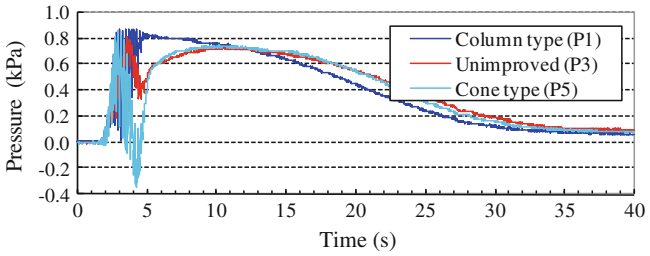

Fig. 11 Time history of excess pore water pressure

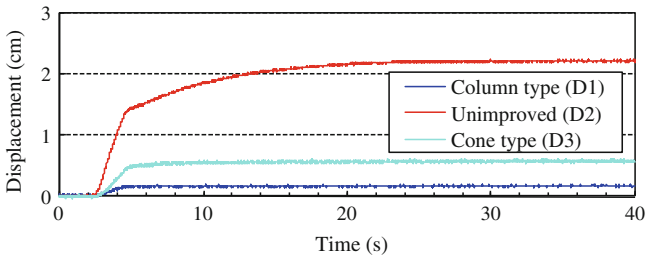

Fig. 12 Time history of settlement of structure model

7 Shaking Table Test to Clarify Effectiveness Against Long Duration of Shaking

To investigate the relation between the duration time of shaking and settlement of house, shaking table tests were conducted using the model ground. Figure 13 illustrates cross-sections of top and side view of a model ground with locations of transducers. The container, materials, and the way to make model ground were similar as shown in Chap. 14. The tests were conducted by using a composite ground which consists of two parts. One was improved ground where thirty-six logs were installed which was shown in left-side of Fig. 13 and the other was unimproved ground. The density of loose liquefiable sand layer was controlled from 40–60 % by preliminary shaking using 300 sinusoidal waves with a frequency of 5 Hz, whose amplitude was 100 gal. A model of log was measured 12 mm diameter and 200 mm long. A model of house was made by water-resistant wood that measured 150 mm^2 and 112 mm high. The ground contact pressure of house was 1.5 kN/m^2 which was scaled down one-tenth of two-story wooden house with a mat foundation. Input wave used in the tests was sinusoidal wave

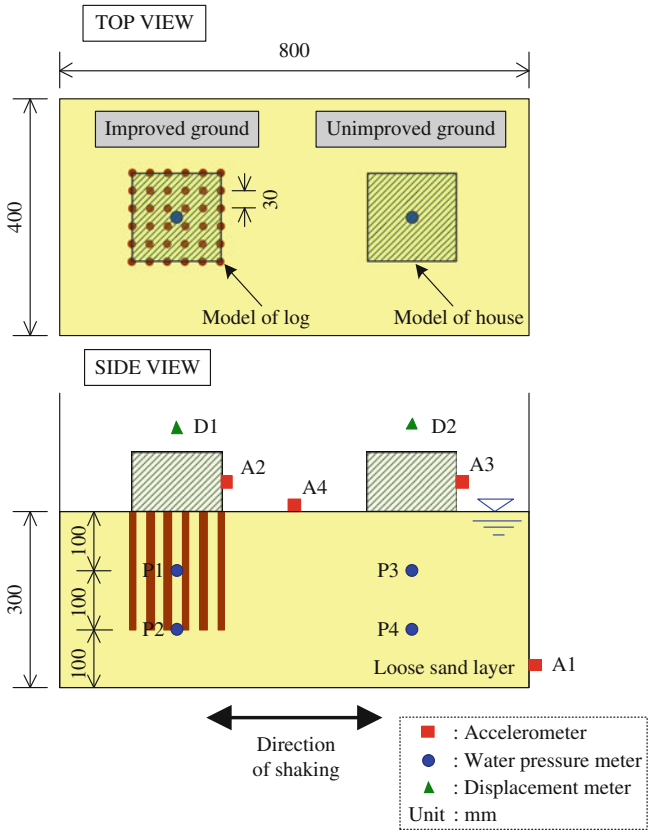

Fig. 13 General view of model ground and transducers

with a frequency of 5 Hz and a peak magnitude of 120 gal. The duration time of shaking was 10, 30, and 60 s.

Figure 14 shows residual settlement of house in relation to the duration time of shaking. It is obvious that the settlement of house increased with increase of shaking time in case of unimproved ground, but the settlement was reduced about one-twentieth in case of the improved ground though the duration time was 60 s. In the previous study (Yoshida et al. 2010), it is clear that bearing the capacity of ground where logs were installed could be improved due to densifying the loose sand around logs, dissipating the water pressure along the periphery of logs and restraining the shear deformation by composite ground with soil and wood in addition to skin friction of log. According to the results as previously described, it

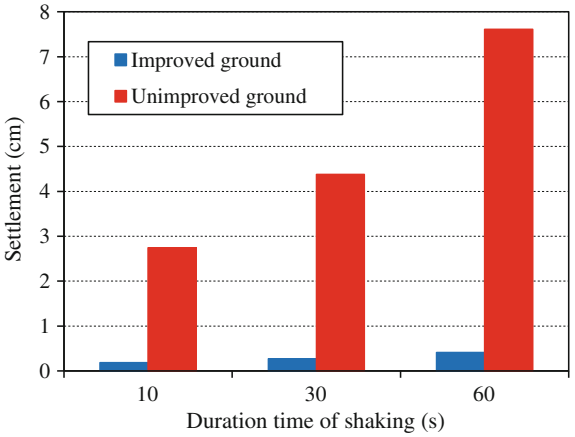

Fig. 14 Relationship between duration time of shaking and settlement of house

is considered that these effects would be expected even if the duration time of shaking might increase.

8 Shaking Table Test to Investigate How to Apply Log Pilling for Existing House

To propose how to apply the technique of log pilling for existing house, shaking table tests were conducted using the model ground. Figure 15 illustrates cross-sections of top and side view of a model ground with the locations of transducers. The container, materials, model of house, and the way to make model ground were similar as shown in Chap. 14. A model of log measured 12 mm diameter and 300 mm long. Four types of ways to install logs were adopted in this study. Case 1 was the ground without installing logs. In Case 2, the logs were installed around the foundation of house. The top and bottom of log did not be fixed. In Case 3, the top of logs were fixed. In Case 4, the logs were installed into the ground with an inclination of 15°. The relative density of loose sand layer was about 40 %. Input wave used in the tests was sinusoidal wave with a frequency of 5 Hz and a peak magnitude of 120 gal. The duration time of shaking was 20 s.

Figure 16 shows the time histories of settlement of house. It is clear that the log pilling around the foundation of house (Cases 2, 3, and 4) was effective to reduce the settlement of house as compared to the unimproved ground (Case 1). Though most settlement in all cases occurred during shaking, the settlement stopped with the end of shaking in case of improved ground. The most effective way was Case 4 and the settlement was reduced to about one-third of unimproved ground. If the

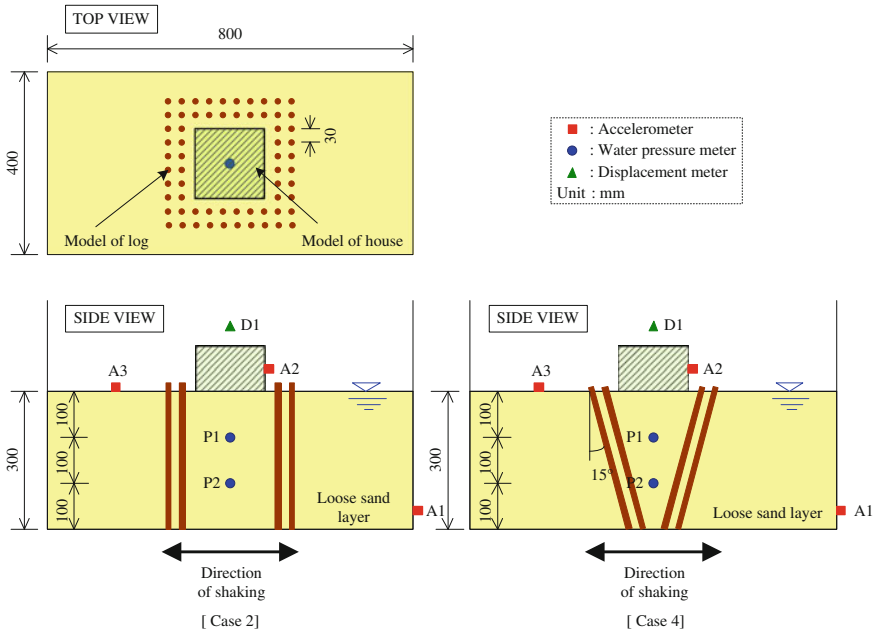

Fig. 15 General view of model ground and transducers

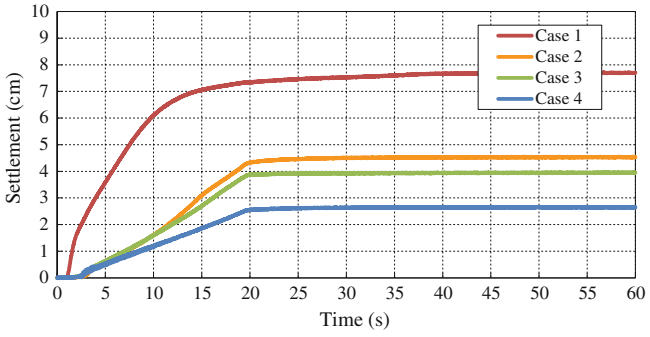

Fig. 16 Time histories of settlement of house

ground liquefies below the base of house, the house settles and the liquefied soil moves laterally. Therefore, the logs around the foundation of house can prevent the lateral movement of soil. This function was more effective by fixing the top of logs in Case 3. Furthermore, it is confirmed that the most effective way to install logs was Case 4 because the deformed area could be smaller by installing logs with the inclination.

9 Conclusions

The three kinds of test were conducted in order to evaluate the soundness of former wood used as the pile of bridge in the soil under the water level. Furthermore, a series of shaking table tests were conducted in a 1-g gravity field in order to evaluate the performance of the logs installed in liquefiable sand layers during earthquakes and to propose the liquefaction countermeasure technique by log piling for residential houses. The following conclusions may be made on the basis of the experimental study:

1. The level of decay of the wood pile made of the Japanese cedar which was retrieved from the riverbed was very low, and they have kept the soundness as the wood pile even though they were buried in the soil under the water level for 59 years.
2. The logs installed in the liquefiable soil layer could increase the resistance of ground against liquefaction. This effect was caused by the following four effects: (1) replacing the loose sand with logs, (2) densifying the loose sand by installing the log, (3) restraining the shear deformation by fixing the top of logs into gravel layer, (4) dissipating the water pressure along the periphery of logs.
3. The bearing capacity of ground where logs were installed would be expected due to the skin friction of logs even if the duration time of shaking might increase.
4. The log pilling around the foundation of house was effective to reduce the settlement of house. The most effective way was to install logs with the inclination because the deformed area below the house could be smaller.

Acknowledgments The authors wish to thank the students who were graduated from Fukui National College of Technology for their cooperation in experiments. This research was partially supported by the Ministry of Education, Culture, Sports, Science and Technology, Grant-in-Aid for Scientific Research (C), No.19560501, Scientific Research (A), No.20246078 and Scientific Research (C), No.22560504.

References

Numata A, Uesugi A, Yoshida M, Kubo H (2008) Investigation of wood piles retrieved from the Asuwa River. In: Proceedings of 10th world conference on timber engineering, No. 407, p 6 (CD-ROM)

Yoshida M, Numata A, Uesugi A, Kubo H, Gensai H, Nomura T (2007) Investigation of soundness for wood piles retrieved from Asuwa River. In: Proceedings of the 62th annual meeting of Japan Society of civil engineers, pp 183–184 (in Japanese)

Yoshida M, Numata A, Uesugi A, Kubo H, Miyajima M (2008) Experimental study on countermeasure against soil liquefaction by using Japanese cedar logs. In: Proceedings of the 63th annual meeting of Japan Society of civil engineers, pp 43–44 (in Japanese)

Yoshida M, Numata A, Motoyama H, Kubo H, Miyajima M, Nomura T (2009) Shaking table tests on countermeasure against soil liquefaction by using Japanese cedar logs. In: Proceedings of the 64th annual meeting of Japan Society of civil engineers, pp 533–534 (in Japanese)

Yoshida M, Miyajiam M, Numata A (2010) Liquefaction countermeasure technique by using logs for carbon storage against global warming. In: Proceedings of the 5th international conference on recent advances in geotechnical earthquake engineering and soil dynamics, No.4.33a, p 7 (CD_ROM)

Damage Analysis on Buildings in Towns and Villages in Wenchuan Earthquake 2008

Bo Song, Fuqiang Qi and Zhongmao He

Abstract Based on the field investigation of building damage in towns and villages in Sichuan and Gansu province by Wenchuan Ms 8.0 earthquake, the damage characteristics of buildings are studied and the damage phenomena are analyzed in this paper. The seismic damage results showed that the buildings with professional design and construction performance well in the earthquake, but some buildings, including raw-soil structure buildings, bricks timberwork buildings and RC frame structures, which were without aseismic design and the main form of buildings in towns and villages, were badly damaged. Combining the seismic damage characteristics, the new revised contents of Chinese Code for Seismic Design of Building are discussed and it analyzes the effects of the earthquake on new code. Considering the construction situation of buildings in towns and villages in China, the key issues concerning seismic design of building are discussed and several seismic fortification measures and suggestions on seismic design of buildings in towns and villages proposed.

Keywords Wenchuan earthquake · Buildings in town and village · Damage phenomena · Seismic design

B. Song (✉) · F. Qi
Department of Civil Engineering, University of Science & Technology Beijing, Xueyuan Road 30, Beijing 100083, China
e-mail: songbo@ces.ustb.edu.cn

Z. He
Gansu Science Research Institute of Civil Engineering, Lanzhou 730020, China

F. Wang et al. (eds.), *Progress of Geo-Disaster Mitigation Technology in Asia*, Environmental Science and Engineering, DOI: 10.1007/978-3-642-29107-4_16,

1 Introduction

On May 12, 2008, an Ms 8.0 earthquake occurred in Wenchuan, Sichuan province, China. Until May 27, 2008, 67,183 people died, 361,822 were injured, and all kinds of buildings, especially buildings in villages and towns suffered serious damages. Since the earthquake occurred in a mountainous region of Western China, it presented many new damage characteristics of buildings in towns and villages, which brings many new problems to earthquake disaster prevention and mitigation.

Since the focal depth of the earthquake was only 10–20 km, the earthquake belongs to shallow inland earthquakes. The massive energy released was widely spread by seismic waves, and the earthquake was felt in most of provinces and cities of China, such as Beijing, Gansu, Guizhou, Ningxia, Shanxi, Shanxi, Henan, Hubei, Shanghai, etc. Because Gansu province is close to the Sichuan province, the earthquake disasters were very serious. In this paper, based on site investigation on the buildings in towns and villages in Longnan city, which is situated in the junction area of Sichuan and Gansu province, the damage characteristics of buildings are studied.

Longnan city is about 200 km away from Wenchuan, as shown in Fig. 1. Its seismic fortification intensity is 8 degrees and the design earthquake acceleration is 0.20 g, which is equal to the intensity of Wenchuan earthquake. The typical building damages in towns and villages in Longnan city were analyzed in the paper.

2 Earthquake Damage Investigation of Buildings in Longnan, Gansu Province

In the site investigation of building damages, more than hundreds of residential buildings and 99 public buildings were investigated. In the mountainous area, most residential buildings were made of raw-soil structures, timberworks, bricks and masonry concrete structures and so on. The investigated public buildings were mainly of irregular structures and large span structures. The raw-soil structure buildings and timberwork buildings were seriously damaged, and the heavily damaged buildings accounted for 78 %. The main support walls collapsed, wooden frames collapsed and tilted, the transverse and longitudinal joints of wooden frame loosened, tenon structures were damaged seriously, and the span purlins and roof tiles fell down. The masonry concrete structures constructed without columns were also gravely damaged, especially the ground floor, where the walls succumbed to shear failure, containing diagonal cracks, ‘X’ form cracks and horizontal cracks. The masonry concrete structures of large span multi-ribbed slab frame structures as well suffered grave damages. Although no obvious cracks could be seen on most of the reinforced concrete structures, the damages on non-structural bodies such as in-filled walls were so obvious.

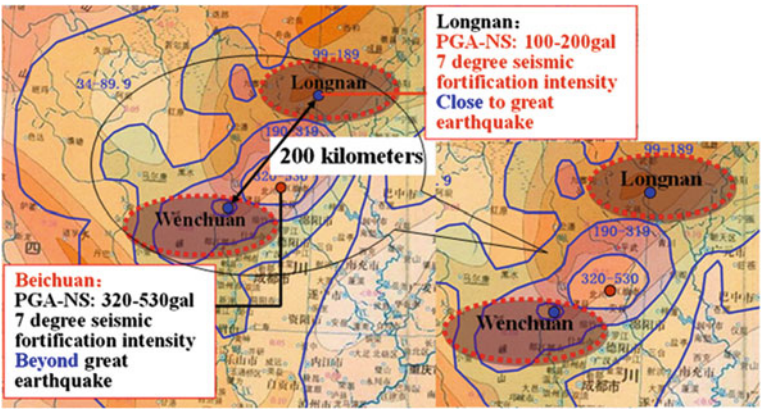

Fig. 1 The geographic position of Longnan city

2.1 The Raw-Soil Structure Buildings and Timberwork Buildings

The raw-soil structure buildings and timberwork buildings were the main types of buildings in towns and villages, which were basically built before the 1970s with single layer and the beams were placed on the walls directly. So these buildings were designed without considering seismic loading, hence the grave damages during the earthquake as shown in Figs. 2 and 3. Because the raw-soil structure buildings are weak in integrity, lack of connecting structures between the walls will make the buildings greatly susceptible to crack and collapse subject to horizontal seismic forces. Though the Code for Seismic Design of Building (GB50011-2010) specifies that in design of raw-soil structure buildings, the junctions of outer and inner walls should set a layer of bamboo muscle, batten and so on, the damaged buildings lacked such connecting structures, even some buildings had no foundations, the site investigation further revealed that the walls were too high and spans too large compared with the specifications in the code. So the raw-soil structure buildings collapsed because the shaking cracks developed due to shaking during the earthquake were too large. The purlins and crossbeams were set on the wall directly, and they were not subject to concentrated loads. Because the strength of walls was insufficient, the walls always crack under service. So when the earthquake occurred, the purlins and crossbeam collided with walls, which caused the cracks to increase.

The main problems with the timberwork buildings were that the components corroded and decayed, the section of timberwork weakened, the strength of components connection was insufficient, and the floor height was too high. The main reasons of the buildings in towns and villages collapsed in the earthquake were that the buildings were not designed in accordance with the provisions of the seismic design codes and the building materials did not meet the requirements. So in high seismic fortification intensity town areas, it is important to strengthen the legality of building construction and the supervision to improve the quality of buildings.

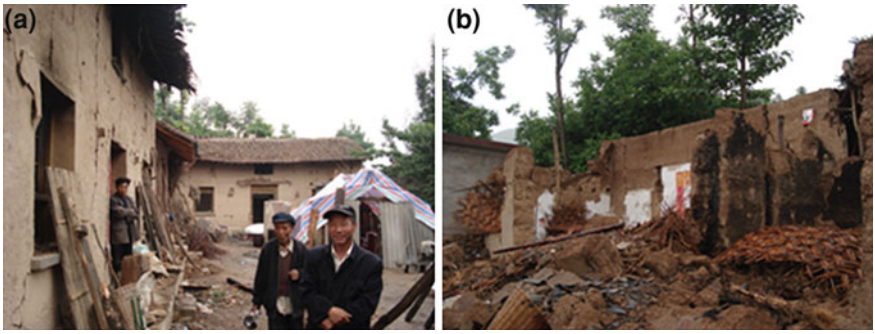

Fig. 2 The collapsed raw-soil structure buildings, **a** before earthquake, **b** after earthquake

Fig. 3 The collapsed timberwork buildings

2.2 The Masonry Timber Buildings

Besides the raw-soil structure buildings and bricks timberwork buildings, masonry timber buildings are also another common type of local dwellings. The main support wall were mostly brick walls with thickness 120, 180 or 240 mm, and the roof were triangular wooden frames. Some masonry timber buildings were designed without seismic measures, lack of connection components, and roof trusses were installed directly on the brick wall, so these types of buildings are always of poor integrity. Figure 4a shows the masonry timber buildings under construction. Under vertical loads, the structures are relatively stable, but subject to horizontal earthquake, the maintenance walls were easily tilt, which leads to severe earthquake damages such as local collapse or overall collapse. In the earthquake, most masonry timber buildings were damaged seriously and some of the buildings built relatively earlier completely collapsed as shown in Fig. 4b. The masonry timber structures have the same problems with the raw-soil structure buildings, such as the purlins put directly on the brick walls. The improper constructions and connections made the masonry timber structures lose the aseismic ability.

Fig. 4 The destroyed masonry timber buildings

2.3 The Masonry Concrete Buildings

The masonry concrete buildings were a new type of buildings adopted by local residents in recent years, most of which were with two layers. The investigation showed that some buildings usually set ring beams at the ground and at top of the first floor, but rarely at the top of second roof, and did not have constructional columns. In the earthquake, the damages on the buildings consisted of cracks on the walls, damage at the connection of vertical walls and horizontal walls, damage at doors and windows, tilted walls, collapses and so on. Some buildings adopted improper force transmission structures, thus the serious damages on such buildings as shown in Fig. 5. It is clearly seen that the second layer column was cut off. The loads acting on upper layer column can not transfer to the foundation via a proper load transmission path, but directly acted on the lower beam, which caused big concentrated force and 'X' form cracks on masonry structures under the beams. The second layer bearing structures were equal to three large bays, and the walls between windows of the three large bays were damaged with 'X' form cracks. Figure 6 shows the bearing wall badly damaged due to poor load transmission. The irregular structures are more susceptible to damages in an earthquake; such designs should therefore be avoided.

In disaster areas, there were some buildings whose major structures were not damaged, but the areas along joints between adjacent buildings (insufficient to serve as aseismic joints) were badly damaged as seen in Fig. 7. More so for the structures with the form 'L' in planar view, because the stiffness as well as the deformations in the two directions differs much, so it needs more deformation space in the junction area. But in the towns and villages, some buildings are without aseismic joints or sub-standard joints.

The in-filled walls of frame structures were also destroyed, no matter whether there were connecting structures or not, many infill walls cracked or collapsed, as shown in Fig. 8. Most of infill walls were of big building blocks made of fragile materials, and the mortar strength and saturation can not meet the requirements, so the deformation of infill walls could not remain bound to the major structures, as

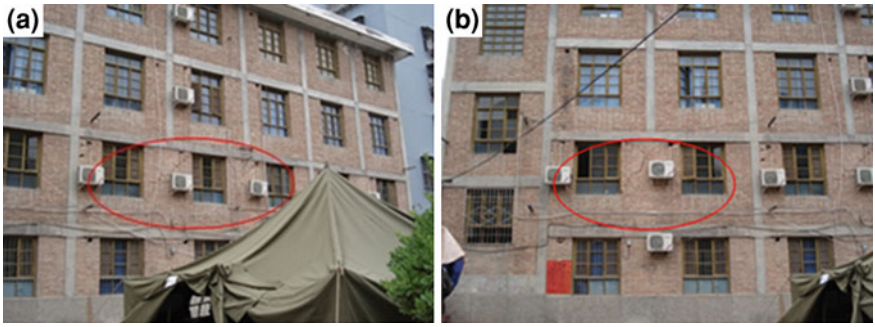

Fig. 5 The building with improper load transmission path

Fig. 6 Damaged bearing wall of a masonry concrete building

Fig. 7 The damaged buildings without aseismic joints

shown in Fig. 8a and b. Especially the infill walls with line pile suffered severe damages, as shown in Fig. 8c. On the other hand, because the infill walls are asymmetrical in the vertical direction, such as the upper buildings were dwelling house with many infilled walls, and the lower part were market with little infilled wall, even without infilled wall, so the lower part deform much than the upper

Fig. 8 The damaged infilled walls

buildings in the strong earthquake, which caused the infilled wall be destroyed, as shown in Fig. 8d.

2.4 The Bottom Floor of Frame Structures

In the towns and villages, some buildings along the street used framed construction to create some business space, but the bottom frame structures did not erect aseismic walls according to the standards, which made the bottom floor weak in stiffness and strength, and then it form a weak floor. During the earthquake, because the deformation was concentrated, the bottom layer collapsed or tilted as seen in Fig. 9. There were also some bottom frame structure with many aseismic walls in the bottom layer made the stiffness and strength of bottom floor bigger than the second and other upper layers, so the second layer become the weak layer. The strong earthquake force sheared off the weak layer, which cause the second layer to collapse.

Due to its functional requirements, it is hard for the transition layer of bottom frame structures to have stiffness that meets the fortification requirements. Consequently, whether earthquake fortification is considered or not, the performances of bottom frame structures remain poor under strong earthquake and therefore the use of bottom frame structure should be limited in high intensity seismic region.

Fig. 9 The destroyed bottom frame structures

2.5 The Irregular Buildings

Irregular construction is one of the types of buildings seriously damaged in the earthquake. In order to get the novel appearance, many buildings adopted the irregular construction shape, such as split-level building, plane protruding building, and so on. Due to the abrupt changes in the load transmission path, the change points of the structure are susceptible to be damage and lead to the damage of the whole building during an earthquake. Figure 10 shows a meteorological agency building whose main structures are three layers and local structures are four layers. The three layer part and four layer parts were connected together without aseismic joint; this led to the top columns complete fracture. The top floor of another irregular building was also badly damaged, as shown in Fig. 11a, and the change point of a building cracked in the earthquake, as shown in Fig. 11b.

In disaster areas, some masonry concrete buildings were erected with big and heavy precast reinforced concrete beams, which made the constructional column endure big shear forces during earthquake and the shear forces are relatively concentrated thereby ending in the destruction of the columns during the quake. As a result of improper design of the irregular building structures, the plastic hinges occurred at the end of the columns of during the earthquake, as shown in Fig. 12. The building damages showed the phenomenon of 'strong beam-weak column', which is opposite to the design goal of 'strong column-weak beam'.

2.6 The School Buildings with Large Spans

In the investigation of building damages, the large span buildings were also damaged seriously. The Longnan middle school building was an octagonal masonry concrete structure with four floors. The destruction features of the school building with large span showed that the vertical wall of the classroom with cantilevered corridor in one side suffered 'X' form shear cracks, as shown in Fig. 13. The cross wall of large span classroom suffered diagonal cracks, which was about 45°, as shown in Fig. 14.

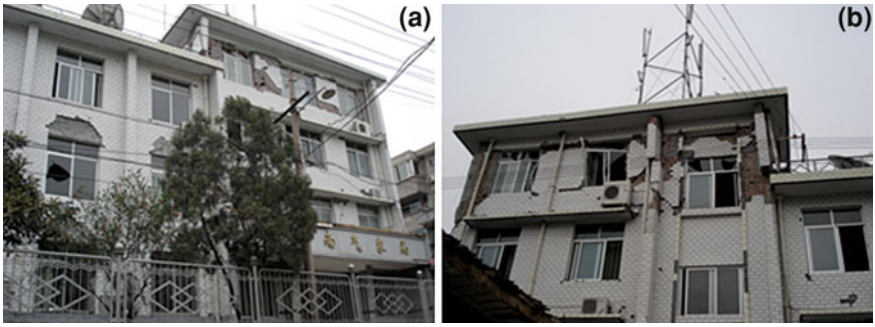

Fig. 10 The damages of Meteorological Bureau building in gansu province

Fig. 11 The damaged irregular buildings, **a** irregular building in planar direction, **b** irregular building in planar direction and facade

A lot of precast slab were used in classroom buildings, and were damaged severely in the earthquake as shown in Fig. 15. The walls endured flexural moment and shear force, and underwent tangential dislocation in the earthquake. So the damaged wall caused the precast slab to fall off. The classroom buildings are large span structures, whose width is rarely smaller than 6 m, and there are rarely any columns in the middle space. The assembly hall and conference room are larger than common classroom. So the precast slab used in these large span structures is contrary to law of small span and intensive walls. In addition, the shelved length of precast slab is limited, and it made the bearing wall be cut off at the position of every layer, therefore the structure has poor integrity. Though the standards require that there should be reliable connection, it is hard to control in construction.

Fig. 12 The phenomenon of 'strong beam-weak column'

Fig. 13 The 'X' form shear cracks of vertical wall

Fig. 14 The diagonal cracks of cross wall

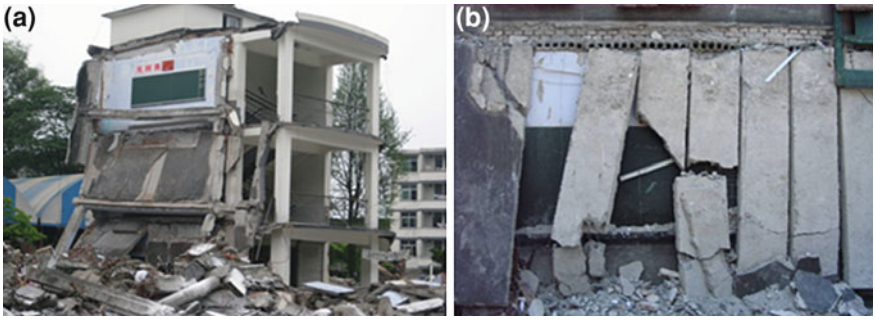

Fig. 15 Buildings with precast slab collapsed seriously

3 Seismic Damage Analysis on Buildings in Towns and Villages

Site investigation also showed that improper location was a main reason for building damages in the earthquake. Some buildings were built in bad geological location, such as slope surface area formed by landslide and debris flow as shown in Fig. 16.

The local buildings were designed with little consideration on proper location. For example, the meteorological agency for instance was built on a raised soil, which is 50 m higher than normal ground. The raised soil has a magnifying effect on seismic responses and the magnifying coefficient can be 1.3–1.5. So the building was damaged seriously not only in the irregular point, but as well at another side of the building which is shown in Fig. 10. So the improper location presents great hidden dangers to buildings, and it should be avoid in building design.

In the earthquake, some buildings were seldom damaged since they had adopted seismic measures. The Fig. 17 provided by Gansu civil engineering science research institute shows an apartment building which adopts rubber bearing shown in Fig. 18. There were no cracks in the apartment building, and also the vase on the air conditioner did not fall. It showed that proper isolation measures are an effective way to improve the aseismic ability of buildings.

4 The Effect of Wenchuan Earthquake on Chinese Code for Seismic Design of Building

In the Wenchuan earthquake, the buildings built, constructed and used according to the active codes did not collapse when subjected to the earthquake whose intensity is one degree higher than the fortification intensity. So, it means that the Code for Seismic Design of Building (GB50011-2001) is effective. But there were some new seismic damage experiments in the earthquake, and some new aseismic technologies were tested in the earthquake. Consequently, based on seismic damage experiments and research achievements, the Code for Seismic Design of

Fig. 16 The buildings built on improper location

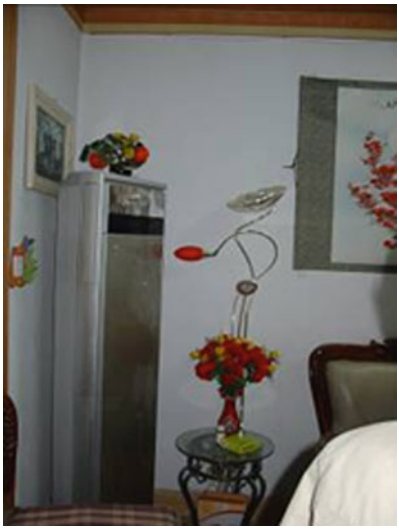

Fig. 17 The building with rubber bearing

Fig. 18 The rubber bearing

Building (GB50011-2001) was revised and published as a new Code for Seismic Design of Building (GB50011-2010).

In the revision, 29 items were revised, and the code strengthened the aseismic design of building in mountainous areas, replenished the aseismic construction of RC buildings, brickwork buildings and steelwork buildings and improved the earthquake-reduction and seismic-isolation design rules.

4.1 Site and Foundation

About site selection and foundation design of buildings in mountainous areas, it puts forward specific aseismic requirements. According to geological, topographic condition and request for utilization, the foundation should adjust measures to local conditions and erect side slope structures complying with the requirements for seismic resistance. The slope should avoid deep cut and high fill, and slopes with poor stability should adopt put back slope or points order slope. The foundation should also keep sufficient distance from the edge of the slope and adopt measures to prevent the foundation being destroyed under earthquakes.

4.2 Building Design and Regularity of Buildings

It firstly proposed that building design should comply with the requirements of seismic concept design and should not adopt too much irregular design. Proper building layout is the most important factor in aseismic design, so it advocates for simple and symmetrical buildings in planar direction and facade. It also puts forward the requirements for contour dimension, lateral force resisting components, mass distribution and bearing capacity and so on, which should be considered in architectural and structural design.

4.3 Structural Systems

Because precast concrete plank is easy to drop and lead to casualties under earthquakes, it requires that cast-in-place concrete plank should be used in high-rise and roof. If the precast concrete plank is used in buildings, it should adopt measures in floor system and structure to guarantee the connections integrity of precast concrete plank.

4.4 Nonstructural Components

It emphasizes that the nonstructural components should be aseismic designed and the relevant items are listed as mandatory provision. It takes the nonstructural

components as a lone content to illustrate and regulate the curtain wall, partition wall, parapet wall, awning, trademark, signboard, ceiling support, large storage and so on as nonstructural components of buildings. The nonstructural components should adopt strengthening measures to endure the seismic force delivered by nonstructural components to major structures. The light material of wall is prior to be used in concrete nonstructural components.

4.5 Isolation and Earthquake-Reduction Design

The technologies of isolation and earthquake-reduction design are relatively mature and it firstly lists the isolation and earthquake-reduction design as mandatory provision.

4.6 Revision About Multilayer Masonry Buildings Bottom Frame Structures and Frame Buildings

Comparing with Code 2001, the Code 2010 not only stipulates that the minimum strength of masonry mortar should be improved, but also specifies much about the minimum distance of ring beams of cross wall. The items about improving the horizontal stiffness of floor system and shear strength of walls, constraining the inclined crack development, and mitigating the effect of differential settlement on building under earthquakes and so on are remarkably improved.

4.7 Revision About Raw Soil Building, Timber Work Building and Stone Structure Building

It revised the wording of strict degree in executing the Codes about the raw soil building, timber work building and stone structure building. It emphasizes that it should be strengthened connection between raw soil walls to improve the integrity of buildings, and it should be strengthened connection of enclosure walls of timber work buildings and the major structure. And the scope of application of stone structure building is strictly controlled.

5 Recommendations on Design of Buildings in Towns and Villages

Because of relative lagging economy, the countryside buildings had some problems of building materials, structural styles and traditional customs, which made the casualties and damaged building in villages more fatal than that in cities.

Through the survey, we found that adopting proper structural measures in countryside buildings is an effective way of mitigating damages in 6 and 7° fortification areas for reinforced concrete frame structures.

For raw-soil buildings and timberwork buildings, it is necessary to strengthen the integrity of buildings and the connection of components. And all of the used irons, clinchers, straws and wooden poles only value 2–5 % of the total cost of buildings. Especially for timberwork buildings, walls and timber structures should connect reliably, and the masonry walls should not completely surround the wood column and should be built outside of the column (Ge et al. 2005; Wang et al. 2004).

For masonry structures, proper constructional columns and ring beams are necessary. The quantity and position of constructional columns should be proper, and avoid the following cases, insufficient longitudinal bars of the constructional columns in building nooks, insufficient anchorage length of longitudinal bars of constructional columns and ring beams, the stirrup of constructional columns at the position of the floors not encryption, the anchorage length of steel tie bars between constructional column and brick walls insufficient or the spacing improper (Hu et al. 2008; Li et al. 2009).

The stairway is the part suffering from earthquake most of the masonry structures and its aseismic ability is weak. So the stairway must be founded properly. According to the Code for Seismic Design of Building (GB50011-2010), the stairway can not be designed in end and nook of the building, also can not install too large window. It should strengthen the connection of each component, and dispose well the relations of nonstructural components and major structure. For constructional column setting, according to its influence on the integral structure, it can set the four corners of the building as first class, the four corners of the stairway as second class, and the junction of inner walls and outer walls as third class. The roof house and additional structures protruding the roof should be paid more attention. Because of the influence of 'whipping effect' in an earthquake, the structures protruding the roof are always damaged more seriously than the lower major structures. So, unless for special requirements and reliable measures adopted, the protruding structures should be avoided in design (Tang 2007).

For reinforced concrete structures, adopting proper structural measures can ensure that the parts where plastic hinges likely occur will have enough ductility, that is to say, the structures have enough plastic rotational capacity and plastic energy dissipation capacity. For beams, we always expect that the plastic hinges occur at the ends, so we should ensure the beam end has good ductility and energy dissipation capacity in design. Besides meeting some requirements for calculation, it also needs to set a series of structural measures, such as controlling the ratio of reinforcement, the beam with a certain number of compression reinforced bars, the proper quantity and usage of stirrups and the well designed sectional dimensions of beams. The structural measures of columns are basically the same as the beams, but the columns not only bear the flexural moments and shear forces, they also endure the axial forces, so there are still requirements for ratio of axial compressive force to axial compressive ultimate capacity of section (Zhong and Song 2008; Yu et al. 2008; Wang et al. 2008, Ye et al. 2008).

For new structural systems, performance-based seismic design (PBSD) should be used. Accompanying with development of PBSD, the building design should meet

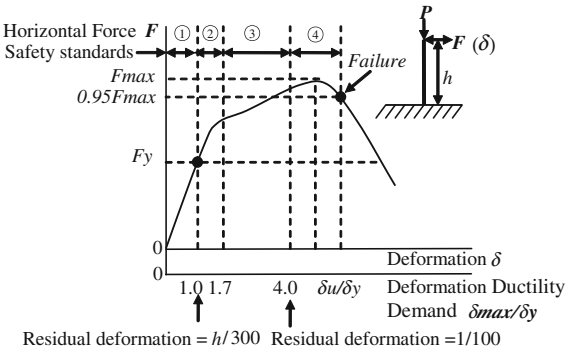

Fig. 19 The multistage seismic design

the requirements for multistage seismic design, shown as Fig. 19. In the Fig. 19, the horizontal axis is the deformation of the structure, which is used to evaluate the performance of the structure after earthquakes, and the vertical axis is the horizontal force on the structure. It divides the goal of seismic performance into four stages. The first stage is corresponding to that the deformation is smaller than the yield deformation of the structure, which also means the residual deformation is smaller than one over three hundred times of the height of the structure. In the first stage, the structure is without any damage. The second stage is corresponding to that the structure occurs plastic deformation and need little repair. In this stage, the deformation ductility demand is always smaller than 1.7. In the third stage, the structure is damaged seriously, but it can be repaired to meet the operating requirements. And the deformation ductility demand is almost between 1.7 and 4.0. In the forth stage, the structure occurs damage, which can not be repaired and the deformation is close to ultimate deformation which means that the structure is close to collapse. The mechanical properties of large complex structures should be determined by using time history seismic analysis and the complex structures should be designed using performance-based seismic design method to control the position of the major structure where plastic hinges occur and the precedence of plastic hinges.

6 Conclusions

Combining with the damage characteristics of buildings in towns and villages at the junction areas of Sichuan and Gansu in the Wenchuan earthquake, the key points on aseismic ability of buildings were discussed and the following recommendations were made.

The site selection of buildings should avoid bad geological location, such as landslide, dilapidation, subsidence, river valley edge, ground fracturing debris flow, and seismogenic zones. The foundation should be reinforced according to the bearing capacity, deformation characteristics and structural characteristics of buildings to ensure that the building will not be damaged due to instable foundation.

Considering the economy, buildings in towns and villages can be constructed in different grades and levels. In a certain period, raw-soil structure buildings can still be the main residential houses, with the economy developing, brick buildings should be encouraged. Irregular structures also need to be avoided and erect proper constructional columns and ring beams to strengthen the seismic capacity of buildings.

The construction of town buildings should be more standardized, and all of the design, construction and supervision should be given more attention and ensure that they meet the requirements of the related laws and regulations.

For the countryside buildings, we should analyze the characteristic of seismic damage, and adopt some simple and effective construction measures to improve the aseismic ability of buildings considering construction cost. There is also need to propose seismic strengthening methods suitable to countryside buildings to mitigate the earthquake damage to old buildings.

Acknowledgments This work was financially supported by the National Natural Science Foundation of China (51078033) to the National Natural Science Foundation of China (51178045) and the Overseas Teacher Project of the Ministry of Education of China (MS2011BJKJ005).

References

Ge XL, Wang YY, Shen SY, Zhang HM (2005) Seism disaster of building in rural area as well as measures of anti-seism and disaster a11eviation. Constr Towns Villages 12:671–674 (in Chinese)

Hu XP, Xu L et al (2008) Wenchuan 8.0 earthquake damage of single-storey industrial plant analysis. J Xi'an Univ Archit Technol 40(5):662–666 (in Chinese)

Li YM, Han J et al (2009) Investigation and analysis of masonry building damage caused by the 5.12 Wenchaun earthquake, Sichuan Province. J Xi'an Univ Archit Technol 41(5):606–611 (in Chinese)

Tang QS (2007) Main earthquake damage characters and earthquake-resistant design of masonry structure. Sci Technol Overseas Buildings Mater 28(6):71–73 (in Chinese)

Wang YY, Yue MG et al (2008) Benefit analysis of RC structures designed under different performance objectives. China Civil Eng J 41(3):37–44 (in Chinese)

Wang YH, Jiang JF, Shi J, Chi JX (2004) Earthquake-resistance performance and protective measures of the timber structural buildings. Earthq Resist Eng Retrofit 5:47–51 (in Chinese)

Ye LP, Lu XZ et al (2008) Damage analysis on buildings in Wenchuan earthquake. Seminar on building damage analysis and reconstruction in Wenchuan earthquake, vol 1, pp 38–49 (in Chinese)

Yu W, Ge XL et al (2008) Damage analysis on buildings in towns and villages around Dujiangyan of Wenchuan Ms 8.0 earthquake. Earthq Resist Eng Retrofit 30(4):45–49 (in Chinese)

Zhong M, Song B (2008) The experience of Sichuan earthquake on urban disaster prevention and mitigation. Seminar on building damage analysis and reconstruction in Wenchuan earthquake, vol 1, pp 623–630 (in Chinese)

Assessing the Simultaneous Effects of Horizontal and Vertical Components of Earthquakes on the Double Layer Barrel Vaults

Arjang Sadeghi

Abstract The earthquake of Kobe of Japan in 1995 had great effect on structural engineering research especially on space structures. Thereafter, a huge effort started to investigate more deeply on the seismic behavior of the space structures. This earthquake happened in a region that there were plenty of such structures and the real behavior of them were studied readily. The Kobe earthquake showed that although the vulnerability of the space structures is not as high as the ordinary buildings, but they are not aseismic. Although there are at the present considerable amount of research on the seismic behavior of the double layer barrel vaults, the available documents on the simultaneous action of the double and triple components of the earthquakes are rare and it is necessary to execute more research to assess the one or multi-directional earthquake effects on these structures. In the current research the effects of horizontal and vertical components of some earthquakes are imposed separately on some models of double layer barrel vaults. In the following the simultaneous action of both the horizontal and vertical components are considered. In all the analysis the dynamic responses of the structures are pursued considering the both material and geometrical nonlinearity. It is shown that, the double layer barrel vaults behave differently against horizontal and vertical components of earthquakes. In fact the horizontal earthquakes are more effective. However, the vertical action by itself increases the action of the horizontal component.

Keywords Horizontal and vertical components · Double layer barrel vaults · Nonlinear behavior · Accellerogram

A. Sadeghi (✉)
Department of Civil Engineering, Azarbaijan Shahid Madani University, Tabriz, Iran
e-mail: a.sadeghi@azaruniv.edu

F. Wang et al. (eds.), *Progress of Geo-Disaster Mitigation Technology in Asia*, Environmental Science and Engineering, DOI: 10.1007/978-3-642-29107-4_17,

1 Introduction

The 1995 earthquake that occurred in Kobe, Japan had a major impact on structural engineering fields with major emphasis on space structures. The impact of the earthquake on engineering structures inspired a huge number of researchers to carry out more precise investigation on the seismic behavior of space structures. The 1995 Kobe earthquake occurred in a region where there were plenty of such space structures and their real behavior during seismic disturbance was observed. The Kobe earthquake showed that although the vulnerability of the space structures is not as high as ordinary buildings, they are not aseismic (Cunieda 1997; Ihsikawa and Kato 1997). Saka et al. (2006) revealed that the joints and the characteristic slender form of the frames have significant effect on the collapse of double layer grids. Kave (2000) studied the effect of the geometric dimensions of the double layer barrel vaults and showed that any increase in the rise-to-span ratio of these structures may make their first-mode period to increase.

Mogaddam (2000), worked on a number of double layer barrel vaults with different configurations and various kinds of support conditions and concluded that the configuration of the barrel vaults significantly affect their first-mode period. However, the configuration showed no meaningful effect on the double layer barrel vaults seismic response. Sadeghi (2010), studied the nonlinear dynamic behavior of a number of double layer barrel vaults and proposed a set of equivalent static earthquake loads for these structures and later tested these formulae. Results of analyses carried out over the structures shows that these formulae were considered in their design stage and also that their response were modified significantly in comparison with others designed without considering the suggested earthquake loads formulae (Sadeghi and Amani 2012).

Although there are presently, considerable numbers of research works on the seismic behavior of the double layer barrel vaults; the available document on the simultaneous action of the double and triple components of earthquakes are rare and it is necessary to carry out more research to assess the one or multi-directional earthquake effects on these structures.

2 Selected Models

To assess the behavior of the double layer barrel vaults against one and two dimensional effects of earthquakes, five models of double layer barrel vaults were selected. These models have different rise-to-spans of 0.1, 0.2, 0.3, 0.4 and 0.5 but their depths, spans and lengths were fixed as 1.5, 30 and 42 m respectively Fig. 1. All the models were designed against dead and snow loading of 500 and 1,500 N/m^2 respectively. The snow loading was considered in both symmetric and asymmetric patterns according to the sixth volume of the National Codes of Buildings of Iran (Iranian National Building Code, Part 6, 2006). The elements were chosen to be

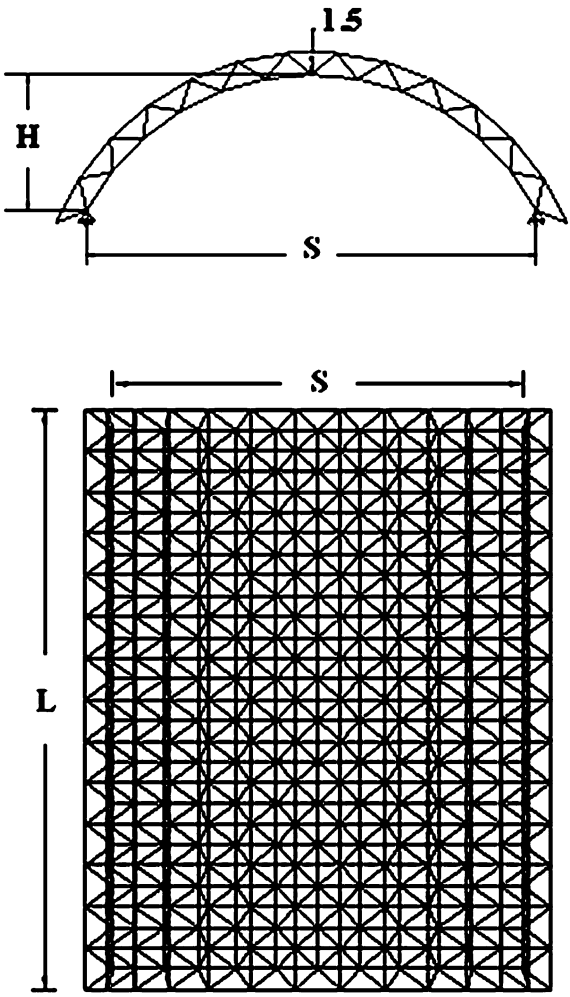

Fig. 1 General layout of double layer barrel vaults

tubular and were designed with the ASD method, Section 10 of the National Codes of Buildings of Iran (Iranian National Building Code, Part 10, 2008). The material used was mild steel with characteristic physical properties such as, $F_y = 2.4E8$, $E = 2.1e11$ N/m^2 and $\upsilon = 0.3$.

The slenderness of the elements was taken to be fixed and equal to 100 and its post-buckling behavior (Eq. 1) was adapted from Ishikawa and Kato (1997).

$$\left(\frac{\sigma}{\sigma_y}\right)^2 + 3.476\left(\frac{\sigma}{\sigma_y}\right) - 11.62\left(\frac{\varepsilon}{\varepsilon_y}\right)\left(\frac{\sigma}{\sigma_y}\right) + 2.1\left(\frac{\varepsilon}{\varepsilon_y}\right) - 0.09241\left(\frac{\varepsilon}{\varepsilon_y}\right)^2 + 1.18 \quad (1)$$

The geometrical configuration of each models was produced by FORMIAN (Nooshin and Disney 1997) and the output was introduced to Mechanical Desktop which its output can be used by design or analysis packages like SAP2000

(Analysis Reference Manual for SAP2000 2008) and ANSYS (Help System 2010). In this research, the design procedure was carried out using SAP2000 and eigenvalue analysis, while the nonlinear dynamic analyses were carried out using ANSYS.

To analyze the models, one should choose elements which can bear both tension and compression. The suitable element in ANSYS for this purpose is COMBIN39. However, for linear analyses purpose, LINK180 element was utilized. Element LINK180, a three-dimensional element which can withstand tension and compression, and lacks rotational stiffness, was used to model the truss element, cable, spring, etc. Elements COMBIN39, is a three-dimensional longitudinal high torsion-resistant element, which has the ability to carry post-buckling behavior along with large deflections. For the introduction of the masses of the structures, element MASS21 was adapted as lumped mass in the upper section nodes of the barrel vaults. Each of the selected models was analyzed three times against the following: the horizontal component of an earthquake; the vertical component of the earthquake; and combined horizontal and vertical components of the earthquakes.

This action is shown by a follower of H for horizontal, V for vertical and HV for horizontal–vertical components after the model index of B1, B2, B3, B4 and B5 standing for the rise-to-span ratios of double layer barrel vaults as 0.1, 0.2, 0.3, 0.4 and 0.5, respectively. The damping ratios of the structures were taken to be 0.02 and were introduced through the Raleigh coefficients of damping (Chopra 2007):

$$\alpha = \xi \frac{2 f_i f_j}{f_i + f_j} \quad \beta = \xi \frac{2}{f_i + f_j} \tag{2}$$

where f_i and f_j and ζ are the frequency of first effective mode, second effective mode and damping ratio respectively.

3 Selected Earthquakes

For the purpose of this dynamic analysis, three strong ground motions of Nahanni of Canada 1985, Northridge of USA 1994 and Chi–Chi of Taiwan 1999 were selected. The common characteristics of these three earthquakes were the fact that they all have big horizontal and vertical PGA's. Table 1 shows the general characteristics of the three selected earthquakes.

Table 1 General information about the selected earthquakes (Chi–Chi, Nahanni and Northridge)

Station: CHY080	Data source : CW8		
Earthquake	Chi-Chi, Taiwan 1999/09/20 (H)	Earthquake	Chi-Chi, Taiwan 1999/09/20 (V)
Record/Component	CHICHI/CHY080-W	Record/Component	CHICHI/CHY080-V
HP (Hz)	0.1	HP (Hz)	0.3
LP (Hz)	50	LP (Hz)	50
PGA (g)	0.968	PGA (g)	0.724
PGV (cm/s)	107.5	PGV (cm/s)	49
PGD (cm)	18.6	PGD (cm)	27.82
Station:6097 Site			
Earthquake	Nahanni, Canada 1985/12/23 (H)	Earthquake	Nahanni, Canada 1985/12/23 (V)
Record/Component	NAHANNI/S1280	Record/Component	NAHANNI/S1-UP
HP (Hz)	0.05	HP (Hz)	0.2
LP (Hz)	62.5	LP (Hz)	62.5
PGA (g)	1.096	PGA (g)	2.086
PGV (cm/s)	46.1	PGV (cm/s)	40.5
PGD (cm)	14.58	PGD (cm)	12.12
Station 24207 Pacoima Dam	Data source: CDMG		
Earthquake	Northridge 1994/01/17 (H)	Earthquake	Northridge 1994/01/17 (V)
Record/Component	NORTHR/PUL104	Record/Component	NORTHR/PUL-UP
HP (Hz)	0.16	HP (Hz)	0.16
LP (Hz)	23	LP (Hz)	23
PGA (g)	1.585	PGA (g)	1.229
PGV (cm/s)	55.7	PGV (cm/s)	49.6
PGD (cm)	6.06	PGD (cm)	11.75

4 Behavior of Double Layer Barrel Vaults Under Different Earthquakes

One of the most important aspects of the behavior of the barrel vaults is consideration of buckling or yield of the members and the locations of these members in the structure. To do this, plans of the barrel vaults were divided into four sections and for each section, a number is assigned for reference (Fig. 2).

All of the models were analyzed dynamically considering both material and geometrical nonlinearity with the three aforementioned earthquakes which led to the generation of many results. However, for brevity, only result of the 1985 Nahanni earthquake of Canada is discussed noting that other results are more or less similar.

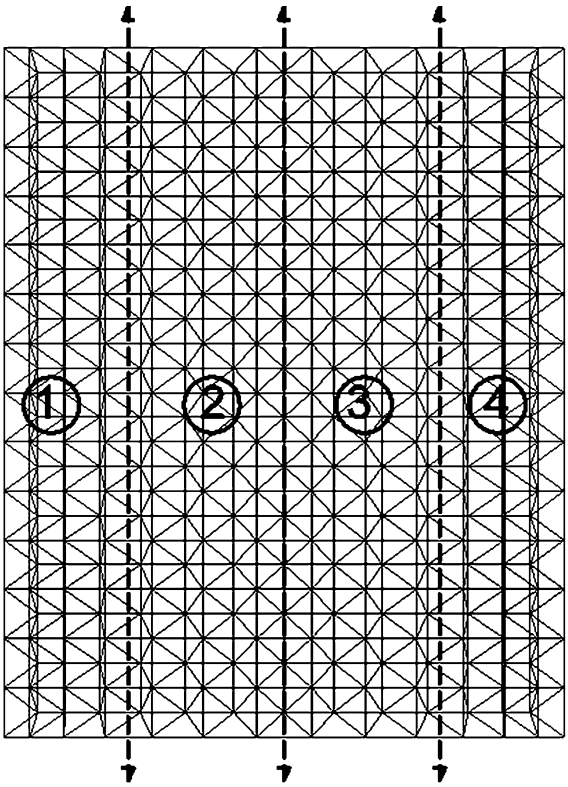

Fig. 2 Division of plan of double layer barrel vaults

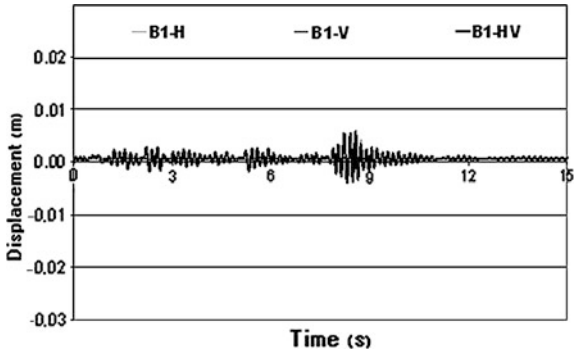

Fig. 3 X-direction displacement time-history of double layer barrel vault in analyses of B1-H, B1-V and B1-HV under Nahanni earthquake

The first model to be discussed is the double layer barrel vault with rise-to-span ratio of 0.1. As shown in Fig. 3, the largest horizontal deflections in the joints of this barrel vault are 0.005, 0.002 and 0.006 m for B1-H (under horizontal component), B1-V (under vertical component) and B1-HV (under the simultaneous action of horizontal and vertical components), respectively. Also, it can be seen

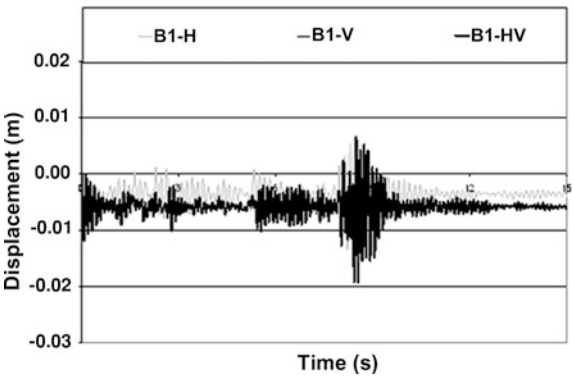

Fig. 4 Y-direction displacement time-history of double layer barrel vault in analyses of B1-H, B1-V and B1-HV under Nahanni earthquake

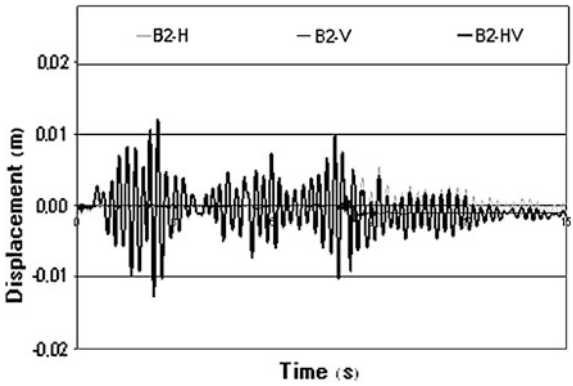

Fig. 5 X-direction displacement time-history of double layer barrel vault in analyses of B2-H, B2-V and B2-HV under Nahanni earthquake

from Fig. 4 that the largest vertical deflections are 0.019, 0.013 and 0.019 m for B1-H, B1-V and B1-HV analyses respectively. The figures imply that there has been no buckling or yield in members, since there is no jump in the joints deflections time histories of the structures.

The second model is the double layer barrel vault with rise-to-span ratio of 0.2, which its behavior was studied under different components of the 1985 Nahanni earthquake. Figure 5 shows that the maximum horizontal deflection in the joints of the structure are 0.012, 0.002 and 0.013 m for B2-H (under horizontal component), B2-V (under vertical component) and B2-HV (under horizontal and vertical components simultaneously), respectively. On the other hand, Fig. 6 shows that the maximum vertical deflections in the model are 0.017, 0.014 and 0.013 m for the analyses of B2-H, B2-V and B2-HV. Figures 5 and 6 show that there are some jumps in the deflections time histories of the barrel vault under the vertical component alone, and simultaneous action of horizontal and vertical components.

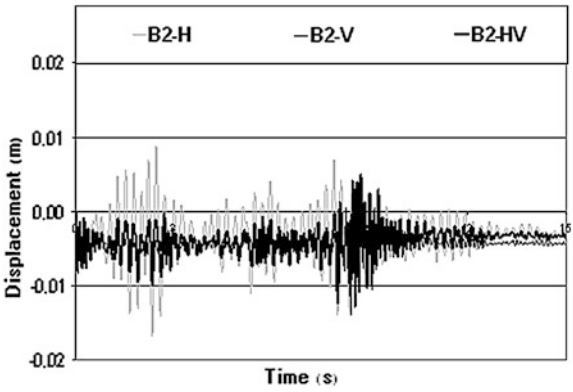

Fig. 6 Y-direction displacement time-history of double layer barrel vault in analyses of B2-H, B2-V and B2-HV under Nahanni earthquake

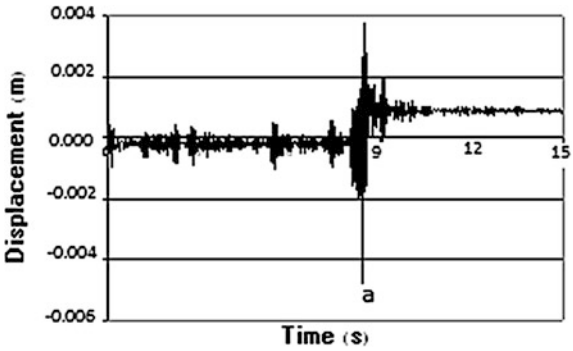

Fig. 7 Axial displacement time-history of first buckled member in analysis B2-V under Nahanni earthquake

This means that some members of the structure have buckled and experienced post-buckling behavior.

The first member buckling for both analyses occurred in the lower section of third region (Fig. 2) at approximately 8.42 s. After some time, more elements buckled and the number of buckled members rose increased to 8 and 12 for the structure under the vertical component, and simultaneous action of horizontal and vertical components, respectively. This indicates that though the horizontal accellerogram could not make the structural elements buckle; but its presence aside of vertical component had an intensifying effect and increased the buckled members and made the barrel vault closer to total collapse.

Investigations on the first buckled member's response reveal that it has experienced the largest deflection at point (a) which corresponds to the jump in the deflection of the critical joint (Figs. 7 and 9). On the other hand, these points coincide with the buckling stress of the element for B2-V and B2-HV analyses respectively (Figs. 8 and 10).

The other model is a double layer barrel vault with rise-to-span ratio of 0.3. The maximum horizontal deflections of the model under horizontal, vertical, and

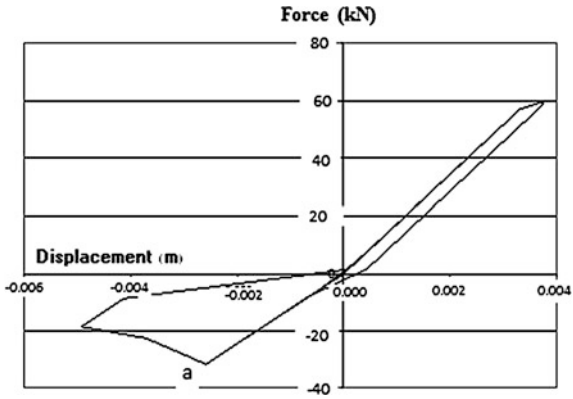

Fig. 8 Postbuckling behavior of the first buckled member in analysis B2-V under Nahanni earthquake

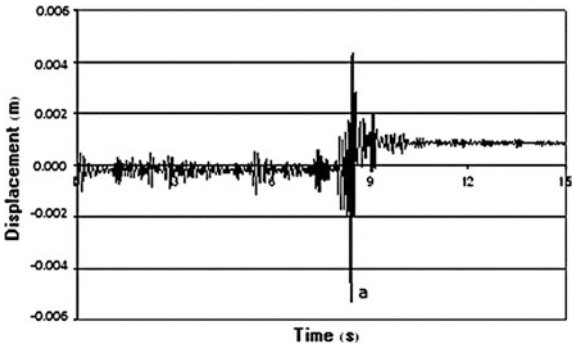

Fig. 9 Axial displacement time-history of first buckled member in analysis B2-HV under Nahanni earthquake

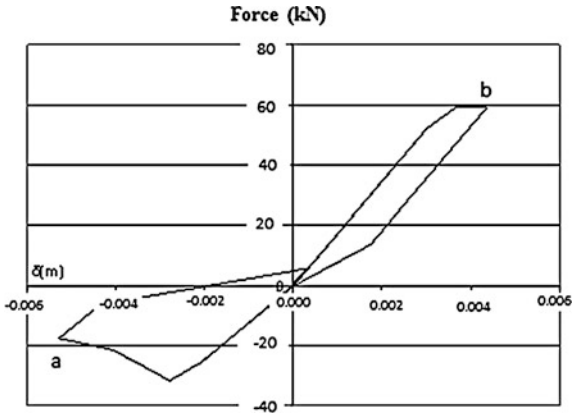

Fig. 10 Postbuckling behavior of the first buckled member in analysis B2-HV under Nahanni earthquake

horizontal and vertical components simultaneous are 0.008, 0.009 and 0.011 m, respectively (Fig. 11). Figure 12 shows the maximum vertical deflections of the structures under similar earthquake components as 0.045, 0.019 and 0.057 m.

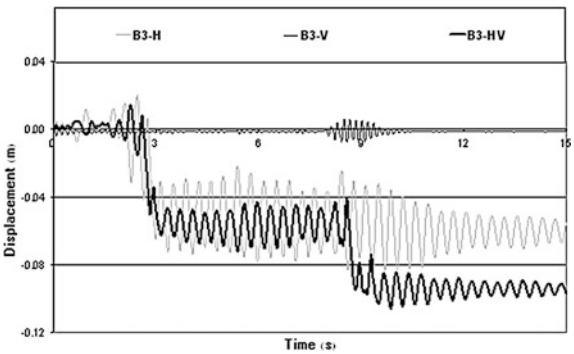

Fig. 11 X-direction displacement time-history of double layer barrel vault in analyses of B3-H, B3-V and B3-HV under Nahanni earthquake

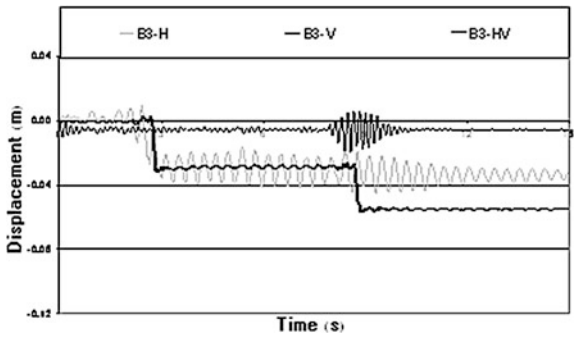

Fig. 12 Y-direction displacement time-history of double layer barrel vault in analyses of B3-H, B3-V and B3-HV under Nahanni earthquake

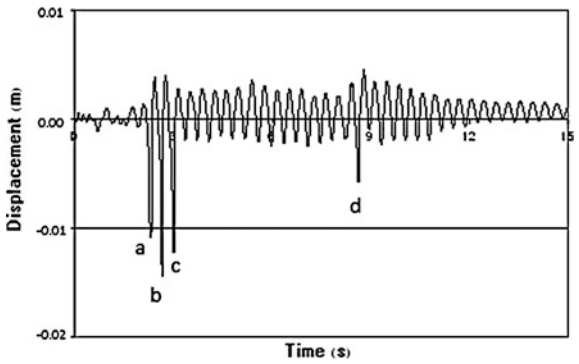

Fig. 13 Axial displacement time-history of first buckled member in analysis B3-H under Nahanni earthquake

It was observed that the horizontal and vertical deflections in the barrel vault were high in comparison with results of the models with lower rise-to-span ratios. Figures 11 and 12 further show that except under vertical component, there are some deflections in the response time histories of the model, which indicate that some members have buckled during the earthquake disturbance. Further investigation reveals that the first buckling occurs in the upper layer of first region at

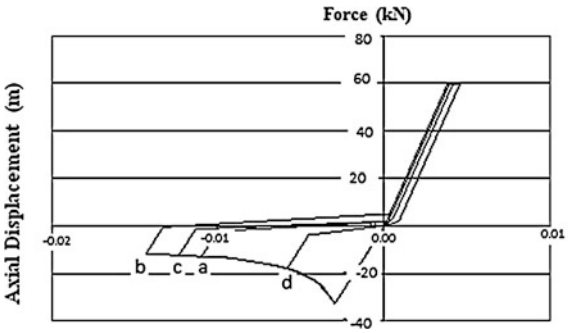

Fig. 14 Postbuckling behavior of the first buckled member in analysis B3-H under Nahanni earthquake

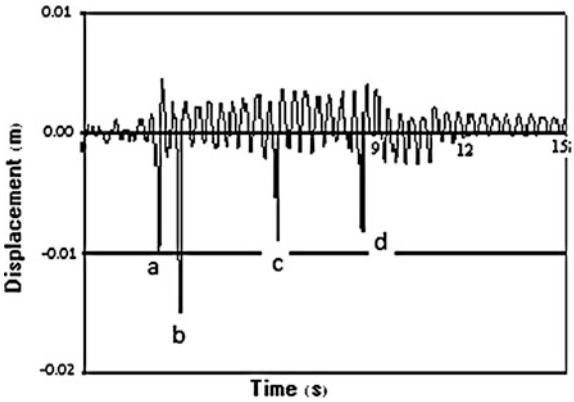

Fig. 15 Axial displacement time-history of first buckled member in analysis B3-HV under Nahanni earthquake

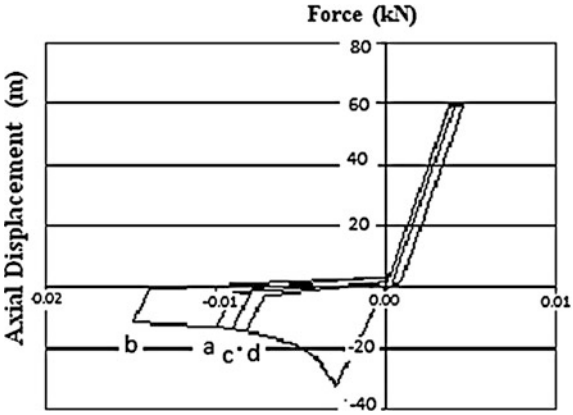

Fig. 16 Postbuckling behavior of the first buckled member in analysis B3-HV under Nahanni earthquake

about 2.32 s (Fig. 2). This implies that the buckling occurrence has got earlier times than the former models. Eventually, the overall buckled elements increased to 58 and 79 for horizontal and simultaneous actions of vertical and horizontal components.

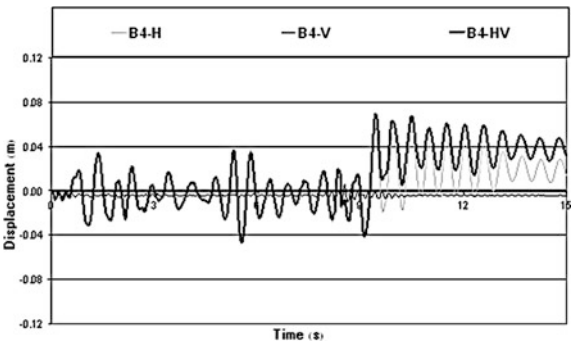

Fig. 17 X-direction displacement time-history of double layer barrel vault in analyses of B4-H, B4-V and B4-HV under Nahanni earthquake

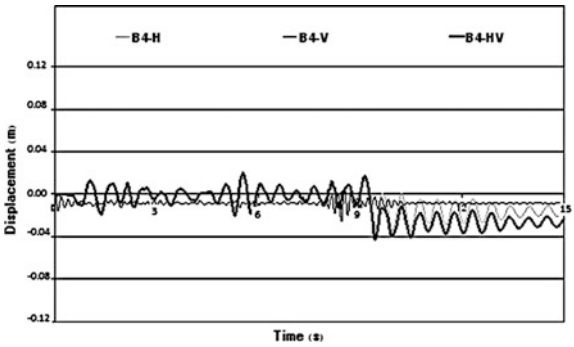

Fig. 18 Y-direction displacement time-history of double layer barrel vault in analyses of B4-H, B4-V and B4-HV under Nahanni earthquake

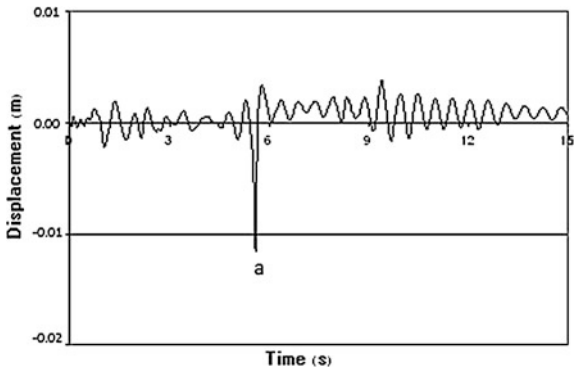

Fig. 19 Axial displacement time-history of first buckled member in analysis B4-H under Nahanni earthquake

The axial deflection time history of the critical element shows that the buckling time (Fig. 13) under the horizontal earthquake component is in consonance with the illustration in Fig. 14. Similar results were obtained for the critical element under the simultaneous action of horizontal and vertical components of the 1985 Nahanni earthquake (Figs. 15 and 16).

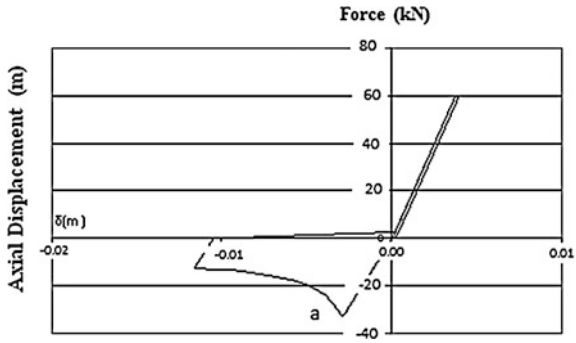

Fig. 20 Postbuckling behavior of the first buckled member in analysis B4-H under Nahanni earthquake

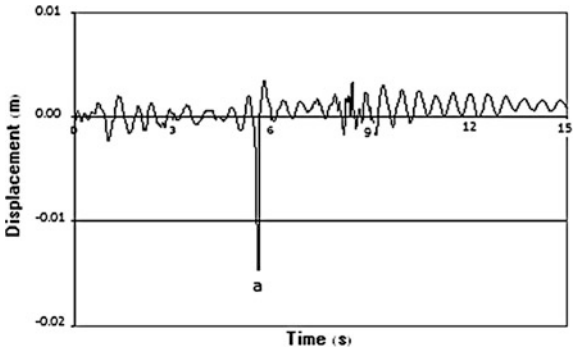

Fig. 21 Axial displacement time-history of first buckled member in analysis B4-HV under Nahanni earthquake

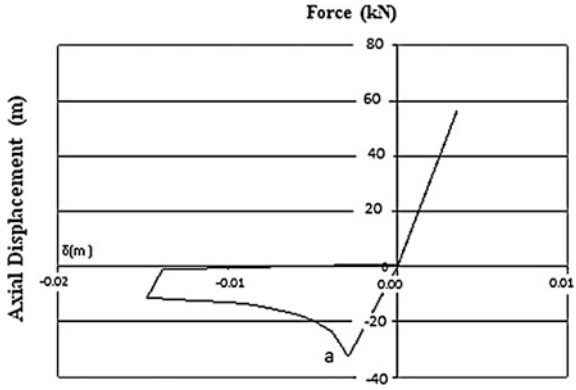

Fig. 22 Postbuckling behavior of the first buckled member in analysis B4-HV under Nahanni earthquake

For the double layer barrel vaults with rise-to-span ratio of 0.4, under different components of the 1985 Nahanni earthquake, the results show that the maximum horizontal deflections in the structure are 0.056, 0.015 and 0.070 m for the horizontal, vertical, and the horizontal–vertical components respectively (Fig. 17). Figure 18 shows that the maximum vertical deflections in the structure are 0.035,

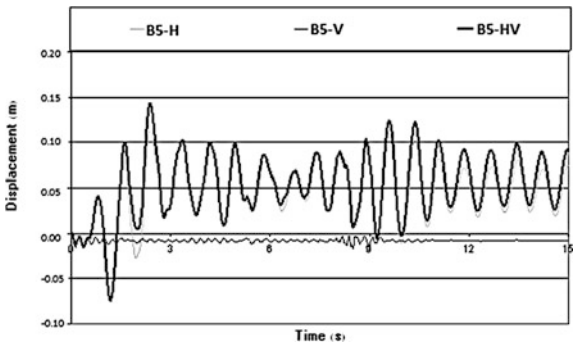

Fig. 23 X-direction displacement time-history of double layer barrel vault in analyses of B5-H, B5-V and B5-HV under Nahanni earthquake

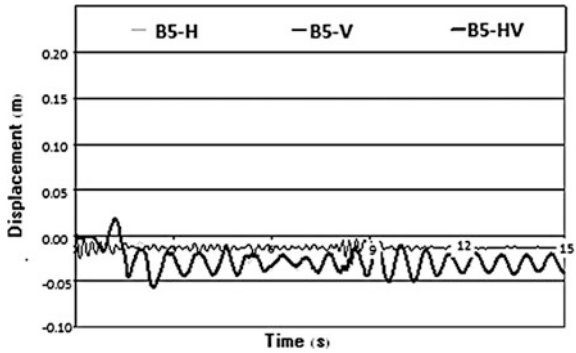

Fig. 24 Y-direction displacement time-history of double layer barrel vault in analyses of B5-H, B5-V and B5-HV under Nahanni earthquake

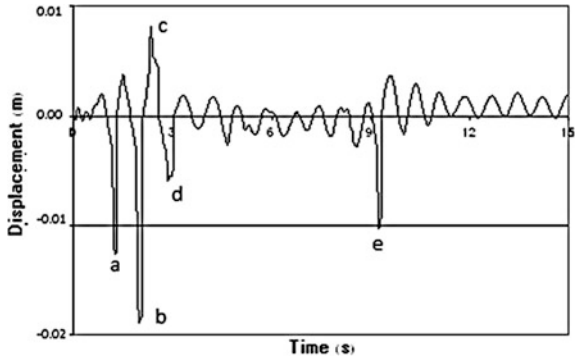

Fig. 25 Axial displacement time-history of first buckled member in analysis B5-H under Nahanni earthquake

0.026 and 0.043 m for the horizontal, vertical, and the horizontal–vertical components of the 1985 Nahanni earthquake. Figures 17 and 18 shows that there are some jumps in the response of the barrel vault under the horizontal and horizontal-vertical components. This again implies that there is buckling in that instance. The first buckling took place at the upper section of the fourth region with maximum time of 5.63 s (Fig. 2). Consequently, the number of buckled element increased to 12 and 27 under the action of horizontal and horizontal-vertical components of the earthquake.

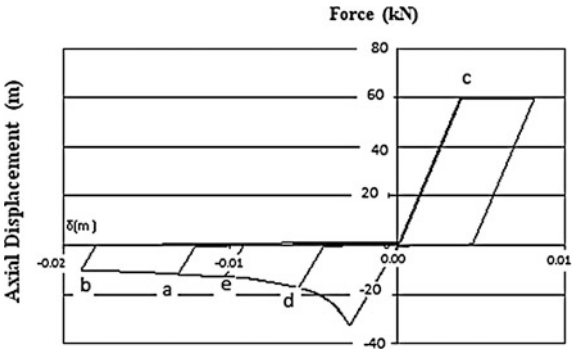

Fig. 26 Postbuckling behavior of the first buckled member in analysis B5-H under Nahanni earthquake

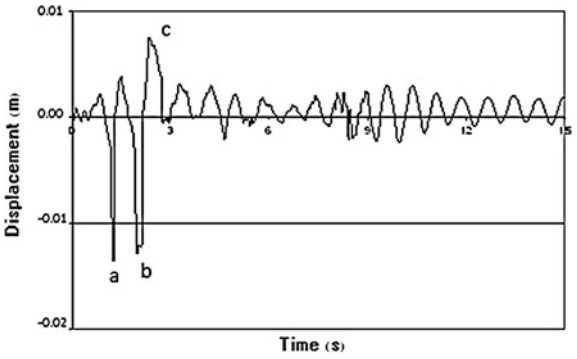

Fig. 27 Axial displacement time-history of first buckled member in analysis B5-HV under Nahanni earthquake

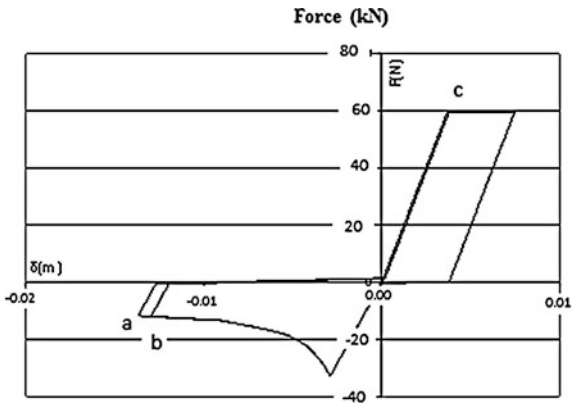

Fig. 28 Postbuckling behavior of the first buckled member in analysis B5-HV under Nahanni earthquake

Consideration of the deflection time history in the critical member under the horizontal component shows that there is a jump in this response (Fig. 19) as well. This jump coincides with the buckling of the member at point (a) in Fig. 20. The time of the buckling can be extracted by noting the jump time in deflection. Similar results can be seen in Figs. 21 and 22 for the structure under the simultaneous action of horizontal and vertical components.

For the double layer barrel vaults with rise-to-span ratio of 0.5, under different components of the 1985 Nahanni earthquake, the results show that the maximum horizontal deflections in the structure are 0.113, 0.016 and 0.143 m for the horizontal, vertical and the horizontal–vertical components respectively (Fig. 23). Also, Fig. 24 illustrates that the maximum vertical deflections in the structure are 0.018, 0.031 and 0.056 m for the horizontal, vertical and the horizontal–vertical components of the 1985 Nahanni earthquake. As Figs. 23 and 24 show, there are some jumps in the response of the barrel vaults under the horizontal and the horizontal-vertical components. This again implies that there is buckling in that instance. The first buckled member is in the upper section of the fourth region at the time of 1.29 s (Fig. 2). Consequently, buckling elements number increased to 44 and 54 due to the effects of horizontal and horizontal-vertical components of the earthquake.

Considering the deflection time history in the critical member under the horizontal component shows that there was a jump in the response (Fig. 25). This jump coincides with the buckling of the member appearing at point (a) (Fig. 26). The time of the buckling can be extracted by noting the jump time in deflection. Similar results can be seen in Figs. 27 and 28 for the structure under the simultaneous action of horizontal and vertical components.

5 Conclusions

The analyzed models which some of their results were presented in this paper show that the vertical component of earthquakes rarely cause the elements of the barrel vaults to buckle; however, they intensify the action of the horizontal component of the earthquake.

Also, the results indicate that the buckling time reduces with increase of rise-to-span ratio of the model under the same earthquake and component. But the combined effect of the horizontal and vertical components does not change the buckling time of the critical element. However, the number of buckled elements increased significantly due to the combined effect of the vertical and horizontal component the earthquake. This implies that the combined actions of the horizontal and vertical earthquake components have no significant effect in the early stage of buckling in a barrel vault. But, it shows a significant strong effect at the pre-failure stage of the barrel vault by occurrence of more buckling in elements.

In brief, from the results presented here, one may conclude that in the stage of design to satisfy serviceability, it is enough to consider the horizontal component of the earthquake action on the structure. However, the limit state design, there is a need of consideration of both of the horizontal and vertical components of the earthquakes simultaneously.

Acknowledgments The author would like to appreciate the Azarbaijan University of Shahid Madani, Iran for their support. The author is also grateful to Professor Nagi Pour and other staff of the University research center for their timely contributions and suggestions.

References

ANSYS (2010) Academic Research, Help System, Coupled Field Analysis Guide, ANSYS, Inc.
Chopra AK (2007) Dynamics of structures, 3rd edn. Pearson/Prentice Hall Co., Englewood Cliffs
CSI (2008) Analysis reference manual for SAP2000. ETABS and SAFE, Berkeley
Cunieda HJ (1997) Earthquake response of roof shells. Int J Space Struct 12(3–4):149–160
Ihsikawa K, Kato S (1997) Elastic—plastic buckling analysis of reticular domes subjected to earthquake motion. Int J Space Struct 12(3–4):205–216
Kave A (2000) Investigation of dynamic behavior of barrel vaults. In: Fifth international conference of civil engineering, Tehran
Ministry of Housing and Urban Development (2006) Iranian National Building Code, Part 6, Minimum Building Loads. Iran, Tehran (in Persian)
Ministry of Housing and Urban Development (2008) Iranian National Building Code, Part 10, Design of Steel Buildings, Iran, Tehran (in Persian)
Mogaddam HA (2000) Seismic Behavior of Space Structures. Int J Space Struct 15(2):119–135
Nooshin H, Disney P (1997) Formian 2. Multi-Science Publishing Co Ltd., Brentwood
Sadeghi A (2010) Effects of earthquakes on some families of the barrel vaults. LAMBERT Academic Publishing Co., Germany, p 443
Sadeghi A, Amani S (2012) Investigation of the benefits of application of earthquake action on the design of double layer barrel vaults. Int J Space Struct vol 27, No 1 15−21
Saka T, Hirano A, Tei Y, Taniguchi Y (2006) Effects of joints and members slenderness ratios on collapse behavior of double layer space grids. New Shell and Spatial Structures, Beijing, 16–19 Oct 2006

Mechanism of Permafrost Landslide Based on GPS and Resistivity Surveying

Wei Shan, Zhaoguang Hu, Hua Jiang, Ying Guo and Chunjiao Wang

Abstract The formation and development of landslide at K178 + 530 section of Bei'an-Heihe expressway was mainly affected by armchair shape topography of the slope, hydrologic and climatic conditions, frost-heave cycles, and geotechnical engineering activities for highway construction. The study employed data obtained from portable global positioning system (GPS) equipment and high-resolution resistivity profiling to characterize landslide mass dynamic characteristics, stratigraphic log profile of the landslide and analyze the motion mechanism of the landslide in K178 + 530 section of Bei'an-Heihe expressway. Lithologic and geological information were obtained from four monitoring wells drilled along the slope. About 40 GPS gauge piles were placed at different positions on the sliding mass on September 13, 2010, to accurately determine the time, direction and rate of movement at different locations and analyze the role of freezing, thawing and rainfall on the sliding mass. The field monitoring campaign lasted for more than 1 year. Between June, and September 2010, we carried out a high-resolution resistivity investigation to obtain resistivity profile logs of the slope. The results show that the landslide material resistivity profile logs show a significant difference before and after the sliding. Result shows that before the movement of the slope, data obtained from resistivity log shows a uniform signature, while after or during sliding, the resistivity signature changed. The change was due to the development of a slip surface within the landslide mass.

Keywords Landslide · Permafrost region · GPS · High-density resistivity method

W. Shan (✉) · Z. Hu · H. Jiang · Y. Guo · C. Wang
Northeast Forestry University, 150040 Harbin, China
e-mail: shanwei456@163.com

F. Wang et al. (eds.), *Progress of Geo-Disaster Mitigation Technology in Asia*, Environmental Science and Engineering, DOI: 10.1007/978-3-642-29107-4_18,

1 Foreword

Landslide is a downward movement of soil, rock or a mixture of both along slopes under the effect of gravity (Kong et al. 2008; GB50021-2001 2002). It is one of the main disasters associated with mountainous regions where near vertical slopes lie close to highways and poses serious threats to lives and properties (Feng et al. 1999; Shan et al. 2008; Liu et al. 2007).

Accurate determination of the sliding surface of a landslide mass and failure characteristics is an important factor in slope stability analysis and landslide prevention programs (He 1991). The purpose of landslide geotechnical engineering investigation is to determine these important parameters which play vital roles in disaster prevention and mitigation (Zhu et al. 2008).

This article utilizes results from GPS technology and high-resolution resistivity profiling to study motion mechanism and failure style of landslides in permafrost regions. The study area is located in Lesser Khingan Range central region at K178 + 530 section of Bei'an-Heihe Expressway, in high altitude permafrost degraded region of China. We used GPS technology to monitor the morphological changes of the landslide and employed high-resolution resistivity profiling to obtain stratigraphic log profile of the landslide which aided in determining the failure surface and other changes in discontinuity of horizontal strata.

2 General Situation of Study Area

2.1 Physical Geography of Study Area

The study area is located in Lesser Khingan Range central region, in high altitude permafrost degraded belt of China. Climatic data of the area shows that spring season is warm and short; summer hot and rainy with cool and short autumn period and cold long winter season. Annual average temperature of the region is −0.8 °C, annual average precipitation is 510–572 mm, with high rainfall intensity between July and September, which accounts for 60 % of annual total precipitation. Winter starts in October and ends in late March or early April. Permafrost deposits dominates the upper part of the slope with maximum seasonal frozen depth is 2.30–2.50 m The geomorphology of the area is mainly low mountains and hills with high topographic relief in high altitude permafrost region (Fig. 1).

Fig. 1 K178 + 530 geographical position

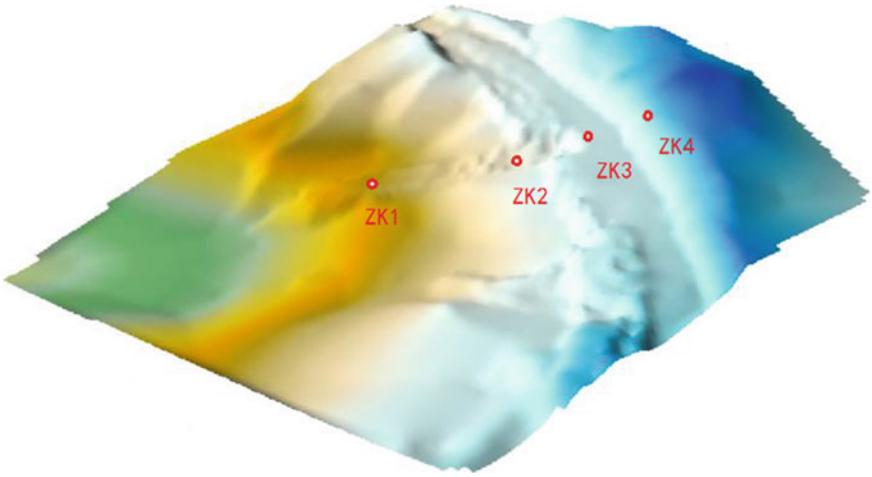

Fig. 2 K178 + 530 drilling holes arrangement

2.2 Geological Structure of Study Area

In order to obtain lithologic and geological characteristics of the landslide section, we drilled four monitoring holes to depths of 14–26 m. Figure 2 shows the arrangement of the monitoring holes.

The stratigraphic log profile of the landslide material is made up of Cretaceous mudstone and sandstone, Tertiary pebbly sandstone, and Quaternary loose sediments. These are further subdivided into the following units:

(1) Subgrade soil or highway construction material: This unit includes subgrade materials, Tertiary pebbly sandstone, Cretaceous mudstone and sandy mudstone with characteristic reddish-brown colouration. It is wet, loose when dry and plastic once saturated. Thickness is about 1–1.5 m at the upper and middle section of log profile.

(2) Silty clay: This layer shows intercalation of silts and clay which enhanced pore water infiltration. It is soft and usually wet, poorly graded, brownish appearance with visible seepage outlets. This unit lies between 1.5–3.8 m on the upper section of the log profile (ZK2 hole), and in depth of 0–6.7 m in the middle and lower sections of the slope (ZK1 hole). Intercalation of fine sand and shale were also observed, with thicknesses which range from 1 cm to 10 cm. Water permeability is also high at the sand-shale contacts.

(3) Tertiary pebbly sandstone: This unit is located in depth range of 3.8–4.5 m, on the upper section of the landslide (ZK1 hole). It is weathered, loose, poorly graded composed pebbles distributed in a fine sand matrix which enhanced surface water infiltration.

(4.1) Weathered siltstone: This unit occupies depth range of 4.5–14.3 m on the upper section of the landslide (ZK1 hole). It shows thin parallel lamination, Sandy structure, bedding construction and week bonding force, all the mineral constituents is weathered into secondary minerals, the locality has clay substance, and the structure has been compromised, the ability of water permeability is vey bad.

(4.2) Weathered mudstone: This unit is located below the silty clay layer at depth range of 6.7–8.0 m for ZK1 hole and below siltstone layer at depth of 14.3 m in ZK2. The rocks are unconsolidated, soft, and relatively impermeable. Colour of weathered sample is gray while fresh sample colour is black.

(5) Completely weathered mudstone: This unit dominates the basal section of the slope which is distributed around ZK1 and ZK2. It shows a massive structure lacking bedding planes with very fine grain sizes and characteristic black-gray appearance for fresh sample and gray for weathered sample (Fig. 3).

3 Formation Mechanism and Morphological Characteristics of Landslide

The formation and development of the landslide at K178 + 530 section of Bei'an-Heihe expressway mainly was affected by the topography, engineering geology, hydrology and climate characteristics, armchair shape topography, active groundwater change, intense freeze–thaw cycle and civil engineering activities. Because of the highway construction, landslide materials dislodged from the unstable slope make up one-third part of exposed soil in the area; perennial fissure

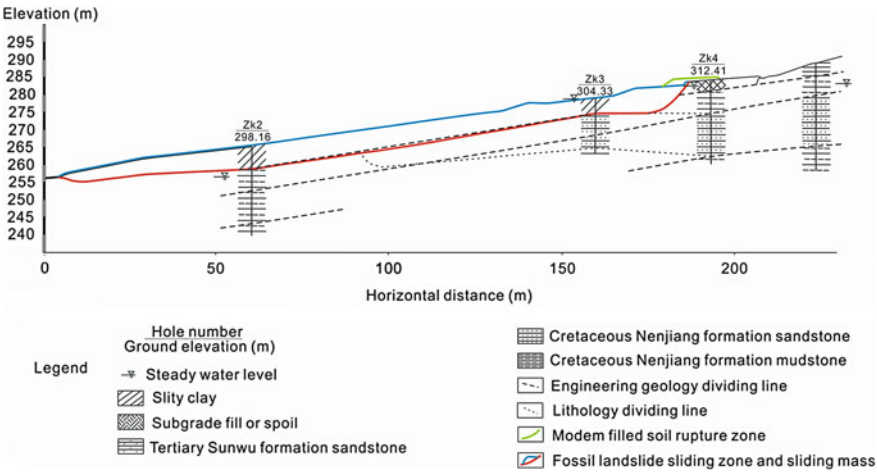

Fig. 3 Geological structure of K178 + 530

spring water flows from the main scarp (left side of the road) of the landslide, eroding the landslide body; high precipitation in rainy seasons and surface water infiltration into the slope increases the shear stress within the slope. Infiltration of snowmelt water, fissure water and rainwater provided water source for landslide liquefaction. High permeable slope material provided channel way for water infiltration while mudstone and sandstone units with low permeability form aquiclude. Rupture surfaces observed within gravelly sand and silty clay above the aquiclude was influenced by infiltration water to reach saturation, forming rupture surface. In late July 2010, the slope started to slide.

Slip surface of the upper part of the slope is located at depth range of 4.5 m, the slip surface is at the interface of gravel sand and siltstone; rock unit underlying the slip surface is poorly consolidated siltstone. Slip surface of the middle and lower parts of the slope is in the depth range of 6.5 m, which is the interface of silty clay and mudstone. The rock unit underlying the slip surface is moderately consolidated mudstone.

This landslide belongs to Chair-bedding push type landslide of superficial area, located at the left side of the embankment road. Soil leftover from the road construction and subgrade filling soil slide along the gully, The 178 + 530 landslide presents a tongue shape, with width of about 20–30 m, acreage of about 5000 m^2; the distance from toe to rear edge is about 200 m. Vertical elevation of the toe section is 254 m while elevation of rear edge is 285 m. Leading edge of the landslide pushes up humus soil of original ground surface to slide forward. And arcuate dislocation in the rear edge, the dislocation was in rang of widen subgrade. There are downtrees at leading edge of the landslide.

4 Landslide Monitoring Based on GPS

4.1 The Arrangement of GPS Monitoring Piles

On 22 of July, 2010, two deformation monitoring pipes on the landslide body were sheared to the depth of 4.2 m and 6.5 m respectively under the ground; the sensor connection lines were also sheared. The result was used in monitoring the motion mechanism of the landslide. We arranged 49 GPS gauge piles at different positions on the landslide on 13 of September, 2010. Using GPS to monitor the moving data of these gauge piles, monitoring cycle is more than 1 year.

The arrangement of GPS gauge piles is shown in Fig. 4. From the rear edge of landslide to the leading edge we respectively arranged 11 rows in order, respectively arranging on the both sides of the outside landslide, the central location on the top of landslide and close to the rear edge of landslide. The distance from the first row to the rear edge of landslide is 15 m, and the numbers from left to right 1#–3#; The distance from the second row to the rear edge of landslide is 30 m, and the numbers from left to right 4#–10#; The distance from the third row to the rear edge of landslide is 50 m. The distance from the forth row to the rear edge of landslide is 70 m. The distance from the fifth row to the rear edge of landslide is 93 m. The distance from the sixth row to the rear edge of landslide is 119 m. The distance from the seventh row to the rear edge of landslide is 134 m. And the others are distribution near the leading edge of the landslide. These GPS monitoring piles can monitor the sliding condition at the upstream and middle stream, as well as the downstream of the landslide. It also can monitor the centre, near the edges and outside locations etc. of the landslide. The monitoring cycle lasted for more than one year.

4.2 Gauge Piles Motion Characteristic at Different Positions

By the first row of gauge piles sliding displacement graph (as shown in Fig. 5), From September 13, 2010 to November 2010, 1#, 2# and 3# gauge piles of sliding displacement were 6.90 m, 8.05 m and 4.12 m respectively. From November 2010 to mid-late May 2011, landslide was not sliding. Until early June 2011, landslide began to slide, and by September 25, 2011, sliding displacements of 1#, 2# and 3# gauge piles were 45.70 m, 65.01 m and 23.82 m in 1 year. In the same cross-sectional inside, slip rate in a central location close to slip rate near the edge.

Figure 6 shows the displacement graph of the second row gauge piles. From the front row and second row sliding displacement graph of gauge piles, from monitoring commencement day (September 13, 2010) to the middle of November, Landslide had been in sliding state. After mid-November, land surface began to freeze, and until the end of May 2011, landslide had been always in steady state. From early June 2011, Landslide began to slide once again. During the same time,

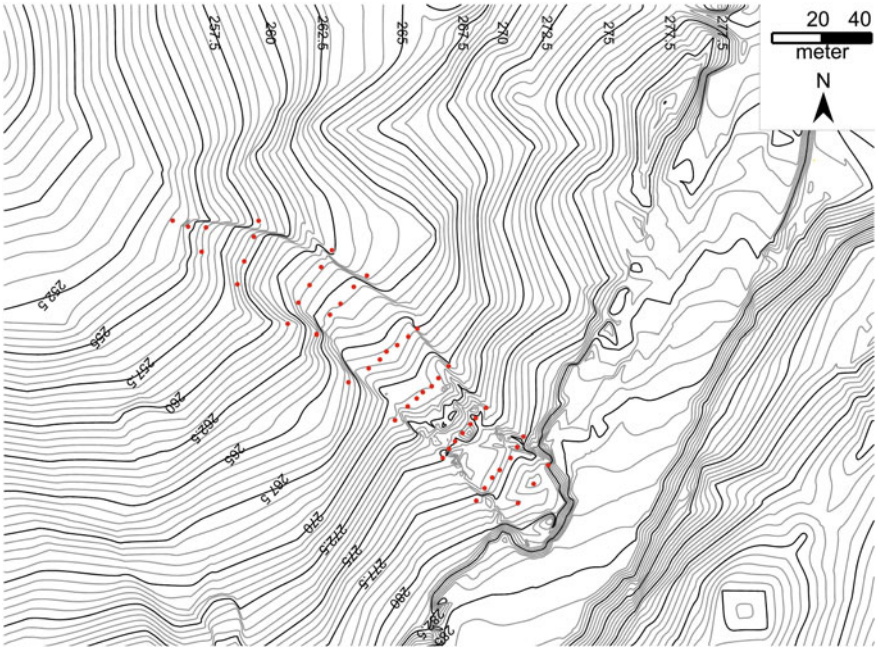

Fig. 4 Arrangement diagram of GPS monitoring piles

Fig. 5 The sliding displacement graph of the first row gauge piles

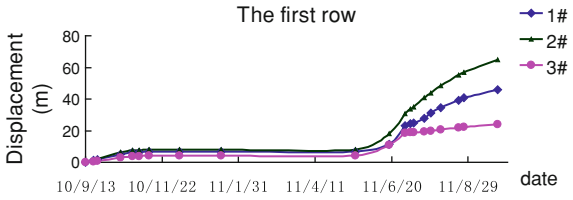

Fig. 6 The sliding displacement graph of the second row gauge piles

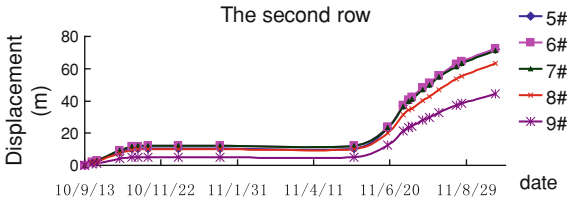

gauge piles sliding displacement in the central location of landslide are obviously bigger than gauge piles of sliding displacement near edge position.

From the gauge pile slip displacement curve (Fig. 7) in the central location of landslide, we can see that, from September 13, 2010 to September 25, 2011, during the 377 days, the gauge pile slip displacement from the first row to the seventh row respectively are 65.01 m, 71.31 m, 64.20 m, 54.23 m, 46.37 m, and 39.43 m.

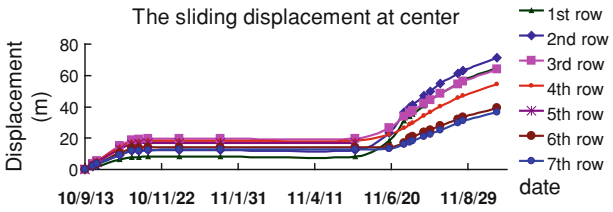

Fig. 7 The gauge pile slip displacement curve in the central location of landslide

It shows that, sliding displacements of different positions are large different during the same time. Sliding displacement of the middle and upper sector is the farthest, sliding displacement of the lower sector is the smallest.

5 Resistivity of Landslide Based on High Density Resistivity Method

5.1 The Arrangement of High Density Resistivity Measuring Line

During application of high density resistivity method in K178 + 530 section, we use 2DRES 2D high-density resistivity method inversion software to inverse least square method, inversion of the program we use is based on least square method which based on quasi-Newton algorithms for Nonlinear optimization, and module width is set to one-second unit electrode spacing to improve monitoring precision. To ensure depth and accuracy, the unit electrode spacing is 3.0 m in the test, sounding almost 30 m.

Figure 8 shows the high density resistivity measuring line at K178 + 530 landslide sections along the landslide (vertical road direction). The measuring line was from median strip, respectively going through the landslide rear edge, drilling ZK2 and drilling ZK1 location and stretching into 177 m along landslide to where is 32 m distance from forefront of landslide, the distance of landslide back edge, drilling ZK2 and drilling ZK1 location from the first electrode respectively are 9 m, and 42 m, and 96 m. The numbers of electrode arrangement: the numbers 1–60 are successively arranged from the median strip of road location to the leading edge of landslide. During the test, Wenner arrangement method was used.

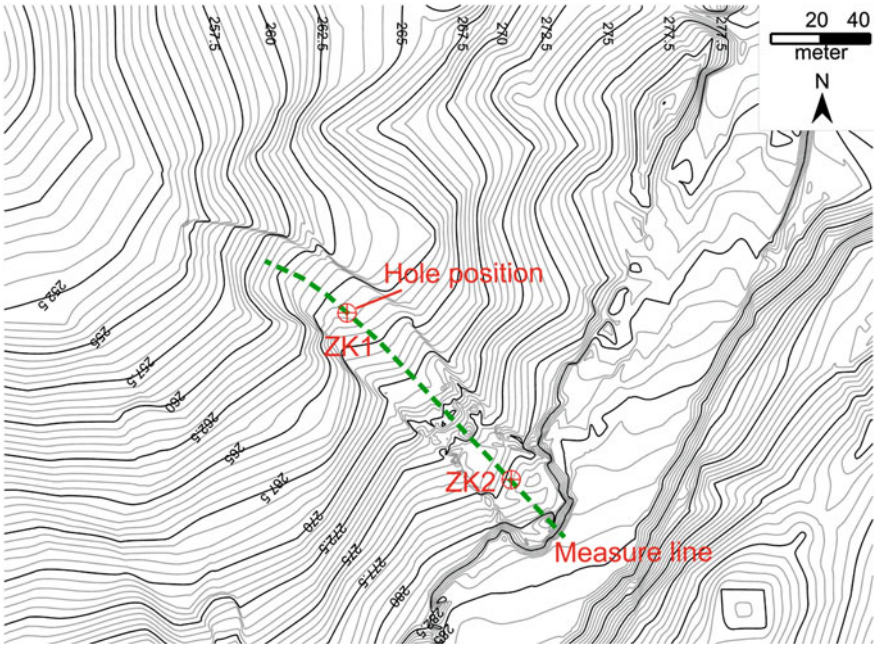

Fig. 8 The high density resistivity measuring line

5.2 The Landslide Soil Resistivity Change Before and After the Landslide Forming

We began investigation and study on K178 + 530 areas from May 2010, before July 22, 2010, K178 + 530 landslides had been in stable state. On July 22, 2010, two deformation monitoring pipes on the landslide body were sheared respectively in the depth of 4.2 m and 6.5 m under the ground, the sensor connection lines were also sheared, accordingly, we determined that the landslide soil began sliding. During the application of high density resistivity method in the process of investigation and study on K178 + 530 landslides, on June 1, 2010, and September 10, 2010, we did twice measure on the landslide, gaining the landslide soil resistivity change before and after the landslide forming.

As shown in Fig. 9 is the inversion images of landslide soil resistivity on June 1, 2010, when the landslide had not yet been formed and the landslide body had not yet started to slide. Through the inversion images of resistivity we could get: before the landslide body formed, landslide body's resistivity values was monotone decreasing with the depth increase, and had no jumping phenomenon of resistivity values.

As Shown in Fig. 10 is landslide soil resistivity inversion image on September 10, 2010. By the resistivity inversion image we can get: there is an obvious layered

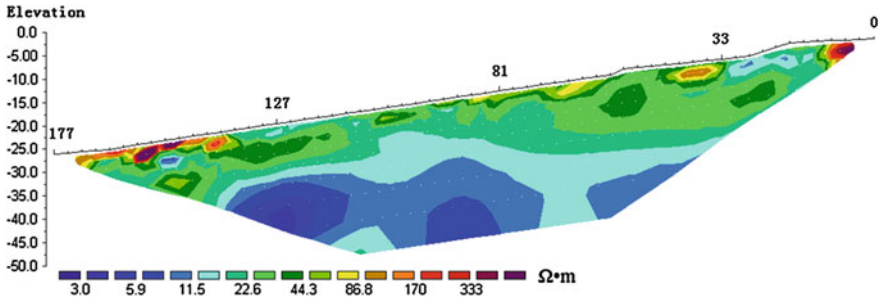

Fig. 9 The inversion images of landslide soil resistivity on June 1, 2010

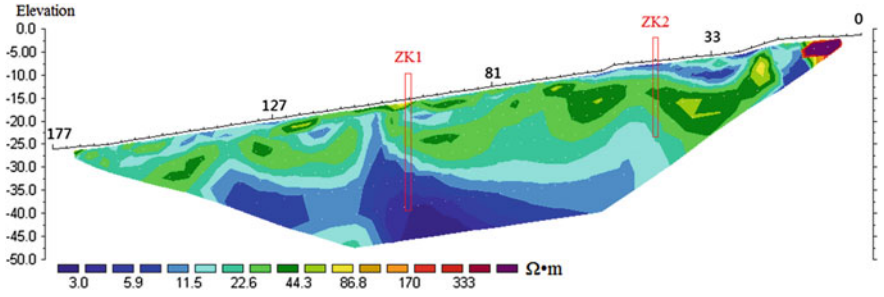

Fig. 10 The inversion images of landslide soil resistivity on September 10, 2010

of landslide soil resistivity and clear differences of sliding surface soil resistivity value after landslide formed.

The first electrode distance of 96 m (drilling 1 position), resistivity value as shown Figs. 10, 11. Depth 0–2.1 m is silty clay, which containing about 15 % of the organic matter as grassroots ect., and resistivity value is 20–67 Ω · m; Depth 2.1–6.7 m is silty clay, which local have weathered sand sandwich, and resistivity value is 15–32 Ω · m; Depth 6.7–8.0 m is mudstone, and its structure is pieces, and resistivity value is 46–54Ω · m; Depth 8.0–26 m is gray mudstone, where is close to ground water level or below ground water level in the underground, and resistivity value smaller is 10–35Ω · m. In 0–2.1 m depth is silty clay that contains a lot of grassroots, water down the plant roots to infiltrate is easy; Below 6.7 m is mudstone, the permeability coefficient is small, water is difficult to infiltrate, forming water-resisting layer. Water is easy to gather in the top surface of mudstone layer, mudstone in water softening disintegration and easy to form the sliding surface. Due to the local weathered sand sandwich, the silty clay in 2.1–6.7 m depth can make water infiltrate easily.

The first electrode distance of 42 m (drilling 2 positions), resistivity value as shown Figs. 10, 12. In 0–4.5 m depth, resistivity value is 10–27Ω · m, the surface layer road building abandon soil give priority to silty clay (Depth 0–3.8 m), resistivity value is 15–27Ω · m, resistivity value of sand gravel (Depth 3.8–4.5 m) is 10–22Ω · m. Below 4.5 m is siltstone, particles smaller and seepage ability is

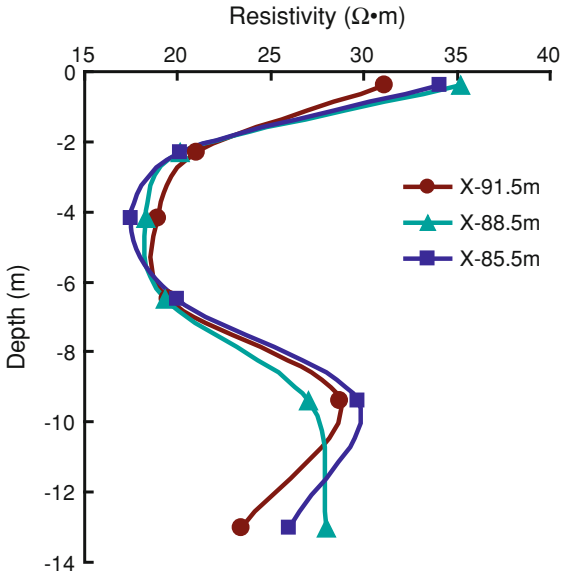

Fig. 11 Resistivity curve of drilling 1 position

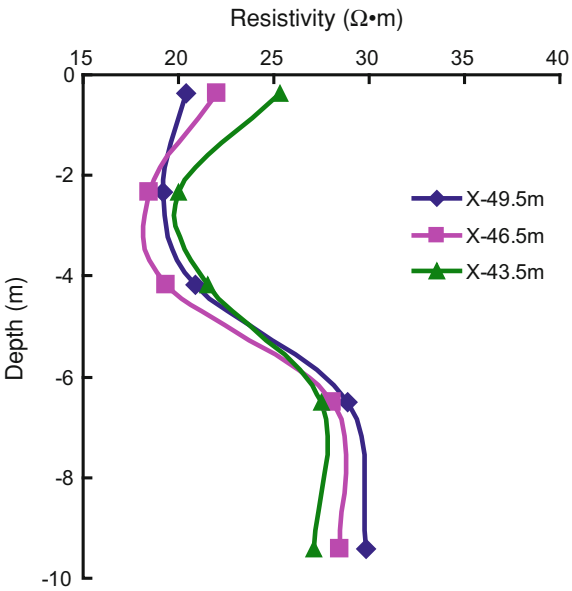

Fig. 12 Resistivity curve of drilling 2 position

poor, forming water-resisting layer. The soil infiltration to 4.5 m depth location is easy to gather and form the sliding surface. In the 4.5 m, the position of sand gravel and siltstone handover, the resistivity apparent stratification. Depth 0–4.5 m, the soil is good permeability, water infiltrates easily; Depth 4.5–9.7 m is siltstone, and resistivity value is 25–54 Ω · m; Depth 9.7–14.6 m is sandstone, and resistivity value is 21–43Ω · m.

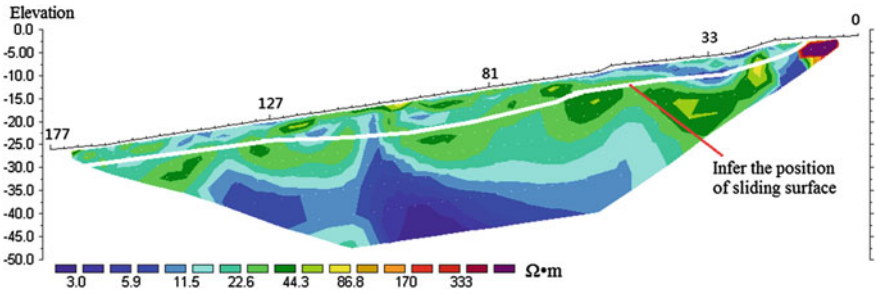

Fig. 13 Infer the position of sliding surface

The resistivity value at the slip surface location showed significant stratification and the resistivity values of its upper and lower show more obvious differences. According to the typical characteristic of the slip surface, we can infer the position of sliding surface, as shown Fig. 13.

6 Conclusion

(1) The slope failure belongs to superficial and translational movement on bedding planes in permafrost region. The soil within the sliding surface is silty clay, which is loose when dry, soft and plastic. The main triggering factor observed was freeze–thaw which has cycle have far-reaching consequences for the landslide, exhibiting intermittent slide and bench slope. There are Drumlin fields on the landslide slope. Snowmelt water, rainwater and fissure water provide groundwater source for the landslide. Tympanites cracks on the slope contribute to atmospheric precipitation pool in the landslide and permeate into the landslide. High permeability of landslide soil mass provides passage for water infiltration; mudstone and sandstone with low permeability form aquifuge while silty clay above the aquifuge is influenced by infiltration water to reach saturation, forming rupture surface.

(2) Different locations on the landslide have large different sliding displacements during the whole monitoring period. The displacement near the main scarp is largest, 50–72.56 m; at the middle of the landslide is 36.69–46.37 m, near landslide toe is 8.25–30 m. On the landslide exists bedding son-landslide, the distance between son-landslide flank and mother-landslide flank is 1.5–4 m, within the same cross section of landslide, the sliding displacement of center is largest, the sliding displacement near landslide flank is smallest.

(3) Sliding velocity of the landslide is large different in different seasons. From mid-November to late May of the following year, Rainfall was very small, the surface layer of ground was frozen, Landslide was at rest all the while; In late May of the following year, Due to the seasonal frozen ground melts and

snow cover melting and infiltrating, Landslide began slipping once again, the sliding velocity of landslide was fastest in this period (from late May to mid-June), sliding velocity of rear edge was 0.89 m/d, sliding velocity of middle landslide was 0.37 m/d, and sliding velocity near toe was 0.16 m/d; Sliding velocity began decreasing in late June, sliding velocity of rear edge was 0.51 m/d, sliding velocity of middle landslide was 0.30 m/d, and sliding velocity near toe was 0.11 m/d; After mid-October, sliding velocity of the landslide was slower, the average was 0.08 m/d.

(4) Using the high-density resistivity method to survey the landslide and its surroundings, and to accurately detect the landslide resistivity value at different locations, according to characteristic of resistivity value, and combined with drilling results, to determine the position of sliding surface: at rear edge, the position of sliding surface was at the depth of 3.2 m apart from the ground; at 30 m apart from rear edge, sliding surface was at the depth of 4.5 m; at the middle landslide, sliding surface was at the depth of 6.5 m; near the landslide toe, sliding surface was at the depth of 4 m, at toe position, sliding surface was at the depth of 2.5 m. Within the same cross section of landslide, sliding surface of center is deepest; sliding surface near landslide flank is shallowest.

(5) At the position of the sliding surface, the resistivity is obviously low, about 7–20Ω m; the resistivity at the position of landslide flank shows a sudden change, obviously large. Resistivity value of soil on the landslide is lower than resistivity value of soil at the same depth of outside landslide.

Acknowledgments This work was financially supported by Heilongjiang Communications Department project and subtopic of the western communication science and technology project "Study on Subgrade Stability Controlling Technology of Expressway Expansion Project Permafrost Melt and Landslides Sections".

References

Feng SR, Feng DX, Ge XR et al (1999) 3D limit equilibrium method for slope stability and its application. Chin J Geotech Eng 21(6):657–661

GB50021-2001 (2002) Geotechnical engineering investigation specification. China Architecture & Building Press, Beijing

He YX (1991) Application of D.C electric sounding for the permafrost exploration along Xinjiang-Xizang highway. J Glaciol Geocryol

Kong FL, Chen C, Sun GJ (2008) Application of multi-electrodes electrical method to landslide investigation in Qingjiang Shuibuya reservoir. Chin J Eng Geophys 5(2):201–204

Liu LH, Zhu DY, Liu DF (2007) Discussion on multiple solutions of safety factor of a slope. Rock Soil Mech 28(8):1661–1664

Shan W, Liu HJ, Yang L et al. (2008) Study of regularity of variation of water content in shallow layer of soil road cutting slopes in seasonally frozen-ground region. Rock Soil Mech 29(sup.):335–340

Zhu Y, Rao Z, Wu B (2008) Organic and gas geochemistry of gas hydrate-bearing sediments from mallik 5L–38 production research well, Mackenzie Delta Canada. Geol surv Can Bull 68(2):311–319

Cut Layer Rocky Landslide Development Mechanism in Lesser Khingan Mountain

Hua Jiang, Zhaoguang Hu, Ying Guo, Chunjiao Wang and Wei Shan

Abstract Bei'an to Heihe expressway utilizes the original second-class highway to widen and expand for expressway, restricted by the original location of old road, widen subgrade of some sections locate in tailing edge of the landslides, influenced by the landform, geological condition, climate and anthropogenic factors, are in unstable states, bring great difficulties to widening and expanding implementation. In process of landslide researching, firstly identify the space form of landslide, analyze the formation mechanism of landslide, evaluate the stability condition and the development tendency of landslide, and then determine the prevention and treatment measures. Took the Bei'an to Heihe expressway cut layer rocky landslide as the research object, employed the geological survey, topographic mapping, geological drilling, indoor test, numerical simulation, field monitoring and theoretical analysis methods to carry an integrated study on the development mechanism and damage mode of the landslide. Through systematic study, drew the conclusions that: the rupture surface is located in completely weathered mudstone; during surveying, the landslide is temporarily in steady state, when the water content continues to increase to 34.7 %, the landslide will reach the state of limit equilibrium; atmospheric precipitation, the island permafrost which scattered in the mountain valley melting water, snowmelt water and seasonally frozen soil thawing water provide a continued water source for landslide, surface water and ground water supply the Cretaceous pore water by infiltration and lateral runoff through surface thermal shrinkage cracks and shallow high permeability rock and soil, low permeability mudstone under the loose overburden forms aquiclude,

Wei Shan (1965), male, professor, doctor of Engineering, doctoral tutor. Research interests: disaster prevention and mitigation of road and bridge engineering.

H. Jiang · Z. Hu · Y. Guo · C. Wang · W. Shan (✉)
Northeast Forestry University, 150040 Harbin, China
e-mail: shanwei456@163.com

F. Wang et al. (eds.), *Progress of Geo-Disaster Mitigation Technology in Asia*, Environmental Science and Engineering, DOI: 10.1007/978-3-642-29107-4_19,

completely weathered mudstone above the aquiclude which is influenced by the Cretaceous pore water to be soften forms rupture surface; due to the permafrost distribution discontinuities and geological conditions difference, the landslide has gradual, low angle, creeping characteristics.

Keywords Expressway · Cut layer rocky landslide · Development mechanism · Damage mode

1 Introduction

Landslide is a phenomenon that the rock and soil of a slope occurs shear failure and significant horizontal displacement along a weak structural zone or maximum shear zone (Hu and Wang 2010; Qiao 2002). Landslide geological disasters have a wide distribution in the world, hazard is very serious, and it not only brings a threat to the safety of human life, but also has a destructive effect on the property, environment, and resource (Zhang et al. 2010). Bei'an to Heihe expressway utilizes the original second-class highway to widen and expand for expressway in Heilongjiang province of China, restricted by the original location of old road, some widen subgrade of K177 + 400 − K180 + 000 section which is situated in the Lesser Khingan Mountain central region locate in tailing edge of the landslides(see Fig. 1), influenced by the landform, formation lithology, geological structure, hydrogeology condition, climate and anthropogenic factors (Duan 1999; Zhang et al. 2000; Li et al. 2002), the landslides are in unstable states, bring great difficulties to widening and expanding implementation.

In process of landslide researching, firstly identify the space form of landslide, analyze the formation mechanism of landslide, evaluate the stability condition and the development tendency of landslide, and then determine the prevention and treatment measures. This article took the Bei'an to Heihe expressway cut layer rocky landslide as the research object, employed the geological survey, topographic mapping, geological drilling, geophysical exploration, indoor test, numerical simulation, field monitoring and theoretical analysis methods to carry an integrated study on the development mechanism and damage mode of the landslide.

2 Field Survey

Bei'an to Heihe expressway landslide section is located in the central region of Lesser Khingan Mountain. The climate of the area belongs to continental monsoon climate, the spring gets warm quickly, the summer is tepidity and rainy, the

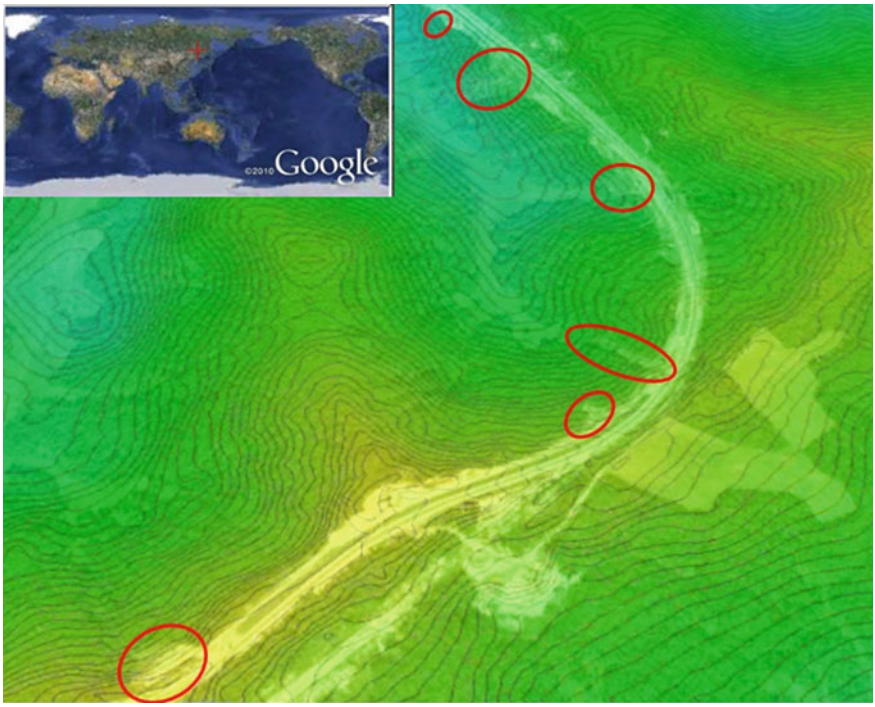

Fig. 1 Aerial view of Bei'an to Heihe expressway landslide section

autumn gets cool fast, the winter is long and cold. The annual average temperature is −0.6 °C. The average annual precipitation is 400–650 mm, and the rainfall concentrates in July to September of the summer. Average sunshine time is 2551.5 h. Frost-free period is 90–120 days.

The tectonic is in the Wuyun-Jieya new rift zone, the south is Shuhe upwarping zone and the north is Handaqi virgation. Surface exposed stratum: the upper Cretaceous Nenjiang formation, Tertiary Pliocene series Sunwu formation, and Quaternary Holocene series modern river alluvium and stack layers. According to the aquiferous medium, supply and drainage conditions, groundwater is divided into Cretaceous pore water, Tertiary pore water and Quaternary pore water three kinds.

According to the field survey, found three sections widening subgrade influenced by landslide, this article aimed at the first landslide, the landform of the landslide is shown in Fig. 2.

The whole landform of landslide area is one ridge at the back, two ridges on the left and right sides, gentle slope terrain in the middle part. The flat shape of landslide body presents a tongue. There are inconspicuous arc cracks on the tailing edge of the landslide, upheaval on the front of the landslide and scaly turf on the surface of the landslide body (see Fig. 2).

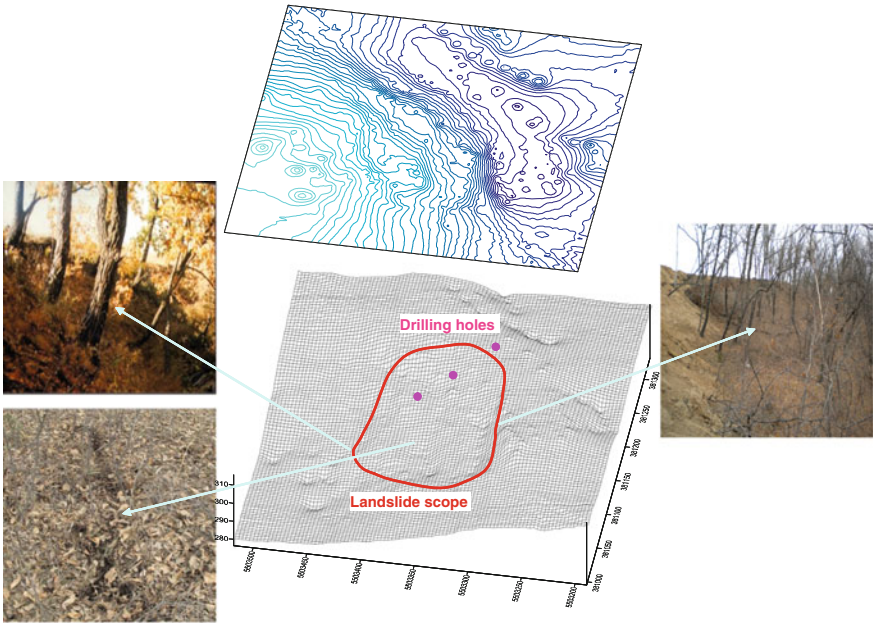

Fig. 2 Tree dimensional terrain of landslide region

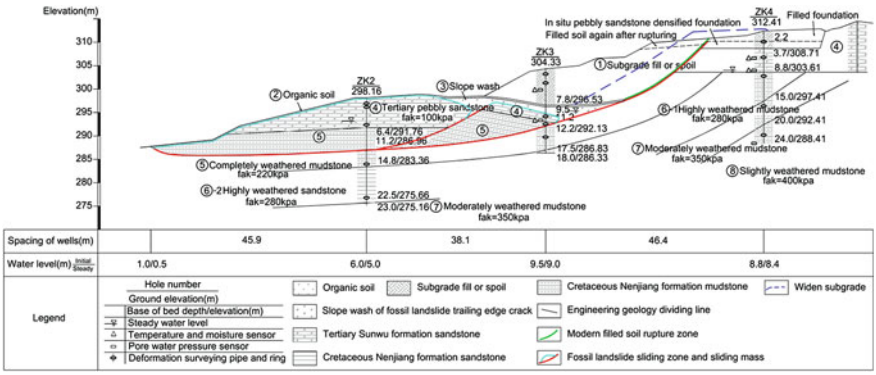

Fig. 3 Landslide engineering geological profile and monitoring equipment arrangement diagram

3 Geological Exploration

To survey the geological condition of the landslide, we arranged three drilling holes and five resistivity measure lines, drilling holes position as shown in Fig. 2. According to the drilling and resistivity surveying results, drew the engineering geological profile as shown in the Fig. 3. Deformations monitoring equipments,

temperature, moisture, pore water pressure sensors were respectively embedded in the holes.

The surface of landslide area mainly consists of Tertiary pebbly sandstone and subgrade abandon soil (sandy clay), high void ratio, many cracks in the soil and weak integrity. The shallow completely weathered mudstone has obvious cracks which have evident water encroached signs; the deep completely weathered mudstone is relatively dense. Through indoor test, the permeability coefficient of sandy clay is 2.74×10^{-6} m/s, Tertiary pebbly sandstone is 2.55×10^{-5} m/s, shallow completely weathered mudstone is 1.74×10^{-6} m/s, and deep completely weathered mudstone is 2.23×10^{-7} m/s.

The permeability coefficient of surface rock and soil and shallow completely weathered mudstone is larger, the permeability coefficient of deep completely weathered mudstone is smaller. When the water penetrates downward through shallow rock and soil and accumulates on the surface of the dense mudstone, the water content of the mudstone layer increased gradually, shear strength decreases significantly. This judgment, the landslide belongs to cut layer rocky landslide, rupture surface is located in completely weathered mudstone.

4 Landslide Stability Numerical Simulation

Limit equilibrium method is the most mature method in landslide stability study (Liu et al. 2007; Hu et al. 2005). The limit equilibrium method is characterized in that only considers static equilibrium condition and soil Mohr–Coulomb failure criterion, need assume rupture surface during calculating. Compared with limit equilibrium, finite element method namely considers the soil static equilibrium, also meets the strain compatibility and stress strain constitutive relation, can serve as a more rigorous theoretical system for slope stability analysis, it needn't assume the shape and position of rupture surface, determines the stability of landslide through stress and strain analysis (Yang et al. 2010; Zhu et al. 2007).

Through geological survey and indoor test analysis, the landslide stability is mainly controlled by the water content of rupture surface rock and soil, employed finite element method to study the law that safety factor of landslide changes with water content of rupture surface soil. The finite element calculation parameters of rock and soil were determined by indoor experiment and engineering analogy method, as shown in Table 1.

The rupture surface soil water content is 32.1 % and saturation is 0.899 during surveying, the slope safety factor is 1.58, the landslide total deformation before damage is shown in Fig. 4. The landslide is temporarily in a steady state, but the rupture surface soil has not reached saturation state, when the water content of the rupture surface soil continues to increase to 34.7 %, saturation reaches 0.972, the safety factor of landslide will be reduced to 1.08, and the landslide will reach the state of limit equilibrium. When the surface soil saturated with water or

Table 1 Physical and mechanical parameters of calculation model

Rock and soil name	Unit weight (g/cm^3)	Cohesion (kPa)	Friction angle (degree)	Modulus of elasticity (MPa)	Poisson's ratio
Subgrade fill or spoil	1.89	21	9	14	0.35
Pebbly sandstone	1.98	5.2	27	26	0.22
Completely weathered mudstone above the rupture surface (natural/saturated)	1.81/ 1.85	16.4/10.3	8/5	15/15	0.36/0.36
Completely weathered mudstone under the rupture surface	1.80	26.6	12	32	0.35
Highly weathered mudstone and sandstone	1.85	34.7	14	70	0.34
Moderately weathered mudstone	1.88	45.5	18	93	0.32
Slightly weathered mudstone	1.91	57.6	19	110	0.3

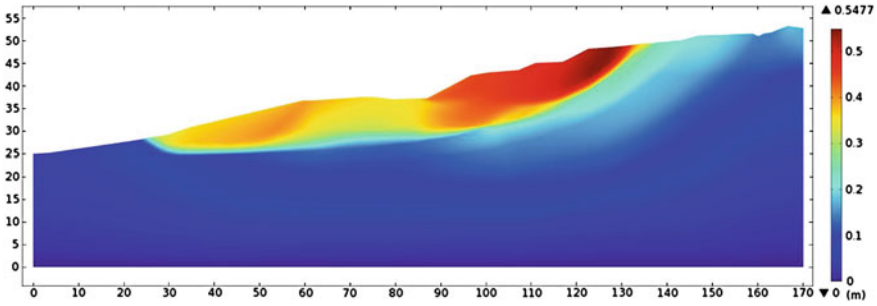

Fig. 4 Landslide total deformation cloud map before damage

abandon soil loading or filling subgrade, the ancient landslide will be likely to slide, and affect the stability of subgrade slope.

5 Field Monitoring

After surveying, we began to collect monitoring data, 32 days later, found that ZK2 and ZK3 deformation monitoring pipe were sheared respectively in the depth of 11.0 m and 12.1 m under the original ground; the temperature, moisture and pore water pressure sensor connections were also sheared; striation appeared on the front of the landslide; many cracks appeared on the mountain surface, and the cracks were in developing trend. Based on these data and phenomena, judged that the slope occurred slide. At that same time, employed GPS to monitor the tube nozzle moving data (see Fig. 5), and paid attention to the pore water pressure data

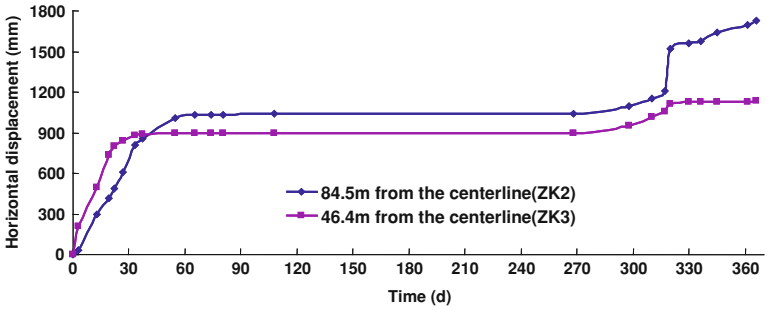

Fig. 5 Curve of nozzle horizontal displacement changes with time

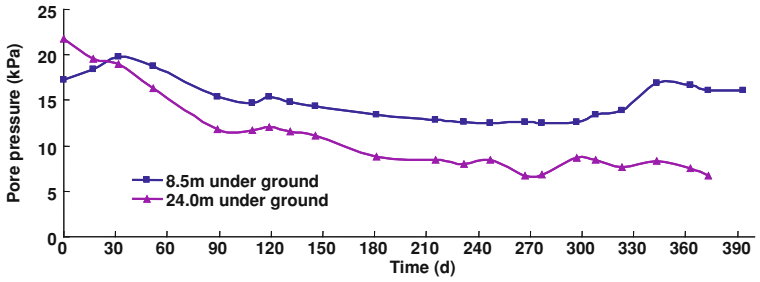

Fig. 6 Curve of ZK4 pore water pressure changes with time

(see Fig. 6) and deformation data of ZK4, the vertical and horizontal displacement of ZK4 were very small.

The landslide began to slide at the rainy season, deep pore water pressure of the region was max of the year, and reached the steady state until winter when the ground began to freeze, the maximum horizontal displacement respectively reached 1.03 and 0.9 m, the landslide formation is mainly influenced by precipitation and permafrost melting. The landslide slid again in the spring melts period of the following year, the seasonal frozen soil layer of the area was completely melted at that time, deep pore water pressure increased rapidly, and the maximum horizontal displacement respectively reached 1.73 and 1.14 m, landslide sliding again is mainly influenced by frozen soil melting and snowmelt.

6 Landslide Development Mechanism

Formation and development of the landslide is mainly affected by the landform, climate and water, geological condition and other factors.

Topography condition: topography of the landslide is upper steep and lower gentle, one ridge at the back, two ridges on the left and right sides, is avail for

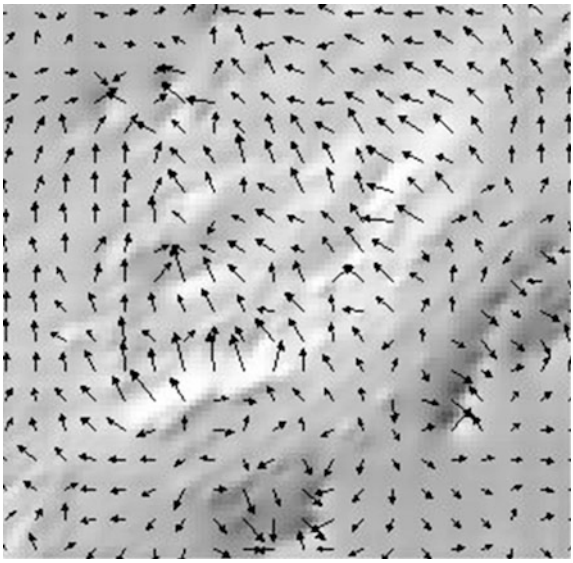

Fig. 7 Landform vector graph of landslide region

surface water and ground water to assemble in landslide (see Fig. 7); the rupture surface is so gentle to retain rainwater for a long time; these provide favourable terrain condition for the landslide development.

The effect of climate and water: atmospheric precipitation and permafrost melting water constantly supply the Cretaceous pore water in the rainy season, snowmelt water and seasonally frozen soil thawing water constantly supply the Cretaceous pore water in the spring thawing period. Under the action of water, unit weight of the slide body increases and shear strength of rupture surface soil decreases.

Geological condition: surface thermal contraction cracks and shallow high permeability soil and rock provide infiltration and lateral runoff channel for surface water and ground water; low permeability mudstone under the loose overburden forms aquiclude, completely weathered mudstone above the aquiclude which is influenced by the Cretaceous pore water to be saturated, the shear strength of the completely weathered mudstone decreases dramatically, then induce the landslide instability.

7 Conclusions

This article employed the geological survey, topographic mapping, geological drilling, geophysical exploration, indoor test, numerical simulation, field monitoring and theoretical analysis methods to carry an integrated study on the development mechanism and damage mode of the Bei'an to Heihe expressway cut layer rocky landslide, drew the conclusions that:

The landslide belongs to cut layer rocky landslide, and the rupture surface is located in completely weathered mudstone.

During surveying, for the rupture surface completely mudstone, the water content is 32.1 %, the landslide is temporarily in steady state, when the water content continues to increase to 34.7 %, saturation reaches 0.972, the safety factor of the slope will be reduced to 1.08, and the landslide will reach the state of limit equilibrium.

Atmospheric precipitation, the island permafrost which scattered in the mountain valley melting water, snowmelt water and seasonally frozen soil thawing water provide a continued water source for landslide, surface water and ground water supply the Cretaceous pore water by infiltration and lateral runoff through surface thermal shrinkage cracks and shallow high permeability rock and soil, low permeability mudstone under the loose overburden forms aquiclude, completely weathered mudstone above the aquiclude which is influenced by the Cretaceous pore water to be soften forms rupture surface.

Due to the permafrost distribution discontinuities and geological conditions difference, the landslide has gradual, low angle, creeping characteristics.

Acknowledgments This work was financially supported by Heilongjiang Communications Department project and subtopic of the western communication science and technology project "Study on Subgrade Stability Controlling Technology of Expressway Expansion Project Permafrost Melt and Landslides Sections".

References

Duan YH (1999) Basic characters of geo-hazards and its development trend in China. Quaternary Sci 19(3):208–216

Hu RL, Wang SS (2010) Main feature and identification method of sliding-surfaces in soil and rock slopes. J Eng Geol 18(1):35–40

Hu XW, Tang HM, Liu YR (2005) Verification of transfer coefficient method applied to landslide stability analysis by physical model test. Rock Soil Mech 26(1):63–66

Li YH, Zhang XY, Cui ZJ (2002) Periodic coupling of debris flow active periods and climate periods during Quaternary. Quaternary Sci 22(4):340–347

Liu HL, Zhu DY, Liu DF (2007) Discussion on multiple solution of safety factor of a slope. Rock Soil Mech 28(8):1661–1664

Qiao JP (2002) Structure and shape of landslide. Chin J Rock Mech Eng 21(9):1355–1358

Yang T, Zhou DP, Ma HM (2010) Point safety factor method for stability analysis of landslide. Rock Soil Mech 31(3):971–975

Zhang CS, Zhang YC, Hu JJ (2000) Spatial and temporal distribution characteristics and forming conditions of Chinese geological disasters. Quaternary Sci 20(6):559–564

Zhang LM, Zheng MX, He M (2010) Study of characteristics of matric suction in landslide slip soils before and after landslide control. Rock Soil Mech 31(10):3305–3312

Zhu YS, Li HL, Cao NE (2007) Finite element method research on road slide stability analysis. J Highw Transp Res Dev 24(4):39–42

The Effect of Freeze–Thaw and Moisture on Soil Strength Index of Cutting Slope

Ying Guo and Wei Shan

Abstract It is the main problem for highway in seasonal frozen regions that soil cutting slope instability causing by freeze–thaw. The change in soil moisture is important factor for soil cutting slope landsliding. Relying on the silty clay slope, which is in the highway expansion project from Fangzheng to Harbin, using field monitoring, and indoor test, the soil moisture varying with ground temperature and the effect of soil moisture on soil physical and mechanical indexes were studied. Field monitoring result indicates that, during the process of soil freezing, there will appear the cracks caused by temperature shrinkage which destroy integrated strength of the slope. Moisture migrates to the freezing-front due to the cracks caused by temperature shrinkage. In the melting period of spring, because of the accumulating water within the cracks, and longer duration of zero temperature below the surface, the melting water is hampered, when soil body temperature reaches 0.1 °C, the frozen water within the soil body melt rapidly. All of these leads to the water content in shallow slope too high, soil shear strength decreases. Triaxial test results show that: When the soil water content is less than the optimum water content, the soil cohesion increases with increasing moisture, when the soil water content is bigger than the optimum water content, the soil cohesion decreases with increasing moisture. The peak value of soil cohesion is near the optimum water content. The internal friction angle of soil decreases with the increasing moisture. Soil cohesion decreases with the increasing freeze–thaw cycles.

Keywords Highway · Cutting slope · Silty clay · Freeze–thaw · Soil moisture

Y. Guo · W. Shan (✉)
Northeast Forestry University, Harbin 150040, China
e-mail: shanwei456@163.com

F. Wang et al. (eds.), *Progress of Geo-Disaster Mitigation Technology in Asia*, Environmental Science and Engineering, DOI: 10.1007/978-3-642-29107-4_20,

1 Introduction

Soil cutting slope shallow land sliding occurs frequently in seasonal frozen areas of Northeast China (Wu et al. 2006; Liu and Wang 2006). The main reason is the moisture transfers to the freezing front during the freezing period, which results in water content increasing in somewhere of shallow slope, then frost heaving occurs under subzero temperature. The association and arrangement among soil particles was changed by frost heaving, then the mechanical properties of the soil changed also (Shan et al. 2009). In the melting period of spring, the frozen layers in shallow slope thawed influenced by kinds of factors such as precipitation, increasing temperature and so on. The melting water was hampered by unfrozen layer under them during their infiltration downward, results in the water content increasing rapidly in the layer between melt layer and frozen layer, and reaching saturation or super saturation state, then the effective stress within the slope reduced, the partial or whole of the shallow slope slide down along the "water saturation layer" under gravity (Niu et al. 2004).

The study of the stability of permafrost slopes appeared earlier (Tarr 1897; McRoberts and Morgenstern 1974; Clark 1988; Zhou and Guo 1982), but mainly is in permafrost plateau (Zhu et al. 1996; Wang and French 1995; Niu and Cheng 2002; Li and Zhao 2002). There is difference between instability in seasonal frozen region and instability in permafrost, mainly is larger changes in temperature and repeated freezing-thawing cycles, which has obvious seasonal characteristics.

Relying on the highway expansion project from Fangzheng to Harbin, the study area is located on the side of Widening from K560 +090 to K565 +690. The terrain graph fluctuation of study area is bigger, the soil of it is sandy clay, whose natural density is 1.8–2.1 g/cm^3, the average height of the cutting slope is 5–15 m, and the average ratio of the slope is 1.5–1.75.

Through on-site investigation, monitoring water content and ground temperature in shallow slope, indoor test of soil physical and mechanical, the soil physical and mechanical nature varied with water content and freeze–thaw cycle, as well as the changes of soil moisture in freeze–thaw cycles.

2 Monitoring of Ground Temperature and Soil Moisture on the Slope

According to meteorological data in Heilongjiang Province, for the ground within 20 cm below the surface, subzero temperature begins to appear in early November every year, and above zero temperature appears in end of March of next year. The maximum freezing depth is about 1.9 m. According to field investigation, the sliding surface of the cutting slope is about 1–1.5 m deep from the slope surface, and the thickness of slip zone is 10–25 cm.

In order to study the effect of weather temperature and plant on ground temperature and soil moisture, two study sites were selected, one is in K560 + 700 (site A, height

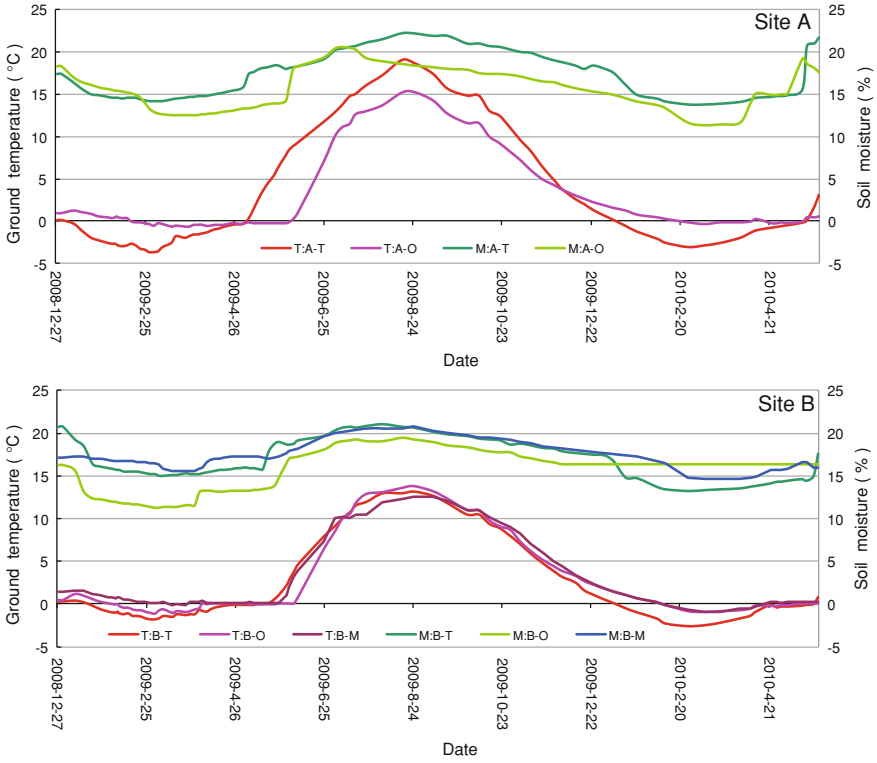

Fig. 1 The curves of ground temperature, soil moisture in 1.4 m depth varying with time

5.6 m, slope ratio 1.75) which planted grass, anther is in K563 + 870 (site B, height 15.3 m, slope ratio 1.75) which planted Lespedeza. On both site, temperature sensors and moisture sensors were buried in the depth of 0.6, 1.4, 2.2 m separately. The sensors in different depth are all in the same drilling hole, site B have three drilling holes which located on top (B-T), middle (B-M) and toe (B-O) of the slope separately. Site A only has two holes (A-T, A-O) and hasn't the hole in middle of the slope. From January 2009 to June 2010, the monitoring of ground temperature and soil moisture of five drilling holes was conducted. Among them, the value of the 1.4 m depth has the most representative, because it is above the maximum freezing depth, as well as near the sliding surface which known from the field investigation above. The next analysis is about the value of 1.4 m depth, and the curves can be seen in Fig. 1.

2.1 Variation of Slope Ground Temperature

In spring of 2009 and 2010, it can be seen from Fig. 1 that, in site A, the lowest ground temperature of two springs was −3.7 °C, −3.1 °C, which was found in A-T,

and happened on March 1st, 2009 and February 25th 2010. The lowest ground temperature of A-O was −0.6 °C and −0.3 °C, which happened on March 2nd, 2009 and April 23rd 2010. In site B, the lowest ground temperature of two springs was −1.8 °C, −2.6 °C, this is found in B-T, and happened on the same date with A-T. The lowest ground temperature of A-M was −1.1 °C, −0.9 °C which happened on March 2nd, 2009 and March 8th 2010. The lowest ground temperature of A-O was −0.9 °C, −1.6 °C which happened on March 1st, 2009 and March 3rd 2010. Since after these dates, the ground temperature of the measuring point begin to go up slowly, and go into the stage of above zero temperature one by one.

The order of appearing above zero temperature for five drilling holes is A-T, B-T, B-M, A-O, B-O, and corresponding appearing time is May 5th, May 11th, May 25th, June 4th, June 7th in 2009. Since after these dates, the ground temperature of five drilling holes begin to rise significantly. It's worth noting that, from top to toe of the slope, the time interval of appearing above zero temperature is about 30 days. Secondly, there is a longer duration of zero temperature.

In summer of 2009, it can be seen from the Fig. 1 that, In site A, the highest ground temperature was 19.1 °C, 15.3 °C, which happened on August 16th and August 24th. In site B, the highest ground temperature was 13.2 °C, 12.6 °C and 13.8 °C, which all happened on August 24th. It is worth noting here, the difference of the highest ground temperature between site A (with turf) and site B (with Lespedeza) is 6.5 °C.

As the weather turns to autumn, the order of appearing subzero temperature for five drilling holes in is A-T, B-T, B-M, B-O, A-O, and corresponding appearing time is January 8th, January 10th, February 7th, February 7th, February 17th in 2010. Since after these dates, the ground temperature of the measuring point begin to go down continuously.

It can be seen from above analysis that, for the ground temperature in 1.4 m depth, whose on the top of the slope is affected by the weather temperature mostly, then is in middle of and on toe of the slope. Secondly, the kind and density of the plant on the slope also affect the ground temperature in 1.4 m depth. Thirdly, it is in spring that there is a longer duration of zero temperature in 1.4 m depth of the slope, but in autumn there has not.

2.2 Variation of Slope Soil Moisture

It can been seen from Fig. 1 that, during the freezing period, the soil moisture curve has a sharp declining when ground temperature is about 0 °C. After that, the ground temperature declines gentle until reaches a minimum value, then the curve rise again slowly, as soon as ground temperature is over the zero temperature, the curve goes up rapidly.

For site A, in 2009 spring, the soil moisture of A-T goes up from 16 % (May 2nd) to 17.4 % (May 5th), at same time, corresponding ground temperature goes up from −0.3 °C to 0.3 °C. The soil moisture of A-O goes up from 13.9 % (May

30th) to 18 % (June 4th), the corresponding ground temperature goes up from −0.2 °C to 0.2 °C. After that, the curve of soil moisture goes up slowly until close or over the value of plastic limit of the soil. The scene situation is, after 2009 spring, there appears cracks near site A (K560 + 420–K560 + 550), then there occur landslide on 7th May 2010.

For site B, in 2009 spring, the moisture curve of B-T has one uplift process, which like site A, but the moisture curve of B-M and B-O have two uplift processes, details are as follows, the soil moisture of B-T go up from 15.8 % (May 14th) to 19 % (May 25th), then the rise turn to gentle, at same time, corresponding ground temperature goes up from 0 °C to 0.1 °C, and keeps straight up till to late July. The soil moisture of B-M first goes up from 15.6 % (March 29th) to 16.9 % (April 9th), corresponding ground temperature go up from −0.2 °C to 0.1 °C, next follows a smooth uplift process, then goes up again from 17.3 % (May 25th) to 19.6 % (June 24th), corresponding ground temperature go up from −0.1 °C to 1 °C. The soil moisture of B-O go up from 11.5 % (March 29th) to 13.2 % (April 3th), corresponding ground temperature go up from −0.9 °C to 0.1 °C, next also follows a smooth uplift process, then goes up again from 13.8 % (May 22th) to 17.2 % (May 30th), corresponding ground temperature go up from 0.1 °C to 6.4 °C.

It can be seen from above analysis that, soil moisture rises up quickly when ground temperature is above 0.1 °C. The moisture of B-T and A-T begin to rise as soon as ground temperature has above zero temperature, and turn to gentle in 3–10 days. The moisture of B-M and B-O increased 1.3 % and 1.7 % when ground temperature rise up to 0.1 °C, but the difference is the ground temperature here continued to maintain near 0.1 °C for 19 days and 65 days separately, then rise up again, during this period, the moisture of B-M and B-O rise up again for 2.3 % and 3.4 % separately.

The cause of above phenomenon is, during the freezing period, there will appear the cracks caused by temperature shrinkage when freezing-front extend to deep slope, the new freezing-front in the soil is formed, then the moisture in soil body migrate to the cold freezing-front, so the curve of moisture here is decline. In spring, the ground temperature rises up, when it reach about 0 °C, the moisture near the freezing-front begins to migrate again under the function of gravity and surface tension, and then there is the first uplift process of the moisture curve. When ground temperature is over 0.1 °C, the melting water from snow and infiltrating water near the freezing-front make the moisture curve have the second uplift process.

3 Effect of Freeze–Thaw on Shear Strength of the Soil in the Slope

In order to study the effect of freeze–thaw cycles, soil moisture and compaction degree on soil shear strength, the soil on the slope was conducted series of experiments. First, the basic physical parameters of the soil in the slope are shown in Table 1.

Table 1 Basic physical properties indicators of silty clay

Liquid Limit (%)	Plastic limit (%)	Plasticity index	Maximum dry density (g/cm3)	Optimum water content (%)
32.5	18.7	13.8	1.90	13

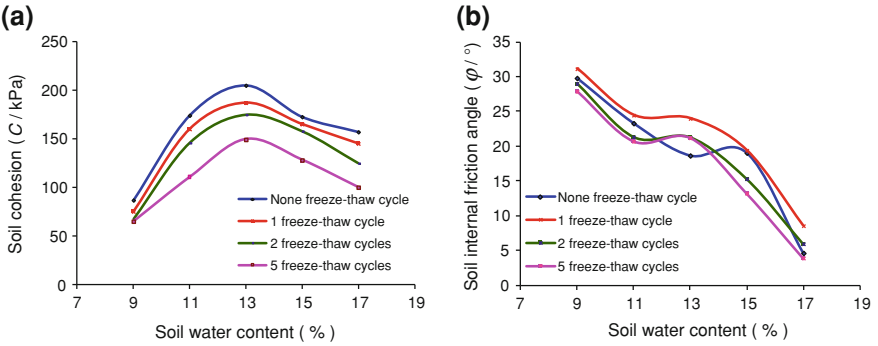

Fig. 2 Moisture-cohesion curves and moisture-internal friction curves before and after frozen-thaw with 95 % soil compaction

Under same 95 % compaction degree, the soil samples with different water content and different freeze–thaw cycles were conducted indoor triaxial test, the results are shown in Fig. 2.

Effect of freeze–thaw cycles and water content on soil cohesion

For silty clay with 95 % compaction degree, Fig. 2a is the relationship curve between soil moisture and soil cohesion under different freeze–thaw cycles. It can be seen that when soil moisture is close to the optimum moisture, soil cohesion reach the peak value. Soil cohesion decreases gradually with increasing freeze–thaw cycles, especially when soil compaction degree is bigger. Under the optimum moisture, after 1, 2, 5 freeze–thaw cycles, the soil cohesion decreases by 18, 30 and 56 kPa separately.

Effect of freeze–thaw cycles and water content on soil internal friction

For silty clay with 95 % compaction degree, Fig. 2b is the relationship curve between soil moisture and soil internal friction angle under different freeze–thaw cycles. It can be seen that soil internal friction angle decreases with increasing soil moisture. When soil moisture increases from 9 to 17 %, after 1, 2, 5 freeze–thaw cycles, the reduction value of soil internal friction angle is 64, 47, 46, 57 % separately.

On the whole, soil cohesion decreases with increasing freeze–thaw cycles. Soil internal friction increases after the first freeze–thaw cycle, and then decreases gradually in later freeze–thaw cycles.

4 Conclusions

Laboratory test results showed that: the soil cohesion increases with increasing of soil moisture. When the soil water content is bigger than the optimum water content, the soil cohesion decreases with soil moisture. Under the same moisture, soil cohesion increases with increasing dry density. The internal friction angle of soil decreases with increasing moisture. Freeze–thaw had a significant effect on soil cohesion and internal friction angle. Soil cohesion decreases gradually with freeze–thaw cycles, soil internal friction increases after the first freeze–thaw cycle, then decreases gradually in later freeze–thaw cycles.

Field monitoring results show that, for the ground temperature in 1.4 m depth, on the top of the slope is affected by the weather temperature mostly. The kind and density of the plant on the slope also affect the ground temperature in 1.4 m depth. During the freezing period, there will appear the cracks caused by temperature shrinkage when freezing-front extend to deep slope, the new freezing-front in the soil is formed, then the moisture in soil body migrate to the cold freezing-front, so the curve of moisture here is decline. In spring, the ground temperature rises up, there is a longer duration of zero temperature in 1.4 m depth of the slope, the moisture near the freezing-front begins to migrate again under the function of gravity and surface tension, and then there is the first uplift process of the moisture curve. When ground temperature is over 0.1 °C, the melting water from snow and infiltrating water near the freezing-front make the moisture curve have the second uplift process.

Because of the accumulating water within the cracks of temperature shrinkage and longer duration of zero temperature below the slope surface, the melting water was hampered, result in high water content in shallow slope, soil shear strength decreases, then cutting slope landslides.

Acknowledgments The authors would like to thank the financial supports provided by the research project of Heilongjiang provincial Science and Technology Department (GZ07 C401), and the Key project of Heilongjiang provincial Transportation Department “Highway Slope Stability and Greening by Vegetation in Cold Regions”.

References

Clark MJ (1988) Advance in periglacial geomorphology. Wiley, New York, pp 325–359

Li YC, Zhao KN (2002) The analysis of landslide in k2023 of QING-Zang highway. J Geol Hazards Environ Preserv 13(4):33–35

Liu HJ, Wang PX (2006) Stability analysis of loss of stability caused by freeze and melt of earthen side slopes of highways. J Harbin Inst Techol 38(5):764–766

McRoberts EC, Morgenstern NR (1974) The stabilityof thawing slopes. Can Geotech J 11:447–469

Niu FJ, Cheng GD (2002) Study on instability of slopes in permafrost regions of Qinghai-Tibet High Plateau. In: Proceedings of the 5th international symposium on permafrost engineering. Permafrost Institute SB RAS Press, Yakutsk, pp 192–197

Niu FJ, Cheng GD, Lai YM (2004) Instability study on thaw slumping in permafrost regions of Qinghai-Tibet Plateau. Chin J Geotech Eng 6(3):402–406

Shan W, Guo Y, Liu HJ (2009) Effect of freeze-thaw on strength and microstructure of silty clay. J Harbin Inst Techol 16:207–211

Tarr RS (1897) Rapidity of weathering and stream erosion in the arctic latitudes. J Am Geol 19:131–136

Wang BL, French HM (1995) In situ creep of frozen soil, Fenghuo Shan, Tibet Pleateau, China. Can Geotech J 32(3):545–552

Wu H, Gao W, Wang GF et al (2006) Cause and control of soil-cutting's sliding collapse in frigid zone. J Nat Disasters 15(3):66–70

Zhou YW, Guo DX (1982) Principal characteristics of permafrost in China. J Glaciol Geocryol 4:1–19

Zhu C, Zhang JX, Cheng P (1996) Rock glaciers in the central Tianshan Mountain, China. Permafr Periglac Process 7:69–78

Long-Term Management of Kosi River Basin

Balmukunda Regmi

Abstract Kosi River starts from Tibet in China, gains momentum in Nepal, enters India to join the Ganges. Kosi is a young river. Chatara as nodal point, Kosi had shifted westward for about 120 km in past 250 years showing a cone (80 km long and 150 km wide alluvial fan) building activity, prior to its embankment in 1959. The major aim of Kosi barrage was to control flood in Bihar; irrigation, hydro-electricity generation, land reclamation, fishing and navigation were less important. Although it prevented major floods in Bihar for about 50 years, the Project was disputed. Some scholars also raised environmental and safety concerns. Kosi is a heavy sediment carrying river (80 million m^3/year). So far no effective method has been developed to avoid siltation upstream of the barrage. The riverbed continued to rise at about 0.05 m per year leading to a situation when it was 4–5 m above the land outside the embankments. Due to sloping landscape, Kosi breached eastern bank in its weakest part and followed some of its old channels. The 2008 flood took 527 lives, inundated 116,000 ha of land and left 234,000 people homeless. The 2008 Kosi flood has been considered as manmade for failure to address the sedimentation problem upstream of the barrage with effective counter measures, no regular repair and maintenance work of the upstream embankments and delay in opening the barrage gates. As a solution, India is lobbying for Kosi 269 m high dam 40 km north of present barrage. The proposal first suggested in 1937 has been opposed by Nepalese scholars. Scientific researches on the ways to reduce the sediment load from upstream and to increase the silt clearing capacity downstream are needed. Nepal–China–India trilateral close cooperation is called for producing a long-term solution.

Keywords Kosi river basin (KRB) · Integrated flood management · Kosi flood

B. Regmi (✉)
Tribhuvan University, Kathmandu, Nepal
e-mail: bmregmi@iom.edu.np; bmregmi@yahoo.co.uk

F. Wang et al. (eds.), *Progress of Geo-Disaster Mitigation Technology in Asia*, Environmental Science and Engineering, DOI: 10.1007/978-3-642-29107-4_21,

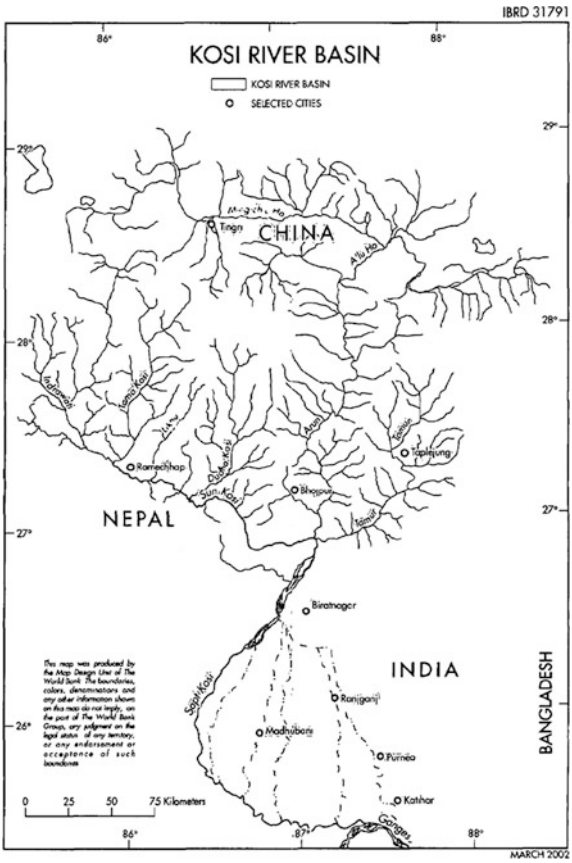

Fig. 1 Saptakosi River watershed (*Source* Salman and Uprety 2002)

1 Introduction

Kosi River starts from Tibet in China, gains momentum in Nepal where it becomes Saptakosi at Chatara, enters India to join the Ganges, as shown in Fig. 1. It has total catchment area of 69,300 km^2 (29,400 km^2 in China, 30,700 km^2 in Nepal and 9,200 km^2 in India). Its watershed includes parts of south Tibet north of Mount Everest and the eastern third of Nepal (Kattelmann 1991). Termed "Sorrow of Bihar", Kosi is a young river. Chatara as nodal point, Kosi had shifted westward for about 120 km in past 250 years showing a cone (80 km long and 150 km wide alluvial fan) building activity (See Fig. 2), prior to its embankment in 1959 and completion of barrage in 1964 following the severe floods in 1953–1954 and subsequent Indo-Nepal Kosi Treaty of 1954.

Through the history, Kosi River has been mainly described as an untameable river that had given northern Bihar continuous problems and solutions are still

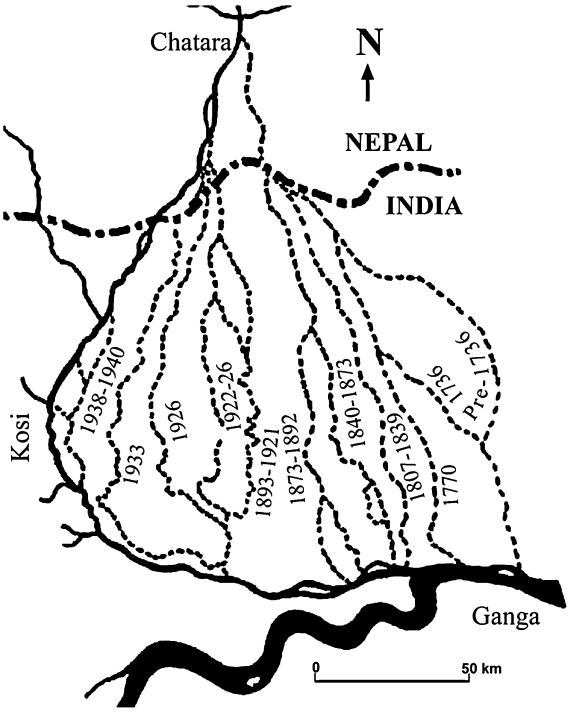

Fig. 2 Position of Kosi River taken from 11 selected historical maps. The channel positions shown in this diagram, illustrate an east–west oscillating movement of Kosi channel (modified after Gole and Chitale 1966)

being developed to cope with the challenge. So far efforts in the past, especially the 1959 embankment, have brought positive results in dealing with Kosi River. Compared to regular inundations and floods, post-barrage events including the 2008 flood are less severe. However, the embankments have failed in many instances, as listed in Table 1.

2 Was There Human Factor in Kosi Flood 2008?

As early as 1966, scientific concerns were shown that the flood embankments could not prevent the shifting tendency of the Kosi course (Gole and Chitale 1966). Although it prevented major floods in Bihar for about 50 years, the Project was disputed. Many scientists continued to caution that Kosi barrage was on verge of breach; worries had been expressed that a disaster was inevitable; the 2008 flood rectified their concerns: it took 527 lives, inundated 116,000 ha of land and left 234,000 people homeless. Figure 3 shows the breached portion and Fig. 4 shows the flow of Kosi during 2008 flood.

Kosi is a heavy sediment carrying river (80 million m^3/year) due to cloudburst, Asian monsoon, masswasting, and Himalayan landslides (Shrestha et al. 2010). No effective measure had been taken to avoid siltation upstream of the barrage. With

Table 1 Breaches in the Kosi embankments

Years	Place breached	Remarks
1963	Dalwa (Nepal)	No casualty
1968	Near Jamalpur in Darbhanga district	
1971	Bhatania approach bund downstream of Bhimnagar	
1980	Near Bahuarawa in Saharsa district	Eroded the eastern embankment but water receded quickly after the breach
1984	Near Hempur village in Saharsa district	Eastern embankment. Affected 50 lakhs of people in Saharsa and Supaul districts
1987	Samani and Ghoghepur villages of the Mahisi block of Saharsa district	Western embankment
1991	Joginia	Eroded the embankment for a stretch of about 2 km, but receded without causing any damage
2008	Kusaha (Nepal)	Affected approximately 3,000 sq km of area; a number of houses, schools, roads, and hospitals were damaged due to the flow of the river. A total of 33,45,545 people and 7,12,140 animals from 993 villages of 412 panchayats of 35 blocks of 5 districts were affected out of which 239 humans and 1,232 animals lives were lost

Source Sinha 2009

help of satellite images and a field visit, Sinha (2009) has concluded that the river has been moving towards the eastern embankment around Kusaha region at least since 1979 and a breach in the embankment at Kusaha was detected as early as 5th August 2008, that a well-defined seepage channel parallel to the eastern afflux bund formed some years ago. The surveys in 1963 and 197 upstream of the barrage showed that the riverbed continued to rise at about 0.05 m per year (Thapa 2004). The river bed around the western afflux bund was observed to be at least 4–5 m higher than the surrounding floodplain level (Mishra 2008; Dixit 2008; Sinha 2009) (See Fig. 5). Due to sloping landscape it was normal for Kosi to breach eastern bank in its weakest part and follow some of its old channels. Worries had been expressed that such a disaster was inevitable; the 2008 flood rectified their concerns: it took 527 lives, inundated 116,000 ha of land and left 234,000 people homeless.

At least three points indicate the 2008 Kosi flood as manmade: failure to address the sedimentation problem upstream of the barrage with effective counter measures, no regular repair and maintenance work of the upstream embankments, and the breach of embankment at a discharge of 144,000 cusecs (cubic feet per second), far below its maximum designed capacity of 950,000 cusecs, due to delay in opening the barrage gates.

Inadequacy of proper communication has been demonstrated by some field research scientists in relation to failure in containing the Kosi floods. (Shrestha

Fig. 3 Kosi flowing in breached portion (Pun 2009)

et al. 2009) (Fig. 6). These include irregularities in working meetings of concerned joint committees and field inspections/monitoring of the barrage.

3 Challenges with Proposed Kosi High Dam

As a solution to the failing Kosi project, India is lobbying for Kosi 269 m high dam 40 km north of present barrage. The proposal first suggested in 1937 has been opposed by Nepalese scholars on many accounts: similar siltation problem, life-span of just 37 years (versus 25 years that of present barrage), submergence of about 324 km^2 of Nepal's fertile river valleys displacing over 75,000 people, and increased possibility of earthquakes in already seismically vulnerable area.

The fact that Nepal is a seismically vulnerable zone is well established. Bilham (1995) has presented some major earthquakes in the Himalayas as given in Fig. 7.

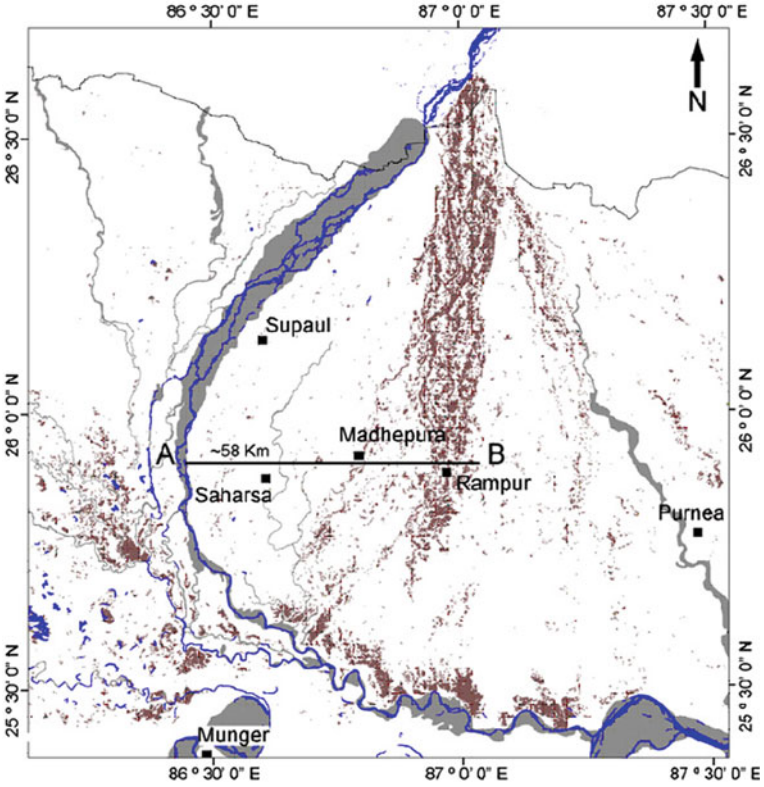

Fig. 4 Kosi megafan showing the flood water flow path after the August 2008 avulsion (after NRSA, http:www.//fmis.bih.nic.in/Kosi_Flood%20Map/aug22-23_Bihar-Nepal-map.pdf). Note a shift of the Kosi channel by about 60 km to the east (as measured along AB). (Chakraborty et al. 2010)

4 The Way Ahead

Kosi River is not just a source of problems; it is also a resource that has immense potential for utilization in economic development. It supplies water to the densely populated South Asia—screening the Department of. Hydrology and. Meteorology, Nepal records from 1977 to 2008 showed its minimum water flow was 6526 cusecs (28 March 2001) and an average discharge of 1564 cumecs. It can fulfil the household and agricultural needs of southern Nepal, Bihar and significant part of nearby areas of India. Besides, it has a potential for hydroelectricity generation of 22,350 MW (of which 10,860 MW is economically exploitable) and it also provides the best option for waterway to landlocked country.

Prudent approach to minimize the Kosi problems would be carrying out scientific research on the ways to reduce the sediment load from upstream and to increase the silt clearing capacity of the river downstream. Nepal–China–India trilateral close cooperation is called for producing a long-term solution.

Fig. 5 Dry Kosi barrage (Pun 2009)

The problem of Kosi flooding is a problem of sediment (Durham Report 2011). Any solution which can deal with sediment that the river supplies to the plains of Bihar will also address issue of unexpected and catastrophic shifts in the river, as occurred in 2008.

The management of Kosi River Basin can benefit from a new "sediment transport system" adopted by Japan that proposed the outline of sediment management policy—integrated sediment system management—in the future in July 1998 by considering all aspects, from mountains include forests to shorelines, and proposed the promotion of total sediment management (Kashiwai 2005) along with the following strategies for specific areas: Areas upstream Mountain and foot of a mountain area, alluvial fan—steep and rapid flow; Hillside works: reducing sediment yield from hillside slope; Check dam: conserving forest area, preventing excess sediment flow to areas downstream; Retarding basin: preventing excess sediment flow to areas downstream; Countermeasures for reservoir sedimentation: reducing reservoir sedimentation. Areas downstream foot protection works: stabilizing embankment; groundsill: preventing scoring, stabilizing riverbed; prohibition of sand and gravel removal: preventing riverbed degradation; riverbed excavation: preventing riverbed aggradations, conserving water quality; spur dike: restoration of pools.

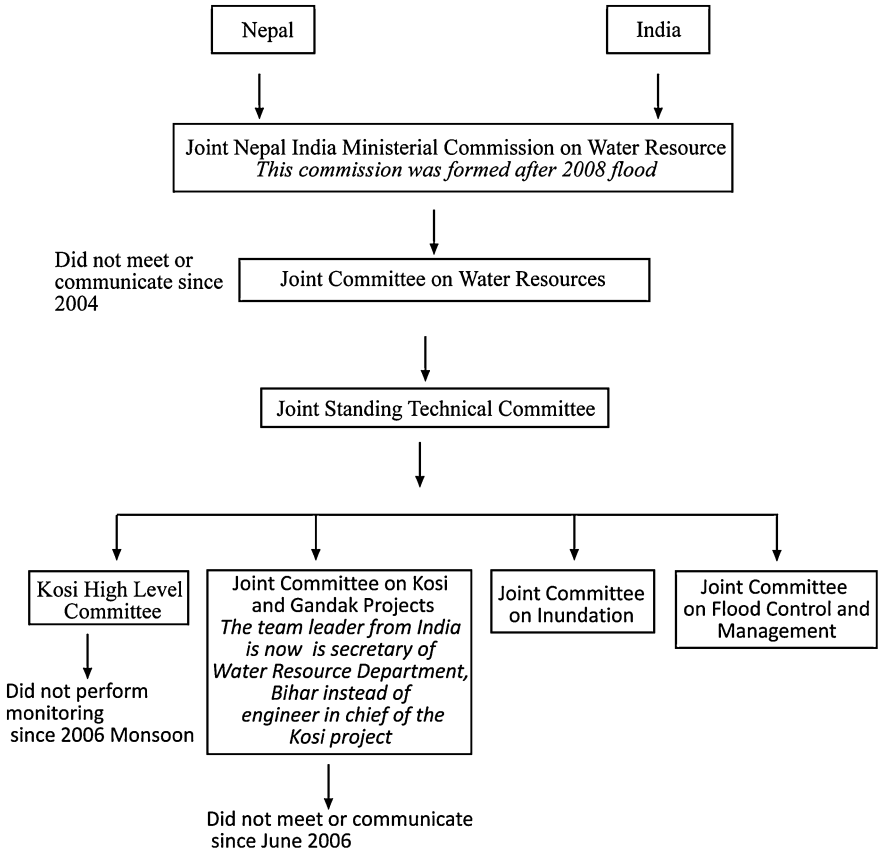

Fig. 6 Communication gaps prior to Kosi flood 2008 (modified after Shrestha et al. 2009)

There is a need to work with the river to allow some degree of dynamic behaviour, but in a way that does not compromise the people and communities on the fan (Kashiwai 2005).

In the plains, a low-cost and sustainable approach should consider breaches to be made and maintained in the embankments that line the river, so that controlled flows of water and sediment can be released down old channels on the Kosi River. By allowing controlled releases of sediment and water during high flows of the Kosi, at levels which can be adequately conveyed by each of the old channels, the uncontrolled and catastrophic shift of the river system could be avoided. This approach would also decrease pressure on the existing flood defences.

The embankments along with rail-road network in the Kosi region have also caused severe drainage congestion resulting in a much longer period of inundation and extensive water logging. Reinstatement of drainage pathway is an urgent need. The paleochannels on the Kosi fan is needed to be identified and reactivated by

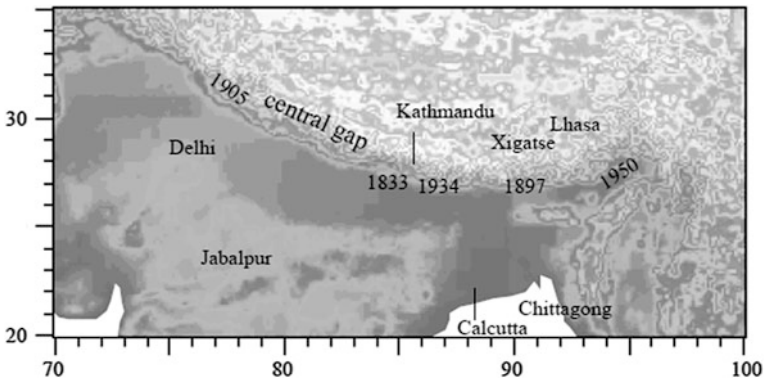

Fig. 7 Approximate Modified Mercalli Intensity VIII zones for five large earthquakes in the Himalaya since 1833 and settlements reporting information concerning the 1833 shock (*white dots*). A great earthquake may not have occurred in the 800 km segment of the Himalaya between the 1905 Kangra and 1934 Bihar earthquakes (Central Gap) for 650 years (Bilham 1995)

connecting them to the main channel using regulation structures and can be maintained as natural channels.

The use of modern technologies such as remote sensing and GIS, GPS-based surveys and echo sounding for river bed and floodplain mapping must be adopted on a routine basis and the database should be continuously updated.

In KRB management, an integrated plan involving all stakeholders (Nepal, India and China) is necessary. It should include engineering and non-engineering methods. Short-term and near future projects should include small-scale dams, strengthening of conservation areas, watershed management, irrigation and hydropower projects in the upper reaches of the basin, and focus on employment generating small-scale eco-friendly industries such as tourism. Long-term targets should include sustainable development, inter-river linkage canal systems, scientific agriculture systems, integrated watershed management, payment for environment and resilience to disasters. Good science, good technology and equitable basin-wise development can succeed in getting support from concerned local communities which leads to further cooperation and trust among the member countries.

References

Bilham R (1995) Location and magnitude of the 1833 Nepal earthquake and its relation to the rupture zones of contiguous great Himalayan earthquakes. Curr Sci 69(2):155–187

Chakraborty T, Kar R, Ghosh P, Basu S (2010) Kosi megafan: historical records, geomorphology and the recent avulsion of the Kosi river. Quat Int 227:143–160

Dixit A (2008) Two neighbors water course (Nepali language). Action Aid Nepal, Kathmandu Nepal

Durham Report (2011): Workshop on 'River dynamics and flood hazard assessment with special reference to the Kosi River' 23 March 2011, Patna, India. Published by the Institute of Hazard, Risk and Resilience, Durham University 2011. Available at http://www.dur.ac.uk/resources/ihrr/KosiRiverreport-IHRR.pdf Accessed 15 May 2011

Gole CV, Chitale SV (1966) Inland delta building activity of Kosi river. J Hydraul Div Am Soc Civil Eng 92:111–126

Kashiwai J (2005), Reservoir sedimentation and sediment management in Japan. Technical 259 memorandum of Public Works Research Institute, vol 3957, pp 240–250

Kattelmann R (1991). Hydrology for the water management of large river basins (proceedings of the Vienna symposium, August 1991). IAHS Publication No. 201

Mishra DK (2008). Serpent tied around the neck: Kosi embankment (Hindi Language). Patna, India, Freedom from Floods Campaign

Pun SB (2009) The Kosi *Pralaya* could the catastrophe have been averted? and what next? HydroNepal. J Water, Eng Environ 4:2–7

Salman SMA, Uprety K (2002) The Kosi River, in conflict and cooperation on South Asia's international rivers. A legal perspective, Van Puymbroeck (ed) The World Bank, Washington DC. Available at http://www-wds.worldbank.org/external/default/WDSContentServer/WDSP/IB/2003/03/29/000094946_03031804015731/Rendered/PDF/multi0page.pdf Accessed 9 May 2012

Shrestha RK, Ahlers R, Bakker M, Gupta J (2010) Institutional dysfunction and challenges in flood control: a case study of the Kosi flood 2008. Economic & Political Weekly vol 45(2), pp 45–53, 9 Jan 2010

Shrestha RK, Ahlers R, Bakker M and Gupta J. Institutional dysfunction and challenges in flood control along the transboundary Kosi River: A Case study of the Kosi Flood 2008. Available at http://www.earthsystemgovernance.org/ac2009/papers/AC2009-0496.pdf (Accessed 23 June 2012)

Sinha R (2009) Dynamics of a river system—the case of the Kosi River in North Bihar. e-J Earth Sci India 2:33–45

Thapa AB. The sorrow of Bihar: Kosi River. Available at http://madhesi.wordpress.com/tag/kosi/ (Acessed 23 June 2012)

Simulation of Evacuation Behaviour During a Disaster for Classes Building of Azarbaijan Shahid Madani University by Using DEM

Saeed Alighadr, Abdolhossein Fallahi, Junji Kiyono and Masakatsu Miyajima

Abstract Safety is a primary consideration in any building. There are many risk factors which can cause casualties such as earthquake, fire, flood, terrorism, etc. One of the important considerations in an emergency situation is evacuation of people. This is of great importance when a large number of people are or gathered together in a confined space such as mosques, subway stations, shopping malls, etc. To predict the evacuation of a place, an effective way is to simulate evacuation behavior. In this paper as a study case, we simulated the evacuation behavior of the Classes Building of Azarbaijan Shahid Madani University by using distinct element method (DEM). In DEM, analysis can compute the position of each element (person) step by step by solving the equation of motion. Human body is modeled as a circular element. Contact force acts on human body through virtual spring and virtual dashpot. Algorithm that can consider avoidance, overtaking, and pass between elements naturally, is used. The parameters used for human body are based on experiments done by Professor Kiyono at Kyoto University. Different cases are considered and evacuation behavior, evacuation time, and density on exits are estimated quantitatively and obtained results are discussed. As results show, number of exits and people have great influences on evacuation behavior.

S. Alighadr · A. Fallahi (✉)
Department of Civil Engineering, Azarbaijan Shahid Madani University,
35 km of Tabriz-Maraghe Road, 53751-71379 Tabriz, Iran
e-mail: fallahi@azaruniv.edu

J. Kiyono
Department of Urban Management, Katsura Campus, Kyoto University,
Nishikyo-ku, Kyoto 615-8540, Japan

M. Miyajima
Graduate School of Natural Science and Technology, Kanazawa University,
Kakuma-machi, Kanazawa, Ishikawa 920-1192, Japan

F. Wang et al. (eds.), *Progress of Geo-Disaster Mitigation Technology in Asia*,
Environmental Science and Engineering, DOI: 10.1007/978-3-642-29107-4_22,

Keywords Evacuation simulation · Emergency evacuation · Emergency evacuation time · Distinct element method · Azarbaijan Shahid Madani University

1 Introduction

Safety is a primary consideration in any building. There are many risk factors which can cause casualties such as earthquake, fire, flood, terrorism, etc. A building not only should service in normal conditions, but also it should service in emergency situations. One of the important considerations in an emergency situation is evacuation of people. This is of great importance when large numbers of people are or gather together in a place. An effective way to predict the evacuation behavior of people in a place is evacuation simulation. One method which can be used for evacuation simulation is distinct element method (DEM). DEM is a numerical method which can calculate each element's position by solving equation of motion step by step. Kiyono et al. (1996) considered circular DEM elements as human beings and investigated behavior of the crowd flow that evacuated from an enclosed space to outside through the passage or the steps. They found that the model they proposed was able to simulate evacuation during a disaster. Kiyono et al. (1998) used DEM to simulate evacuation behavior during a disaster. They used circular elements and proposed an algorithm in which elements can avoid collision and pass each other naturally. They determined DEM parameters such as spring constants and driving force for human body based on experiments and simulated evacuation behavior for the explosion accident occurred at the underground shopping center near Shizuoka Station in 1980. Kiyono et al. (2000) used the same method to simulate the evacuation of an underground mall in Kyoto. Kiyono and Mori (2004) used elliptic elements to simulate emergency evacuation behavior during a disaster and validated the technique by comparing the simulation results with a real pedestrian flow.

Langston et al. (2006) developed a DEM technique for modeling crowd dynamics. They presented each element by three overlapping circles. The model was tested on a single enclosure entry scenario where some model parameters were scaled then it was used on a multi enclosure entry scenario. The potential for further application was demonstrated on hypothetical scenarios on the London Underground. Langston et al. (2009) compared the predicted model behavior with actual video footage shot at various locations around University Park Campus, Nottingham. They found that it did not match well to the video footage when people were moving toward each other, as in case of contra-flow on a walkway. In order to improve the model, they introduced an avoidance algorithm to the model to make it more realistic in those cases.

Alighadr et al. (2011a) did the evacuation simulation for the Mosque of Azarbaijan University of Tarbiat Moallem. They found that number of exits, exits' width, and door opening angle have great influence on emergency evacuation time. Alighadr et al. (2011b) observed effect of exits' width and number of people on

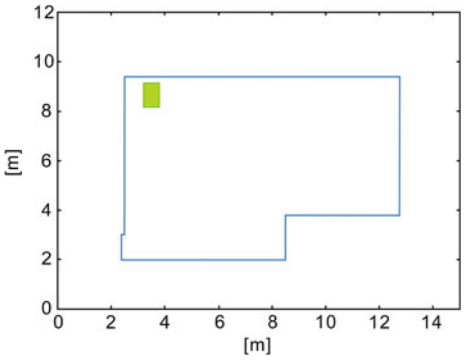

Fig. 1 Plan of the biggest class of the classes building considered for sample class simulation

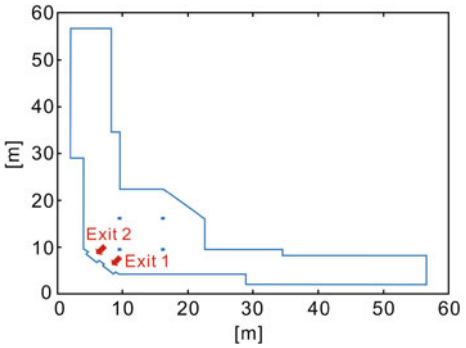

Fig. 2 Plan considered for simulation of classes building

emergency evacuation time and density around exits for Seghatol Islam Mosque of Tabriz Bazaar.

As a study case, we did emergency evacuation simulations of Classes Building of Azarbaijan Shahid Madani University by using DEM. First as a sample of evacuation of classes, we did the simulation for the biggest class of the building. Then by considering the critical situation, all of the people to be in corridors, simulations were done for different considered cases. Emergency evacuation time and density on exits are calculated quantitatively for all considered cases and results of simulations are introduced and compared.

2 Study Case

2.1 Considered Study Case

Study case takes place in the Classes Building of Azarbaijan Shahid Madani University. First as a sample of evacuation of classes, we did the simulation for the biggest class of the building. The considered plan for the class is shown in Fig. 1. Maximum number of students in class is 70 people. The considered plan for

Table 1 Number of people and exits for six considered cases

	Number of people	Exit
Case 1	650	1
Case 2	975	1
Case 3	1300	1
Case 4	650	1 & 2
Case 5	975	1 & 2
Case 6	1300	1 & 2

building's simulations is shown in Fig. 2. The critical situation, all of the people to be in corridors, is considered for building's evacuatuin simulations. Maximum number of people at the full capacity of the building is determined to be 1300 people. The building has two main exit doors. Exit 1 is commonly open and used but exit 2 is closed and barely used. Exit 1 and 2 are shown in also shown in Fig. 2. Six different cases with different number of people and number of exits are considered.

2.2 Considered Simulation Cases for Simulation

As previously mentioned, maximum number of people people at the full capacity of the Classes Building is determined to be 1,300 people. Here we considered 650, 975, 1,300 as different number of people for different cases with one or two exits. Number of people and exits for six considered cases are illusterated in Table 1. As it can be seen, respectively, cases 1, 2, and 3 are identical to cases 4, 5, and 6, in number of people but they have different number of exits (one exit for cases 1, 2, and 3 and two exits for cases 4, 5, and 6). Exits' width are conidered to be 2.2 m and equal to each other.

3 Evacuation Simulation

3.1 Method

Distinct Element Method was used to simulate the emergency evacuation from a confined area. Human body is modeled as a circular element. Contact force acts on human body through virtual spring and virtual dashpot. In DEM, analysis can compute the position of each element (person) step by step by solving the equation of motion. The program simulates movement and decision making by means of adding the psychological forces to the physical forces. Algorithm that can consider avoidance, overtaking, and pass between elements naturally, is used. The governing equations of motions are:

Table 2 DEM parameters for human body

Parameter	Value
Element spring constant (Normal)	1.07×10^4 (N/m)
Element spring constant (Tangential)	5.35×10^2 (N/m)
Element damping coefficient (Normal)	1.245×10^3 (Nsec/m)
Element damping coefficient (Tangential)	2.79×10^2 (Nsec/m)
Virtual spring constant (Normal)	6.62×10^1 (N/m)
Virtual spring constant (Tangential)	3.31×10^0 (N/m)
Virtual damping coefficient (Normal)	9.79×10^1 (Nsec/m)
Virtual damping coefficient (Tangential)	2.19×10^1 (Nsec/m)
Element radius	0.259 (m)
Virtual radius	0.72 (m)
Mass	3.62×10^1 (kg)
Time interval	0.01 (sec)
Acceleration of driving force	0.837 (m/s^2)

$$m_i \ddot{x}_i(i) = f_i^x(t) \tag{1}$$

$$m_i \ddot{y}_i(i) = f_i^y(t) \tag{2}$$

in which is mass of i-th element, f^x and f^y are various forces including driving force act on the element in x and y directions respectively. Assuming that the acceleration is constant between small time intervals, Δt, the following equations can be obtained.

$$\dot{x}_i(t) = \dot{x}_i(t-1) + \ddot{x}_i(t-1)\Delta t \tag{3}$$

$$\dot{y}_i(t) = \dot{y}_i(t-1) + \ddot{y}_i(t-1)\Delta t \tag{4}$$

$$x_i(t) = x_i(t-1) + \dot{x}_i(t-1)\Delta t + \frac{1}{2}\ddot{x}_i(t-1)\Delta t^2 \tag{5}$$

$$y_i(t) = y_i(t-1) + \dot{y}_i(t-1)\Delta t + \frac{1}{2}\ddot{y}_i(t-1)\Delta t^2 \tag{6}$$

The position of each element can be calculated sequentially by solving above equations step by step.

Psychologically people tend to keep a constant distance from others when they walk or run. In this study, this psychological distance is introduced as virtual radius. Independence of element spring, the virtual spring is also introduced. The contact judgment of two elements is determined by calculating the distance between the centers of two elements. The parameters used for human body are based on experiments done by Prof. Kiyono at Kyoto University. These parameters are illustrated in Table 2.

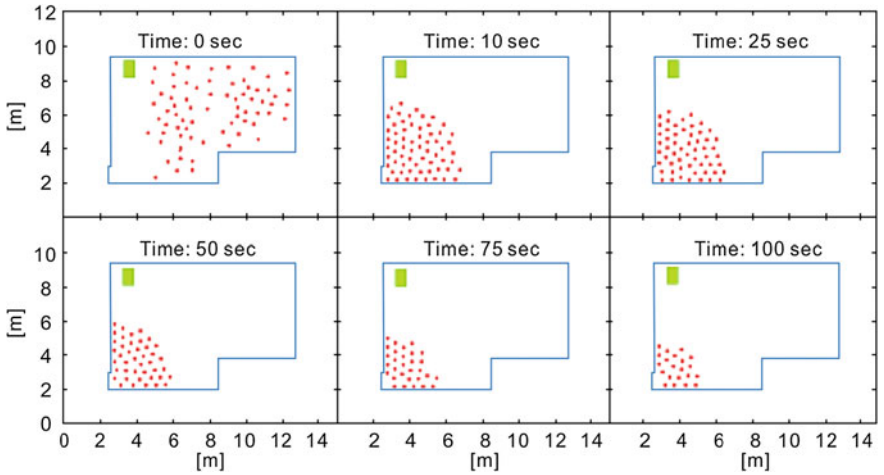

Fig. 3 Snap shots of evacuation behaviour for considered sample class

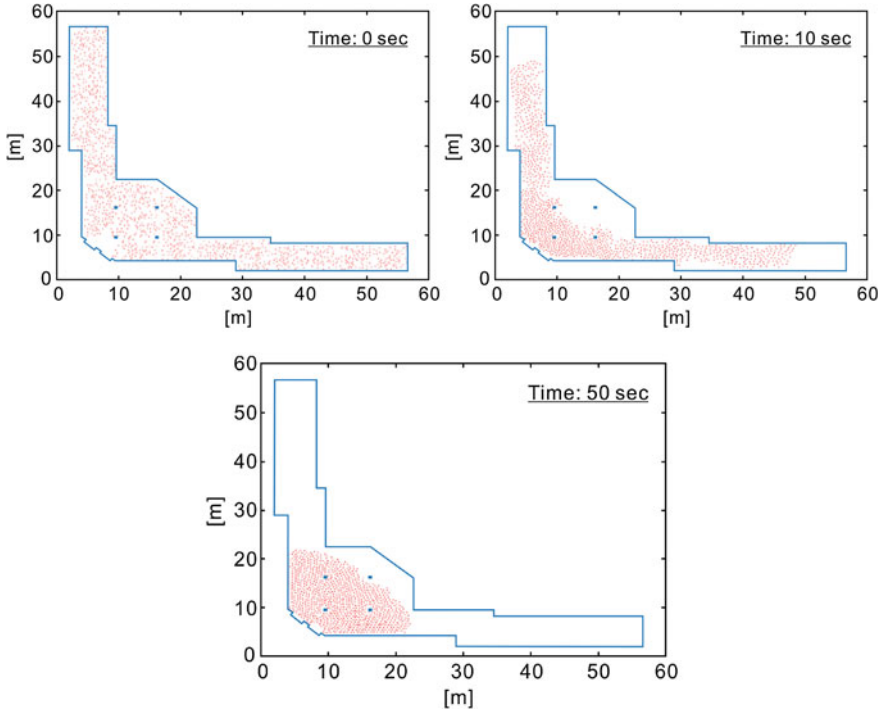

Fig. 4 **a** Snap shot of evacuation behaviour for case 3 at 0 s. **b** Snap shot of evacuation behaviour for case 3 at 10 s. **c** Snap shot of evacuation behaviour for case 3 at 50 s

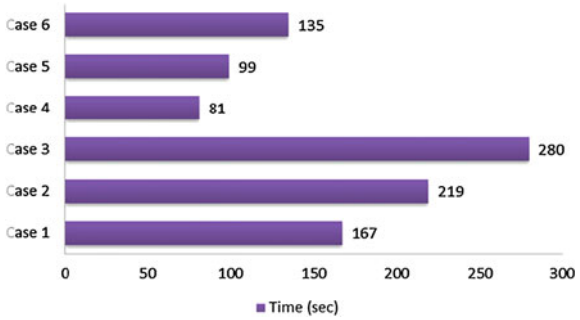

Fig. 5 Evacuation time for different considered cases

3.2 Results of Evacuation Analysis

We did evacuation simulation for considered sample class and the six different considered cases. Snap shots of evacuation behavior for considered sample class are shown in Fig. 3 and evacuation time is calculated to be 146 s. Snap shots of evacuation behavior for case 3 are shown in Fig. 4a, b, c at 0, 10, and 50 s. Evacuation time is calculated to be 167, 219, 280, 81, 99, and 135 for case 1–6, respectively which is shown in Fig. 5. As results show by doubling the number of people, 625–1300, evacuation time increases 1.67 times and by considering two exits instead of one exit, evacuation time decreases 0.47 times. We can conclude that number of people and number of exits have great influence on evacuation time of a place and, of course, it will depend on geometry of plan, exits' width, etc. Time histories of density of people around exits for six considered cases are shown in Fig. 6. Maximum density around exits for different considered cases is illustrated in Table 3. Maximum density near exits is calculated to be 5.26 person/m^2 in average. As it can be seen considering different number of people and number of exits do not have significant influence on maximum density around exits. This is because of geometry of the plan and being the two exits very close each other so congestion of people cannot be avoided.

4 Conclusion

One of the important considerations in an emergency situation is evacuation of people. This is of great importance when a large number of people are or gathered together in a confined space such as mosques, subway stations, shopping malls, etc. To predict the evacuation of a place, an effective way is to simulate evacuation behavior. We did the simulation of evacuation behavior by using DEM for the Classes Building of Azarbaijan Shahid Madani University. Different cases with different number of people and exits are considered. Evacuation behavior, evacuation time, and density around exits are estimated quantitatively. As results show

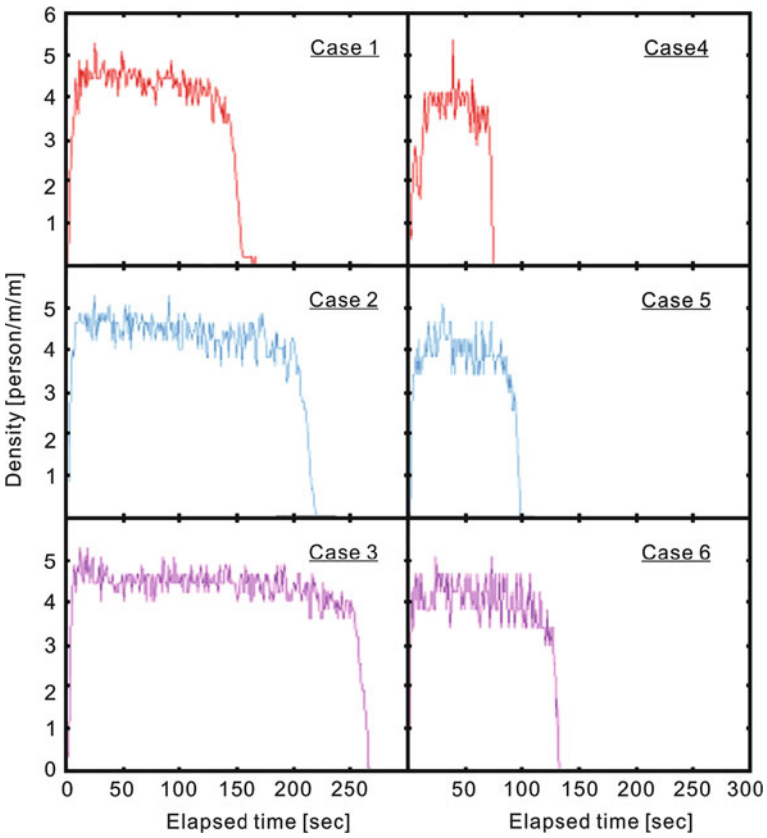

Fig. 6 Time history of density near exits

Table 3 Maximum density around exits

	Maximum density (person/m^2)
Case 1	5.32
Case 2	5.32
Case 3	5.32
Case 4	5.4
Case 5	5.1
Case 6	5.1

by doubling the number of people, 625–1300, evacuation time increases 1.67 times and by considering two exits instead of one exit, evacuation time decreases 0.47 times. So according to current situation of the building, it is better that exit 2 always be open or at least there should be some people responsible to open it at emergency situations.

Maximum density near exits is calculated to be 5.26 person/m^2 in average. Considering two exits instead of one exit does not have significant effect on maximum density of people near exits and that is because of geometry of the plan and being the two exits very close to each other. So it is better that exits have enough distance to reduce congestion of people near exits.

In general, it is recommended that before construction of a building, especially buildings with high number of occupants, simulations to have optimum evacuation behavior to be done.

References

Alighadr S, Fallahi A, Kiyono J, Rizqi FN, Miyajima M (2011a) Simulation of evacuation behavior during a disaster, study case: "Mosque of Azarbaijan University of Tarbiat Moallem". In: First international conference on urban construction in the vicinity of active faults (ICCVAF 2011), Paper code: T4001, Tabriz, Iran, Sept 3–5

Alighadr S, Fallahi A, Kiyono J, Rizqi FN, Miyajima M (2011b) Simulation of evacuation behavior during a disaster, study case: Seghatol Islam Mosque of Tabriz Bazaar. In: Proceedings of the ninth international symposium on mitigation of geo-disasters in Asia, Yogyakarta, Indonesia, pp 39–44, Dec 19–20, ISBN: 978-602-95687-4-5

Kiyono J, Mori N (2004) Simulation of emergency evacuation behavior during a disaster by Use of elliptic distinct elements. In: 13th world conference on earthquake engineering, Paper No.134, Vancouver, BC, Canada, Aug 1–6

Kiyono J, Miura F, Takimato K (1996) Simulation of emergency evacuation behavior in a disaster by using distinct element method. In: Proceedings of civil engineering conference, 537/I-35, pp 233–244 (In Japanese with English abstract)

Kiyono J, Miura F, Yagi H (1998) Simulation of evacuation behavior during a disaster by using distinct element method. In: Proceedings of civil engineering conference, 591/I-43, pp 365–378 (In Japanese with English abstract)

Kiyono J, Toki K, Miura F (2000) Simulation of evacuation behavior from an underground passageway during an earthquake. In: 12th world conference on earthquake engineering, Paper No.1800, Auckland, New Zealand, Jan 30–Feb 4

Langston P, Masling R, Asmar BN (2006) Crowd dynamics discrete element multi-circle model. Saf Sci 44:395–417

Smith A, James C, Jones R, Langston P, Lester E, Drury J (2009) Modeling contra-flow in crowd dynamics DEM simulation. Saf Sci 47:395–404

Catastrophic Deep-Seated Landslide at Xiaolin Village in Taiwan Induced by 2009.8.9 Typhoon Morakot

Su-Chin Chen, Ko-Fei Liu, Lien-Kuang Chen, Chun-Hung Wu, Fawu Wang and Shih-Chao Wei

Abstract Xiaolin village is located in Kaohsiung County, Taiwan. During typhoon Morakot, a deep-seated, dip-slope landslide with an area of 2.5 km^2 and a volume of 2.7×10^7 m^3 occurred and killed more than 400 people. It began at 6:17 a.m. on August 9, 2009 due to heavy rainfall. The mean depth of Xiaolin landslide was 44.6 m. The main sediment slid through an original valley, dammed the Chishan River, and buried a part of the Xiaolin village. Dam-breaking occurred shortly after and buried remaining part of the village. It was the most devastating disaster occurred since the typhoon warning system was established in Taiwan in 1992. This paper gives a detailed report on the event and analyzes the disaster through comparison of the geographical change. The detailed description in this paper can provide important criterion for predicting and emergency response to similar large scale landslide disaster in the future.

Keywords Typhoon Morakot · Deep-seated landslide · Xiaolin landslide · Dam break

S.-C. Chen · C.-H. Wu
Department of Soil and Water Conservation, National Chung Hsing University, 250 Kuo Kuang Rd, Taichung, Taiwan

K.-F. Liu (✉) · S.-C. Wei
Department of Civil Engineering, National Taiwan University, No.1, Sec. 4 Roosevelt Rd, 106 Taipei, Taiwan
e-mail: kfliu@ntu.edu.tw

L.-K. Chen
National Science and Technology Center for Disaster Reduction, 9F., No.200, Sec. 3, Beisin Rd, Sindian District, New Taipei City 231, Taiwan

F. Wang
Department of Geoscience, Shimane University, 1060 Nishikawatsu, Matsue, Shimane 690-8504, Japan

F. Wang et al. (eds.), *Progress of Geo-Disaster Mitigation Technology in Asia*, Environmental Science and Engineering, DOI: 10.1007/978-3-642-29107-4_23,

1 Introduction

Many serious rainfall-induced large scale landslides and debris flows occurred during the last two decades in Taiwan, such as in Typhoon Herb (Lin and Jeng 2000), Typhoon Toraji (Wu and Chen 2009), and Typhoon Morakot (Chen and Huang 2010) just to name a few. There are also many catastrophic dip-slope landslides in the world, such as Vajont dam, Italy with a volume of 2.7×10^8 m^3 in 1963 (Kilburn and Petley 2003), and the snow-melting induced Yigong landslide, Tibet with a volume of 3.0×10^8 m^3 in 2000 (Shang et al. 2003). Large scale landslides often block rivers and form landslide dams. The follow-up dam-breaking event (if any) usually cause serious casualties as well.

Catastrophic landslides often occur without warning since the slight topographic creeping in the early stage is either unnoticed or difficult to be detected (Kilburn and Petley 2003). Their long run-out distance with huge volumes and the lack of response time are the reasons why catastrophic landslides often result in a large number of deaths. Xiaolin landslide (Wu et al. 2011) was one of the typical cases.

Xiaolin village is located in the northeast of Chiahsien Township, Kaohsiung County, Taiwan (Fig. 1). Xiaolin village is one of the earliest settlements in Taiwan. Its history can be traced back to early 1900. The village occupies an area of 47.9 km^2. The population was 1,313. Main industry is tourism and agriculture. Average annual rainfall is 2,018.2 mm. There was no landslide or flood record for the past 70 years.

Villagers live on the east. The bank of Chishan River and around a newly deposited mountain foothill (Fig. 2). The Alishan with altitude 1,008 m is on the west and the Yushan with altitude 1,664 m is to the east. River bank is at an altitude of 345 m. Xiaolin village is separated into two parts.The south part with altitude 430–450 m is 80 m above river bottom. The north part with the altitude 370–380 m is only 10 m above river bottom (Fig. 2). During the disaster, the north part was completely wiped out but the south part was not affected at all. Since this paper concentrates on the landslide disaster, we shall refer the north part of Xiaolin village as Xiaolin village from here on.

2 The Xiaolin Deep-Seated Landslide Event

The Xiaolin landslide is located in east bank of the Chishan River. The maximum accumulated rainfall brought by Typhoon Morakot is over 3,000 mm and occurred in the Alishan just west to the village. The rain gauge nearest to Xiaolin village is the Chiahsien station. The accumulated rainfall amount for typhoon Morokat is 2,142 mm (Fig. 3) at Chiahsien station. This 4-day event accumulated amount had already exceeded 60% of the average annual rainfall 2,839 mm in this area and was projected to be a 500 year return period event.

To describe the whole event in time and space, we combined the rainfall variation from Aug 6th to 10th and water level variation at Nanfeng bridge (just upstream to Xiaolin village and right above the major landslide) as well as at

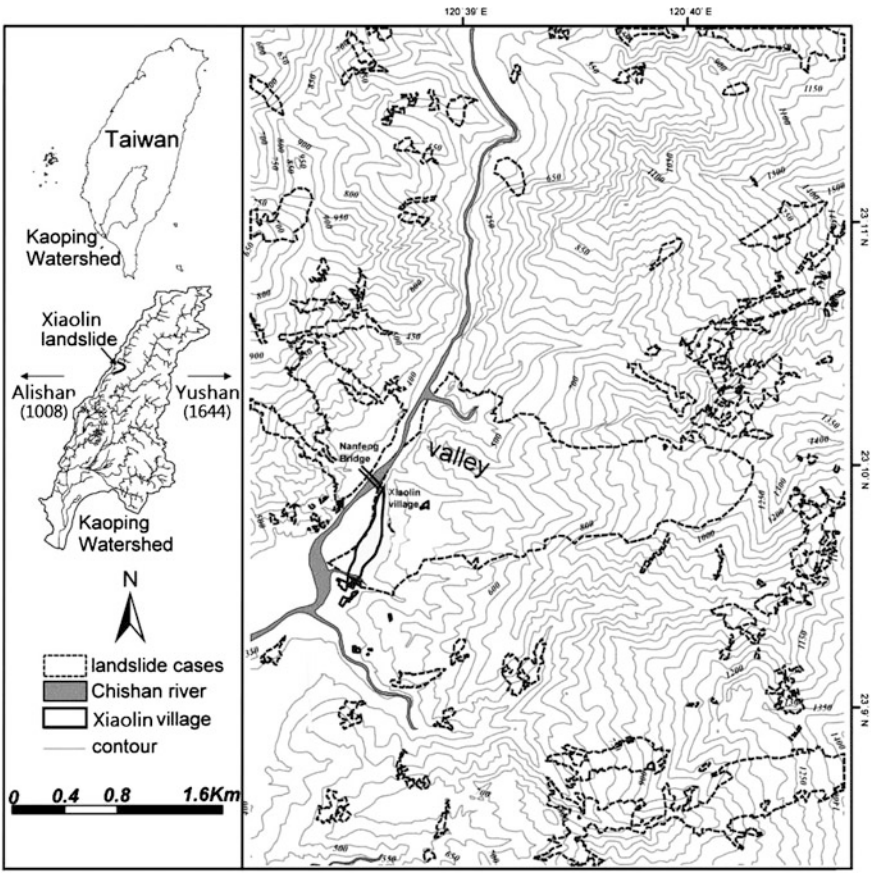

Fig. 1 The location of the Xiaolin landslide

Sanlin bridge (27 km downstream of Xiaolin Village) in Fig. 3. Then the whole event can be described as follows.

(1) 8:30, August 6th: The Central Weather Bureau in Taiwan announced land warning for typhoon Morakot. Water level at Nanfeng Bridge was 368.8 m and at Sanlin Bridge was 116.1 m. Both water levels were normal at that time.
(2) 17:00 August 7th: Soil and Water Conservation Bureau in Taiwan notified Chiahsien Township officer that the accumulated rainfall amount would soon exceed the debris flow warning threshold 500 mm. Yellow alert was announced. Villagers should get ready to leave.
(3) 23:00 August 7th: Accumulated rainfall exceeded 500 mm. Red alert for debris flows was effective. All villagers must evacuate immediately according to the evacuation law.
(4) 6:00 August 8th: Accumulated rainfall amount exceeded 700 mm. Hourly rainfall intensity was 48.5 mm and 3 hours accumulated rainfall reached

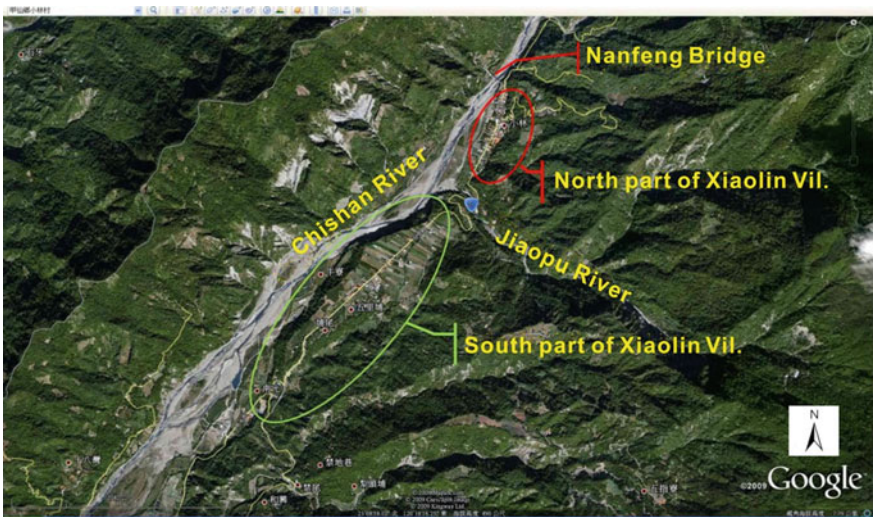

Fig. 2 *Red circle* indicates the disaster area

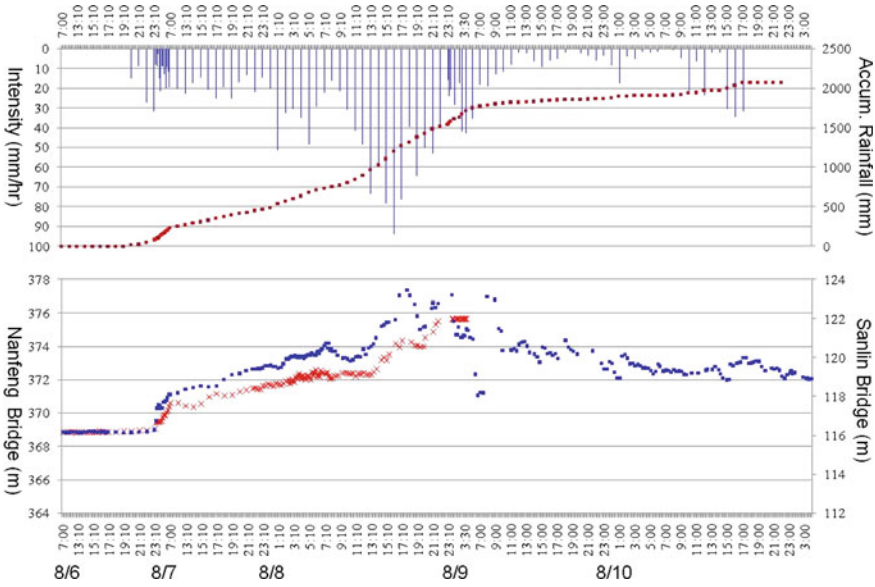

Fig. 3 Combined rainfall and water level for Xiaolin Village disaster event. *Red crosses* indicate water level at Nanfeng Bridge (just upstream to Xiaolin village). *Blue dots* indicate water level at Sanlin Bridge (27 km downstream of Xiaolin Village)

67.5 mm. Flooding warning was also issued by Water Resources Agency. The water level at Nanfeng bridge was 372.6 m.

(5) 15:30 August 8th: Chishan River just besides Xiaolin Village flooded and overflowed to Route 21 which is the only road connected to outside from

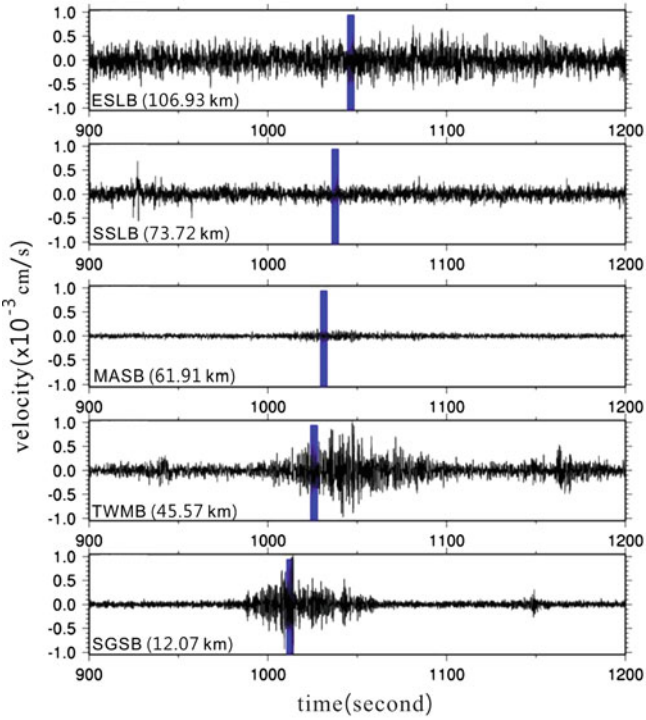

Fig. 4 SSA data for Xiaolin Village slide from 5 earthquake seismographs from nearby stations. The distance marked on *lower left* corner of each record is the distance from the station to Xiaolin landslide. The calculated vibration source is at Xiaolin landslide

Xiaolin Village. The accumulated rainfall amount was 1,100 mm. Water level at Nanfeng Bridge was 373.5 m. Hourly rainfall intensity was 94 mm. These number has exceeded all previous records for the past 70 years.

(6) 21:00 August 8th: Road traffic was completely blocked due to heavy flood. Accumulated Rainfall was 1,485 mm. Water level at Nanfeng Bridge was 374.8 m.

(7) 23:30 August 8th: Water level at Nanfeng Bridge reached the peak 375.6 m. This is the height of the bridge and the highest level can berecorded. Water level at Sanlin Bridge was 123.2 m and started to decrease.

(8) 3:30 August 9th: Flood in Xiaolin Village reached the height of adult's waist. Villagers started to evacuate to high ground. But water level at Sanlin Bridge decreased to 121.1 m. It was due to downstream embankment destruction.

(9) Arond 6 a.m. August 9th: Survivors from Xiaolin Village recalled three huge sounds (one large, two small). This could be the initiation of the catastrophic slide.

(10) 6:17:47.7 August 9th: Broadband array system for earthquake detection in Taiwan collected wave form records for the slide event. Through Source Scanning Algorithm (SSA), event source was identified at 1 km underground at (23.1407 N 120.6480 E) just besides Xiaolin Village (Fig. 4) (Lin

Fig. 5 Xiaolin Village after disaster. *Top* photo is taken from Chishan River and looking upstream while the *lower* photo is looking downstream. The only house survived is the one in the top photo on the *right*

et al. 2010). It should be the slide process. Chishan River had no water but huge boulders remained. This indicated a barrier lake was formed due to landslide. The water level at Sanlin Bridge decreased to 120 m.

(11) 7:00 August 9th: Rainfall started to decrease to hourly intensity of 18 mm. Accumulated rainfall was 1,770 mm. Sanlin Bridge water level decreased to its lowest 118.1 m at 7 a.m. This shows the natural dam had blocked the upstream flow.

(12) Around 7:40 August 9th: Hourly rainfall intensity was 13 mm and accumulated rainfall was 1,802 mm. The water level at Sanlin Bridge increased from 118.2 to 123.1 m in 20 min. This indicated the breach of natural dam had occurred. Remaining part of Xiaolin Village was buried by debris flows (Fig. 5). Estimating from the flow velocity, the breaching should occur around 6:40–6:60. An aerial photo of Xiaolin Village is shown in Fig. 6.

Fig. 6 **a** A satellite photo of the Xiaolin landslides. All later figures are based on this photo (Date of the photo: August 17, 2009; photo source: Formosat-2 Satellite Image). **b** Aero photo of Xiaolin Landslide (from Water Resource Agency, Taiwan)

Fig. 6 (continued)

(13) 9:00 August 9th: Hourly rainfall intensity was 8 mm and accumulated rainfall was 1,822 m. Water level at Sanlin Bridge decreased from 123 m to 121.5 m in 30 min and decreased to 120.4 m in 2 hours. Debris flows also destroyed Chiahsien dam operation center and all nearby bridges 25 km downstream (Fig. 7). The effect of the Xiaolin landslide had already propagated more than 80 km downstream.

3 Xiaolin Landslide Investigation

The geological setting of the Xiaolin landslide is shown in Fig. 8. The Xiaolin landslide was mainly located in Tangenshan sandstone and with small portion in Yenshuikeng shale. The age of the Tangenshan sandstone is Miocene to Pliocene, and its content is thick-bedded sandstone and muddy sandstone. The age of the Yenshuikeng shale is Pliocene, and its content is massive shale. The thickness of Tangenshan sandstone and Yenshuikeng shale are approximately 450–500 m and 200–250 m, respectively. Two active faults, i.e. the Chishan fault and the Wulipu fault are close to the site. A new east–west strike fault was found according to the field investigation after the Xiaolin landslide (Lee et al. 2009). In addition, there are two folds, Xiaolin syncline and Jiashian anticline, go through the landslide

Fig. 7 Flood destroyed Chiahsien dam operation center (*top*) and nearby bridges (*bottom*)

area, while Shihchangeli syncline is adjacent to the east ridge of Xiaolin landslide. The aforementioned three folds strike to northeast and the fold axes plunge to the southwest. The flanks of the three folds dip gently with the angles of 10–20°, but occasionally with dipper angles of 30–40° (Keng 1965).

After the landslide, exposed rocks at the collapse area showed that the sediments were mainly dark gray shale occasionally inter-bedded with sandstone. The bedding plane of the sandstone with strike in WNW-ESE dipping to the southwest direction was observed at some outcrops. The bedding plane and a steep joint striking in the EW direction were thought of weak planes of the landslide mass at north and south sides, respectively. The collapse mass, which slid toward west mainly consists of shale, and the slide surface was mainly within the shale formation. Therefore, it is suspected that the whole layer of sandstone above a weak layer was mobilized due to extremely high accumulated rainfall amount.

All field data used in the analysis was obtained on the field survey conducted on November 4, 2009, 3 months after the disaster. 5mX5m DEM is used to analyze the

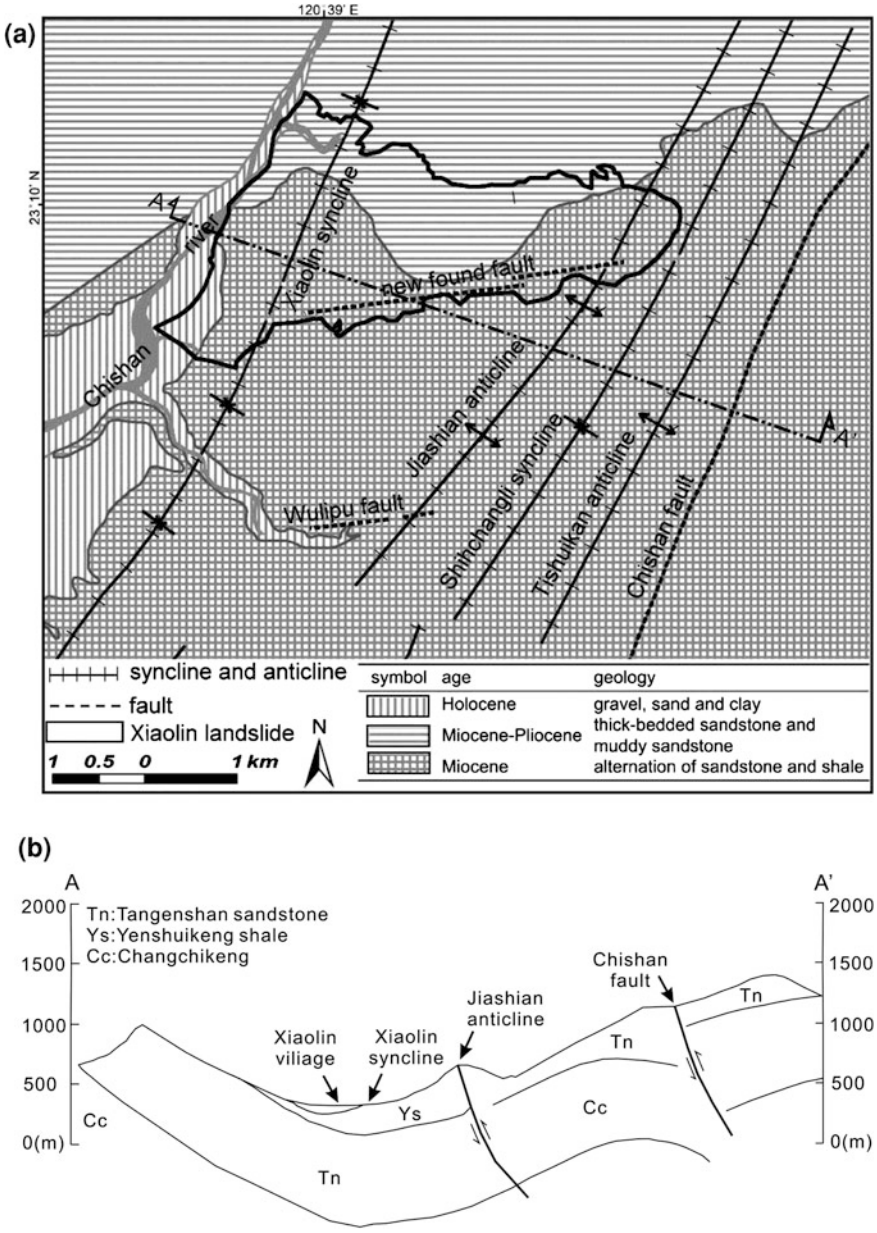

Fig. 8 **a** 1/50000 geological map of the Xiaolin landslide (from Central Geological Survey). *Red line* indicates the landslide area. **b** Strata profile along *Blue dotted line* in **a** *Arrow* indicates the movement of the layer. Cc is the Changchikeng Formation which is an alteration of sandstone and shale

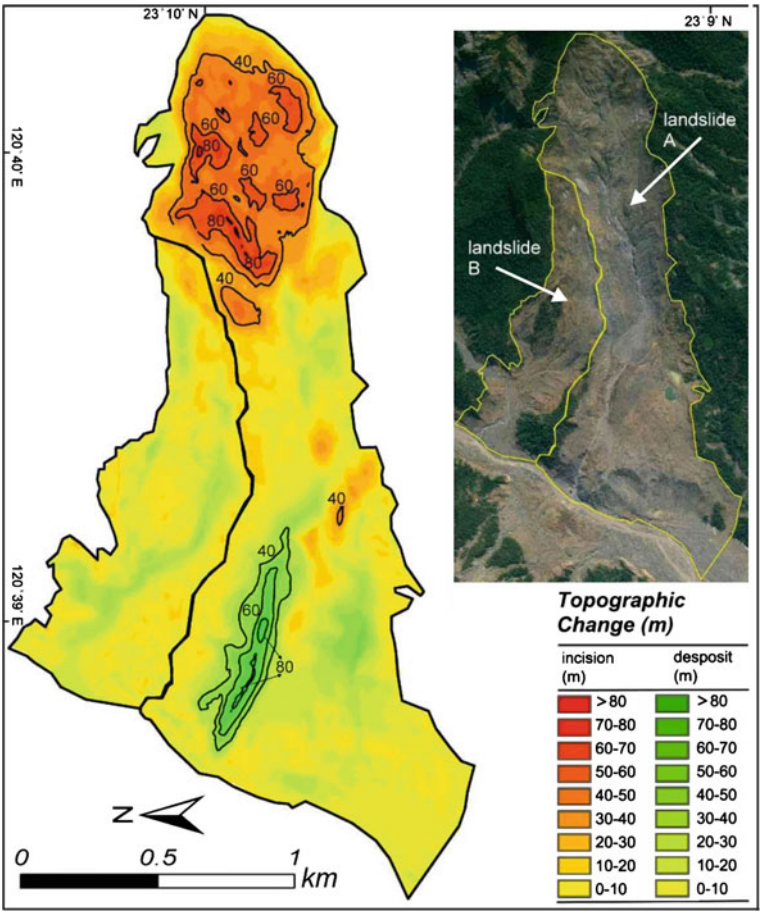

Fig. 9 Topographic change of the Xiaolin landslides (figure from Wu et al. 2011)

topographic changes of the Xiaolin landslide before and after Typhoon Morakot (Fig. 9). The area and volume of the Xiaolin landslide are 2.5 km^2 and 2.7 × 107 m^3. The areas with slope greater than 20° were reduced by 13.8 % after the slide. From the field investigation, Xiaolin landslide can be divided into Landslide A on the right and Landslide B to the left (Fig. 9) and they were separated by the ridge. In what follows, we shall discuss these two landslides separately. Landslide A is the major landslide and is the reason for the disaster. Therefore, we discuss Landslide A first.

3.1 Major Landslide (Landslide A)

Landslide A is the major slide which leaded to the disaster. The source area and volume of Landslide A are 1.9 km^2 and 2.55 × 10^7 m^3 and was located at an

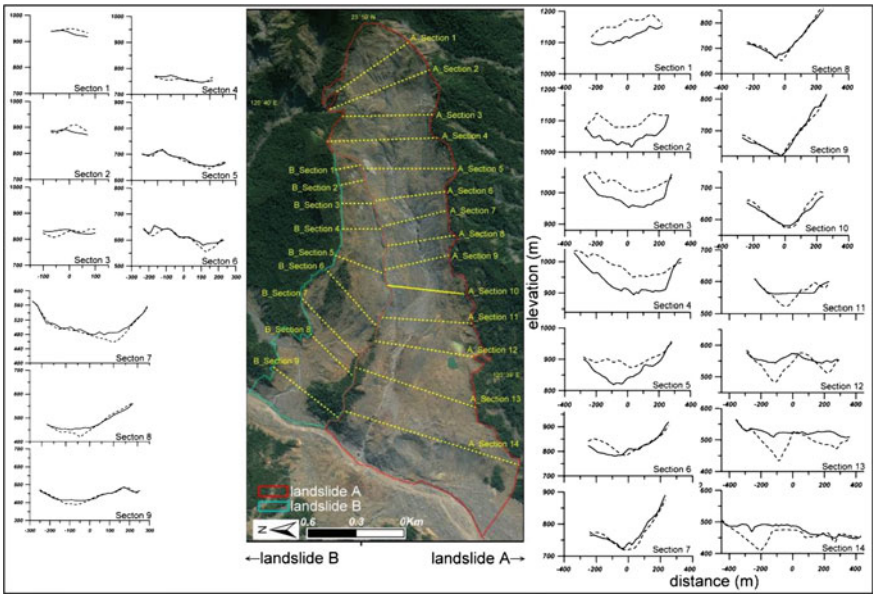

Fig. 10 The elevation variation before (*dashed line*) and after (*solid line*) Typhoon Morakot. There are 14 cross-section lines for Landslides A and 9 cross-section lines for B (figure from Wu et al. 2011)

elevation greater than 800 m. The mean incised depth in its source area is approximately 38.1 m. The estimated deposited volume of Landslide A after the disaster is approximately 1.5×10^7 m^3, and is located at an elevation less than 600 m. This means roughly 1.05×10^7 m^3 of the deposited material was transported downstream by debris flows induced from the collapsed dam. The whole process is described in the previous section as what happened between 5:30 and 7:20 August 9th. The average deposition depth after the disaster is approximately 11.3 m with the highest deposition greater than 80 m (Fig. 9). To examine the topographic change in more details about Landslide A, we delineate 14 cross-sectional transects for Landslide A in Fig. 10. The deep incision in Landslide A occurred between Sections 1 and 5, with the deepest incision located on the northern hill slope at Sections 4 and 5. The region between Sections 6 and 10 is slightly deposited and the region between Sections 11 and 14 is the major depositional zone. The main deposition area occupies part of the original valley (see Fig. 9). Section 10 is the location where the slide changed its direction. That is why major deposition occurred after Section 10. This also means the huge slide moved more than 600 m as a whole without stopping.

To further explore the Landslide A, we draw more longitudinal profiles in incised region and analyze them by employing both DEM and field investigation. Profile d1, d2 and d3 in Fig. 11 start from the top of the main scarp and end at Section 10 where slide changes direction. The elevation change of d1, d2 and d3 are drawn in Fig. 12. The maximum incised depth was 66.9 m at 1,000 m upstream from Section 10. The

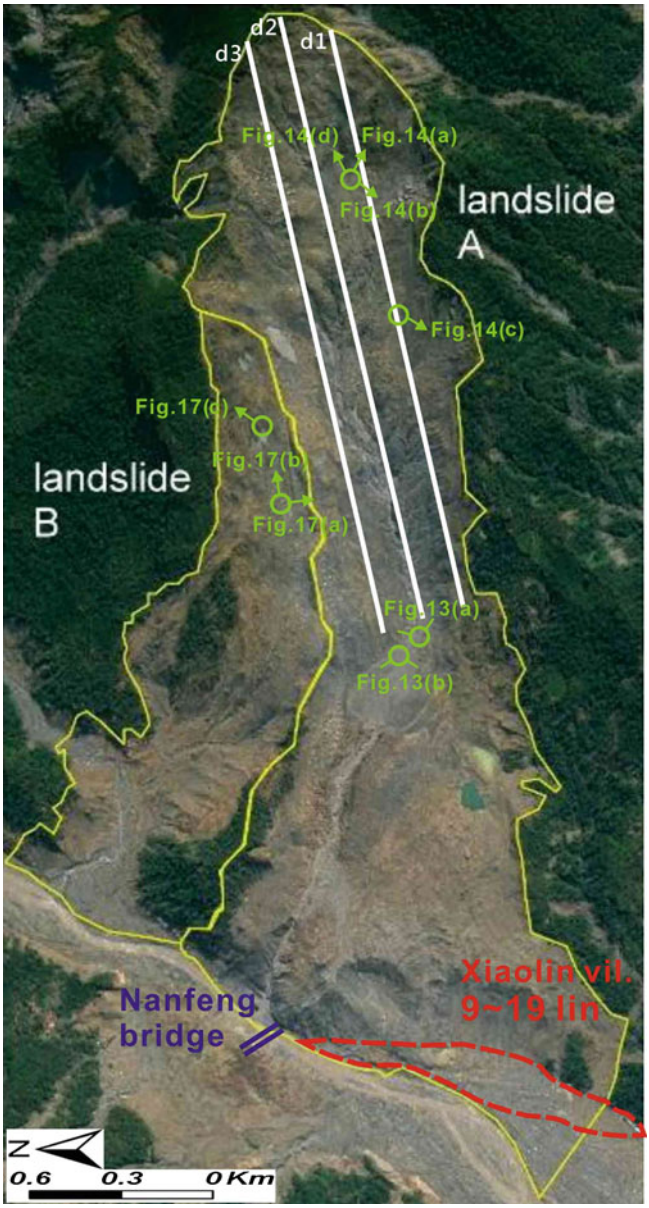

Fig. 11 Detailed topographic changes are shown for longitudinal line d1, d2 and d3. Field photos were taken at location marked by *green circle*. *Arrows* indicate the direction a photo was taken (figure modified from Wu et al. 2011)

profile shows an 1,100 m long source region (from 500 to 1,600 m upwards of Section 10). This is the major slide area. From Section 10 to 500 m upwards, topography remains almost the same. This is the sliding area.

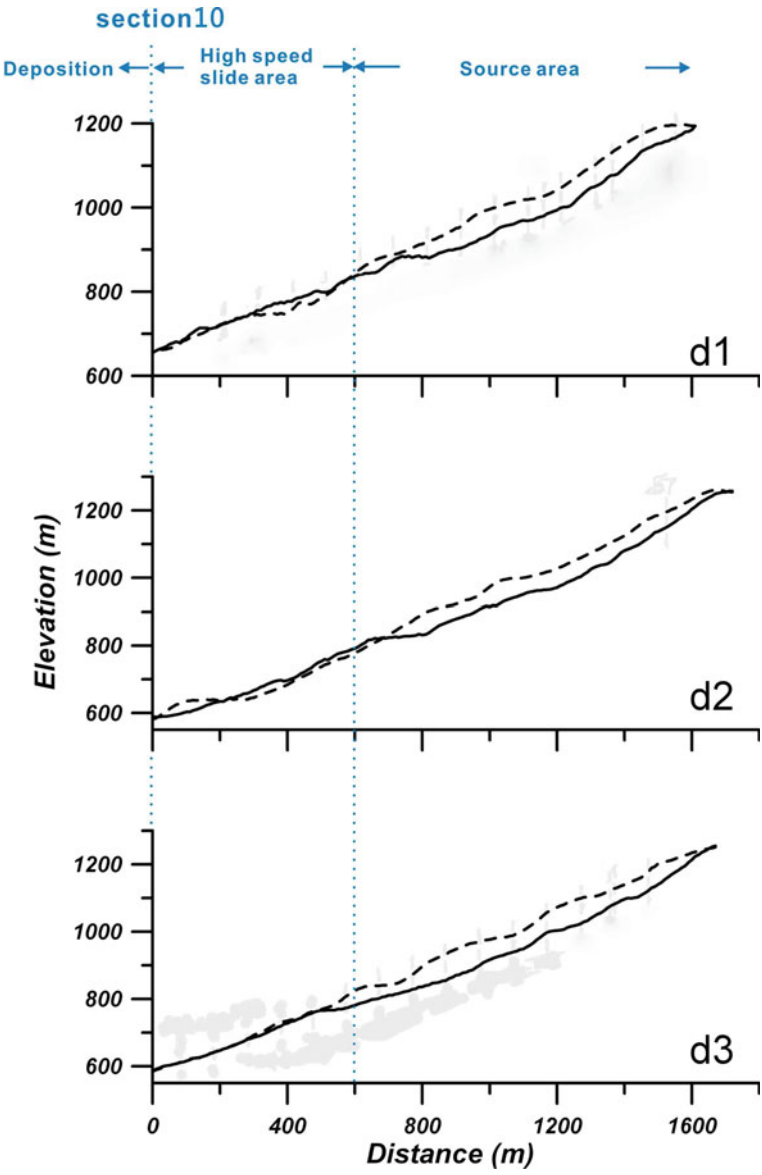

Fig. 12 The elevations before (*dashed line*) and after (*solid line*) Typhoon Morakot along the longitudinal lines d1, d2 and d3 of the main Xiaolin landslides (figure modified from Wu et al. 2011)

If we examine the satellite photo in Fig. 6 carefully, there is a platform (between A_section 10 and A_section 12 in Fig. 10 and around location marked with Fig. 13b in Fig. 11). The shape of the platform looks like a deposition fan with length 220 m and maximum width 200 m. But there is no deposition at all on

that platform. Furthermore, there are clear path of long scratching or sliding evidence existing. As we examine the location in the field, there are many shallow pools exist. These evidences show that this is a platform created as the result of a high speed slide. The tail of the high speed slide stopped at the end of the platform with all vegetation still remains the same as the top of the source area.

If we go further upwards to the source area (Fig. 14), many dip-slope landslides can be found as shown in Fig. 13a. Combining all the above information and field investigation, we can summarize the movement of Landslide A in Fig. 15. Landslide A has a mean and maximum landslide depth of 44.6 and 85.6 m, respectively. The landslide was a dip-slope landslide that moved along the lower sandstone layer. Landslide A, moved toward down slope like a huge rock mass at 6:17 a.m. on August 9, 2009. The huge dip-slope landslide slid down with high speed until it hit Chiashien River and created a natural dam. The duration of the huge landslide was less than 3 min. Afterward, the landslide dam failed in 20 min.

To show a complete variation of the longitudinal profile, the difference of elevation and volume along the baseline GG' in Fig. 15 is given in Fig. 16. Clear boundaries can be seen, i.e. the incised area, the transport area, and the deposit area with the elevation of >800, 600–800, and <600 m, respectively.

3.2 Landslide B

The source area and volume of Landslide B are 0.6 km^2 and 1.6×10^6 m^3, respectively. Its source area is located at elevation between 700 and 1,000 m. The mean incised depth in the source area is approximately 9.8 m, and the depositional zone of Landslide B is located at the region with elevation less than 700 m. The mean deposition depth is approximately 7.1 m with a rather uniform distribution along the path. Its deposition area is upstream to Landslide A and did not form natural dam.

We delineate nine transects for Landslide B in Fig. 10 to evaluate the topographic change before and after Typhoon Morakot. As can be seen, most colluviums in Landslide B were deposited on the southern hill slope in Sections 6–9. But there is no large variation of topography. Therefore, it is just a typical shallow layer slide. There was not enough momentum or mass to have large scale effect. The field photos of Landslide B are shown in Fig. 17 which shows the deepest part of the source area. The deepest landslide with a maximum depth of 32.5 m is located in the southern hill slope of Landslide B. The rock mass outcrops in Fig. 17 clearly appear on these photos. There is water flowing on the surface of rocks in Fig. 17a indicates the ground water level is high. Large boulders were seen on top of fine grain material near the deposition zone (Fig. 17a). Therefore, Landslide B is assumed to be another dip-slope landslide.

Fig. 13 Field survey of the Xiaolin landslides. Photo taken from central platform at Section 10. The sliding surface around here dipped to S50°W, and the dip angle was 23°; **a** uphill source area, **b** downhill view

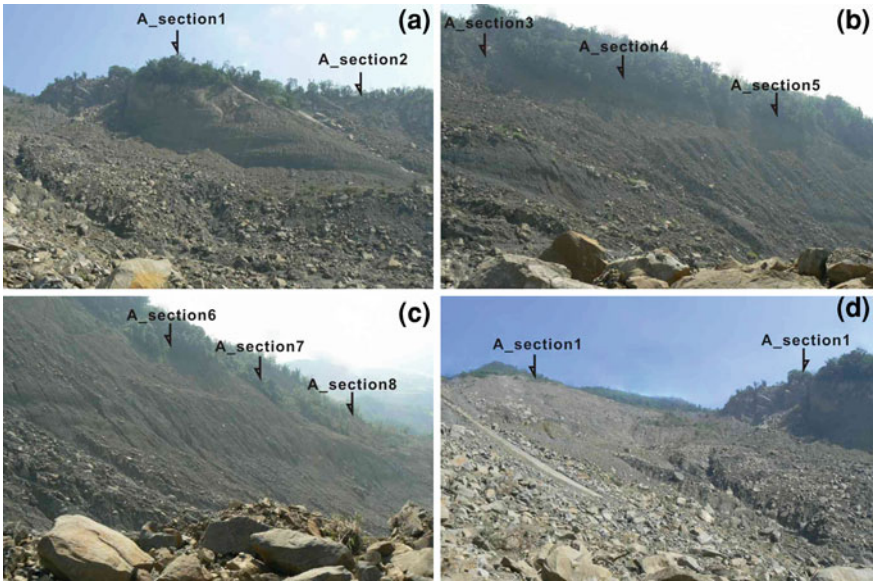

Fig. 14 Field survey photos of the Xiaolin landslide. Photos were taken in the source area with locations and photo taken directions indicated in Fig. 11 (photo from Wu et al. 2011). Sections marked on photo is the location of sections indicated in Fig. 10

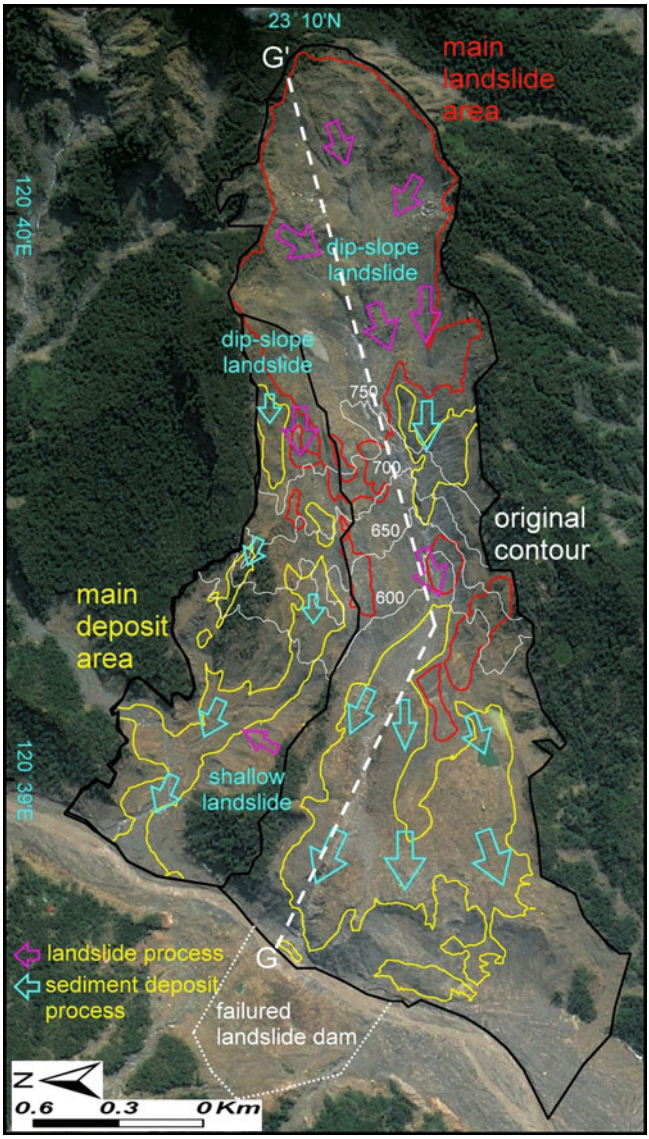

Fig. 15 Xiaolin landslides: *black line* depicts the complete landslide area. The *red line* indicates the area with landslide depth > 10 m. The *yellow line* indicates the area with deposit depth > 10 m. The *purple* and *blue arrows* indicate the landslide process and sediment deposit processes, respectively. The estimated deposit area of the landslide dam is plotted as the *white dotted line*. The GG' line is the longitudinal section with the maximum incision. The detail depth variation along GG' is plotted in Fig. 16 (figure from Wu et al. 2011)

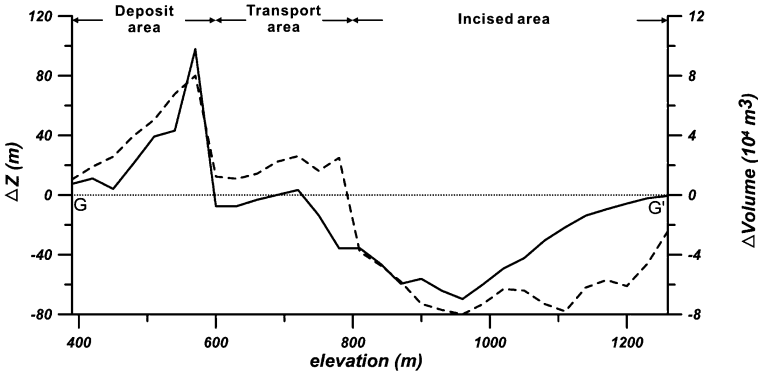

Fig. 16 The difference of elevation (△Z, *dashed line*) and volume (△V, *solid line*) with the base area of 1 m^2 along GG' line in Landslide A of Xiaolin landslide (figure from Wu et al. 2011) The horizontal axis is the elevation not the horizontal distance used in Fig. 12

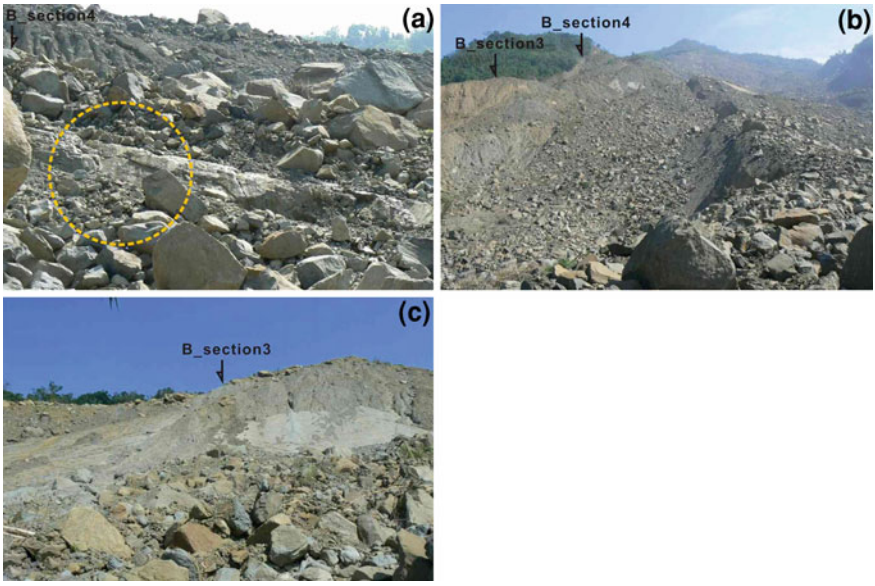

Fig. 17 Field survey pictures of Landslide B. Photo location and directions are indicated in Fig. 11. **a** The ridge separates landslide A and B. *Circle* indicates the location where ground water flows to the surface. **b** *Upstream* view with clear trace of shallow layer slides. **c** Highest point of landslide B (figure from Wu et al. 2011)

4 Conclusion

A heavy rainfall over 500-year return period during Typhoon Morakot, induced serious disasters in southwestern Taiwan. Xiaolin landslide was a deep-seated, dip-slope landslide with an area of 2.5 km^2 and a volume of 2.7 $\times$ 10^7 m^3. It began at

6:17 a.m. on August 9, 2009 due to heavy rainfall. The mean depth of Xiaolin landslide was 44.6 m. Part of the sediment slid through the original valley and dammed the Chishan River. The village was completely wiped out due to the combined effect of landslide and dam-break. The record-breaking rainfall could be the reason for slide as well as for the dam-break.

Two things were learned from this disaster. First, people live in areas such as Xiaolin village, where road connection to outside can be easily affected by disaster, should be evacuated as early as possible. Second, large scale landslide can create vibration in shallow ground layer and can be picked up by seismometers. This can be of future use for emergency response for large scale landslides. The detailed time sequence for the whole event should be very valuable to emergency response of similar event.

Acknowledgments The authors would like to thank Professor C.T. Lee and Dr. W.N. Wang for providing us useful geologic information and constructive comments. Special thanks for National Science and Technology Center for Disaster Reduction, Taiwan for providing part of the data in this paper.

References

Chen SC, Huang BT (2010) Non-structural mitigation programs for sediment-related disasters after the Chichi Earthquake in Taiwan. J Mountain Sci 7:291–300

Keng WP (1965) Geology of the Minsheng-Chiahsien area, Southern Taiwan. Bulletin Geol Surv Taiwan 16:3–15

Kilburn CRJ, Petley DN (2003) Forecasting giant, catastrophic slope collapse: lessons from Vajont, Northern Italy. Geomorphology 54:21–32

Lee CT, Dong JJ, Lin ML (2009) Geological investigation on the catastrophic landslides in Siaolin village, southwestern Taiwan. Sino-Geotechnics 122:87–94

Lin ML, Jeng FS (2000) Characteristics of hazards induced by extremely heavy rainfall in Central Taiwan—Typhoon Herb. Eng Geol 58:191–207

Lin CH, Lin HK, Ando M, Shin TC (2010) Detection of landslides and submarine slumps using broadband seismic networks. Geophys Res Lett 37:L22309. doi:10.1029/2010GL044685

Shang Y, Yang Z, Li L, Liu DA, Liao QL, Wang YC (2003) A super-large landsl1ide in Tibet in 2000: background, occurrence, disaster and origin. Geomorphology 54:225-243

Wu CH, Chen SC (2009) Determining landslide susceptibility in Central Taiwan from rainfall and six site factors using the analytical hierarchy process method. Geomorphology 112:190–204

Wu CH, Chen SC, Chou HT (2011) Geomorphologic characteristics of catastrophic landslides during typhoon Morakot in the Kaoping Watershed, Taiwan. Eng Geol 123(2011):13–21

Failure and Motion Mechanisms of a Rapid Loess Flowslide Triggered by Irrigation in the Guanzhong Irrigation Area, Shaanxi, China

Tonglu Li, Jifei Zhao, Ping Li and Fawu Wang

Abstract Rapid loess flowslides induced by irrigation often occur in the loess irrigation area, which have resulted in serious damages to farmlands, residential houses and loss of lives. A typical case of the Gaolou flowslide in Guanzhong irrigation area, Shaanxi Province of China was investigated. Laboratory tests suggest that the loess flowslide has a loose structure and that the saturated moisture content is higher than the liquid limit. As the loess slope starts to fail, the saturated loess of the sliding zone quickly fluidizes and then flows on the relative dry-hard path because the loess structure is damaged by the shear force to produce a high excess pore pressure in the lower portion of the displaced mass, while negative pore pressure is produced between the displaced mass and the ground surface because of pore pressure dissipation on the dry ground. So the shearing zone is within the lower portion of the displaced mass other than on the ground surface, which makes part of the displaced mass cohere on the ground as seen at the site. The triaxial tests for the loess specimens suggest that fluidization occurs at the source area in the beginning and maintains in the moving process, which produces a quick and long run-out flow. The modified Sassa K's simulation model for landslide motion is applied to simulate the motion scenarios of this case.

Keywords Rapid flowslide · Irrigation · Loess · Fluidization

T. Li (✉) · J. Zhao · P. Li
Department of Geological Engineering, Chang'an University, Xi'an, 710054 Shaanxi, China
e-mail: dcdgx08@chd.edu.cn

F. Wang
Department of Geoscience, Faculty of Science and Engineering, Shimane University, Matsue 690-8504, Japan

F. Wang et al. (eds.), *Progress of Geo-Disaster Mitigation Technology in Asia*, Environmental Science and Engineering, DOI: 10.1007/978-3-642-29107-4_24,

1 Introduction

Flowslide is a typical type of landslide frequently occurring in countries of Southeast Asia, such as in Taiwan, Japan, Philippine, Malaysia and Indonesia. They are generally triggered by heavy rainfalls and results in catastrophic disasters. However, in the Chinese loess area, the loess flowslide have been recorded with the number triggered by irrigation being higher than those triggered by rainfall. Loess is deposited in the arid-semiarid region with annual precipitation between 450–650 mm/a, which is far lower than that in the oceanic areas. Even the loess area often has rainstorms or mould rains, but loess has a very low permeability, most of the rainwater runs off other than infiltrates into soil, so the heterogeneous loess flowslides could possibly occur in the gullies where there have existed enough slumped materials. Therefore, the rain-triggered loess flowslides do not dominate in the loess region. Since 1970s, lots of irrigation systems have been built and utilized in the loess area. It essentially solves the draught problem of agricultural development, but leakages of the irrigation canals and free-flow of water have triggered a large number of landslides. Loess flowslide has caused a great economic loss to agricultural activities and causalities to local dwellers. This research focuses on the Gaolu loess flowslide which occurred in Gaolou village, Daming town, Huaxian County, Shaanxi Province of China in Oct. 6, 2006. Based on the field investigation, laboratory tests and numerical simulations, the authors summarize the geological conditions of the landslide origin, and the mechanisms of the landslide initiation and movement.

2 Geological Characteristics of the Loess Flowslide

There are some loess flowslides triggered by irrigations scattered in the Guanzhong irrigation area. The area is located in the center of Shaanxi Province and accords with the Weihe rift region. Many pieces of highlands among the branches and the trunk of the Weihe River stand in the rift. These highlands are the dissected loess platforms, and the surfaces of them are irrigation farmlands. The area has a long history of irrigation and now has a very dense channel system. Leakage of the channels and free-flow irrigations induced a large number of landslides at the side slopes of the loess platforms. Loess flowslides are minor in number but results in high fatality because of their quick outburst and long run-out.

Investigations carried out in the Guanzhong irrigation area suggests that the loess flowslide occurs in distinct geological conditions, including topography, hydrogeology and soil property.

Topographically, loess flowslides occur in narrow loess gullies, which develop at the sides of the platforms. As the top end or the side of the gully slumps, the displaced loess may change to mud-flow moving down along the gully and stops at the outlet of the gully. Hydrogeologically, loess has a relative impermeable bed at

higher levels on which perched underground water could be formed during the irrigation activities on top of the slope. The landslide may shear out on the impermeable bed because of water softening. For soil properties, the soils above the impermeable bed should be as loose as the saturated moisture content is higher than the liquid limit. In this case, the soil in the shear zone of the landslide could fluidize quickly as it starts to fail, which means it may change from solid state to liquid state. The reason, as explained below, can be attributed to liquefaction caused by extra pore pressure in the shear zone. Otherwise, for the soils with the saturated moister content is less than liquid limit, they may change to a plastic state with creep deformation other than flow under shearing action.

A typical case is the Gaolou flowslide which occurred in Gaolou village, Daming town, Huaxian County, about 120 km to the east of Xi'an city, on Oct. 6, 2006. Figure 1 shows the location of the landslide and Guanzhong irrigation area. The flowslide occurred on the top end of a loess gully, which has eroded out on the side of a loess platform. Gaolou village just lies on the outlet of the gully. While the flowslide was occurring, most of the displaced material moved down along the gully's floor and thereafter accumulated on the outlet of the residential area, where it killed 12 people and destroyed 94 rooms related to 24 families. In the morning, most of the local people went out to work in the farmland; otherwise, there could have been more casualties. Soon after the accident, the authors investigated the site, surveyed the topographic map and the main longitudinal section. Figure 2 shows that the source area of the slide was an armchair-shape after the failure. The back scarp is vertical and arc-like in horizon with height of 30 m, while the inner bottom is gentle with slope angle of 14°. The flow path (Fig. 3) is a U-shaped gully that has a flat bottom and vertical sidewalls transversely. The outside of the gully is an open gentle area on which the Gaolou village lies and the flow mass deposited (Fig. 4). Figure 5 is the topographic contour map of the whole sliding area and (Fig. 6) is the main geological. It shows that the flow path is not straight, as the displaced mass moved forward first, then oriented to the left along the gully floor. The landslide descended a vertical distance of 75 m over a horizontal distance of 320 m measured from the top of the back scarp to the outer margin of the deposit. It also can be seen from Figs. 2 and 3 that there was a little material leaving in the source area and the path. Size of the deposit is measured to be 2.7×10^4 m^3.

The geological profile shows that the whole slope outcrops loess, in detail, it can be recognized as loess-paleosol sequences belonging to later (Q_3) to middle (Q_2) Pleistocene deposits. Of which, Q_3 is composed of L_1 (Loess 1) and S1 (paleosol 1), while Q_2 is of L_2 to L_8 according to the Standard Chinese Loess Profile (Kula and An 1989. On the back scarp, L_1, S_1, L_2, S_2, L_3 and S_3 can be clearly seen (Fig. 2), among which, S_3 appears at the bottom of the sliding area, on which the landslide may shear out. Therefore, the landslide occurred in the Q_3 and upper Q_2 loess, which have a loose structure and vertical joints. The slide cut off a water channel that the remained openings still hang on the top of the scarp. Under the channel, the loess was soaked by water to form a down-spread wet zone and some sinkholes can be seen around the back scarp. Because there was no rainfall before the event, the slide can be attributed to leakage of the channel. The residents

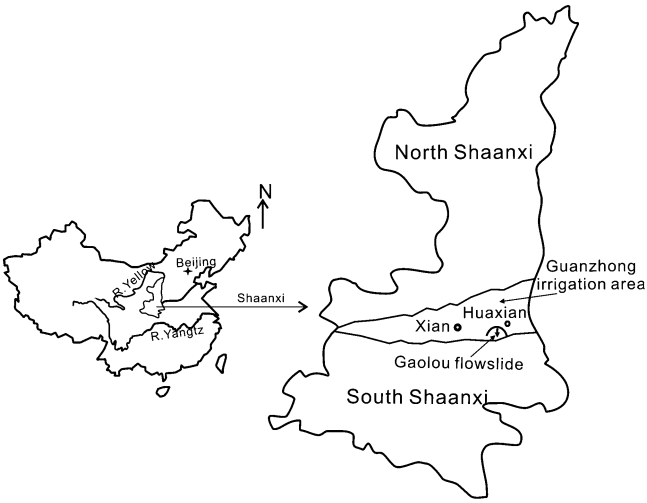

Fig. 1 Location of the Gaolou flowslide in Guanzhong irrigation area, China

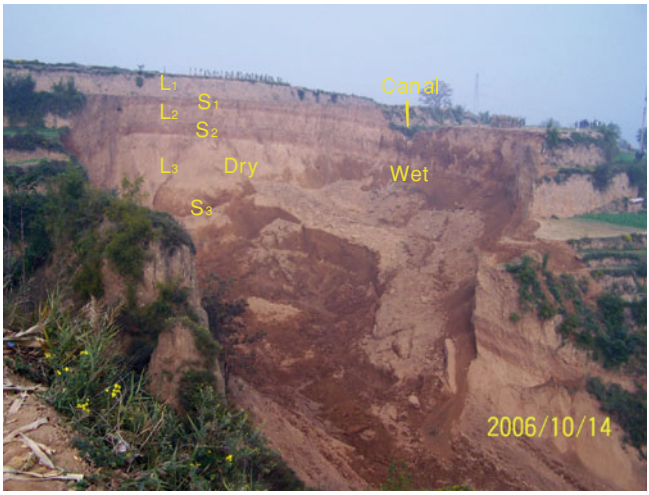

Fig. 2 The source area of the Gaolu flowslide

said that the channel had flowed water for 13 days before the accident, but a little water flowed ahead of the slide.

In general, loess has low permeability, but in top of slopes, unloading may make the vertical joints in the loess to open, which provides the well paths for leakage water to flow down, consequently, the water erosion could further enlarge the joints to form sinkholes. The sinkholes allow more water to penetrate down into the loess. As leakage water got to the paleosol S_3 which is a relatively firm and impermeable bed, a perched water layer is formed on the impermeable bed. With

Fig. 3 The flow path of the Gaolu flowslide

rising of the water table as well as increasing of the pore pressure, the slope failed. Zhang et al. (2008) described the landslide movement as three phases according to the witnesses' description, the first phase occurred when very soft "mud" flew down quickly and was followed immediately by the second phase when "dry" soils descended, destroying the houses and burying 11 people As the residents rushed to rescue the buried people, soon the third phase occurred when they saw the debris coming down. Two of them could not escape in time and were caught by the debris. The movement process implies that there is a lot of water taken in the displaced mass and the gully. As the slope fails, fluidization occurs first in the lower part of the saturated loess, then the dry loess of the upper part "floating" on the fluidized loess rushed down. The water in the loess and in the gully was pushed ahead to form mud flow down first, then the main sliding mass arrived. There were some saturated soils remained in the source area and on the path after while they flew down as debris.

Fig. 4 The deposit of the Gaolu flowslide

Fluidization is defined by the properties of the loess in the source area. In site investigation, a 30 m deep shaft was excavated on the top of the back scarp for sampling. The shaft goes through the loess layers from L_1 to S_3 and the samples were taken on the wall in space distance of 2 m, then laboratory tests were conducted to measuring the loess properties.

Figure 7 shows the logging curves of the shaft, of which the indexes include void ratios, moisture contents, saturated water contents, plastic limits, liquid limits, and plasticity indexes. The void ratios of the loess generally exceed 0.9, so it is a loose material. The index of plasticity is between 8 and 15; it can be classified as silty clay according to "the code of foundation and basement design for buildings (China national standard)". It is obvious that the upper portion of the loess L_1–L_3 has saturated moisture content a little higher than the liquid limit, while the lower S_3 has moisture content less than the liquid limit. The loose structure and low cohesion make the upper portion of the loess easy to slump and fluidize as flowslide.

3 Mechanism of the Loess Flowslide

It is obvious that leakage of channel water into the slope played a unique role in the initiation of the flowslide, because there were neither rainfalls nor earthquakes recorded before the slide occurred. To study the initiation and motion mechanism, additional undisturbed samples were taken at 28 m depth in the excavated shaft of the landslide. The sampling depth accords with the lower portion of the saturated loess. Particle size distribution of the sample was analyzed with the Laser Grain Size Analysis Equipment. The curve of particle size versus accumulative content in percentages is shown in Fig. 8. It suggests that the loess consists of 10 % fine

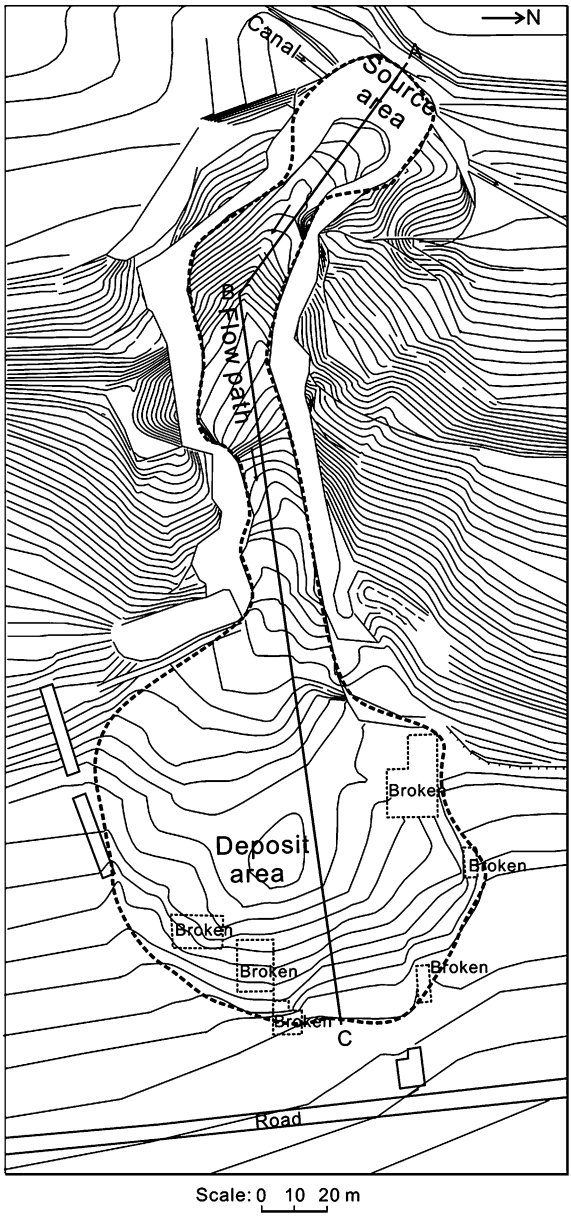

Fig. 5 The measured map of the landslide after failure

sand (>50 μm), 69 % silt (5–50 μm), and 21 % clay (<5 μm), of which silt takes up the main portion.

Consolidated undrained tri-axial test was used to study the geotechnical properties of the slope material. Each specimen was carefully cut to a cylindrical shape with a height of 8 cm and a diameter of 3.9 cm. All of the specimens were

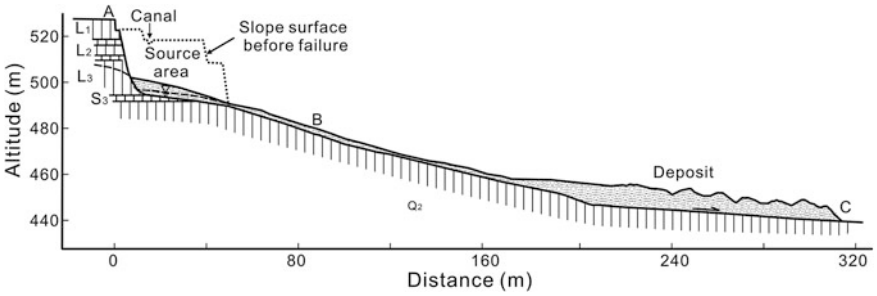

Fig. 6 Longitudinal profile of the landslide

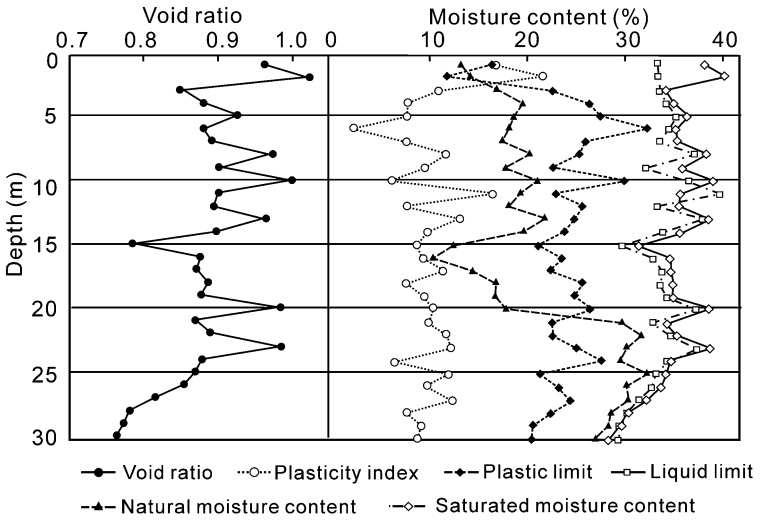

Fig. 7 The logging curves of the basic physical indexes of the samples collected from the shaft

saturated by injecting CO_2 for 30 min and then slowly filling de-aired water in 20 cm pressure head. Saturation was ensured by obtaining a B value of exceeding 0.95 (Skempton 1954). The saturated specimens were consolidated under a given confining pressure, and then sheared by constant axial strain rate of 0.04 mm/min in undrained conditions. The specimens were consolidated and tested at confining pressures (σ_3) of 100, 200, 300, 400, and 500 kPa. Termination condition of the test at each confining pressure is as the axial strain reaches at 20 %. The tests were conducted on the LSB-1 Stress–strain Controlled Seepage Tri-axial Equipment (Made in China). Figure 9 presents the test results of axial stress versus strain curves, pore pressure versus axial strain curves, and total and effective stress path. It can be seen that pore pressure was increasing with the deformation progressing, at last get to and hold on a high level, which resulted in a remarkable decrease in effective stress. As the axial stress gets to 10–15 %, pore pressures reach the peak, which take up about 50, 65, 75, 83, 90 % of the total stress at the confining

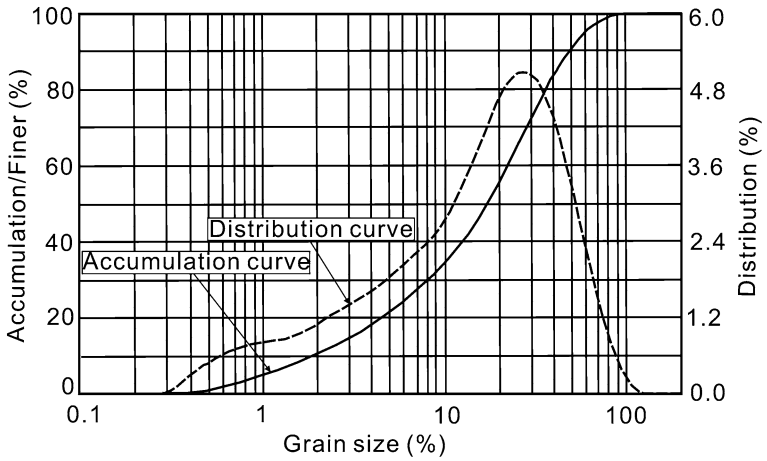

Fig. 8 Curve of particle size versus content and accumulative content of the loess sample

pressure of 100, 200, 300, 400, and 500 kPa respectively. In actual situation, it is not difficult to imagine that a quick collapse may produce a higher pore pressure than those in the tests, so fluidization may occur. From the test results, the loess have residual effective cohesion c of 10 kPa, and friction angle φ of 20.8°, and total cohesion c of 50 kPa, and friction angle φ of 8.1°. As the displaced mass starts to move, cohesion c has been eliminated, total friction angle φ is only of 12°, a little lower than 14° slope angle of the sliding surface in the source area, but much lower than the 24°slope angle of gully's floor. Therefore, the moving mass could achieve a high acceleration and consequently a high speed on the path.

To further understand the motion mechanism, the movement simulation is conducted by the modified Sassa (1988) motion model. Sassa K originally proposed the model. Wang and Sassa (2002) found in the ring-shear test results that as a saturated sliding mass moves for a long distance, the shearing strength τ_{ss} in motion is normal stress independent, that means the mobilized motion friction angle will adjust with the variation of the sliding mass thickness in the motion process. Therefore, he introduced a parameter B_{ss} in the model to modify the apparent friction angle. B_{ss} is named accumulation possibility of excess pore pressure which is determined by the properties of the soil in the sliding zone, existing state of groundwater and drainage condition etc. It is an empirical index, and a range of value was proposed in three cases. The first case is that the unsaturated sliding mass moves on dry surface, with $B_{ss} = 0.0-0.1$. The second is sliding mass moves on fully saturated surface or saturated sliding mass moves on impermeable surface, with $B_{ss} = 0.9-1.0$. And the third is that saturated sliding mass moves on dry and permeable surface, with $B_{ss} = 0.1-0.9$.

For the motion simulation, three sets of data are necessary (1) The thickness data of the sliding mass; (2) topographic data of the sliding surface; and (3) physical and mechanical parameters data of sliding mass, sliding zone and moving path. Because we have measured the topographic map (Fig. 5) after failure

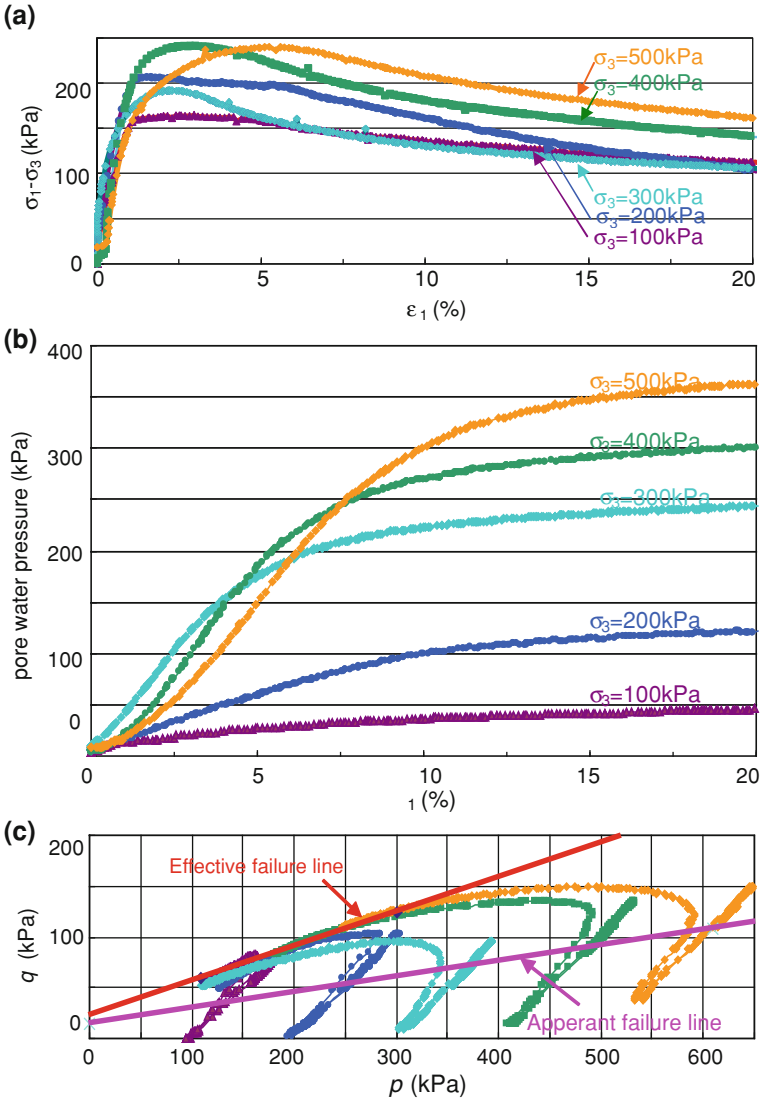

Fig. 9 The consolidated-untrained tri-axial test results of the loess specimens. **a** Axial stress versus axial strain; **b** Pore water pressure versus axial strain; **c** The total and effective stress path (Max shear stress versus mean normal stress. The legend denotes different confining stress

with Total Station Equipment, the contour map of the sliding surface was worked out based on the measured map by taking off the deposits in the slide area, the thickness of which have been determined during site investigation. The original topographic map before failure (Fig. 10a) was reconstructed by comparing the measured map after failure and the satellite imagine before failure, so the thickness

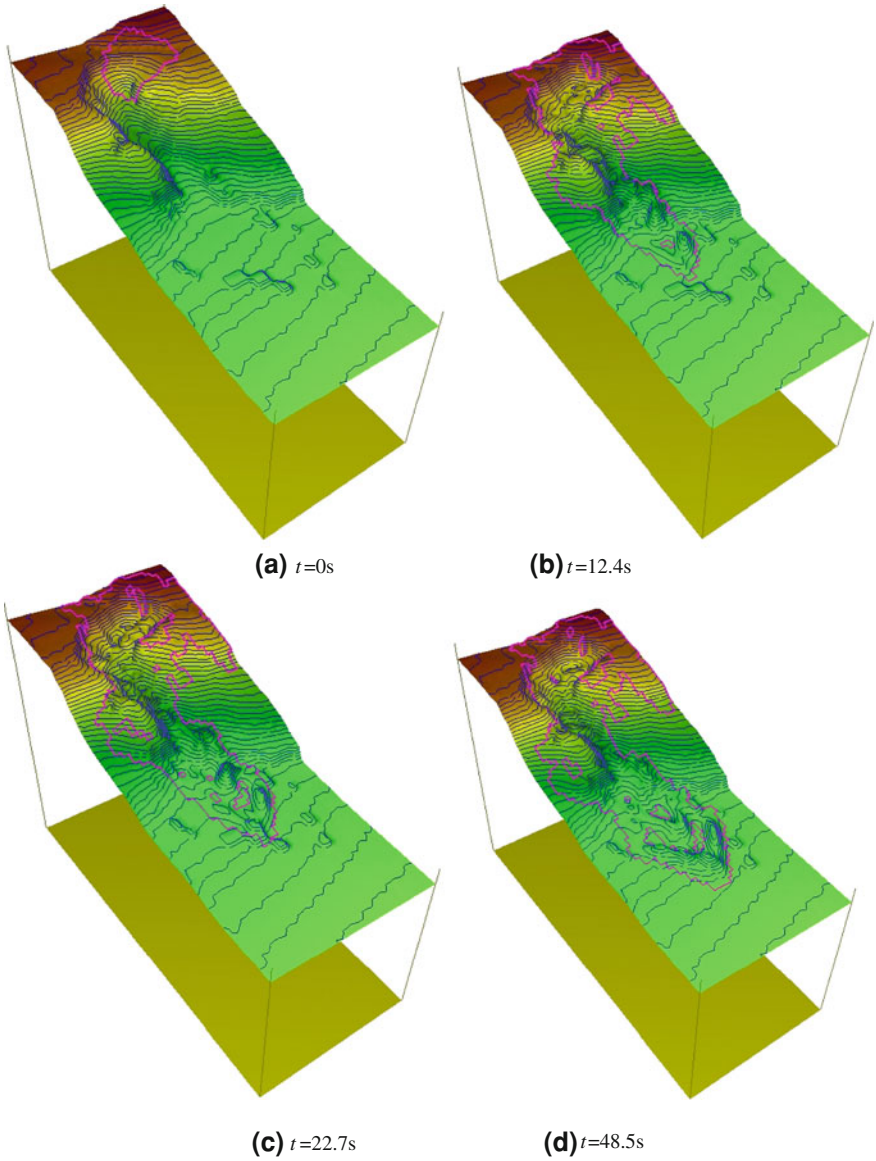

Fig. 10 Motion simulation results of the landslide

of the sliding mass before failure was estimated by the difference on the maps before and after failure in the source area.

Based on the character of the sliding area and the soil test results analyzed above, companying with back-analysis results, the physical and mechanical data are provided in Table 1. The three portions of the sliding zone, the flow path and

Table 1 The data for the landslide simulation

Position	τ_{ss}/kPa	φ'/°	K	B_{ss}	γ/kN/m^3
Sliding zone	1.0	11.3	0.70	1.0	19
Flow path	5.0–8.0	30	0.70	0.91–0.95	19
Deposit zone	10	35	0.70	0.80	19

Note τ_{ss}—Stable shearing strength in motion; φ—Residual effective friction angle; K—Coefficient of lateral pressure; B_{ss}—accumulation possibility of excess pore water pressure; γ—Unit weight

the deposit zone have different parameters underlying their water content and soil characters.

Figure 5 was meshed as 34 × 81 square elements with mesh size of 5 × 5 m, and the whole model is 170 m in width and 405 m in length, then the data file of the thickness of the sliding mass at the nodes was edited. The file and the data in Table 1 were applied in the LS-RAPID software to simulate the landslide motion. Figure 10a, b, c d show the simulation results at the time t = 0, 12.4, 22.7, 48.5 s, which reflects the flowing process of the displaced mass. The movement maintained 48.5 s from the beginning to the end. There are 24200 m^3 of displaced mass flowing from the source area. By comparing the measured topographic map Fig. 5 and the simulated result Fig 10d, a very good correspondence is established and the simulated thickness of the flowslide after failure fits the actual results of site investigation.

4 Conclusion

A typical case study and field investigation of the rapid loess flowslide induced by irrigation was carried out. It suggests that there are three aspects of geological conditions for this type of landslide. First is that there is a high slope which is cut by a long steep gully. Second is that there is a loose loess layer on the upper slope whose saturated water content is higher than liquid limit. Third is that there is an impermeable bed at the upper part of the slope or the gully which may form a perched aquifer. As the irrigation water infiltrates into the slope, rising of the perched water level resulted in failure of the upper slope, thereafter, fluidization occurrs to induce a rapid long run-out down the slope. Based on conventional and triaxial tests, the initiation mechanism was illustrated. Numerical simulation was conducted to simulate the moving process and determine the final covering range, which produces a good correspondence with the actual situation.

Acknowledgments This research work was supported by National Natural Science Foundation of China (NSFC-40972182). The support from this agency is gratefully acknowledged.

References

Kula G, An ZS (1989) Palaeogeogr Palaeoclimatol Palaeoecol 72:203–225
Skempton AW (1954) The pore-pressure coefficient A and B. Geotechnique 4(4):143–147
Sassa K (1988) Geotechnical model for the motion of landslides. In: Proceedings of the 5th international symposium on landslides, vol 1, pp 37–56
Wang FW, Sassa K (2002) A modified geotechnical simulation model for the areal prediction of landslide motion. In: Proceedings of the 1st European conference on landslides, Prague, pp 735–740
Zhang DX, Wang GH, Luo CY, Chen J, Zhou YX (2008) A rapid flowslide triggered by irrigation in China. Landslide 6:55–60

Shallow Slope Failure and Protection Method Along a Highway in a Seasonally Frozen Area in China

Wei Shan, Fawu Wang, Ying Guo, Yuying Sun, Atsuo Takeuchi and Chunjiao Wang

Abstract Shallow slope failure occurred frequently along the Jiamusi-Harbin section of Tong-San highway in Heilongjiang Province (Jia-Ha highway), China in April and May every year since the highway construction involving cut-slopes, in 1997. Because seasonally frozen areas are widely distributed in this area, the melting of frozen soil is thought to be the main reason for the slope failure. We selected two different slopes, one protected by geotechnical countermeasure works of steel–concrete frame but which failed, and another that was protected by bio-technical countermeasure works which included trees, and remained stable, to analyze the possible mechanism of the shallow slope failure at the cut-slopes in this area, and the suitability of the countermeasure works.

Keywords Shallow slope failure · Highway cut-slope · Seasonal freeze area · Biotechnical countermeasure

W. Shan · Y. Guo · Y. Sun · C. Wang
Engineering Reconnaissance and Design Institute, Northeast Forestry University, No.26 Hexing Road, 150040 Harbin, China
e-mail: shanwei456@163.com

F. Wang (✉)
Department of Goesciences, Faculty of Science and Engineering, Shimane University, Matsue, Japan
e-mail: wangfw@riko.shimane-u.ac.jp

A. Takeuchi
Natural Groundwater Research Institute, 2-11-18 Yanagawa, Otsu, Shiga 520-0014, Japan

F. Wang et al. (eds.), *Progress of Geo-Disaster Mitigation Technology in Asia*, Environmental Science and Engineering, DOI: 10.1007/978-3-642-29107-4_25,

1 Introduction

Tong-San highway is one of the longest highways in China. It starts from Tongjiang City, Heilongjiang Province located in the Northeast, and ends at Sanya City, Hainan Province located in Southern China. The entire length is 5,700 km, and crosses different climate zones. Jiamusi-Harbin section (Jia-Ha highway) is the north part of the Tong-san highway, and is located in a seasonally frozen area.

Topography in this area is low hills with wavy gentle slopes. During the first several years after the opening of the highway in 1997, many shallow slope failures occurred in the cut-slopes. Figure 1 shows a typical case of this kind of slope failure. The thickness of the displaced soil mass is limited to about 1 m, but the sliding mass moves for a long distance, generally 3–5 m. Sometimes it reaches the driving path of the highway, and hinders the traffic. For most cases, the shallow slope failures damaged the landscape and had resulted in an eyesore for drivers, hindered the drainage at the side of the highway, and increased the cost for maintenance. This kind of slope failure generally occurred on a slope, with an angle of 33.7° (1:1.5), and a slope height of about 5–25 m.

Through the statistical survey, it is clearly found that the shallow slope failures always occur in April and May when the temperature becomes high enough to make the frozen layer in the slope melt, but the effective countermeasure methods to protect this kind of slope failure are not available. In this research, done for the purpose of preventing this kind of slope failure in the highway, two kinds of countermeasure works were designed for study that would be suitable for the slope protection in the seasonally frozen area. One countermeasure is a geotechnical approach using a steel–concrete frame to support the shallow surface soil layer (Figs. 2 and 3); the other is through a biotechnical approach using plants and grass (Fig. 4).

Figure 2 shows the slope situation protected by the steel–concrete frame. The steel–concrete beam of the frame is 0.4 m wide and 0.4 m thick. It was fixed to the slope by a steel pile of 1.8–2.0 m long, and formed two lanes of rectangles, 2 m long and 3 m wide for each. As can be seen in the Fig. 2a, the horizontal beam in the second line was curved down at two sides because of the pressure coming from the soil in the upper rectangle, and the resistance coming from the lower supporting beam. In Fig. 2b, the failure of the lower supporting beam can be observed. In Fig. 2c, the subsidence and sliding displacement along the slope direction of the upper horizontal beam is obvious. From this kind of evidence, it is clear that this kind of continuous stiff countermeasure work is not suitable in this area.

Figure 3 shows another type of geotechnical countermeasure approach. The hollow blocks were used to stabilize the surficial soil. The purpose of the empty hollow space was for growing grass. However, as seen in Fig. 3, these blocks were ineffective for the slope protection. Because the root of the grass is too short, it cannot supply enough resistance to stop the surficial soil deformation. The weight of the block is also too weak to keep it on the deformed slope. As a result, this kind of discrete stiff countermeasure work is also not suitable for slope stabilization in the frozen area.

Fig. 1 Shallow slope failure occurred along the Jia-Ha highway

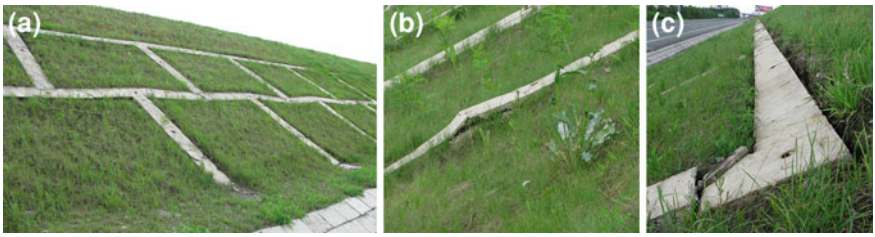

Fig. 2 Highway slope protected by steel–concrete frame. Failure occurred in the structures

Fig. 3 Slope failure in Jia-Ha highway protected by hollow blocks

Conversely, the countermeasure work applied through a biotechnical approach with the plants known as Amorpha fruitcosa (abbreviated as AF) and Lespedeza (abbreviated as LP) achieved great success. As shown in Fig. 4, AF and LP have performed well for slope protection in this area. They have made not only an

Fig. 4 Highway slope covering with Amorpha fruitcosa (AF) (*left*) and Lespedeza (LP) (*right*)

Fig. 5 Rich leaves of Amorpha fruitcosa (AF) (*left*) and Lespedeza (LP)

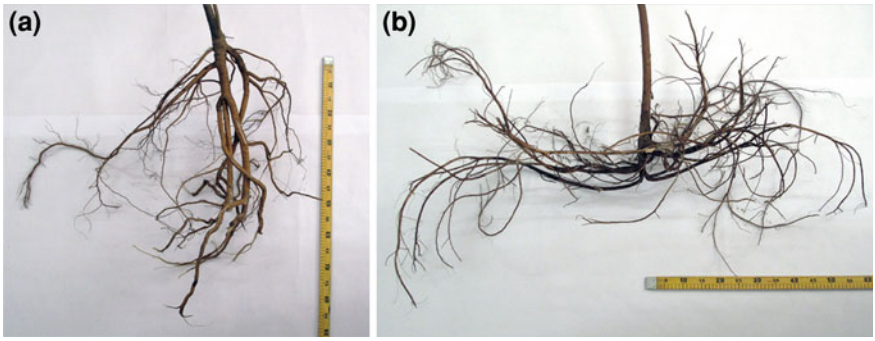

Fig. 6 Roots of Amorpha fruitcosa (AF) (*left*) and Lespedeza (LP)

improved aesthetic affect in summer and autumn, but they also can keep the slope stable during the melting season around April and May when slope failure frequently occurred in other parts having similar geometric and geological conditions.

AF and LP are two kinds of small plants which can grow well in a cool area, like that in northeastern China (Fig. 5). They have dense leaves that can prevent rainfall infiltration to the slope directly and stop surface erosion. They also have substantial roots, and the roots are long and strong (Fig. 6). Especially, AF has a

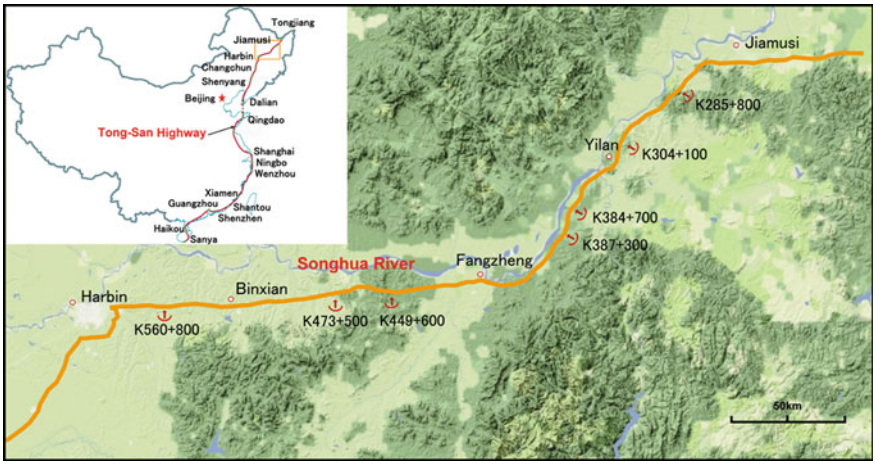

Fig. 7 Site map and the distribution of the shallow slope failure along the Jia-Ha highway

long main root at the center, and some side roots around the main root. Special characteristics for AF are that there are many small hair-roots developing from the main root and side roots, and all of the roots are curved. These characteristics make the AF fix well with the surface soils, and have a good water exchange with soils. The main root of LP is not so long or strong, and the hair roots are not so substantial when comparing with AF, however, LP has more side roots than AF, and the side roots are much longer than that of AF.

Concerning the effect of tree roots in reinforcing slopes, a lot of work has been published (Waldron 1977; Preston and Crozier 1999; Schmidt et al. 2001; Roering et al. 2003). Through a case study on landslides, Wu et al. (1979) analyzed the strength of tree roots, and proposed the Wu-Waldron model. Wu et al. (1988) also conducted an in situ shear test with roots in the soil. However, there are few investigations on root effects for seasonally frozen slope stability. In this paper, we will first investigate the mechanism of the shallow slope failure in the seasonally frozen area through field investigation and in situ measurement of soil conditions. Then, through a comparative study, we will examine the reason that the two kinds of plants can successfully protect the shallow slope from failure in the seasonally frozen area.

2 Site Characteristics

Figure 7 is a site map of the Tong-San highway in general and a zoomed area of the Jia-Ha highway. The Tong-San highway connects the eastern part of China from the northern-most to the southern-most parts, and this area is the most important area for the Chinese economy. In the zoomed area of the Jia-Ha highway, many shallow landslides occurred along the highway. This figure shows the statistical survey result

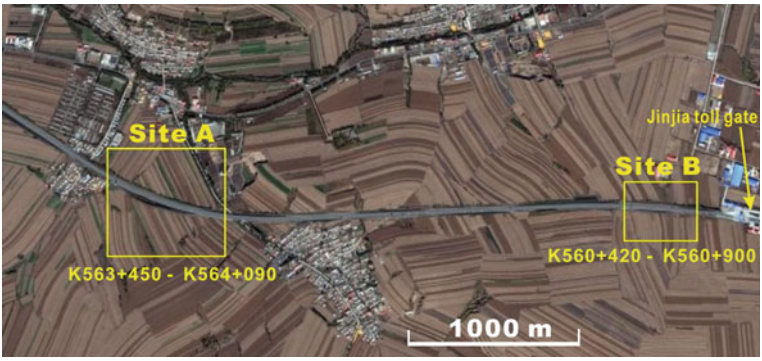

Fig. 8 Google Earth image of the study area at the Jia-Ha highway near Harbin City in 2009

from 2008. A general characteristic is that all of the shallow landslides occurred at the southern slope of the highway. One possible factor may be that the groundwater from the hills passes through those slopes and flows to the river, making those slopes a high groundwater area. The other factor may be the evaporation caused by sunshine. The southern slopes have less evaporation than the northern slopes, and this will affect the depth difference in the groundwater in both sides, i.e., the groundwater level is shallow in the southern slopes, and deep in the northern slopes. With the two factors, the groundwater is more abundant and shallower in the southern slopes than the northern slopes, and this will contribute to the slope failures in the southern slopes in during the seasonal melt.

Due to good access from the Harbin city, two sites, Site-A and Site-B, were selected along the Jia-Ha highway, near the Jinjia toll gate (Fig. 8). Site-A is covered with AF and LP, and Site-B is reinforced with steel–concrete frame. At both sites, small grasses were covering the slopes in summer and autumn.

The Jia-Ha highway is located at the south bank of the Songhua River in the southeast part of Heilongjiang province, northwest part of Zhangguangcai Ridge in the small range of Changbai-san mountain system. It crosses Yilian county, Fangzheng county and Binxian county of Harbin City. The highway passes mostly mountainous and hilly areas, higher in elevation at the south and lower at the north, where steep hills and sparsely distributed with hilly formations. The topography in this area is fluctuates in elevation, and the altitudes range between 150 and 250 m. Surface drainage mostly is unobstructed with the exception of some low-lying sections. Ground vegetation mostly is arable land and woodland, and woodland is mainly shrubbery, including secondary forests and artificially planted forests. The natural division of the road is classified as level-II_2, which is a severe frozen zone on a piedmont plain. The surface deposits along the highway are mostly Quaternary alluvium. No activity was found in fault zones, and the geological stability is good.

The stratum structure along the highway is mainly colluvium of later Pleistocene (Q3). The upper is yellow sandy loam, silt-mixed clay, and its thickness is between 3 and 20 m. In some parts, the thickness can reach 30 m. The soils are

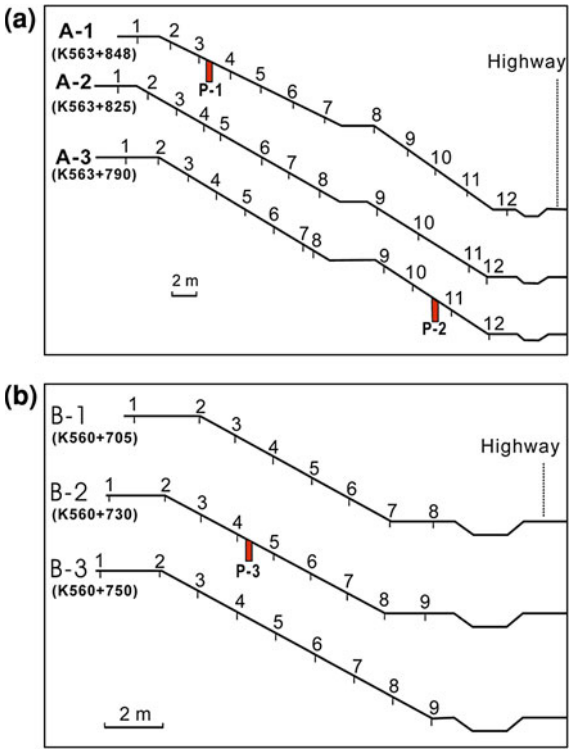

Fig. 9 Working sections in Site-A (*upper*) and Site-B (*lower*)

mostly middle or low consolidated clay. At the base, yellow gravel and grey gravel is distributed. Parts of these gravels have a clay lenticular layer, and the thickness is between 5 and 15 m. The rock is mainly yellow and white granite, with a sandy and gravel-like weathering zone at the top.

The climate of this region is a continental seasonal windy climate of the North Temperate Zone. It is characterized by hot and rainy summers, cold and dry winters, windy and dry springs, and cool autumns with early frost. The rainy season concentrates in June to the end of August. The average annual temperature is 3.2 °C, with a record high of 36.4 °C, and a record low of −41 °C. The average annual rainfall is 542.6 mm. The maximum thickness of snow accumulation is 500 mm and the maximum depth of frozen soil ranges from 1.8 m to 2.2 m. The stable ground freezing starts in late November, and the stable ground melting occurs in mid-April of the next year. The average annual evaporation is 1418.8 mm, prevailing wind is southwest in direction with a maximum wind speed of 30 m/s and average wind speed of 4.3 m/s.

Two sites, Site A (see Fig. 4) and Site B (see Fig. 2), were selected for the field monitoring and study. For each site, measurements were conducted along three sections (Fig. 9).

To study the mechanism of the shallow slope failure that often occurred between April and May, the following field investigation and measurements were conducted in this period.

(a) Along the three sections in Site-A and Site-B, respectively, portable penetration tests were conducted. The measurement stopped when the frozen layer was penetrated. The depth is about 2–3 m. At the same points, ground temperature was measured at the slope surface. Because the length of the sensor is just 1 m, only 1 m below the surface was measured.
(b) Three trenches (P-1, P-2 and P-3) were excavated at the three different cover types, AF, LP, and grass, respectively. In the trenches, repeated measurements from winter to spring on hardness of soil, density, water content, were made at different depth, to clarify the parameter change and the effect of the different plants and cover.
(c) Soil samples were taken from the slope, and ring shear tests were conducted on the saturated soil, to investigate the shear resistance behavior during shearing.
(d) In situ direct shearing tests were conducted on the slope soil with different plant roots, including those of AF, LP and grass.

Through the test analysis, (a) to (c), the mechanism of the shallow slope failure in the seasonally frozen area was clarified. From the test results of (d), a reasonable conclusion was obtained for using biotechnical approach preventing this kind of failure. The following gives an explanation of the details.

3 Mechanism of Shallow Slope Failure Along the High way in the Seasonally Frozen Area

Field investigation and ring shear tests were conducted to study the mechanism of the shallow slope failure. Among them, portable penetration tests with ground temperature measurements were conducted on 26–30 April 2008, when shallow slope failure started to appear at a different part of the highway slope. In the period between November 2007 to May 2008, three trenches were opened in three types of ground containing different plants, i.e., AF (the trench P-1), LP (the trench P-2) and grass (the trench P-3). Monitoring on water content (using a moisture sensor) was conducted, and the tendency of water content change was obtained.

3.1 Portable Penetration Tests and Ground Temperature Measurements

Portable penetration tests and ground temperature measurements were conducted at Site-A and Site B, three sections for each, up to the depth of 2.5 m. Figures 10 and 11 present the ground temperature measurement results for Site-A and Site-B, respectively, while Figs. 12 and 13 present the portable penetration test results.

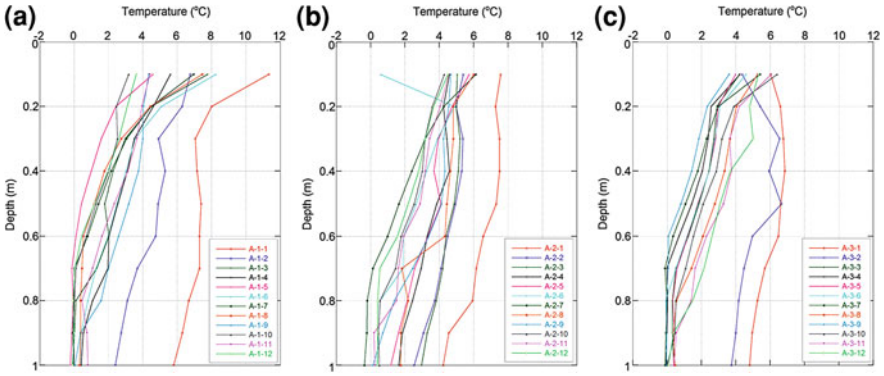

Fig. 10 Ground temperature measurement (Site-A)

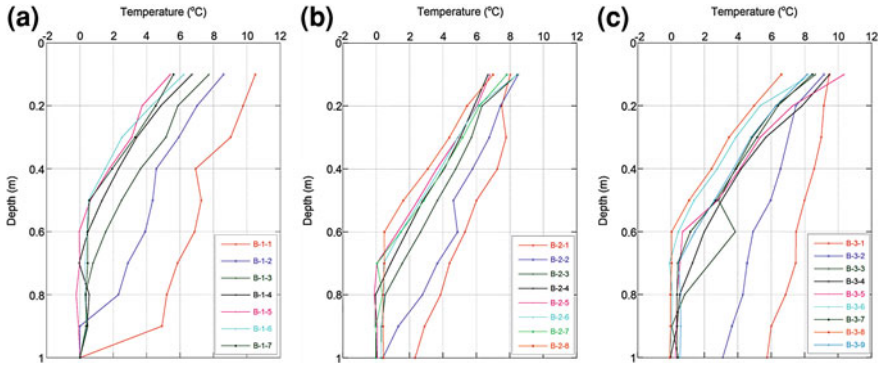

Fig. 11 Ground temperature measurement (Site-B)

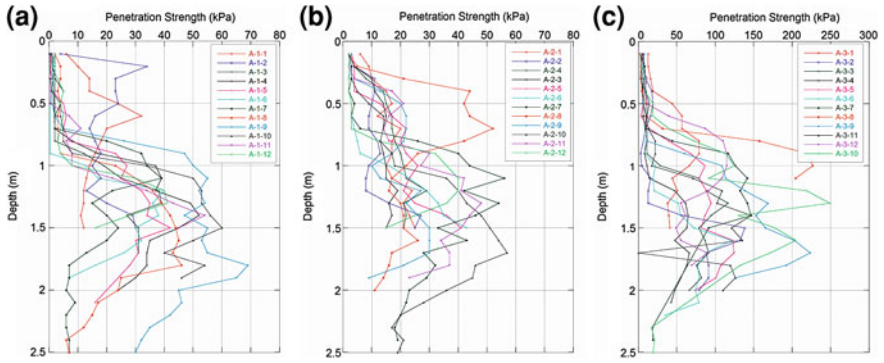

Fig. 12 Penetration test results (Site-A)

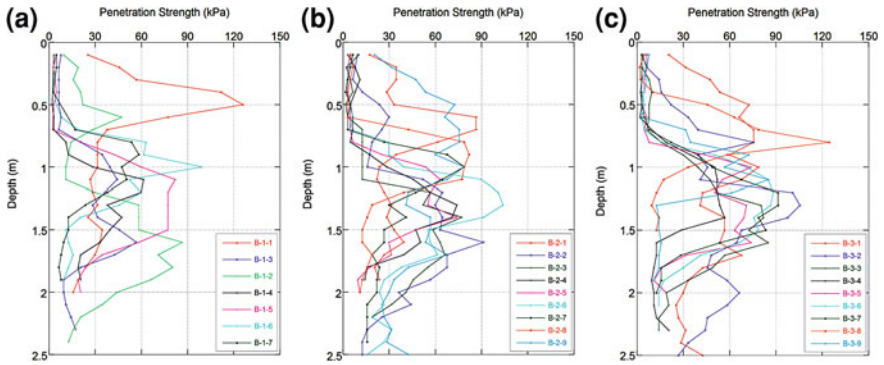

Fig. 13 Penetration test results (Site-B)

Ground temperature was measured every 0.2 m, up to 1 m deep, because of the limitation of the length of the temperature sensor. Figures 10 and 11 show the results. Due to the existence of the frozen layer, the ground temperature decreased to zero degrees when the depth reached about 0.6–0.7 m. For the same depth, those points around the middle slope have relatively lower temperatures compared to the others at the upper slope, and lower slope, indicating that the groundwater concentrated more in the middle slope than in the other parts. Especially, the ground temperatures at the upper slope (see point 1 and 2) did not decrease to zero, with respect to the melting process of the frozen layer which had already melted in this period if it existed.

Figures 12 and 13 are the results for the portable penetration tests in Site-A and Site-B, up to the depth of about 2.5 m. For the middle slope and lower slope at the depth smaller than 1.0 m, the penetration resistance corresponded well with the ground temperature; when the ground temperature was higher than zero degrees, the penetration resistances nearly equaled zero. Wen it reached the frozen layer, the resistance became much larger. At about 1.5 m, the resistance began to decrease, perhaps due to the fact that the penetration head passed through the frozen layer. Because the ground surface was quite dry for the two points at the upper slope, the penetration resistances were quite higher than the other parts. This may be the reason why the shallow slope failure mostly occurred at middle slope, and did not occur at the upper slope.

3.2 Trench Investigation and Soil Property Measurement

Figure 14 shows the monitoring results at the trenches under the conditions of different plant covering, i.e., grass only, AF, and LP. Through November to the next May, the water content ranged at 10–20 % for the AF and LP covering, while it ranged at 18–25 % for the grass only covering (through March to May). The

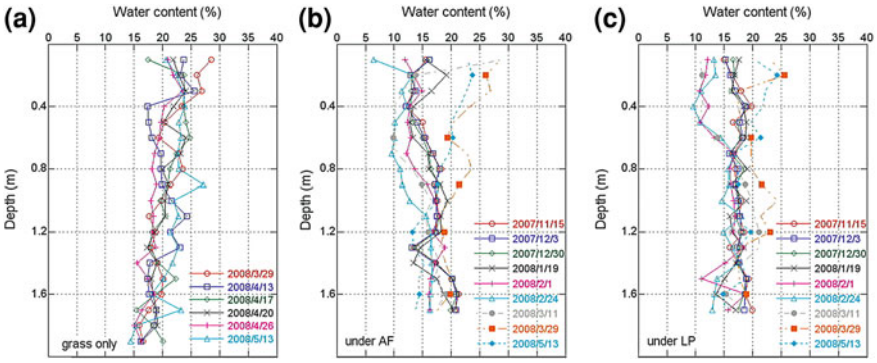

Fig. 14 Annual change of water content under different plants or grass covering

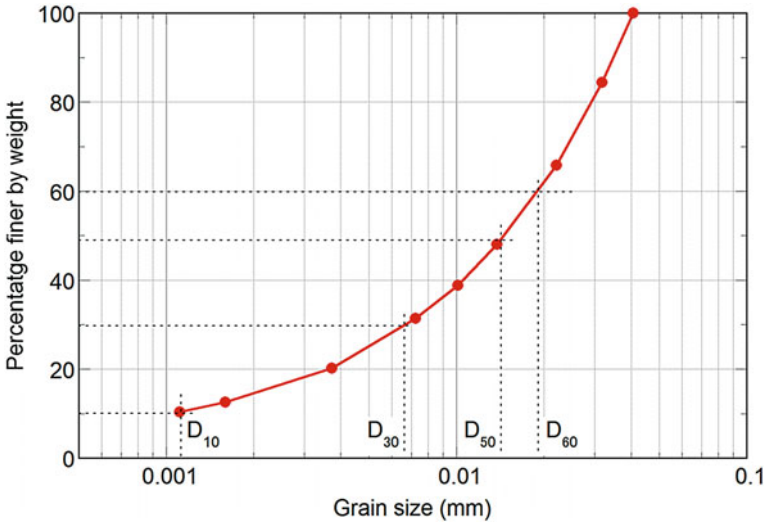

Fig. 15 Grain size distribution curve of the soil sample taken from Site-A

water content is obviously higher with the grass-only covering than that of AF and LP. Maybe one of the effects of the AF and LP plants protecting slope failure is through decreasing the water content in the slope. When water content is lower, the effect from frozen should be weaker.

To measure the permeability of the slope soil, undisturbed samples were taken from 0.3 m, 0.6 m and 1.4 m in depth, respectively, from the trench P-2. Using the falling head permeability test, a range from $1.4*10^{-6}$ to $3.8*10^{-6}$ m/s was obtained, which shows a low permeability of the soil.

3.3 Shear Test with Ring Shear Apparatus

To measure the soil mechanical parameters, soil sample was taken from the Site-A, where the slope had no vegetation covering and showed heavy deformation. Figure 15 is the grain size distribution curve of the soil sample.

According to the curve, the effective grain size d_{10} is 0.0012 mm, and the average grain size D50 is 0.015 mm. Uniformity coefficient C_u and coefficient of curvature C_c are 15.8 and 2.03, respectively. Also, the plastic index I_p of this soil was measured as 13.8. So, the soil can be classified as silty clay with good gradation.

With the ring shear apparatus DPRI-5 developed at the Disaster Prevention Research Institute, Kyoto University (Sassa et al. 2004), a velocity controlled test was conducted on the soil sample. The test procedure was as follows.

(1) Place the oven-dried disturbed sample in the shear box;
(2) Saturate the sample with carbon dioxide and de-aired water;
(3) Consolidate the specimen under the normal stress of 50 kPa;
(4) Change the shear box to undrained condition, and measure the degree of saturation of the specimen by increasing the normal stress to 100 kPa. A pore water pressure of 48 kPa was obtained. This means that the pore pressure parameter under direct shear condition, BD value reached 0.96, showing a near-full saturation condition was achieved for the specimen.
(5) Change the shear box to a drained condition, and let the specimen normal consolidated under the normal stress of 100 kPa. The normal stress level was adopted based on the consideration of the field stress condition and precision of the apparatus.
(6) Change the shear box to undrained condition again, and shear the specimen with a constant velocity of 2 mm/s. Because the specimen is silty clay, the permeability of the specimen was low. This shearing velocity was expected for good monitoring of the pore water pressure. Referring to Sassa et al. (2004), the pore water transducer was located 2 mm far from the shear zone. When sandy soil with high permeability was sheared, the generated pore water pressure can be measured exactly in time, but when the specimen has low permeability, a time lag will be generated for the pore water pressure measurement.

Figure 16 shows the test result, indicated as effective stress path. After shearing, the shear resistance reached the peak strength at point A, where the peak strength is 40.2 kPa. The apparent friction angle, which is defined as the angle of the line connecting the original point to that point, with shear resistance as its vertical coordinate, and initial total stress as its horizontal coordinate, at the peak value of the shear resistance (point A') is 22.2°. It means that when the melting occurs suddenly at a frozen slope steeper than 22.2°, slope deformation will be generated. It should be mentioned that this result is obtained under a fully undrained condition. In the actual situation, when the draining process is permitted, the slope angle allowing the slope to be stable, will be bigger. From point A to point B, a drop-down of the shear strength from 40.2 kPa to 22.6 kPa occurred. This means that an excess pore water

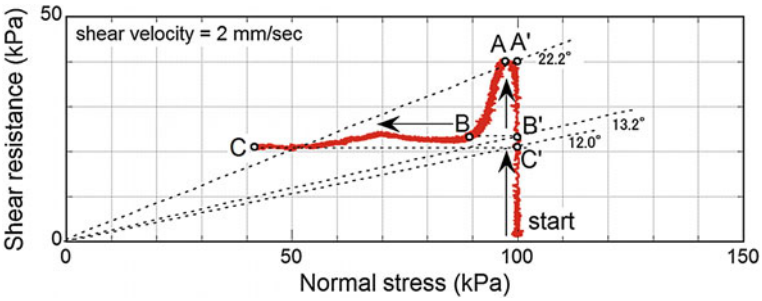

Fig. 16 Effective stress path of the velocity controlled undrained ring shear test on the sample taken from the highway slope

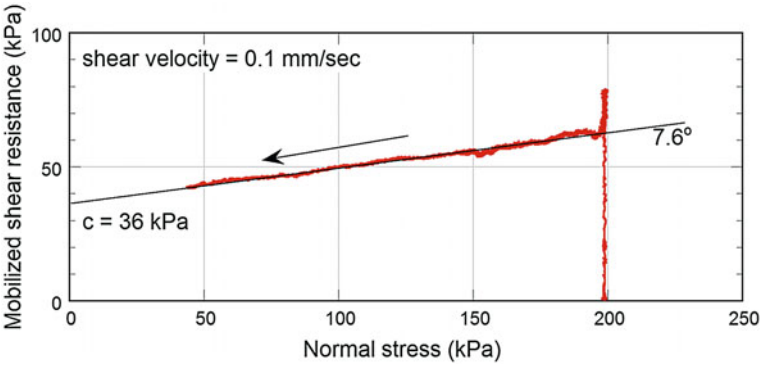

Fig. 17 Drained ring shear test results to measure the residual shear resistance of the soil

pressure generation process occurred in this period. Because of the low permeability of the soil sample, the stress path did not follow a straight failure line. At point B, the apparent friction angle decreased to 13.2°. The sudden drop-down of the shear resistance can make the displaced slope material move for long distance, even if the slope angle is as gentle as 13.2°. When keeping the shearing, the stress path moved from point B to point C, there is no obvious drop-down of the shear resistance in this period, and the decrease of the apparent friction angle is just 1.2°. At the end of the test, i.e., point C, the shear resistance was kept as 20 kPa. Because of the low permeability of the soil, it is not clear how much the generated excess pore pressure is at point C, and it is clear as to whether the 20 kPa shear resistance is the cohesion of the soil or not. However, this test result can reasonably explain the actual phenomenon of slope failure that occurred in the melting season, and the long distance behavior of the shallow landslide.

Figure 17 shows the result of drained ring shear test, which was conducted for the purpose of obtaining residual shear strength of the soil. After fully saturated, the specimen was consolidated at a normal stress of 200 kPa. Then shearing, with

Fig. 18 Photo of the in situ direct shear equipment with a small AF within

a constant shearing velocity of 0.1 mm/s was conducted. After the shear resistance reached the peak value, the normal stress was decreased from 200 kPa at a rate of 2.64 Pa/s. It is expected that a residual friction envelope is obtained, because the shear velocity is slow and the unloading rate is small. However, the result is a line with 8.7° of friction angle, and cohesion of about 40 kPa. This test also verified that the permeability of the soil has very low permeability, and low shear resistance when it is fully saturated.

Although the test results did not show the same tendency as that with sandy soil, which has high permeability (Sassa et al. 2004), it gives very important hints explaining the mechanism of the shallow slope failure which occurred during the melting season at the Jia-Ha highway. Because the soil has very low permeability, during the melting season, the water will saturate the nearby soil and keep the soil in fully saturated condition; when the initial stress condition of the slope makes the shallow soil failed, high excess pore water pressure will be generated. In turn, the shear resistance becomes lower and lower, and induces obvious slope deformation or a long-distance shallow landslide. Based on this mechanism, the countermeasure work to control the shallow slope failure should follow the principle of improving the drained condition of the slope, and increasing the shear resistance of the shallow soil.

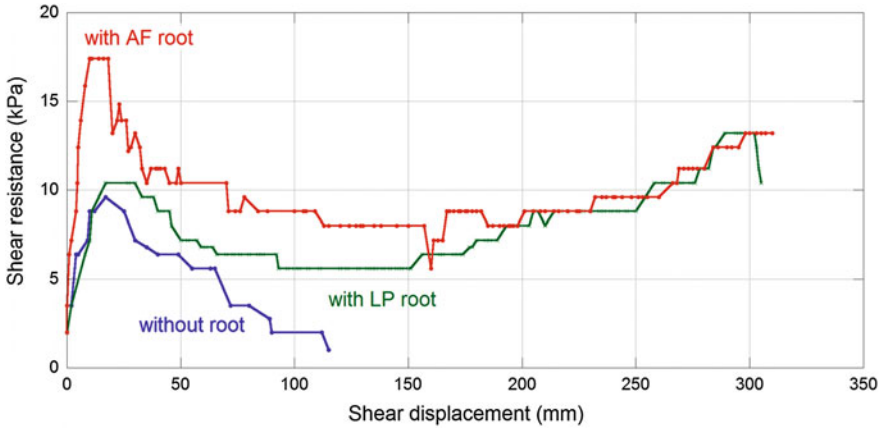

Fig. 19 In-situ direct shear tests on the surface soil with AF root, with LP root, and without tree roots

4 The Advantage of the Biotechnical Approach to Countermeasures

As introduced previously, AF and LP have good performance in the deformation control in the highway slope. To clarify the mechanism, in situ direct shear tests were conducted on the shallow slope containing the roots of AF and LP. Figure 18 shows the equipment used. In the real slope, a specimen with single AF or LP root was cut to the dimension of 0.5 m long, 0.5 m wide and 0.2 m thick. Shearing surface is fixed at 0.1 m deep. 0.2 m thick surface soil was eroded. No extra normal stress was loaded. By pushing the upper shear box along the two guide bolts, the shear resistance was obtained and the shear displacement was also recorded at the same time. Because the root of AF or LP is longer than the thickness of the shear box, the roots can contribute to the shear resistance.

Figure 19 shows the test results on three different types of specimens, i.e., with AF root, with LP root, and without any root. It shows that the specimen with AP root has the largest peak shear resistance, and the peak shear resistances for the specimen with LP root and the specimen with root, have no obvious difference. However, along the increasing of shear displacement, those with roots are quite higher than those without root. At the shear displacement of 120 mm, the specimen without root lost all of the shear resistance, while those with tree root show an increasing tendency, although the shear displacement increased. When the shear displacement exceeded 150 mm, there is no obvious difference between the AF root and LP root.

This test verified the function of the AF root and LP root in the slope stabilization of the frozen highway slope in the melting season. As shown in the in situ permeability test result, the AF and LP root can also improve the permeability of the soil. As indicated by these tests, the AF and LP can be considered suitable plants to prevent slope failure in the similar area, and AF is better than LP.

5 Conclusions

Through field investigation, long period in situ monitoring, laboratory tests, and in situ tests for purposes clarifying the mechanism of the shallow slope failure in a seasonally frozen area, and to find a suitable protective method along the highway, the following conclusions were obtained, and it is hopeful that they will be used in the actual applications.

(a) The shallow slope failure in Jia-Ha highway occurred as the result of a combination of low permeability of the slope soil, low undrained shear resistance of the soil, and substantial groundwater supplementation. To stop the slope failure, countermeasure works aiming to improve the draining effect and increase soil strength should be adopted.
(b) The roots of AF and LP have positive effects that increase soil shear resistance, and improve the drainage effect of the soil. The bushes themselves like AF and LP, can also prevent the infiltration of the rainfall to the slope. AF and LP can be recommended for the countermeasure work in the highway slope protection in this seasonally frozen area.
(c) Concrete frame structure should be avoided in the seasonally frozen area, because their stiff structure cannot resist the creep-like slope deformation.

Acknowledgments This paper is a part of a comprehensive study on landslides in seasonally frozen areas, which was recognized as a member project of International Project on Landslides (IPL M-132) titled "Study of shallow slope stability for earthen cut-slope of high-rank highway in seasonally frozen regions" (Project leader: Wei Shan and Fawu Wang). The support from International Consortium on Landslides (ICL) is appreciated. We will also like to delivery our thanks to Transportation Bureau of Heilongjiang Province, China for the financial support to the key scientific project of "Using Vegetation to Stabilize Slopes along High Grade Roads and Tree-planting Methods in Cold Area" (2003–2010), and Scientific Bureau of Heilongjiang Province for the financial support to the key-research project of "Vegetation Protection System for Cutting Slopes along High Grade Roads in Seasonal Frozen Area" (2007–2011). Dr. Lin Yang, Mr. Aiqing Zhang, Mr. Dayong Zhang and Mr. Hua Jiang joined the field investigations.

References

Preston NJ, Crozier MJ (1999) Resistance to shallow landslide failure through root-derived cohesion in east coast hill country soils, North Island, New Zealand. Earth Surf Proc Land 24:665–675

Roering JJ, Schmidt KM, Stock JD, Dietrich WE, Montgomery DR (2003) Shallow landsliding, root reinforcement, and the spatial distribution of trees in the Oregon Coast Range. Can Geotech J 40(2):237–253

Sassa K, Fukuoka H, Wang GH, Ishikawa N (2004) Undrained dynamic-loading ring-shear apparatus and its application to landslide dynamics. Landslides (1)1:7–19

Schmidt KM, Roering JJ, Stock JD, Dietrich WE, Montgomery DR, Schaub T (2001) The variability of root cohesion as an influence on shallow landslide susceptibility in the Oregon Coast Range. Can Geotech J 38:995–1024

Waldron LJ (1977) The shear resistance of root-permeated homogeneous and stratified soil. Soil Sci Soc Am J 41:843–849

Wu TH, McKinnell WP, Swanston DN (1979) Strength of tree roots and landslides on Prince of Wales Island Alaska. Can Geotech J 16(1):19–33

Wu TH, Beal PE, Lan CC (1988) In situ shear test of soil-root systems. J Geotech Engrg 114(12):1376–1394

A Coupled Hydrology/Slope Kinematics Model for Developing Early Warning Criteria in the Kalitlaga Landslide, Banjarnegara, Indonesia

Fikri Faris and Faisal Fathani

Abstract The tropical climatic condition of Indonesia brings consequences of high activity of landslide in the area. Although, studies of landslide activity and rainfall as triggering factor have been introduced in many research papers, the implementation of the research on the regional area which has particular geological and climate condition is significant. This study has potential meaning to develop early warning systems that may avoid damage and loss of human lives in the area. In this research, field monitoring data have been assessed in Kalitlaga Village, Banjarnegara Regency, Central Java Province to develop coupled hydrology/slope kinematics model of landslide. To simulate the groundwater levels in the landslide, a hydrological model with two series of tank represented the geological setting of the area is applied. Groundwater output from the model was used in visco-plastic kinematics model to simulate the velocity of landslide movement. Calibration and verification of the model on the recorded data of groundwater and displacement data showed good results. The peak velocity from the combined model is then classified based on rainfall record of the previous landslide which happened near the area. Velocity that considered being critical condition is used as additional precursor of early warning system of Kalitlaga landslide.

Keywords Hydrological model · Visco-plastic · Tank model · Early warning system

F. Faris (✉)
Graduate Student of Interdisciplinary Graduate School of Science and Engineering, Shimane University, 1060 Nishikawatsu, Matsue 690-8504, Japan
e-mail: farisonsky@yahoo.com

F. Faris · F. Fathani
Department of Civil and Environmental Engineering, Faculty of Engineering, Universitas Gadjah Mada, Jalan Grafika No. 2, Yogyakarta 55281, Indonesia

F. Wang et al. (eds.), *Progress of Geo-Disaster Mitigation Technology in Asia*, Environmental Science and Engineering, DOI: 10.1007/978-3-642-29107-4_26,

1 Introduction

Field investigations and laboratory analysis have revealed that the implementation of early warning system in landslide studies is important in landslide disaster management and control. A reliable landslide early warning system directly associates with good warning criteria. Comprehensive study about landslide mechanism derives warning criteria which integrates the triggering factors and probable landslide events. In the focus of rainfall triggered landslides, hydrological factors and its influences on landslide stability should be assessed to improve a better understanding of particular landslide mechanism.

To facilitate landslide assessment and early warning system development, preliminary investigation and real-time field monitoring equipment was set up in Kalitlaga Village, Banjarnegara District, Central Java Province of Indonesia as a pilot project (Fathani et al. 2008). The development of the project in the area was part of the Asian Joint Research Project for early warning system on landslides disaster management, which consists of the International Consortium on Landslides (ICL), Gadjah Mada University (GMU) and Disaster Prevention Research Institute of Kyoto University (DPRI/KU). As part of the project, real-time field monitoring equipment such as rain-gauges, groundwater level sensors and extensometers were employed to obtain data of precipitation, groundwater level and landslide mass displacement, respectively. These data are essential for the landslide assessment, prediction and early warning system development.

2 Landslide Study Area

2.1 Kalitlaga Landslide

The studied area is in Kalitlaga village which is located in Pagentan District, Banjarnegara Regency of the Central Java Province of Indonesia (Fig. 1). The lithological composition of the area is characterized by Rambatan Formation which consists of shale, marl and calcareous sandstone (Condon et al. 1996). Specifically, the geological structure of this area was inclined stratigraphic of sediment layers which consist of montmorillonite clay covered by colluvial deposits (Karnawati et al. 2008).

In view of the imminent landslide hazard in the area, a landslide monitoring system was established in order to assess, track, monitor and record the sequence and failure mechanism of the slope due to intermittent rainfall. The installed field monitoring equipment, as previously discussed, consist of outdoor unit and indoor unit. The outdoor unit, which is made up of strategically positioned sensors and electronic gadgets like long-span extensometers, rain-gauges, internet protocol (IP) cameras and water pressure sensors, records information observed from the field, while the indoor unit processes, stores, and sends real-time information via a GPRS modem which is displayed on a web-server (Fathani et al. 2008). For the further analysis concern, a reliable data of topography and aerial photo has been reserved through Balloon

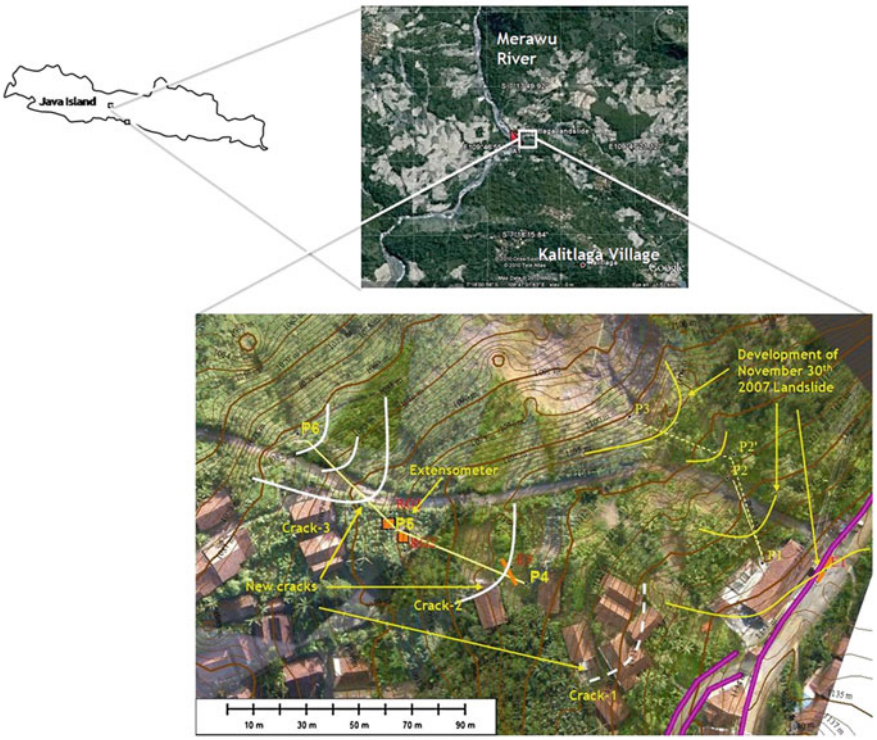

Fig. 1 Location of Kalitlaga landslide

Photogrammetry System which combines balloon aerial photography and digital photogrammetry for low-altitude aerial mapping. The balloon carries out a digital camera up to 400 m above the ground level and takes aerial photographs in appropriate viewing angle. The digital photogrammetry processes photo-restitution to produce 3D model from multi-view aerial photograph (Rokhmana 2007).

2.2 Hydrological Influence on Landslide Activity

From hydrological point of view, groundwater is highly affected by rainfall activity and infiltration rate that controlled by land surface condition. Since there is a lot number of cracks and cultivated area comprise the landslide body, the rainfall can be easily infiltrate into the soil and become groundwater. Angeli et al. (1998) considered that the rapid piezometric response is attributed to an infiltration process through a superficial system of interconnected cracks. This system not only works as a fast flow-path from the ground surface to water table, but is also capable to discharge the infiltrated water rapidly.

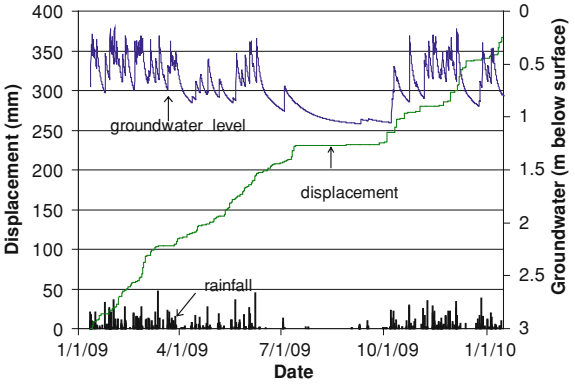

Fig. 2 The influence of groundwater flow against soil mass displacement

The water pressure sensor attached in an observing well showed that the ground water fluctuation is highly affected by rainfall event. The observation by field monitoring also revealed that there is a high influence of groundwater fluctuation to soil mass displacement that is recorded in specific area (Fig. 2). Based on this fact, a sound geotechnical model which appropriately predicts the soil mass displacement by considering hydrological factor is needed to be developed.

2.3 Hydrological Model

In some studies, hydrological model used for estimating groundwater level considers the geological formation that occurs in particular area. Hong et al. (2005) have taken the three cascading tank into consideration based on the geological formation that is indicated from the investigation of borehole in Zentoku landslide on Shikoku Island, Japan. Angeli et al. (1998) also represented the incorporation of geological structure in hydrological model in the study of Alverà landslide, Italy. The developed model in Alverà consists of two reservoirs that represent the root zone and the clay layer. Each of studies introduced different hydrological model according to particular geological formation in the study area. Developed hydrological model in both studies that is previously described needs actual groundwater level data and rainfall data to verify the results.

In this study, required data to support the development of the model are already obtained through pilot project that has been established in Kalitlaga landslide. The general geological condition in the site, such as geomorphology of the area, the lithology, geological structure and slope stratigraphy has been studied through geological investigation. The specific geological formation in the area arises some consideration of hydrological concept which is can be described schematically with tank model.

The tank model consisted of two series of tank as shown in Fig. 3. This model was based on assumption that the first tank represented the water balance at the surface that was controlled by runoff and infiltration while the second tank represented the colluvium layer. The first tank is used to simulate the surface run-off

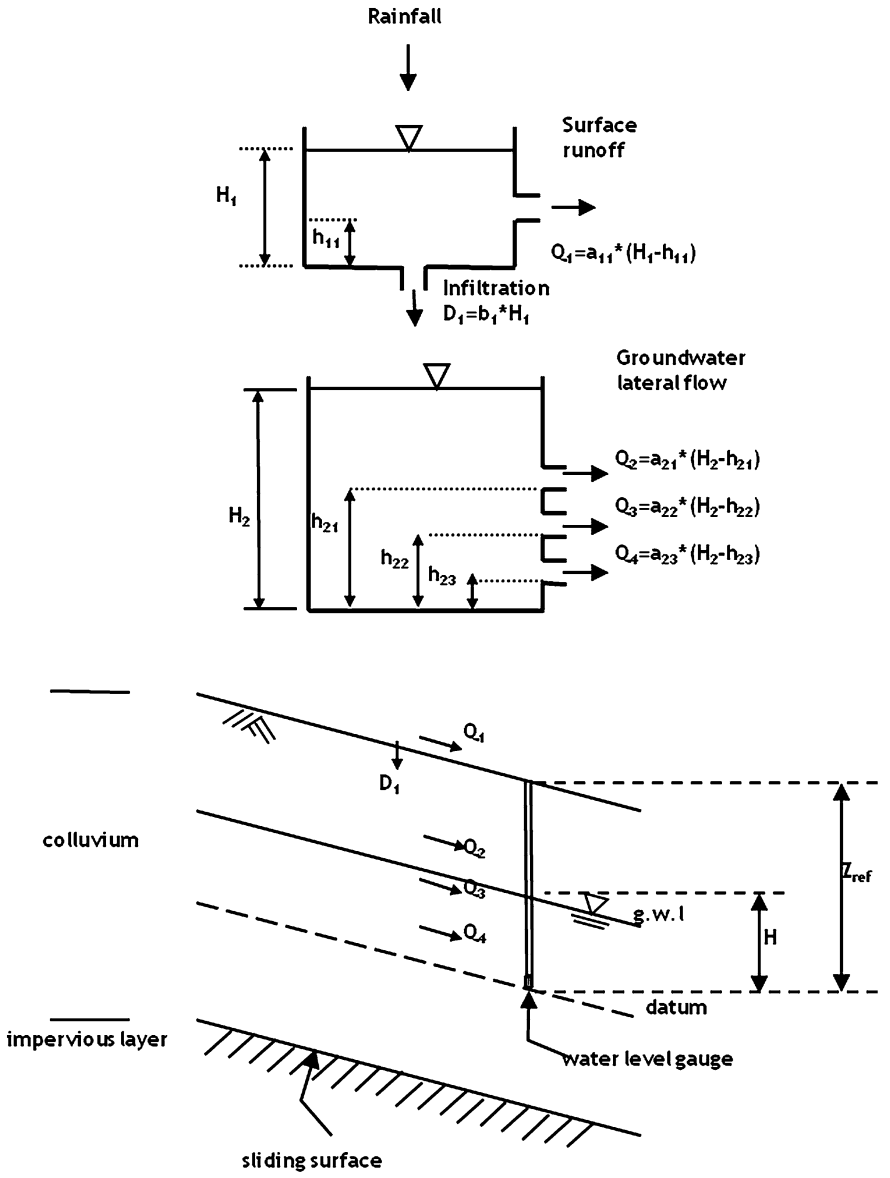

Fig. 3 Tank model configuration in Kalitlaga landslide

and infiltration into colluvium soil. Once the rainfall enters the first tank, then it is distributed to the lower outlet D_1, in case the previous water level at the first tank is still below h_{11}. Otherwise, if the water level at the first tank is same as or higher

Table 1 Parameters of tank model

Parameters	Value
s	100.0
b_1	0.4
a_{11}	0.03
a_{21}	0.01
a_{22}	0.16
a_{23}	0.0025
h_{11}	1
h_{21}	7
h_{22}	2
h_{23}	0

than h_{11}, then the rainfall becomes runoff Q_1. The height h_{11} corresponds to soil moisture capacity. Once the water level at the first tank surpasses h_{11}, one can interprets that the soil is already saturated and the next rainfall adding up will becomes surface runoff. The second tank represents the input and output of water at the borehole, thus the fluctuation of water level in the second tank corresponds to groundwater level. The second tank receives discharge from infiltration D_1 that subsequently distributed to three outlets of the second tank, which represent the disparity of soil permeability at the borehole.

Land surface and geological condition highly control the infiltration and groundwater fluctuation. Since there is a lot number of cracks and cultivated area comprise the landslide body, the rainfall can be easily infiltrate into the soil and become groundwater. However, groundwater does not exist homogenously under the ground. Groundwater tends to congregate into such a stream due to the diversity of soil permeability (Takeuchi 1981). The lateral flow from recharge area, which is affected by existence of cracks, asperity and concave-like shape of landslide base, is assumed to contribute on this phenomenon. Groundwater stream mechanism can be illustrated as "underground river" with some catchments area. However, neither the extent of this area, nor its geohydrological properties are known, and both entities are difficult to assess (Angeli et al. 1998). Although there is no inflow from upper slope that explicitly represented in tank model, the scale factor (s) is used to represents the inflow from catchments area surrounding the landslide. The scale factor (s) obtained by calibration and one can conclude it as the representation of catchments area broadness. This factor is applied as multiplier factor of total height of the last tank in tank model (H).

2.4 Result of Hydrological Model

This simulation needs consistent and continuous rainfall data and groundwater level. Thus, rainfall event January 11, 2009–June 19, 2009 which is adequately supported by continuous groundwater level data considered as stored data. The heights, the coefficients and the numbers of outlets at the last tank are determined by trial and error until the simulated groundwater level presents a good corresponding relation with the real

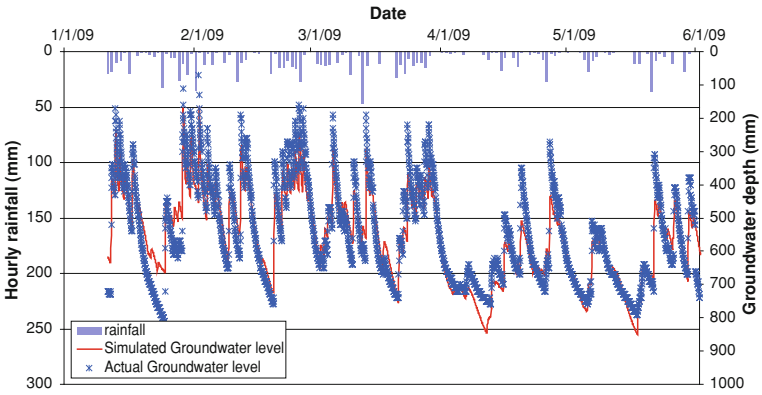

Fig. 4 Simulation result of the groundwater level from tank model

groundwater level. This relation can be expressed by the linear regression which results the simulated levels in boreholes in millimetres. Table 1 shows adjusted coefficient values and height of the outlets to satisfy required condition.

The verification used statistical parameter of coefficient of correlation (R) and volume error (V_e) which are obtained from linear relationship of simulated groundwater level with the actual groundwater from field monitoring. The result of simulation is shown in Fig. 4. The red curve that displays the estimated hydrological response to the rainfall during the chosen intervals proves that the tank model could simulate the groundwater with a good precision. The graphic also shows high response of groundwater level due rainfall activity. The possible reasons of this phenomenon, possibly, are the occurrence of cracks and highly cultivated land which eases infiltration. The obtained coefficients of correlation confirm the good corresponding between these two parameters ($R = 0.927$). The volume error (V_e) of simulation result against the observed data also gives permitted value ($V_e = 0.042\ \% < 5\ \%$).

2.5 Visco-Plastic Assumption for Slope Kinematics Model

Slow slope movements are typically associated with "creep" behaviour, since the soil can be characterized by a viscous response, implying the presence of a resisting force that is activated only when the soil mass starts to move (Ranalli et al. 2009).

For continuously moving landslides, a dynamic analysis should be adopted instead a classical static approach (Ranalli et al. 2009; Corominas et al. 2005). A classical static analysis is suitable to determine the slope safety factor, but is not able to model the actual kinematics of the soil mass behaviour. In the limit equilibrium stability analysis, the soil shear strength is usually defined by the Mohr–Coulomb criterion, and the instability condition occurs when the equilibrium is modified by a pore water pressure increase and a consequent reduction of the effective stress level. For a given piezometric level, a constant instability force could exist and initiate a

slope movement with constant acceleration and a corresponding velocity, linearly increasing with time. When these conditions fail, a possible explanation is the effect of a viscous resisting component of the material. In this case, the mass velocity can be related to the excessive shear stress by different viscous laws, like the Bingham's law, which shows a yield point and a subsequent linear relationship (Ranalli et al. 2009):

$$v = 0 \quad \tau < \tau_0 \tag{1}$$

$$v = (z/\eta)(\tau - \tau_v) \quad \tau \geq \tau_0 \tag{2}$$

where v is the velocity (m/s), z is the shear band thickness (m), η is the dynamic viscosity (N.s.m^{-2}), τ is the driving shear stress (N/m^2), and τ_0 (N/m^2) is the resisting shear strength (yield strength). The resisting shear strength τ_0 can be defined by the Mohr–Coulomb failure criterion at the residual strength state (Van Asch and Van Genuchten 1990). This yield strength line can be described by the following equation:

$$\tau_0 = c'_r + \sigma' \tan \phi'_r \tag{3}$$

where: τ_0 = the yield strength; c'_r = the residual cohesion; σ' = the effective normal stress; and ϕ'_r = the residual friction angle.

Once the frictional resistance of weight is overcome it starts moving in creep phase with a velocity controlled by the viscous resistance of the dash-pot which is expressed by:

$$\tau = \eta_B v \tag{4}$$

where η_B corresponds to viscous characteristic of the soil in the dash-pot and v is the velocity the sliding block (Angeli et al. 1996) (Fig. 5) which also represent the analogy of infinite slope with a viscous deforming layer (Fig. 6).

The viscous parameter C is defined as the ratio between the material dynamic viscosity η and the thickness of the shear band z. The term $C = \eta/z$ is called as the coefficient of dynamic viscosity. As a consequence, the contribution to resistance can be expressed as $\tau = Cv$ which analogous to the Bingham's expression for viscous characteristic of the oil in the dash-pot $\tau = \eta_B\, v$. The C value obtained from the calibration process (Ranalli et al. 2009; Angeli et al. 1996).

The dynamics of the landslide are governed by the difference between driving forces (F), that depend basically on weight and slope, which are constant and resisting forces (F_r) are sensitive to water pressure at the slip surface (Corominas et al. 2005). The momentum equation can be written as:

$$F - F_r = ma \tag{5}$$

where m is the mass (kg) and a the acceleration (m.s^{-2}). Resisting forces can be estimated using Mohr–Coulomb criterion which considers cohesion and friction parameter. By using infinite slope condition, forces are computed over a unit surface, and therefore shear stresses are considered in what follows;

$$\tau - [c' + (\sigma - p_w) \tan \phi'] = ma \tag{6}$$

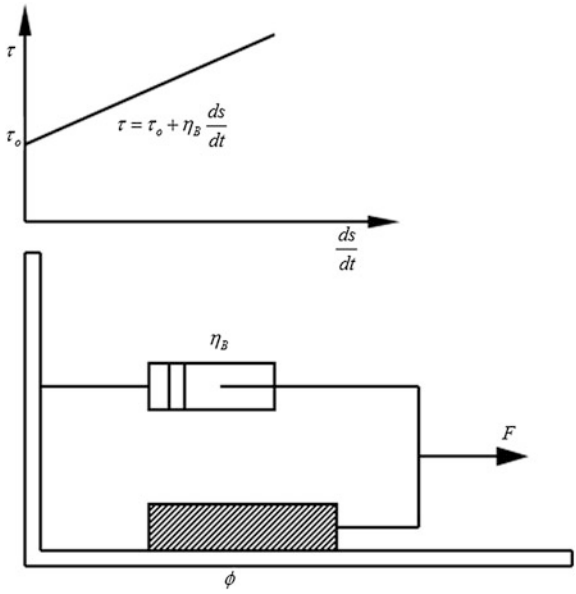

Fig. 5 Model of Bingham body

where τ is driving shear stress, c is the cohesion, σ is the normal stress, p_w the pore water pressure and ϕ' the friction angle, all magnitude projected to the slip surface. Figure 6 is already presents the variables used in this approach.

Corominas et al. (2005) suggested that as the landslide creep movement is considered as dynamic, thus a viscous term should be included in Eq. (7). That is:

$$\tau - [c' + (\sigma - p_w)\tan\varphi'] - \tau_v = ma \tag{7}$$

Viscous forces are usually dependent on the strain rate of the shear zone. For a Bingham typemodel, this relation is linear and becomes:

$$\tau_v = \eta v / z \tag{8}$$

where, η is the viscosity, v is the velocity and z is the thickness of the shear zone. Expression (7) can be introduced in Eq. (9) to give differential equation for a single point, assumed representative of the whole landslide:

$$\gamma l \sin\alpha\cos\alpha - \left[c' + \left(\gamma l\cos^2\alpha - p_w\right)\tan\phi'\right] = m\frac{dv}{dt} + \eta\frac{v}{z} \tag{9}$$

Pore water pressure was not measured directly, but it was estimated from readings of depth of groundwater level. Assuming a parallel flow to the slope surface:

$$p_w = \gamma_w \cos^2\alpha h = \gamma_w \cos^2\alpha(l - D_w) \tag{10}$$

where γ_w is the specific weight of water, l the thickness of the sliding mass and D_w the depth of groundwater level.

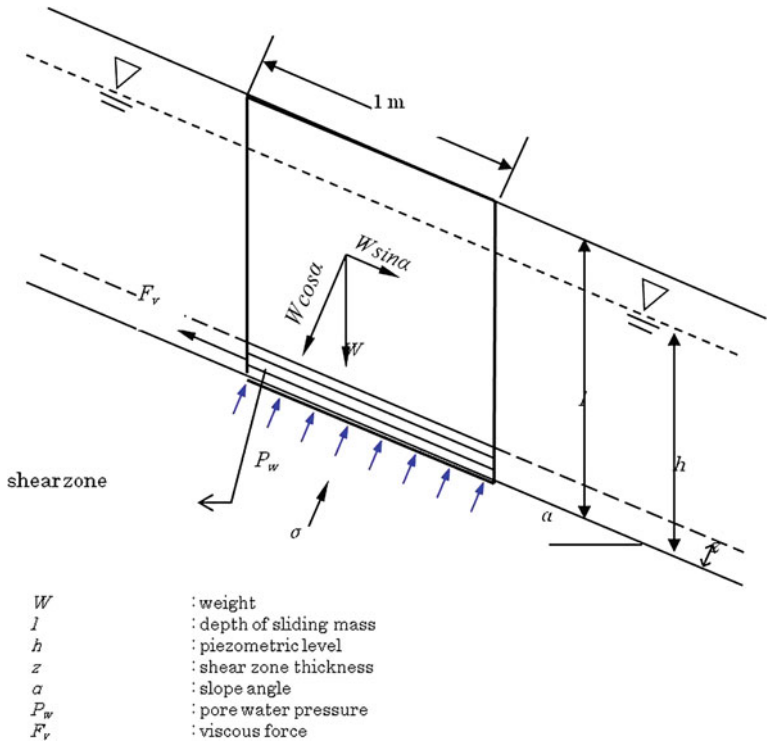

Fig. 6 Infinite slope with a viscous deforming layer (z)

The governing equation which expressed in Eq. (9) is considered as first order ordinary differential equation. By means of integration, this equation can be solved analytically in terms of velocity by considering the following form:

$$\frac{dy}{dx} + yP(x) = Q(x) \tag{11}$$

In order to match up the governing equation to general form, the Eq. (9) need to be modified by dividing both two side with terms m. Hence, the Eq. (9) can be rewritten as Eq. (12) that is:

$$\frac{dv}{dt} + B = A \tag{12}$$

where

$$A = \frac{\gamma l \sin\alpha \cos\alpha - [c' + (\gamma l \cos^2\alpha - p_w)\tan\varphi']}{m} \tag{13}$$

and

Table 2 Soil parameter

Parameter	Value
Saturated unit weight, γ_{sat} (kN/m^3)	20.8
Effective internal friction angle, ϕ' (degree)	15.4
Effective cohesion, c' (kN/m^2)	10.4

$$B = \frac{\eta}{z \cdot m} \tag{14}$$

Through integration procedure, the Eq. (12) yields the solved governing equation:

$$v = \frac{A}{B}\left(1 - e^{-Bt}\right) \tag{15}$$

3 Combined Hydrological and Slope Kinematics Modelling

The simulated groundwater level from tank model were used as input to the kinematics model to directly obtain displacement values as a function of precipitation. The soil parameters that used in kinematic model are obtained from laboratory test of index properties and CU triaxial test which is shown in Table 2. The result of the displacement simulation of Wire 4–5 and Wire 5–6 for the period January 2009–January 2010 are shown in Figs. 7 and 8, respectively. The distinctive parameter between these two simulations is the coefficient of dynamic viscosity (C). This parameter determined through calibrations process until the simulated displacement curve and actual displacement curve are considered to be have a good fit. Wire 5–6 shows the most responsive and highest velocity among the extensometers, thus it is considered to be used for further development of early warning criteria.

Obviously, the use of this model and its parameters are limited to local conditions and being a representative for particular area. However, it is believed that this area can be a sort of additional precursor of landslide warning system for the surrounding areas which have more susceptible against landslide prone, i.e. steeper slope and highly populated.

4 Early Warning Criteria

The importance of early warning system arises when other mitigation efforts in avoiding landslide and protecting landslide mass considered being costly and ineffective, meanwhile human lives threatened by landslide disaster anytime.

A good early warning system should give an accurate prediction of landslide occurrences. This kind of ideal early warning system is built by comprehensive understanding of landslide mechanism and supported by representative and accurate data. Thus, the addition of supporting data may increase the accuracy of prediction.

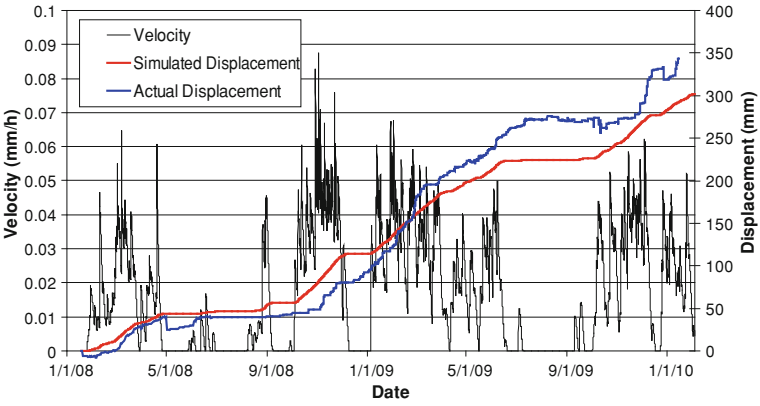

Fig. 7 Simulated velocity, simulated displacement and actual displacement of Wire 4–5

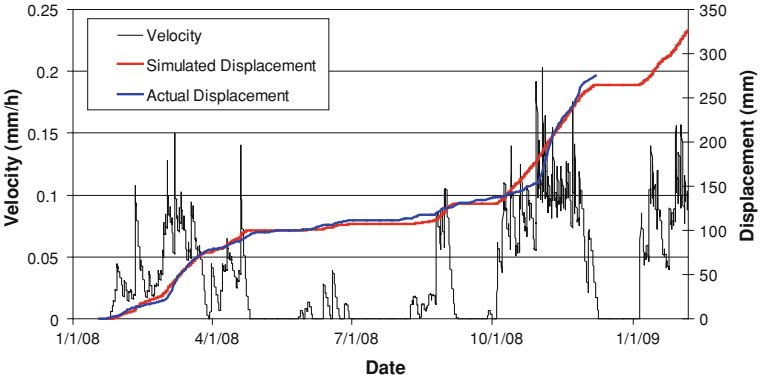

Fig. 8 Simulated velocity, simulated displacement and actual displacement of Wire 5–6

Formerly, the developed model is able to generate landslide mass creep velocity based on real-time rainfall data obtained from the field. In this particular region of Kalitlaga landslide, where the real-time monitoring implemented, some high precipitation would not emerge a dangerous velocity since the landslide mass just tends to creep. However, in case of other steeper slopes at surrounding area, such kind of precipitation might be disastrous. Hence, it needs to correlate the landslide mass creep velocities in this monitored area with some real landslide event which has happened in vicinity area. Usually, several rainfall data need to be collected in order to support a reliable prediction. However, in this case, the only available data once landslide occurred in Kalitlaga on December 30th 2007 just near the currently studied landslide location is daily rainfall intensity data. However, to develop early warning criteria, the determination of hourly rainfall intensity should be included. Thus, the hourly rainfall distribution is generated based two methods of rainfall distribution; Tadashi Tanimoto method and Alternating Block Method

Table 3 Landslide mass velocity class

Velocity class	Range (mm/h)
Class 1 (C1)	<0.15
Class 2 (C2)	>0.15

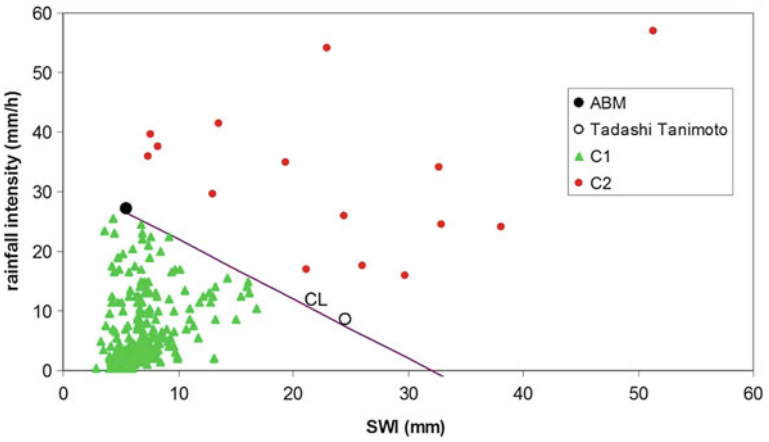

Fig. 9 SWI and hourly rainfall plots and recorded peak velocities from the model

(ABM). Tadashi Tanimoto method based on his study about rainfall distribution in Java Islands, whereas ABM method using some formulas in determines the rainfall duration and distribution (Aras 2007).

Subsequently, these rainfall data were stored in previously developed model to generate soil water index (SWI) of each rainfall event. SWI is defined as the total water level height of the tanks series (Okada 2001). In this study, a new proposed method to built early warning criteria is described by associating the Soil Water Index (SWI) and landslide mass velocity as additional precursor. The determination of SWI from critical rainfall event is achieved initially and its further correlation with landslide mass velocity from the combined model taken into account afterward.

The generated SWI from each rainfall scenario is plotted in X–Y graph. The critical line (CL) is then drawn by intersecting two scenarios which is expressed by line $Y = -X + 32$. This line is considered as the safest based on available data.

In order to build some additional precursor using landslide mass velocity from particular site, it is needed to divide the velocities into several categories/classes. The velocities are divided in two classes described in Table 3. The velocity range is categorized using line CL as demarcation line between velocity ranges. The plot of peak velocity is generated from developed combined simulation using recorded 2 years rainfall data from January 18, 2008 to January 18, 2010 is shown in Fig. 9.

5 Conclusions

The combined model reliability is strongly depending on data recording validation. The reliable and continuous data leads to high performance of both hydrological model and kinematics model and their combination. Recently, this model is considered as the representative of particular landslide area. However, further study of comparable landslide on similar geological condition with better quantification and verification is expected to provide more understanding of landslide movement triggered by rainfall.

The combined hydrological model and kinematics model showed a good agreement between computed and actual displacement using estimated parameter of tank model. The simulated velocity is possible to be correlated to rainfall parameter generated by hydrological model to develop early warning criteria. The determination of early warning criteria by means of rainfall data analysis and soil water index (SWI) obtained from developed tank model gives a line form of critical line (CL) $Y = -X + 32$ where x-axis and y-axis corresponds to SWI and hourly rainfall, respectively. In the mitigation point of view, landslide mass velocities obtained from the combined model result contributed in being additional precursor in early warning criteria by dividing landslide velocity range into two classes.

References

Angeli M, Gasparetto P, Menotti RM, Pasuto A, Silvano S, Uniti CS et al (1996) A visco-plastic model for slope analysis applied to a mudslide in Cortina d'Ampezzo, Italy. Eng Geol 29:233–240

Angeli G, Buma J, Gasparetto P, Pasuto A (1998) A combined hillslope hydrology/stability model for low-gradient clay slopes in the Italian Dolomites. Eng Geol 49:1–13

Aras A (2007) Karakteristik aliran sungai Serayu di bendung gerak Serayu Kabupaten Banyumas, Jawa Tengah. Undergraduate thesis. Civil and environmental engineering department. Gadjah Mada University. Yogyakarta.

Condon WH, Pardyanto L, Ketner KB, Amin TC, Gafoer S, Samodra H (1996) Geological map of the Banjanegara and Pekalongan Sheet, Jawa. Geological Research and Development Centre, Bandung

Corominas J, Moya J, Ledesma A, Lloret A, Gili JA (2005) Prediction of ground displacements and velocities from groundwater level changes at the Vallcebre landslide (Eastern Pyrenees, Spain). Landslides, (Oct 2004), pp 83–96

Fathani TF, Karnawati D, Sassa K, Fukuoka H, Honda K (2008) Landslide monitoring, prediction and early warning in Banjarnegara, Indonesia. Star, 4–6 Sept 2008

Hong Y, Hiura H, Shino K, Sassa K, Suemine A, Fukuoka H et al (2005) The influence of intense rainfall on the activity of large-scale crystalline schist landslides in Shikoku Island Japan. Landslides 2:97–105

Karnawati D, Fathani TF, Sudarno I, Andayani B (2008) Development of community-based landslide early warning system in Indonesia. In: Proceeding of the first world landslide forum, Tokyo, 18–21 Sept 2008, pp 305–308

Okada K, Makihara Y, Shimpo A, Nagata K, Kunitsugu M, Saito K (2001) Soil water index. Tenki 47:36–41

Ranalli M, Gottardi G, Medina-cetina Z, Nadim F (2009) Uncertainty quantification in the calibration of a dynamic viscoplastic model of slow slope movements. Landslides 7(1):31–41

Rokhmana CA (2007) The low cost monitoring system for landslide and volcano with digital photogrammetry. In: Proceedings of Joint Convention HAGI-IAGI-IATMI, Bali

Takeuchi A (1981) Method of investigating groundwater-vein-streams by measuring one-meter-depth in landslide areas (II). J Jpn Assoc Groundw Hydrol 23(1):1–27

Van Asch T, Van Genuchten P (1990) A comparison between theoretical and measured creep profiles of landslides. Geomorphology 3:45–55

Dynamic Analysis of Earthquake Amplification Effect of Slopes in Different Topographic and Geological Conditions by Using ABAQUS

Yasuhiro Mitani, Fawu Wang, Austin Chukwueloka Okeke and Wenhao Qi

Abstract Natural disasters like earthquake and tsunami can trigger slope failure or affect the stability of slopes. Geodisasters associated with slope failure has affected the socio-economic development of many developed and developing countries of the world. In dynamic analysis of slope stability due the seismic loading, it is important to understand the amplification effect on the slope due to topographic and geologic conditions. However, because the topographic and geological structures are too complicated, the amplification effects are not clear. This study tries to analyze the amplification effects on slopes by using Abaqus, FEM software. Analysis was conducted on the amplification effect of a homogeneous slope due to the effects of slope height, slope angle, seismic movement, and dip angle of alternating layers of tuff and shale. Also, the amplification effect of the north–south and east–west strike directions of slopes around the Shimane nuclear power plant (Shimane-NCPP) was also simulated. In this study, amplification factor will be defined as the ratio of output peak acceleration to the input acceleration. Results obtained show (1) that the amplification factor becomes lower when the slope height is increased for the slope crest and the middle part of the slope; (2) amplification factor of the slope crest becomes relatively high when the slope angle is high while amplification factor at the foot of the slope becomes relatively low at the same slope angle; (3) amplification tendency does not show obvious difference for seismic waves on the dip angle of the slope strata; (4) north–south trending strike direction of slopes around the Shimane-NCPP show high amplification factor near the slope crest while the east–west trending strike direction of slopes around the Shimane-NCPP shows high amplification factor near the slope toe.

Y. Mitani (✉) · F. Wang · A. C. Okeke
Faculty of Science and Engineering, Department of Geoscience, Shimane University,
1060 Nishikawatsu-cho, Matsue 690-8504, Japan
e-mail: wangfw@riko.sjimane-u.ac.jp

W. Qi
Institute of Engineering Mechanics China Earthquake Administration,
29 Xuefu Road, Harbin, China

F. Wang et al. (eds.), *Progress of Geo-Disaster Mitigation Technology in Asia*,
Environmental Science and Engineering, DOI: 10.1007/978-3-642-29107-4_27,

Keywords Slope topography · Slope structure · Amplification of seismic acceleration · ABAQUS

1 Introduction

Natural disasters like earthquakes, tsunamis, landslides, debris avalanches and monsoons have continued to pose great threats to important engineering facilities like oil refineries, underground mining stations, hydropower plants and most recently, nuclear power plants (NCPPs). Nuclear power plants, which are sometimes built near Japan coasts, are often prone to many natural and man-made disasters. Good knowledge and understanding of the geological and topographic condition of the area around nuclear power plants is vital in disaster mitigation, early warning and prevention. This research focuses on the Shimane nuclear power plant (also referred to as Shimane NCPP), which is located near the Japan sea in western part of Japan. The disastrous effects of the 2011 9.0M_S Tohoku earthquake and tsunami in Japan have drawn the attention of the Japanese government in finding lasting solutions to reduce risks associated with earthquakes and tsunami-triggered disasters due to its proximity (9 km), to the nearest city of Matsue, capital of Shimane Prefecture.

Many landslide sites exist in Chugoku, Sanin area (Fig. 1), with Shimane Prefecture having higher distribution of landslide occurrences. The understanding of the geological and topographic conditions of steeply inclined chains of mountains and confined valleys in the Sanin area is necessary in long-term disaster mitigation, and prevention programme. It is also important to put relevant countermeasures in place especially around the geological structures surrounding the Shimane NCPP due to earthquake effects because earthquakes with magnitudes greater or equal to 6 have occurred several times in the past in Sanin area (Fig. 2).

Slope failure due to earthquake is affected by distance from the seismic origin, shock of seismic affects slope direction, slope geometry and internal structures of the slope material. In order to evaluate the risk associated with slope failure, it is necessary to conduct dynamic analysis and to investigate the slope amplification effect by considering dynamic load due to seismic movement.

The Shimane NCPP is located near the Japan sea with slopes of different vertical elevations, attitudes (strike and dip directions), and slope angles. Figure 3 shows part of the slopes around the NCPP with inclined beds of tuffs and shale. The structural style of the slopes shows alternating beds of shale and tuffaceous sands with mean thickness of 15 m for the shale layers and 20 m for the tuff layers.

Structural and topographic characteristics of slopes around the Shimane NCPP have a tendency of amplifying seismic acceleration and triggering slope failure. Also, materials on the slopes may easily yield to shear stress along weak bedding planes. Some researchers (Gaztas 1987; Athanasopoulos et al. 1999; Qi et al. 2003; Cetin et al. 2004), observed the amplification effect on topography by comparing earthquake damages between slope toe and slope crest. Some researchers (Luzi and Pergalani 2000; Sepulveda et al. 2005), got the amplification effect on topography according to

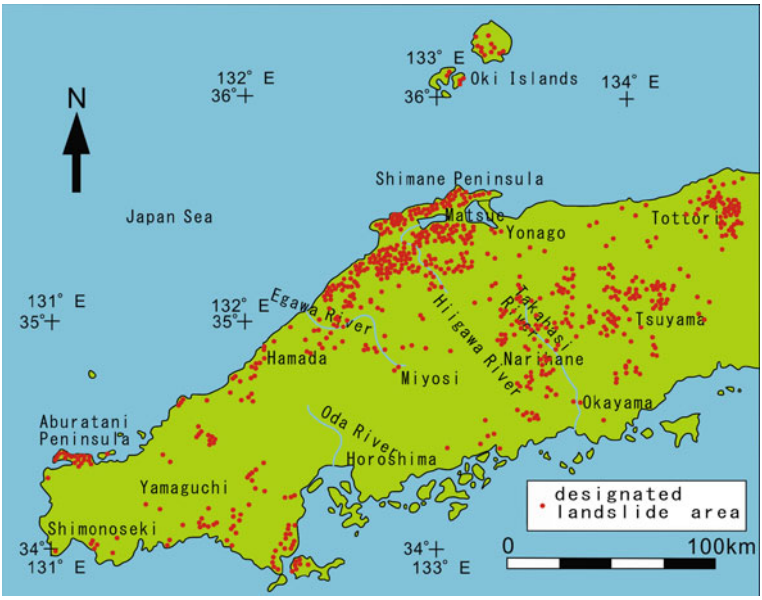

Fig. 1 Designated landslide area in Chugoku area

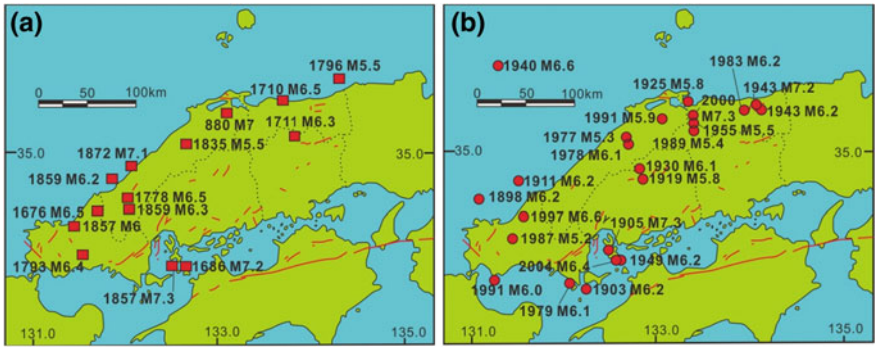

Fig. 2 Epicentral distribution of historic earthquake in Chugoku area (Japan Society of Engineering Geology 2010)

accelerometric records monitored at different places on a slope; some records show that the peak acceleration on the slope crest is three times (3x) larger than peak acceleration obtained at the foot of the slope. Laboratory tests like centrifuge test (Brennan and Madabhushi 2009) and shaking table tests (Wang et al. 1987; Xu et al. 2010) were also used to simulate the seismic performance of slopes. In recent years, some numerical simulation works have been carried out to study the effect of topography on slopes during earthquakes using FEM and DEM softwares (Qi et al. 2003; Xu et al. 2008).

From the above literatures, studies of the effect of slope topography on the behavior of slopes during earthquake are based on limit slopes which were

Fig. 3 Slope with alternately distributed shale layers and tuff layers

investigated after an earthquake disaster or tested in the laboratory. In numerical simulation, almost all slope models are modeled as a uniform slope models with single faces. Therefore, real slopes with double faces and slope structure are not considered. The slopes are numerically analyzed based on FLAC^{3D} software by which it is difficult for model building.

In practical cases, some nuclear plants are constructed in sites surrounded by mountain slopes similar to the Shimane NCPP. It is necessary to study the effect of topography and slope structures on seismic acceleration response based on the special double-faced slope models extracted from real slopes around the Shimane NCPP using ABAQUS software, which is user-friendly and convenient for model building.

2 Topography and Geological Summary in Study Field and Slope Movement in Same Field

Slopes around the Shimane NCPP were affected by geotechnical and civil engineering works carried out prior to the installation of the nuclear reactors. These construction works affected the attitudes of strata composing the slopes and made the slopes prone to geological disasters. The Shimane NCPP is surrounded by slopes with slope heights ranging between 50 and 70 m in the eastern part of the plant, 100–120 m in the southern and western parts of the plant. Observation

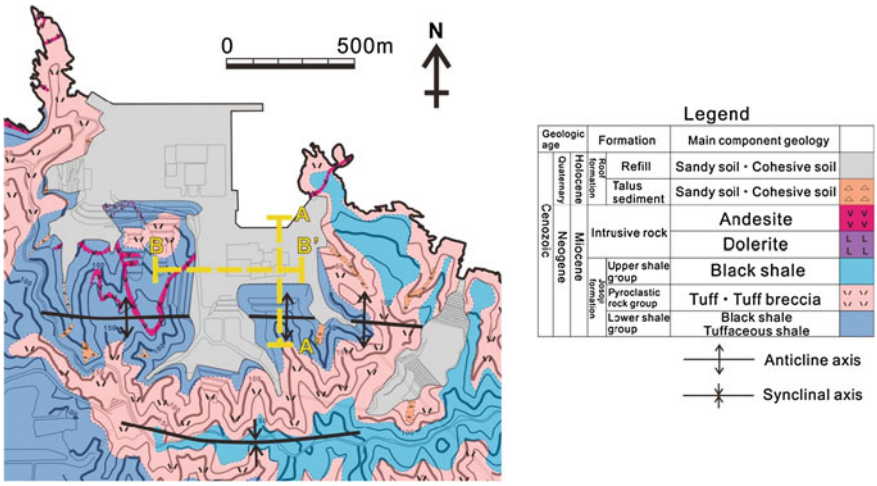

Fig. 4 Geologic map of Shimane nuclear power plant area

revealed that slopes in the west and southern part of the nuclear reactor have been stabilized by cutting and excavation. The Shimane NCPP is underlain by the Josoji Formation which is composed of sedimentary rocks of the Miocene (tuff breccias, lapilli tuff, tuffaceous shale and shale) and intrusive rocks (andesite and dolerite) as bedrock. Many clay seams in the sedimentary rocks lie parallel to the bedding planes. Figure 4 shows the geologic map of the area (Kurooka et al. 2005).

In Kashima-cho Matsue, Shimane Prefecture, rockfalls occurred in the Etomo area on July 16th 2010. Also, another landslide occurred around an elderly nursing home around Kitakoubu on January 5th 2011. Figure 5 shows rockfall in Etomo area and landslide site near the nursing home. Two persons were killed by the rockfall disaster around Etomo area while no fatality was recorded by the landslide disaster in Kitakoubu except for buildings that were affected by the landslide. Assessments and field analysis shows that the two disasters were triggered by the combined effect of snow and rainfall. Deposits of the two disaster sites are primarily part of the Josoji Formation having the same geologic and geotechnical properties with that of the Shimane NCPP.

3 Research Method and Its Verification

3.1 Model Building

To study the amplification effect of slopes due to topographic and geological condition of the slope material, a homogenous slope model and a slope model with alternating layers of tuff and shale were built using ABAQUS software (Fig. 6). The homogenous slope model was taken to be wholly composed of tuffaceous material

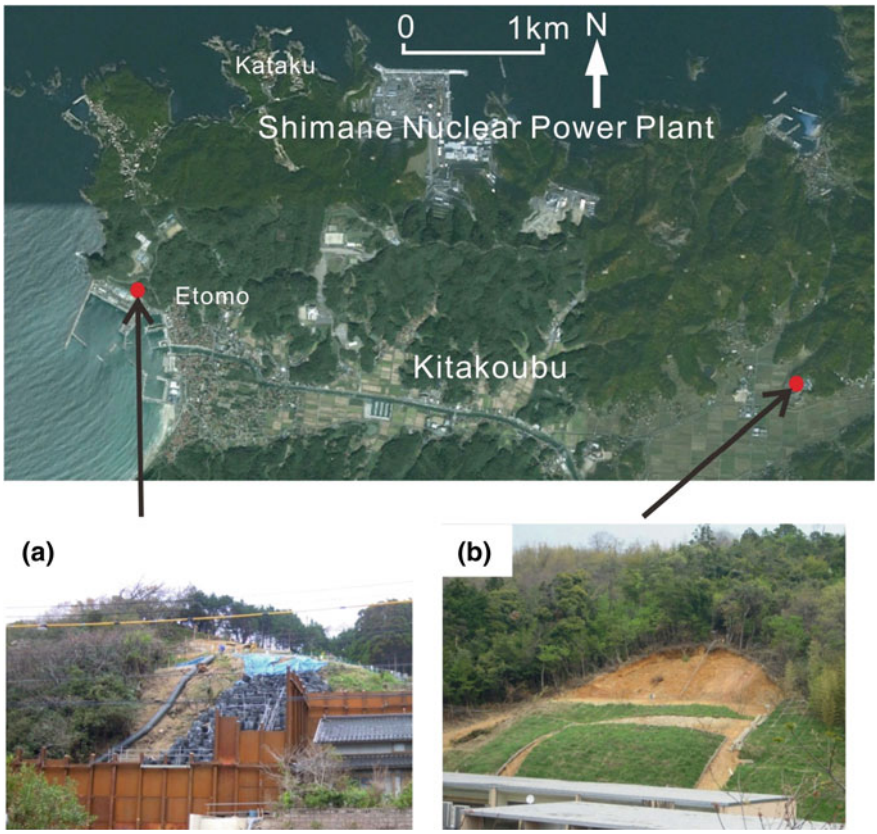

Fig. 5 Occurred slope movement in Kashima-cho. **a** Rockfall occurred in Etomo area. **b** Landslide occurred in Kitakoubu

while the thickness of the layers in the slope model with alternating layers of tuff and shale is 20 m and 15 m respectively. Geomechanical parameters (Hoek 2000) of the models are shown Table 1. Detailed geological cross-section (Fig. 7) shows that slopes in the north–south region, and east–west region of the nuclear power reactors #1 and #2 were extracted in order to analyze the stability of the slopes (Fig. 8).

The dynamic behavior of a continuous body with an infinite area was analyzed using finite element method (FEM). The equation governing the dynamic analysis is represented as follows:

$$[M]\{\ddot{x}\} + [C]\{\dot{x}\} + [K]\{x\} = \{f\} \tag{1}$$

$[M]$: mass matrix, $[C]$: damping matrix, $[K]$: stiffness matrix, f: external force, x:nodal point displacement. The Rayleigh damping is assumed to initiate the damping.

$$[C] = \alpha[M] + \beta[K] \tag{2}$$

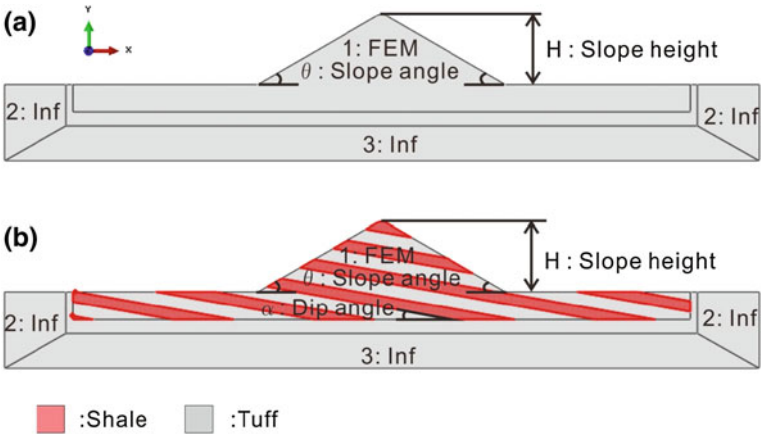

Fig. 6 Homogenous slope model and slope model with alternately distributed layers. **a** Homogenous slope model. **b** Slope model with alternately distributed layers (*1*, analysis area; *2*, lateral boundary area; *3*, bottom boundary area)

Table 1 Mechanics parameters of four materials used in the modeling

Material	Density (kg/m^3)	Elastic modulus (MPa)	Poisson ratio	Cohesive strength (MPa)	Friction angle (°)	Dilate angle (°)	Thickness (m)	Damping (%)
Shale	2,100 (2,300)	2.0E + 09 (6.0E + 09)	0.28 (0.26)	1.0E + 06 (2.0E + 06)	27 32	2 5	15	3
Tuff	2,200	4.0E + 09	0.27	1.5E + 06	30	4	20	3
Lateral boundary	2,200	4.0E + 09	0.27					
Bottom boundary	2,500	9.0E + 09	0.25					

α, β are constant. Damping rate of 3 % formerly adopted by Qi (2011) was employed in carrying out the slope simulation. The damping of 3 % was set using $\alpha = 2.134$, $\beta = 0.0009009$.

In this study, to simulate such semi-infinite bodies as slopes (Fig. 6), all the boundary areas (2 Inf & 3 Inf) were set as infinite elements. If the boundary conditions are not set, the sides and bottom of slope will be limited which makes the slope an unrealistic model. By setting the infinite element on the bottom and sides of the model, it is possible to get rid of the side and bottom boundaries of the model which makes the slope model functional. Mohr–Coulomb models are set at the region of seismic effect, and elastic model are set to boundary infinite elements. The seismic wave acceleration data was set between the upper part of the bottom boundary and the bottom of the slope model. The underground record during the 2000 western Tottori M7.3 earthquake is chosen as input earthquake acceleration. This study used many earthquake records (Table 2) in order to adjust the earthquake motion frequency, the epicentral distance, the distance from earthquake source fault, and subsurface foundation conditions.

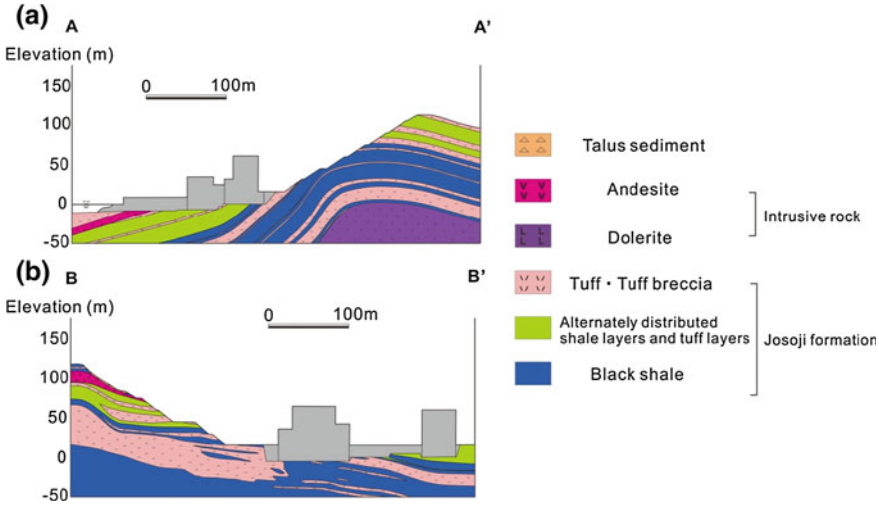

Fig. 7 Geological section of slopes around the Shimane-NCPP. **a** Section of north–south direction slope. **b** Section of east-south direction slope (Chugoku Electric Power Company 2000 with modification)

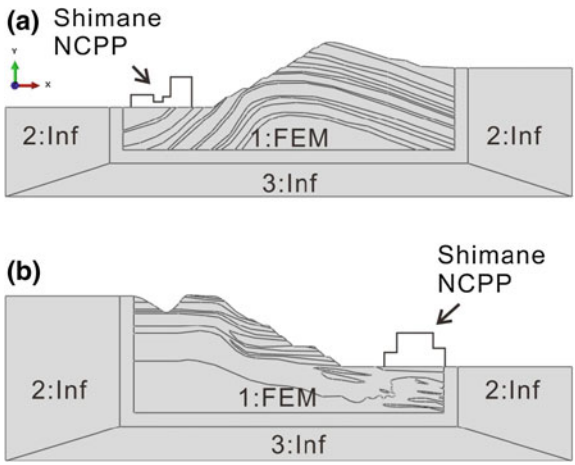

Fig. 8 Slopes model around Shimane Nuclear Power Plant. **a** North–south direction slope. **b** East–west direction slope (*1*, analysis area; *2*, lateral boundary area; *3*, bottom boundary area)

3.2 Verification of the Model Building Way by Centrifuge Test Result

To validate the reliability of the model-building which will be used in this study, the centrifuge test results, which was obtained from the University of Cambridge (Brennan and Madabhushi 2009), about amplification of seismic acceleration at slope crests, were used as a reference criterion (Fig. 9). A corresponding ABAQUS slope model was built, which uses the same geotechnical parameters and

Table 2 Site code list of using seismic records

Site code	Site name	Lat	Lon	Surface alt (m)	Install depth (m)	Prefecture	Epicentral distance (km)
OKYH07	Shingou	35.0461	133.3196	564	100	Okayama	26
OKYH08	Tetsuta	34.9071	133.4081	430	100	Okayama	41
OKYH09	Yubara	35.1777	133.6792	405	100	Okayama	32
OKYH14	Hokubou	34.9331	133.6232	218	100	Okayama	45
SMNH01	Hakuta	35.2931	133.2630	170	101	Shimane	8
SMNH02	Nita	35.2203	133.0882	340	101	Shimane	24
SMNH10	Mihonoseki	35.5547	133.3031	9	200	Shimane	31
SMNH12	Yoshida	35.1603	132.8583	380	101	Shimane	46
TTRH02	Hino	35.2281	133.3936	410	100	Tottori	7
TTRH04	Akasaki	35.4636	133.6333	114	207	Tottori	33

infinite element boundary condition (Fig. 10). Under the same seismic response regularity with the centrifuge model: as (1) at the bottom of the slope, the peak value and the waveform are almost the same as the input wave, (2) at the top of the slope which is far from the crest, the peak value is slightly larger than the input wave, but the waveform is almost the same as the input wave (3) at the crest of the slope, the peak value is about 2.5 times higher than that of the input wave, and the waveform is almost the same with the input wave. The result shows that the seismic wave was amplified at the crest. All the results show that the method is practically acceptable.

4 The Effect of Topography and Slope Structure on Seismic Acceleration Response

4.1 Studied Slope Models

In order to study the effect of the slope topography (slope angle and slope height) and slope structure (dip angle) on seismic performance of slopes, slopes models were built (1) to study the effect of slope angle. Four homogenous slope model with heights of 100 m and different slope angles of 20, 30, 40, and 50° (2) to study the effect of slope height. Six homogenous slope models with angle of 30° and different slope height as 50 m, 75 m, 100 m, 125 m, 150 m, and 175 m (3) to study the effect of dip angle. Six alternating tuff-shale bed slope models with slope angle of 30°, slope height of 100 m, and different dip angles as 10, 15, 20, 25, 30, and 40° which present different relationships with the slope angle. Output points of slope models are red points shown in Fig. 11.

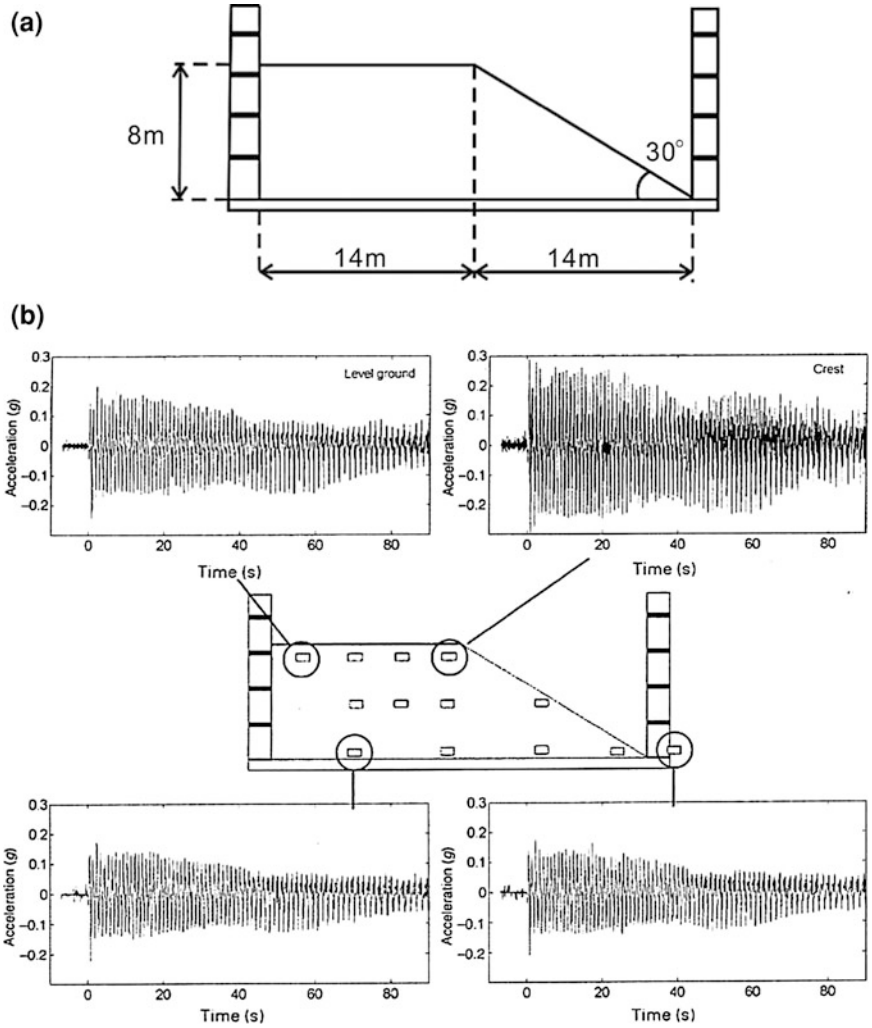

Fig. 9 The centrifuge test (Brennan and Madabhushi 2009). **a** The test model of the centrifuge test. **b** The result of the centrifuge test

4.2 Slope Topography and Structural Effect on Seismic Acceleration Response

Using north–south seismic record observed at Hino-cho Tottori prefecture as an example, the output waveform of a homogenous slope model with height of 100 m and slope angle of 30° and the intercalated slope model of tuff and shale with height of 100 m. Slope angle of 30° and dip angle of 10° are shown Figs. 12 and 13.

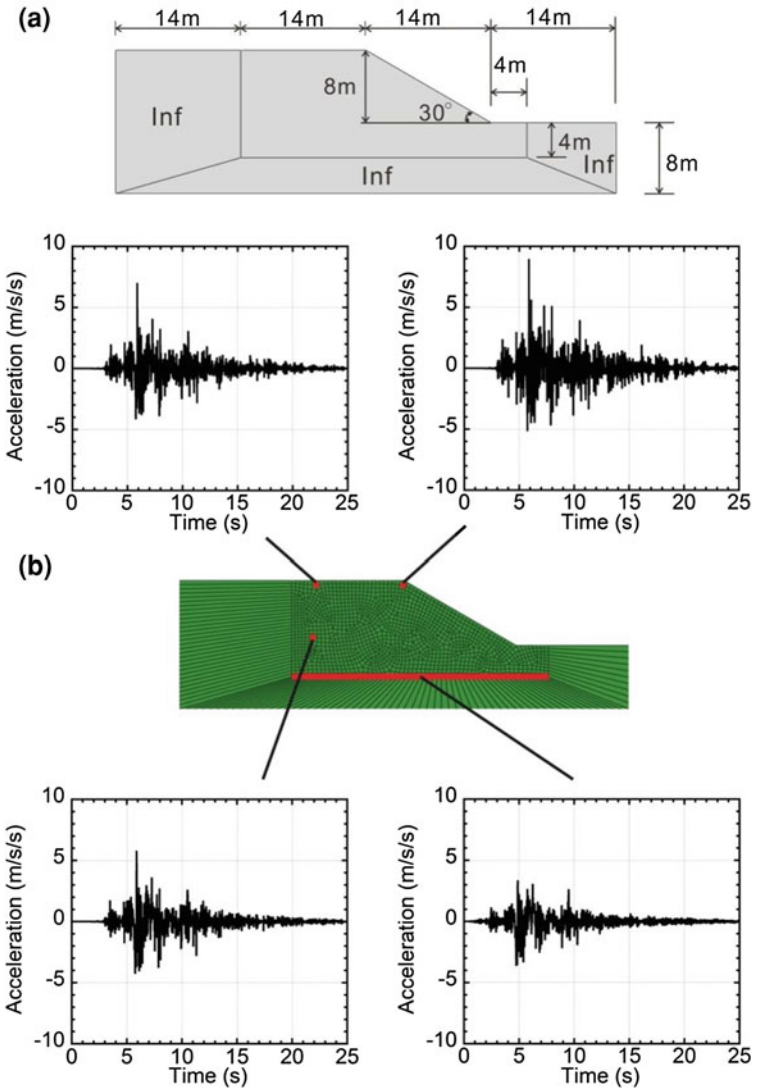

Fig. 10 The validation analysis of ABAQUS model. **a** The validation model1. **b** The validation result

For the analysis of the acceleration waveform at each point of the homogeneous slope (Fig. 12), the peak amplification at the crest is relatively higher than the peak acceleration at other points. Similar results were obtained as earthquake data were varied in the simulation. In acceleration waveform of each point of the alternating tuff-shale bed slope (Fig. 13), the peak amplification at the crest is obviously higher than the peak acceleration at other points in the same way as the effect of homogeneous slope. In this study, amplification factor is defined as the ratio of output peak acceleration to the input acceleration.

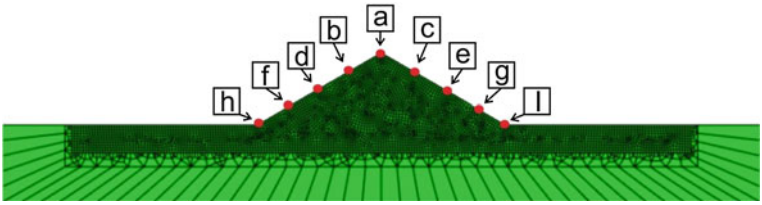

Fig. 11 Output points of slope model

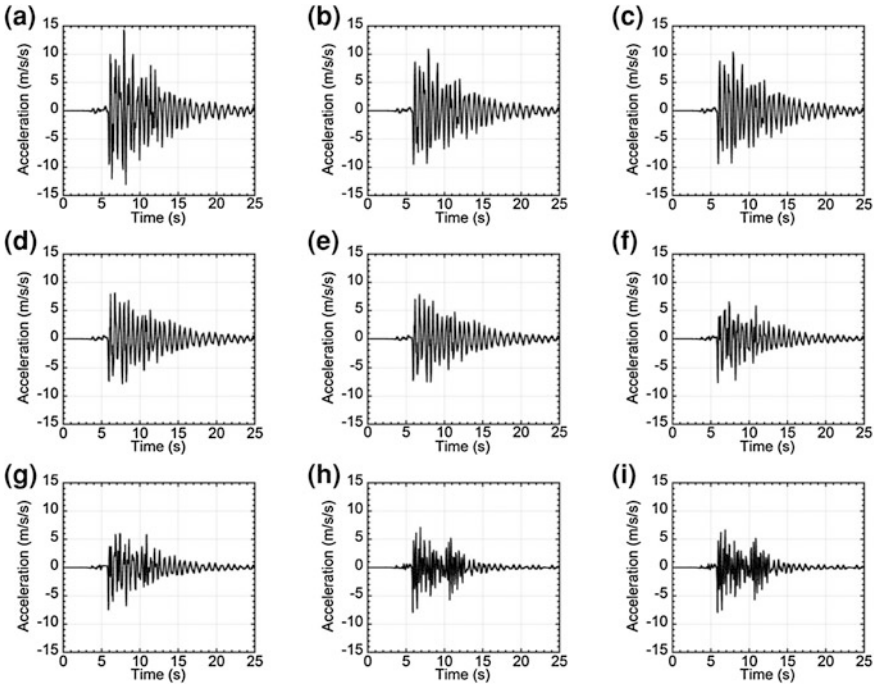

Fig. 12 Output acceleration waveform of a homogenous slope with height of 100 m, slope angle 30° (Using NS seismic record observed at Hino-cho)

Amplification factors of the slope crest were simulated using seismic records which were plotted against each epicentral distance and distance from earthquake source fault (Fig. 14). Distance of the KiK-net observation point from earthquake source fault were estimated using related model of source fault and position in Bateer et al. (2011) and fault model in Horikawa et al. (2001). In amplification factors of each epicentral distance, the slope model with height of 100 m and slope angle 30° shows a decreased tendency for amplification factor for the same epicentral distance, while result from the other model showed no decreased tendency for amplification factor for the same epicentral distance. In amplification factors of each distance from earthquake source fault, the slope model with height of 100 m and slope angle 30° shows a decreased tendency for amplification factor with

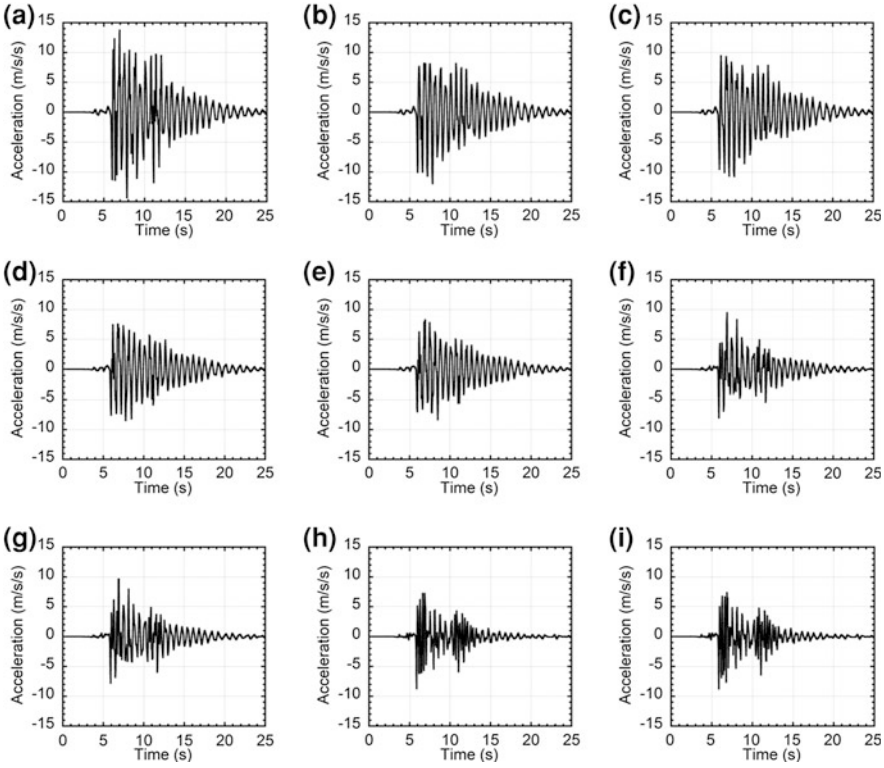

Fig. 13 Output acceleration waveform of an alternately distributing layered slope with height of 100 m, slope angle 30°, and dip angle 30° (Using NS seismic record observed at Hino-cho)

larger distance while the other showed no decreased tendency for amplification factor with the same distance. Because Western Tottori earthquake is of left lateral fault, there is no influence on the effect on the upper circle.

For analysis of the earthquake response due to different slope heights, the amplification factor at the crest region was relatively higher than the middle and toe part of the slope (Fig. 15). Around these areas, the amplification factor becomes relatively low when the slope height is increased. At the slope toe, amplification factor did not show similar trend due to the effect to different slope heights.

For analysis of earthquake response due to different slope angles, the amplification factor at the crest region was relatively higher than the middle and lower part of the slope (Fig. 16). At the upper part of the slope, amplification factor becomes relatively high when the slope angle is high; however, amplification factor at the slope toe shows a steady decrease in value. Amplification factor at the middle part of the slope did not show similar trend as a result of the difference in slope angles.

Because the peak acceleration value and the acceleration waveform output on the left and right sides of the homogeneous slopes were nearly uniform, the waveform of the acceleration of the slope on the left side was adopted.

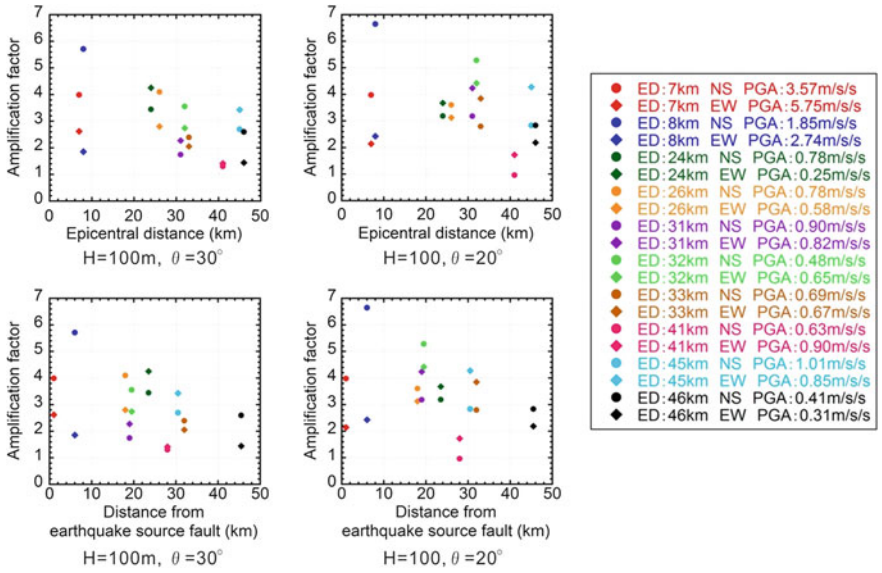

Fig. 14 Amplification factor of seismic record of each epicenter distance and amplification factor of seismic record from each distance from earthquake source fault

For analysis of earthquake response due to different dip angles, the amplification factor at the crest region was higher than the middle and lower part of the slope which is similar to the trend of the homogeneous slope (Fig. 17). As physical parameters of the shale bed were changed to a slightly higher strength than that of the tuff, the same result was obtained (Fig. 18). However amplification tendency due to change in dip angles of the beds was very negligible.

5 Slope Topography and Structural Effect on the Failure Style of the Slope

In order to ascertain the critical failure zone, data obtained from the Hyogoken-Nanbu earthquake were magnified and used as input seismic motion (Fig. 19). Based on the results of slope failure due to slope height, slope angle and dip angle, the diagram illustrating the slope failure mechanism is shown Figs. 20, 21 and 22.

The degree of uniformity associated with the failure style of the slope is mainly due to the combined effect of the slope height, slope angle and dip angle which are easy to find as (1) the possible sliding surface is almost the same in Fig. 20; the slope height has no obvious effect on the slope failure style; (2) the possible sliding surface becomes higher with the slope angle is increased according to Fig. 21; the slope angle controls the slope failure styles; (3) Fig. 22 shows the possible sliding due to different dip angle. Plastic strain occurred at the rear part of the slope for all slope models. When the dip angle of the bedding plane is lower than the

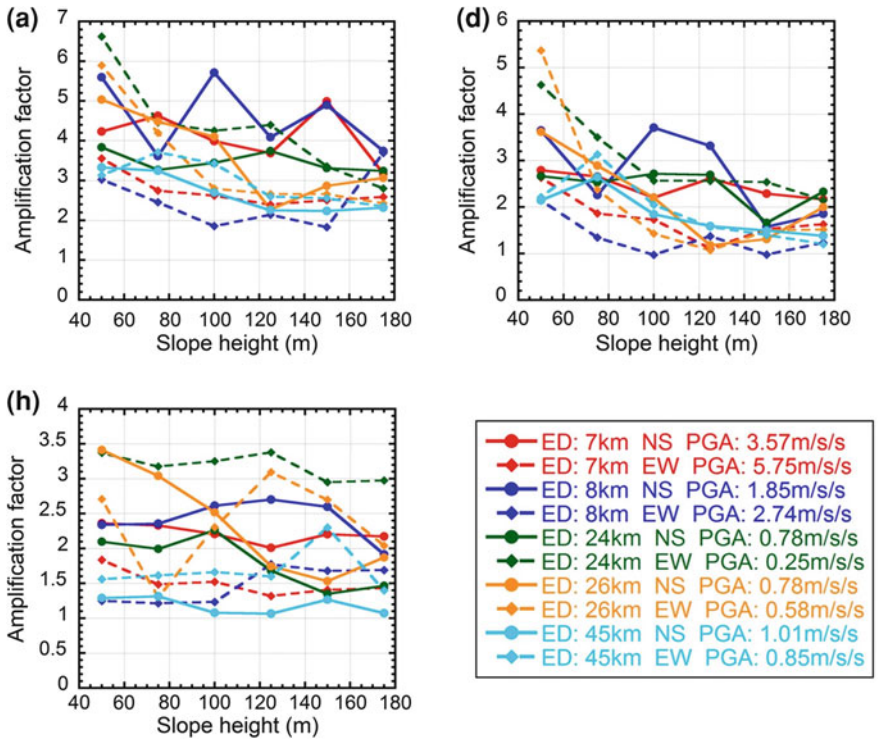

Fig. 15 Amplification factor due to different slope height. **a** The peak of slope. **b** The slope middle. **c** The slope foot (a), (d) and (h) are similar with Fig. 11

inclination angle of slope, sliding surface occurs along the weak layer. When the dip angle of the bedding plane is larger than the inclination angle of the slope, the sliding surface occurs without being affected by the stratum.

6 Amplification Effect of Slopes Around the Shimane-NCPP

To analyze the slopes around the NCPP, samples collected from the field were subjected to uniaxial compression test. However, geotechnical parameters of the rock samples are not complete due to lack of special geotechnical equipment.

The dynamic elasticity modulus and dynamic Poisson's ratio were estimated from the relationship between P-wave velocity and density and S-wave velocity and density in Ludwig et al. (1970). Shear strength of rocks were computed using the formula (3) by Yamaguchi and Nishimatsu (1991) if the tensile strength and compressive strength can be gotten.

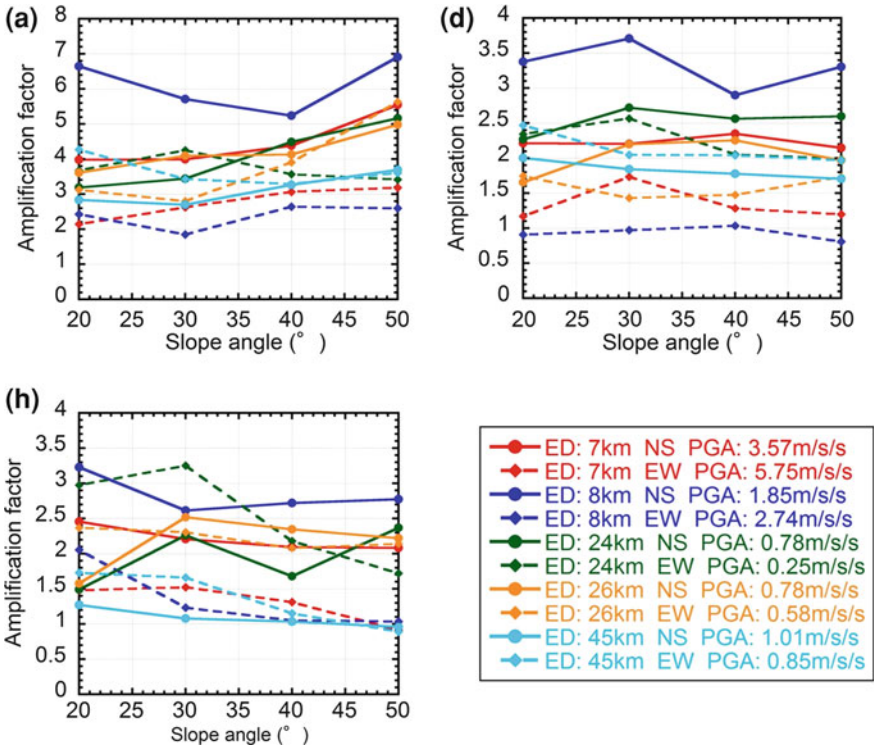

Fig. 16 Amplification factor due to different slope angle. **a** The peak of slope. **b** The slope middle. **c** The slope foot

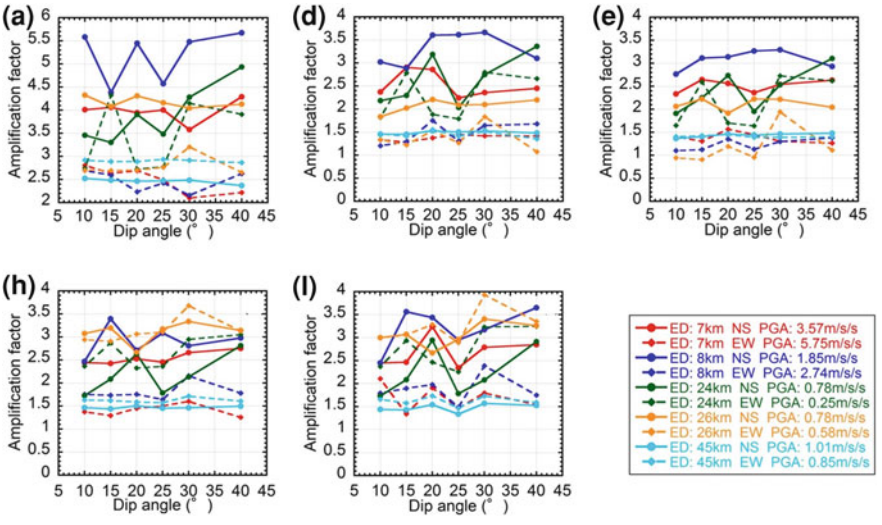

Fig. 17 Amplification factor due to different dip angle (shale strength is weaker than tuff strength). **a** The peak of slope. **b** The slope middle. **c** The slope middle. **d** The slope foot. **e** The slope foot

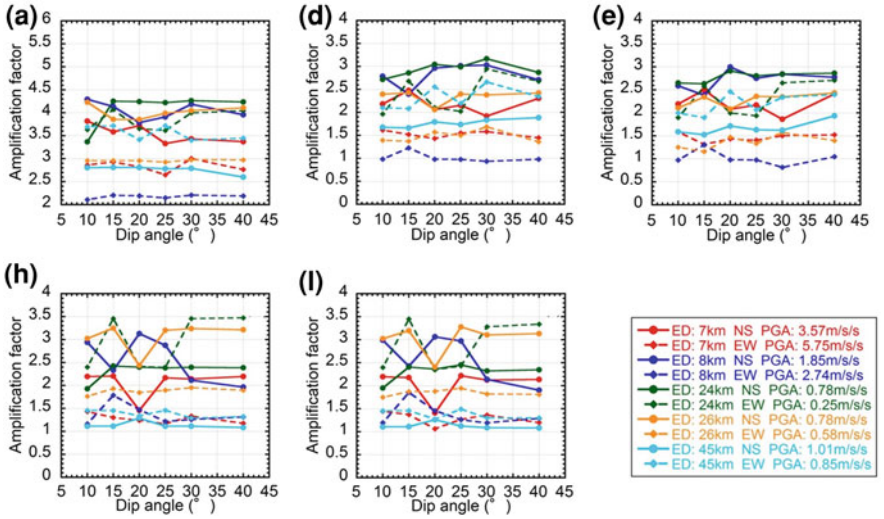

Fig. 18 Amplification factor due to different dip angle (tuff strength is weaker than shale strength). **a** The peak of slope. **b** The slope middle. **c** The slope middle. **d** The slope foot. **e** The slope foot

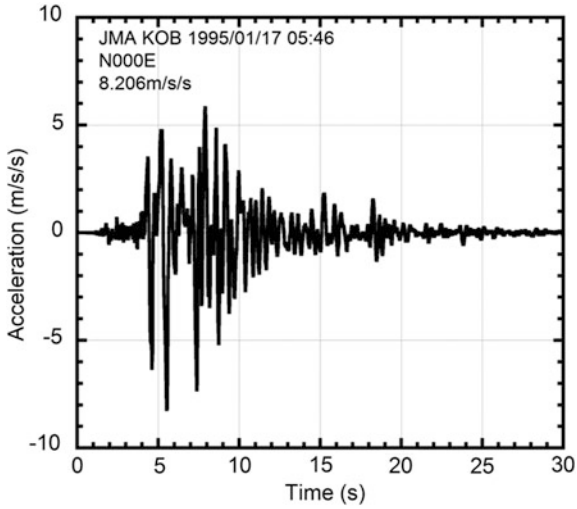

Fig. 19 Acceleration waveform of Hyogoken-Nanbu Earthquake (Observed at Kobe Marine Observatory)

$$S_s = \frac{S_c \cdot S_t}{2\sqrt{S_t(S_c - 3S_t)}} \tag{3}$$

S_s: shear strength, S_s: the compressive strength, S_t: the tensile strength. However, considering these methods, many previous studies were consulted to obtain the

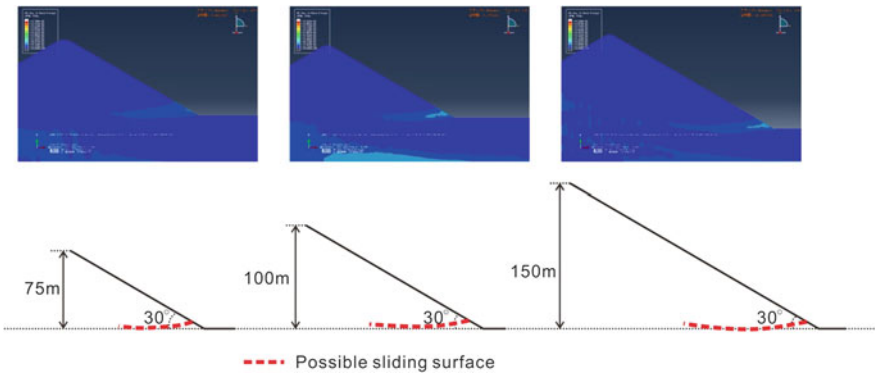

Fig. 20 The effect of the slope angle on the slope failure style

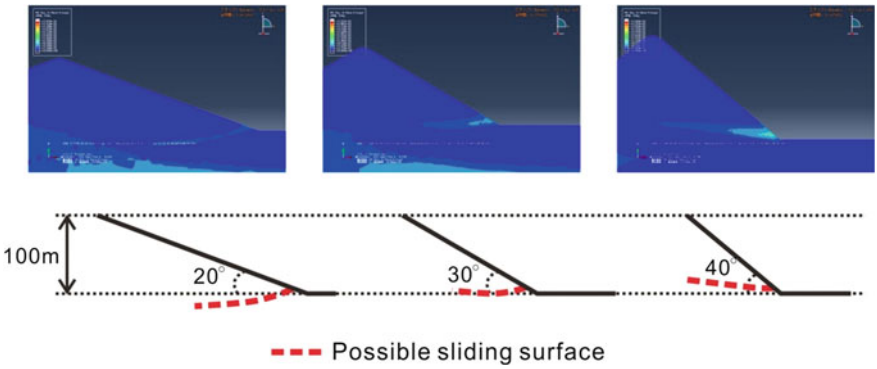

Fig. 21 The effect of the slope height on the slope failure style

geotechnical parameters. In this study, input value was adopted based on test result of laboratory analysis (Table 3). Simulation was carried out on each slope using seismic record of five different combinations. Slopes located in the north–south direction were simulated using seismic records in the N–S direction while slopes in the east–west axis were simulated using seismic records in the E-W direction.

Figure 23a shows the amplification factor of slopes in the north–south at each output point. Outputs number 8 and 9 which corresponds to the slope crest show high deflections in amplification factor. The amplification factor is also high at the lower part of the slope (Fig. 24). In using seismic records, the amplification factor of the N–S seismic record observed at Shingou-cho was high while the amplification factor of the N–S seismic record observed at Hokubou-cho was the low.

Figure 23b shows the amplification factor of slopes in the east–west axis at each output point. Outputs number 2 and 3 corresponding to the cut earth slope show higher amplification factors. However, the amplification factor is low at the upper part of the slope (Fig. 24). Using seismic records, the amplification factor of

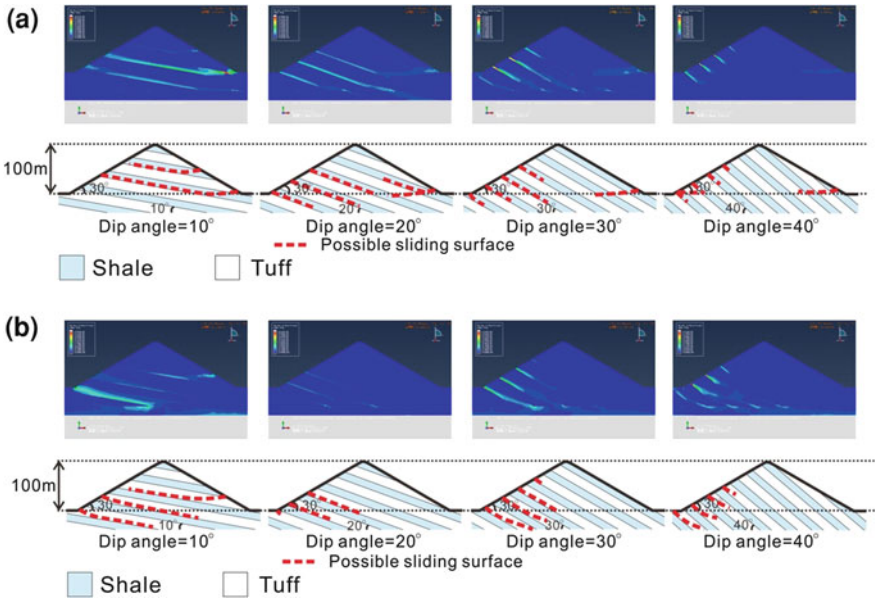

Fig. 22 The effect of the dip angle on the slope failure style. **a** shale strength is weaker than tuff strength. **b** tuff strength is weaker than shale strength

Table 3 Mechanics parameters of eight materials used in the modeling

Material	Density (kg/m^3)	Elastic modulus (MPa)	Poisson ratio	Cohesive strength (MPa)	Friction angle (°)	Dilate angle (°)	Damping (%)
Shale	2,300	9,000	0.25	3.5	33	4	3
Hard Shale	2,530	20,577	0.23	6.7	38	7	3
Tuff	2,430	12,044	0.24	4.0	35	5	3
Alternate layer of tuff and shale	2,350	10,500	0.245	3.75	34	4.5	3
Andesite	2,700	42,000	0.2	13	46	11.5	3
Dolerite	2,700	42,000	0.2	13	46	11.5	3
Lateral boundary	2,430	12,044	0.24				
Bottom boundary	2,700	42,000	0.2				

the E-W seismic record observed at Shingou-cho is high. On the other hand, amplification factors of the E-W seismic record observed at Hokubou-cho and the E-W seismic record observed at Hakuta-cho are low.

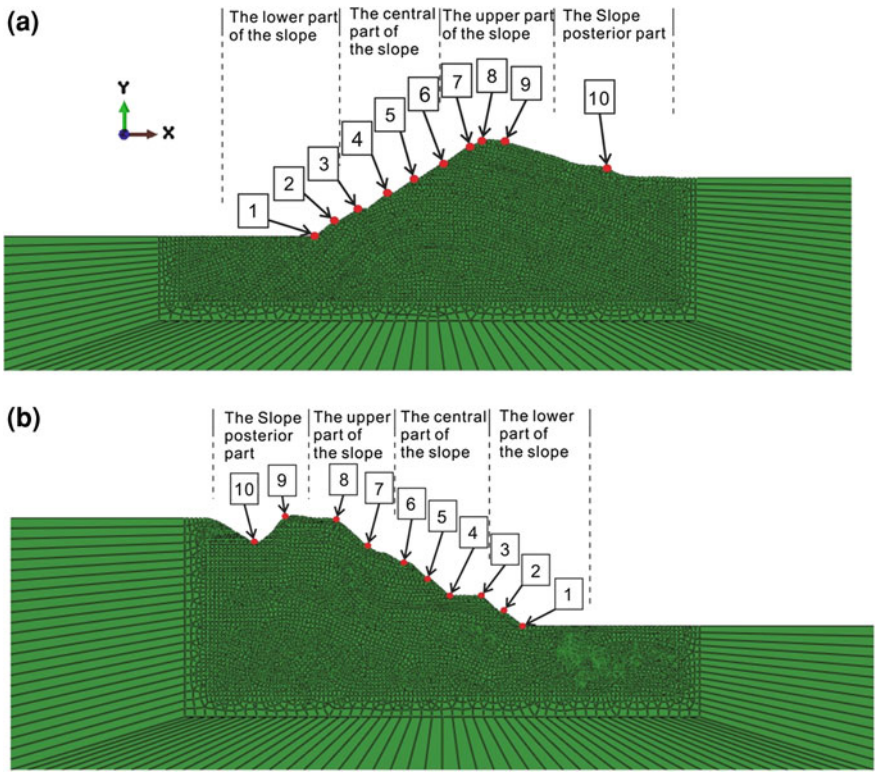

Fig. 23 Output points of slope models around Shimane Nuclear Power Plant. **a** Output points of north–south direction slope. **b** Output points of east–west direction slope

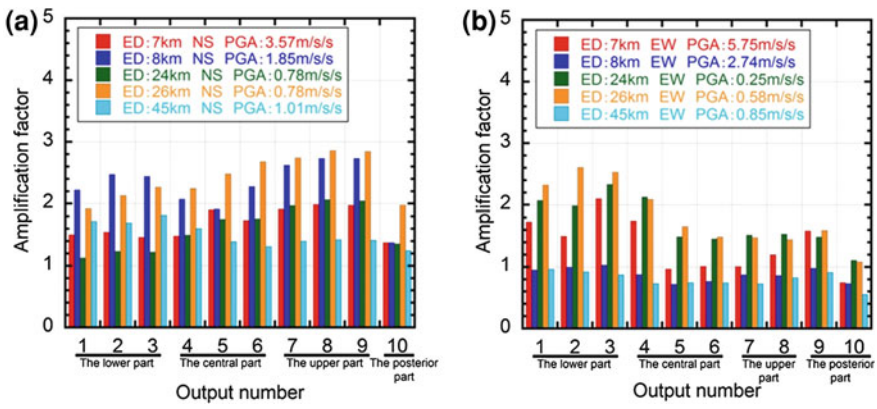

Fig. 24 Amplification factor of slope models around Shimane Nuclear Power Plant. **a** Amplification factor of north–south direction slope. **b** Amplification factor of east–west direction slope

7 Conclusions

The following conclusions were drawn from our study of the effect of topography and dip angles on slope seismic acceleration using FEM program ABAQUS.

1. For amplification effect due to different seismic movement, amplification factor of the slope with height of 100 m and slope angle of 30° becomes lower when the epicentral distance and distance from earthquake source fault is large; however amplification factor on other slopes does not show obvious change.
2. For amplification effect due to topographic conditions, amplification factor of the slope crest and the middle section becomes relatively low when the slope height is large. Amplification factor of the slope crest and toe becomes relatively high when the slope angle is large; however amplification factor of the slope toe becomes relatively low.
3. For amplification effect due to geological structure, amplification tendency does not show obvious difference on the dip angles of the beds.
4. For slopes affected by topography and geologic conditions, possible sliding surface becomes high as slope angle increases. When the dip angle of the bedding plane is lower than the angle of inclination of the slope, sliding surface appears along the weak layer. When the dip angle of the bedding plane is larger than the angle of inclination of the slope, the sliding surface appears without being affected by the beds.
5. Slopes in the north–south aris around the Shimane-NCPP show higher amplification factor near the slope crest, while the east–west trending slopes around the Shimane-NCPP show higher amplification factor near the slope toe.
6. FEM ABAQUS is a useful tool for dynamic analysis of slope response under seismic loading.

References

Athanasopoulos GA, Pelekis PC, Leonidou EA (1999) Effects of surface topography on seismic ground response in the Egion (Greece) 15 June 1995 earthquake. Soil Dyn Earthq Eng 18:135–149

Bateer H, Ishii Y, Maruyama K, Terada H, Suzuki S, Nakamura A (2011) Distribution and scale of landslides induced by recent reverse-fault earthquakes in Japan. J Jpn Landslide Soc 48(1):23–38

Brennan AJ, Madabhushi SPG (2009) Amplification of seismic accelerations at slope crests. Can Geotech J 46:585–594

Cetin KO, Isik N, Unutmaz B (2004) Seismically induced landslide at Degirmenedere Nose, _Izmit Bay during Kocaeli (_Izmit)—Turkey earthquake. Soil Dyn Earthq Eng 24:189–197

Chugoku Electric Power Company (2000) Permit application of construction change of Shimane nuclear power plant and nuclear reactor. Change of the nuclear reactor facility first and second and additional building of the nuclear reactor third

Digital Strong-Motion Seismograph Network KiK-net. http://www.kik.bosai.go.jp/kik/

Gazetas G (1987) Seismic response of earth dams: some recent developments. Soil Dyn Earthq Eng 6(1):3–47

Hoek E (2000) Rock engineering (Course notes). Available for downloading at 'Hoek's Corner': http://www.rocscience.com/education/hoeks_corner

Horikawa H, Sekiguchi H, Iwata T, Sugiyama Y (2001) A fault model of the 2000 Tottori-ken Seibu earthquak. Active fault and Palaeoseismicity research, report, No.1, pp. 27–40

Japan Society of Engineering Geology (2010) Engineering geology of Chugoku and Shikoku area, p 9

Kurooka K, Sogabe A, Iwata N (2005) A cause and estimation of physical characteristic of clay seam in Shimane nuclear power station. Japan Society of Engineering Geology Chugoku and Shikoku Branch Office

Ludwig WJ, Nafe JP, Drake CL (1970) Seismic refraction. In: Maxwell A (ed) The sea, vol 4. Wiley Inter Science, New York, 4, pp 57–84

Luzi L, Pergalani F (2000) A correlation between slope failures and accelerometric parameters: the 26 September 1997 earthquake (Umbria–Marche, Italy). Soil Dyn Earthq Eng 20:301–313

Qi WH (2011) FEM seismic analysis on the effect of topography and slope structure for landsliding potential evaluation. Master Thesis for National Graduate Institute for Policy Studies, Tsukuba, Japan

Qi SW, Wu FQ, Sun JZ (2003) general regularity of dynamic response of slopes. Science in China (Series E), 46 (suppl.): 120–132

Sepulveda SA, Murphy W, Jibson RW, Petley DN (2005) Seismically-induced rock slope failures resulting from topographic amplification of strong ground motions: the Case of Pacoima Canyon, California. Eng Geol 80:336–348

Wang CY, Wang SJ (1987) Seismic stability of slope of Er'tan reservoir. Engineering Geomechnics problem of rock mass (7th). Science press, Beijing, China

Xu GX, Yao LK, Li ZH, Gao ZM (2008) Dynamic response of slopes under earthquakes and influence of ground motion parameters. Chin J Geotech Eng 30:918–923

Xu Q, Liu H, Zou W, Fan X, Chen J (2010) Large scale shaking table test study of acceleration dynamic response characteristics of slopes. Chin J Rock Mech Eng 29(12):2420–2428

Yamaguchi U, Nishimatsu Y (1991) Rock mechanics handbook (3rd). pp 142–144

Experimental Study on the Influence of Cable Diameters on the Impact Forces Caused by Submarine Landslide

Tomokazu Sonoyama, Fawu Wang, Mitsuki Honda and Yohei Kuwada

Abstract Recently, it has been known that submarine communication cables are frequently cut by submarine landslides and turbidity currents. When a cable failure occurred, the economic loss is vast for cable restoration coupled with temporary or permanent breach in the stop of the information transmission. The aim of this study is to use experimental approach to analyze and understand the mechanism and effect of submarine landslides on communication cables. Experiments were carried out considering for factors: (1) Effect of motion velocity of submarine landslide; (2) Effect of submarine landslide volume; (3) material composition of the landslide; and (4) Effect of different diameters of cable. Result obtained from the experiment shows that the impact force on the communication cable model is high for submarine landslides with low motion velocity. It was observed that a critical velocity exists for the impact force. The impact forces decreases until the velocity gets to the critical point, and then it turns to increase with the velocity. In addition, larger cables are subjected to larger impact forces. When the diameter of the cable is increased by 14 %, the impact force also increase by 50 %.

Keywords Submarine landslides · Turbidity currents · Cable · Impact force · Velocity · Cable diameter

T. Sonoyama (✉) · F. Wang · M. Honda · Y. Kuwada
Department of Geoscience, Shimane University, Matsue, Nishikawatsu 1060, Shimane 690-8504, Japan
e-mail: tomokazu.sonoyama@gmail.com

F. Wang et al. (eds.), *Progress of Geo-Disaster Mitigation Technology in Asia*, Environmental Science and Engineering, DOI: 10.1007/978-3-642-29107-4_28,

1 Introduction

Communication cables that cross the oceans between continents all over the world are an essential system and very important for international communication. These cables may be damaged due to the occurrence and motion of submarine landslides, causing interruption in data transmission and international data transmission, and even of international communications. The economic loss is vast when cables are cut, due to the cost of cable restoration and the loss of information transmission. For instance, many communication cables were cut in the south sea of Taiwan after an earthquake in December 2006. Based on broken time records of the cables, it was concluded that a landslide was triggered by the earthquake, and the cables were cut by the impact of submarine landslides which emanated from the continental slope towards the deeper part of the sea (Hsu 2008). According to a report by ICPC (2009), there were 2162 cable breaks globally between 1960 and 2006. Of these at least 20 % were directly influenced by submarine landslides or turbidity currents.

Submarine landslides were initially studied for the need of resource development in the ocean (Shanmugam 2000). For the purposes of clarifying the mechanisms of geo-hazards such as tsunami, many investigations and exploration have been conducted in the ocean of North Europe, especially in Norway and the United States. Geophysical approaches have mainly been employed during field investigations, and the topographic features of the oceans have gradually been clarified. It has been observed that common features of submarine landslides are that: (1) the motion of submarine landslides influences large areas; (2) the motion can continue even at very gentle slopes, as low as 0.1° (Kokusho and Takahashi 2008). Mohrig et al. (1998) conducted model tests in the laboratory and confirmed that the mechanism of submarine landslides involves a hydroplaning phenomenon, i.e., a water layer is formed at the base of the submarine landslide during its motion. The hydroplaning phenomenon can result in low shear resistance of the submarine landslide, so that it moves for long distance even at a gentle slope.

Many features of submarine landslides and the damage they cause to communication cables are unclear, because these events occur beneath the sea's surface. Direct observation of submarine landslides would be extremely expensive and difficult because of their unpredictability. Our interest in submarine landslides lies in disaster mitigation of communication cables. In this study, we seek to understand the impact of submarine landslides on communication cables. For this purpose, an apparatus to simulate the relative motion of submarine landslide and cable was developed in the laboratory and series experiments were conducted. Although it is difficult to reproduce the deep water conditions, we hope the test results can provide some hints for communication cable design and cable positioning in the ocean.

2 Submarine Landslide Apparatus

An experimental apparatus to study submarine landslide was developed for this study. The apparatus consists of a wheel-shaped hollow disc with an axle shaft at the center and a trough at the inner circumference. The axle is connected to a motor so the apparatus can rotate in the vertical plane. The trough of the circular disc contains mixtures of sand and water used in simulating the submarine landslide. Under the action of gravity, water and soil always stay in the lower part of the apparatus. When the frame of the apparatus is rotated, the water and soil mix, and motion relative to the frame bottom occurs in a similar way to a submarine landslide or gravity flow. In this paper, we use the term "landslide" to refer to mass motion, and use the term "gravity flow" to refer to the motion of a flowing mixture.

Figure 1 is a sketch showing water and soil in the apparatus and the sensor settings (Wang et al. 2011). The height of the apparatus is 1.9 m, while the diameter and thickness of the rotatory part are 1.8 m and 0.4 m, respectively. The maximum height of water and soil in the apparatus (lower part) is 0.3 m. Three types of sensors were set at the bottom center of the rotatory frame. These are: (1) shear stress sensors to measure the shear resistance at the bottom of the landslide model. Six main sensors were set at equal intervals, and three additional sensors were installed in one interval; (2) Normal stress sensor. This is used to measure the normal stress generated by water and soil when the sensor comes to the lowest point; (3) Pore water pressure transducer. This is used to measure the maximum water pressure when the sensor reaches the lowest point. In point [A] of Fig. 1, the normal stress sensor, pore water pressure transducer, and one of the six main shear stress sensors are located along one line parallel to the axle, so that the three sensors can reach the lowest point at the same time. Using the pore water pressure data, it is easy to find the lowest point. Using the data at the lowest point, the apparent frictional coefficient during the rotation of the apparatus rotation can be obtained from dividing the shear resistance by normal stress. This parameter can be used to evaluate the mobility of the model landslide.

A model cable is set above point [A] to measure the force of impact by the mixture of water and soil. The comparison between the impact force and landslide mobility can be conducted because the cable and the set of sensors are located at the vertical line when point [A] comes to the lowest point. The height and diameter (size) of the cable can be changed for different tests.

The speed of the rotary part of the apparatus is controlled by a motor connected to a power source. The speed at the bottom of the rotatable part ranges between 0.013 and 0.78 m/s. A data logger and battery were fixed in the axial part of the apparatus, so that data collection is carried out in an independent unit.

The main purpose of the apparatus is to simulate the movement of submarine landside relative to the ocean bottom and the cable. In actual cases, the ocean bottom is fixed and the landslide moves. In our apparatus, the landslide body is kept in the lower part while the frame is rotated. In real cases, the lengths of submarine

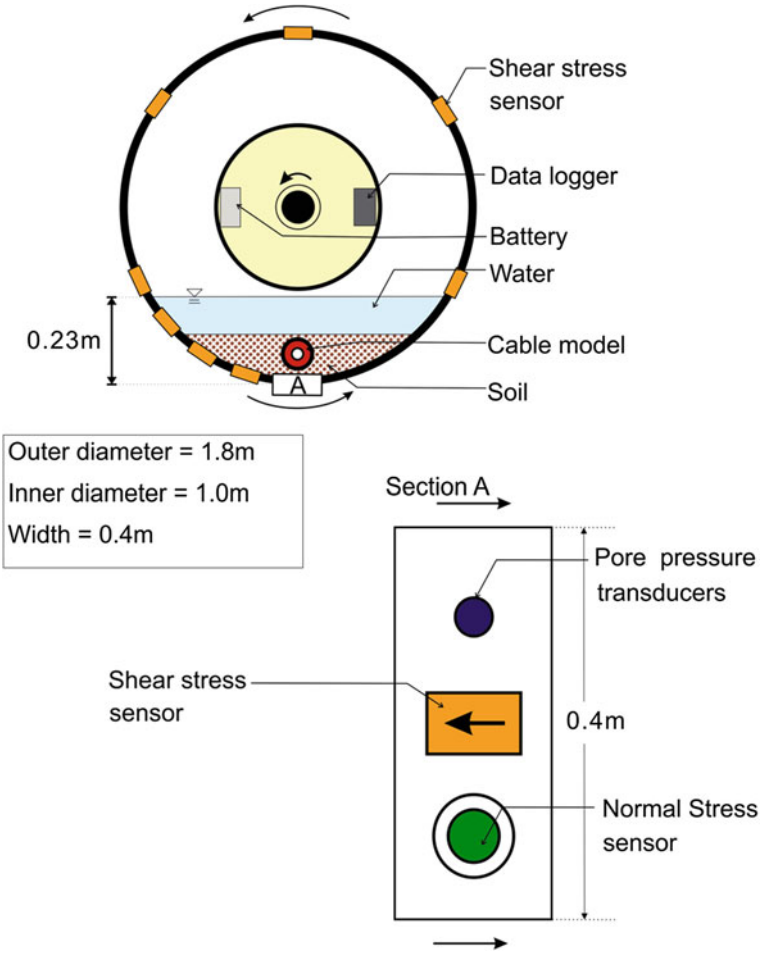

Fig. 1 Sketch showing water and soil in the apparatus and sensor setting

communication cables are always in hundreds or thousands of kilometers, so axial deformation is hardly observe. In the model test, the two ends of the model cable are fixed, and the impact force from moving water and soil can be measured.

3 Properties of the Soil Sample Used in the Test

Silica sand no.7 and no.8 were used in this test. Silica sand is a construction material mainly used in civil and geotechnical engineering works. It has a uniform grain size distribution with 92–98 % quartz and small amount of feldspar. Grain shapes are angular to sub-angular. Table 1 shows the properties of the two samples.

Table 1 Properties of the testes soil samples

Properties	Silica sand no.7	Silica sand no.8
Specific gravity	2.64	2.64
Maximum void ratio	1.30	1.594
Minimum void ratio	0.71	0.778
Mean grain size (mm)	0.16	0.045
Effective grain size D10 (mm)	0.09	0.018
Uniformity Coefficient (Uc)	2.1	3.17

4 Model Cables Used to Measure the Impact Force

Cables with different diameters are used in practice. Their diameters range from 17 mm to 55 mm. Thicker cables are used in shallow waters near coastlines to prevent damage from fish and human activity, whereas thinner cables are used in deep ocean floors. Most landslides occur in deep oceans, and hence thin cables are generally those cut by such events. For example, the submarine landslides and turbidity currents that destroyed cables during the 2006 Taiwan earthquake were mostly generated at a depth of 2,500 m or less (Hsu 2008). In our tests, vinyl chloride cables of diameters, 19 mm, 21 mm, 23 mm, and 25 mm, were used as model cables. These diameters are almost similar to the sizes of cables used in deep seas, and are almost the same as those destroyed in the 2006 earthquake in Taiwan.

Length of the model cables is 0.378 m. Two screw holes were made at both ends to fix the cable to the frame of the apparatus. To measure the impact force, strain gauges were fixed onto the model cable as shown in Fig. 2. Five strain gauges were positioned at equal intervals on the front and back sides of the model cable, forming three channels (ch). There were two gauges in ch1, four gauges in ch2, and four gauges in ch3, respectively. The strain gauges can measure the deformation or strain on the cable caused by the impact force from the submarine landslide model. Through calibration with known load, the impact force can then be obtained.

Considering the actual case, only sediments move on the seafloor, and sea-water keeps stable related to the seafloor, it is necessary to obtain the impacted force caused by the sediment motion only. For this purpose, the impact forces caused by water were obtained by the water-only-test at different rotating velocity with different cables. Through subtracting the impacted force caused by water only from the measured impact force caused by the mixture of sediments and water, the impacted force caused by sediments only can be obtained.

5 Test Results With the Model Cables

In this study, four types of tests were carried out to investigate the effect of landslide motion velocity, landslide volume, material composition of submarine landslides, diameter and setting height of cables. The details are listed below.

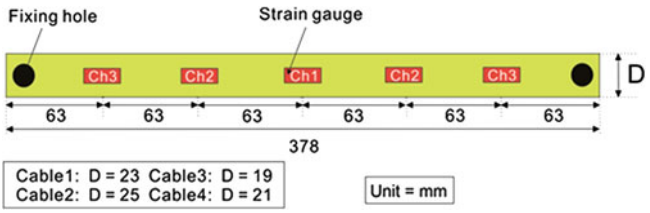

Fig. 2 Strain gauge installed cable model

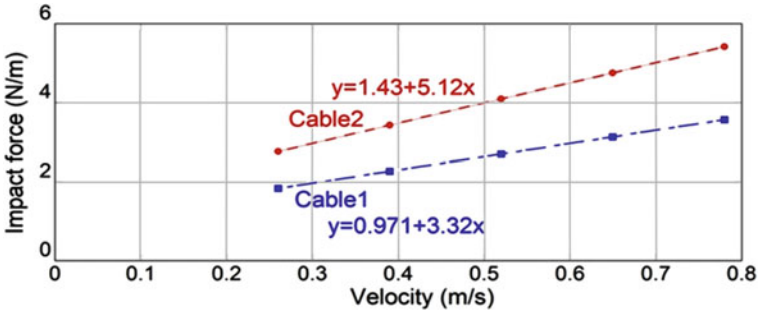

Fig. 3 Impact force due to water for four cables at different rotation velocity

1. Tests were conducted at five different constant velocities, i.e., 0.26 m/s, 0.39 m/s, 0.52 m/s, 0.65 m/s, and 0.78 m/s;
2. Tests were conducted at eight different of sand samples, i.e., dry mass amount of 10 kg, 20 kg, 30 kg, 40 kg, 50 kg, 60 kg, 70 kg, and 80 kg, respectively;
3. Two types of soils (silica sand no.7 and no.8) were used in different tests to observe the effect of soil type;
4. Two types of cable model with diameters of 0.023 m (i.e., cable-1) and 0.025 m (cable-2) were used to evaluate the effect of cable thickness.

In these tests, the cable model was set at a height of 0.08 m above the bottom of the rotatory part (point A in Fig. 1). The maximum depth of the water and soil mixture was fixed at 0.23 m for all tests. To obtain the impact force due to water, water-only-tests were conducted at first, and the results for cable-1, 2, 3 and 4 are shown in Fig. 3.

6 Tests with Different Mass at Different Velocity

Figure 4 shows result of one of the analysis. Silica sand no. 7 of mass, 40 kg was used in the analysis. Rotation velocity was 0.26 m/s. The peak normal stress was 3.2 kPa, and peak pore water pressure was 2.1 kPa. Peak effective stress was

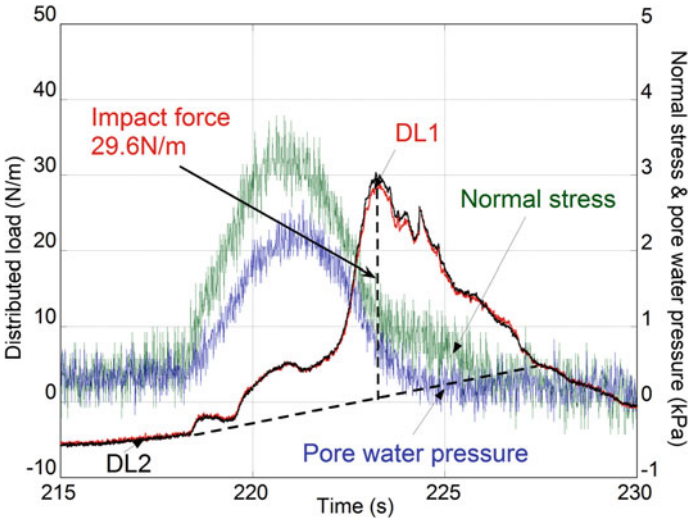

Fig. 4 Test results with silica sand no.7 (40 kg) rotated at a velocity of 0.26 m/s

computed to be 1.1 kPa. With a time lag to the peak normal stress and pore water pressure, the peak impact force was the result obtained for the peak impact force is 29.6 N/m. During the test, we observed that the landslide moved as a mass, as a mass due to the very low rotation velocity of the apparatus.

Figure 5 shows the results when the rotation velocity was increased to 0.78 m/s and kept constant. Compared with the results in Fig. 4, the impact force clearly became smaller, and reached a value of 6.27 N/m. During this test, we observed that the soil and water were well mixed, forming a homogenous dense fluid. We describe the mixture for the test shown in Fig. 4 as a landslide, and that in Fig. 5 as a gravity flow. When the landslide mass transforms to a gravity flow, impact force decreased considerably.

7 Tests with Different Soils

The tests with two different soils showed different tendencies. Figure 6 shows a test result with silica sand no.8, using silica sand no.8 (40 kg) as an example. At the lowest velocity of 0.26 m/s, an impact force of 6.07 N/m was obtained. This impact force is considerable smaller than that obtained from the same test with silica sand no.7.

In Fig. 7, impact forces obtained from the tests with silica no.7 and no.8 are plotted together for comparison. The plot shows that: 1) the impact forces in test with silica sand no.8 are generally smaller than those of silica sand no.7; 2) Silica sand no.8 did not behave as a mass, but behaved as a semi-viscous flow which have lower impact force.

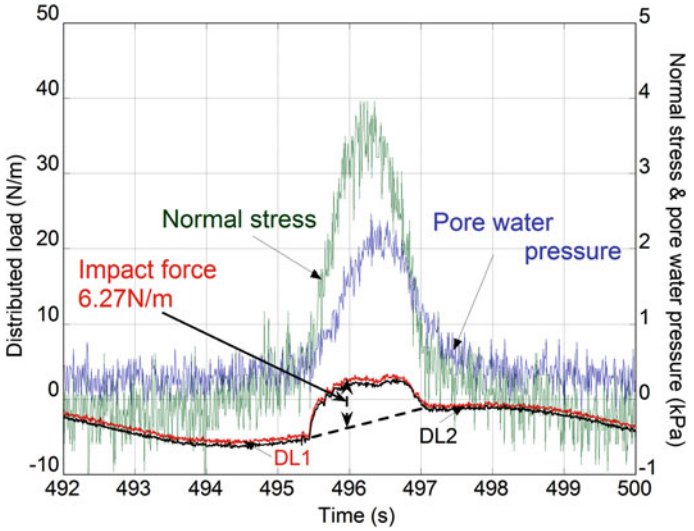

Fig. 5 Test results with silica sand no.7 (40 kg) rotated at a velocity of 0.78 m/s

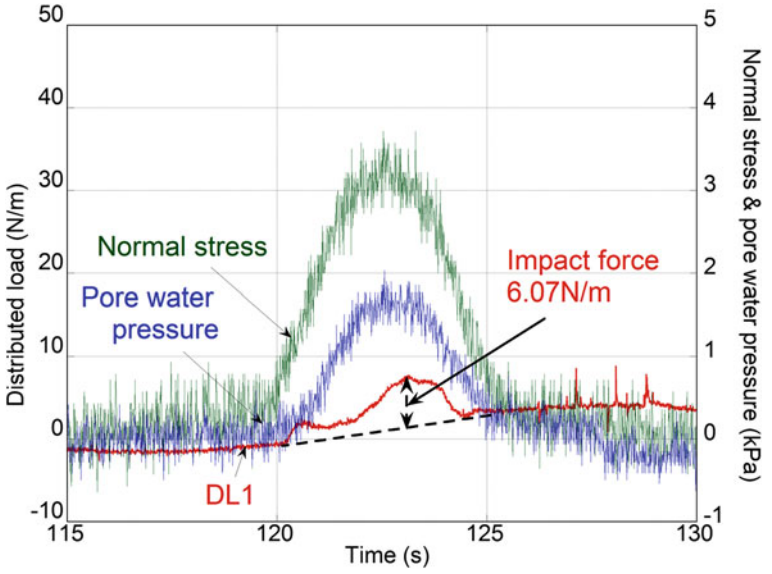

Fig. 6 Test results with silica sand no.8 (40 kg) rotated at a velocity of 0.26 m/s

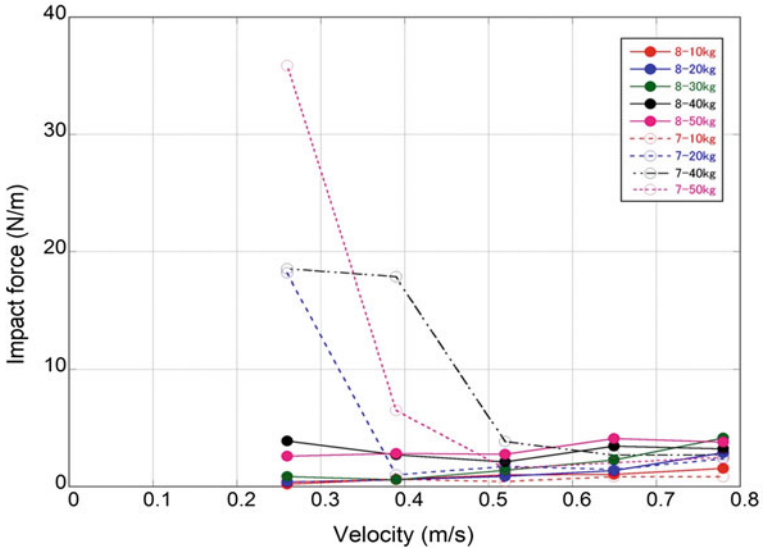

Fig. 7 Test result comparison between silica sand no.7 and no.8

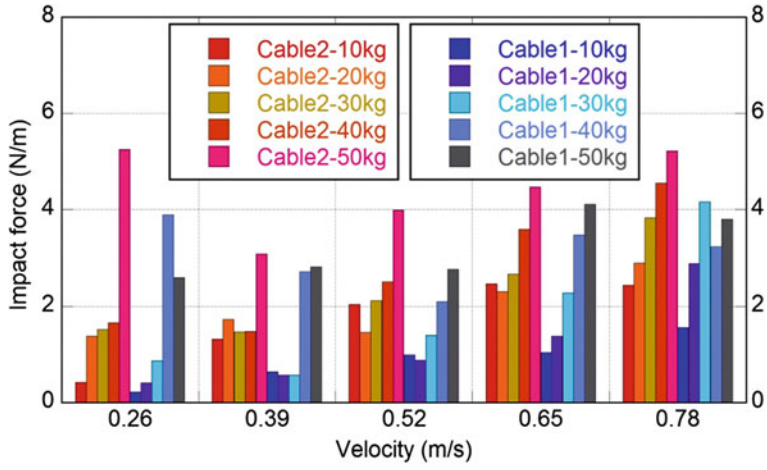

Fig. 8 Test result comparison by using Cable-1 (0.023 m diameter) and Cable-2 (0.025 m diameter)

8 Test with Different Cable Models

Figure 8 shows results obtained by using cable models with different diameters. Cables with diameters of 0.022 m and 0.025 m are referred to as Cable-1 and Cable-2, respectively. The mass quality used in the test is also shown in the legend. Obviously, the larger diameter cable is subjected to larger impact force. Although

the difference in diameter is as small as 3 mm (about 14 % of the cable diameter), the impact forces in Cable-2 are almost 1.5 times greater than cable-1 averagely.

9 Conclusions

Our preliminary test results have been presented in this paper. Although the dimension of the test apparatus are quite small compared to actual submarine landslides, and the difficulty in obtaining quantitative results from these experiments, some qualitative tendencies related to the impact on cables from submarine landslides were obtained. Conclusions from the model tests and work planned for the next stage of research are given below.

1. At the same rotation velocity, impact force increased with increased soil volume. Next phase of this research will concentrate on evaluating the heights of the two layers formed during the analysis (muddy water in the upper layer, and landslide mass or turbidity flow in the lower layer) should be measured. Methods of measuring the degree of turbidity or density, method to evaluate Reynolds number and Froude number must be developed.
2. Larger cables are subjected to high impact forces. When the diameter of the cable is increased by 14 %, the impact force became to 1.5 times greater. To clarify the relationship between cable diameter and impact force, we recommend that a higher number of different sized cables be used in subsequent analysis.
3. The sliding body shows different behavior depending on the velocity. When the velocity was small, it behaved as a sliding mass, but when the velocity was high, it became a turbidity flow. The tests show that the velocity at the turning point depends on the volume of the soil mass. The next stage of this study will try to analyze the factors affecting the critical velocity at the turning point should be clarified in the next stage.
4. Samples with silica sand no.8 behaves as gravity flow at lower velocity than that of silica sand no.7. This may be due to higher buoyancy potential for finer grain size than for coarser grains.

Acknowledgments This study was funded by a scientific research grant (No. 20310109) from the MEXT of Japan. Okeke Austin checked and corrected English of this paper.

References

Hsu SK (2008) Turbidity currents, submarine landslides and the 2006 Pingtung earthquake off SW Taiwan. Terr Atmos Ocean Sci 19(6):767–772

ICPC (2009) Submarine cables and the oceans: connecting the world. 11–25:29–53

Kokusho T, Takahashi T (2008) Earthquake-induced submarine landslides in view of void redistribution. Geotechnical Engineering for Disaster Mitigation and Rehabilitation (Eds: Liu HL, Deng A, Chu J.), Nanjing, China, 2008. Part 3:177-188

Masson DG (2006) Submarine landslides: processes, triggers and hazard prediction. Phil Trans R Soc A15 364:2009–2039

Mohrig D, Whipple KX, Hondzo M, Ellis C, Parker G (1998) Hydroplaning of subaqueous debris flows. Geol Soc Am Bull 110:387–394

Shanmugam G (2000) 50 Years of the turbidite paradigm (1950s–1990s): deep-water processes and facies models-a critical perspective. Mar Pet Geol 17:285–342

Wang FW, Sonoyama T, Honda M (2011) Experimental study on submarine landslide impact forces acting on cables. In: Proceeding of International Conference and Field Trip on Landslides (ICFL-Japan-2011), Nagaoka—Kyoto—Kochi 45–53

Sonoyama T, Wang FW, Honda M (2011) Experimental study on the influence of diameter and setting height of cables on the impact forces caused by submarine landslide. In: The Ninth International Symposium on Mitigation of Geo-disasters in Asia, Yogyakarta 83–87

Numerical Simulation of Failure Process of the Qianjiangping Landslide Triggered by Water Level Rise and Rainfall in the Three Gorges Reservoir, China

Hufeng Yang, Wenxing Jian, Fawu Wang, Fanhe Meng and Austin Chukwueloka Okeke

Abstract The Qianjiangping landslide is a large translational rock slide which occurred in July 14, 2003 shortly after the water level reached 135 m in the Three Gorges Reservoir, China. The landslide destroyed 346 houses, took 24 lives and rendered 1,200 people homeless. In order to understand the failure process of the landslide, numerical simulation was conducted on Qianjiangping slope before sliding. Based on pre-failure characteristics and structural conditions of the landslide, topographic and geological profile of Qianjiangping slope was reconstructed. Seepage field of the Qianjiangping slope before sliding was simulated with the SEEP/W module of GeoStudio software. The results show that the groundwater table rose and infiltrated into the slope during the rise in water level, and the slope surface became partially saturated during the period of continuous rainfall. Using the groundwater table data, the failure process of the Qianjiangping slope was simulated with Flac^{3D} software. The result shows that the shear strain increment, displacement and plastic state region of the slope increased greatly after water level rise and continuous rainfall. Consequently, the landslide was triggered by the combined effects of water level rise and rainfall. The simulated results of the shear strain increment, displacement and plastic state region of the slope show that the failure surface was located in the weak carbonaceous shale layer, and was retrogressive in the lower part of the slope and progressive in the upper part. Analysis of the simulation results before and after the

H. Yang · F. Wang (✉) · A. C. Okeke
Department of Geoscience, Shimane University, Matsue, 690-8504 Shimane, Japan
e-mail: wangfw@riko.shimane-u.ac.jp

W. Jian
Three Gorges Research Center for Geo-hazards, Ministry of Education,
China University of Geosciences, Wuhan, 430074 Hubei, China

F. Meng
Guangxi Communications Planning Surveying and Designing Institute,
No.1 Beiyili, Renmin Road, Nanning, 530011 Guangxi, China

F. Wang et al. (eds.), *Progress of Geo-Disaster Mitigation Technology in Asia*,
Environmental Science and Engineering, DOI: 10.1007/978-3-642-29107-4_29,

water level rise and rainfall, it was observed that reservoir water level rise was the main triggering factor for the Qianjiangping landslide.

Keywords Numerical simulation · Qianjiangping landslide · Water level rise · Rainfall · Three Gorges Reservoir

1 Introduction

The Qianjiangping landslide is located in Shazhenxi Town beside the Qinggan-he River, a tributary of the Yangtze River (Fig. 1). It is a large translational rockslide which occurred in July 14, 2003 shortly after the water level in the Three Gorges Reservoir rose to 135 m. This catastrophic landslide destroyed 346 houses, took 24 lives and rendered 1,200 people homeless. The direct economic loss caused by this landslide was about 7 million USD (Wang et al. 2004; Wang et al. 2008). Previous studies on the deformational characteristics and the failure mechanism of the reservoir landslide have been undertaken by many researchers. Wang et al. (2003, 2005) concluded that Qianjiangping landslide was a reactivated landslide based on geotechnical site investigation and geoenvironmental conditions. According to stress history analysis and U-series dating of interbedded shear zone, Li et al. (2008) considered that the Qianjiangping landslide was a first-time rock slide.

The occurrence of Qianjiangping landslide was naturally considered to be the combined effect of reservoir water level rise and continuous rainfall. Results from notable research works showed that the influence of reservoir water level rise was much greater than rainfall effect (Dai et al. 2004; Yin and Peng 2007; Xiao et al. 2007; Wen et al. 2008). However, some researchers proposed that structural vulnerability of the geomaterial and intense rainfall within the region contributed to the landslide, while the reservoir water level rise and slope undercutting accelerated the occurrence of the slide (Liao et al. 2005).

In order to understand the deformational characteristics and the failure mechanism of the Qianjiangping landslide, a detailed numerical simulation was conducted on the seepage field and the failure process of the landslide under water level rise and rainfall effect was analyzed.

2 Geological Conditions

2.1 Geomorphology

2.1.1 After Failure

The Qianjiangping landslide has a characteristic tongue-like shape with slope length of 1,200 m and maximum width of 600 m (Figs. 2 and 3). After the slope

Fig. 1 Location map of the Qianjiangping landslide in the Three Gorges Reservoir, Hubei Province, China (Wang et al. 2004)

Fig. 2 Front-on view of the Qianjiangping landslide (Taken by Zhang, July 15, 2003)

Fig. 3 View of the Qianjiangping landslide from the upstream side of the Qinggan-he River (Taken by Wang, March 15, 2004)

failed, the exposed planar slip surface was found on the main scarp. The toe of the landslide crossed the Qinggan-he River and some of the landslide material were deposited at the opposite bank of the river (Fig. 4). The elevation of the toe of the slip surface was about 100 m. The middle and upper part of the sliding mass slid

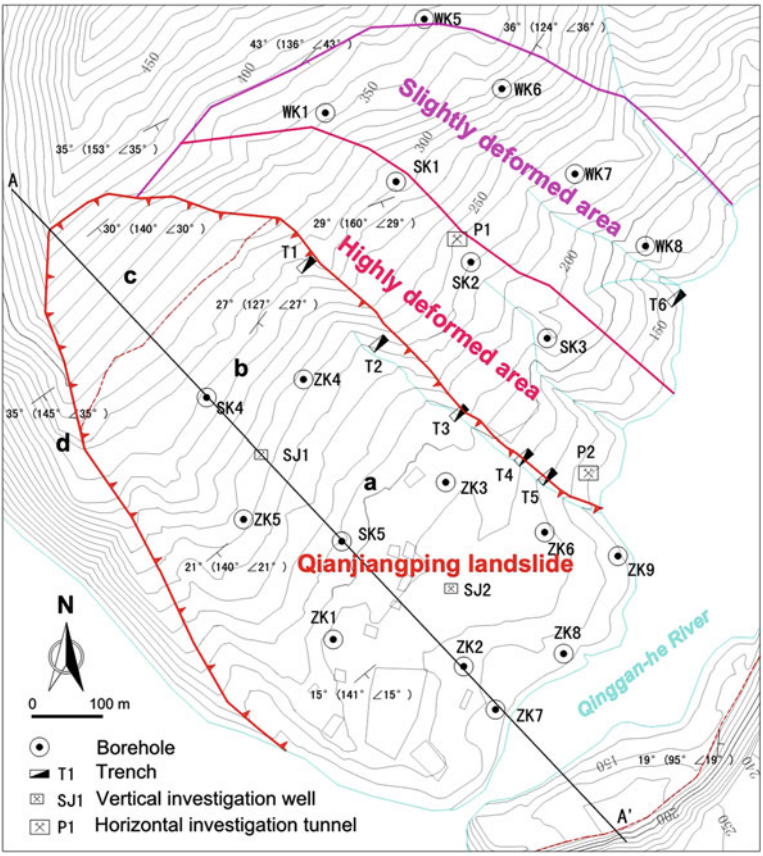

Fig. 4 Topographical map of the Qianjiangping landslide after the 2003 sliding event

along the planar slip surface. A slight rotation and a steep scarp were noticed at the proximal part and left lateral flank of the landslide (Fig. 5).

2.1.2 Before Failure

Figure 6 shows a 3-Dimensional pre-failure stage representation of the Qianjiangping landslide. The site is located on the channel bend of the Qinggan-he River. Two gullies exist at the eastern side of the landslide. The west lateral boundary was open and a cliff existed at the western side of the slope toe which has been reshaped by erosional effects of the Qinggan-he River over a long period of time. Based on these characteristic features and previous geological data of the landslide, the pre-failure topographic and geological profile of the Qianjiangping slope was reconstructed (Fig. 7). From stratigraphic log profile and borehole data, the lithology of the sliding mass was divided into highly weathered layer and slightly weathered layer.

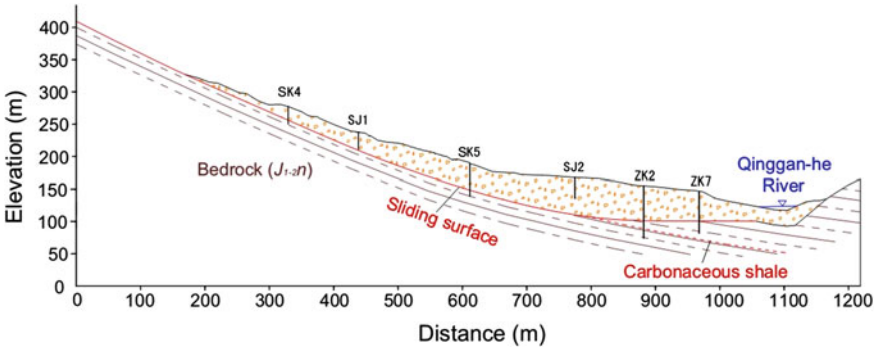

Fig. 5 Main section (A–A′) of the Qianjiangping landslide after the 2003 sliding event

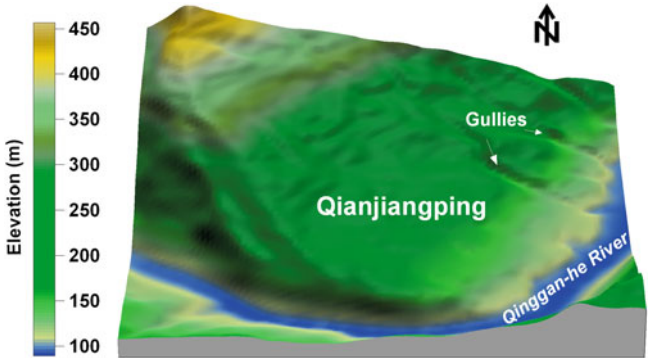

Fig. 6 3-Dimensional pre-failure stage representation of the Qianjiangping landslide

2.2 Lithology

2.2.1 Sliding Mass

The sliding mass is mainly composed of blocky rock mass. The rock mass is comprised of feldspathic-quartz sandstone, fine sandstone, and muddy siltstone interbeds. Fragmented rock mass which dominates the area are slightly to highly weathered. The average thickness of the sliding mass is about 25 m, and the maximum thickness is about 50 m. Because the middle-upper part of the sliding mass slid along a planar surface, the attitude of the strata remained the same with no noticeable discontinuity or rotation (Fig. 8a). However, a slightly rotational movement occurred at the proximal end of the sliding mass (Fig. 5). The strata show a near-horizontal attitude. The disjointed rocky blocks can be found at the upper part of the sliding mass. The volume of each block ranges from 0.5 to 1.0 m^3 (Fig. 8b).

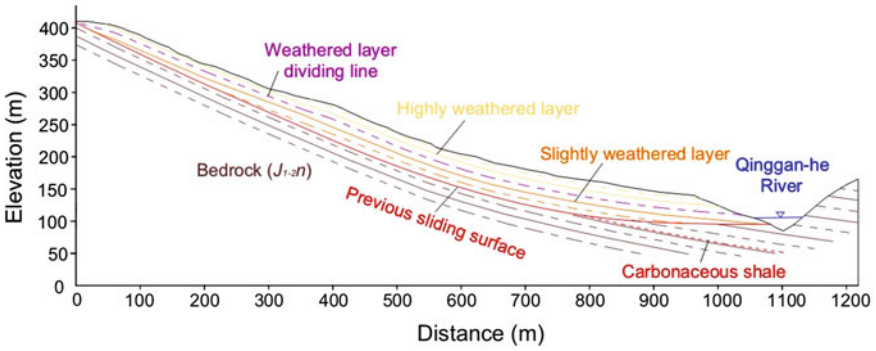

Fig. 7 Reconstructed main section of the Qianjiangping landslide before the 2003 sliding event

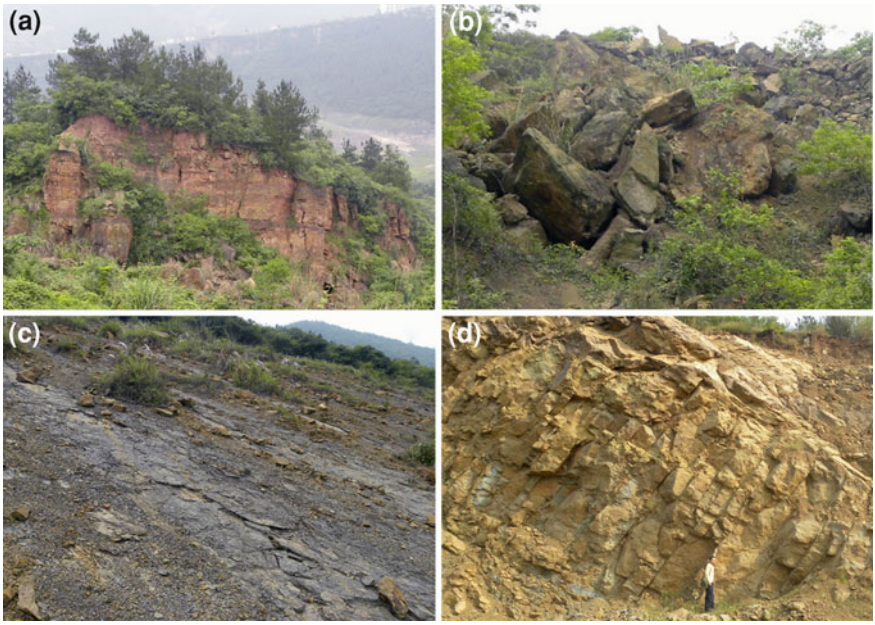

Fig. 8 Photos of **a** blocky rock mass at the middle-upper part of sliding mass; **b** disjointed rocky blocks at the upper part of sliding mass; **c** carbonaceous shale on the main scarp; **d** bedrock near the main scarp. Locations of these photos are shown in Fig. 4

2.2.2 Sliding Zone

After the Qianjiangping landslide occurred, carbonaceous shale was found along the failure surface on the main scarp (Fig. 8c). In order to study the characteristics of the sliding zone, two horizontal investigation tunnels were drilled by the China Three Gorges University in the highly deformed area (Fig. 4). The sliding zone is about 40 cm thick and was in a plastic state.

2.2.3 Bedrock

Composite stratigraphic units in the slope are fine sandstone and silty mudstone of the Lower Jurassic Niejiashan Formation (J_{1-2n}). Field investigation shows characteristic structural features like fractures and joint on the slightly weathered bedrock (Fig. 8d). Analysis of initial stratigraphic log profiles obtained from boreholes after the slope failed indicted that the rock samples in the deeper part of the slope are fresh and consolidated but are weathered at the upper part of the slope.

2.3 Geological Structure

The site is located at a dip-structure slope. The dip directions of the strata range from S30 to S70°E. The dip angle varies from 15 to 30°, with the upper section having a greater dip angle value than the lower section (Fig. 4). Field investigation shows that the driving force that initiated the slope movement was provided by the steep structural style of the rocks. The continuous intercalations of silty sandstone and very weak carbonaceous shale layer within the rocks also contributed to the instability of the slope.

2.4 Hydrogeology

2.4.1 Surface Drainage

Within the landslide site, elevation of watershed ranges from 420 to 560 m. The major river in the area, the Qinggan-he River has several tributaries and gullies with an area of approximately 1 km^2. These gullies naturally remain dry except during rainy season period. Two main gullies are located at the left and right side of the drainage area. During the rainy season period, large volumes of rainfall flows into these gullies, and are discharged into the Qinggan-he River (Fig. 4).

2.4.2 Groundwater Discharge and Recharge

Groundwater data around the Qianjiangping landslide area and its environs are limited. Data obtained from vertical investigation wells drilled on the landslide and horizontal investigation tunnels shows that the phreatic zone within the slope material is very deep below the surface, and groundwater discharge into the tunnels and pits is negligible. Artesian contact springs were observed along planes of discontinuities and contacts between the sandstone and mudstone units. Groundwater recharge is mainly controlled by the amount of rainfall, infiltration rate and level of reservoir water.

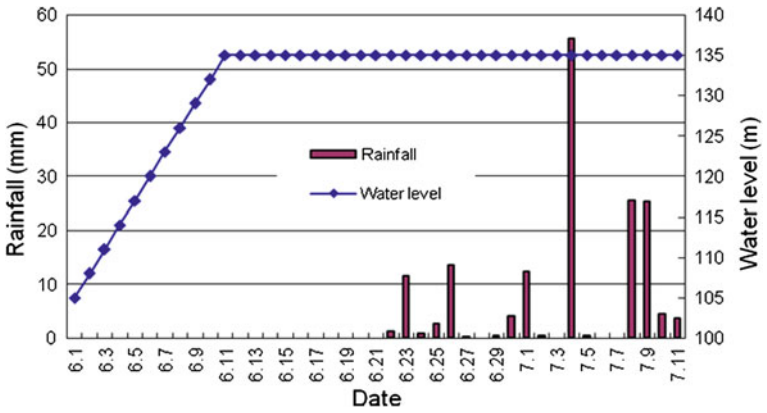

Fig. 9 Diagram of computing conditions

3 Numerical Simulation of Seepage Field

3.1 Computing Conditions

Based on water level variation data obtained from the Three Gorges Reservoir and local precipitation information, the diagram of the computing conditions are shown in Fig. 9. From the figure, it can be observed that the rise in water level was reasonably controlled to maintain a constant inflow rate. The computing conditions were divided into four steps. The first step is the initial condition when the water level is 105 m. The second step is the sudden increase in water level from 105 to 135 m in 10 days (June 1st–11th). Rate of water level increase was 3.0 m per day. The third step is that water level maintained a constant value of 135 m for 10 days (June 11th–21st). The fourth step is that water level maintained a constant value of 135 m with continuous rainfall for 20 days (June 22nd–July 11th).

3.2 Model Setup

A 2-Dimensional numerical simulation model was established based on the reconstructed pre-failure geological profile. The front part of the numerical simulation model reached the riverbed of the Qinggan-he River, while the rear end of the numerical simulation model stopped close to the watershed of the Qianjiangping slope. Figure 10 shows the finite element mesh used to analyze the seepage field. The green, yellow, and orange groups represent highly weathered rock, slightly weathered rock, and bedrock respectively. The thin red layer between the yellow group and the orange group is the sliding zone. The 2-Dimensional model with horizontal distance of 1,130 m and maximum height of 420 m is composed of 6,244 elements and 6,523 nodes.

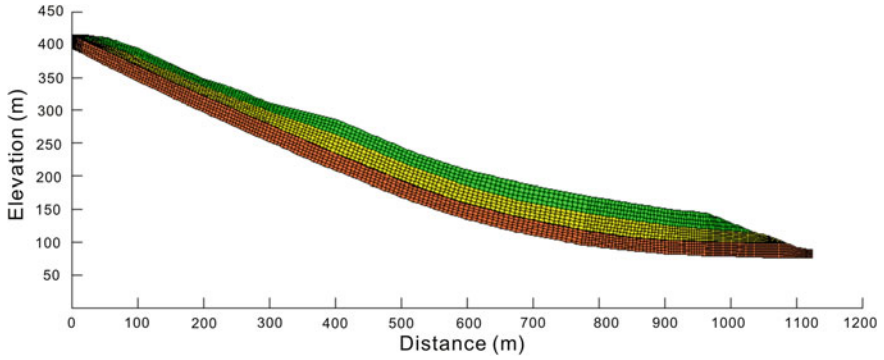

Fig. 10 Mesh for calculation of 2-Dimensional numerical model

The steady and transient state of finite element seepage analyses was simulated using SEEP/W module of GeoStudio software. For the first step (initial condition), the steady-state of finite element seepage analysis was applied. Head (or constant pressure) boundary conditions were specified at the slope toe to simulate the constant water level of 105 m for a long period as the initial condition. For the second, third, and fourth steps, the transient stage of finite element seepage analysis was used to correctly simulate the mechanisms of the reservoir water level rise and rainfall. Unlike the first step, the boundary condition of the slope toe was a head (or constant pressure) versus time function that specified the filling rate of the reservoir. The nodes along the slope surface were specified as flux boundary which is equal to the infiltration rate. No flow boundary condition was assumed for all other boundaries.

3.3 Geotechnical Parameters

Finite element method (SEEP/W module of GeoStudio software) was used for the seepage field simulation. Various soil hydraulic functions are necessary in the solution of the seepage partial differential equation (Eq. 1). Well-defined soil properties are relevant in obtaining a reliable result. Because of the limitation of samples, the difficult task of measuring the unsaturated hydraulic conductivity function directly was overcame by predicting the unsaturated hydraulic conductivity from a predicted volumetric water content function. The SEEP/W module of GeoStudio software has four methods available for developing a volumetric water content function. Based on the test data from previous investigation reports, Fig. 11 shows the volumetric water content functions using Van Genuchten estimation model. Once the volumetric water content functions and saturated hydraulic conductivity have been specified, the hydraulic conductivity function can be estimated using built-in predictive methods of the SEEP/W module of GeoStudio software (Fig. 12).

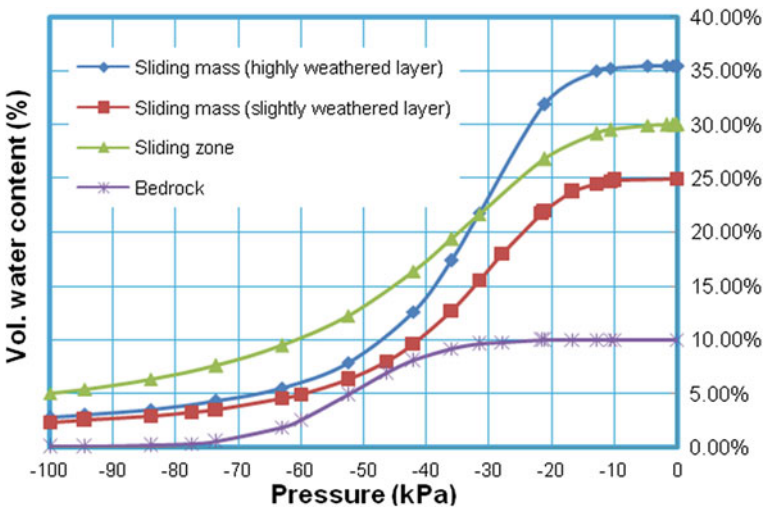

Fig. 11 Volumetric water content function

$$\frac{\partial}{\partial x}\left(k_x \frac{\partial H}{\partial x}\right) + \frac{\partial}{\partial y}\left(k_y \frac{\partial H}{\partial y}\right) + Q = \frac{\partial \theta}{\partial t} \tag{1}$$

where H is the total head, k_x is the hydraulic conductivity in the x-direction, k_y is the hydraulic conductivity in the y-direction, Q is the applied boundary flux, θ is the volumetric water content, and t is the time.

3.4 Simulation Results

3.4.1 Simulation Result of the First Step

Figure 13a shows the phreatic line (blue line) under static initial water level of 105 m. From the simulation result, it can be found that the phreatic line is almost horizontal. The result shows that the phreatic zone is far below the surface. Hydraulic gradient under steady state is negligible. From field hydrogeological investigation, the main gullies on the slope are often dry. In addition, based on data obtained from boreholes, vertical investigation wells and horizontal investigation tunnels, the groundwater table was found to be deep. Therefore, it reveals that the computed result is relevant and can be considered as the initial condition for the next steps.

3.4.2 Simulation Result of Second Step

Using simulation result of the first step as initial condition, seepage field in transient state was computed under rapid rise in water level from 105 to 135 m. Figure 13b

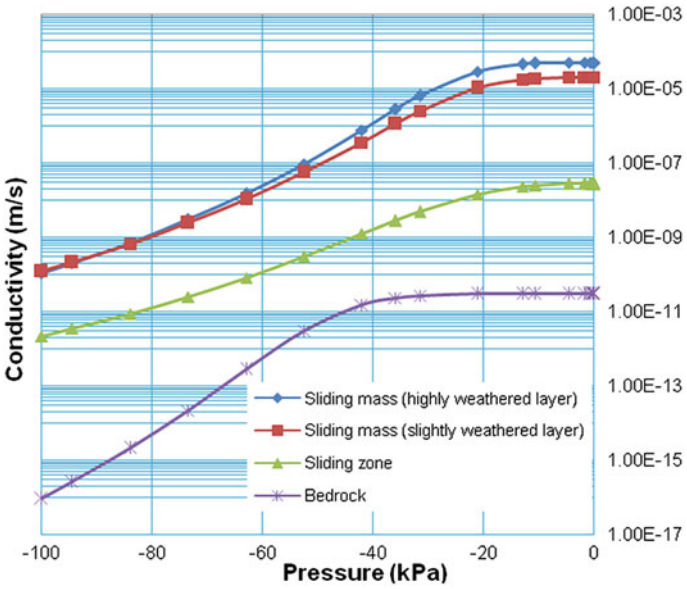

Fig. 12 Hydraulic conductivity function

shows the simulation result of phreatic lines for each day. It can be easily observed that these phreatic lines show a concave upwards pattern as reservoir water flows into the slope mass. The main reason for this phenomenon is that hydraulic conductivity of slope mass is smaller than the speed at which reservoir water level rises. The simulated result shows that only the phreatic line in shallow slope surface under water level rose immediately with water level. While the inside phreatic lines rose with a time lag.

3.4.3 Simulation Result of Third Step

Figure 13c shows the simulation result of the phreatic lines as water level maintained a constant value of 135 m for 10 days. When compared with these phreatic lines for 10 days, the curved phreatic lines became gradually straight. In addition, variation rate of the first few days were bigger than the latter. At the beginning when the water level reached 135 m, the reservoir water rapidly flowed into the slope mass under high hydraulic gradient. As the phreatic lines became relatively straight, the advantage of high hydraulic gradient began to reduce.

3.4.4 Simulation Result of Fourth Step

Figure 14 shows the phreatic lines of the 9th, 13th, 16th and 20th day during early rainy season. Combined with the computing condition, saturated area appeared in the middle part of the shallow slope surface at the 9th day during the early rainy

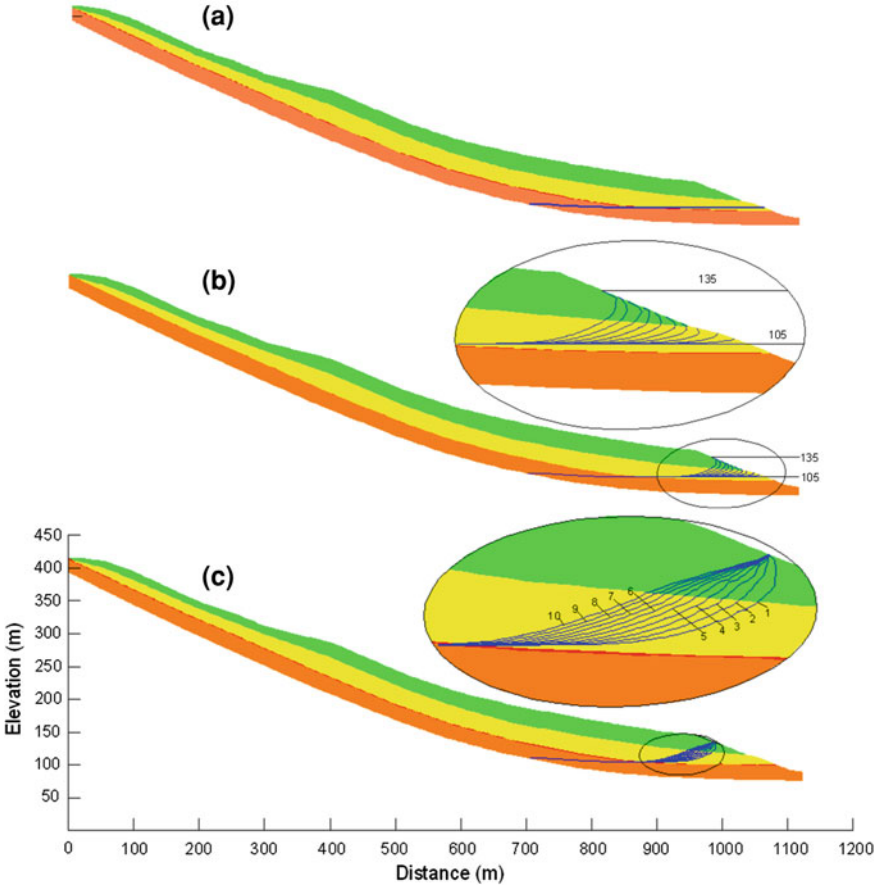

Fig. 13 Phreatic line under initial water level of 105 m (**a**), water level rapid rising from 105 to 135 m (**b**), water level remaining at 135 m for 10 days (**c**)

season (Fig. 14a). Saturated area became larger after heavy rainfall (almost 55 mm) at the 13th day (Fig. 14b). Over the next three days, there were small amount of precipitation. In addition, surface and groundwater gradually infiltrated into the slope mass. Therefore, saturated area of the shallow slope surface became smaller on the 16th day (Fig. 14c). This process was followed by continuous rainfall (almost 60 mm) during the next 4 days. On the 20th day, saturated area of shallow slope surface became larger again (Fig. 14d).

Figure 15 shows the groundwater level of the 1st, 5th, 9th, 13th, 17th and 20th day after it began to rain. Reservoir water continually infiltrated into the slope mass as water level maintained a constant value of 135 m. Groundwater level in the slope mass increased over time as a result of steady influx of reservoir water. Due to the hydraulic conductivity difference between the slide mass and the sliding zone, groundwater level formed an S-shaped curve near the sliding zone.

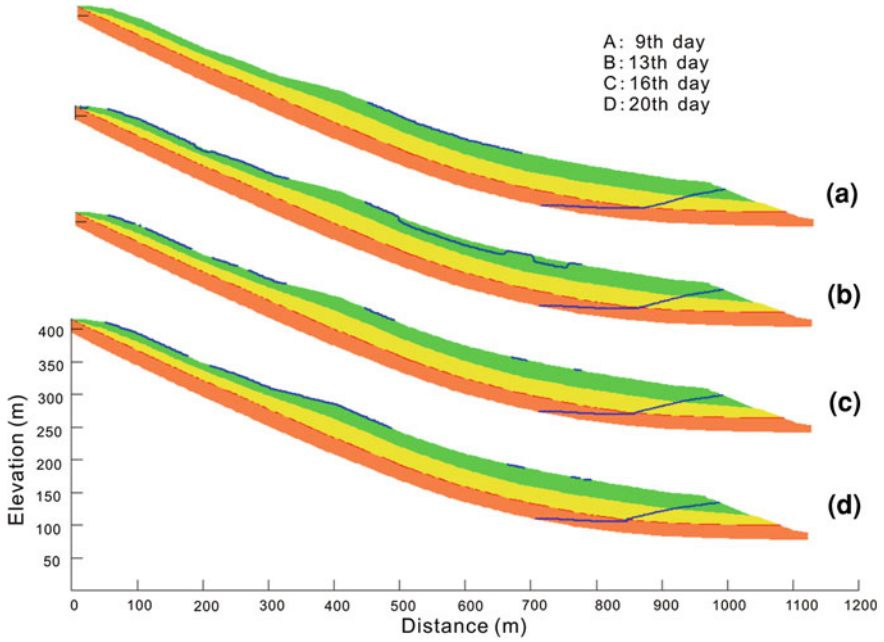

Fig. 14 Phreatic line of the 9th day (**a**), 13th day (**b**), 16th day (**c**), and 20th day (**d**) after rainfall beginning

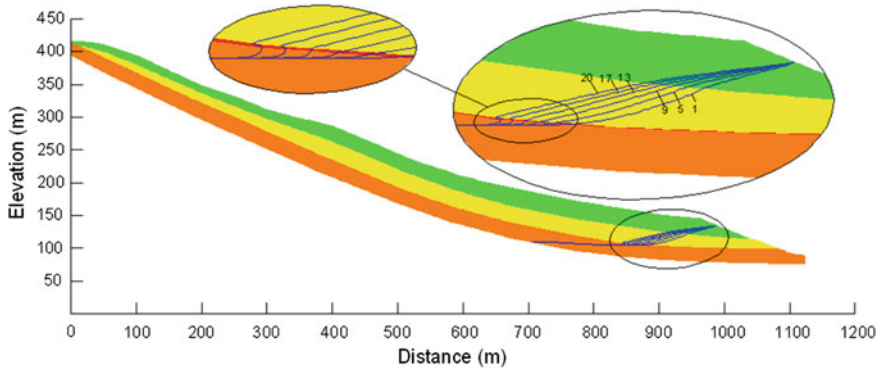

Fig. 15 Groundwater level of the 1st, 5th, 9th, 13th, 17th, and 20th day after rainfall beginning

By analyzing these simulation results, it can be concluded that rainfall primarily affected the saturated area of shallow slope surface while groundwater level at the proximal part of the slope was controlled by the reservoir.

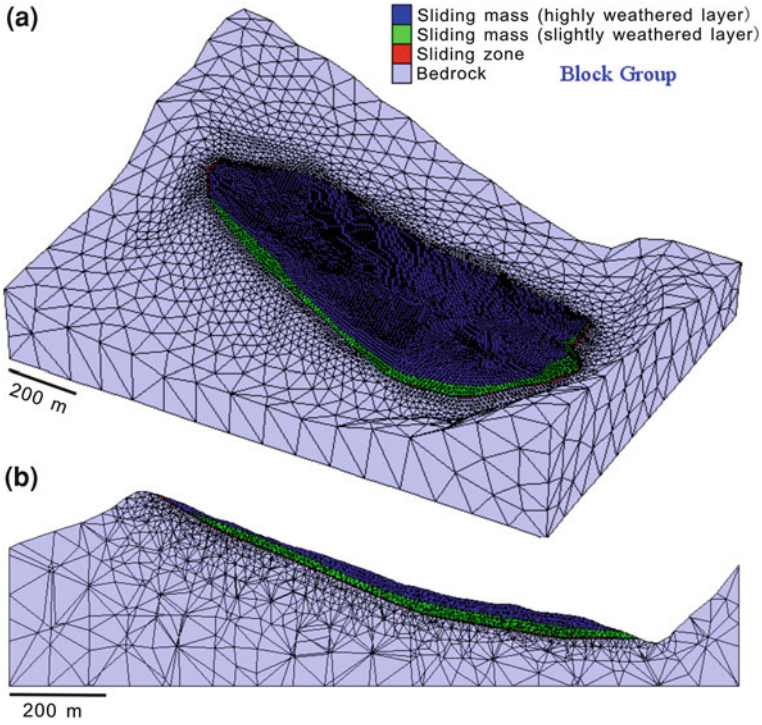

Fig. 16 Mesh for calculation of 3-Dimensional numerical simulation model (**a**) and main section (**b**)

4 Numerical Simulation of Failure Process

4.1 Model Setup

To avoid boundary effect, the size of the numerical simulation model was made to be larger than the size of the landslide. The front boundary of the model crossed the Qinggan-he River and reached the scarp of the opposite bank. The back boundary was beyond the watershed. The right boundary reached the grand scarp and the Qinggan-he River. The left boundary reached the main gully on the Qianjiangping slope.

In this study, finite differences program FLAC^{3D} (Fast Lagrangian Analysis for Continuum in 3-Dimensional) was used to study the failure processes of the Qianjiangping landslide. The mesh for finite difference analysis is shown in Fig. 16. The 3-Dimensional model was composed of 197,538 elements and 41,395 nodes. According to the slope lithology, the materials were divided into four groups: bedrock (light blue group), sliding zone (red group), slightly weathered rock (green group), and highly weathered rock (blue group). Roller boundaries were applied to the four sides and the bottom of the model, while the slope surface was free.

Table 1 Geotechnical parameters for numerical simulation

	Slide mass (highly weathered)	Slide mass (slightly weathered)	Sliding zone	Bedrock
Unite weight (kN/m^3)	22.5	24.5	16.3	25.0
Saturated unit weight (kN/m^3)	23.5	25.5	20	26.0
Bulk modulus (Pa)	6.94×10^8	1.11×10^{10}	4.17×10^7	2.03×10^{10}
Shear modulus (Pa)	1.81×10^8	4.55×10^9	1.92×10^7	1.16×10^{10}
Cohesion (kPa)	100	150	22	4000
Friction angle (°)	30	40	15	42
Tension strength (Pa)	2.0×10^6	4.0×10^6	2.0×10^5	2.0×10^7

For numerical simulation of the failure process, the same computing conditions were used. Based on groundwater level of seepage simulation at the end of each computing step and topographic feature of the Qianjiangping slope, simplified 3-Dimensional groundwater table was obtained to study the failure process using FLAC^{3D}. Then, pore pressure of different computing conditions was assigned to the corresponding nodes of 3-Dimensional numerical simulation model by calculation program respectively.

4.2 Geotechnical Parameters

Majority of the geotechnical parameters were obtained from field investigation reports obtained from the China Three Gorges University. The parameters in the investigation report were determined by laboratory test, in situ test, geotechnical and theoretical analysis. Some parameters were calculated using theoretical formula. The geotechnical parameters are shown in Table 1. For the simulation of failure process using FLAC^{3D}, the slope materials were assumed to be perfectly elasto-plastic and satisfy the Mohr–Coulomb failure criterion. Considering the decrease in shear strength as slope material becomes saturated, the shear strength of the material below groundwater table was reasonably decreased in the calculation program.

4.3 Simulation Results

4.3.1 Simulation Result of Shear Strain Increment

Figure 17 shows the simulation result of shear strain increment under water level increase and rainfall. It is necessary to say that uniform interval value was used to visually show the progressive changes in the process. Therefore, if shear strain increment of some zone is beyond maximum value of the contour, it is represented as a white color zone.

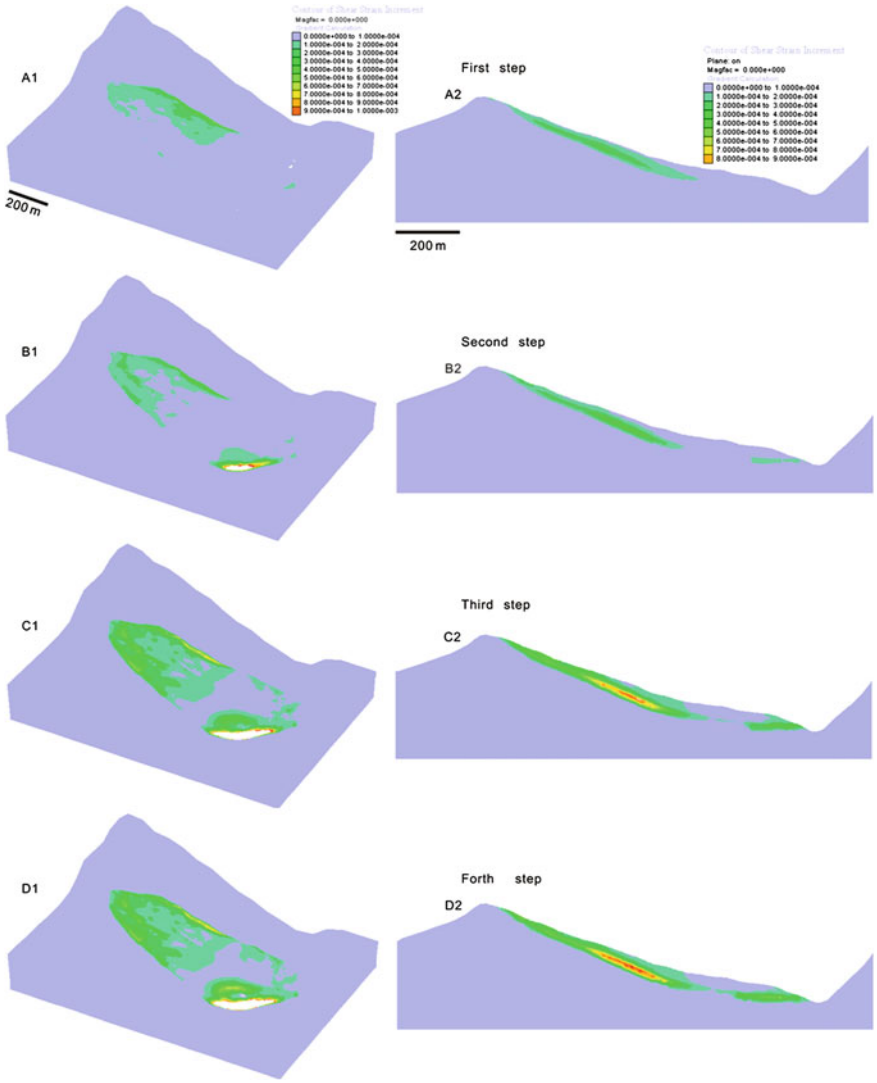

Fig. 17 Simulation result of shear strain increment

(1) When water level was kept at 105 m, maximum value of shear strain increment appeared at the left side of the slope half and upper section of the slope mass. From the main section, maximum value of shear strain increment appeared at the middle and upper part of the sliding zone.
(2) When water level rose from 105 to 135 m with inflow rate of 3 m per day, there was a sharp increase in shear strain value at the right-hand side of the slope toe. The shear strain increment observed at the right-hand side of slope also showed a gradual increase in value. Compared with the main section of

the first computing step, the region of shear strain increment appeared at the proximal end of the sliding zone. However, little or no change was observed at the middle and upper side of the sliding zone.

(3) When water level was kept at 135 m for 10 days, the shear strain increment at the proximal end of the slope increased instantaneously, especially near the cliff at the right-hand side of the slope toe. The maximum value of shear strain increment at the middle and upper side of the slope also increased gradually causing the region of concentrated shear strain strength to expand. From the main section, the maximum shear strain increment at the middle and upper part of the sliding zone also showed a steady positive change in value with the region of concentrated shear strain increment extending towards the slope toe. Conversely, the region of concentrated shear strain increment at the proximal end of the slope toe extended towards the upper part of the slope.

(4) Under the effect of rainfall and rise in reservoir water level, the maximum value of shear strain increment increased gradually and the regions of concentrated shear strain increment were almost connected.

From the simulation results of different computing steps, some qualitative analyses were conducted. At initial condition, region of concentrated shear strain increment appeared along the bedding planes of the sliding zone. This was because shear strain kept increasing along the weak interlayer located at the steeply inclined part of the slope under the effect of gravity for a long period of time. During reservoir water level rise, groundwater level in the proximal section of the slope mass increased gradually. The region of concentrated shear strain increment shows continuous expansion due to the combined effect of high pore pressure and decrease in shear strength as reservoir water infiltrates into the slope mass.

4.3.2 Simulation Result of Displacement

Figure 18 shows the simulation result of displacement under rainfall and steady rise in water level. Due to the relatively high difference in value of displacement with each computing step, it was not feasible to use uniform interval value for each step. Therefore, simulation result of each computing step had its own contour. From results obtained from the simulation, qualitative analyses were conducted as follow:

(1) At the initial condition, the obvious displacement appeared at the middle and upper side of the slope with maximum displacement is 2 cm.

(2) When water level rose from 105 to 135 m with inflow rate of 3 m per day, the displacement increased rapidly at the right-hand side of the slope toe with maximum displacement of 4 cm. From the main section, small displacements occurred at the proximal section of the slope under the effect of water level rise.

(3) When water level was kept at 135 m for 10 days, displacement increased rapidly at the right-hand side of the slope toe with maximum displacement of 10 cm. When compared with the main sections of different computing steps,

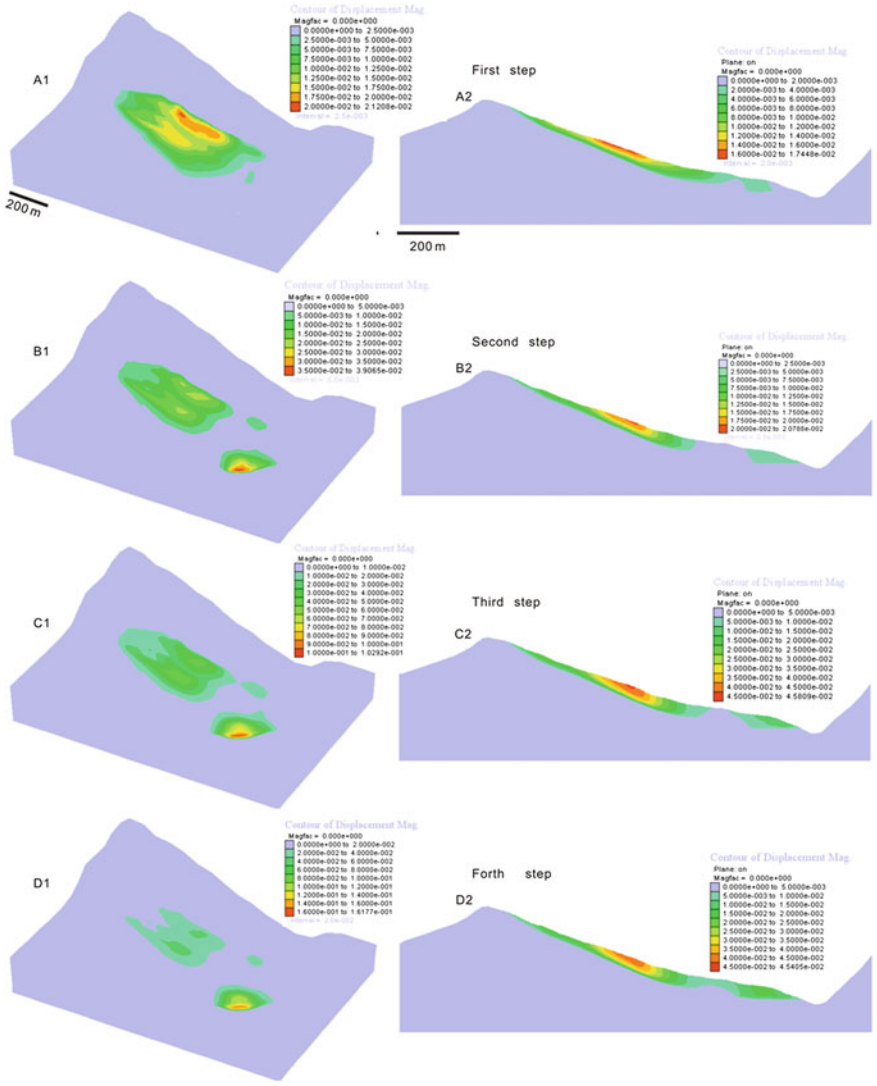

Fig. 18 Simulation result of displacement

displacement at the proximal section of the slope was seen to be greater than others. At the center of the slope, maximum displacement reached 4.5 cm.

(4) Under the effect of rainfall and reservoir water level rise, maximum displacement almost reached 16 cm. From the main section, it can be observed that the initial localized deformation gradually developed into a regional deformation.

From the modeling results of different computing steps, obvious displacement initially appeared at the middle and upper side of the slope. After the reservoir

water level increased, the displacement increased rapidly at the right side of the slope toe due to increase in pore pressure and decrease in shear resistance of the slope material with landward movement of moisture. Under the effect of rainfall infiltration, shear stress showed a gradual increase around the middle and upper side of slope. Meanwhile, shear resistance within the proximal side of the slope decreased gradually due to rise in water level. Finally, the total failure process of the slope occurred at the end of the rainfall period. Simulation results were generally consistent with previous failure record.

4.3.3 Simulation Result of Plastic State

Figure 19 shows the simulation result of plastic state under different computing steps.

(1) Before reservoir water level increased, some blocks at the left side of the middle and upper section of the slope and the sliding zones were already in plastic state.
(2) When water level rose from 105 to 135 m with an inflow speed of 3 m per day, some blocks at the right side of the slope were in plastic state. From the main section, it can be observed that the region of plastic state continued to expand.
(3) When water level was kept at 135 m for 10 days, some blocks at the slope toe were in plastic state. The probability of connectivity of plastic state along the sliding zone also increased slowly.
(4) Under the effect of rainfall and reservoir water level increase, plastic state at the slope toe expanded gradually. Meanwhile, plastic state at the middle section of the slope showed a gradual contraction. The plastic states were almost connected. It indicated that the slope was in a critical state at the end of the fourth computing step.

5 Conclusions

Field investigations which include topographic, geological and hydrogeological analyses were conducted to study the factors which contributed to the slope failure. In order to understand the failure process of the landslide, numerical simulation was conducted on the Qianjiangping slope. Based on simulation results of seepage field and failure processes, the following conclusions were reached:

(1) Rainfall primarily affected the saturated area of the shallow slope surface while groundwater level at the proximal part of the slope was controlled by changes in reservoir level.

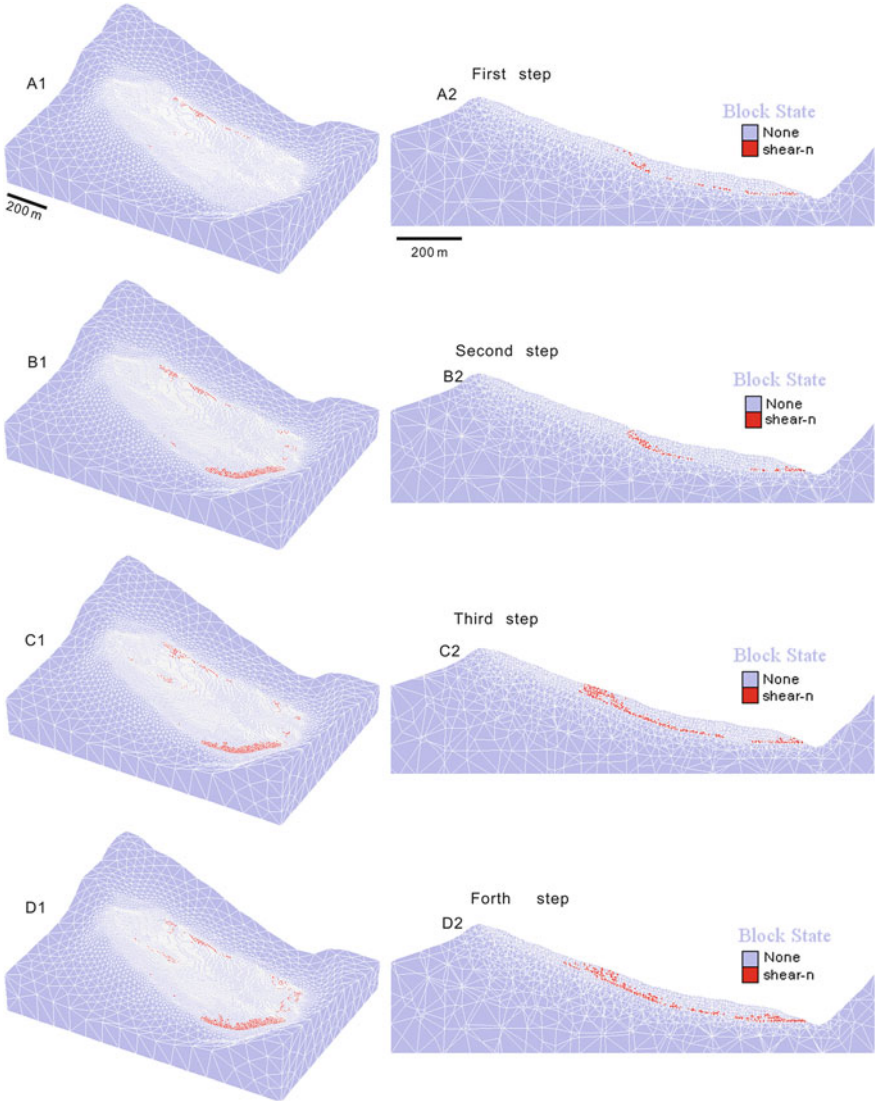

Fig. 19 Simulation result of plastic state

(2) Before the effect of rainfall and reservoir water level increase, there was obvious displacement at the middle part of the shallow slope surface. Regions of high shear strain increment appeared along the bedding planes of the sliding zone under the effect of gravity. Shear resistance of the slope material at the proximal section gradually decreased due to increase in pore pressure and decrease in shear strength of the slope material as a result of a steady rise in reservoir water level. As the rainy season period ends, the slope reached a maximum critical state.

(3) The simulation results of the shear strain increment, displacement and plastic state region of the slope show that the sliding surface was located along the weak carbonaceous shale layer, and was retrogressive in the lower part of the slope and progressive in the upper part of the slope. When compared with simulation results obtained before and after water level rise and rainfall, it was observed that reservoir water level rise was the main triggering factor for the Qianjiangping landslide.

Acknowledgments The authors' wish to thank the National Natural Science Foundation of China (NSFC) for this scientific research grant (No.40972184 Representative: Wenxing Jian). We appreciate the support received from the China Three Gorges University and the headquarters of the Three Gorges Geological Disaster Prevention, Chinese Ministry of Land and Resources for providing us with literature on the Qianjiangping landslide. The authors sincerely wish to thank Fusong Fan, Tingting Zhang and Li Zhou from the China University of Geosciences (Wuhan) for their constructive comments on the numerical simulation.

References

Dai FC, Deng JH, Tham LG, Lee CF (2004) A large landslide in Zigui County, Three Gorges area. Can J Geotech Eng 41(6):1233–1240

Li SD, Li X, Liu YH, Sun XS (2008) Geological evolution process of sliding zone in Qianjiangping landslide. Hydrogeol Eng Geol 35(2):18–23 (in Chinese with English abstract)

Liao QL, Li X, Dong YH (2005) Occurrence, geology and geomorphy characteristics and origin of Qianjiangping landslide in Three Gorges Reservoir area and study on ancient landslide criterion. Chin J Rock Mech Eng 24(17):3146–3153 (in Chinese with English abstract)

Wang FW, Zhang YM, Huo ZT, Matsumoto T, Huang BL (2004) The July 14, 2003 Qianjiangping landslide, Three Gorges Reservoir, China. Landslides J Int Consort Landslides 1(2):157–162

Wang FW, Zhang YM, Huo ZT, Peng XM, Wang SM, Yamasaki S (2008) Mechanism for the rapid motion of the Qianjiangping landslide during reactivation by the first impoundment of the Three Gorges Dam reservoir China. Landslides 5(4):379–386

Wang ZH, Yang RH (2005) The activity characteristics and movement style of Qianjiangping landslide in the Three Gorges Reservoir region. Chin J Geol Hazard Control 16(3):5–11 (in Chinese with English abstract)

Wang ZH, Yang RH, Wang Y (2003) An airborne remote sensing survey of Qianjiangping landslide in Zi-Gui Shanxisha Town. Remote Sens Land Resour 57(3):5–9 (in Chinese with English abstract)

Wen BP, Shen J, Tan JM (2008) The influence of water on the occurrence of Qianjiangping landslide. Chin Hydrogeol Eng Geol 35(3):12–18 (in Chinese with English abstract)

Xiao SR, Liu DF, Hu ZY (2007) Study on geomechanical model of Qianjiangping landslide, Three Gorges Reservoir. Rock Soil Mech 28(7):1459–1464 (in Chinese with English abstract)

Yin YP, Peng XM (2007) Failure mechanism on Qianjiangping landslide in the Three Gorges Reservoir region. Chin Hydrogeol Eng Geol 34(3):51–54 (in Chinese with English abstract)

Laboratory Experiments on Landslide Dam Failure Due to Piping: An Evaluation of 2011 Typhoon-Induced Landslide and Landslide Dam in Western Japan

Austin Chukwueloka Okeke, Fawu Wang, Tomokazu Sonoyama and Yasuhiro Mitani

Abstract Laboratory experiments were carried out to study erosional processes of landslide dam failure due to piping phenomenon with an evaluation of landslides and landslide dam triggered by 2011 Typhoon in Nara and Wakayama Prefectures of western Japan. Landslide dam models were built in a flume box with flume bed slope of 5°. To initiate piping, cylindrical pipe was laid in the dam at different horizontal and vertical locations. Four erosional stages were observed from the experiments. They include: appearance of wet spot/pipe development, continuation, progression, and breach. Stability and longevity of landslide dams due to piping were analyzed by varying heights of dams (H_D), downstream slope angles, and horizontal positions of pipe. Results obtained show that stability and longevity of landslide dams depend on downstream slope angle, height and size of dams, and the erosive forces acting on the dam material. Results obtained from petrologic analysis of rock samples from the landslide and landslide dam sites show that the geomaterial of the areas are grain-supported which could lead to initiation of internal erosion and pipe formation.

Keywords Wet spot · Backward erosion · Suffusion · Piping · Breach · Weathering

1 Introduction

Landslides and landslide dams are common geoenvironmental disasters occurring in tectonically active mountain belts of the world. Landslides occur as a result of rapid down-slope movement of soil and rock material under gravitational influence, while

A. C. Okeke · F. Wang (✉) · T. Sonoyama · Y. Mitani
Department of Geoscience, Shimane University, Matsue, 690-8504, Shimane, Japan
e-mail: wangfw@riko.shimane-u.ac.jp

F. Wang et al. (eds.), *Progress of Geo-Disaster Mitigation Technology in Asia*, Environmental Science and Engineering, DOI: 10.1007/978-3-642-29107-4_30,

natural dams such as landslide dams and moraine dams are common in steep confined valleys of mountainous regions. Triggering factors of landslides and landslide dams have been recorded in many parts of the world. Among these factors, snowmelt and rainfall constitute 90 % of studied landslide dams while volcanism, earthquake, devegetation and others make up the remaining 10 %. Landslide dams unlike earth dams are made up of heterogeneous materials that are poorly sorted, unconsolidated or moderately consolidated lacking filter zones to control internal seepages and piping (Costa and Schuster 1988). Loss of cohesion, internal friction angle of hillslope materials, increase in hillslope angle and relief have been observed to be preparatory factors for slope and landslide dam failures. The above-mentioned factors may be enhanced by stress released along intrinsic zones of weakness, repeated earthquake shaking, rock mass shattering along tectonic fault zones and slope debuttressing following deglaciation or precursory landsliding (Korup and Tweed 2007). Landslide dams have been classified into six categories based on their relation with the valley floor. The failure time and magnitude of resulting floods are dependent on dam size and geometry, compositional material of the impoundment, volume and magnitude of the impoundment, and other factors like geotechnical design methods (Costa and Schuster 1988). Detailed research and investigation on collected data from Japan, western USA and Italy have shown that a common feature of these regions was a high frequency in dam formation along or near active margins of tectonic plates. In particular, there was a correlation between landslide dam density and areas of crustal shortening, where orogenic events have provoked the formation of large-scale movement and deep narrow valleys which could easily be blocked by a landslide (Ermini and Casagli 2003).

Field and laboratory studies on earth and natural dam failure have been reported by Mizuyama et al. (2006), Catane et al. (2011), Gregoretti et al. (2010), Watanabe and Rothacher (1996), Jones (1990); Hayashi et al. (2003), Worman (1993); Fujisawa et al. (2009).

Chang and Zang (2010) carried extensive research on Tangjiashan and Xiaogangjian landslide dam induced by the 2008 Wenchuan earthquake in China. They developed a physically-based model to stimulate the breaching process of the landslide dam and a spreadsheet to numerically implement the model and discovered that the erodibility of the two landslide dams vary significantly with depth. The authors concluded that the model can predict breach evolution, erosion rate and outflow hydrograph. Shang et al. (2003) gave a comprehensive detail of the April, 2000 landslide dam failure along the Zhama Creek in southeastern Tibet with dam height of 100 m, maximum bottom width of 250 m and an axial length of 1,000 m. Xu et al. (2009) used interpretations generated from a series of aerial photographs and satellite images to identify 256 landslide dams caused by the Wenchuan earthquake. Results obtained from their study show a high concentration of landslide dams near the Yingxiu-Beichuan fault line. Mizuyama et al. (2006) estimated outflow discharge rate from landslide dam outburst with flume experiment. The authors developed a numerical simulation model to estimate both peak flow discharge and flow hydrograph. They applied their method to a historical flood, resulting from outburst of Taka-isoyama landslide dam in the Naka-

gawa River of Tokushima, Japan. Results obtained from the calculation conformed to field survey data. Awal et al. (2009) combined 3-D slope stability model with transient seepage flow model for numerical simulations. From experiments performed using flume box to measure movement of moisture in dam body and observe slip surface, they concluded that the predicted moisture profile at different locations within the dam body and the critical slip surface were quite close to results obtained from experiments. Fujisawa et al. (2010) analyzed the 2004 typhoon-induced landslide in Otomura city, Japan using various monitoring systems and proffered many risk-management methods.

Internal erosion in earth and natural dams can be defined as downstream removal of dam materials due to seepage action while piping is initiated by retrogressive (slow and continuous) internal erosion of dam materials with the formation of a 'pipe'. Internal erosion in landslide dams and earth dams occur when the combined effect of seepage forces and hydraulic head are greater than the erosion resistant forces of the dam material. These resistant forces are dependent on the geomechanical and geotechnical properties of the dam.

Fell et al. (2005) enumerated four hydrodynamic conditions governing internal erosion and piping. These are: there must be a continuous supply of water and a seepage flow path; the flow path must have erodible material which can easily be transported by water; an impervious exit must be available for escape of eroded material; and pipe can only be formed in a dam if the material is strong enough to form a roof for the developing pipe. Four phases of erosional process have been reported in the works of Fell et al. (2003). These erosional phases include: initiation, continuation, progression, and breach formation.

This paper studies two deep-seated landslides and landslide dam formed as a result of torrential rainfall caused by typhoon-12 in the western part of Japan and tries to analyze the failure processes due to piping phenomenon in landslide dams using a laboratory landslide dam model. The study has become more important due to an increase in rural expansion, infrastructural and industrial developments especially in mountainous regions.

Tanabe city Landslide: At exactly 00:30 h of 4th September 2011, a torrential rainfall was brought by a powerful slow moving typhoon also referred to as Typhoon 12. A landslide of approximately 50,000 m^3 in volume was triggered in Fudono, Tanabe city of Wakayama Prefecture by the typhoon and its attendant rainfall. The length of the landslide was about 290 m with maximum width of 130 m, slip height of 40 m and relative height of 170 m (Fig. 1). The landslide materials were easily liquefied after travelling a short distance and became debris flow submerging many houses on its flow path. Five fatalities were recorded.

Gojo city Landslide dam: A deep-seated landslide dam occurred in Gojo city in the early hours of 4th September, 2011 killing five people, and destroying houses in its path. Ten people were declared missing. Slope length of the landslide was 550 m with relative height of 350 m, slip height of 30 m and maximum width of 200 m (Fig. 2). The landslide material inundated Kumamo River, travelling in the opposite direction of the stream flow, and blocked the river. A spillway has been constructed to avert imminent disaster.

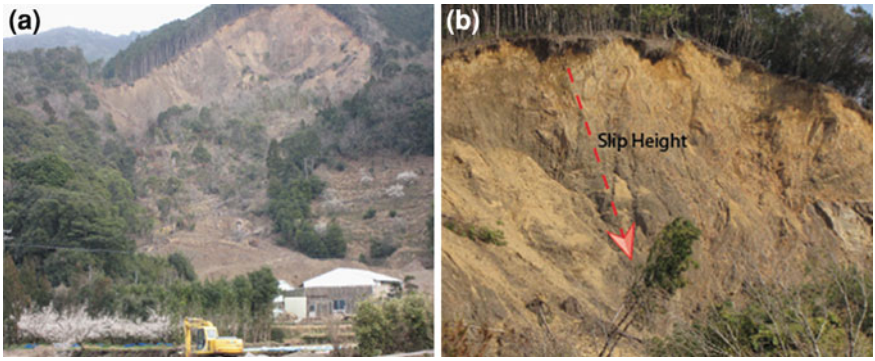

Fig. 1 **a** Front view of Fudono Tanabe city landslide showing the slope **b** Main scarp of the landslide showing vertical slip height

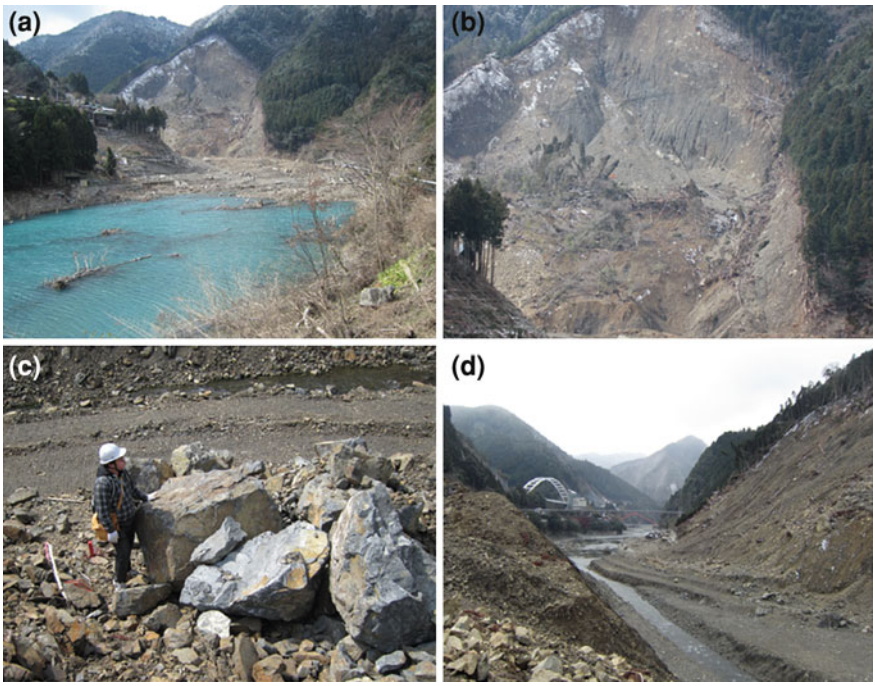

Fig. 2 Ui, Gojo city landslide dam showing: **a** Downstream view of the landslide dam and Kumamo River inundated by the landslide material; **b** Main scarp of the landslide with near-vertical vegetation; **c** Large-sized blocks of dislodged rocks; **d** Temporary drainage channel excavated to mitigate disaster

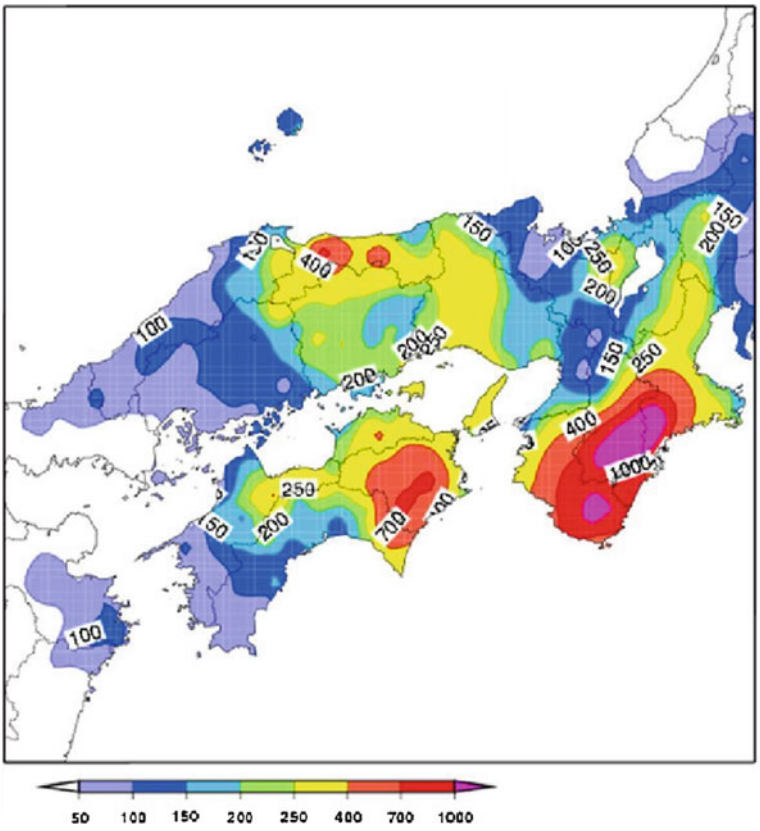

Fig. 3 Rainfall distribution map of mainland Japan for 4th September, 2011

2 Triggering Factor

The passage of a severe tropical cyclone (named Typhoon 12) over Japan caused torrential rain to fall throughout Japan with highest recorded intensity around Kii Peninsula, western Japan (Fig. 3). Total amount of precipitation exceeded 1,000 mm in the Kii Peninsula with Nara Prefecture recording more than 1,652.5 mm. The typhoon displaced lots of people, damaged properties worth $600 million and caused more than 70 fatalities.

3 Geology and Geomorphic Setting of the Landslides

The two landslide sites are located in Kii Peninsula, of the western part of Japan. Kii Peninsula is located at the southern region of mainland Japan (Lat: 34° N, Long: 1,360 E), and bestrides Mie, Nara, Osaka and Wakayama Prefectures. Total length of

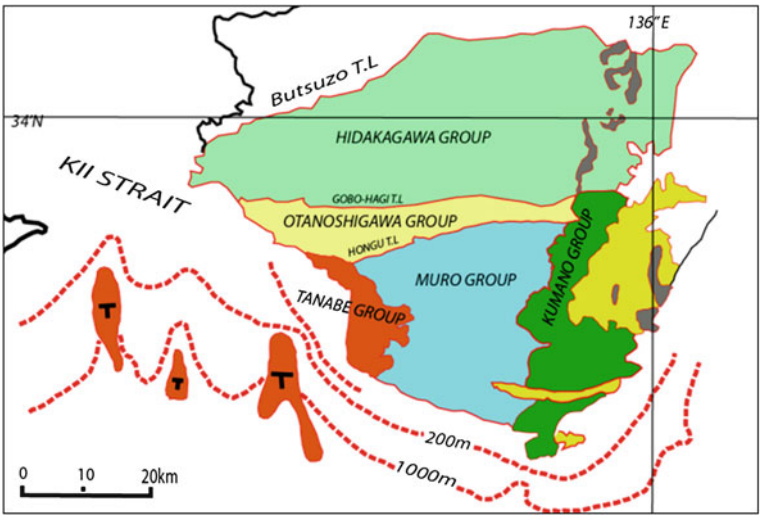

Fig. 4 Geologic map of Kii Peninsula (Modified after Taira et al. 1982)

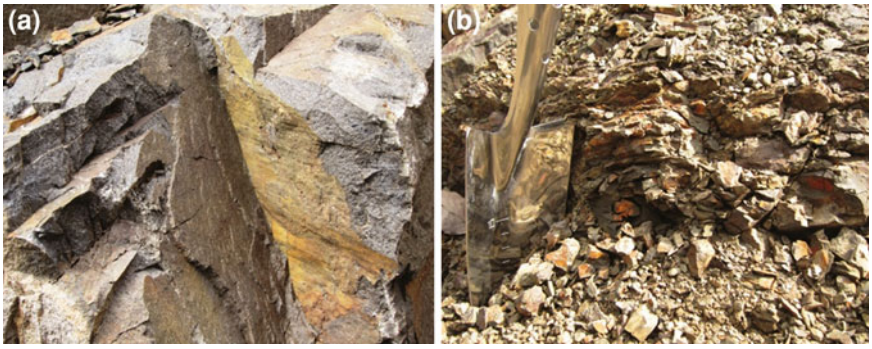

Fig. 5 Structural features of geomaterials within the two sites showing: **a** Foliated layers of Tanabe landslide material **b** Faults, joints, shear zones and foliated layers of Gojo landslide dam material

coastline is about 1,956 km. Kii Peninsula is underlain by deposits of Shimanto Supergroup which has been divided into three Groups: Upper Cretaceous Hidakagawa, Paleogene Otonashigawa and Muro Groups with Miocene Kumano and Tanabe Groups overlying them (Taira et al. 1982). Landslide material of Tanabe district, Wakayama Prefecture belongs to Eocene Otonashigawa Group which is composed of alternations of sandstone and mudstone, cherts, granites, pelitic schists and acid tuffs (Figs. 4 and 5). The strata have strike directions trending ENE–WSW, with dip direction to the north having varying dip amounts.

Landslide material of Ui, Gojo area, Nara Prefecture belongs to the Upper Cretaceous Hidakagawa Group of the Miyama Formation containing alternations of sandstone and mudstone with cherts, granite, felsic tuffs and greenstone (Fig. 5). Dense

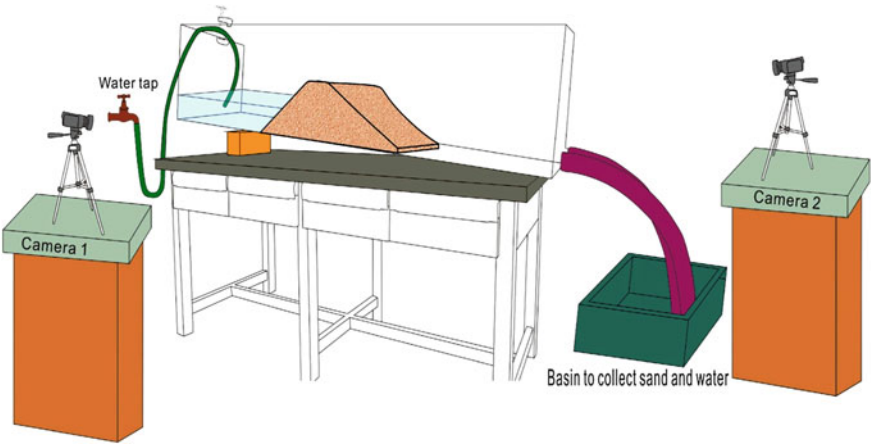

Fig. 6 Schematic diagram of the laboratory experimental set-up

vegetation covered the upper steeply inclined slope. The Kumamo River flows along the valley floor. The landslide dammed the river with travel distance of approximately 1.5 km upstream of the river. Similar landslide events in the Gojo area have been recorded in the works of Fujisawa et al. (2010); Hattanji and Moriwaki (2009).

4 Experimental Methods and Apparatus

Series of experiments were carried out in a transparent rectangular flume box of dimension, 200 cm × 45 cm × 45 cm with two drainage outlets of diameters, 4 cm each at the downstream end. Upstream lake was provided by a drainage hose fed by a water tap. The flume box rests on a flat table and makes an angle of 5° with the flat table (Fig. 6). The front and side sections of the box were graduated in meters of 5 cm scale while the center of the front section was graduated in meters of 1 cm scale. Silica sand number 8 was used to build different sized dam models, 70 cm downstream of the upstream end (Fig. 7). Series of experiments were conducted with dam heights of 20, 25, 30, and 35 cm. Downstream slope angles were varied from 35 to 45° while horizontal and vertical positions of pipe were varied in all the experiments. The sand samples used were mixed with a little water to obtain moisture content necessary to hold the sand grains together. The upstream lake was recharged at a constant rate of 77 cm^3/s. To initiate piping in the dam model, transparent perspex pipe of 1.8 cm in diameter and 67 cm long was used. Holes were bored at exactly 1 cm spacing along the pipe to ensure uniform distribution of water within the dam. The cylindrical pipe was placed at the center of the dam and inclined at an angle to the floor of the flume box. Radially-opposite holes bored on the cylindrical pipe were terminated at 35 cm mark which corresponds to the downstream horizontal distance. To study the mechanism of pipe development, two video cameras and stopwatch were used to record the failure processes and time at which each erosional stage was attained.

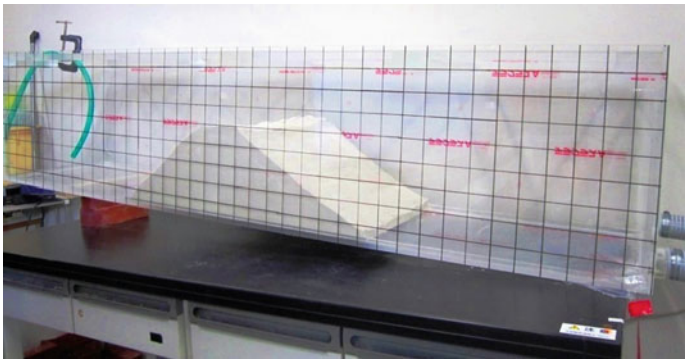

Fig. 7 Side-view of the landslide dam model in a flume box

Table 1 Summary of experiments and final breach time

Test No.	Dam height (cm)	Dam width (cm)	Horizontal pipe position (cm)	Vertical pipe position (cm)	Breach time (s)
1A	20	45	15	10	685
1B	25	45	15	10	648
1C	30	45	15	10	610
1D	35	45	15	10	566
2A	25	45	5	6	786
2B	25	45	10	6	701
2C	25	45	15	6	630
2D	25	45	20	6	600
2E	25	45	25	6	568
3A (35°)	35	45	10	15	602
3B (40°)	35	45	10	15	565
3C (45°)	35	45	10	15	548

5 Experimental Results

Experiments were carried out considering different horizontal locations of pipe, varying downstream slope angles, effect of dam height and pipe enlargement. The width of the dam crest (10 cm) and slope of the flume box (5°) were constant for all the experiments (Table 1). The experiments observed four erosional failure phases proposed by Fell et al. (2003). The appearance of wet spot on the downstream dam face is taken to be the end of internal (backward) erosion and beginning of piping (Fig. 8).

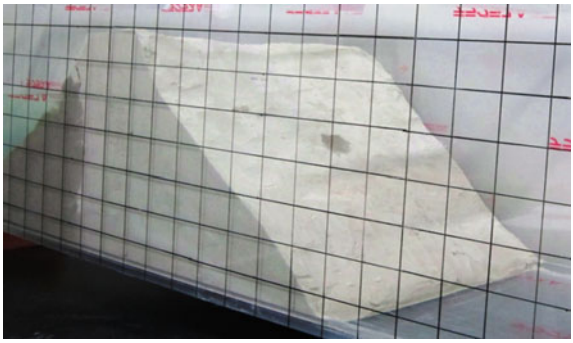

Fig. 8 Appearance of wet spot on the downstream face of the landslide dam model

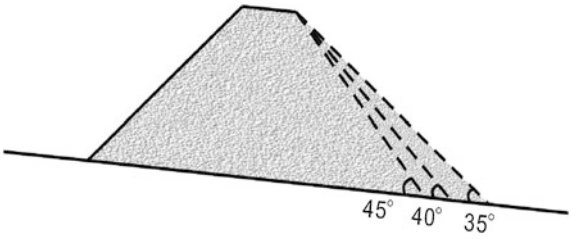

Fig. 9 Side view of dam showing different downstream slope angles

6 Effect of Downstream Slope Angle

The experiment was performed with pipe kept at a vertical height of 15 cm at the upstream dam face. Downstream slope angles were plotted against time of wets spot development and breach formation (Fig. 9). Wet spot appeared on the downstream dam faces at $T_w = 122$, 127, and 138 s for downstream slope angles of 45, 40 and 35° respectively. The three landslide dams attained breach stage at $T_b = 548$, 565 and 602 s respectively (Fig. 10).

7 Effect of Dam Height (H_D)

Different heights of dam ($H_D = 20$, 25, 30, and 35 cm), were plotted against time of wet spots appearance, progression stage and breach formation (Fig. 11). The experiments were performed with vertical height of pipe fixed at 10 cm on the upstream dam face (Fig. 12). Wet spots appeared on the downstream dam faces at $T_w = 110$, 118, 120, and 125 s for $H_D = 20$ m, 25, 30 and 35 cm respectively. The pipe progressed at $T_p = 142$, 150, 154 and 165 s for the same dam heights and breached at $T_b = 685$, 648, 610, and 566 s for $H_D = 20$, 25, 30 and 35 cm respectively (Fig. 13).

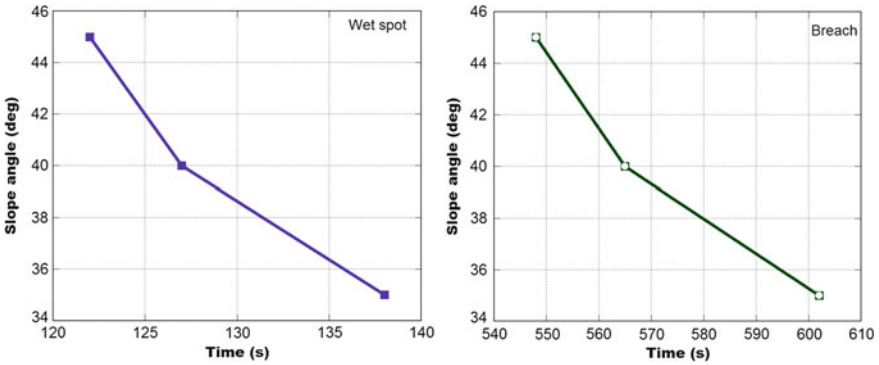

Fig. 10 Plots of downstream slope angles against time of development at each stage

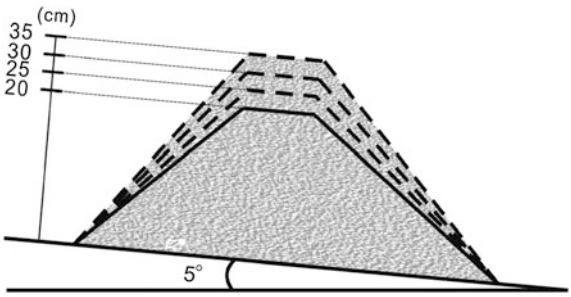

Fig. 11 Side view of dam showing different vertical heights

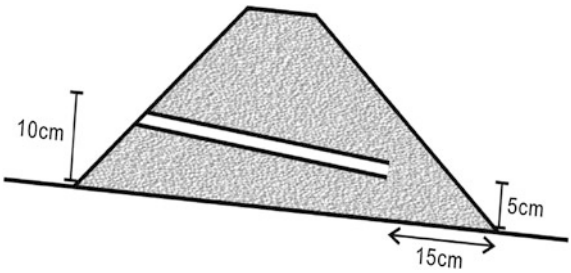

Fig. 12 Side-view showing vertical location of pipe at both faces of the dam

8 Effect of Horizontal Pipe Location

For vertical height of pipe on the upstream dam face fixed at 6 cm (Fig. 14), horizontal pipe locations were plotted against time of different stages of erosional process (Fig. 15). Wet spots appeared on the downstream dam face at $T_w = 45, 66, 119, 196$ and 320 s while the pipe progressed at $T_p = 124, 160, 210, 288$ and 349 s respectively for pipe positions at 5, 10, 15, 20 and 25 cm respectively (Fig. 16).

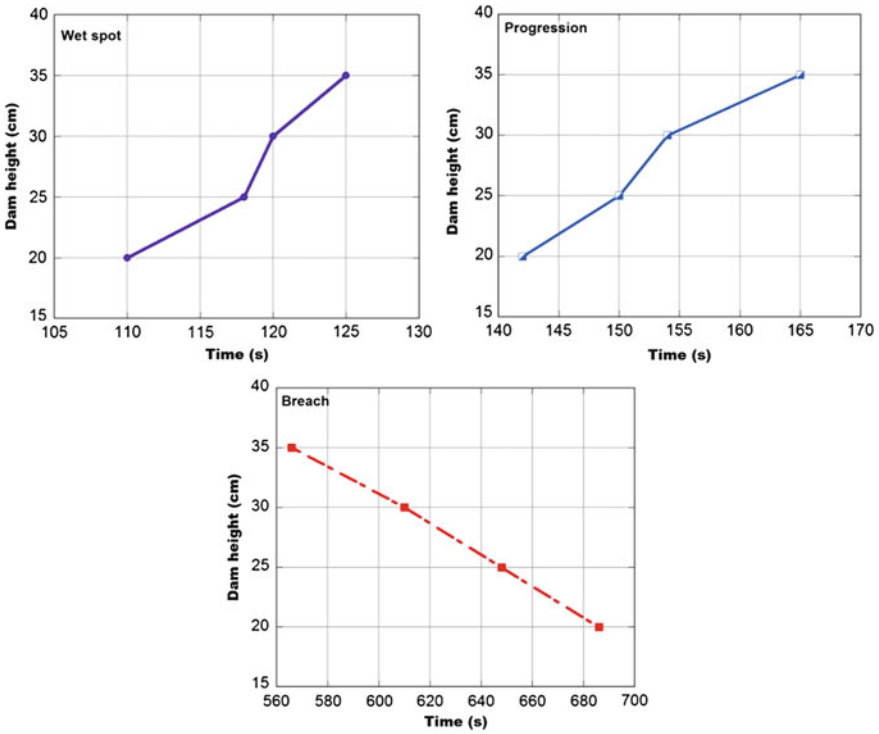

Fig. 13 Plots of dam heights against time of development at each stage

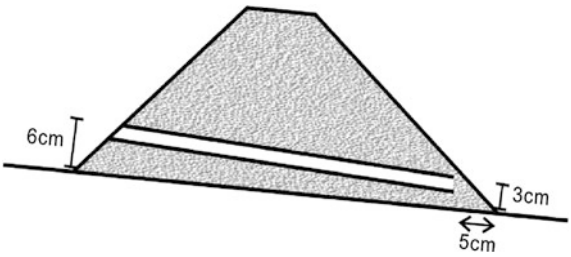

Fig. 14 Side-view showing vertical location of pipe at both faces of the dam

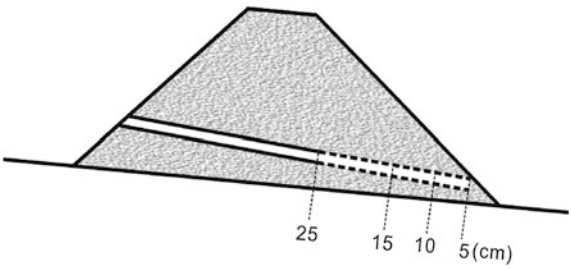

Fig. 15 Side-view of the dam model showing different horizontal positions of pipe

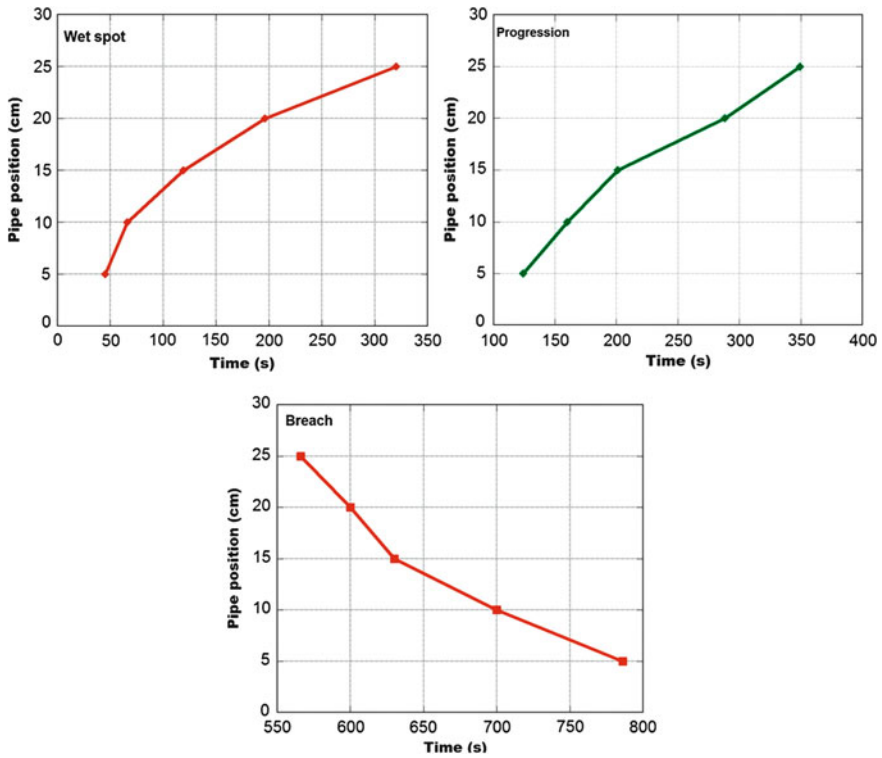

Fig. 16 Plots of horizontal pipe positions against time of development at each stage

9 Effect of Dam Height to Pipe Enlargement

For the same vertical position of pipes at the upstream dam face, values obtained from the enlarging pipes were plotted against corresponding times of the enlargement for $H_D = 20$, 25, 30, and 35 cm respectively (Fig. 17). As height of dam (H_D) is increased from 20 to 35 cm, hydraulic head into the dam increased due to relative volume of upstream lake which increased the erosive forces leading to breach formation. The plot shows that breach bottom widths (W_b) of 13, 15, 21 and 26 cm were formed at $T_b = 685$, 648, 610, and 566 s for dam heights (H_D) of 20, 25, 30, and 35 cm respectively.

10 Discussions

Mechanisms controlling landslide dam failure due to piping and internal/seepage erosion have been divided into four stages. These failure processes are initiation, continuation, progression and breach. In this research, we initiated internal erosion

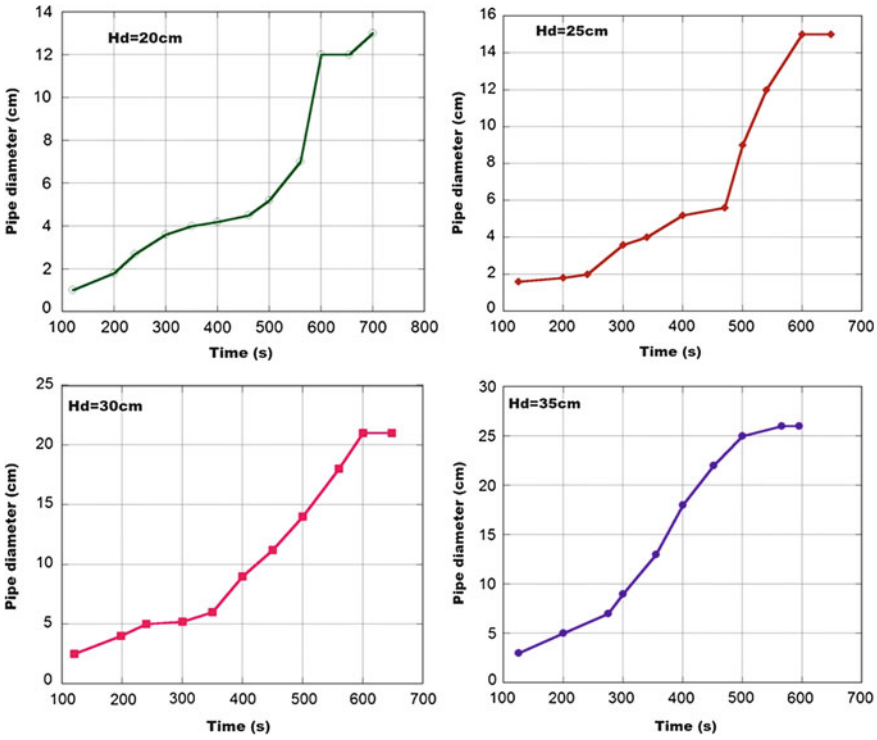

Fig. 17 Plots of vertical heights of dam against pipe diameter/enlargement

to monitor its continuation to form pipe, progression by increase in pipe diameter due to erosion and breach formation. This was achieved with a small diameter perspex pipe which was carefully placed in the dam material. Continuation in this research is defined as formation of 'wet spot' on the downstream dam face due to backward erosion (slow but continuous detachment and entrainment of soil particles), while progression and breach are pipe widening, collapse, and removal of dam crest. Backward erosion occurs only if hydraulic head into the dam is high enough to dislodge soil particles (Crosta and Prisco 1999).

Results obtained from experiments on the effect of downstream slope on dam longevity shows that at steeper slopes, landslide dams are unstable due to the effect of piping as pipe develops within a short time interval. Analysis of plots indicates that downstream dam slope angle is one of the fundamental factors controlling landslide dam longevity.

Results obtained from plots of various dam heights (H_D) against time of failure shows that for various erosional processes, wet spot and pipe enlargement takes a longer time to develop for dams of higher heights (H_D) but fails catastrophically in a short period. Conversely, dams of lower height (H_D) forms wet spot within a short time but fails after a long time. At higher dam heights (H_D), volume of upstream lake increases significantly, while at lower dam heights (H_D), upstream

Table 2 Summary of geometrical parameters of selected historical landslide dams

References	Location	Date formed	Dam volume, V_D (10xm3)	Dam width, W_D (m)	Dam height, H_D (m)	Dam erodibility	Breach time T_B (h)
Costa and Schuster (1991)	Totsu River, Nara, Japan	20/08/1889	2.5	350	80	Medium	–
Costa and Schuster (1991)	Tsao-Ling, Taiwan	10/08/1942	191	1600	217	Medium	4.5
Costa and Schuster (1991)	Tsao-Ling, Taiwan	15/08/1979	40	–	90	Medium	3
Costa and Schuster (1991)	Naka River, Japan	25/07/1892	3.3	330	80	Medium	–
Huang et al. (2008)	Tangjiashan, China	12/05/2008	20.37	611.8	82	Medium	14
Lee and Duncan (1975)	Mantaro River, Peru	25/04/1974	1300	3800	175	Medium	12
Costa and Schuster (1991)	Ojika River, Japan	01/09/1683	3.8	400	70	Low	–

lake volume depends on erosive forces into the dam. Ermini and Casagli (2003) stated that dam longevity is dependent on the capacity of the upstream lake and the hydraulic head in the dam. Geomorphological characteristics-dam height (H_D), dam volume (V_D), and watershed area (A_b)-have been used in predicting longevity and stability of landslide dams (Ermini and Casagli 2003). Catastrophic landslide dams of high magnitude and size have been recorded in Japan (Table 2), and other parts of the world. They include the 1953 Arida River landslide dam, Japan (H_D, 60 m; V_D, 2,600 $\times$ 10^3 m^3), 1984 Otaki River landslide dam, Japan (H_D, 40 m; V_D, 12,500 $\times$ 10^3 m^3), 1911 Murgab River landslide dam in Tajikistan (H_D, 500 m; V_D, 2,200,000 $\times$ 10^3 m^3). Costa and Schuster (1988) on analyzing landslide dam longevity listed three factors which control stability and life span of landslide dams. These factors are: (1) geotechnical properties of the dam, (2) nature and size of dam, and (3) rate of water inflow into the dam.

Results obtained from analysis of horizontal positions of pipe shows that time of complete failure of dams are shorter for pipes placed at far distances away from downstream toe but longer for pipes placed very close to the dam toe. Close observation show that at the same upstream discharge rate, erosive forces act faster within the dam than near the dam toe where most of the toe materials have liquefied. Once suffusion and backward erosion have been able to reach the

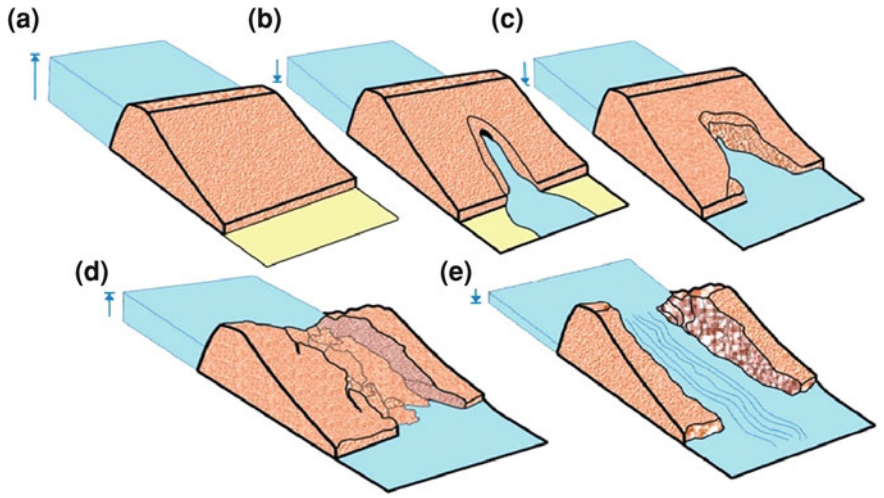

Fig. 18 Stages of the erosional process showing **a** Internal erosion and wet spot development; **b** Continuation; **c** Progression; **d** Temporary breach with collapse of dam roof and **e** Final breach formation

downstream dam face (formation of wet spot), pipe enlargement, progression and breach occur instantaneously.

11 Observed Failure Processes During the Analysis

Four failure processes were observed from the laboratory analysis. They include: formation of wet spot, continuation, progression and breach (Fig. 18). Decrease in level of upstream lake depends on the vertical positions of pipe, hydraulic head into the dam and erodibility of the dam material. The time it takes for wet spot to appear on the downstream dam face depends on initial horizontal location of pipe which is influenced by soil particle dislodgement and entrainment by suffusion and backward erosion. Conversely, for different horizontal and vertical position of pipes, it was observed that downstream face wetting time and pipe enlargement was different. Pipes buried very close to downstream dam toe form wet spots faster but take longer time to reach breach stage, while pipes at farther distance cause failure within short period of time.

The appearance of wet spot on the downstream dam face marks the end of internal erosion and the beginning of piping (Fig. 18a). The time between wet spot appearance and upstream lake outburst due to piping is negligible (Fig. 18b). Depending on the lake volume, downstream slope angle and dam height, piping progresses unabated with steady drawdown of upstream lake (Figs. 18c, 19 and 20). This is preceded by collapse of dam crest due to removal of material support. Collapse of dam crest causes a steady rise in upstream lake due to channel way

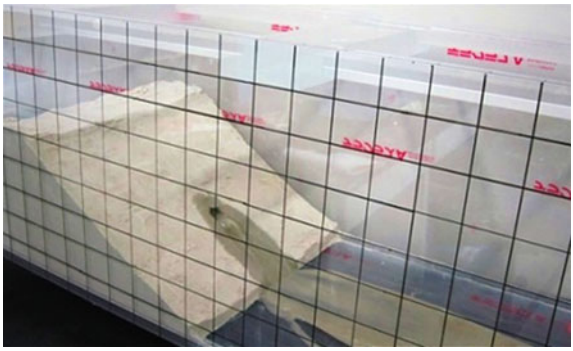

Fig. 19 Progression stage of piping

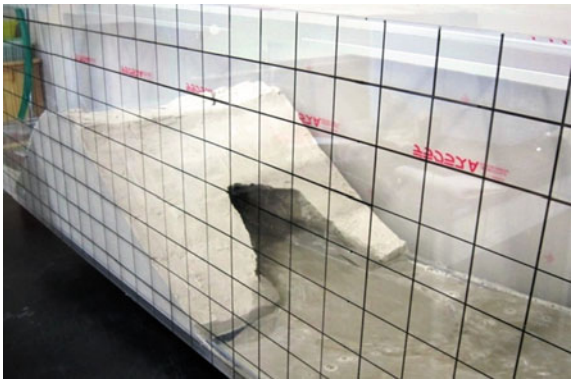

Fig. 20 Pipe enlargement with tension cracks on the downstream dam face

Fig. 21 Temporary breach formation as upstream lake rises steadily due to collapse of dam roof

impoundment (Figs. 18d, 20 and 21). The rise in lake level is dependent on the recharge rate. Erosion cycle continues as soon as the erosive forces of the lake are able to dislodge and entrain sand grains head-ward. The end of the failure process is marked by formation of wide gully/channel with thin walls on both sides of the dam (Fig. 18e).

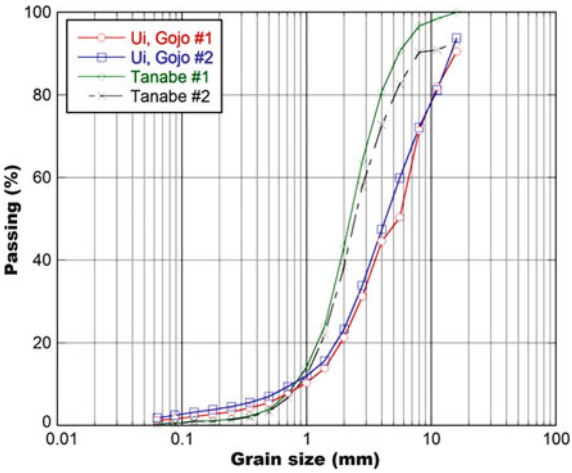

Fig. 22 Cumulative particle size distribution of four representative geomaterials of the two locations

12 Grain-Size Analysis

Stability and failure mechanism of landslides and landslide dams are dependent on geomechanical and geotechnical properties of the material. Grain size analyses of landslide dam material have been one of the basic tools in landslide dam assessment studies (Casagli and Ermini 1999; Costa and Schuster 1988; Casagli et al. 2003; Korup et al. 2003).

Cumulative grain size distribution curves of four representative sand samples collected from the Tanabe landslide and Gojo landslide dam sites are shown in Fig. 22. The curves show that Tanabe landslide materials are moderately to poorly sorted while Gojo landslide dam materials are moderately sorted. Frequency diagrams of the sand samples are generally bimodal except for Fudono Tanabe 1 which shows unimodal distribution (Fig. 23). The distribution shows relative large amount of grains with diameters of phi = +0.5 to −4.0. This distribution could lead to internal erosion and piping especially for Gojo landslide dam geomaterials.

13 Rock Microscopy

Photomicrograph of four representative rock samples collected from the two locations are shown in Fig. 24. Detailed microscopic analysis indicates that the geomaterials have undergone high degree weathering. Rock samples of Fudono Tanabe are reddish-brown in color. Generally, petrographic examination of materials from the two locations indicates that major minerals (feldspars,

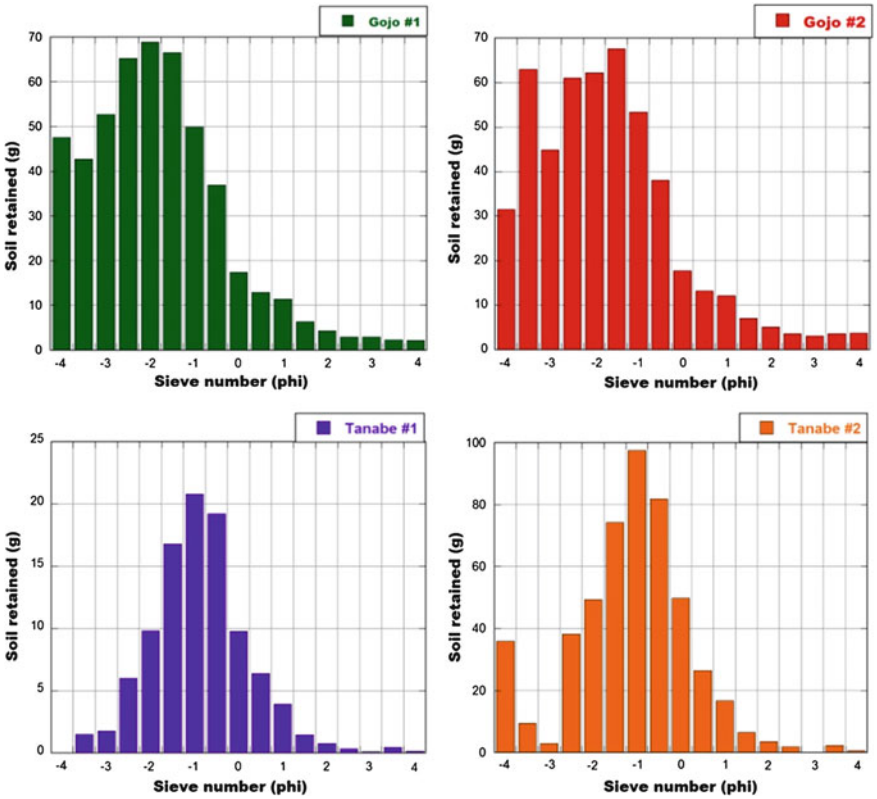

Fig. 23 Frequency diagram of four representative geomaterials

plagioclase, biotite), composing the rocks show variation in the degree of weathering. In some parts, the minerals are highly weathered while in other parts, the minerals are unaltered. At areas where weathering and mineral alteration are high, reddish-brown rings rich in ferric oxides are seen around the altered grains. Xenolith-filled fractures and foliated zones are major structural features. Breccias and detrital matrix are characterized by densely folded and fractured grains. Pre-fault mineral grains of folded biotite were observed within the fractured zones. Fresh samples of plagioclase, k-feldspars, and biotite dominated layers of criss-crossed gouges and fractures (Zangerl et al. 2006). Small-scale seepages, internal erosion and piping could occur in these areas due to microfracturization, irregular joints, veins and veinlets which have weakened the interlocking bonds between the mineral grains.

The characteristic structural and mineralogical compositions of rocks within Shimanto Supergroup have been highlighted in the works of Taira et al. (1982)

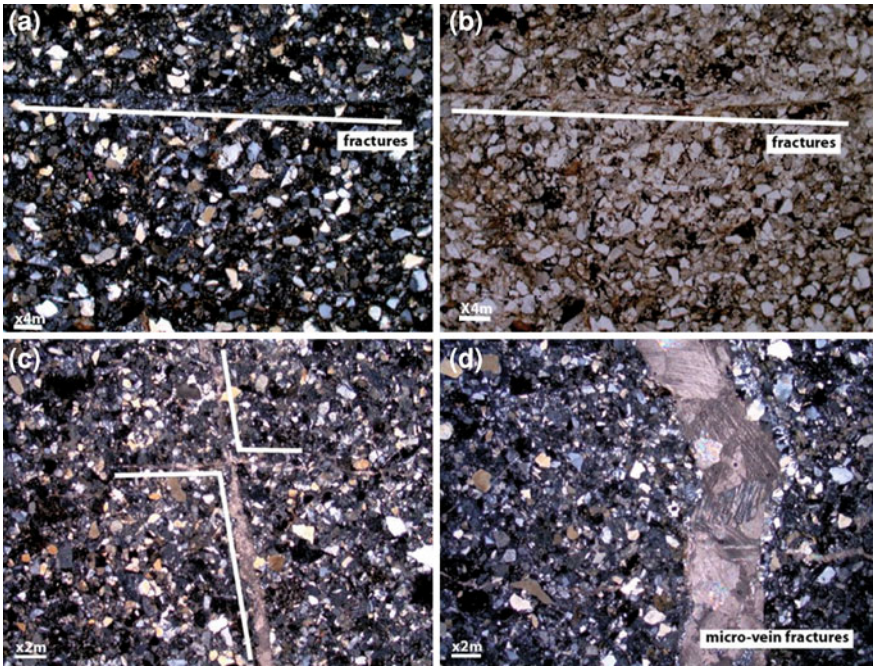

Fig. 24 Micro structural features of rock samples showing: **a** and **b** Fractures and joints, **c** Crossed vein fractures and, **d** Xenolith-filled veins and veinlets

14 Conclusions

Based on field investigations we carried out on the 2011 typhoon-induced landslide and landslide dam sites in the Fudono Tanabe and Ui Gojo areas of Wakayama and Nara Prefectures. We performed laboratory experiments to study the mechanism and processes of landslide dam failure due to piping phenomenon. Piping was initiated by placing a perforated cylindrical plastic pipe at a distance away from the downstream dam face. Laboratory experiment showed that landslide dam failure by piping starts with the formation of a wet spot on the downstream dam face with gradual but steady widening of the formed pipe. Laboratory experiments showed that the controlling factors in landslide dam longevity and stability are downstream slope angle, dam geometry, horizontal position of pipe and erodibility of the dam material. The experiment showed that the time of breach formation (T_b) is largely controlled by the area of the flume box used. Many researchers have obtained different breaching times (T_b) with different flume box dimensions. In real cases, landslide dams are more stable and last longer for lower heights, lower downstream slope angles, and longer dam widths and fail within minutes or days for higher heights, steeply inclined downstream slope angles and very short dam widths. Analysis of geomaterials from the two sites showed that internal erosion and piping could occur in the geomaterials

due to the nature of the grain sizes and microstructural characteristics of the weathered rock components of geomaterials of the Fudono Tanabe landslide and Gojo landslide dam. The results and interpretations presented in this research are preliminary findings which we hope to improve in subsequent papers. We will not fail to recommend that detailed sedimentological and petrologic studies need to be carried out on geomaterials of the two sites to better understand the structural controls affecting the two sites.

Acknowledgments This research was financially supported by government of Japan, ministry of education, science and technology (MEXT).

References

Awal R, Nakagawa H, Kawaike K, Baba Y, Zhang H (2009) Three dimensional transient seepage and slope stability analysis of landslide dam. Ann Dis Prev Res Inst Kyoto Univ No. 52B

Casagli N, Ermini L (1999) Geomorphic analysis of landslide dams in the Northern Appennine. Trans Jpn Geomorph Union 20(3):219–249

Casagli N, Ermini L, Rosati G (2003) Determining grain size distribution of material composing landslide dams in the Northern Appennines: sampling and processing methods. Eng Geol (Amsterdam) 69:83–97

Catane SG, Zarco MAH, Cordero CJN, Kaimo RAN, Saturay RM Jr (2011) Laboratory experiments on steady state seepage-induced landslides using slope models and sensors. Sci Diliman 23(1):17–30

Chang DS, Zhang LM (2010) Simulation of the erosion process of landslide dams due to overtopping considering variations in soil erodibility along depth. Nat Hazards Earth Sys Sci 10:933–946

Costa JE, Schuster RL (1988) The formation and failure of natural dams. Geol Soc Am Bull 100:1054–1068

Costa JE, Schuster RL (1991) Documented historical landslide dams around the world. US Geological Survey Open-file Report, pp 91–239

Crosta G, Prisco C (1999) On slope instability induced by seepage erosion. Can J Geotech 36:1056–1073

Ermini L, Casagli N (2003) Prediction of the behaviour of landslide dams using geomorphological dimensionless index. Earth Surf Proces Landf 28:31–47

Fell R, Wan CF, Cyganiewicz J, Foster M (2003) Time for development of internal erosion and piping in embankment dams. J Geotech Geoenviron Eng ASCE 129(4):307–314

Fell R, MacGregor P, Stapledon D, Bell G (2005) Geotechnical engineering of dams. Taylor and Francis Group plc, London

Fujisawa K, Kobayashi A, Aoyama S (2009) Theoretical description of embankment erosion owing to overflow. Geotechnique 59(8):661–671

Fujisawa K, Marcato G, Nomura Y, Pasuto A (2010) Management of a typhoon-induced landslide in Otomura (Japan). Geomorphology 124:150–156

Gregoretti C, Maltauro A, Lanzoni S (2010) Laboratory experiments on the failure of coarse homogenous sediment natural dams on a sloping bed. J Hydraul Eng 136:868–879

Hattanji T, Moriwaki H (2009) Morphometric analysis of relic landslides using detailed distribution maps: implications for forecasting travel distance of future landslides. Geomorphology 103:447–454

Hayashi M, Van der kamp G, Schmidt R (2003) Focused infiltration of snowmelt in partially frozen soil under small depressions. J Hydrol 270:214–229

Huang MH, Jin F, Yang WJ (2008) Breaching flood simulation o Tangjiashan landslide dam. In: Proceedings of the 2008 annual conference of Chinese Hydraulic Engineering Society, pp 961–966 (in Chinese)

Jones JAA (1990) Piping effects in humid lands. In Higgins CG, Coates DR (eds.) Groundwater geomorphology. Geological Society of America, Special paper 252, pp 111–138

Korup O, Tweed F (2007) Ice, moraine and landslide dams in mountainous terrain. Q Sci Rev 26:3406–3422

Korup O, McSaveney MJ, Davie TRH (2003) Sediment generation and delivery from large historic landslides in the Southern Alps, New Zealand. Geomorphology 61:189–207

Mizuyama T, Satohuka Y, Ogawa K, Mori T (2006) Estimating the outflow discharge rate from landslide dam outburst. Univ Academic Press, Tokyo, pp 365–377

Shang Y, Yang Z, Li L, Liu D, Liao Q, Wang Y (2003) A super-large landslide in Tibet in 2000: background, occurrence, disaster, and origin. Geomorphology 54(3–4):225–243

Taira A, Okada A, Whitaker JH, Smith AJ (1982) The Shimanto belt of Japan: cretaceous-lower miocene active-margin sedimentation. Geol Soc 10:5–26 (London, Special Publications)

Watanabe T, Rothacher D (1996) The 1994 Luggye Tsho glacier lake outburst flood. Bhutan Himal MtiRes Dev 16(1):77–81

Worman A (1993) Seepage-induced mass wasting in coarse soil slopes. J Hydraul Eng 199:1155–1168

Xu Q, Fan X, Huang R (2009) Landslide dam triggered by the Wenchuan earthquake, Sichuan Province, Southwest China. Bull Eng Geol Environ 68:373–386

Zangerl C, Loew S, Eberhardt E (2006) Structure, geometry and formation of brittle discontinuities in anisotropic crystalline rocks of the Central Gotthard Massif. Switz Eclogae geol Helv 99:271–290

Comprehensive Treatment Methods of Chaancun Landslide in Dalian City, China

Min Zhang, Lei Nie and Shulin Dai

Abstract For the past few years, the occurrence of the Chaancum landslide in Dalian city of China has caused great economic loss of about Yuan 46,000,000. The landslide affected the Lvshun highway, Wangjiadian reservoir and the safety of lives and properties of local residents. This has prompted the need to stabilize the slope to avert future disaster associated with landslide and to minimize economic loss and infrastructural damages within the area. This paper discusses the treatment design process. From the beginning to the end, several treatment plans are designed. In line with the principles of safety, reliability and economy, a comprehensive treatment system composed of cut slope, slope foot project, anti-slide piles, and drainage is put forward at last. The treatment plan changes can reflect the dynamic design idea.

Keywords Landslide · Comprehensive treatment · Dynamic design

1 Introduction

As the population increases continuously, human's action space is steadily expanded, and the scale of our project increases steadily. Considering the effect of global climate change and human activities, landslide disasters are seemingly becoming more and more frequent in mountainous regions. In order to mitigate personal safeties and properties, effective treatment measures should be taken before the overall sliding (Au 1985; Yin et al. 2000; Schuster and Lynn 2001). On

M. Zhang (✉) · L. Nie · S. Dai
College of Construction Engineering, Jilin University, Ximinzhu Street 938, Changchun 130026, China
e-mail: zhangmin7913@126.com

F. Wang et al. (eds.), *Progress of Geo-Disaster Mitigation Technology in Asia*, Environmental Science and Engineering, DOI: 10.1007/978-3-642-29107-4_31,

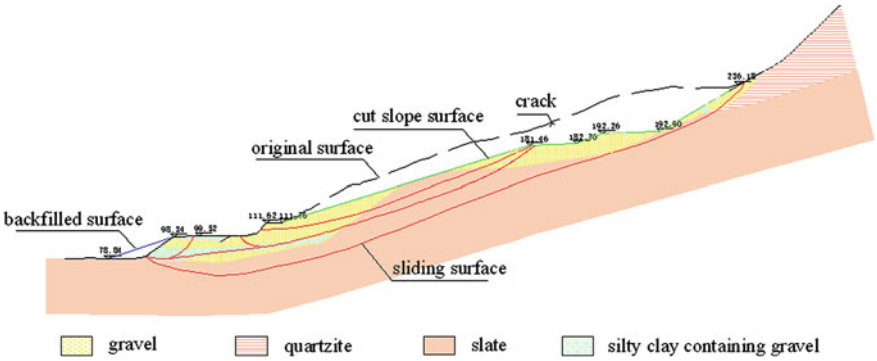

Fig. 1 Slope morphology of the vertical section (first plan)

the other hand, design of landslide treatment should be considered on the principle of economy reasonable and technology feasible (Ghebretensae and Yu 2002; Nie and Fu 2004), so the treatment design is a complex process.

The motion velocity of the Chaancun landslide increased between October, 2009 and August, 2010. Field observation shows that if countermeasures are not carried out on the slope, a catastrophic landslide may be triggered in no distant time. This paper designed some stabilization processes for the slope and tries to explain the methods employed in the design.

2 Comprehensive Treatment Plan

In order to mitigate the hazard, comprehensive treatment methods including cut slope, backfilled soil in the slope toe, anti-slide piles, and drainage were proposed. A lot of remediation plan have been designed between April, 2010 and January 2011. Three of them are introduced as follow.

2.1 The First Plan

Cut slope and backfilled Cut slope and backfilled soil in the slope toe should be done to improve the overall stability of the landslide. The cut slope is designed into a two-way tilt. After the slope cut, there will be two platforms on the vertical section and gently inclined on the cross section (shown in Figs. 1, 2). The total volume of cut slope is 913,000 m^3, and 40,000 m^3 of backfilled soil.

Anti-slide pile After cut slope, the rectangle anti-slide piles are used, and the section size is 3 × 4 m. Piles A1 are used to anchor the middle of the slope. Piles A2 are to make sure the sliding surface in the east of the slope stable. The design of pile A1 is show in Fig. 3, and Table 1 is the design parameters of pile.

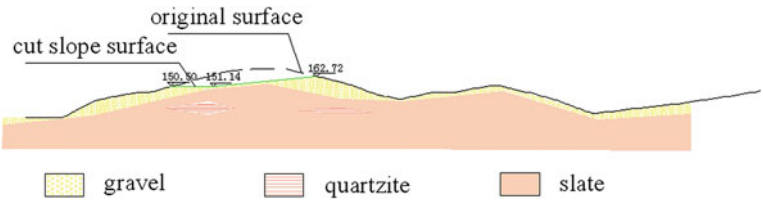

Fig. 2 Slope morphology of the cross section (first plan)

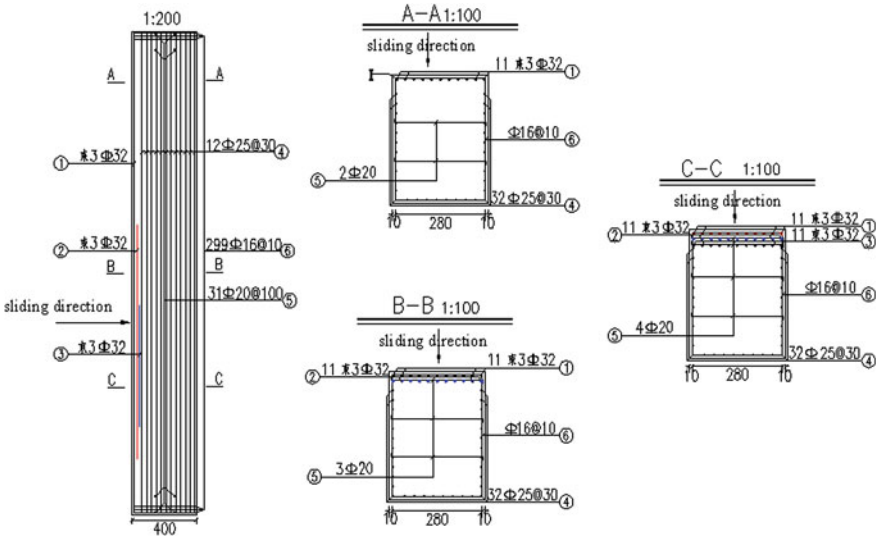

Fig. 3 Reinforcement of pile A1

Drainage After the cut slope of Chaancun landslide, two platforms will be formed, so the blind ditches should be constructed in the end of the platforms. At the same time, open ditches were constructed at the east side of the slope. Fig. 4a is the shape of the blind ditch, and Fig. 4b is the open ditch. Fig. 5 is the whole design of comprehensive treatment methods of the first plan.

2.2 The Second Plan

Cut slope and backfilled In this plan, the depth of cut slope is deeper than the first plan. Cut slope is not only to improve the overall stability, but to cut down pile length. After the slope cut, there will be three platforms on the vertical section and gently inclined on the cross section (Figs. 6, 7). The total volume of cut slope is 1,280,000 m^3, and 196,000 m^3 of backfilled soil.

Table 1 Design parameters of anti-slide pile of the first plan

Pile number	Spacing (m)	Total number of piles	Length of one pile (m)
A1	8	28	30
A2	8	13	33

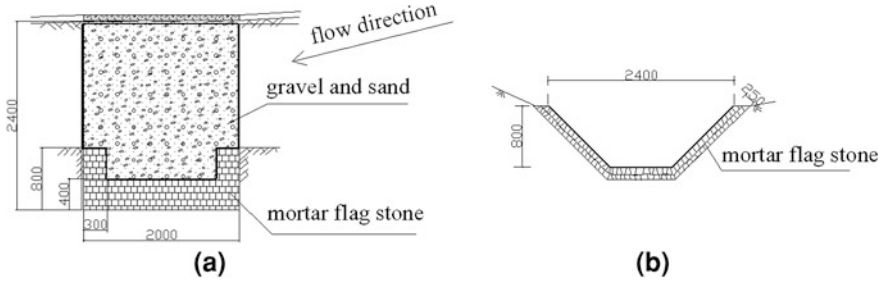

Fig. 4 Blind ditch and open ditch

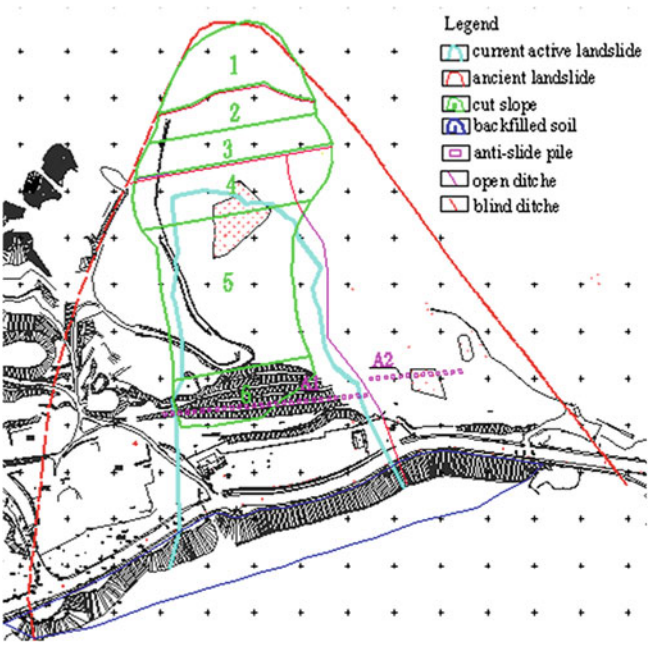

Fig. 5 Comprehensive treatment methods of the first plan

Anti-slide pile After cut slope, the rectangle anti-slide piles are used, and the section size is 3 × 4 m. Piles B1 are used to anchor the lower sliding surface. Piles B2 keep the middle sliding surface and the upper sliding surface stable in the middle of the slope. Piles B3 are to make sure the sliding surface in the east of the

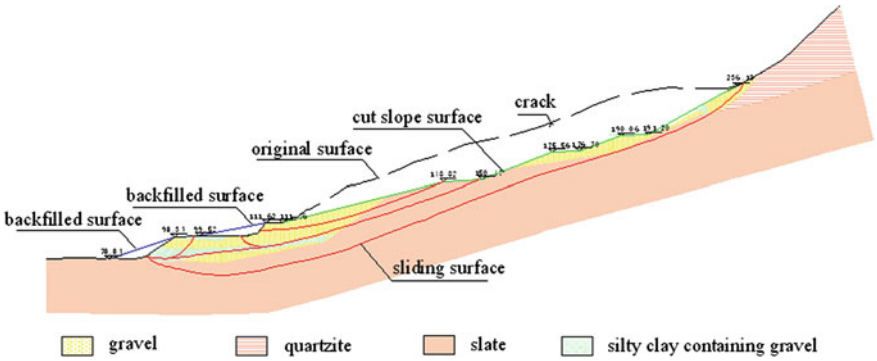

Fig. 6 Slope morphology of the vertical section (second plan)

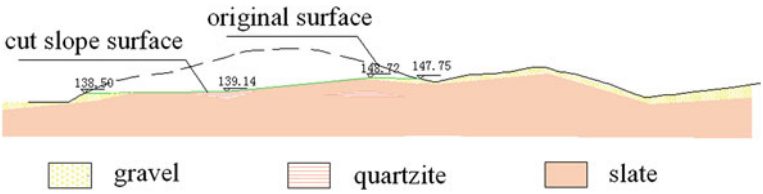

Fig. 7 Slope morphology of the cross section (second plan)

Table 2 Design parameters of anti-slide pile of the second plan

Pile number	Spacing (m)	Total number of piles	Length of one pile (m)
B1	8	27	33
B2	8	27	30
B3	6	19	33

slope stable. Table 2 is the design parameters of pile. The reinforcement design is similar to Fig. 3.

Drainage The blind ditches should also be constructed in the end of the platforms. But open ditches should be constructed in both side of the slope, along the natural valley. Figure 8 is the whole design of comprehensive treatment methods of the second plan.

2.3 The Third Plan

Cut slope and backfilled In this plan, the depth of cut slope is the deepest (shown in Figs. 9, 10). The total volume of cut slope is 2,366,000 m^3, and 59,000 m^3 of backfilled soil.

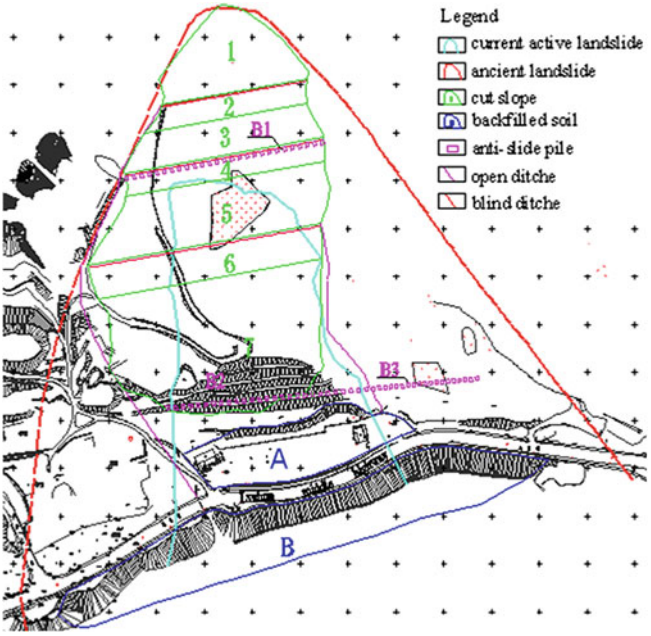

Fig. 8 Comprehensive treatment methods of the second plan

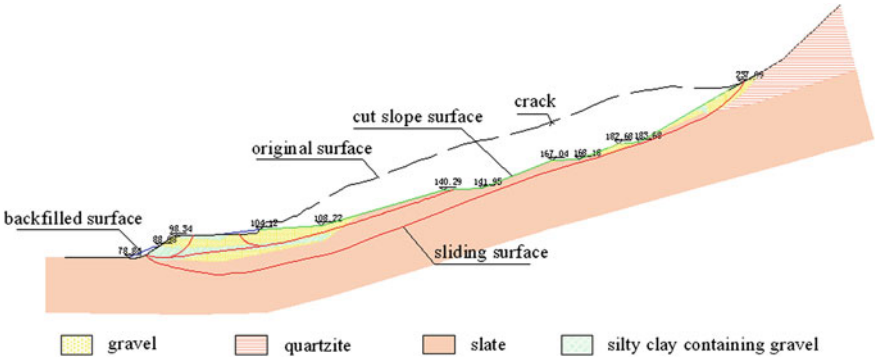

Fig. 9 Slope morphology of the vertical section (third plan)

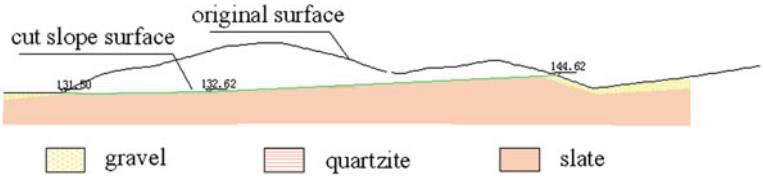

Fig. 10 Slope morphology of the cross section (third plan)

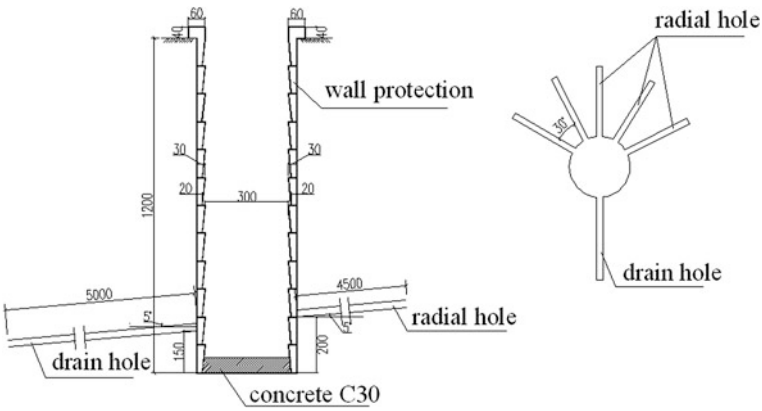

Fig. 11 Borehole combined drainage

Anti-slide pile After cut slope, the middle of the slope is stable. So only a row of anti-slide piles is needed to retain the east of the slope safety. The section size of the rectangle pile is still 3 × 4 m. The spacing is 10 m, the total number is 10, and the length of one pile is 21 m.

Drainage Open ditches and blind ditches are also used in this plan, but the position has a little difference. Borehole combined drainage is used to drain the groundwater. The borehole combined drainage is composed with shaft and radial well. The shaft is dug in the slope body, and drilled five radial holes. Groundwater seeps into the five radial hole and collects in the shaft, then flow into the drainage pipe and is discharged through an outlet (Fig. 11). Figure 12 is the whole design of comprehensive treatment methods of the third plan.

3 Treatment Design Idea

The treatment plan change form the first plan to the third reflects the design idea. In the first plan, because the most dangerous load combination is not considered, especially the rare rainstorm condition. So the cut slope is smaller, and the number of anti-slide piles is not very large. Then the following plans are improved. In the second plan, more anti-slide piles to keep stable. But rectangular piles need manual digging holes, the construction process is complex, and has a high cost. Meanwhile, we know the earth from the cut slope can be used for sea reclamation, so the third plan is designed as more cut slope and less anti-slide piles. And great attention is paid to the role of groundwater, borehole combined drainage is used. One unique advantage of this remediation plan is that it is cost and time efficient with high probability of stabilizing the slope for a very long period.

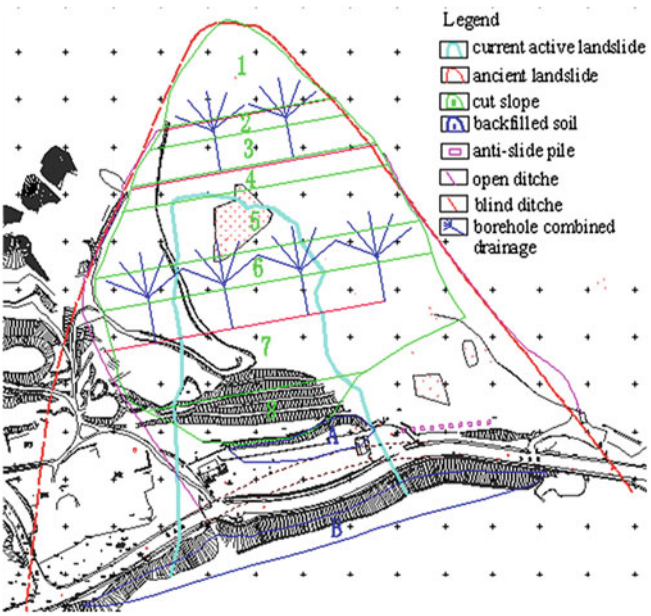

Fig. 12 Comprehensive treatment methods of the third plan

4 Conclusions

(1) Comprehensive treatment methods with more cut slope and less anti-slide piles, slope foot project, ditches and borehole combined drainage were proposed. The proposed remediation plans are cost efficient, feasible and can be applied in slope stabilization.
(2) An optimized treatment plan depends on the type of stabilization technique used, and the understanding of the geological condition of the affected area.

Acknowledgments This research was funded by the Liaoning Hydrogeology and Engineering Geology Survey Institute and J-i-lin University, China. We are grateful to our colleagues who contributed to the success of this research.

References

Au SWC (1985) Rain-induced slope instability in Hong Kong. Eng Geol 51(1):1–36
Ghebretensae N, Yu QY(2002) Optimum of landslide administer methods of expressway-taking Zhongli landslide on Yanji to Tumen expressway as example. World Geol 21(1):67–70
Nie L, Fu FL (2004) Landslide harness on expressway of northeast China. J Eng Geol 12 (suppl):321–324

Schuster RL, Lynn MH (2001) Socioeconomic impacts of landslides in the western hemisphere. U.S. Geological Survery Open-file Report 01–9276

Yin KL, Han ZS, Li ZZ (2000) Progress of landslide researches in the world. Hydrogeol Eng Geol 5:1–4

Research on Unstable Rock Stability Evaluation and Rockfall Motion Characteristics of Chenjiashanping

Shulin Dai, Chenglei Liu, Yan Xu and Tingxin Yu

Abstract Unstable rock relicts in Chenjiashanping are part of the major geodisasters which were contributed by the effect of the 2008 (8.0 M_S) Wenchuan earthquake in Chenjiashanping with epicenter, 80 km west-northwest of Chengdu, Wenchuan County in Sichuan Province of China. Xiangzhang slope hosts lots of displaced unstable blocks of rocks tilting in different directions with sizes ranging from few centimetres to tens of meters. These unstable rocks are composed of highly weathered sandstone and alluvial gravelly soils, which have been cut by multiple sets and co-sets of irregular fractures and joints. Once these unstable rocks topple or slide, they will cause severe effect on the lives and properties of the local people living just below the Xiangzhang slope in Shimen Village. In view of this, this paper analyzed the probable failure mechanism, speed, motion characteristics of these unstable rocks, and proposed some geotechnical engineering remediation works which would contribute in geodisaster mitigation and prevention.

Keywords Unstable rock · Stability evaluation · Rockfall motion characteristics

1 Introduction

A deadly earthquake measuring 8.0 on the Richter scale struck Sichuan Province of China on Monday, May 12, 2008 at exactly 14: 28: 01 CST. The earthquake killed 69, 197 people with Sichuan Province recording 68, 636 fatalities. Information

S. Dai (✉) · C. Liu · Y. Xu · T. Yu
Construction Engineering College, Jilin University, Ximinzhu Street 6,
130026 Changchun, China
e-mail: daisl@jlu.edu.cn

F. Wang et al. (eds.), *Progress of Geo-Disaster Mitigation Technology in Asia*,
Environmental Science and Engineering, DOI: 10.1007/978-3-642-29107-4_32,

Fig. 1 Unstable rock No. 1

obtained from the China Earthquake Administration (CEA), asserted that the earthquake occurred along the Longmenshan thrust fault along the border of the Indo-Australian Plate and Eurasian Plate. The earthquake's epicenter was located in Wenchuan County, Sichuan Province with epicentral distance of 80 km and focal depth of 19 km. Chenjiashanping is located in Shifang city of China, which is not far from the epicenter of the Wenchuan earthquake. The devastating earthquake led to geoenvironmental disasters, triggering the collapse of Xiangzhang slope in Chenjiashanping. After the earthquake-triggered landslides, mudslides, rockfalls and debris avalanche, many unstable rocks still exist on top of the Xiangzhang slope. These unstable geomaterials are composed of strongly weathered sandstone and alluvial gravelly soil. These rock materials have been affected by multiple sets of fractures, irregular joints and mylonitic shear zones. Once the crags failure takes place, it will affect the safety of lives and properties of people who dwell in the lower part of the Shimen village.

2 Characteristics and Failure Style of the Unstable Rocks

2.1 Characteristics of Unstable Rocks

Figures 1, 2, 3, 4 and 5 shows the unstable rocks of the Chenjiashanping slope. Table 1 shows the characteristic geometry of the unstable rocks.

2.2 Unstable Rocks Failure Style

Analysis of the unstable rock form, development scale, basement and bottom layer characteristics, and spatial distribution characteristics shows that the rocks may fail by sliding while No. 1 and 2 unstable rock may fail by toppling.

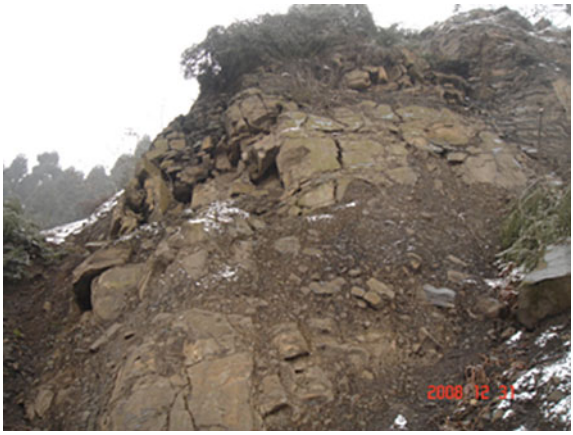

Fig. 2 Unstable rock No. 2

Fig. 3 Unstable rock No. 3

Fig. 4 Unstable rock No. 4

Fig. 5 Unstable rock No. 5

Table 1 Basic characteristics of unstable rocks

Number	Length (m)	Width (m)	Area (m^2)	Thickness (m)	Volume (m^3)
1	37	43	1591	5	7955
2	70	55	3850	5	19250
3	47	20	940	8	7520
4	83	31	2573	4	10292
5	52	27	1404	4	5616

3 Unstable Rocks Stability Evaluation

3.1 Toppling Stability Evaluation

No. 1 and 2 unstable rock is cut seriously by multiple sets of fractures. Lots of dangerous blocks of rocks are shown in Figs. 1 and 2. The toppling evaluation model of the unstable blocks is shown in Fig. 6. As the blocks fails by toppling, they will rotate around the C axis. Then the coefficient of stability will be calculated using the following equation:

$$K = \frac{W \times a + \frac{1}{2}[\sigma_t]\frac{(H-e)^2}{\sin^2\beta}}{P \times h_0 + Q(\frac{1}{3}\cdot\frac{e_1}{\sin\beta} + \frac{H-e}{\sin\beta})} \tag{1}$$

Where didn't consider tensile strength of the base, W, is gravity of unit length dangerous rock block (KN), P is the under earthquake force of unit length dangerous rock block (KN), Calculation by $P = \xi W$, ξ is horizontal earthquake coefficient, β is angle of fracture surface of the dip (deg.), H is height of dangerous rock block (m), e is depth of fracture (m), e_1 is depth of water filling (m), Q is the

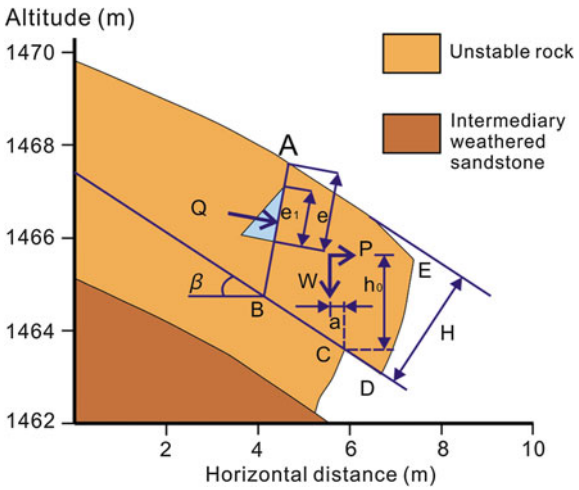

Fig. 6 Toppling stability evaluation model

Table 2 Result of toppling stability evaluation

Numbers	No. 1 unstable rock	No. 2 unstable rock
Heavy rain conditions	0.938	0.901
Earthquake condition	0.882	0.833

hydrostatic pressure in the fractured layers (KN, a is horizontal distance between point of dangerous rock block center and the point of overturning (m), h_0 is the vertical dimension between earthquake force and the point of overturning (m, [σt] is 0.7 times tensile strength standard values of dangerous rock block.

The results of the toppling stability evaluation are shown in Table 2. The result shows that blocks No. 1 and 2 will fail by toppling due to the combined effect of heavy rainfall and earthquake.

3.2 Sliding Stability Evaluation

Simulation model of the sliding stability evaluation is shown in Fig. 7. The sliding stability analysis considers the formula below;

$$K = [(W\cos\alpha - U)\tan\varphi' + c'L]/W\sin\alpha \tag{2}$$

where K is the stability coefficient, W is the weight of unstable rock (KN/m), α is angle of slip surface (deg.), U is fissure water pressure (KN/m), $U = 1/2\gamma_w h_w^2$, h_w is height of water filling into the fractures at the posterior border (m), c' is cohesion of

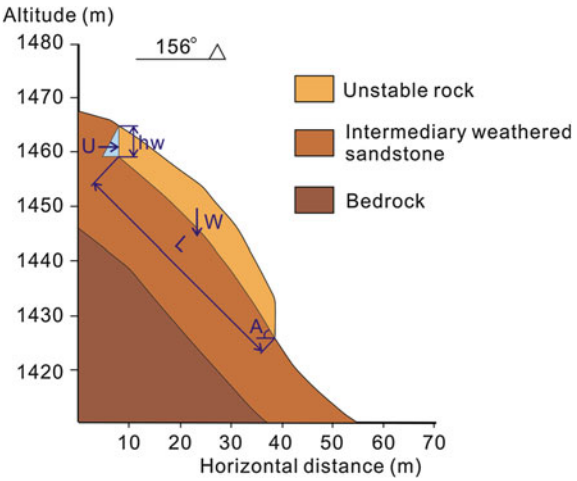

Fig. 7 Sliding stability evaluation model

Table 3 Suggested physical and mechanical parameters of unstable rock

Working condition	Condition 1, natural state			Condition 2, Heavy rains state		
	Severe (KN/m^3)	C (kPa)	φ (deg.)	Severe (KN/m^3)	C (kPa)	φ (deg.)
Unstable rock	23.0	60	36	23.5	50	32

Precaution, working condition three (natural state and earthquake) parameters as working condition 1

Table 4 Results of unstable rock sliding stability evaluation

Unstable rock Numbers	1	2	3	4	5
Condition 1	1.347	1.356	1.386	1.495	1.421
Condition 2	1.135	1.130	1.160	1.227	1.165
Condition 3	1.029	1.026	1.046	1.125	1.075

slip surface (kPa), φ' is friction angle of the slip surface (deg.), L is the horizontal distance of the slip surface (m).

Three working conditions are considered. Physical and mechanical parameters of the unstable rocks under different working conditions are shown in Table 3, with earthquake peak dynamic acceleration taken to be 0.2 g. Result obtained from the computation for the sliding stability of the unstable rock is shown in Table 4.

Standard safety coefficient of the sliding stability evaluation is shown in Table 5.

From the computed result, the rocks are stable under normal undisturbed state and are also stable under the combined effect of heavy rainfall and earthquake. Analysis of results obtained from the evaluation of the unstable rocks show that some of the unstable rocks will yield to the effect of gravity and topple under heavy rainfall and earthquake effect.

Table 5 The standard of sliding stability of unstable rock

Conditions of dangerous rock mass	Unstable	Basic stability	Stable
Condition 1	<1.0	1.0 ~ 1.3	>1.3
Condition 2	<1.0	1.0 ~ 1.2	>1.2
Condition 3	<1.0	1.0 ~ 1.15	>1.15

Table 6 The final velocity of rockfall at the foot of the slope

Rock Numbers	1	2	3	4	5
Velocity (m/s)	22.2	27.1	25.7	24.9	20.3

4 Research on Rockfall Motion Characteristics

4.1 Analysis of Rockfall Movement Velocity

Using the undisturbed natural state of the unstable rocks on the Xiangzhang slope, mathematical formula proposed by Nieme Roy Nish was used to calculate the motion velocity of the rockfall (Hu 1989) (Eq. 3)

$$V_j(i) = \sqrt{V_0^2(i)+2gH_i(1 - K_i ctg\alpha_i)} \tag{3}$$

where V_0 (i) is the starting point speed of the rockfalls (m/s), when $\alpha_i - 1 > \alpha_i$, $V_0(i) = V_j(i-1)\cos(\alpha_{i-1}-\alpha_i)$, when $\alpha_i - 1 < \alpha_i$, $V_0(i) = V_j(i-1)$, V_j (i) is movement velocity of the rockfalls at the end of the before slope (m/s), Hi is the vertical height of each line of the ramp (m).

The final velocity of rockfall is shown in Table 6.

4.2 Calculation of Rockfalls Buckjump

Result obtained from the rockfall buckjump calculation shows high vertical and maximum vertical deviations when the rocks fall from the slope surface to the slope toe (Huang et al. 2007; Huang and Liu 2008). Maximum horizontal distance between the rockfall and the slope surface is obtained from Eq. 4:

$$L_{max} = \frac{V_0^2(tg\alpha - ctg\beta)^2}{2gtg\alpha(1 + ctg^2\beta)} \tag{4}$$

The vertical distance between the rockfall and the slope surface is obtained from Eq. 5.

$$H_{max} = L_{max} tg\alpha \tag{5}$$

Table 7 The calculation results of buckjump

Rock Numbers	1	2	3	4	5
Buckjump distance (m)	4.83	4.85	1.38	4.97	4.56
Buckjump height (m)	2.15	1.86	0.37	1.81	1.57
Buckjump height (m)	2.15	1.86	0.37	1.81	1.57

Table 8 The calculation results of rockfalls bounce

Rock Numbers	1	2	3	4	5
Bounce distance (m)	13.06	17.59	11.77	14.22	9.00
Bounce height (m)	1.04	2.21	0.58	0.93	0.56

Where V_0 is the foot velocity of rockfall at the end of the slope (m/s), β is the angle between speed with the direction and the longitudinal axis (deg.).

The result obtained from the computation of the rockfall buckjumps are shown in Table 7.

4.3 Rockfalls Bounce Calculation

Rock bounce calculation mainly obtains the maximum height of rockfall in building slope as well as the intercept meet falling platform (Lv et al. 2003).

The furthest distance of falling bounce is:

$$L_{max} = \frac{V_0^2}{g} \sin 2\gamma \tag{6}$$

The maximum height of rockfalls bounce is:

$$H_{max} = \frac{V_0^2}{2g} \sin^2 \gamma \tag{7}$$

where V_0 is the foot velocity of the rockfall at the end of the slope (m/s), γ is angle of reflection (deg), φ is incident angle (deg). Usually, take the foot of hillside Angle as incident angle, ρ is coefficient of restitution, as 0.5, λ is transient friction coefficient, as 0.3.

The furthest distance of the rocks bounce is shown in Table 8.

5 Proposed Geotechnical Remediation Plan

In order to check and control geodisasters associated with rockfalls and rockslips, geotechnical engineering remedial measures should be applied on the affected areas (Liu et al. 2005, Zhang and Zhou 2009). Results obtained from the analyses

shows that bioengineering planting of special trees on the slopes, construction of retaining walls with minimum height of 3.0 m, and other geotechnical slope stabilization techniques would help to check, mitigate and prevent probable rockfall disaster in the area.

6 Conclusion

(1) Blocks of rocks around Chenjiashanping area are stable under normal natural conditions and have been found to be in stable state under the combined effect of heavy rainfall or earthquake disturbance. Result from numerical analysis shows that rocks No.1 and 2 will fail by toppling under heavy rainfall or earthquake disturbance.
(2) In order to control and mitigate disasters associated with rockfalls, high quality concrete reinforcements should be constructed to hold the unstable rocks together. Also, planting of special carpet grasses, cover trees and construction of retaining walls should be considered.
(3) Results obtained from rockfall motion characteristics show that the minimum height of the proposed retaining wall should be 3.0 m while the minimum horizontal distance from the foot of the slope should be 8 m.

References

Hu HT (1989) Collapse and rockfall. China railway publishing house, Beijing (in Chinese)
Huang RQ, Liu WH, Zhou JP, Pei XJ (2007) Experimental study of motion features in rolling stone. Chinese J Geotech Eng 29(7):1296–1302
Huang RQ, Liu WH (2008) Study on the movement characteristics of rolling rock blocks on platform. Chinese J Adv Earth Sci 23(5):517–523
Liu YP, Nie L, Li GJ (2005) Falling rock movement characteristic and reinforcement measures of a high steep slope. Chinese J Hydrogeol Eng Geol 32(1):30–33
Lv Q, Sun HY, Zhuo SK, Wang HB, Shang YQ (2003) Evaluation models of rockfall trajectory. Chinese J Natural Disasters 12(2):79–84
Zhang TB, Zhou LH (2009) The movement characteristics and reinforcement measures of highway landslide rockfall. Chinese J Hydropower design 25(3):40–42

Research on the Early-Warning Model with Debris Flow Efficacy Coefficient Based on the Optimal Combination Weighting Law

Yichen Zhang, Lei Nie and Yanliang Wang

Abstract Early-warning of debris flow plays an important role in disaster mitigation and prevention. Based on optional combination weighting law, the warning model with debris flow efficacy coefficient was built considering the evaluation factors including deposits of loose materials along the gully, gradient of mountain slope, effective precipitation in three dimensions, vegetation coverage rate, relative height difference, watershed area, and total amount of precipitation in a single day. The debris flow which occurred in the city of Dunhua, China was analyzed and evaluated; the data have been used in disaster warning in flood seasons. The result shows that early-warning model with debris flow efficacy coefficient is feasible and practical, and can be regarded as a new method of debris flow warning.

Keywords Debris flow · Efficacy coefficient · Optimal combination weighting law · Early-warning model

1 Introduction

The geological condition of China is relatively complex, with drastic plate tectonism, coupled with the fact that China is one of the countries in the world that suffer the influence of debris flow. Lots of fatalities, damages to properties, and

Y. Zhang (✉) · Y. Wang
Central Monitoring Station of Geology and Environment,
Jilin, 130021 Changchun, China
e-mail: weifenfangcheng@tom.com

Y. Zhang · L. Nie
College of Construction Engineering, Jilin University,
Jilin, 130021 Changchun, China

F. Wang et al. (eds.), *Progress of Geo-Disaster Mitigation Technology in Asia*,
Environmental Science and Engineering, DOI: 10.1007/978-3-642-29107-4_33,

obstruction of highways are recorded every year especially during the rainy season periods due to debris flow avalanches. In 2010, flash floods and debris avalanche occurred in Gansu Zhouqu area of China, causing severe damages to properties and displacement of local dwellers. So the development of debris flow disasters early warning research is of great significance in disaster mitigation and prevention.

The efficacy coefficient method is a method that based on multi objective planning theory, to assess indicators according to the quality standard; the function can be transformed into the measurement evaluation scores of evaluation object and carry out overall evaluation. The method according to the evaluation of the complexity of the object, from the different sides to calculate score to the object, has the characteristics of objective, accurate. The key advantage in the application of the efficacy coefficient method is in determining weights of each index size of which the weight coefficient directly reflects in the efficacy coefficient forecast model for the relative degree of importance, whether it is reasonable or not directly affect the prediction accuracy. The existing evaluation methods mainly include two categories: subjective method and objective analysis method. Subjective judgment by experts to determine the weight coefficient of evaluation index points to realizing the quantitative to qualitative changes But the shortcomings of this method is that the result which is influenced by subjective factors is too large; objective analysis method is based on the index data, the objective information extraction and analysis to determine the weight coefficient of size, which is characterized by strong objectivity, but ignored the experts in determining the weight coefficient of the important role, the calculation results are often not convincing. This paper will focus on the subjective judgment preference ratio method and objective analysis method of entropy function method for optimization. Optimization model is used to determine the weight coefficient of each index which is combined with the efficacy coefficient method to establish the early warning model of debris flow effect coefficient based on the optimal weights combination theory.

2 Efficiency Coefficient Method

Efficiency coefficient method is sometimes referred to as efficiency function method. Is a quantitative method that reflects many indices and comprehensive analysis for each evaluation index to determine a satisfied value and an impermissible value, and regard the satisfied values as the upper limit and the impermissible value as the lower limit, and calculate the satisfied value degree of each index, and determine the index function value, and determine the comprehensive evaluation value through the weighted evaluation, so as to evaluate the comprehensive status of the research object. The evaluation steps are as follows:

(1) Selection of the evaluation index
The evaluation index should be representative, typical and independent in evaluating a system, and should reflect the general situation of evaluation target as much as possible (Abdou and Savoy 2006).
(2) Defining the evaluation index of the satisfied value and impermissible value
There should be determined satisfied value and impermissible values for each evaluation index. Satisfied value is the given value according to people's or industry experience; impermissible value is generally the acceptable minimum or maximum value of the evaluation index.
(3) Single efficacy coefficient of evaluation index
In the evaluation index system, single efficacy coefficient can be determined by the following rules according to the characteristics of each index. There are 4 styles in total. The very large variable is the variable that the higher the index value, the higher the coefficient of individual efficacy; the very small variable is that the smaller the value of the index, the higher the single efficacy coefficient; the stable-type variable is that single efficacy coefficient is the highest when the index value at a certain point; the interval-type is that single efficacy coefficient is the highest when the index value in a range.
The computational formula of single efficacy coefficient of the very large variable is as follows.

$$g1_i = \begin{cases} \dfrac{x_i - x_{ni}}{x_{yi} - x_{ni}} \times 40 + 60, & x_i < x_{yi} \\ 100, & x_i \geq x_{yi} \end{cases}$$

The computational formula of single efficacy coefficient of the very small variable is as follows.

$$g2_i = \begin{cases} \dfrac{x_i - x_{ni}}{x_{yi} - x_{ni}} \times 40 + 60, & x_i > x_{yi} \\ 100, & x_i \leq x_{yi} \end{cases}$$

The computational formula of single efficacy coefficient of the stable-type variable is as follows.

$$g3_i = \left(1 - \frac{|x_i - x_{yi}|}{|x_{ni} - x_{yi}|}\right) \times 40 + 60$$

The computational formula of single efficacy coefficient of the interval-type variable is as follows.

$$g4_i = \begin{cases} \left(1 - \dfrac{x_{\min} - x_i}{x_{\min} - x_{n\min}}\right) \times 40 + 60, & x_i < x_{\min} \\ 100, & x_{\min} \leq x_i \leq x_{\max} \\ \left(1 - \dfrac{x_i - x_{\max}}{x_{n\max} - x_{\max}}\right) \times 40 + 60, & x_i > x_{\max} \end{cases}$$

where, $g1_i$ is the number of single efficacy coefficient of the very large variable, x_i is the actual values of the evaluation index for i, x_{yi} is the satisfaction value of evaluation for i and x_{ni} is the unsatisfied value of evaluation for i. Where, x_{max} is the maximum value of the interval-type variable, x_{min} is the minimum value of the interval variable, x_{nmax} is the unsatisfied function of the maximum value and x_{nmin} is the unsatisfied function of the minimum value.

(4) General efficacy coefficient

The general efficacy coefficient of the evaluation object is calculated according to single efficacy coefficient and weight coefficient of evaluation index. The computational formula is as follows.

$$G = \sum_{i}^{m} g_i \times \omega_i$$

where, G is the general efficacy coefficient of evaluation object, g_i is the single efficacy coefficient of evaluation index for i and ω_i is the weight coefficient of evaluation for i.

3 Optimal Combination of Empowerment Theory

The main purpose of optimization theory is to find the optimal solution in many programs. The optimal combination of empowerment theory is considered with *m* objects and *n* attributes, and under the conditions of group decision model which contains *L* decision-making participants, coordinating several single model weights, and selecting preferred one (Chen 2003; Meng et al. 2009). In this paper, the weight determined preference ratio method and entropy method were chosen to optimize the combination, and dealt with an optimization problem instead of weight problems. Finally, the weight determination met the subjective judgment and objective analysis of combinatorial optimization.

4 Preference Ratio Method

Preference ratio method is a subjective judgment based on the evaluators to evaluate the importance of indicators (Bay and Pazzani 2001). It is based on pairwise comparison of all participating indicators to determine the indicators of the evaluation results of the actual contribution rate. Different from the traditional scale of the AHP method, the evaluation of the preference ratio has been re-defined (Table 1). To a certain extent, the method both reflects the will of the experts, and also with the actual situation.

The number of known evaluation is n, $C = \{c_1, c_2, \ldots c_n\}$ In order to facilitate the model, it may be assumed in order of importance among the various indicators

Table 1 Ratio scale between factors

The relative preference of indicators Ci and Cj	Ratio scale value
Ci is very stronger	5.0
Ci is much stronger	4.0
Ci is stronger	3.0
Ci is slightly stronger	2.0
Ci and Cj is similar	1.0
The comparison of Cj and Ci	Reciprocal of the ratio
Middle level of the two	Average value of the ratio scale

as $c_1 \geq c_2 \geq \cdots \geq c_n$. $a_{ij}(i,j = 1,2,\ldots,n)$ are defined as the ratio scale values of c_i and c_j, the following equations can be created:

$$\begin{cases} a_{11}p_1 + a_{12}p_2 + \cdots + a_{1n}p_n = np_1, \\ a_{22}p_2 + a_{23}p_3 + \cdots + a_{2n}p_n = (n-1)p_2, \\ \cdots\cdots \\ a_{n-1,n-1}p_{n-1} + a_{n-1,n}p_n = 2p_{n-1}, \\ p_1 + p_2 + \cdots + p_n = 1_{\text{o}} \end{cases}$$

where, $0 \leq p_j \leq 1$, $j = 1,2,\ldots,n$; p_j is the wanted weight.

5 Entropy Method

Entropy was named by the founder of information theory in Mathematical Theory of Communication in 1948. It is commonly known as information entropy. In information systems, information entropy is a measure of the information on the degree of disorder. The greater its value, the higher the degree of disorders of the information and the smaller the utility value of the information. Conversely, the smaller the information entropy, the smaller the degree of disorders of the information and the greater the value of the usefulness of the information, the more it contributes to the evaluation results. The entropy method is used (Wang et al. 2006, 2010; Wei and Yan 2001), and the data information is used to determine the weight coefficient, as follows:

With m objects and n evaluations, each index attributes value of b_{ij} (b_{ij} represents i index of the j object attribute values), the information entropy is a dimensionless quantity, therefore, before calculating the weight of each index of the data is normalized. Standardized decision matrix is $B = \{b_{ij}\}_{m\times n}$. Command:

$$k_{ij} = \frac{b_{ij}}{\sum_{i=1}^{m} b_{ij}}, \quad i = 1,2,\ldots m; \quad j = 1,2,\ldots n$$

Table 2 Relationship between the debris flow early warning level and the evaluation dimensions in Dunhua area

Early warning level	C ($10^4 m^3/km^2$)	E (°)	F (mm)	G (%)	H (m)	I (km^2)	J (mm)
I	<1	<15	<60	>60	<60	<0.10	<30
II	1–3	15–25	60–80	45–60	60–80	0.10–0.50	30–50
III	3–5	>45	80–100	30–45	80–100	0.50–1.0	50–70
IV	5–7	25–32	100–120	15–30	100–120	1.0–1.5	70–100
V	>7	32–45	>120	<15	>120	>1.50	>100

C along the ditch loose materials deposits, *E* hillside slope, *F* effect rainfall in 3 days, *G* fraction of green vegetation, *H* relative relief, *I* drainage area, *J* rain that day

And the information entropy is:

$$h_j = -(\ln n)^{-1} \sum_{i=1}^{m} k_{ij} \ln k_{ij}, \quad j = 1, 2 \ldots n$$

Information entropy can be used to measure the information utility value of the index. In a completely disordered system, the degree of orderliness is zero, and its entropy value is max. $h_j = 1$, the utility value of information evaluation of h_j is 0. Therefore, the information utility value of an indicator depends on the difference between the information entropy index h_j and 1. So the j indicator weights: $q_j = \frac{1-h_j}{\sum_{j=1}^{n}(1-h_j)}, \quad j = 1, 2, \ldots n$

Research on the Early Warning Model of Debris Flow Efficacy Coefficient Based on the Optimal Combination Empowerment Theory: In the Case of the Typical Disaster Point in Dunhua City.

(1) Establishment of the relationship between evaluation index and early warning level

The evaluation index of the early warning model of debris flow uses the selected factors, of which, C—along the ditch loose materials deposits; E—hillside slope; F—effect rainfall in 3d; G—fraction of green vegetation; H—relative relief; I—drainage area; J—rain that day.

Take the debris flow gully in recent 10 years of the Dunhua city disaster history for example, and take the quantitative method and discrimination standards about the predisposition of the debris flow gully estimated in the Debris Flow Disaster Prevention and Control Engineering Exploration Norms, GT/T 0220-2006 as the basis, and conduct statistical analysis based on the combination of the evaluation dimensions and the actual situation of the debris flow in the research area, so that we established the relationship between the debris flow early warning level and the evaluation dimensions in Dunhua area as follow (Table 2).

Table 3 The satisfaction value of the various index

Eigen Value		C ($10^4m^3/km^2$)	E (°)	F (mm)	G (%)	H (m)	I (km^2)	J (mm)
Satisfaction value		7	32–45	120	15	120	1.50	100
No valve	Upper limit		55					
	Lower limit	1	15	60	60	60	0.10	30

C along the ditch loose materials deposits, *E* hillside slope, *F* effect rainfall in 3 days, *G* fraction of green vegetation, *H* relative relief, *I* drainage area, *J* rain that day

(2) Evaluation of the Satisfaction Value and No Value of the index
Combined range of values and variable attributes are shown in Table 2. The satisfaction value of the various indices were determined and presented in Table 3. The satisfaction value is inclined to the highest standard according to the index theory to the greatest extent, which is hard to be confirmed because of the complicated geological environment, like highest standard of relative relief, along the ditch loose materials deposits; rainfall condition is different in all the areas. No value is meant to the lowest standard according to the index theory, like the lowest standard of the hillside slope and rainfall condition is 0 while in the actual geological environment conditions it is no possible for debris flow to happen under the circumstances and it is no necessary to warning. Therefore, to evaluate the satisfaction value and No value of the index, the evaluation index of the geological environment condition class is divided into severity and normal based on the high incidence stated in the Debris Flow Disaster Prevention and Control Engineering Exploration Norms, while the rainfall condition is based on statistical rule of index and possibility of the debris flow in the study area combined with previous research results.

(3) Single efficacy coefficient calculation
In early warning of debris flow evaluation index system, single efficacy coefficient of the relative relief along the ditch loose materials deposits, 3-D effective rainfall, catchment area and daily rainfall data are calculated as extremely large variables while fraction of green vegetation as extremely small variables. Result obtained by the research team shows that when the slope elevation is low, the slope material will become unstable due to the effect of stream erosion. On the other hand, when the slope elevation is high, the loose rock mass will fail by abrupt slump causing the slope materials to be easily transported to the gully downstream as the solid fragments are difficult to be accumulated. The increase of the slope and the slope surface deposits are not in a simple linear relationship, but with a range of slope (32–45°), where the rock and soil accumulation can reach the maximum, so the single efficacy coefficient is calculated with the single efficacy coefficient of the interval type variables.

(4) Determination of the weight coefficient with the optimal combination empowerment theory
With the optimal combination empowerment theory, the weight coefficient of the 3-D effect of daily rainfall along the ditch loose deposits, drainage area,

Table 4 Mudslides warning level

Warning level	Total efficacy coefficient	Illustration
I	≤60	Lower possibility, no warning
II	60–70	Low possibility, no warning
III	70–80	High possibility, yellow warning
IV	80–90	Higher possibility, orange warning
V	≥90	Highest possibility, red warning

Table 5 Evaluation index of the typical disaster areas in Dunhua city

Disaster area	Fraction of green vegetation (%)	Loose deposits ($10^4 m^3/km^2$)	Slope (°)	Drainage area (Km^2)	Relative relief (m)
Debris flow in the Jianghe village, Dapuchai town	20	3.0	30	0.40	150
Debris flow in the Yujia Village, Daqiao town	30	3.0	35	0.25	130
Debris flow in the Sandaogou village, Guandi town	25	2.2	30	1.00	170
Debris flow in the Xiaodonggou village, Yanminghu town	30	3.0	40	0.50	130

hillside slope, relative relief, fraction of green vegetation in the order of importance are 0.3142, 0.2771, 0.1243, 0.1066, 0.0710, 0.0710, 0.0355.

(5) Classification of the early warning level
Total efficacy coefficient can be calculated by the formula, which is used as an evaluation standard. It is based on the efficacy coefficient principles and the research results of YingchaoWang and Yuequan Shang; so the early warning level of the debris flow can be divided according to the numerical values. Released to the society, the levels are I II III, and yellow for I which means the possibility of debris flow is high and orange for II which means higher and red for III which means the highest (Table 4).

(6) Models of the early warning in different geological disaster areas
With the specific evaluation index (Table 5) of the selected disaster areas in Dunhua city and the calculation (Table 6) of the single efficacy coefficient of the index in spite of the index rainfall, we can get the relationship equation of the total efficacy coefficient about the effect of rainfall with models of the early warning in different geological disaster areas.
Debris flow in the Jianghe Village, Dapuchai Town:

Table 6 The single efficacy coefficient of the typical disaster areas in Dunhua city

Disaster area	Fraction of green vegetation	Loose deposits	Slope	Drainage area	Relative relief
Debris flow in the Jianghe village,Dapuchai town	64	73	95	68	67
Debris flow in the Yujia village,Daqiao town	73	73	100	64	64
Debris flow in the Sandaogou village, Guandi town	69	68	95	86	69
Debris flow in the Xiaodonggou village, Yanminghu town	73	73	100	71	64

$$G = \left[\frac{r_a - 60}{60} \times 40 + 60\right] \times 0.3142 + \left[\frac{r_0 - 30}{70} \times 40 + 60\right] \times 0.2771 + 30.0967$$

Simplified to

$$G = 0.21r_a + 0.16r_0 + 48.28$$

Debris flow in the Yujia Village, Daqiao Town:

$$G = 0.21r_a + 0.16r_0 + 48.32$$

Debris flow in the Sandaogou Village, Guandi Town:

$$G = 0.21r_a + 0.16r_0 + 49.90$$

Debris flow in the Xiaodonggou Village, Yanminghu:

$$G = 0.21r_a + 0.16r_0 + 49.07$$

Of which, r_a–3d effect rainfallr_0–rainfall that day. To sum up, $r_0 \geq 30$, $G \in [70, 80)$, release III;$r_0 \geq 30$, $G \in [80, 90)$, release IV;$r_0 \geq 30$, $G \geq 90$, release V.

6 Conclusions

(1) In the debris flow early warning model, the effective factor of the optimal combination of empowerment theory was used to determine the weight coefficient which overcomes the problem that the preference ratio method of subjective factors is too large and the entropy method is far too objective. To achieve the optimal combination of subjective and objective, the early warning model can be used more scientific and rational, and with great significance, it's a meaningful exploration.

(2) The model was applied to Dunhua City geological disasters in flood season warning analysis, the warning results was in line with the debris flow pattern,

and it can play an active role in disaster prevention and mitigation, so the model is more reliable. It provides a new method for debris flow warning.

References

Abdou S, Savoy J (2006) Statistical and comparative evaluation of various indexing and search models. LNCS 4182(2006):362–373

Bay SD, Pazzani MJ (2001) Detecting group differences: mining contrast sets. Data Min Knowl Disc 5(3):213–246

Chen HY (2003) Research on optimal combination determining weights method for multiple attribute decision making. Oper Res Manag Sci 12(2):6–10

Meng FQ, Li GJ, Wang Q (2009) Application of optimal combination weighting law in the debris flow risk assessment. Yangtze River 40(22):40–42

Wang MY, Zhang FM, Liu Z (2006) Evaluation method of the multi-attribute scheme based on entropy weight of fuzzy information. Syst Eng Electron 28(10):1523–l525

Wang YC, Shang YQ, Sun HY (2010) Study of prediction of rock burst intensity based on efficacy coefficient method. Rock Soil Mech 31(2):529–534

Wei QL, Yan H (2001) A method of transferring polyhedron between the intersection-form and the sum-form. Comput Math Appl 41(10–11):1327–1342

Influence of the Heat Transfer Efficiency of Oil Shale In Situ Fragmentation

Chen Chen, Wei Wang, Youhong Sun, Wei Guo, Xuanchen Yan, Hongyan Wang, Guijie Zhao, Jiwei Wen, Qian Fang and Xinpeng Liu

Abstract The increase of the phase of oil shale in situ fragmentation was suggested in the initial phase of in situ mining, which was against problems in the existing in situ oil shale mining technology. By theoretically analyzed this method of in situ mining, making oil shale beds in hole base broken into small pieces of size and the formation of cracks through hydraulic or other technical means, the heat transfer efficiency of small size of oil shale after fragmentation would be greatly improved. Taking fluid heating as example, the certification of theoretical calculation was done. Through the experimental comparison of the subcritical water extraction of shale oil and oil shale TGA instrument pyrolysis which had been completed by others, we analyze the shale oil extraction rate of large size and small size of oil shale. Experimental results shown that both electrical heating or fluid heating method, shale oil extraction rate of the small size of oil shale was significantly increased than the larger size of oil shale. Theory and experiments shown that the oil shale in situ fragmentation would have an impact on heat transfer efficiency for in situ mining of oil shale, the heat transfer efficiency after in situ fragmentation will be a significant improvement than broken before.

Keywords Oil shale · In situ mining · In situ fragmentation · Heat transfer efficiency

C. Chen (✉) · W. Wang · Y. Sun · W. Guo · X. Yan · G. Zhao · J. Wen · Q. Fang · X. Liu
College of Construction Engineering, Jilin University, 130026 Changchun, China
e-mail: chenchen@jlu.edu.cn

H. Wang
College of Chemistry, Jilin University, 130012 Changchun, China

F. Wang et al. (eds.), *Progress of Geo-Disaster Mitigation Technology in Asia*, Environmental Science and Engineering, DOI: 10.1007/978-3-642-29107-4_34,

1 Introduction

In the recent years, as global demand for oil and international oil prices continued to rise, countries around the world are actively looking for alternatives for oil resources. Oil shale, as alternatives for oil, more attention has been paid. It has important practical significance to vigorously develop oil shale (Niu and Chen 2006). The world's oil shale reserves are about 550 billion tons. If they are converted into oil, reserves are equivalent as 5.4 times as the amount of current proven natural crude oil recoverable (Liu and Liu 2006).

The way to extract shale oil from oil shale is basically divided into two categories worldwide: ex-situ retorting and underground conversion process. The mining of the ex-situ retorting is of high cost, but also produces a large number of "three wastes" (waste gas, waste water, and waste residue) which brought serious environmental pollution and destruction of the ecological environment. The technique of oil shale in situ mining belongs to the underground conversion process, which is a relatively economical and environmentally friendly shale oil preparation technique.

The principle of in situ oil shale mining technology is as follows. By directly heat to the underground oil shale beds, making them crack and generate oil and gas production, oil and gas were finally explored by production wells (Gao et al. 2007; Fang et al. 2009; Qian et al. 2008). The main methods of existing oil shale in situ mining were electrical heating and fluid heating, but the heat transfer efficiency in these two methods were not high. It in general cost more than 3 years in electrical heating to extract shale oil and gas. The heat loss in the fluid heating was very large. So how to improve heat transfer efficiency of in situ mining are the urgent problems which we are facing now.

2 The Existing Oil Shale In Situ Mining Technology

At present, the in situ oil shale mining technologies are up to dozens. The most mature of which is ICP technology of Shell, whose research has been carried out field trials but not for commercial exploitation. Other in situ mining techniques are still in the laboratory research stage.

According to the heating methods, in situ mining of oil shale can be divided into three types of process of electrical heating, fluid heating, and radiation heating (Harold 2005). In which the underground conversion of ICP Technology of Shell, Electrofrac TM of Exxon—the Mobil and GFC technologies of EP are adopted the way of the electric conduction heating on the oil shale formation.

The electrical heating with high power consumption and slow heating, which costs several years on heating to output oil and gas. Besides it has high cost, easily damaged heating element is and low rate of oil and gas recovery.

The CRUSH technology of Chevron, in situ mining technology of EGL and the convection heating technology of Taiyuan University of Technology all take the fluid heating method to heat the oil shale formation. The speed of fluid heating is relatively quicker. Due to the role of fluid pressure, the cracks will not be closed. So the oil and gas export faster out of the strata but not easy to control, which is easy to form the short-circuit of the fluid that the fluid flow is too fast, without the oil shale heat exchanger. The system is more complex with higher cost.

Radiation heating technology is a new development concept. The current technology of radiation heating methods to heat the shale beds mainly consist of LLNL's RF technology and critical flow radio frequency technology of Schlumberger/Raytheon2CF. Radiant heating is with strong penetrating and quick heating speed, but with higher cost and difficult to control. So the technology is very difficult. And because of the low permeability of the oil shale formation, in order to explore oil and gas smoothly, the corresponding oil shale formation should be fractured so that to increase its porosity and permeability (Liu 2009).

3 Analysis on Heat Transfer in the Process of Oil Shale In Situ Fragmentation

Although the in situ oil shale mining technology has been developed for decades, disadvantages of high energy consumption and cost are still widespread. There are the following reasons mainly:

1. Oil shale is a poor conductor of heat. The heat transfer efficiency is very low for the large size of oil shale, no matter in electric heating or fluid heating.
2. Second, in the natural state, oil shale is a kind of argillaceous shale with low permeability and porosity, whose penetration rate is of 0.0001–0.000001 mD. The kerogen occurs in solid form in the oil shale and forms the integration with oil shale. So the tiny underground bedding is in a closed state completely. However, if the internal oil (gas) wants to be discharged from the dense oil shale into the extraction wells, there must be cracks in the system so that the oil (gas) can effectively communicate with the extraction wells. Even if the oil shale exists some natural fractures as well as generated cracks in the case of heat expansion, but still not easy to meet needs of oil and gas discharged from the oil shale (Wang et al. 2010; Arens 2001; Chen et al. 2007; Qian and Wang 2006; Liu et al. 2006; Ru and Zhu 2009; Yan and Jiang 2000).

In order to solve the above problem, the increase of the phase of oil shale in situ fragmentation was suggested in the initial phase of in situ mining. Firstly, make underground oil shale in a certain volume within kinds of technical means to break into small pieces of volume. Then do the subsequent in situ heating.

First use a variety of effective horizontal hole drilling and rock breaking technology and hydraulic transport technology in the corresponding position

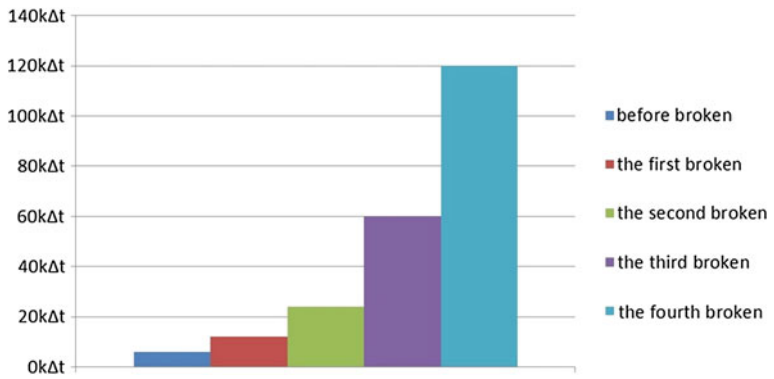

Fig. 1 Compared of heat transfer rate in before broken and four sizes of oil shale after

where oil shale buried to form an underground space (broken space). Then use a variety of technical measures on the oil shale above this level length to fracture and fluid (gas) force, making the large size of oil shale into the small size. Compare the small size of oil shale after broken with the large size before broken, the overheated area of the broken oil shale, oil and gas channel will significantly increase, heat transfer efficiency can be significantly higher.

Taking the fluid heating method as example to verify the theoretical calculations, assuming a large size cube of oil shale before broken with dimensions of $100 \times 100 \times 100$ cm, whose heat transfer cross-section area is of 6 m^2, assumed an ideal case, fully formed the rules of the small size of the cube oil shale page blocks after broken.

Assuming that four possible kinds of small size of oil shale can form after broken. Four ones are respectively marked as the first, the second, the third and the fourth broken, whose corresponding dimensions are $50 \times 50 \times 50$ cm, $25 \times 25 \times 25$ cm, $10 \times 10 \times 10$ cm, and $5 \times 5 \times 5$ cm, as well as the total area of each heat transfer cross-section respectively are 12 m^2, 24 m^2, 60 m^2, and 120 m^2.

According to the heat transfer rate equation, in heat transfer (Yang and Tao 2006):

$$\Phi = KA\Delta t$$

Φ-heat flux, K-heat transfer coefficient, A-cross-sectional area of the heat transfer, Δt-the average temperature difference.

As before and after broken the lithology of oil shale are the same, the heat transfer coefficient K are unchanged. And the minimum temperature for pyrolysis of oil shale is the same. So the average temperature difference will not change. The results of calculation heat flux are shown in Fig. 1. The heat transfer rate can be described by the heat flux, so we can use Fig. 1 to characterize the four cases of heat transfer rate before and after fragmentation.

From Fig. 1, we can conclude that the heat transfer rate of oil shale after broken is higher than the one of before. In the first breakage, the heat transfer rate after broken is two times than broken before. In the second breakage, the heat transfer rate after broken is four times than broken before. In the third breakage, the heat transfer rate after broken is ten times than broken before. In the fourth breakage, the heat transfer rate after broken is twenty times than broken before. By the definition of heat transfer efficiency, it shows that the maximum theoretical heat transfer rate of oil shale is certain. So the heat transfer efficiency will be significantly improved after broken.

4 Experimental Study on the Impact of In Situ Crushing on the Heat Transfer Efficiency

Zhao-hui Xu and others analyzed pyrolysis factors of oil shale in the Liushuhe basin in Daqing by thermal gravimetric analyzer; the pyrolysis experiment was done by selected cylindrical oil shale particles whose sizes were of 2×2, 4×4, 6×6, 8×8 mm (diameter $\times$ height). The experimental results show that the oil production rate decreased with the increase of the oil shale particle size.

The reason is that the poor thermal conductivity of oil shale. When the particle size increases, there are large temperature difference between the surface and the center of the oil shale. The greater particle size of the oil shale, the greater difference of the temperature, the longer required time of heat passed. The increase in particle size also conducts the difficult of diffusion for the center pyrolysis product and increases the chance of thermal polycondensation and secondary pyrolysis. So the small particle size of oil shale has more advantages on oil yield and conversion time (Wang et al. 2010). TGA instrument heating belongs to electrical heating. So we can know that when we use electrical heating, the small size of oil shale heat transfer efficiency is higher than the large size of oil shale.

In order to verify the actual impact of in situ oil shale fragmentation on the heat transfer efficiency in the fluid heating mode, we conducted experiments of using the near-critical water (NCW) to extract shale oil. NCW is the compressed liquid water with temperature between 180–350 °C. As the supercritical water (SCW), NCW has the mass transfer performance (low viscosity and high diffusion coefficient). In addition, it can be used not only as a solvent, but also as a reactant and a catalyst (Sun 2007). Hong-yan Wang from Jilin University put forward a technology which uses NCW as a medium for underground oil shale in situ pyrolysis to extract organic compounds from low-permeability oil shale. The technology has applied for a patent.

Three different sizes of oil shale were chosen to take experiments. In which the physical dimension of the small size of oil shale was 3–5 cm (right in Fig. 2). The one of the large size of oil shale was 10 cm (left in Fig. 2). There was a medium

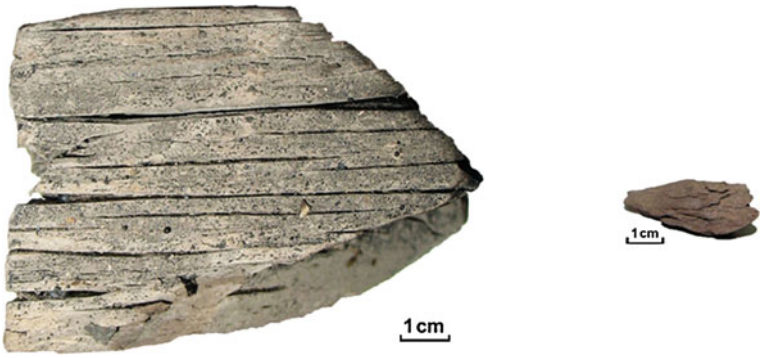

Fig. 2 The physical figure of the large size and the small size of oil shale

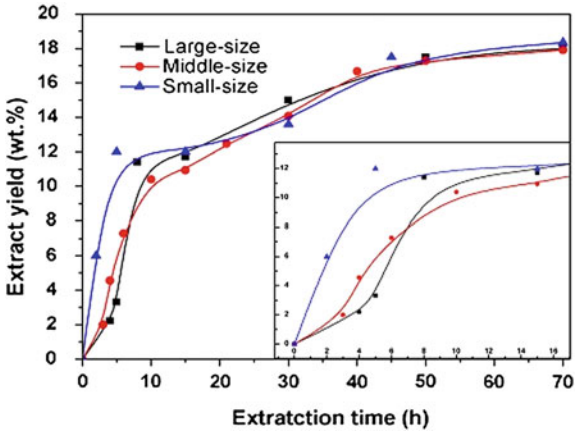

Fig. 3 The experimental results of the shale oil extraction by NCW

size between them. The experimental results were shown in Fig. 3, within the picture shown the extraction curves of first 16 h.

The extraction rate of small size of the oil shale was the highest in the first 16 h as Fig. 3 shown. The maximum difference between the extraction rate of the small size of oil shale and the large size can reach about 7 %. After 16 h, the extraction rate of three sizes of oil shale began to converge. In order to make the extraction rate up to 10 %, it costs about 10 h for large size of oil shale. While it only cost 5 h for the small size. The heat transfer rate of small size oil shale was significantly higher than the large size.

No matter in the electrical heating experiments or in the fluid heating experiments, the results both shown that the heat transfer efficiency of the small size (volume) of oil shale was higher than the large size (volume). So the in situ fragmentation had an impact on the heat transfer efficiency. And the heat transfer efficiency after broken was higher than the one before broken.

5 Conclusion

1. Against the problem that the existing in situ mining technology for oil shale was of low heat transfer efficiency, to increase the process of in situ fragmentation for oil shale was suggested in the initial stage of the in situ mining, which was to crush the large size of oil shale into the small size.
2. Taking the fluid heating as example, the theoretical calculation was done on the heat transfer efficiency of the four sizes of oil shale after broken in the ideally situation and before broken. The calculation results shown that the heat transfer efficiency of four sizes of oil shale after broken were respectively two times, four times, ten times, and twenty times as the ones before broken.
3. The heat transfer efficiency of the small size of oil shale was higher than the large size, no matter in the mode of electrical heating or fluid heating.

References

Arens VJ (2001) Physical and chemical geotechnology. Moscow Publishing House of Moscow State Mining University, pp 426–427

Chen C, Zhang ZP, Wang M (2007) The new model of mining oil shale in Jilin Province. China Min Mag 16(5):55–57

Fang CH, Zheng DW, Liu DX (2009) Development direction and trends of in situ mining technology on oil shale. Energy Tech Manag 2:78–80

Gao SX, Cao KG, Meng QP (2007) Production technology of oil shale. Jilin Geol 26(1):45–48

Harold J (2005) Sources with conductive material for in situ thermal processing of an oil shale formation: United States of America,6929067[P].2005-08-16

Liu R, Liu ZJ (2006) Oil shale resource situation and potential analysis on comprehensive development in China and abroad. J Jilin Univ: Earth Sci Ed 36(6):892–898

Liu ZJ, Dong QS, Ye SQ (2006) The situation of oil shale resources in China. J Jilin Univ: Earth Sci Ed) 36(6):869–873

Liu DX, Wang HY, Zheng DW, Fang CH, Ge ZX (2009) World progress of oil shale in situ exploitation methods. Nat Gas Ind 9(5):28–132

Niu JH, Chen DY (2006) Foreign underground conversion mining method of oil shale. J Jilin Univ: Earth Sci 36(6):1027–1030

Qian JL, Wang JQ (2006) The world's oil shale. Energy of China 28(8):16–19

Qian JL, Wang JQ, Li SY (2008) World oil shale development & utilization trends. Sino-Global Energy 13(1):11–15

Ru FG, Zhu GF (2009) World oil shale production technology. Foreign Oil Field Eng 25(1):1–5

Sun H (2007) Influence of near-critical water on organic chemical reactions. Mat Chem Eng, pp 1–2

Wang HY, Liu ZW, Ning N (2010) Oil shale resources and development technology. Petroleum Industry Press, Beijing, pp 81–86 (in Chinese)

Yan C, Jiang XM (2000) Utilization of chinese oil shale energy. Energy of China 9:22–26

Yang SM, Tao WQ (2006) Fourth edition of heat transfer. Higher Education Press, Beijing, p 13 (in Chinese)

The Damage Mechanism and Estimation of Stability of Dasen Shukong Slope

Shuheng Sun, Hepeng Zhang and Qing Dong

Abstract Detailed geotechnical field investigation was carried out on the Dasen Shukong slope to understand the structural controls affecting its stability which is the probable failure zone between Quaternary gravels and bedrock. Result obtained from the investigation shows that the slope belongs to water pressure-driven landslide and will collapse with increase in rainfall intensity. By means of analysis of combination relationship between the main control structure plane and fissure, the safety factor is 0.615, of which the slope must be treated.

Keywords Slope · Rainfall · Water pressure-driven · Damage mechanism · Estimation of stability

1 Introduction

Problems of slope stability in traffic engineering, water conservancy, hydropower engineering and industrial and civil building engineering exist universally and they are the key of success to the projects in a certain degree. The past few years have witnessed los of scholarly works on the failure mechanism and stability analysis of the slope (Liu et al. 2005a; Zhu et al. 2007; Quan 2004; Huo et al. 2009). And for the gravel soil landslip that obviously exists potential slide plane, the mechanical

S. Sun (✉) · H. Zhang
Hydrogeology and Engineering Geology Survey Institute of Liaoning, 116037 Dalian, China
e-mail: sunsh0849@163.com

Q. Dong
Dalian Admin Station of State Land Resources and Housing, Dalian, 116001 Liaoning, China

F. Wang et al. (eds.), *Progress of Geo-Disaster Mitigation Technology in Asia*, Environmental Science and Engineering, DOI: 10.1007/978-3-642-29107-4_35,

Fig. 1 Loose accretion at the front of the slope

mechanism of destruction can be mainly water pressure drives type (Liu et al. 2005b, 2003; Xu et al. 2006; Ke 2010). So the slope can stay stability in natural stress state. But because the water has many adverse effects such as erosion dissolution, softening effect, physical chemistry effect and mechanics effect on the slope, in the action of factors like rainfall or rising of ground water, the rocks' properties get worse and the shear strength of glide plane gets lower which makes the slope be instable and forms landslip.

Because of the obvious contact surface of gravel soil and underlie rocks which form potential glide plan and the tension fissures at the end of upper slip mass that provide the circulation channels for rainwater, Dasen Shukong slope belongs to typical slope of water pressure drives type.

2 Engineering Geological Conditions of the Slope

2.1 Topography

The physiognomy type of slope is low hilly area of tectonic denudation whose hill top is rounded. The hill slope is lumpy and the terrain is relatively steep with a total slope gradient of 22–35°. There is vegetation growing on the slope and the bed rock of part ground that is composed by thick quartzite splint rock of Sinian bridge group is naked. The total terrain is high in the west and low in the east and undulating. The ground elevation is 87.56–157.81 m while the ground weight difference is 70.25 m. The photograph of loose accretion at the front of the slope is shown in Fig. 1.

Fig. 2 Incline deformation of impounding reservoir at the end of the slope

2.2 Geologic Structure

There are no large wrinkles and fault structures round the slope. There are slates at the bottom of the slope and artificial miscellaneous fill and gravel soil at the top of the slope. The contact zone of rock and soil is parallel with the slope with a low undulation.

The quartzite whose attitude is 260°∠20° exposes on the top of slope and there are some rock rupture phenomena developing inside the rock.

2.3 Meteorological and Hydrological Conditions

The area of the slope belongs to warm temperate zone humid and subhumid marine climate with the year average temperature of 10.6 °C and average rainfall of 662.0 mm. In the area, the maximum amount of precipitation in 10 min is 20.5 mm, in 1 h is 68 mm, in arbitrary 24 h is 149.4 mm and in 1 day is 144.4 mm. A continuous maximum amount of precipitation is 178.6 mm while the average evaporation capacity of many years is 1647.2 mm and the maximum depth of frozen earth is 0.93 m. There are no surface rivers or other water in the area and there is only one flood internalcepting trench which is south-north outside the fence of Dasen Shukong Company. There is a small impounding reservoir on the slope whose incline deformation is shown in Fig. 2.

2.4 Ground Water

During engineering geological investigation, the cover depth of ground water was 3.6–4.3 m in the confine and depth of the slope. According to investigation, the ground water type of the slope is mainly fissure water of bedrock. The ground

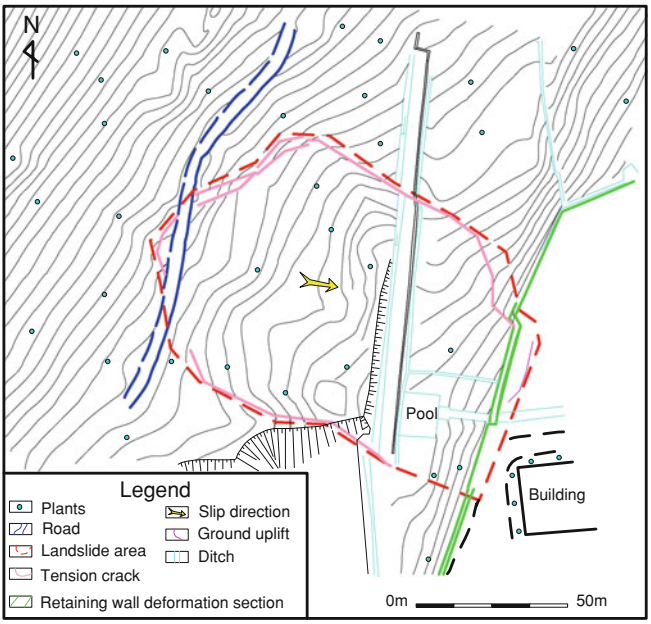

Fig. 3 Plane sketch map of the slope

water exists in the weathering fractures of slate and is seasonal. In rainy season, the rock in medium slope is in moist state, and there is a little water permeating from bedrock fissures with the infiltration capacity of less than 0.01 L/s. But where is no water in dry season. In the process of this reconnaissance, because it was raining in Dalian with an amount of precipitation of more than 50 mm, the ground water of slope and slope toe outflew like a stream along the fissures of caving soil. In the process of misering, the water seepage of drill holes was serious and at the same time, the infiltration capacity of the lower slope increased which indicated that the ground water of the inside slope connected well. The catchment area of upper slope was 0.34 km^2. The plan sketch map of the slope is shown in Fig. 3.

3 Characteristics of the Slope

3.1 Type and Structure of the Slope

The slope is mainly composed by quaternary period miscellaneous fill, gravel soil and Sinian strongly-medium weathered slate.

In which, miscellaneous fill (Q_{4ml}): brown, taupe, black brown and loose. It is mainly composed by gravels, dimension stones and cohesive soil. The content of cohesive soil is 30–50 % and is 50–70 % of gravels and dimension stones. The

Table 1 Major physical mechanism parameters

Lithology	Type of structure plan	Combination degree	Weight(kN/m^3)	Cohesion (kPa)	Friction angle (°)
Miscellaneous fill	Weak structure plan	Bad	19.5	3.03	17.32
Gravel soil	Weak structure plane	Worse	21.0	10.0	16.12
Strongly weathered slate	Rigid structure plane	Bad	23.5	40.0	10.00
Medium weathered slate	Rigid structure plane	Ordinary	26.5	70.0	32.00

gravels and dimension stones are mainly quartzite and in angular-subangular state with a common grain diameter of 3.0–10.0 cm and partly more than 30 cm to the maximum of 200 cm. This layer forms from artificial accumulation backfilling and mostly distributes on the upper surfaces of the slope.

Gravel soil (Q_{4dpl}): brown, loose slightly dense. It is mainly composed by gravels and cohesive soil. The content of cohesive soil is 30–60 and 40–70 % of gravels. The gravels are mainly quartzite and in angular-subangular state with a common grain diameter of 0.5–2.0 cm and partly more than 10 cm. This layer commonly exists on the upper surfaces of the slope.

Strongly weathered slates (Z_{2c}): tawny and gray yellow. They have fragmentation and granular structures and obvious stratifications. The joints develop and in high degree of crushing which are mostly in fragment state. A small part of the surface is clastic and most drill holes, test borings and prospect holes have disclosures.

Medium weathered slates (Z_{2c}): brown and gray yellow. They have layer structures and obvious stratifications. The joint fissuring develops and the core of the rock is cracked that is partly massive and short cylindroid. The structure plans combine badly. The basic quality grade of the rock is IV and there are disclosures in local area whose thickness is 1.5 m.

3.2 Physical Mechanism Properties of the Slope

According to the shearing tests of big area and the wild field testing experiments and on the basis of "Code for Investigation of Geotechnical Engineering" (GB50021), the article respectively makes statistical analysis of indexes such as cohesion, friction angle and weight of the rock and soil, identifies and contrasts outdoor the initial data of physical mechanism indexes and revises the initial data after eliminating the abnormal one. Then the article confirms the average value, standard value and eigenvalue and finally determines the standard value of physical parameter of the slope by statistical results. The major physical mechanism parameters of the slope are shown in Table 1.

4 Analysis of Failure Mechanism

4.1 The Hazard Reasons

The landform of Dasen Shukong slope belongs to low hilly slope foot and the lithology of the slope is slate. The slope is covered with quaternary period artificial filled soil and gravel mixed soil, which are loose with a thickness of 2–7.5 m. By technology means of misering, test pitting, costeaning and geophysical prospecting, the author confirms that the slope inside develops consequent main control structures and the upper structure develops on the contact surface of soil and strongly weathered broken rocks, and the lower develops on the contact zone of soil and strongly weathered rocks with a local thickness of 1.0 m and the state of fold lines. In the condition of heavy rainfall from August 13–17th, 2007, a little surface water was excreted by the cut drainage system and most infiltrated to supply the ground water. Because the scuppers of the retaining wall at the slope toe did not drain freely and the catchment area at the top was large, a great quantity ground water converged in the slope. As long time rain soaked, the rock and soil reached to saturation, which increased the weight of slope and reduced the strength of the rock and soil. The contact surface between quaternary period loose layer and strongly weathered slate was separated, and added with the lubrication of rain, the rock and soil slip downward on its own gravity and caused the landslide.

4.2 Starting Mechanism

The starting mechanism of this slope belongs to water pressure-driven type. On the condition of heavy rains, the hydraulic gradient of ground water in the slope increases suddenly and ground water discharge is blocked, so the pore and cracks are filled with water. The slipping deformation becomes larger in the combine action of hydrostatic pressure and pore water pressure generated along the slip plane by hydrodynamic pressure. In the meantime, the strength of rock and soil become weaker in the soaking of water, then the slope loses balance and the landslide happens.

5 Slope Stability Analysis

5.1 Analysis of the Main Control Structure Plane and Fissure

To analyze the mechanics relationship of the main control structure plane and the slope, the article first analyzes the internal structure plane in the surveying. By

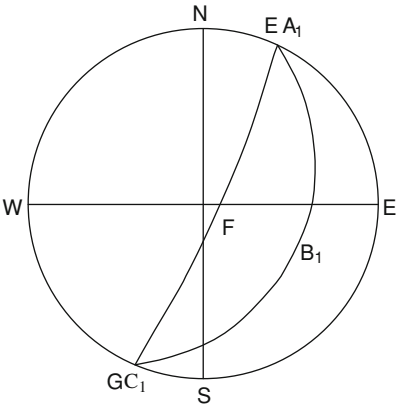

Fig. 4 Stereographic projection of the slope structure

means of analyzing the type and form of the main control structure plane, it analyzes the relationship of structure plane and slope aspect by stereographic method.

There is a large slipping structure plane in this slope section and a contact surface of rock and soil on the top of the slope. In the contact zone of soil and strongly weathered slate, the main control slipping structure plane is in the state of fold lines by the limit of the original terrain with a tendency of 120° and a dip angle between 20 and 45°. The attitude of retaining wall surface is 120°∠80°. The main control structure plane is parallel with the slope and the dip angle of structure plane is less than that of slope surface, which belongs to syntropy extroversive structure plane and is instable. The whole sliding makes the ground in front of the slope uplift as arc-shaped. The slip mass has angles of rupture up along the upheaval deformation, which forms easily slipping slope and is the main instable factor of the slope section. The stereographic projection of the slope structure is shown in Fig. 4.

5.2 Calculation of Stability of the Slope

By means of analyzing the shape characteristics, sliding surface, characteristics of sliding soil and physical mechanics parameter of the slope, stability factor is calculated. And hydrogeology conditions, geotechnical engineering conditions, architectural feature, deformation and failure trend are obtained. This paper finds that the slope may slip and has the condition for fold line slipping. So we can calculate it with the formula of fold line slipping method. The profile map for calculation is shown in Fig. 5.

The adoption of parameters is mainly the measured value, and partly from calculation or experience. The stable factor of the slope is 0.615 and according to

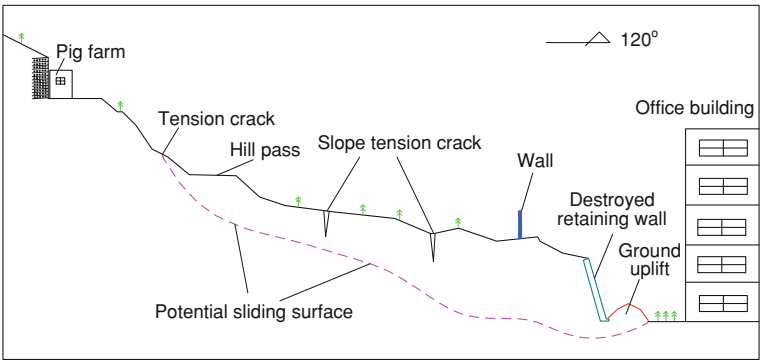

Fig. 5 Profile map of the slope

"Specification of Geological Investigation for Landslide Stabilization", the slope is instability and needs to be treated because its stable factor is less than 1.

6 Conclusion

1. The slope of Dasen Shukong is composed by quaternary period miscellaneous fill, gravel soil and slate, and belongs to the type of slipping along the contact surface of loose accumulation horizon and bed rock.
2. The shear strength of the sliding surface is weak, and the degree of combination is low, which is disadvantageous to the stability of the slope.
3. The slope belongs to water pressure-driven type and the strength of slope significantly reduces on the effect of rainfall. So it slips easily.
4. The capacity of staying stable of the slope itself is bad estimated form the combine relationship of the main control structure plane and the attitude of the fissures. By calculation, the safety factor of the slope is 0.615 and the slope is in instable state. So the slope needs to be treated.

References

Huo YX, Huang RQ, Ju NP (2009) Deformation mechanism and stabilization measures of broken granitic rock slope that experienced Wenchuan earthquake. J Eng Geol 17(3):317–321

Ke YB (2010) Instability mechanisms and reinforcing treatment of granite residual soil slope under rainfall infiltration condition. Bull Soil Water Conserv 30(5):12–15

Liu XW, Liu G et al (2003) Analysis on rainfall influence on slope deformation and failure. Chin J Rock Mech Eng 22(Suppl 2):2715–2718

Liu CH, Chen CX, Feng XT (2005a) Study on mechanism of slope instability due to reservoir water level rise. Rock and Soil 26(5):769–773

Liu CH, Xu J, Cao CL et al (2005b) Analysis of bedding-slip failure mechanism of rock slope due to hydraulic drive. Chin J Rock Mech Eng 24(19):3529–3533

Quan FW (2004) The control and mechanism of the slope slipping with fracture structure. Highway 6:8–12
Xu JC, Shang YQ, Wang JS (2006) Study on relationship between slope-mass slide displacement and precipitation of loose soil landslide. Chin J Rock Mech Eng 25(Supp 1):2854–2860
Zhu XD, Shang YQ (2007) Sensitivity analysis on failure mechanism of debris slope. J Disaster Prev Mitig Eng 27(1):86–90

Prediction of the Jiatanchang Reservoir Bank Collapse in the Three Gorges Reservoir Area

Linlin Zou and Lei Nie

Abstract After the impoundment of the Three Gorges Reservoir, slopes around the reservoir bank and other geological structures near the reservoir were affected by the sudden reservoir water level increase. Geomaterials around the reservoir bank suffered mechanical strength reduction due to the effect of the reservoir which shows periodic rise and fall in water level. Loss of shear strength within the reservoir bank may affect the stability of slopes around the reservoir bank. In this paper, the Jiatanchang reservoir bank was analyzed; it is divided into two parts based on geological characteristics. By the use of Limit Equilibrium Theory and Kachugin Graphic Method,the whole stability and local bank collapse were analyzed and predicted with the determination of the failure mode. Final result was combined with the urban planning and ecological management data, and remediation plans were put forward.

Keywords Stability analysis · Bank collapse prediction · Kachugin Graphic Method

1 Introduction

Jiatanchang reservoir bank is located in Jiangjin District of Chongqing City, China. It is on the left bank of the Sunxi River which is a secondary tributary of the Yangtze River. Figure 1 shows the topographic base map of Jiangjin District. The bank spreads along Yudong and Jiangnan school road covering a distance of more

L. Zou (✉) · L. Nie
College of Construction Engineering, Jilin University, Ximinzhu Street 938, 130026 Changchun, China
e-mail: zoull@jlu.edu.cn

F. Wang et al. (eds.), *Progress of Geo-Disaster Mitigation Technology in Asia*, Environmental Science and Engineering, DOI: 10.1007/978-3-642-29107-4_36,

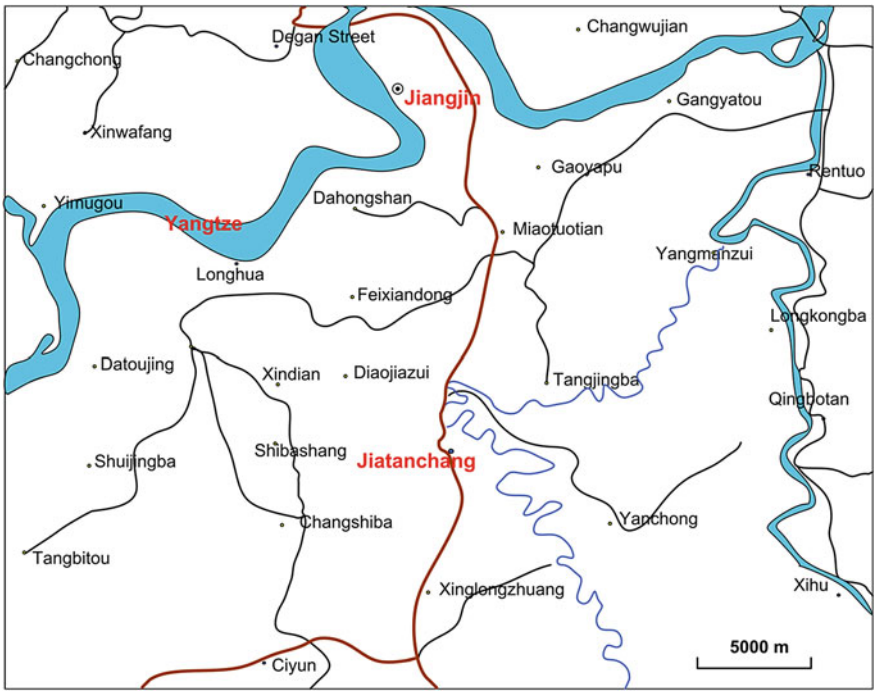

Fig. 1 Traffic position graph

than 500 m. The perennial low water level of the Sunxi River is 181.2 m and the flood level is 193 m. As water level in the Three Gorges Reservoir rises to 175 m, the Jiatanchang reservoir water level also rises to 184.7 m.

2 Bank Segmentation and Geological Characteristics

The reservoir shows a long strip planar shape while the longitudinal profile shows a convex shape; the geomaterial of the reservoir is composed of rock fillings, silty clay, and gravel. The underground water types are pore water in loose rocks and fissure water in the alluvial rock deposits. The reservoir bank was divided into two distinct parts according to the basic principles of bank segmentation taking the small stream under the Jiatan bridge as boundary marker.

Part I: spreads along Yudong Road covering a horizontal distance of 200 m with main scarp elevation of 188 m and slope toe elevation of 200 m having overall relative height of 12 m and slope gradient ranging between 30° and 35°.

Part II: spreads along Jiangnan school Road covering a horizontal distance of 300 m with main scarp elevation of 188 m and slope toe elevation of 194 m. The slope gradient ranges between 25° and 35° with relative vertical height of 6 m.

3 Collapse Prediction and Evaluation

The prediction of the failure style of slopes at the reservoir bank was carried out with initial constructive evaluation of the possible arc-shaped failure plane within the slope material. To understand the probable dynamics controlling the slope stability, graphic method of prediction was employed and the final slope morphology was determined. For the parts that would not produce integral sliding failure, local bank collapse should be predicted.

4 Integral Stability Analysis

For this bank is reverse slope, and the dip angles between contact surfaces are less than 5°, the cemented and dense gravel has formed a natural protective layer of reservoir bank, so the broken-line sliding failure along surfaces would not occur. Therefore the stability coefficient of arc slide inside the Quaternary is analyzed by Limit Equilibrium Theory to identify the probable failure surface, and then integral stability analysis is conducted by Bishop and Janbu Methods.

(1) Profile Selection: According to bank segmentation, profile 1-1 and profile 2-2 were selected in computing the stability analysis of Part I and Part II (Figs. 2 and 3).
(2) Geotechnical parameters of the geomaterial: The geotechnical parameters of the silty clay deposit and land-filling materials were obtained from field in situ sampling, tests, horizontal and vertical borehole data and laboratory analysis (Table 1).
(3) Calculated Conditions and Load Combination: Self weight, surface load, rainstorm and flood are mainly considered to identify the calculated conditions and load combination. According to the actual situations of this bank, Table 2 shows the calculated conditions and load combination.
(4) Stability Calculation: Calculation is conducted in six different conditions by Bishop and Janbu Methods, Table 3 shows the detailed results.
(5) Integral Stability Analysis: The results show that profile 1-1 and 2-2 are both stable, therefore integral sliding failure would not occur. The failure mode of bank collapse is erosion type, and local collapse should be predicted.

5 Local Collapse Prediction

For slopes around the reservoir bank, Kachugin Graphic Method was applied in forecasting the stability of the slope (Liu et al. 2007; Wang et al. 2000).

(1) Principle of Kachugin Graphic Method: According to topographic and geological profile of the area, the stable slope angle of above water surface level

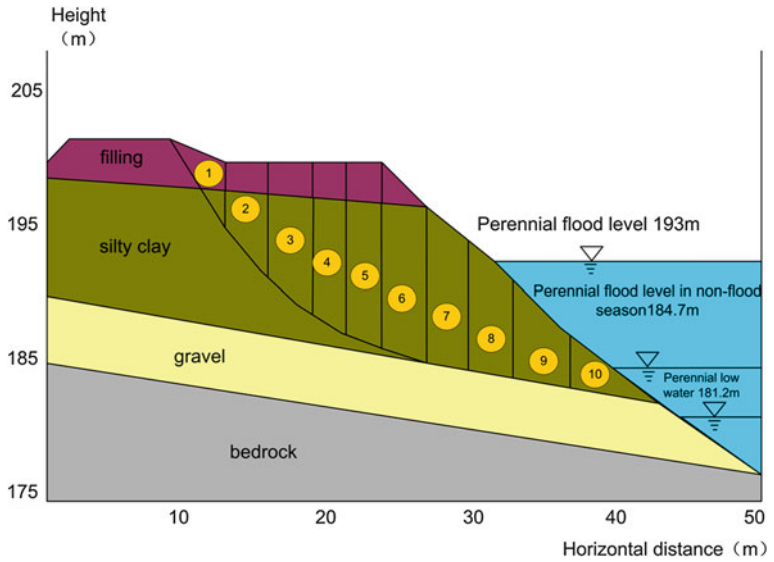

Fig. 2 Sub-strip diagram of profile 1-1

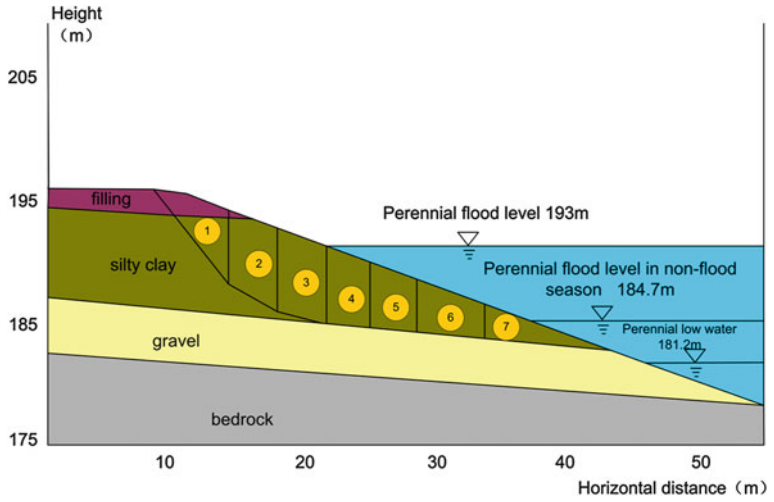

Fig. 3 Sub-strip diagram of profile 2-2

amplitude area and under-water in different rock layers are adopted, and the corresponding slope angle in different water levels are drawn. The connection of stable slope angles in different sections represents the final boundary line of reservoir bank.

Table 1 Calculation parameters

Soil Layer	Status	C (kPa)	Φ (°)	γ (kN/m^3)
Filling	Natural	8.0	23.0	19.0
	Saturated	6.0	18.0	20.0
Silty clay	Natural	28.8	15.9	19.6
	Saturated	16.2	12.4	20.0

Table 2 Calculated conditions and load combination

Calculated Conditions	Load Combination
I	Self weight + surface load + annual flood level
II	Self weight + surface load + flood level every 20 years in non-flood season + rainstorm every 20 years in non-flood season
III	Self weight + surface load + flood level every 50 years + rainstorm every 20 years
IV	Self weight + surface load + flood level every 20 years in non-flood season down to annual flood level in non-flood season
V	Self weight + surface load + flood level every 20 years in non-flood season down to annual flood level in non-flood season + rainstorm every 20 years in non-flood season
VI	Self weight + surface load + flood level every 50 years down to annual flood level + rainstorm every 20 years

Table 3 Calculation results

Profile	Method	Calculated Conditions					
		I	II	III	IV	V	VI
1-1	Bishop	1.432	1.464	1.306	1.291	1.284	1.256
	Janbu	1.482	1.415	1.348	1.288	1.269	1.238
2-2	Bishop	1.572	1.614	1.563	1.440	1.314	1.284
	Janbu	1.527	1.554	1.559	1.349	1.269	1.234

Table 4 Recommended values of stable slope angle

Lithology	The stable slope angle under water (°)	The stable slope angle of level amplitude area (°)	The stable slope angle above water (°)
Silty clay	10°	15°	28°
Filling	10°	20°	30°

(2) Parameters: The stable slope angles are determined by physical and mechanical properties of rock, statistics of slope survey and analysis of initial condition of the reservoir Tang et al. (2006) (Table 4).

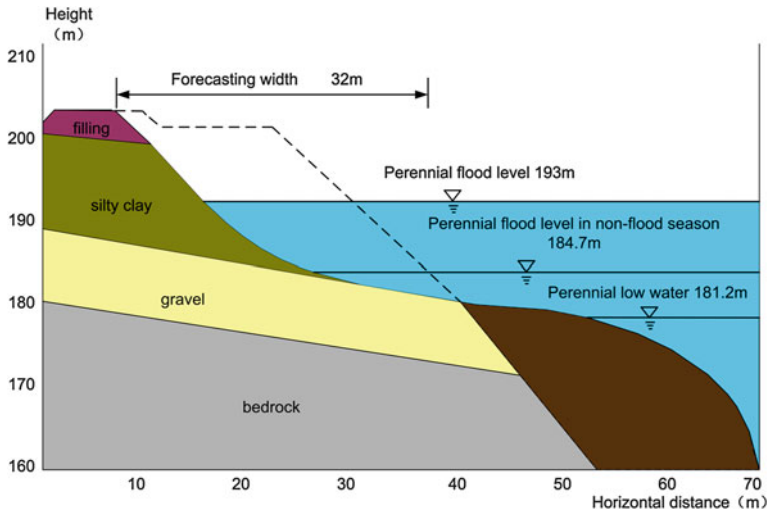

Fig. 4 Forecasting range of bank collapse of profile 1-1

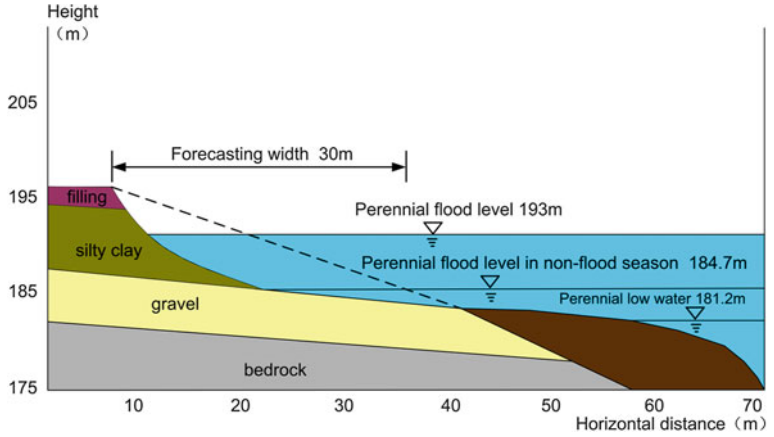

Fig. 5 Forecasting range of bank collapse of profile 2-2

(3) Forecasting results: According to the principles of graphic method and the suggested values of slope angle, the bank collapse of two profiles is predicted (Xiao et al. 2009; Zeng 2008), Figs. 4 and 5 show the forecast ranges.
(4) As the lowest baseline for urban construction is 192 m, the intensity of reservoir bank reformation is graded, shown in Table 5.

Table 5 Forecasting results

Profile	Forecasting width(m)	Forecasting height(m)	The intensity of reservoir bank reformation
1-1	32	201	Strong
2-2	30	194	Strong

6 Conclusions

(1) By analyzing and calculating, Part I and Part II are basically stable in six different conditions which will not produce integral sliding failure, and the failure modes of both parts are erosion types.
(2) The forecasting boundaries by Kachugin Method are basically the same with the bank boundaries after destruction. The forecasting widths of Part I and Part II are 32 and 30 m, and the intensity of bank rebuilding is strong.
(3) The affecting objects of Part I are three residents, comparing to engineering treatment measures, relocation of avoidance is suggested, and the affecting objects of Part II is Jiangnan School Road, the slope protection measures are suggested.

References

Liu YG, Wu ZS, Wu AH (2007) Approximate forecasting methods for reservoir bank destruction and shore protection. Res Soil Water Conserv 14:270–275

Tang MG, Xu Q, Huang RQ (2006) Study on the forecasting parameters of the bank failure and the influence factors in the yangtze three gorges project region. J Chengdu Univ Technol (Sci Technol Edition) 33:460–464

Wang YM, Tang JH, Ling JM (2000) Study on prediction method for reservoir bank caving. Chinese J Geotech Eng 22:569–571

Xiao HB, Chen Q, Zhang B (2009) Prediction of Ganzixi bank collapse in the three gorges reservoir area. J Eng Geol 17:228–232

Zeng H (2008) Prediction of reservoir bank collapse of Pingyikou bank slope in three gorges reservoir area. J China Three Gorges Univ (Natural Sci) 30:27–30

Investigation Method of Flowing Groundwater in Natural Condition Using Temperature Factor

Atsuo Takeuchi, Kensaku Matsumoto and Tsuyoshi Harasawa

Abstract Various types of soil disaster related with groundwater behaviour. Especially, flowing groundwater flows in very local area causes destabilization of the soil structure. It is very important to understand the mechanism of soil disasters. However, exploration of flowing groundwater in local area is very difficult because of heterogeneity of soil quality and groundwater condition. This paper has provided principle and measurement results of two types of exploring method of flowing groundwater. One-meter Depth Temperature method is developed to get information of flowing groundwater route reflected by the ground surface. One-meter Depth Temperature is simple, inexpensive and stable method to detect the local flowing groundwater. We can get information of existence of flowing groundwater by measuring one-meter depth soil temperature, simply. Multipoint Temperature Logging method is also developed. We can get information of vertical location of layers with flowing groundwater. Boring hole was used in Multipoint Temperature Logging method. Measurement of vertical temperature distribution of temperature decreasing process indicates the location of the layers with flowing groundwater. Results of these two methods indicated the three dimensional location of existence of the flowing groundwater in detail.

Keywords Flowing groundwater · One-meter depth temperature method · Multipoint temperature logging method

A. Takeuchi
Natural Groundwater Research Institute, 2-11-1, Yanagawa, Otsu-city, Shiga 520-0014, Japan

K. Matsumoto (✉) · T. Harasawa
Department of Civil and Environmental Engineering, Gunma University, 1-5-1, Kiryu-city, Gunma 376-8515, Japan
e-mail: kemastu@gunma-u.ac.jp

F. Wang et al. (eds.), *Progress of Geo-Disaster Mitigation Technology in Asia*, Environmental Science and Engineering, DOI: 10.1007/978-3-642-29107-4_37,

1 Introduction

Groundwater problems are closely related to bank and slope failure. One of the important factors of theses disasters is groundwater in shallow layer and rainfall infiltration. We reported that results of field measurements indicate existence of flowing ground water in local area as different type from layer type groundwater (Takeuchi 1980). Furthermore, even if in the same soil layer, there is several flowing groundwater with various water level with various water head in it, in some case. Therefore, it is important to obtain information of flowing groundwater in various layers to solve the problems of soil disaster which are related to groundwater. In other word, information of the groundwater in natural condition is important to solve the various soil disasters.

One-meter Depth Temperature method and Multipoint temperature Logging method was developed to obtain the information of the flowing groundwater in natural condition. We introduce the principle and summary of these two methods.

2 Investigation Method of Flowing Groundwater Using Temperature Factor

2.1 One-Meter Depth Temperature Method

One-meter Depth Temperature method is one of the investigation methods of flowing groundwater. Soil temperature in shallow layer fluctuates in one year. However, fluctuation of soil temperature in one day is less than 0.1° in one-meter depth layer. On the other hand, flowing ground water temperature in deeper than one-meter depth is almost constant. Figure 1 shows temperature fluctuation of flowing groundwater and soil in one-meter depth in a year. Difference of temperature between flowing groundwater and soil in one-meter depth causes spatial temperature distribution. If the flowing groundwater exits near measurement point, measured one-meter depth soil temperature becomes lower than normal temperature in summer, or becomes higher than normal temperature in winter. Figure 2 shows illustration of difference of one-meter depth temperature with flowing groundwater from normal one-meter depth temperature in summer and winter. Indicator of One-meter Depth Temperature method is difference between fluctuate one-meter depth soil temperature and constant flowing groundwater temperature. Therefore, if one-meter depth soil temperature and flowing groundwater temperature are almost same, One-meter Depth Temperature method is not applicable. Usually, more than 2.5° difference between one-meter depth soil temperature and flowing groundwater temperature is necessary for application of One-meter Depth Temperature method. Figure 3 shows flow chart of sequence of operation of One-meter Depth Temperature method. At first, measurement points setting and one-meter hole digging are conducted. Then,

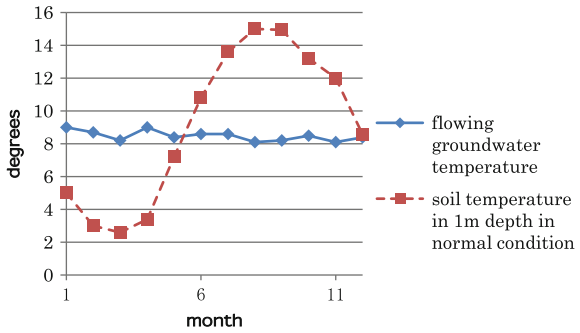

Fig. 1 Temperature fluctuation of flowing groundwater and soil in one-meter depth in a year

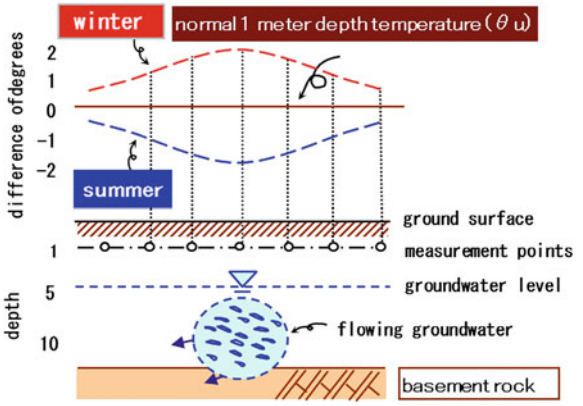

Fig. 2 Illustration of difference of one-meter depth temperature with flowing groundwater from normal one-meter depth temperature in summer and winter

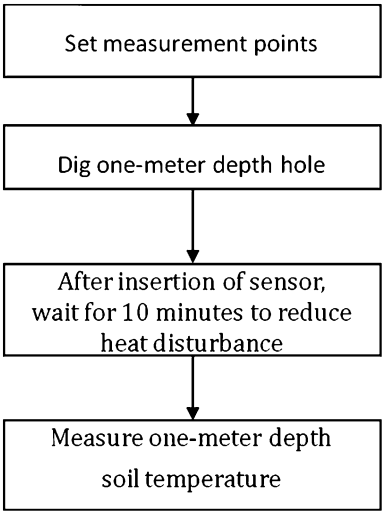

Fig. 3 Flow chart of sequence of operation of one-meter depth temperature method

Fig. 4 Equipment of one-meter depth temperature method

Table 1 Example of measurement conditions of one-meter depth temperature method

Research object	Interval of measurement line (m)	Interval of measurement point (m)
Landslide	5–20	5–10
Leakage of riverbank	2–3	2–5
Leakage of reservoir	3–5	1–3
Infiltration water	1–2	1–50
Working place of tunnel	1–100	1

sensor is inserted to measure the soil temperature. After that, it needs 10 min to reduce the heat disturbance by digging. Finally, the temperature is measured. Figure 4 shows equipment of One-meter Depth Temperature method. And Table 1 shows example of measurement conditions. Example result of One-meter Depth Temperature method is shown in Fig. 5. Field measurement was performed in winter. Therefore, soil temperature in one-meter depth is 7.5°. And flowing groundwater temperature is 15.5°. Plane distribution of measurement results of One-meter Depth Temperature method indicated route of flowing groundwater. Figure 6 shows the other example of measurement results of One-meter Depth Temperature method in summer. By connecting low temperature point, we could obtain route of the flowing groundwater.

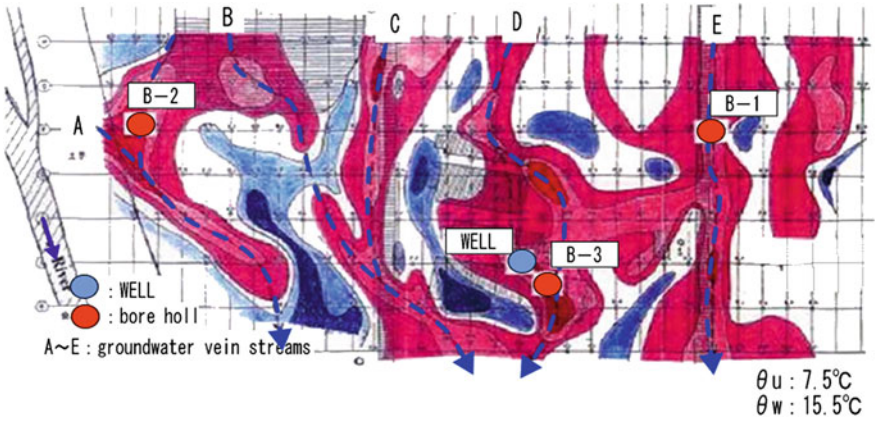

Fig. 5 Example of one-meter depth temperature method in winter

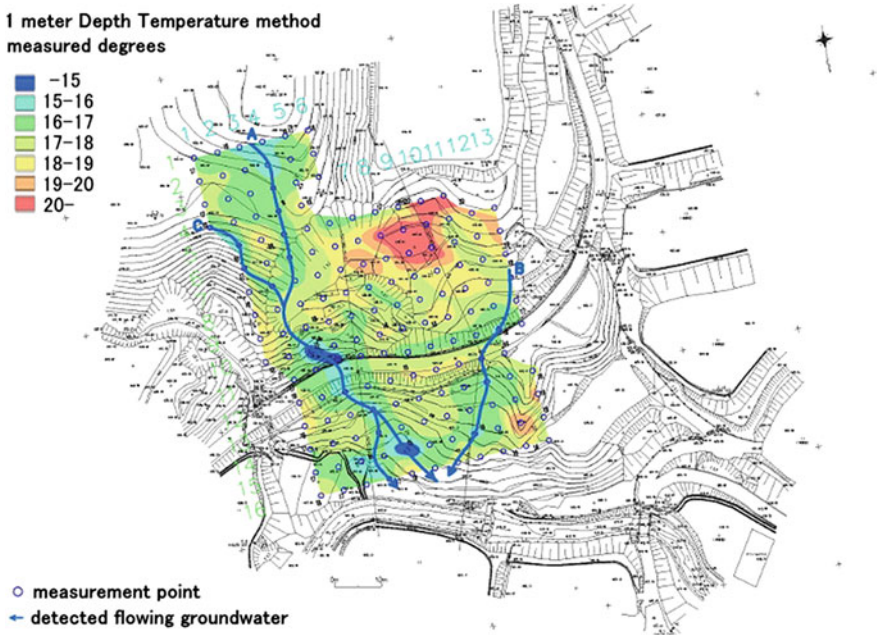

Fig. 6 Example of one-meter depth temperature method in summer

2.2 Multipoint Temperature Logging method

We can obtain the route of the flowing groundwater on ground surface plane by One-meter Depth Temperature method. It is also necessary to obtain information of depth of the flowing groundwater to solve various soil disasters. Flowing groundwater is exists in various depth with various water head, normally. Flowing

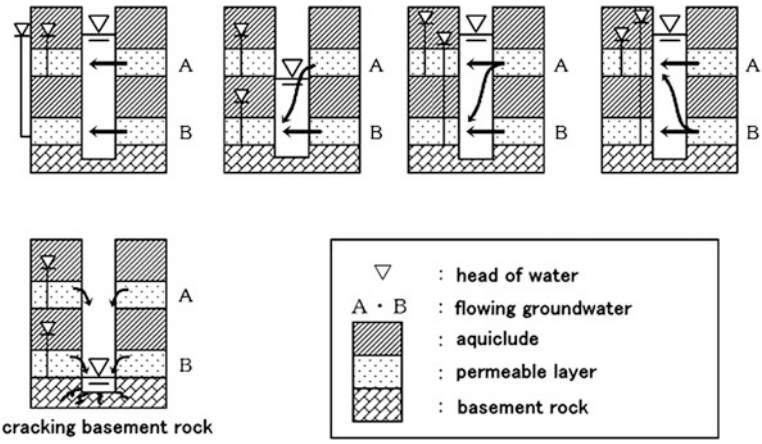

Fig. 7 Illustration of flowing groundwater type

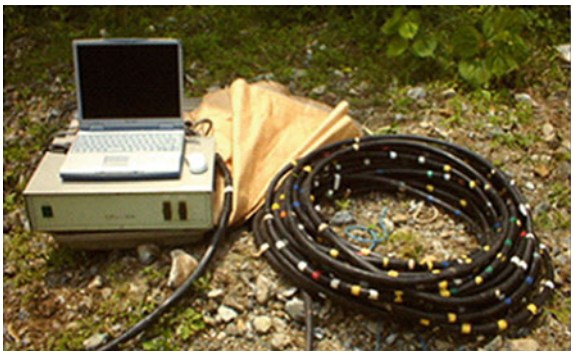

Fig. 8 Equipment of multipoint temperature logging

groundwater type is shown in Fig. 7. Therefore, Multipoint Temperature Logging method was developed. Multipoint Temperature Logging is one of the well logging methods for getting information of flowing groundwater condition by vertical temperature distribution in boring hole. At first, 60° hot water is poured in boring hole. Decreasing process of vertical temperature distribution of hot water in boring hole is measured during 30 min. In layer with flowing groundwater, decreasing ratio of hot water in boring hole is higher than the other by cooling effect of flowing groundwater. Accordingly, we can obtain the information of depth, number and thickness of flowing groundwater. Figure 8 shows equipment of Multipoint Temperature logging method. Example of measurement results by Multipoint temperature Logging method is shown in Fig. 9. In Fig. 9, left figure shows temperature distribution and right figure shows temperature restoration ratio distribution during temperature decreasing process in 30 min, respectively. Restoration ratio (R) is calculated by

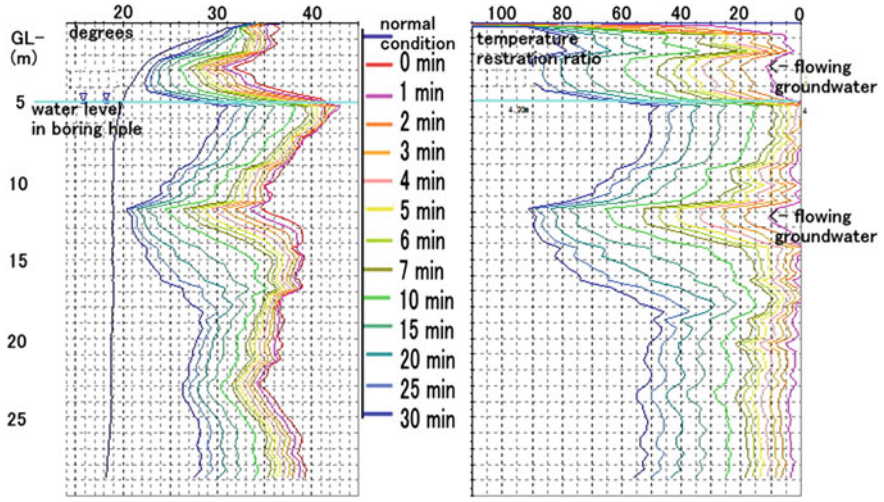

Fig. 9 Example of measurement result of multipoint temperature logging

$$R = \frac{\text{initial hot water temperature} - \text{temperature in anytime}}{\text{initial hot water temperature} - \text{natural temperature}} \quad (1)$$

There is water level in normal condition in GL-5 m. Above the normal water level, there is a remarkable part which shows high temperature restoration. It indicates that there is a flowing groundwater. In GL-12 m, there is another flowing groundwater, too. This result shows that 2 flowing groundwater is exist at this boring point.

3 Conclusions

Principle and the results of One-meter Depth Temperature method and Multipoint Temperature Logging method were described. Result of One-meter Depth Temperature showed the area which had high possibility of existence of flowing groundwater on the ground surface plane. Results of the Multipoint Temperature Logging method showed that there were two flowing groundwater. The width and vertical location of two flowing groundwater was also indicated. According to these results, effectiveness of One-meter Depth Temperature and Multipoint Temperature Logging were shown.

Reference

Takeuchi A (1980) Method of investigating groundwater-vein streams by measuring one-meter depth in landslide areas part 1. J Jpn Assoc Groundw Hydrol 22(2):11–39

Rheological Behaviour and Compressive Strength of Cement Bentonite Grout Slurry

Abdulhakim G. H. Al-Kholidi, Sun Youhong and Sun Zhifeng

Abstract Grouting is a special technique generally applied in civil and geotechnical engineering works all over the world. Sustainable development of the grouting sector can be achieved by careful mixing and application of correct quantities of cement and bentonite compounds. In order to improve the efficiency of grout slurries, laboratory experiments were carried out to study the rheological behaviour and compressive strengths of cement–bentonite admixtures due to different volumes of water used in preparing the slurries. Moreover, the choice of grout slurries depends on the geotechnical characteristics of the geomaterial like voids, open cavities, fractures, particle sizes and fissures. This has led to the development of grouts with low water content, as well as the need to avoid problems of durability encountered due to high content of water or cement which would be necessary to reach the best economic solution. Therefore, water–cement–bentonite admixtures with correct ratios of grout materials are preferred over others due to its low production cost and efficiency.

Keywords Rheological · Compressive strength · Dynamic viscosity · Fluidity · Bleeding · Temperature

A. G. H. Al-Kholidi · S. Youhong (✉)
College of Construction Engineering, Jilin University, Chang Chun, China
e-mail: syh@jlu.edu.cn

A. G. H. Al-Kholidi
e-mail: alkholidi70@yahoo.com

S. Zhifeng
Siping Northeast Geotechnical Engineering Company, Siping, China
e-mail: sunnyyy830@yahoo.com

F. Wang et al. (eds.), *Progress of Geo-Disaster Mitigation Technology in Asia*, Environmental Science and Engineering, DOI: 10.1007/978-3-642-29107-4_38,

1 Introduction

Grouting technology is applied in civil and engineering works to improve geomechanical properties of rock masses by injecting slurries of high compressive strength, stability and impermeability into open cavities, fissures and voids. Therefore the overall planning and management of grouting quality, quantities are very important to prevent loss of water through the foundation. Grouting can improve deformability of rock masses Kohkichi et al. (1997). Anagnostopoulos (2005) defined grouting as a civil engineering process which involves careful injection of grout slurries into voids, fissures and open cavities in soil and rock Formations or other engineering foundations. Although there are many kinds and related compounds of grout materials which can be used to fill open fissures, different results have been obtained as a result of different physical and chemical characteristics of the materials. The knowledge of the properties of grout materials and the ratio of water to the material is necessary in grouting technology. Grouting and rheological behaviour of grouting materials started in France and became popular in the twentieth century. Over the years, a lot of research work have been published in grouting technology and have been widely applied in bridge construction and tunnelling, and also in oil, gas and water wells. The measurement and control of rheological parameters of grout material are very important in grouting (Bangoyina 2008). Rheological characteristics of cement grouts are depend on the ratio of water to cement in the mix Viet Hung et al. (2011). However, many countries all over the world are using ordinary portland cement (OPC) in hydropower projects due to its high strength, durability and other physical properties that can easily be controlled, in addition to its use as a cementitious material Kasemchaisiri and Tangtemsirikul (2007). Therefore, cement–bentonite admixtures have been successfully applied in backfilling works as a result of its high strength properties. Hence, this paper concentrates on the characteristic behaviour of cement and bentonite when they are mixed with different known quantities of water. In order to reduce bleeding in grout mixes and carry out successful injection, it is necessary to use bentonite and silica fume Tan Ozcan et al. (2005). Chemical admixtures have been observed as one of the factors affecting the setting time of grout materials Shamarana et al. (2008). It has been observed that initial consistency of cement- and cement–bentonite-based grouts prior to injection influences the process after grouting Bangoyina (2008).

2 Theoretical Significance and Application Value

According to the principles and theory of grouting, there is a relationship between the degree of injectability, particle sizes and width of fissures. So, we will study the effect of the ratio of water to water–cement–bentonite mix; the rheological behaviour and compressive strength of cement–bentonite grout slurry in order to obtain the optimum proportions of high efficiency and performance. The parameters have been varied in the range of 0.4–5.

3 Academic Views

Although grouting technology is popular in the world, several problems related to rheological behaviour and compressive strengths of composite grouts are yet to be solved. One of these problems is the rheological behaviour of cement–bentonite materials when they are mixed with different known quantities of water. Many literatures have been published on grouting technology and rheological behaviour of grout slurries. Yang and Chang (2003) used percentage water content values of OPC which ranged between 50 % and 90 % to study the strength characteristics of the mixture at different cement–water ratios. Vintzileou and Fezans (2008) observed that grouting of vulnerable masonry at cement–water mix of 50:70 % was efficient. But the fluidity can be decreased. In addition to water content being very high, it can also cause excessive residual water permeability. So the shape of the fracture depends on the properties of the grout Kleinlugtenbelt et al. (2006), Although OPC is used to inject rock masses in which breadth of fissures is bigger than 0.2 mm Zhichu et al. (2003), large-sized cement particles can cause agglomeration of solids, which in turn obstructs and prevent complete grouting of the crack Mirza et al. (2002). Also thick grout suspension can be adopted for the injection of the upper zone of rock loosened by excavation basting Nonveiller (1989) Fluid mass and column mass evolution according to time Saiyouri et al. (2008). Hence grouting efficiency of a fan depends on the flow system. Compressive strength is an important performance measurement which is applied in the design technology of grouting; Lucie et al. (2003) measured the compressive strengths of grouts at 7 and 28 days. For all the different ratios studied, density measurements were also carried out in 24 h interval Rosquoe (2003). However, a gradual stiffening of the paste and change in rigidity was observed after 5 h of curing for all the activated blends Maria et al. (2003). Wei et al. (2010) through laboratory experiments observed that high temperatures affect bentonite materials in grout slurries which lead to less leaching.

4 Materials Proportions and Testing Procedures

4.1 Material Investigation

The laboratory materials used in the experiments were prepared using eleven different ratios of tap water, OPC and bentonite clay of chemical formula: [Al_2, Mg_3) Si_4O_{10} $OH_2{\cdot}nH_2O$].

The chemical properties of the cement used in the analysis are given in Table 1.

Initially, the slurries were formed by mixing water and bentonite. After thorough mixing, cement was added; the total production time from the initial time the materials were mixed to the time of pressing of the final slurry was 8 min; 7 min middle speed and 1 min was slowly. Table 2 shows the basic characteristics of the mixer.

Tables 3, 4 show the different quantities of water content from 5 to 0.4 kg, cement (1 kg) and bentonite 5 %, 0 % according to Eq. (4) indicated in subsection

Table 1 Chemical composition of cement

Component	$3CaO{\cdot}SiO_2$	$2CaO{\cdot}SiO_2$	$3CaO{\cdot}Al2O_3$	$4CaO{\cdot}AlFeO_3$
Portland cement %	40–55	20–30	2.5–15	10–19

Table 2 Mechanical properties of mixer

Mixing vane speed (clockwise)	Mixing tube capacity	Volume (l)	Mixing drums	Voltage power supply
80 ± 4 r/min	60 ± 2r/min	15	ϕ 380 × 250 mm	380–1500 W

Table 3 Composition of water, cement and bentonite for each batch at bentonite 5 %

Water (kg)	5	4	3	2	1	0.9	0.8	0.7	0.6	0.5	0.4
Cement (kg)	1	1	1	1	1	1	1	1	1	1	1
Bentonite (%)	5	5	5	5	5	5	5	5	5	5	5

Table 4 Composition of water, cement and bentonite for each batch at bentonite 0

Water (kg)	5	4	3	2	1	0.9	0.8	0.7	0.6	0.5	0.4
Cement (kg)	1	1	1	1	1	1	1	1	1	1	1
Bentonite (%)	0	0	0	0	0	0	0	0	0	0	0

(5.5) for each batch. Test procedures for determine rheological behaviour and compressive strength.

4.2 Distribution Analysis

Using the mixtures were prepared in 1–11 batches for $B = 5$ % and 1–11 with $B = 0$ mixed using mixer are shown in Tables 3, 4 the illustration for the experiment design shown in Fig. 1.

4.3 Research Contents

Therefore grouting by using water: cement: bentonite is applicable material for successfully backfilling.

And to provide higher levels of properties so we studied such as:

Water: Cement: bentonite (5 % and 0 %) has shown in Tables 3, 4.
Compressive strength at (7 and 28 days).

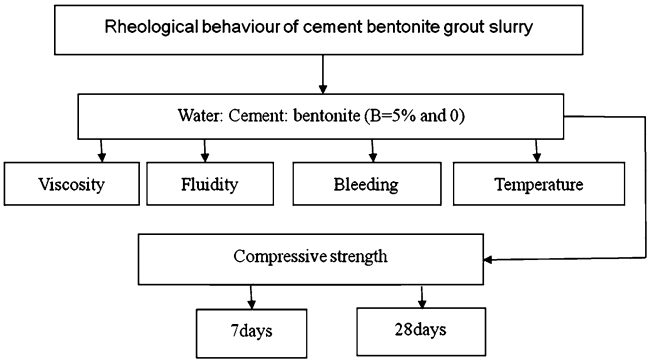

Fig. 1 Illustration for the experiment design process approach

Fig. 2 March flow cone for viscosity measurement

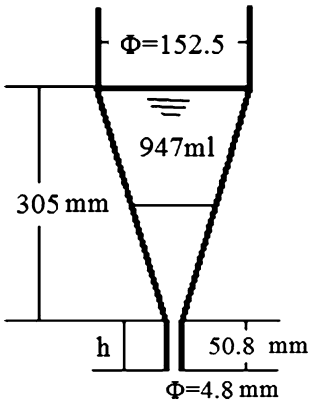

Rheological behaviour which consists:

- Viscosity
- Fluidity
- Bleeding
- Temperature

4.4 Composition of Grout Mixture

The mixing tap water had a temperature of 21 °C and the grout temperature following the end of mixing was (21–24.88 °C). After finishing of mixing and get fresh slurry for different ratios Table 3 were test as follow: temperature—bleeding—viscosity—fluidity—compressive strength (Figs. 2, 3).

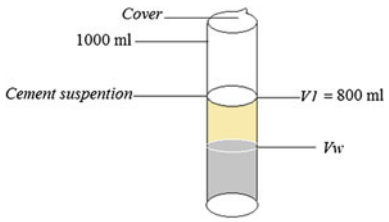

Fig. 3 Graduated cylinders

4.5 The Compressive Strength

Compressive strength of samples is significantly important in engineering geology. It is an important design parameter for tunnels, rock slopes and rock foundations; it is also used as input parameter in some rock mass classification systems Cevik (2011). On the other hand, the effects of pressures at different depths on the mechanical properties of rocks are commonly simulated in a laboratory by load frame which has been used to determine the compressive strength and is measured by using three cylinders with dimension: 15 × 15 × 30 cm (Fig. 4). In order to determine 7 and 28 days measure compression strength from each sample (Fig. 5) and different ratios as follow: (1:1, 0.9:1, 0.8:1, 0.7:1, 0.6:1, 0.5:1, 0.4:1) of slurry with in unit's Kilonewton per square meter (kN/m2), breaking cylindrical concrete specimens in a compression testing machine and it is calculated from the failure load divided by the cross sectional area resisting the loads as presented in Figs. 4, 5 and as illustrated in Eq. (1):

$$Compressive\ Strength = \left(\frac{Maixmum\ load}{Cross\ setion\ area}\right) \tag{1}$$

Whereas the wet specimens, were first immersed in water for 27, 28 days before testing.

4.6 Viscosity

Viscosity is defined as the resistance of a liquid to flow which is the opposite of fluidity. Test was carried out to characterize the effect of water and bentonite by using March flow cone as shown in Fig. 2. According to API standard which allows one quart (946 ml) of slurry to flow out of the funnel and are expressed as time in second. Therefore, viscosity is calculated upon the flow time value.

Hence the grouting efficiency of a fan depends on the flow system.

Fig. 4 Typical compression to failure using compression testing machine

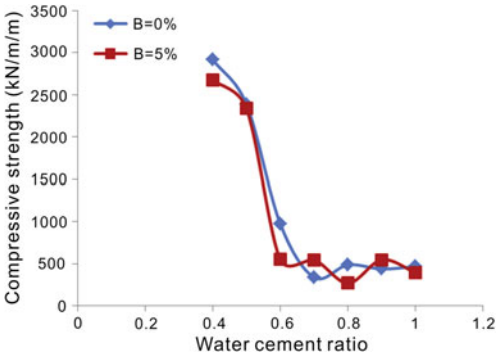

Fig. 5 Compressive strength test result $B = 0$ % and 5 % (7 days)

4.7 Fluidity (Q)

Fluidity is defined as the tendency of a liquid to flow easily; it is an important factor considered in grout mix designs. In addition to if the flow rate is considered constant during the test we can calculate the initial fluid filling level using Eq. (2) below:

$$Q = \frac{V}{T} \tag{2}$$

where:

Q: is the flow rate of suspension, V: is a volume of suspension that has flown out of the cone and

T: is flow time.

4.8 Bleeding

It was measured every: 15, 30, 45, 60, 90, 120, 150, 210, 240 mins by using graduated cylinders which height was 1000 ml with cover and was added suspensions until 800 ml (Fig. 3)

We can calculate the bleeding from the formula as presented in Eq. (3):

$$Bleeding\ \% = \frac{Vw}{V1} \tag{3}$$

where:

V_1: Volume of sample at beginning of test (800) ml

V_w: Volume of decanted bleed water by ml.

The bentonite ratio is presented in Eq. (4):

$$B = 5\ \%\ (Water + Cement) \tag{4}$$

4.9 The Temperature

Temperature is measured by using a thermometer through a glass tube sealed with mercury that expands or contracts as the temperature rises or falls.

5 Test Results and Discussion

Figure 4 shows the result obtained in the laboratory analysis with compression testing machine designed for conducting compression test on concrete specimens, rocks and others by applying external load on the rock model. Loading is accomplished by the upward movement with the help of a centering pin, the effect of loading speed on the plate ultimate strength of steel plates subjected to dynamic axial compressive load, the compressive strength test results on the samples tested at 7 and 28 days For $B = 5$ %, from the 7 days are between (270.40–2675.59) and (339.50–3344.50) kN/m2. From the 28 days as compare with (0.4:1, 0.5:1, 0.6:1, 0.7:1, 0.8:1, 0.9:1 and 1:1).Also the compressive strength at 0.8:1:0.05 was the least of values. There is a direct correlation between compressive strength and water content of the sample; compressive strength decreases with increase in water content. Figures 5, 6 are presented the compression strength for $B = 5$ % and 0 % of 7 and 28 days. The samples (0.4:1:0.05, 0.5:1:0.05, 0.6:1:0.05, 0.8:1:0.05, 1:1:0.05) with $B = 0$ % were higher strength than $B = 5$ % but samples as (0.7:1:0.05, 0. 9:1:0.05) were the least, we conclude that when we add bentonite 5 % to cement not be affected the increase compressive strength except ratios (0.7:1:0.05, 0.9:1:0.05).

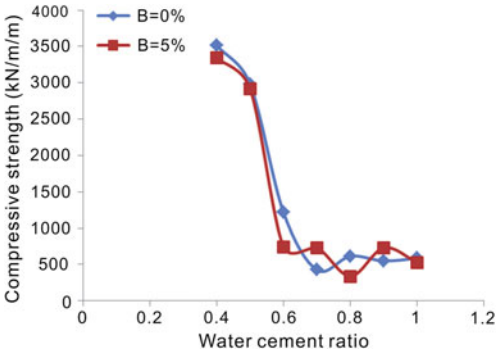

Fig. 6 Compressive strength test result $B = 0$ % and 5 % (28 days)

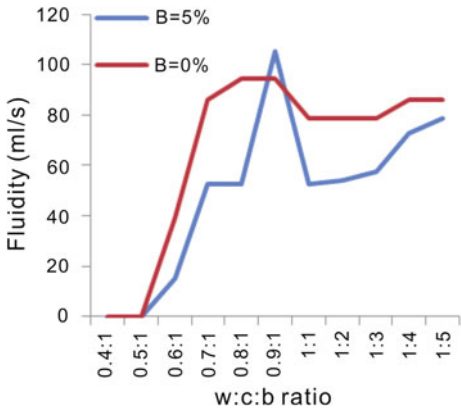

Fig. 7 Suspension fluidity at $B = 5$ %, $B = 0$ %

Figures 7, 8 present the suspension fluidity and viscosity for $B = 5$ % and $B = 0$. The results obtained show that the flow of the grout slurry was determined by a flow cone Fig. 2. However, slurry grouting W/C/B for different ratios was tested, the efflux time for these grouts between 9–63 s. In addition to these effect bentonite on flow of suspension except to 0.9:1:0.05. As expected, flow time and dynamic viscosity of slurry grouting increases with decrease water ratio to cement: bentonite (5 %) except to 0.9:1:0.05 as showing in Fig. 8. A W/C/B ratio of 0.8 1:0.05 viscosity and flow time are low whereas the viscosity is much higher for a 0.6:1:0.05 but for ratios 0.5:1:0.05 and 0.4:1:0.05 are doesn't flow see curves presented in Fig. 7. For understanding consideration of the unflow due to agglomeration of solid particles, in addition to the density remains increase as W/C/B decrease for 0.4:1:0.05 is much higher. As expected, flow time and dynamic viscosity of slurry grouting increases with decrease water ratio to cement: bentonite (5 %) except to 0.9:1:0.05. Low viscosity and low flow ability grouts are effect for injection into fissures. Voids, and joints but high viscosity grouts might be effect to limit flow of slurry to fill it. The test results showed there affect on flow time and plastic viscosity with using $B = 5$ % than $B = 0$ %.

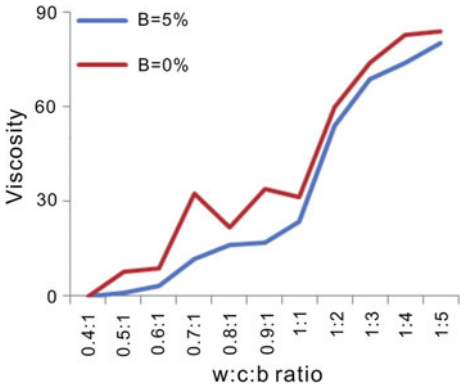

Fig. 8 Viscosity at $B = 5$ %, $B = 0$ % for 0.4:1–5:1

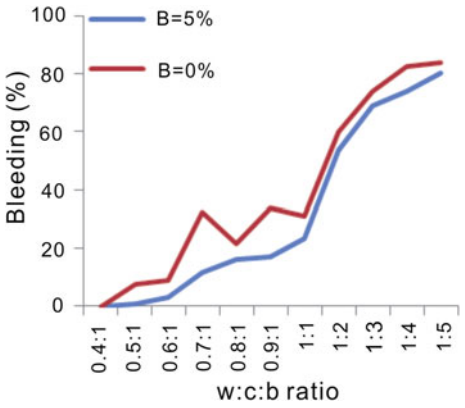

Fig. 9 The relation between water content % and water; cement: bentonite

Figure 9 shows the relation between water content and water: cement: bentonite. The results obtained show that there is an effect with use bentonite on Bleeding of water, with increasing bentonite on slurry the water content was decrease for all of the ratios except (0.9:1:0.05) this correlation is presented in Fig. 10. W/C/B ratios up to 1:1:0.05 have high water content as follow: (5:1:0.05, 4:1:0.05, 3:1:0.05, 2:1:0.05), but the mixing ratios less than 1:1:0.05 have low water. Also the process of bleeding for all these ratios studies have high bleeding during 1 h from 3 h but with about less than 6 % light bleeding within 2 h. Also ratio 2:1:0.05 was the high time period until the bleeding stop but no bleeding from various occurred in ratios 0.4:1:0.05 and 0.5:1:0.05 with using ($B = 5$ % and $B = 0$ %).

5.1 Temperature

The specific heat of water is constant but the heat of cement specific heat of OPC past increased with temperature to an extraordinary extent. However with the development of grouting technology the proportion of deep well is increasing,

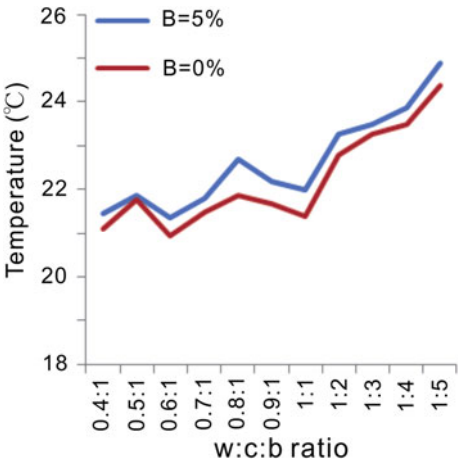

Fig. 10 The relation between water content % and water; cement: bentonite

hence big temperature difference from top and bottom, which effects of the injection slurry. Also When cement and bentonite were mixed with water the temperature rise occurs immediately and steady state temperature, then an appreciable and continues at diminishing rate for 20 min. The temperature was rise at $B = 5$ % than $B = 0$ % as illustrated in Fig. 10.

6 Conclusions

Cement grout usually consists of two basic materials: cement and water admixtures. Bentonite is sometimes added to improve the physical properties of the grout. The research team conducted several laboratory experiments in order to study the effects of ratio of water at B = 5 % and B = 0 on rheological behaviour and compressive strength of grouts when they are mixed with different volumes of water. This is done to obtain a good mixing ration of water, cement and bentonite which will be used in dam construction. The following conclusions were drawn from the study:

1. Test results show that there is a marked effect on dynamic viscosity, fluidity, bleeding and temperature as different volumes of water are mixed with cement and bentonite.
2. Water–cement–bentonite admixtures with different ratios show high bleeding and thickening time due to high water content, while slurries with low water content has higher quality but low viscosity which inadvertently affects its efficiency during injection.
3. We also observed that water–cement–bentonite admixture with ratios less than 0.6:1:0.05 caused the agglomeration of solid particles which also caused the bleeding time to be very high with time range of 1 and 3 h.

Acknowledgments The authors would like to thank the reviewers of this paper for their valuable suggestions and comments. We are also grateful to Messrs Li Qiang, Wang Tong, Aadil Yousif and other staff of the Jilin University, China, for their constructive comments and contributions.

References

Kohkichi K, Tetsuo I, Yoshitada M et al. (1997) In situ experimental studies on improvement of rock masses by grouting treatment. Rock Mech Miner Sci 34(3–4):138.e1–138.e14

Anagnostopoulos CA (2005) Laboratory study of an injected granular soil with polymer grouts. Tunn Undergr Space Technol 20(6):525–533

Bangoyina P (2008) Ageing and large-consolidation of cement based grouts. University of Twente, Netherlands, pp 71 (in english)

Viet Hung N, Remond S, Gallias JL (2011) Influence of cement grouts Composition on the rheological behaviour. Cem Concr Res 41(3):292–300

Kasemchaisiri R, Tangtemsirikul S (2007) Methods to determine water retain ability of porous fine aggregate. Constr Build Mater 21(6):1322–1334

Tan Ozcan, Zaimoglu Sahin, Hinislioglu Sinan, Altun Selim (2005) Taguchi approach for optimization of the bleeding on cement-based grouts. Tunn Undergr Space Technol 20(2):167–173

Shamarana M, Ozkan N, Keskin SB, Uzal IO, Yaman TK (2008) Evaluation of natural zeolite as a viscosity-modifying agent for cement-based grouts. Cem Concr Res 38(7):930–937

Yan MG, Chang ZH (2003)Theory and practice of Grouting drainage and anchorage of rock mass, Water pub Press, China, pp 62–76(in Chinese)

Vintzileou E, Fezans AM (2008) Mechanical properties of three-leaf stone masonry grouted with ternary or hydraulic lime-based grouts. Elsevier Sci Ltd 30(8):2265–2276

Kleinlugtenbelt R, Bezuijen A, Van Tol AF (2006) Model tests on compensation grouting. Tunn Undergr Space Technol 21(6):729–732

Zhichu HM, Mingxiang C, Xurong CA (2003) Develop technology for wet-ground fine cement slurry with its applications. Cement Concr Res China 33(5):729–732

Mirza J, Mirza MS, Roy et al (2002) Basic rheological and mechanical properties of high-volume fly ash grouts. Constr Build Mater 16(6):353–363

Nonveiller E (1989) Grouting theory and practice. Elsevier, Amsterdam

Saiyouri N, Bouasker M, Khelidj A (2008) Gas permeability measurement on injected soils with cement grout. Cem Concr Res 38(1):95–103

Lucie S, Mohammed S, Peter JM (2003) Influence of mix proportions on rheology of cement grouts containing limestone powder. Cement Concr Compos 25(7):737–749

Rosquoe T, Alexis A, Khelid A, Philpot A (2003) Experimental study of cement grout: rheological behavior and sedimentation. Cem Concr Res 33(5):713–722

Maria S, Konsta G, Surendra PS (2003) Hydration and properties of novel blended cements based on cement kiln dust and blast furnace slag. Cem Concr Res 33(8):1269–1276

Wei YL, Hsieh HF, Peng YS, Yang JC, Wang HP, Lina CY, Shih WL, Hsu C (2010) Thermal detoxification and bloating of chromium (VI) with bentonite. Nucl Instrum Methods Phys Res 619(1–3):108–111

Cevik A, Akcapinar Sezer Ebru, Cabalar AF, Gokceogluc C (2011) Modeling of the uniaxial compressive strength of some clay-bearing rocks using neural network 11(2):2587–2594

Editors Biography

Dr. Fawu Wang is an Associate Professor in the Department of Geoscience, Interdisciplinary Graduate School of Science and Engineering, Shimane University, Japan. His current research interest covers submarine landslides, landslide dams, and landslides triggered by earthquake, rainfall, and water level variation in reservoirs.

Dr. Masakatsu Miyajima is a Professor in the School of Environmental Design, Kanazawa University, Japan. For more than 30 years, he participated and led on many reconnaissance of surveys of damages caused by earthquake on infrastructures. His main research interest is in lifeline earthquake engineering.

F. Wang et al. (eds.), *Progress of Geo-Disaster Mitigation Technology in Asia*, Environmental Science and Engineering, DOI: 10.1007/978-3-642-29107-4,

Dr. Tonglu Li is a Professor in the School of Geological Engineering and Geomatics, Chang'an University, China. His research interest is on failure mechanism of loess landslides; he has also built geotechnical design models for the disaster mitigation. He has studied loess stratigraphy and loess properties as a basis for the landslide research.

Dr. Wei Shan is a Professor in Northeast Forestry University, China. He is a board member of the International Consortium on Landslides (ICL) and network coordinator for landslides in cold regions. His main research interest is in geo-environmental disasters in cold regions.

Dr. Teuku Faisal Fathani is an Associate Professor in the Department of Civil and Environmental Engineering of Gadjah Mada University, Indonesia. He has been actively involved in research on disaster risk mitigation of landslides, fast floods, earthquakes, and volcanic eruptions.